D 2022

U.PORTO
FEUP FACULDADE DE ENGENHARIA
UNIVERSIDADE DO PORTO

INNOVATIVE APPROACH FOR OLIVE MILL WASTEWATER RECLAMATION: INTEGRATED HETEROGENEOUS FENTON OXIDATION USING OLIVE MILL SOLID RESIDUES AND MEMBRANE FILTRATION PROCESSES

BRUNO MIGUEL MIRANDA ESTEVES

TESE DE DOUTORAMENTO APRESENTADA
À FACULDADE DE ENGENHARIA DA UNIVERSIDADE DO PORTO EM
ENGENHARIA DO AMBIENTE

Innovative approach for olive mill wastewater reclamation: integrated heterogeneous Fenton oxidation using olive mill solid residues and membrane filtration processes

International cotutelle thesis presented to the

University of Porto and **University of Granada**

for the degrees of

Doctor of Philosophy in Environmental Engineering (by the University of Porto) and

Doctor por la Universidad de Granada (by the University of Granada)

by

Bruno Miguel Miranda Esteves

PhD thesis co-supervision between the University of Porto and the University of Granada

Supervisor: Prof. Dr. Luis Miguel Palma Madeira, University of Porto

Supervisor: Prof. Dr. Francisco José Maldonado-Hódar, University of Granada

Department of Chemical Engineering, Faculty of Engineering, University of Porto

Department of Inorganic Chemistry, Faculty of Sciences, University of Granada

January 2022

“And so it goes...”

— Kurt Vonnegut

ABSTRACT

The management of effluents generated by the olive oil industry – olive mill wastewater (OMW) – poses a complex and persistent environmental challenge to this sector due to OMW intrinsic properties, including high organic load, acidic pH, and presence of toxic and hardly-biodegradable substances such as phenolic compounds. The main goal of this work was to study the oxidative treatment of OMW by the heterogeneous Fenton-like process (also known as catalytic wet peroxide oxidation, CWPO), repurposing solid by products of the same agro-industry as precursors for the preparation of Fe-supported carbon-based materials. Envisaging a circular economy model for the sector, the integration of a downstream direct contact membrane distillation (DCMD) unit was also evaluated to potentially recover water suitable to be reused in the same industry (e.g., for crops irrigation or machinery/facilities washing activities).

Preliminary Fenton/Fenton-like homogeneous phase experiments were performed with discontinuous and continuous reactors to evaluate the viability of the proposed catalytic process in organic matter degradation, phenolic content (TPh) removal, and toxicity reduction. A synthetic solution replicating the polyphenolic fraction occurrence in real OMW was first used. Several operational variables were parametrically evaluated, including pH, H_2O_2 and Fe^{2+} dosages and temperature (in the batch reactor), as well as space-time values (for the operation of the continuous stirred-tank reactor – CSTR). Under the best operational conditions defined in the parametric study, >98% TPh removal and chemical (COD) and biochemical oxygen demand (BOD_5) oxidation efficiencies of 75% and 70%, respectively, were achieved at steady-state in the CSTR. Based on the previous findings, the treatment of real OMW was evaluated by both Fenton (Fe^{2+}/H_2O_2) and Fenton-like (Fe^{3+}/H_2O_2) systems, and additional operational parameters were tested, namely the effect of pH readjustments during the process, reagents addition method, and Fe/H_2O_2 mass ratio. A correlation between TPh removal and OMW toxicity reduction in the treated samples (assessed by the *Vibrio fischeri* inhibition) was established. Moreover, it was found that the ferric chloride salt used acted as a coagulant/flocculant agent after the oxidative step, further improving the process efficiency. The global reductions achieved after optimization of the process were similar to those reported for the synthetic solution, albeit the considerably higher load of the real OMW.

In order to solve the problems associated to the use of homogenous processes, both heterogeneous catalysts and processes for adsorption and catalysis of OMW were developed

and tested. Experiments in the heterogeneous phase were then conducted using several carbon-based materials (used as adsorbents and/or catalysts) synthesized from different supports (chars and activated carbons, AC) prepared from olive stones (OS) and olive tree pruning (OTP). The synthesis process was tuned by changing the materials' activation conditions (physical, with CO_2, or chemical, with KOH). These materials were used as adsorbents or iron-supports (catalysts), by adjusting the Fe impregnation procedure, and also different properties regarding the active metallic phase (iron salt precursor and loading). All materials were extensively characterized by numerous complementary techniques, and their properties correlated to the adsorptive/oxidative behavior towards specific contaminants (namely phenolic acids) and wastewater's lumped parameters of quality assessment (e.g., TOC, COD). Preliminary studies showed that the adsorptive capacity of the prepared ACs towards phenolic compounds of OMW was mainly controlled by the larger micropores and by the surface area of the materials. The oxidative activity and stability of the catalysts were first evaluated in batch reactors, using a synthetic polyphenolic formulation. Due to the developed porosity and morphology, and better distribution of surface metallic nanoparticles, Fe/AC catalysts performed better than analogous Fe/biochars, while the OS derived AC catalyst (OSAC-Fe) was catalytically more active (higher H_2O_2 conversion efficiency and TOC, TPh, and toxicity reductions) and stable (less Fe-leaching) than OTPAC-Fe. Catalysts supported onto commercial-AC materials (used for comparison) led to globally higher efficiencies but presented less stability, which is a key factor for industrial implementation.

Three impregnation routes were evaluated in the most promising material (OSAC-Fe) – incipient wetness impregnation (IWI), wet impregnation (Ads), and hydrothermal precipitation (HT) – resulting in catalysts with distinct Fe-loadings, particle sizes, and surface dispersion. All catalysts were able to remove *ca*. 80% TPh and 50% TOC, but based on the stability (evaluated in consecutive reaction cycles), kinetic rate constants and removal rates, OSAC-Fe-IWI was selected as the most promising of the three catalysts and used in further experiments. Additionally, the Fe-precursor (iron nitrate, ferrous chloride) and resulting Fe-loading (1–5 wt.%) were varied. The most promising sample was found to be the one prepared with $Fe(NO_3)_3$ salt and 5 wt.% load, which was selected for the depuration of different samples of OMW (with varying initial load) under continuous operation mode in a fixed-bed reactor (FBR). At a fixed feed $[H_2O_2]/[COD]$ of 2.3 ±0.1 g H_2O_2/g O_2, no pH adjustments, W_{cat}/Q = 1.33 g min/mL and 60 °C, TPh removals of 57–71% and COD reductions of 26–34% were attained at steady-state,

depending on OMW initial load. The resulting effluents also showed an overall reduction of eco-toxicity and improvement of biodegradability indices. Fixing the same operating conditions and increasing the contact time (W_{cat}/Q) by 2-fold, TPh and COD removals were increased to 79–81% and 37–45%, respectively, also maintaining high H_2O_2 conversions during the entire operation time.

The resulting treated samples of OMW allowed the membrane distillation unit operation at higher fluxes than those registered for analogous untreated samples, and the integrated process also showed higher rejections of organic matter from the feed solution. Under defined operational conditions (Q = 100 mL/min, $T_{permeate} \approx 18$ °C, $T_{feed} \approx 66$ °C), the produced permeate water stream presented several parameters below the legislated thresholds required for irrigation purposes, including total suspended and dissolved solids – TSS (<10 mg/L) and TDS (<89 mg/L), respectively – as well as TPh (<0.01 mg GA_{eq}/L), BOD_5 (<40 mg/L), and dissolved Fe (<0.06 mg/L). Moreover, the resulting concentrated OMW retentate stream was successfully recirculated to the FBR, maintaining the same removal efficiencies previously attained.

RESUMO

A gestão das águas residuais geradas pela indústria de extração de azeite – águas ruças (*olive mill wastewater*, OMW) – constitui uma problemática ambiental que persiste neste setor dadas as características intrínsecas deste tipo de efluentes, como a elevada carga orgânica, o pH ácido e o alto teor em substâncias tóxicas e dificilmente biodegradáveis, nomeadamente compostos fenólicos. O objetivo principal deste trabalho foi o estudo do tratamento de OMW pelo processo oxidativo tipo-Fenton (em sistema heterogéneo), reaproveitando para tal os subprodutos sólidos deste setor como precursores para a preparação de materiais de carbono como suporte da fase ativa de ferro. Com vista à adoção de um modelo de economia circular para este setor, foi ainda avaliada a integração de uma unidade de destilação por membrana após o processo catalítico de modo a recuperar água com características potencialmente adequadas para a sua reutilização na mesma indústria (por exemplo, para irrigação de cultivos ou atividades relacionadas com a lavagem de máquinas/lagar).

Foram realizados ensaios preliminares pelos processos Fenton/tipo-Fenton em fase homogénea, em reatores a operar em modo descontínuo e contínuo, para avaliar a viabilidade deste tipo de processo oxidativo na degradação de matéria orgânica, eliminação do conteúdo fenólico (TPh) e redução da toxicidade da OMW. Foi inicialmente usada uma solução sintética (com diferentes compostos fenólicos) que simula a ocorrência da fração polifenólica num efluente real, e avaliou-se o efeito de diversas variáveis operatórias, incluindo o pH da solução, a concentração de H_2O_2 e de Fe^{2+}, a temperatura de reação, assim como o tempo de residência (no caso do reator contínuo perfeitamente agitado). Para as melhores condições operatórias definidas no estudo paramétrico, obtiveram-se remoções superiores a 98% para TPh, bem como de 75% e 70% para a carência química (CQO) e a bioquímica de oxigénio (CBO_5), respetivamente, em regime de estado-estacionário do reator contínuo. Com base nestes resultados, estudou-se também o tratamento de um efluente real pelos processos Fenton (Fe^{2+}/H_2O_2) e tipo-Fenton (Fe^{3+}/H_2O_2), tendo sido avaliados outros parâmetros operatórios, como o efeito dos ajustes do pH da solução ao longo do tempo, o método de adição de reagentes, e a razão mássica Fe/H_2O_2. A partir deste estudo foi possível estabelecer uma correlação entre as remoções de TPh e a redução da toxicidade do efluente produzido (avaliada pela inibição da bactéria *Vibrio fischeri*). Além disso, verificou-se que o sal de cloreto de ferro(III) também atua como agente coagulante/floculante após a oxidação, promovendo assim as eficiências de remoção do

processo global. As remoções globais dos parâmetros indicadores da qualidade do efluente (nomeadamente CQO e TPh) após otimização do processo foram semelhantes às alcançadas com a solução sintética, apesar da carga orgânica consideravelmente superior do efluente real.

Para solucionar os problemas associados ao processo Fenton em fase homogénea, foram desenvolvidos catalisadores e testados sistemas heterogéneos para adsorção e catálise de OMW. Para tal, procedeu-se inicialmente à preparação de vários materiais de carbono, tanto carbonizados (*biochar*) como carvões ativados (*activated carbon*, AC) a partir de caroços de azeitona (*olive stone*, OS) e restos de poda das oliveiras (*olive tree pruning*, OTP). O método de síntese dos materiais de carbono foi ajustado através da modificação das condições de ativação dos precursores orgânicos (ativação física com CO_2, ou química com KOH). Estes materiais foram usados como adsorventes ou suportes de ferro (catalisadores), otimizando-se também os processos de impregnação e a fase metálica ativa (precursor usado e teor de Fe do catalisador). A caracterização morfológica e química dos materiais foi realizada por vários métodos e técnicas complementares, e as suas propriedades correlacionadas com a atividade adsortiva/oxidativa para contaminantes específicos (nomeadamente compostos fenólicos), bem como para os restantes parâmetros globais de caracterização de águas residuais (p.ex. CQO, carbono orgânico total – COT). Os resultados experimentais mostraram que a adsorção dos compostos fenólicos nos ACs é principalmente controlada pelos microporos de maior dimensão e também pela área superficial dos materiais. A capacidade oxidativa e estabilidade dos catalisadores foram inicialmente avaliadas em testes realizados num reator fechado (*batch*) com uma solução sintética polifenólica. Dado o maior desenvolvimento de porosidade e morfologia, bem como a melhor distribuição das nanopartículas metálicas na sua superfície, os catalisadores de ferro desenvolvidos a partir de ACs obtiveram melhores resultados do que os análogos preparados em *biochars*. Além disso, o catalisador obtido a partir de caroços de azeitona (OSAC-Fe) mostrou ser cataliticamente mais ativo (i.e., apresentou maior eficiência de conversão de H_2O_2 e redução de COT, TPh e toxicidade) e mais estável (menos lixiviação de Fe) do que o preparado a partir de restos de poda de oliveira (OTPAC-Fe). Usando catalisadores suportados em ACs comerciais (selecionados para referência de comparação) foi possível aumentar a eficiência de remoção de contaminantes, mas de uma forma geral estes apresentam menor estabilidade, um fator determinante para aplicação à escala industrial.

Com base nos resultados catalíticos obtidos com o material mais promissor (OSAC-Fe), foram posteriormente testados três métodos de impregnação da fase ativa (Fe) – impregnação seca

(IWI), por via húmida (Ads) e por precipitação hidrotermal (HT). Obtiveram-se catalisadores com alguma heterogeneidade no teor de ferro, tamanho de partículas e dispersão superficial. Todos os materiais foram capazes de remover cerca de 80% de TPh e 50% de COT, mas com base nos resultados de estabilidade (avaliada em ciclos consecutivos de reação), no cálculo das constantes cinéticas de reação e taxas de remoção, o catalisador OSAC-Fe-IWI foi selecionado como sendo mais promissor dos três para os ensaios seguintes. De seguida, fez-se variar o percursor de ferro (nitrato de ferro, cloreto de ferro(II)) e a sua concentração (1–5% em peso) no catalisador. O material selecionado, i.e. o mais promissor (preparado com $Fe(NO_3)_3$ e teor de 5% em peso), foi então utilizado para o tratamento de amostras de OMW (com carga orgânica inicial variável) num reator de leito fixo a operar em modo contínuo. Fixando a razão mássica inicial de $[H_2O_2]/[CQO]$ em 2,3 ±0,1 g H_2O_2/g O_2, sem ajustes de pH, e com o sistema a operar a 60 °C e W_{cat}/Q = 1,33 g min/mL, foram alcançadas remoções de TPh e CQO na ordem dos 57–71% e 26–34%, respetivamente, em estado estacionário. Os efluentes tratados também apresentaram uma redução apreciável da ecotoxicidade e uma melhoria global dos índices de biodegradabilidade. Fixando as mesmas condições operatórias e duplicando o tempo de contato (W_{cat}/Q), as remoções de TPh e CQO aumentaram para 79–81% e 37–45%, respetivamente, mantendo também as conversões de H_2O_2 elevadas durante o processo.

As amostras de OMW tratadas permitiram a operação da unidade de destilação por membrana a fluxos superiores aos registados com amostras de efluente não tratado, sendo que o processo integrado também apresentou maiores rejeições de matéria orgânica da solução de alimentação. Nas condições operacionais definidas (Q = 100 mL/min, $T_{permeado} \approx 18$ °C, $T_{alimentação} \approx 66$ °C), o caudal de água produzida no lado do permeado apresentou vários parâmetros abaixo dos valores limite de emissão (VLE) para descarga de águas de rega, incluindo os sólidos suspensos e dissolvidos totais – SST (<10 mg/L) e SDT (<89 mg/L), respetivamente – bem como TPh (<0,01 mg GA_{eq}/L), CBO_5 (<40 mg/L) e Fe dissolvido (<0,06 mg/L). Além disso, o efluente concentrado acumulado no lado do retido foi encaminhado de novo para o reator de leito fixo, mantendo-se as mesmas eficiências de remoção por oxidação alcançadas anteriormente.

RESUMEN

El tratamiento de las aguas residuales generadas por la industria oleícola durante la extracción del aceite de oliva (OMW, por sus siglas en inglés) resulta en un reto complejo para el sector, ya que su vertido produce importantes problemas ambientales debido a su intrínseca alta carga orgánica, pH ácido y altos contenidos en fenoles, que inducen una alta actividad fitotóxica y antibacteriana. El principal objetivo de este trabajo ha sido el desarrollo de tratamientos oxidativos del OMW mediante procesos tipo Fenton heterogéneos (oxidación catalítica con peróxido de hidrógeno, CWPO), reutilizando otros residuos sólidos de la producción de aceite (huesos de aceituna, restos de poda) como materiales de partida en la preparación de los catalizadores usados, catalizadores de Fe soportados en materiales de carbón. Siguiendo este modelo de economía circular, también se evaluó la integración de una unidad de destilación por membrana de contacto directo (DCMD) aguas abajo para recuperar potencialmente agua apta para ser reutilizada para riego de cultivos o actividades de lavado de maquinaria.

Se realizaron experimentos preliminares tipo en fase homogénea con reactores discontinuos y continuos para evaluar la viabilidad del proceso catalítico propuesto en la degradación de la materia orgánica presente en el OMW, la eliminación del contenido fenólico (TPh) y la reducción de la toxicidad. Inicialmente se usó una disolución sintética que simula la fracción polifenólica en el OMW real y se evaluaron varias variables operacionales, incluyendo pH, dosis de H_2O_2 y Fe^{2+}, temperatura (reactor discontinuo), así como los parámetros espaciales en la operación del reactor continuo de tanque agitado. En las mejores condiciones de trabajo se logró una reducción del TPh >98%, así como de la demanda química de oxígeno (DQO, 75%) y 70% y bioquímica (DBO_5, 70%) en estado estacionario del reactor continuo. Sobre esta base se evaluó el tratamiento de una muestra real de OMW con sistemas Fenton (Fe^{2+}/H_2O_2) y tipo Fenton (Fe^{3+}/H_2O_2), y se probaron parámetros de operación adicionales, a saber, el efecto de los reajustes de pH durante el proceso, el método de adición de reactivos y la relación másica Fe/H_2O_2. Se estableció la correlación entre la eliminación de TPh y la reducción de la toxicidad del OMW (inhibición de *Vibrio fischeri*). Además, la sal de cloruro férrico utilizada actuó como agente coagulante/floculante después del proceso oxidativo, mejorando aún más la eficiencia del proceso. Las reducciones globales logradas después de la optimización del proceso fueron similares a las reportadas para la solución sintética, a pesar de la carga considerablemente mayor presente en la muestra de OMW real.

Para evitar los problemas asociados al uso de la fase homogénea se desarrollaron catalizadores y procesos heterogéneos. Se realizaron experimentos de adsorción y catálisis. Inicialmente se preparan diversos materiales de carbón, tanto carbonizados (*biochars*) como carbones activados (AC) preparados a partir de hueso de aceituna (*olive stone*, OS) y restos de poda del olivo (*olive tree pruning*, OTP). El proceso de síntesis se ajustó cambiando las condiciones de activación de los precursores (activación física con CO_2, o química con KOH). Estos materiales se usaron como adsorbentes o soportes de catalizadores de Fe, optimizando también los procedimientos de impregnación y la fase metálica activa (sal de Fe y carga). Todos los materiales se caracterizaron ampliamente mediante técnicas complementarias y sus propiedades se correlacionaron con el comportamiento en procesos de adsorción/oxidación de los contaminantes (ácidos fenólicos) presentes en el OMW, junto con los parámetros típicos de las aguas residuales (p. ej., COT, DQO).

Los resultados mostraron que la capacidad de adsorción de los compuestos fenólicos en ACs está controlada principalmente por los microporos más grandes y el área superficial de los materiales. La actividad oxidativa y la estabilidad de los catalizadores se evaluaron primero en reactores discontinuos, utilizando una formulación polifenólica sintética. Debido a la mayor porosidad, morfología y mejor dispersión de las fases activas, los catalizadores Fe/ACs funcionaron mejor que sus análogos Fe/*biochars*. Igualmente, el catalizador derivado del ACs obtenido a partir de hueso (OSAC-Fe) fue catalíticamente más activo (mayor eficiencia de conversión de H_2O_2 y reducciones de COT, TPh y toxicidad) y estable (menos lixiviación de Fe) que el OTPAC-Fe, soportado sobre el ACs obtenido de restos de poda. Los catalizadores soportados en materiales comerciales de CA (utilizados para comparación) conducen en general, a eficiencias más altas, pero presentan menos estabilidad.

Se evaluaron tres rutas de impregnación del soporte más prometedor (OSAC): impregnación incipiente (IWI), adsorción (Ads) y precipitación hidrotermal (HT). Además, se variaron el precursor de Fe (nitrato, cloruro) y la carga de Fe (1–5% en peso) resultante de los catalizadores. De esta forma, se obtuvo una batería de catalizadores con distintas cargas de Fe, tamaños de partículas y dispersión superficial. Todos los catalizadores fueron capaces de eliminar alrededor del 80% TPh y 50% COT, pero en base a la estabilidad en ciclos consecutivos, las constantes cinéticas y las tasas de eliminación (calculadas para descartar el efecto de las diferentes cargas de Fe entre las muestras), se seleccionó la muestra OSAC-Fe-IWI preparada con $Fe(NO_3)_3$ y una carga del 5% en peso, como la más prometedora.

El catalizador seleccionado se utilizó para la depuración de diferentes muestras de OMW (con carga inicial variable) en modo de operación continua en un reactor de lecho fijo (FBR). Con una alimentación fija $[H_2O_2]/[DQO]$ de 2,3 ±0,1 g H_2O_2/g O_2, sin ajustes de pH, W_{cat}/Q = 1,33 g min/mL y 60 °C, se logró reducir el contenido fenólico TPh entre el 57–71% y una reducción del DQO entre 26–34% a temperatura constante y en estado estacionario. Los efluentes resultantes también mostraron una reducción general de la ecotoxicidad y una mejora de los índices de biodegradabilidad. Fijando las mismas condiciones de operación y aumentando el tiempo de contacto (W_{cat}/Q) al doble, las remociones de TPh y DQO incrementaron hasta el 79–81% y 37-45%, respectivamente.

Las muestras de OMW tratadas con CWPO permitieron el uso de las membranas DCMD a flujos más altos que los registrados para muestras análogas sin tratar, y el proceso integrado también mostró rechazos más altos de materia orgánica de la solución de alimentación. En las condiciones operativas definidas (Q = 100 mL/min, $T_{permeado} \approx 18$ °C, $T_{alimentación} \approx 66$ °C), la corriente de agua de permeado presentó valores en varios parámetros por debajo de los umbrales legislados requeridos para fines de riego, incluidos los sólidos suspendidos y disueltos totales – SST (<10 mg/L) y SDT (<89 mg/L), respectivamente, así como TPh (<0,01 mg GA_{eq}/L), DBO_5 (<40 mg/L) y Fe disuelto (<0.06 mg/L). Además, la corriente concentrada resultante del retenido, se recirculó con éxito al FBR, manteniendo las mismas eficiencias de eliminación alcanzadas anteriormente.

ACKNOWLEDGMENTS

First and foremost I would like to acknowledge and express my gratitude to both my supervisors, Prof. Dr. Luis Madeira and Prof. Dr. Francisco Maldonado-Hódar, for all the tutoring, guidance, immeasurable help, and patience throughout the last four years. It was a great pleasure to work with you both, and I sincerely hope we may find ourselves again in future endeavors. I would also like to acknowledge Prof. Dr. Ádrian Silva for the help provided in the final stretch of this PhD thesis.

I would also like to thank Carmen Rodrigues for the support and friendship during this journey that began in 2014 in the E 203A laboratory, and more recently to Sergio Morales Torres for the friendliness by which I was welcomed in the laboratories of the Faculty of Sciences of the UGR. This work has been immensely facilitated by both of your help and guidance.

To the great companion and friendship developed during the last four years within the two research groups I was part off, a big “thank you” to: Emanuel Sampaio, Joana Martins, Catarina Faria, Cláudio Rocha, Salomé Macedo, Miguel Soria, Pedro Cerqueira, Cristina Caeiro, João Brito, Rita Fernandes and Sofia Alves from the E -146 laboratory at FEUP – as well as past members – Joel Silva and Vanessa Lima. To Jésica Castelo Quibén, Stefanía Betancur Márquez, Jimena Castro, Safa Benjedim, Luisa Pastrana Martínez, Álvaro Molina Perez and Diana Vilella at the UGR, and also Aléx González, my heartfelt thank you for the warm welcoming at Granada.

To Liliana Pereira, José Luis Moreira and Fátima Ferreira from the DEQ to all the assistance.

To my mother, brother, and grandparents.

To my family, Patrícia and Mariana.

This thesis was financially supported by: LA/P/0045/2020 (ALiCE) and UIDB/00511/2020 - UIDP/00511/2020 (LEPABE) funded by national funds through FCT/MCTES (PIDDAC); Project NORTE-01-0247-FEDER-39789 funded by European Regional Development Funds (ERDF) through North Portugal Regional Operational Programme (NORTE 2020); Project NORTE-01-0145-FEDER-000069, supported by NORTE 2020, under the PORTUGAL 2020 Partnership Agreement, through the ERDF; and Spanish Project ref. RTI2018-099224-B-I00 from ERDF/Ministry of Science, Innovation and Universities - State Research Agency (MCIN/AEI/10.13039/501100011033/FEDER). I'm also grateful to FCT for the financial support through the PhD grant (SFRH/BD/129235/2017), with financing from National and the European Social Funds through the Human Capital Operational Programme (POCH).

LIST OF CONTENTS

ABSTRACT I

RESUMO V

RESUMEN IX

ACKNOWLEDGMENTS XIII

LIST OF CONTENTS XV

LIST OF FIGURES XXI

LIST OF TABLES XXIX

LIST OF ACRONYMS AND ABBREVIATIONS XXXI

LIST OF VARIABLES XXXIII

PART I. INTRODUCTION 1

1. GENERAL INTRODUCTION 3

1.1. RELEVANCE AND MOTIVATION 4

1.2. OBJECTIVES 5

1.3. THESIS OUTLINE 6

REFERENCES 9

2. STATE-OF-THE-ART 13

2.1. OLIVE OIL INDUSTRY 14

2.1.1. Brief characterization of the sector 14

2.1.2. Olive mill wastewater: characteristics and environmental issues 19

2.1.3. Management practices and EU environmental policy 22

2.1.4. OMW treatment/valorization technologies 24

2.2. ADVANCED OXIDATION PROCESSES 27

2.2.1. Fenton process 28

2.2.1.1. Free radical mechanism 28

2.2.1.2. Key operational parameters 29

2.2.1.3. OMW treatment by Fenton processes 31

2.2.2. Catalytic wet peroxide oxidation 36

2.2.2.1. Heterogeneous catalysts for CWPO 37

2.2.2.2. Activated carbon as support for catalysts synthesis 40

2.2.2.3. OMW treatment by CWPO 45

2.3. MEMBRANE TECHNOLOGY 51

2.3.1. Membrane distillation 53

2.3.2. Application of MD for OMW treatment/valorization 56

2.4. SUMMARY 61

REFERENCES 62

PART II. ANALYTICAL METHODS 75

3. ANALYTICAL METHODS AND CHARACTERIZATION TECHNIQUES 77

3.1. METHODS FOR WASTEWATER ANALYSIS 78

3.2. MATERIALS CHARACTERIZATION TECHNIQUES 79

3.2.1. TGA 79

3.2.2. N_2 and CO_2 adsorption 80

3.2.3. SEM 81

3.2.4. XRD 81

3.2.5. TEM 81

3.2.6. XPS 82

3.2.7. FTIR 82

3.2.8. pH_{pzc} 82

REFERENCES 83

PART III. TREATMENT OF OMW BY HOMOGENEOUS PROCESSES 85

4. SYNTHETIC OLIVE MILL WASTEWATER TREATMENT BY FENTON'S PROCESS IN BATCH AND CONTINUOUS REACTORS OPERATION 87

ABSTRACT 88

4.1. INTRODUCTION 89

4.2. MATERIALS AND METHODS 89

4.2.1. Synthetic wastewater preparation 89

4.2.2. Experimental procedure 90

4.3. RESULTS AND DISCUSSION 92

4.3.1. Batch catalytic tests 92

4.3.2. Selection of iron salt 92

4.3.2.1. Influence of H_2O_2 and Fe^{2+} doses 93

4.3.2.2. Influence of pH 98

4.3.2.3. Effect of the reaction temperature 100

4.3.3. CSTR catalytic tests 102

4.3.4. Overall performance of the batch and CSTR reactors: biodegradability and toxicity evaluation 105

4.4. CONCLUSIONS 107

REFERENCES 109

5. TREATMENT OF HIGH-STRENGTH OMW BY COMBINED FENTON-LIKE OXIDATION AND COAGULATION/FLOCCULATION 113

ABSTRACT 114

5.1. INTRODUCTION 115

5.2. MATERIALS AND METHODS 116

5.2.1. Olive mill wastewater 116

5.2.2. Experimental procedure *117*
5.3. RESULTS AND DISCUSSION 119
5.3.1. Iron salt selection and pH control *119*
5.3.2. Reagents addition strategy *122*
5.3.3. Fe^{3+}/H_2O_2 ratio *126*
5.3.4. Photo-Fenton-like oxidation *129*
5.3.5. Toxicity and quality of the treated effluent *130*
5.4. CONCLUSIONS 134
REFERENCES 136
PART IV. TREATMENT OF OMW BY HETEROGENEOUS PROCESSES 139
6. SPECIFIC ADSORBENTS FOR THE TREATMENT OF OMW PHENOLIC COMPOUNDS BY ACTIVATION OF BIO-RESIDUES FROM THE OLIVE OIL INDUSTRY 141
ABSTRACT 142
6.1. INTRODUCTION 143
6.2. MATERIALS AND METHODS 144
6.2.1. Synthesis of materials *144*
6.2.2. Adsorbates and adsorption runs *144*
6.2.3. Regeneration studies *147*
6.3. RESULTS AND DISCUSSION 147
6.3.1. Textural and chemical characterization of the adsorbents *147*
6.3.2. Adsorptive performance of the ACs in the treatment of simulated OMW *151*
6.3.3. Performance of ACs in the adsorption of single phenolic compounds *158*
6.3.4. Regeneration of adsorbents *169*
6.4. CONCLUSIONS 172
REFERENCES 174
7. FITTING BIOCHARS AND ACTIVATED CARBONS FROM RESIDUES OF THE OLIVE OIL INDUSTRY AS SUPPORTS OF FE-CATALYSTS FOR THE FENTON-LIKE OXIDATION OF SIMULATED OMW 179
ABSTRACT 180
7.1. INTRODUCTION 181
7.2. MATERIALS AND METHODS 181
7.2.1. Catalysts synthesis *181*
7.2.2. Synthetic wastewater and experimental procedure *183*
7.3. RESULTS AND DISCUSSION 184
7.3.1. Textural and chemical characterization *184*
7.3.2. Treatment of simulated OMW *196*
7.3.3. Further considerations *203*
7.4. CONCLUSIONS 205

REFERENCES 207

8. INTEGRATION OF OLIVE STONES IN THE PRODUCTION OF FE/AC-CATALYSTS FOR THE CWPO TREATMENT OF SYNTHETIC AND REAL OLIVE MILL WASTEWATER 211

ABSTRACT 212

8.1. INTRODUCTION 213

8.2. MATERIALS AND METHODS 213

8.2.1. Catalysts synthesis 213

8.2.2. Wastewater and experimental procedure 214

8.3. RESULTS AND DISCUSSION 216

8.3.1. Catalysts characterization 216

8.3.2. CWPO of synthetic OMW 223

8.3.2.1. Adsorption experiments 223

8.3.2.2. Catalytic experiments 225

8.3.2.3. Catalysts stability and reuse 228

8.3.2.4. Scavenging tests and catalytic mechanism 230

8.3.2.5. Kinetic studies 232

8.3.3. CWPO application to real OMW 234

8.3.3.1. Catalyst selection 234

8.3.3.2. Influence of key operational parameters: pH and H_2O_2 dose 235

8.3.3.3. Evaluation of the treated wastewater quality 237

8.4. CONCLUSIONS 239

REFERENCES 241

9. SUSTAINABLE IRON-OLIVE STONE BASED-CATALYSTS FOR FENTON-LIKE OMW TREATMENT: DEVELOPMENT AND PERFORMANCE ASSESSMENT IN CONTINUOUS FIXED-BED REACTOR OPERATION 245

ABSTRACT 246

9.1. INTRODUCTION 247

9.2. MATERIALS AND METHODS 248

9.2.1. Catalysts synthesis 248

9.2.2. Synthetic polyphenolic solutions and real OMW 248

9.2.3. Catalytic runs 250

9.3. RESULTS AND DISCUSSION 252

9.3.1. Textural and chemical characterization of the materials 252

9.3.2. Catalysts screening: batch reactor 257

9.3.2.1. Selection of Fe-precursor 257

9.3.2.2. Selection of Fe-loading 260

9.3.3. Fixed-bed reactor operation 262

9.3.3.1. Catalytic bed stability 262

9.3.3.2. Effect of temperature, H_2O_2 feed dose, and flow rate 263

9.3.3.3. Effect of synthetic solution composition 266

9.3.3.4. Application to real OMW samples 269
9.4. Conclusions 271
References 273
10. INTEGRATION OF CATALYTIC WET PEROXIDE OXIDATION AND MEMBRANE DISTILLATION PROCESSES FOR OMW TREATMENT AND WATER RECOVERY 277
Abstract 278
10.1. Introduction 279
10.2. Materials and methods 280
10.2.1. Chemicals, materials, and olive mill wastewater 280
10.2.2. Fixed-bed reactor set-up: CWPO experiments 281
10.2.3. DCMD experimental set-up 283
10.3. Results and discussion 284
10.3.1. FBR experiments 284
10.3.2. DCMD experiments 286
10.3.3. DCMD-retentate recirculation to the FBR 293
10.4. Conclusions 295
References 296
PART V. CONCLUSIONS 299
11. CONCLUSIONS AND FUTURE WORK 301
11.1. Conclusions 302
11.2. Limitations and future work 305
A. APPENDIX – SUPPORTING INFORMATION FOR CHAPTER 4 309
B. APPENDIX – SUPPORTING INFORMATION FOR CHAPTER 7 313
C. APPENDIX – SUPPORTING INFORMATION FOR CHAPTER 8 321
D. APPENDIX – SUPPORTING INFORMATION FOR CHAPTER 9 329
E. APPENDIX – PUBLICATIONS AND SCIENTIFIC COMMUNICATIONS 335
Scientific publications in peer-reviewed international scientific journals 336
Oral communications in scientific meetings 337
Poster communications in scientific meetings 338

LIST OF FIGURES

Fig. 2.1 Average worldwide olive oil production (in %) for the last decade campaigns (2010–2020), according to figures published by IOC (data collected from December 2021) [8]. 15
Fig. 2.2 Stages of the different olive oil extraction processes with indication of the main inputs/outputs. 16
Fig. 2.3 Evolution of the olive oil extraction systems used in Portugal (1998–2020). Data collected from INE (Instituto Nacional de Estatística) [19]. 18
Fig. 2.4 Overlook of the different OMW treatment processes from several research articles published between 2006-2021 (based on Scopus database search with combinations of keywords such as "OMW" or "olive mill wastewater" with "CWPO", "Ion Exchange", etc.). 25
Fig. 2.5 Diagram representation and classification of several AOPs for water/wastewater treatment. 27
Fig. 2.6 (a) Mineralization degree and (b) leaching values over time using catalysts with different particle sizes (data taken from ref. [168]). 39
Fig. 2.7 Activated carbon's porous structure schematic representation and classification (adapted from [188]). 40
Fig. 2.8 Scanning electron microscopy (SEM) micrographs of (a) carbonized olive stones, (b) KOH/AC (2:1 wt. ratio), (c) KOH/AC (2:1 wt. ratio) with particle size range 0.63–0.80 mm, (d) direct chemical activation (KOH) of raw olive stones (taken from ref. [194]). 43
Fig. 2.9 (a) Concentration of residual H_2O_2 in solution over time and (b) total degradation of phenolic content according to the number of H_2O_2 injections (taken from ref. [97]). 48
Fig. 2.10 Adequacy of traditional membrane technologies as a function of the size or molecular weight of the target compound (adapted from [233]). 52
Fig. 2.11 Schematic representation of (A) direct contact membrane distillation (DCMD), (B) vacuum membrane distillation (VMD), (C) air gap membrane distillation (AGMD), and (D) sweeping gas membrane distillation (SGMD) configurations. 55
Fig. 2.12 Permeate flux (J) of OMW over time before and after microfiltration or coagulation/flocculation pre-treatments at T_{feed} = 40 °C and $T_{permeate}$ = 20 °C (taken from ref. [38]). 57
Fig. 4.1 Fenton's oxidation experimental set-up for batch (a) and CSTR (b) operation. TT – thermometer, pH – pH meter, MB – magnetic bar, MSC – magnetic stirrer controller, TC – temperature controller. 91
Fig. 4.2 Influence of the iron salt used as catalyst on the TOC and TPh removal efficiency (%) along time. Experimental conditions: $[Fe^{2+}/Fe^{3+}]$ = 50 mg/L, $[H_2O_2]$ = 2.0 g/L, pH_0 = 3.7, T = 30 °C. 93
Fig. 4.3 Effect of H_2O_2 dose on the TOC removal efficiency (%) along time on the batch runs. Experimental conditions: $[Fe^{2+}]$ = 50 mg/L, pH_0 = 3.7, T = 30 °C. 94
Fig. 4.4 Effect of H_2O_2 concentration on TOC (▩) and TPh (□) removal efficiencies and efficiency of oxidant use (η H_2O_2) (···•···) after the batch runs, for Fe^{2+} concentrations equal to (a) 25, (b) 50, and (c) 100 mg/L. Experimental conditions: pH_0 = 3.7, T = 30 °C, t = 300 min. 95
Fig. 4.5 Influence of initial pH value on TOC (▲) and TPh (□) removal after Fenton's oxidation batch runs. Experimental conditions: $[H_2O_2]$ = 2.0 g/L, $[Fe^{2+}]$ = 100 mg/L, T = 30 °C, t = 300 min. 99

Fig. 4.6 Influence of reaction medium temperature on the TOC (▲) and TPh (□) removal after Fenton's oxidation batch runs. Experimental conditions: [H_2O_2] = 2.0 g/L, [Fe^{2+}] = 100 mg/L, pH_0 = 5.0, t = 300 min. 100
Fig. 4.7 (a) % TOC degradation for constant temperature (T = 30 °C) throughout the entire reaction (×) *vs*. unadjusted temperature (T_0 = 22 °C) (○); (b) reaction's temperature variation throughout the experiments. Experimental conditions: [H_2O_2] = 2.0 g/L, [Fe^{2+}] = 100 mg/L, pH_0 = 5.0, t = 300 min. 102
Fig. 4.8 Effect of H_2O_2 dose fed on TOC and TPh removal efficiency, in transient regimen, for the CSTR runs. Experimental conditions: [Fe^{2+}]$_{feed}$ = 100 mg/L, pH_0 = 5.0, T = 30 °C, τ = 90 min. 104
Fig. 4.9 Effect of space-time (τ) on TOC (▲) and TPh (□) removal efficiencies, at steady-state, for the CSTR runs. Experimental conditions: [H_2O_2]$_{feed}$ = 2.0 g/L, [Fe^{2+}]$_{feed}$ = 100 mg/L, pH_0 = 5.0, T = 30 °C. 105
Fig. 5.1 Comparison of Fenton (Fe^{2+}/H_2O_2) and Fenton-like (Fe^{3+}/H_2O_2) reactions, with and without pH adjustments, on the (a) TOC removal, (b) pH evolution, (c) H_2O_2 concentration profile, and (d) temperature profile along time. Experimental conditions: [Fe^{2+}/Fe^{3+}] = 1.0 g/L, [H_2O_2] = 25 g/L, pH_0 = 3.0, T_0 = 25 °C. 120
Fig. 5.2 Effect of the different reagent addition methods on (a) TOC removal, (b) H_2O_2 concentration profile, and (c) temperature profile over time for. Experimental conditions: [Fe^{3+}] = 1.0 g/L, [H_2O_2] = 25 g/L, pH_0 = 3.0, T_0 = 25 °C. 123
Fig. 5.3 Overall COD and TPh removal (after Fenton oxidation and Fenton + coagulation/flocculation processes) and BOD_5:COD ratio of the final effluent for the different reagent addition methods tested. Experimental conditions: [Fe^{3+}] = 1.0 g/L, [H_2O_2] = 25 g/L, pH_0 = 3.0, T_0 = 25 °C, t = 240 min. 125
Fig. 5.4 (a) TOC removal and (b) H_2O_2 concentration over time for different Fe^{3+}/H_2O_2 ratios. Experimental conditions: [Fe^{3+}] = 0.75–1.25 g/L, [H_2O_2] = 15–30 g/L, pH0 = 3.0, T_0 = 25 °C, and H_2O_2 gradually added until t = 90 min. 127
Fig. 5.5 Overall COD and TPh removal (after Fenton oxidation and Fenton + coagulation/flocculation processes), and BOD_5:COD ratio of the final effluent for the different [Fe^{3+}]/[H_2O_2] ratios tested. Experimental conditions: [Fe^{3+}] = 0.75–1.25 g/L, [H_2O_2] = 15–30 g/L, pH_0 = 3.0, T_0 = 25 °C, t = 180 min, and H_2O_2 gradually added until t = 90 min.. 128
Fig. 5.6 Comparison of TOC removal over time for the photo-Fenton-like and Fenton-like processes. Experimental conditions: [Fe^{3+}] = 1.0 g/L, [H_2O_2] = 25 g/L, pH_0 = 3.0, T_0 = 25 °C, I = 500 W/m^2, and H_2O_2 added gradually until t = 90 min 130
Fig. 5.7 Inhibition of the *V. fischeri* bacteria of the OMW before and after the combined treatment process for different contact time (5, 15, and 30 min) 131
Fig. 5.8 Relationship between *V. fischeri* inhibition (%) and residual TPh (g/L) after the combined treatment process, for different contact times (5, 15, and 30 min). 132
Fig. 6.1 HRSEM micrographs highlighting the morphology of (a) OSAC and (b) OTPAC. 148
Fig. 6.2 (a) N_2 adsorption-desorption isotherms (P/P_0 is the relative pressure between the equilibrium pressure and the saturation vapor pressure of N_2) and (b) pore size distribution of the adsorbents. 148
Fig. 6.3 High resolution XPS spectra of the O1s spectral region for the different biosorbents. 151
Fig. 6.4 Total phenol removal as a function of adsorption time (dashed lines: PFO model adjustment; solid lines: PSO model adjustment). Experimental conditions: C_0 = 150 mg/L (30 mg/L each phenolic compound) at 25 °C, W_{ads} = 75 mg, pH_0 = 3.5–3.8 152

Fig. 6.5 Kinetic curves for competitive adsorption onto (a) OSAC, (b) OSAC/KOH, and (c) N samples (dashed lines: PFO model; solid lines: PSO model). Experimental conditions: C_0 = 150 mg/L (30 mg/L each phenolic compound) at 25 °C, W_{ads} = 75 mg, pH_0 = 3.5–3.8. 152
Fig. 6.6 Adsorption isotherms of (a) gallic acid and (b) vanillic acid (solid lines: experimental data fit with Langmuir isotherm; dashed lines: fit with Freundlich isotherm). Experimental conditions: 25 °C, C_0 = 25–350 mg/L, W_{ads} = 25 mg, V = 50 mL, pH_0 = 3.5–3.8. 159
Fig. 6.7 Kinetic curves for (a) gallic acid and (b) vanillic acid adsorption at C_0 = 150 mg/L, 25 °C, V = 50 mL, pH_0 = 3.5-3.8 (dashed lines: fitting of PFO model to experimental data; solid lines: fitting of PSO model). 162
Fig. 6.8 Intraparticle diffusion adsorption kinetics for (a) gallic acid and (b) vanillic acid at C_0 = 150 mg/L, 25 °C, V = 50 mL, and pH_0 = 3.5–3.8. 165
Fig. 6.9 Relationship between equilibrium adsorption capacities (qe) and the textural characteristics (S_{BET} and W_0 (N_2)) of the adsorbents for gallic and vanillic acids (C_0 = 150 mg/L); q_e values for TPh on competitive runs shown for comparison (same experimental conditions). 167
Fig. 6.10 (a) TG and (b) DTG profiles of gallic acid (GA) and vanillic acid (VA) decomposition. 170
Fig. 6.11 (a) TG and (b) DTG profiles of fresh and spent OSAC/KOH after adsorption of GA or VA. 171
Fig. 6.12 Kinetic curves for (a) gallic and (b) vanillic acids using regenerated samples at C_0 = 150 mg/L and 25 °C (PSO model adjustment). 172
Fig. 7.1 TG-DTG profiles for the carbonization of OS and SD residues. 185
Fig. 7.2 HRSEM images of (A) SDC-AC, (B) OSC-AC and (C) OS-AC/KOH supports (without Fe). 186
Fig. 7.3 Pore size distribution obtained by QSDFT applied to N_2-adsorption isotherms for selected activated carbon supports and Fe-derivative catalysts: effect of Fe-impregnation. 188
Fig. 7.4 Morphology of (A) OSC-AC-Fe, and (C) SDC-AC-Fe; (B, D) detail of Fe-nanoparticles coating the carbon surface. 189
Fig. 7.5 XRD patterns of the catalysts tested; standard patterns of Fe_3O_4 and α-Fe_2O_3 (JCPDS cards no. 19-0629 and 33-0664, respectively) are also presented. 190
Fig. 7.6 HRTEM images of (A) OSC-AC-Fe, (B) OS-AC/KOH-Fe, (C) SDC-AC-Fe, and (D) N-Fe catalysts. 191
Fig. 7.7 Relationship between the surface Fe and O atomic contents (%) for all the prepared catalysts. 192
Fig. 7.8 O1s XPS spectral region of the different catalysts. 195
Fig. 7.9 Fitting the $Fe2p_{3/2}$ spectral region of OSC-AC-Fe and SDC-AC-Fe. 196
Fig. 7.10 (a) TPh removal efficiencies by adsorption and catalytic processes, and H_2O_2 consumption for each catalyst after 4 h of reaction; (b) evolution of TOC conversion as a function of reaction time for CWPO experiments (inset: mean Fe-leaching values after the reaction). 196
Fig. 7.11 Comparison of phenolic compounds' removal by adsorption or CWPO using OSC-AC-Fe and N-Fe catalysts. 199
Fig. 7.12 Influence of the specific surface area (S_{BET}) on the TPh and TOC removals by adsorption and catalysis (in mg/L). 200
Fig. 7.13 H_2O_2 consumed *vs.* experimental and theoretical TOC removals for each catalyst. 202

Fig. 7.14 TPh/TPh_0 *vs*. inhibition (%) of the *V. fischeri* bacteria after 30 min in contact with the different solutions after CWPO. 203
Fig. 8.1 HRSEM micrographs of samples: (A) OSAC-Fe-IWI and (C) OSAC-Fe-HT; (B) and (D) show details of Fe-particles coating OSAC-Fe-IWI and OSAC-Fe-HT surfaces, respectively 217
Fig. 8.2 (a) N_2 adsorption-desorption isotherms at -196 °C; (b) pore size distribution of the materials obtained by QSDFT applied to N_2 adsorption isotherms. 218
Fig. 8.3 XRD patterns of the synthetized catalysts. Standard patters of α-Fe_2O_3 (ICDD card no. 33-0664) and Fe_3O_4 (ICDD card no. 19-0629) are shown for reference. 220
Fig. 8.4 HRTEM images of Fe-catalysts: (A-C) OSAC-Fe-IWI, (D-F) OSAC-Fe-Ads, and (G-I) OSAC-Fe-HT. 221
Fig. 8.5 O1s XPS spectral region of the different catalysts. 222
Fig. 8.6 Fitting of the $Fe2p_{3/2}$ spectral region of the different catalysts. 223
Fig. 8.7 Comparison of total phenolic content (TPh) adsorption over time by the OSAC support and derived Fe-catalysts (solid lines: pseudo-second order kinetic model fitting). [Cat] = 0.5 g/L, T_0 = 25 ºC, and pH_0 = 3.5. 223
Fig. 8.8 Comparison of TOC and TPh removals by adsorption (dashed bars), and adsorption + oxidation = CWPO (blank bars) after 240 min of reaction. H_2O_2 consumptions for CWPO runs are shown in the right y-axis. [Cat] = 0.5 g/L, [H_2O_2] = 1.0 g/L, T_0 = 25 ºC, and pH_0 = 3.5. 226
Fig. 8.9 Removal of phenolic compounds over time by CWPO (normalized concentrations) using: (a) OSAC Fe IWI, (b) OSAC-Fe-Ads, and (c) OSAC-Fe-HT (PA – Protocatechuic acid; VA – Vanillic acid; Ty – Tyrosol; GA – Gallic acid; CA – Caffeic acid). [Cat] = 0.5 g/L, [H_2O_2] = 1.0 g/L, T_0 = 25 ºC, and pH_0 = 3.5. 227
Fig. 8.10 Effect of catalyst dosage on the removal of TPh: (a) 0.5 g/L (75 mg), (b) 1.0 g/L (150 mg), and (c) 2.0 g/L (300 mg). [H_2O_2] = 1.0 g/L, T_0 = 25 ºC, and pH_0 = 3.5. 227
Fig. 8.11 Total phenolic content removal in consecutive cycles using: (a) OSAC-Fe-IWI, (b) OSAC-Fe-Ads, and (c) OSAC-Fe-HT. Inset graphs show Fe leached (wt.%) after each run. 229
Fig. 8.12 Comparison of TPh removal efficiencies in the absence *vs*. presence of DMSO quencher for all catalysts (DMSO:H_2O_2 molar ratio of 10). 231
Fig. 8.13 (a) TOC, COD, and TPh removals of real OMW samples, and H_2O_2 conversions by OSAC-Fe-IWI and OSAC-Fe-Ads (after 240 min); (b) Inhibition (%) of the Vibrio fischeri at different contact times in the presence of ten-fold diluted OMW sample and after CWPO. 234
Fig. 8.14 Conversion efficiencies after 240 min with OSAC-Fe-IWI catalyst with different (a) initial pH ([Cat] = 2.0 g/L, [H_2O_2] = 1.0 g/L, T_0 = 25 °C), and (b) H_2O_2 dosages ([Cat] = 2.0 g/L, pH_0 = 4.9, T_0 = 25 °C); (c) Efficiency of degradation *vs*. H_2O_2 conversions (right y-axis: H_2O_2 consumed (g/L)). 236
Fig. 9.1 Scheme of the up-flow fixed-bed reactor (FBR) experimental set-up. 251
Fig. 9.2 (a) N_2-adsorption/desorption isotherms and (b) pore size distribution (PSD) of OSAC support and derived Fe-catalysts (2 wt.% Fe). 253
Fig. 9.3 XRD patterns of the two fresh catalysts prepared to theoretical Fe-loads of 2 wt.%, and OSAC $Fe(NO_3)_3$ after 48 h of continuous use. ICDD cards of α-Fe_2O_3 and Fe_3O_4 shown for reference. 254
Fig. 9.4 STEM images (1st column), mapping (2nd column), and EDX-spectrum (3rd column) of OSAC-$FeCl_2$ (a, b, c) and OSAC-$Fe(NO_3)_3$ (d, e, f), as well as OSAC-$Fe(NO_3)_3$ after 48 h of operation in the fixed-bed reactor (g, h, i). 255

Fig. 9.5 XPS spectra and fitting of the derived Fe-catalysts (2 wt.% Fe) and of a used sample of OSAC-Fe(NO_3)$_3$: (a, b, c) O1s and (d, e, f) Fe2p$_{3/2}$ regions. 257
Fig. 9.6 (a) TPh/TPh$_0$ in consecutive adsorption/catalytic runs with OSAC and derived Fe-catalysts (2 wt.% Fe); (b) Fe leaching (wt.%) with indication of the cumulative % after each run (open symbols); Inset graph: Fe concentration in solution (mg/L). [Cat] = 2.0 g/L, [H_2O_2] = 1.0 g/L, pH$_0$ = 3.5, 20 °C. 258
Fig. 9.7 (a) TPh/TPh$_0$ over time in consecutive runs; (b) Fe leaching (wt.%) with indication of the cumulative % after each run (open symbols); Inset graph: concentration of Fe in solution (mg/L), (c) TOC/TOC$_0$, (d) H_2O_2 conversion with different OSAC-Fe(NO_3)$_3$ catalysts. [Cat] = 2.0 g/L, [H_2O_2] = 1.0 g/L, pH$_0$ = 3.5, 20 °C. 261
Fig. 9.8 Stability tests for OSAC-Fe(NO_3)$_3$ catalyst (5 wt.% Fe): normalized TPh and H_2O_2 over time. Right y-axis: pH values at the reactor outlet. Q = 0.75 mL/min, [H_2O_2]$_{feed}$ = 0.75 g/L, pH$_0$ = 3.5, 20 °C. 262
Fig. 9.9 Parametric assessment of the FBR operation: steady-state TPh removals (open symbols: TPh removal considering the thermal degradation effect), TOC removal efficiencies and H_2O_2 conversions for different operational conditions. 264
Fig. 9.10 Normalized profiles for the removal of parent phenolic compounds from the different synthetic solutions tested in the fixed-bed reactor. Q = 0.75 mL/min, [H_2O_2]$_{feed}$ = 0.75 g/L, pH$_0$ = 3.5, 20 °C. 267
Fig. 9.11 Steady-state TPh and TOC removals and H_2O_2 conversions for each solution under distinct operational conditions. Coloured bars: Q = 0.75 mL/min, [H_2O_2]$_{feed}$ = 0.75 g/L, pH$_0$ = 3.5, 20 °C (as reported on Fig. 9.10); Blank bars: Q = 0.75 mL/min, [H_2O_2]$_{feed}$ = 1.50 g/L, pH$_0$ = 3.5, 60 °C. 268
Fig. 10.1 Schematic representation of the combined experimental set-up: (1) recirculating water bath; (2) magnetic stirrer hot plate; (3) 3-neck flask with OMW+H_2O_2; (4) combined pH and temperature electrode; (5) reflux condenser; (6) peristaltic pump; (7) jacketed FBR; (8) retentate; (9) permeate; (10) heat/cool exchangers (both connected to separate recirculating water baths – not graphically represented); (11) DCMD module; (12) conductivity meter; (13) thermocouples. 282
Fig. 10.2 COD and TPh concentrations (mg/L) over time at the FBR feed and outlet streams for (a) OMW-5× and (b) OMW-7.5×. Experimental conditions: [H_2O_2]$_{feed}$/[COD]$_{feed}$ = 2.3 ±0.1 g H_2O_2/g O_2, W_{cat}/Q = 2.66 g min/mL, T = 60 °C, Q = 0.75 mL/min, pH$_0$ = 4.0 ±0.2. 285
Fig. 10.3 (a) DCMD permeate flux and (b) H_2O recovery over time for DW and for OMW samples (before and after CWPO pre-treatment). Experimental conditions: T_{feed} ≈ 57 °C and $T_{permeate}$ ≈ 18 °C (ΔP ≈ 16.5 kPa), Q = 100 mL/min. 287
Fig. 10.4 Visual comparison of a neat-PTFE membrane with the used ones in DCMD after 4 h of operation for the different feed solutions tested. Experimental conditions: T_{feed} ≈ 57 °C and $T_{permeate}$ ≈ 18 °C (ΔP ≈ 16.5 kPa), Q = 100 mL/min. 288
Fig. 10.5 (a) DCMD permeate flux and (b) TDS rejection over time for CWPO pre-treated samples of OMW-7.5× Experimental conditions: $T_{permeate}$ ≈ 18 °C, Q = 100 mL/min. 292
Fig. 10.6 Concentration of COD, TOC, and TPh (permeate) after the integrated process (CWPO+DCMD), initial values of OMW-7.5× presented for reference. Right y-axis shows the global rejection for each parameter. Experimental conditions: $T_{permeate}$ ≈ 18 °C, Q = 100 mL/min, t = 3 h. 293

Fig. 10.7 (a) COD, TOC, and TPh of different retentates after recirculation to the FBR with indication of oxidation efficiencies in steady-state (yy-axis). DCMD experimental conditions: T_{feed} ≈ 57 °C, $T_{permeate}$ ≈ 18 °C, ΔP ≈ 16.5 kPa, Q = 100 mL/min; FBR: $[H_2O_2]_{feed}/[COD]_{feed}$ =2.3 ±0.1 g H_2O_2/g O_2, W_{cat}/Q = 2.66 g min/mL, T = 60 °C, pH_0 = 4.0 ±0.2; data for the FBR refer to its steady-state operation). 294

Fig. A.1 Effect of H_2O_2 dose on the TOC removal efficiency (%) along time on the batch runs of the synthetic OMW Fenton's oxidation for $[Fe^{2+}]$ = 25 (a) and (b) 100 mg/L. Experimental conditions: pH_0 = 3.7, T = 30 °C, t = 300 min. 310

Fig. A.2 Effect of H_2O_2 dose on the TOC removal efficiency (%) along time on the batch runs of the synthetic OMW Fenton's oxidation. Experimental conditions: $[Fe^{2+}]$ = 200 mg/L, pH_0 = 3.7, T = 30 °C, t = 300 min. 310

Fig. A.3 Evolution of pH values for the batch runs of the synthetic OMW Fenton's oxidation. Experimental conditions: $[Fe^{2+}]$ = 200 mg/L, $[H_2O_2]$ = 2.0 g/L, pH_0 = 3.7, T = 30 °C, t = 300 min. 311

Fig. A.4 Effect of space-time (τ, min) on (a) TOC and (b) TPh removal efficiencies, in transient regimen, for the CSTR runs. Experimental conditions: $[H_2O_2]_{feed}$ = 2.0 g/L, $[Fe^{2+}]_{feed}$ = 100 mg/L, pH_0 = 5.0, T = 30 °C. 311

Fig. B.1 N_2 adsorption/desorption isotherms for the supports and corresponding Fe-catalysts tested. 314

Fig. B.2 C1s spectral region of OSC-Fe and OSC-AC-Fe catalysts. 315

Fig. B.3 Adsorption runs using the catalysts prepared: removal of each phenolic compound (C/C_0) over time. Experimental conditions: [Cat] = 0.5 g/L, T = 25 °C, pH = unadjusted. 316

Fig. B.4 Catalytic effect of H_2O_2 on the removal of phenolic compounds (C/C_0) over time. Experimental conditions: $[H_2O_2]$ = 1 g/L, T = 25 °C, pH = unadjusted. 317

Fig. B.5 Catalytic runs using the Fe/AC catalysts prepared: removal of phenolic compounds (C/C_0) over time. Experimental conditions: $[H_2O_2]$ = 1 g/L, [Cat] = 0.5 g/L, T = 25 °C, pH = unadjusted. 318

Fig. C.1 EDX microanalysis of the OSAC-Fe-IWI catalyst surface with the mapping of elements C, Fe, and O in the sample. (1) Fe-particles and (2) carbon support. 322

Fig. C.2 FTIR spectra of OSAC support and derived OSAC-Fe-IWI catalyst. 323

Fig. C.3 Adsorption of phenolic compounds over time (normalized concentrations) by: (a) OSAC, (b) OSAC-Fe-IWI, (c) OSAC-Fe-Ads, and (d) OSAC-Fe-HT (PA – Protocatechuic acid; VA – Vanillic acid; Ty – Tyrosol; GA – Gallic acid; CA – Caffeic acid). [Cat] = 0.5 g/L, T_0 = 25 ºC, and pH_0 = 3.5. 323

Fig. C.4 pH variation over time for the CWPO runs. [Cat] = 0.5 g/L, $[H_2O_2]$ = 1.0 g/L, T0 = 25 ºC, and pH_0 = 3.5. 324

Fig. C.5 Removal of phenolic compounds over time by CWPO (normalized concentrations) using: (a) OSAC-Fe-IWI, (b) OSAC-Fe-Ads, and (c) OSAC-Fe-HT. [Cat] = 1.0 g/L, $[H_2O_2]$ = 1.0 g/L, T_0 = 25 ºC, and pH_0 = 3.5. 324

Fig. C.6 Removal of phenolic compounds over time by CWPO (normalized concentrations) using: (a) OSAC-Fe-IWI, (b) OSAC-Fe-Ads, and (c) OSAC-Fe-HT. [Cat] = 2.0 g/L, $[H_2O_2]$ = 1.0 g/L, T_0 = 25 ºC, and pH_0 = 3.5. 325

Fig. C.7 Variation in H_2O_2 consumption in consecutive cycles using: (a) OSAC-Fe-IWI, (b) OSAC-Fe-Ads, and (c) OSAC-Fe-HT. 325

Fig. C.8 HPLC chromatograms of the initial synthetic solution and after 60 min of reaction with OSAC-Fe-IWI ([Cat] = 2.0 g/L, $[H_2O_2]$ = 1.0 g/L, T_0 = 25 ºC, and pH_0 = 3.5). 326

Fig. C.9 COD degradation along time under different initial pH values ([OSAC-Fe-IWI] = 2.0 g/L, $[H_2O_2]$ = 1.0 g/L, and T_0 = 25 ºC). 326

Fig. C.10 (1) Ten-fold diluted OMW, (2) OMW after CWPO (240 min) with OSAC-Fe-IWI deposited, and (3) OMW after CWPO without catalyst. 327
Fig. C.11 AOS and COS indices variation over time during the real OMW treatment by CWPO ((Cat] = 2.0 g/L, $[H_2O_2]$ = 0.50 g/L, $pH_0 \approx 4.9$, T = 25 °C). 327
Fig. D.1 Chemical structures of the phenolic acids selected as model compounds. 330
Fig. D.2 Adsorption profiles of each phenolic compound over time obtained by HPLC using (a) OSAC-$Fe(NO_3)_3$, (b) OSAC-$FeCl_2$, and (c) OSAC support. [Cat] = 2.0 g/L, pH_0 = 3.5, 20 °C. 330
Fig. D.3 (a) Total organic carbon (TOC) removal and (b) H_2O_2 conversion along time in consecutive 300-min cycles using OSAC-$Fe(NO_3)_3$ and OSAC-$FeCl_2$ catalysts (2 wt% Fe). [Cat] = 2.0 g/L, $[H_2O_2]$ = 1.0 g/L, pH_0 = 3.5, 20 °C. 331
Fig. D.4 TPh and TOC profile at the fixed-bed reactor's outlet in a non-catalytic run. Q = 0.75 mL/min, pH_0 = 3.5, 20 °C. 331
Fig. D.5 TPh concentration profile at the fixed-bed reactor outlet in a catalytic run performed with dissolved iron. $[H_2O_2]_{feed}$ = 0.75 g/L, $[Fe]_{feed}$ = 2.1 mg/L; Q = 0.75 mL/min, pH_0 = 3.5, T = 20 °C. 332
Fig. D.6 Thermal degradation (in %) promoted by different operating temperatures for each parent phenolic compound in solution after 6 h. Q = 0.75 mL/min, $[H_2O_2]_{feed}$ = 0.75 g/L, pH_0 = 3.5. 333
Fig. D.7 HPLC chromatograms of synthetic solutions before and after CWPO in the fixed-bed reactor. Q = 0.75 mL/min, $[H_2O_2]_{feed}$ = 1.50 g/L, pH_0 = 3.5, 60 °C. 333

LIST OF TABLES

Table 2.1 Estimated input/output data for different olive oil extraction systems (adapted from refs. [12–14]). 17

Table 2.2 Summary of the main physicochemical characteristics of OMW according to the extraction method. 20

Table 2.3 Phenolic compounds identified in different OMW samples, according to scientific literature data. 21

Table 2.4 Summary of Fenton and Fenton-like processes applied for OMW treatment, either as single stage units, or combined with other treatment processes. 34

Table 2.5 Main research findings on the treatment of simulated and real OMW by catalytic wet peroxide oxidation. 49

Table 2.6 Summary of membrane distillation technologies applied for the treatment and/or valorization of OMW. 59

Table 4.1 Main characteristics of the synthetic effluent (average values). 90

Table 4.2 Key reactions occurring in Fenton's system in the presence of sulfate ions (adapted from [9]). 97

Table 4.3 Comparison between residual [H_2O_2] in solution at the early stage of the Fenton process (15 and 30 min) and at the end of the experiment (300 min), for the 20–50 °C range of temperatures tested in the batch runs. Experimental conditions: [H_2O_2] = 2.0 g/L, [Fe^{2+}] = 100 mg/L, pH_0 = 5.0, t = 300 min. 101

Table 4.4 Characterization of the synthetic effluent after the batch (after 180 and 300 min) and CSTR (for τ = 120 and 180 min) Fenton's oxidation runs, with respective removal efficiency percentages (within brackets). 106

Table 5.1 Physicochemical characterization of the OMW sample as collected and after the 12 h sedimentation.. 117

Table 5.2 Physicochemical characteristics of the OMW before and after the combined process for two Fe^{3+}:H_2O_2 ratios (supernatant's mean values). Legal discharge limits for industrial effluents into (a) water bodies in force in Portugal and (b) into municipal collectors of Braga Municipality (northern region of Portugal) are also presented. 133

Table 6.1 Chemical characteristics of the phenolic compounds used. 146

Table 6.2 Textural characteristics and pH_{pzc} of the adsorbents. 150

Table 6.3 Elemental analysis (atomic content, %), species percentages and corresponding binding energies (in brackets, eV) of the different adsorbents determined by XPS analysis. 151

Table 6.4 Fitted kinetic parameters of the competitive adsorption runs using the PFO and PSO models. 156

Table 6.5 Langmuir and Freundlich isotherm models' parameters for gallic and vanillic acids. 161

Table 6.6 Fitted parameters for the pseudo-first order and pseudo-second order kinetic models. 163

Table 6.7 Intraparticle diffusion parameters for the adsorption of gallic and vanillic acids. 166

Table 6.8 Comparison of maximum adsorptive capacities (mg/g) of various low-cost adsorbents derived from agro-industrial residues for different organic pollutants (at 25 °C). 169

Table 7.1 Summary of synthesis conditions, nomenclature of catalysts and yield values of the carbonization/activation processes. 182

Table 7.2 Physicochemical characterization of the synthetic effluent; overview of OMW characteristics from different sources: storage pond (weathered), olives washing and centrifuges. 183

Table 7.3 pH_{pzc} and textural characteristics of supports and corresponding catalysts. 187

Table 7.4 Atomic surface composition determined by XPS analysis of the prepared catalysts. 192
Table 7.5 Distribution of oxygen and iron species on the catalysts surface. 193
Table 8.1 Textural characteristics and pH_{pzc} values for the OSAC support and derived Fe-catalysts. 216
Table 8.2 Elemental analysis of the prepared catalysts determined by XPS (atomic content %). 222
Table 8.3 Calculated adsorption parameters for PSO kinetic model fitting. 224
Table 8.4 Summary of TPh and TOC removals, H_2O_2 conversions, and Fe leaching after each run. 228
Table 8.5 Kinetic parameters of TPh depletion for the stability cycles after saturation of the catalysts ($(-r)_0$: mg/min·g_{Fe}; k_{app}: L^2/mg·min·g_{Fe}). 233
Table 8.6 Apparent rate constants of H_2O_2 consumption (k_{app}: L/min·g_{Fe}). 234
Table 8.7 Physicochemical properties of OMW before and after CWPO, and legal discharge limits for industrial effluents: (a) direct discharge to natural water resources, (b) industrial discharge in municipal collectors; values and standard deviations reported result from 3 independent analyses. 238
Table 9.1 Phenolic compounds selected for each formulation used. 249
Table 9.2 Physicochemical properties of the polyphenolic solution and filtered sample of OMW used (supernatant, non-diluted). 250
Table 9.3 Textural characteristics of the OSAC support and derived OSAC-Fe catalysts, Fe loadings (wt.%) obtained from AAS analysis. 252
Table 9.4 Elemental analysis (atomic content %), species percentages and corresponding binding energies (in brackets, eV) of the derived Fe-catalysts (2 wt.% Fe), and of a used sample of OSAC-Fe$(NO_3)_3$, determined by XPS. 256
Table 9.5 Physicochemical properties of the different OMW samples (diluted 30, 15, 7.5 and 5-fold) after CWPO (values at steady-state); removal percentage values shown in parentheses. $[H_2O_2]/[COD]$ = 2.3 ±0.1 g H_2O_2/g O_2, Q = 0.75 mL/min, pH_0 = 3.5, 60 °C. 270
Table 10.1 Main physicochemical characteristics of OMW supernatant before and after dilution. Legislated discharge limits for irrigation water and industrial wastewater are shown for reference. 281
Table 10.2 Permeate characterization after 4 h of DCMD; rejection % shown between brackets. Experimental conditions: T_{feed} ≈ 57 °C and $T_{permeate}$ ≈ 18 °C (ΔP ≈ 16.5 kPa), Q = 100 mL/min. 290
Table 10.3 Retentate characterization after 4 h of DCMD; concentration factors of the retentate ($\theta_{4\,h}$) shown in brackets. Experimental conditions: T_{feed} ≈ 57 °C and $T_{permeate}$ ≈ 18 °C (ΔP ≈ 16.5 kPa), Q = 100 mL/min. 291
Table A.1 Relative percentage of phenolic compounds in relation to the total phenolic content (wt.%) of different untreated OMW, according to literature survey. 312
Table A.2 Outlet H_2O_2 concentration (g/L) at steady-state for different H_2O_2 feed doses to the CSTR. Experimental conditions: $[Fe^{2+}]_{feed}$ = 100 mg/L, pH_0 = 5.0, T = 30 °C, τ = 90 min. 312
Table B.1 Chemical characteristics of the selected phenolic compounds. 319
Table C.1 Distribution of oxygen and iron species on the catalysts' surface. 328
Table C.2 TOC removal efficiencies (%) for the consecutive catalytic cycles (after 240 min). 328
Table D.1 Physicochemical characterization of the initial OMW samples used. 334

LIST OF ACRONYMS AND ABBREVIATIONS

AAS	Atomic absorption spectroscopy
AC	Activated carbon
Ads	Adsorption
AGMD	Air gap membrane distillation
AOP	Advanced oxidation process
AOS	Average oxidation state
APHA	American Public Health Association
BEA	Beta zeolite
BET	Brunauer–Emmett–Teller
BOD_5	Biochemical oxygen demand (5-day)
BTC	Benzene-1,3,5-tricarboxylic acid
CA	Caffeic acid
CNF	Carbon nanofibers
CNT	Carbon nanotubes
COD	Chemical oxygen demand
COS	Carbon oxidation state
CSTR	Continuous stirred-tank reactor
CWAO	Catalytic wet air oxidation
CWPO	Catalytic wet peroxide oxidation
DAD	Diode-array detector
DCMD	Direct contact membrane distillation
DLD	Delay-line detector
DMSO	Dimethyl sulfoxide
EDG	Electron donating group
EDX	Energy dispersive X-ray
EU	European Union
FAOSTAT	Food and Agriculture Organization Corporate Statistical Database
FBR	Fixed-bed reactor
FTIR	Fourier-transform infrared
FWHM	Full width half maximum
GA	Gallic acid
HPLC	High-performance liquid chromatography
HPM	High-pressure membrane
HRSEM	High-resolution scanning electron microscopy
HRT	Hydraulic retention time
HRTEM	High-resolution transmission electron microscopy
HT	Hydrothermal precipitation
HTC	Hydrothermal carbonization
ICDD	International Centre for Diffraction Data
IE	Ion exchange
INE	Instituto Nacional de Estatística
IOC	International Olive Council
IUPAC	International union of pure and applied chemistry
IWI	Incipient wetness impregnation
LEP	Liquid entry pressure
M	Merck® activated carbon

MBR	Membrane bioreactor
MD	Membrane distillation
MF	Microfiltration
MOF	Metal-organic framework
MSC	Mathematical/model selection criterion
N	Norit® activated carbon
NF	Nanofiltration
O&G	Oil and grease
OD	Osmotic distillation
OH	Olive husk
OMW	Olive mill wastewater
OP	Olive pomace
OS	Olive stone
OSAC	Olive stone activated carbon
OSC	Olive stone char
OSG	Oxygenated surface groups
OW	Olive wood
PA	Protocatechuic acid
PFO	Pseudo-first order
pH_{pzc}	pH at point of zero charge
PILC	Pillared interlayered clay
PMP	*p*-methoxyphenol
PNP	*p*-nitrophenol
PP	Polypropylene
PSD	Pore size distribution
PSO	Pseudo-second order
PTFE	Polytetrafluoroethylene
PVDF	Polyvinylidene fluoride
QSDFT	Quenched solid density functional theory
RH	Organic compound
RMSE	Root mean square error
RO	Reverse osmosis
SA	Syringic acid
SD	Sawdust
SDAC	Sawdust activated carbon
SDC	Sawdust char
SEM	Scanning electron microscopy
SGMD	Sweep gas membrane distillation
STEM	Scanning transmission electron microscopy
TC	Total carbon
TDS	Total dissolved solids
TEM	Transmission electron microscopy
TGA	Thermogravimetric analysis
TG-DTG	Differential thermogravimetric analysis
TOC	Total organic content
TKN	Total Kjeldahl Nitrogen
TMP	Transmembrane pressure
TPh	Total phenolic content
TS	Total solids

TSS	Total suspended solids
Ty	Tyrosol
UF	Ultrafiltration
VA	Vanillic acid
VMD	Vacuum membrane distillation
VOC	Volatile organic compounds
VrA	Veratric acid
VSS	Volatile suspended solids
WFD	Waste Framework Directive
WL	Weight loss
XPS	X-ray photoelectron spectroscopy
XRD	X-ray diffraction
ZVI	Zero-valent iron
4-HbA	4-Hydroxybenzoic acid

LIST OF VARIABLES

A_0	(min^{-1})	Pre-exponential factor
C	(mg/L, g/L)	Concentration
D	(rad)	Full-width at half maximum
d_p	(mm)	Particle diameter
d_{XRD}	(nm)	Average Fe-crystallite size
E_A	(kJ/mol)	Activation energy
h	(mg/g·min)	Initial adsorption rate
J	($L/h·m^2$, $kg/h·m^2$)	Permeate flux
k	(min^{-1})	Rate constant
k_{app}	($L^2/mg·min·g_{Fe}$)	Apparent kinetic constant (per active metal phase)
K_F	($(mg/g)·(mg/L)^n$)	Freundlich constant
K_{id}	($mg/g·min^{1/2}$)	Intraparticle diffusion rate constant
K_L	(L/mg)	Langmuir constant
k_1	(min^{-1})	Pseudo-first order rate constant
k_2	(g/mg·min)	Pseudo-second order rate constant
L_0	(nm)	Mean micropore width
P	(Pa, kPa)	Pressure
P/P_0	-	Relative pressure
Q	(L/h, mL/min)	Flowrate
q_e	(mg/g)	Equilibrium adsorption capacity
q_m	(mg/g)	Maximum adsorption capacity
q_t	(mg/g)	Adsorption capacity (at time t)
R	(kJ/mol·K)	Ideal gas constant
S	(m^2)	Effective membrane area
S_{BET}	(m^2/g)	BET surface area
t	(min, h)	Time
T	(K, °C)	Temperature
V	(mL, L)	Volume
V_{gas}	(cm^3/g)	Adsorbed gas volume per adsorbed mass unit
V_{meso}	(cm^3/g)	Volume of mesopores
V_T	(cm^3/g)	Total pore volume

W_0	(cm^3/g)	Volume of micropores
W	(g)	Mass of catalyst/adsorbent
$(-r)$	($mg/min \cdot g_{Fe}$)	Reaction rate (per active metal phase)

Greek letters

α	(%)	Separation coefficient
β	-	Concentration factor
ΔP	(kPa)	Pressure difference
ΔT	(°C)	Temperature difference
γ_{Fe}	(g_{Fe}/g_{Cat})	Iron content per mass of catalyst
δ	(µm)	Membrane thickness
τ	(min)	Space-time
θ	-	Bragg's angle
λ	(Å)	X-ray wavelength

Subscripts

ads	Adsorbent
cal	Calculated
cat	Catalyst
eq	Equivalent
exp	Experimental
FC	Folin-Ciocalteau
theor	Theroretical

PART I

INTRODUCTION

CHAPTER 1

GENERAL INTRODUCTION

This chapter outlines the relevance and motivation of the proposed PhD thesis and provides a brief introduction to the subject of study. The main scientific and technological goals are established and the thesis outline is presented.

1.1. RELEVANCE AND MOTIVATION

The worldwide production of olive oil has substantially increased in the last three decades due to the technological conversion of many olive mills from traditional batch press processes to continuous operation centrifugation ones. Although traded globally, the extraction of olive oil is often carried out regionally in geographically dispersed facilities and through both extraction systems. Proper management of the large amount of waste/wastewater generated by this activity is a cost-ineffective process, particularly for small-to-medium-sized facilities. Olive mill wastewater (OMW) presents dark color, acidic pH, foul odor, and a high concentration of organic compounds (including, among many others, polyphenols, tannins, and lipids) [1,2]. Untreated disposal of OMW has been reported to cause several environmental hazards related to soil and water contamination, foul-smell, and plants growth inhibition [3,4]. OMW concentration in open air evaporation ponds or controlled land disposal are the most common practices among producers, while dried and de-oiled solid by products are typically sent to burn for energy recovery [5].

Several approaches have been applied for the treatment of OMW, including physical, biological, and chemical processes (as well as their combination) [1,6–8]. Dilution, evaporation, sedimentation, filtration, and centrifugation are simple physical treatments commonly employed in olive mills, but slow (in some cases) and ineffective [9]. Biological processes alone are not able to overcome the high organic load; moreover, micro-organisms' activity is inhibited by the toxicity of the pollutants, jeopardizing most biological treatment units [10,11].

Rising above such problems, several advanced oxidation processes (AOPs) have been studied for OMW treatment [12]. Among them, Fenton-based technologies have been distinguished for being able to oxidize complex organic compounds under mild conditions of temperature and pressure, employing simple and low-cost systems [13]. They are based on the reaction between ferrous ions (acting as the catalyst) and hydrogen peroxide in an acidic medium, producing hydroxyl radicals ($^{\bullet}OH$) that attack the organic molecules in a fast and non-selective way. However, the formation of a Fe-containing sludge and the narrow pH of operation are the main disadvantages of the homogeneous Fenton process. To overcome this problem, heterogeneous catalytic systems have been developed with Fe or Fe-oxides (or other transition metals) incorporated into porous supports using different carbon materials [14–16], clays [17], and

zeolites [18]. The vast and complementary experience of both thesis supervisors in this area was a major incentive for the proposal of a joint cotutelle thesis model for this work.

Among all possible supports for the catalyst, activated carbons (ACs) are particularly attractive thanks to their high porosity and surface area, stability in acid and basic media, and easily tunable surface chemistry [19]. Based on these properties, AC materials synthesized from solid residues of this industry (such as olive stones, wood from pruning, or olive pomace) could constitute a promising alternative to recycle and valorize such by-products, in line with the circular economy trend and the sustainability of the production processes [20,21]. The resulting AC materials may then be used as adsorbents or as solid matrixes for supporting the metallic active phase and be used in the heterogeneous Fenton oxidation (also known as catalytic wet peroxide oxidation, CWPO) of OMW.

Furthermore, as water becomes scarcer and more costly to obtain or purify, it is vital to prioritize wastewater treatment and reuse at its source. It is therefore proposed a combined treatment scheme that allows the downstream recovery of water by a separation process comprising a hydrophobic membrane distillation unit. The membrane unit should benefit from the potential of the oxidation process to reduce the organic load of the feed stream, and thus improve the production of water by reducing the decline of the membrane unit efficiency (e.g., by the concentration polarization effect, and membrane fouling or scaling) [22]. The integrated process would allow for solid and liquid waste recovery/reuse, as treated wastewater would be potentially used locally for crops irrigation or machinery washing.

1.2. OBJECTIVES

The main scientific and technological goals of this PhD thesis are:

- To evaluate the potential of Fenton and Fenton-based oxidation technologies for the treatment of OMW, particularly for the elimination of refractory organic substances (including the polyphenolic fraction) responsible for its eco- and phyto-toxicity. Moreover, reduction of the effluent's high organic load and enhancement of its biodegradability is also envisaged;
- The valorization of organic residues generated during the different steps of olive oil production (including olive stones and olive tree pruning) as carbon materials (e.g., biochars and ACs) for environmental applications related to adsorption and catalysis,

mainly focusing on the synthesis of iron-based catalysts for OMW treatment by the heterogeneous Fenton process;

- To optimize the morphological and chemical properties of the carbon materials by tuning the synthesis/activation process, as well as the active phase nature and dispersion of derivative Fe-catalysts to improve their catalytic performance and stability. This activity was favored by the expertise of the co-supervisor and specific equipment available in the R&D laboratories at the University of Granada;
- To find the best catalyst for the CWPO of target contaminants in a synthetic/simulated effluent. Screening of the prepared catalysts should initially be carried out in batch reactors as smaller amounts of samples are required. Then, the best catalyst(s) would be used in a tubular fixed-bed reactor (FBR) operating continuously, with inherent optimization of the operating conditions. Likewise, the expertise of the supervisor on catalytic reactors and processes, as well as the availability of experimental set-ups and analytical apparatus at the LEPABE laboratories, were essential for the ensuing tasks;
- The application of the selected catalytic system for OMW reclamation (using real effluents from a Portuguese olive oil manufacturer) and process optimization through a parametric study of various operational variables;
- To apply water-permeable membranes to recover the treated water by developing a combined AOP-membrane system. A direct contact membrane distillation (DCMD) unit is set to be integrated after the fixed-bed reactor and the operational conditions optimized to recover the highest possible amount of water, also evaluating the compliance with legislated values for safe disposal or use.

1.3. THESIS OUTLINE

In addition to the present Chapter 1, where the main scientific objectives and motivation behind this thesis are defined, the document is divided into ten additional chapters.

Chapter 2 presents an overlook of the past and current status of the olive oil processing industries, the main residues generated by this agro-industrial sector, as well as OMW characteristics, environmental risks, and current management practices. A thorough review of the scientific literature on this topic is discussed, focusing on the application of homogeneous Fenton/Fenton-based technologies, the development and use of heterogeneous catalysts for

CWPO, and the potentials of membrane technology for OMW treatment/reclamation. The two introductory chapters comprise Part I of this thesis.

Part II consists of Chapter 3, where the analytical methods and materials' characterization techniques adopted in this work are described.

Before the development and application of heterogeneous catalysts, homogenous Fenton and Fenton-like experiments were performed in both discontinuous and continuous reactors to evaluate the viability of the proposed process in OMW's organic matter degradation, phenolic content mineralization, and toxicity reduction. The results of these preliminary studies were compiled in Part III, where Chapter 4 reports the application of the classic homogeneous Fenton reagent for the treatment of a synthetic solution simulating OMW's polyphenolic composition. Several operational parameters, including Fe^{2+} and H_2O_2 dosages, pH, temperature, and space-time values, were sequentially evaluated for batch and continuous operation. In Chapter 5, the efficiency of Fenton/Fenton-like processes for the depuration of high-strength OMW samples is described. Different operational parameters such as type of iron salt used as catalyst, the effect of pH readjustments during the process, reactants addition methods, and Fe/H_2O_2 mass ratio, were evaluated in this study.

Part IV addresses the synthesis, characterization, and testing of several biochars and activated carbons derived from two raw organic by-products (olive stones – OS – and olive tree pruning – OTP) used as phenol adsorbents, as well their derivative heterogeneous Fe-based catalysts for the CWPO of OMW. Because adsorption is always the first step of the catalytic process, the interaction of the different ACs with the simulated OMW mixture was analyzed in the absence of H_2O_2 to determine their adsorption performance. The kinetics of adsorption and the adsorption isotherms were analyzed applying different models and results are presented in Chapter 6. In Chapter 7, the activity and stability of the resulting materials were screened for the oxidation of a synthetic polyphenolic solution and results compared to those obtained with catalysts supported onto commercial-AC materials (used for reference). The catalysts' activity towards adsorption and catalytic oxidation of the model pollutants in solution were correlated with their morphological and surface chemistry properties. Following the results of the previous screen tests, Chapter 8 reports the application of the most promising AC-supported catalyst impregnated with Fe: olive stone activated carbon (OSAC-Fe), prepared under sequential carbonization (under an inert N_2 atmosphere) and physical activation (under CO_2 atmosphere). Three distinct Fe-impregnation routes onto the OSAC-support were evaluated and the resulting catalysts used for the CWPO of

a synthetic solution. The two most promising materials were then tested for the depuration of real OMW samples under smooth operational conditions. The resulting effluent's phenolic character, toxicity behavior, and organic load were evaluated and checked for compliance with legal discharge limits.

Chapter 9 describes the operation of a FBR for continuous OMW treatment. Similar to the experimental layout reported in the previous chapter, the treatment of actual OMW samples and assessment of the process' efficiency was preceded by a parametric study of different synthesis conditions of the OSAC-catalysts, namely the iron salt precursor used and the Fe-loading. The catalysts were evaluated for the oxidation of synthetic solutions with distinct compositions, highlighting specific pollutant/catalyst interactions occurring in each case. Chapter 10 describes the operation of the proposed integrated treatment scheme, including the operation of the FBR and DCMD units for olive mill wastewater treatment and water recovery through the membrane separation unit. The possible recirculation of the retentate stream to the CWPO unit is also studied, and the quality of the produced permeate stream is evaluated.

Finally, Chapter 11 in Part V presents the main conclusions drawn from this PhD thesis, some of its limitations, and perspectives of future work.

REFERENCES

1. Amor, C.; Lucas, M.S.; García, J.; Dominguez, J.R.; De Heredia, J.B.; Peres, J.A. Combined treatment of olive mill wastewater by Fenton's reagent and anaerobic biological process. *J. Environ. Sci. Heal. - Part A Toxic/Hazardous Subst. Environ. Eng.* **2015**, 50, 161–168.
2. Nieto, L.M.; Hodaifa, G.; Rodriguez, S.; Giménez, J.A.; Ochando, J. Degradation of organic matter in olive-oil mill wastewater through homogeneous Fenton-like reaction. *Chem. Eng. J.* **2011**, 173, 503–510.
3. Ochando-Pulido, J.M. A review on the use of membrane technology and fouling control for olive mill wastewater treatment. *Sci. Total Environ.* **2016**, 563–564, 664–675.
4. Ntougias, S.; Gaitis, F.; Katsaris, P.; Skoulika, S.; Iliopoulos, N.; Zervakis, G.I. The effects of olives harvest period and production year on olive mill wastewater properties - Evaluation of Pleurotus strains as bioindicators of the effluent's toxicity. *Chemosphere* **2013**, 92, 399–405.
5. Roig, A.; Cayuela, M.L.; Sánchez-Monedero, M.A. An overview on olive mill wastes and their valorisation methods. *Waste Manag.* **2006**, 26, 960–969.
6. Lucas, M.S.; Beltrán-Heredia, J.; Sanchez-Martin, J.; Garcia, J.; Peres, J.A. Treatment of high strength olive mill wastewater by Fenton's reagent and aerobic biological process. *J. Environ. Sci. Heal. - Part A Toxic/Hazardous Subst. Environ. Eng.* **2013**, 48, 954–962.
7. Ochando-Pulido, J.M.; Victor-Ortega, M.D.; Martinez-Ferez, A. Performance modeling and cost analysis of a pilot-scale reverse osmosis process for the final purification of olive mill wastewater. *Membranes* **2013**, 3, 285–297.
8. Ioannou-Ttofa, L.; Michael-Kordatou, I.; Fattas, S.C.; Eusebio, A.; Ribeiro, B.; Rusan, M.; Amer, A.R.B.; Zuraiqi, S.; Waismand, M.; Linder, C.; et al. Treatment efficiency and economic feasibility of biological oxidation, membrane filtration and separation processes, and advanced oxidation for the purification and valorization of olive mill wastewater. *Water Res.* **2017**, 114, 1–13.
9. Gebreyohannes, A.Y.; Mazzei, R.; Giorno, L. Trends and current practices of olive mill wastewater treatment: Application of integrated membrane process and its future perspective. *Sep. Purif. Technol.* **2016**, 162, 45–60.
10. Fajardo, A.S.; Rodrigues, R.F.; Martins, R.C.; Castro, L.M.; Quinta-Ferreira, R.M. Phenolic wastewaters treatment by electrocoagulation process using Zn anode. *Chem. Eng. J.* **2015**, 275, 331–341.
11. Silva, A.M.T.; Nouli, E.; Xekoukoulotakis, N.P.; Mantzavinos, D. Effect of key operating parameters on phenols degradation during H_2O_2-assisted TiO_2 photocatalytic treatment of simulated and actual olive mill wastewaters. *Appl. Catal. B Environ.* **2007**, 73, 11–22.
12. Ochando-Pulido, J.M.; Pimentel-Moral, S.; Verardo, V.; Martinez-Ferez, A. A focus on advanced physico-chemical processes for olive mill wastewater treatment. *Sep. Purif. Technol.* **2017**, 179, 161–174.
13. Hodaifa, G.; Ochando-Pulido, J.M.; Rodriguez-Vives, S.; Martinez-Ferez, A. Optimization of continuous reactor at pilot scale for olive-oil mill wastewater treatment by Fenton-like process. *Chem. Eng. J.* **2013**, 220, 117–124.
14. Duarte, F.; Maldonado-Hódar, F.J.; Madeira, L.M. Influence of the characteristics of carbon materials on their behaviour as heterogeneous Fenton catalysts for the elimination of the azo dye Orange II from aqueous solutions. *Appl. Catal. B Environ.* **2011**, 103, 109–115.
15. Duarte, F.M.; Maldonado-Hódar, F.J.; Madeira, L.M. Influence of the iron precursor in the preparation of heterogeneous Fe/activated carbon Fenton-like catalysts. *Appl. Catal. A Gen.* **2013**, 458, 39–47.
16. Esteves, B.M.; Rodrigues, C.S.D.; Boaventura, R.A.R.; Maldonado-Hódar, F.J.; Madeira, L.M. Coupling of acrylic dyeing wastewater treatment by heterogeneous Fenton oxidation in a continuous stirred tank reactor with biological degradation in a sequential batch reactor. *J. Environ. Manage.* **2016**, 166, 193–203.
17. Ramirez, J.H.; Costa, C.A.; Madeira, L.M.; Mata, G.; Vicente, M.A.; Rojas-Cervantes, M.L.; López-Peinado, A.J.; Martín-Aranda, R.M. Fenton-like oxidation of Orange II solutions using heterogeneous catalysts based on saponite clay. *Appl. Catal. B Environ.* **2007**, 71, 44–56.
18. Queirós, S.; Morais, V.; Rodrigues, C.S.D.; Maldonado-Hódar, F.J.; Madeira, L.M. Heterogeneous Fenton's oxidation using Fe/ZSM-5 as catalyst in a continuous stirred tank reactor. *Sep. Purif. Technol.* **2015**, 141, 235–245.
19. Navalon, S.; Dhakshinamoorthy, A.; Alvaro, M.; Garcia, H. Heterogeneous Fenton catalysts based on activated carbon and related materials. *ChemSusChem* **2011**, 4, 1712–1730.
20. Demiral, H.; Demiral, I.; Karabacakoğlu, B.; Tümsek, F. Production of activated carbon from olive bagasse by physical activation. *Chem. Eng. Res. Des.* **2011**, 89, 206–213.

21. Ubago-Pérez, R.; Carrasco-Marín, F.; Fairén-Jiménez, D.; Moreno-Castilla, C. Granular and monolithic activated carbons from KOH-activation of olive stones. *Microporous Mesoporous Mater.* **2006**, 92, 64–70.
22. Wang, Y.; Wang, J.; Liu, L.; Cao, Z.; Wang, J.; Jia, M.; Ji, X. Treatment of coal gasification brine by membrane distillation: Effect of mixed fouling and pretreatment on process performance. *Desalination* **2021**, 499, 114820.

CHAPTER 2

STATE-OF-THE-ART

This chapter provides a brief overlook of the olive oil processing industry, the main residues generated, and current management practices of the most environmentally troublesome waste stream: olive mill wastewater (OMW). Advanced oxidation processes (AOPs), particularly Fenton-based technologies, are known for their ability to degrade a wide range of contaminants, even under mild operational conditions. To tackle the main drawbacks of the homogeneous Fenton process (i.e., the generation and downstream management of iron-rich sludge and the narrow pH of operation), the development of heterogeneous catalysts – where the catalytic active phase is supported into a solid matrix – has become the focus of recent scientific studies. The mechanism and operational parameters controlling the process, also known as catalytic wet peroxide oxidation (CWPO), will be reviewed throughout this chapter. The most recent developments in heterogeneous catalysts' synthesis and control are presented, with emphasis on activated carbon-supported catalysts prepared from organic residues. The most relevant state-of-the-art on Fenton and CWPO processes for OMW depuration is also presented and discussed. Moreover, since a combined OMW treatment and water recovery approach is envisaged, membrane separation technologies will be briefly addressed, highlighting the application of membrane distillation (MD) processes for OMW treatment/valorization.

2.1. OLIVE OIL INDUSTRY

The pollution of water sources, intensified by industrialization, fast urbanization, and climate changes, is a rising global crisis that threatens humans, wildlife, and environmental health. Contamination of water caused by industrial wastewater runoffs and non-compliant discharges, along with inefficient and/or excessive consumption of water, are, according to the European Commission, the leading factors threatening freshwater sources and disrupting aquatic ecosystems [1].

Agricultural and industrial activities are responsible for the major share of water consumption and pollution globally. In particular, the food processing industry is among the largest water-consuming activities per ton of product processed, with tap and groundwater representing a great fraction of its needs, which almost always entails financial costs to obtain and/or to purify [2].

According to the Food and Agriculture Organization Corporate Statistical Database (FAOSTAT) data on crops around the world, the water footprint of the olive oil processing industry (i.e., the sum of water used in all steps and unit operations required for extraction of olive oil) can be as high as 14 500 m^3 per ton of oil extracted [3–5]. Despite the seasonal production, wastewaters generated by olive mills may represent upwards of 50% relative to the total water inputs, depending on the extraction process used. As water becomes scarcer, it is of vital importance to prioritize wastewater treatment and reuse to maintain the sustainability of natural and urban water cycles [6].

The unsustainable use of resources and the exponential growth of waste produced yearly calls for a fast shift in the paradigm of “production-consumption-disposal” to circular economy models that favor the adoption of “waste-to-value” standards across all major polluting activities, as referenced in the revised Waste Framework Directive (WFD) of the European Union (EU) [7].

2.1.1. Brief characterization of the sector

Olive oil extraction is one of the utmost traditional agro-industrial activities in countries around the Mediterranean Sea. Olive oil extraction in that region represents approximately 91% of the total produced globally, corresponding to an estimated 3.2 million metric tons of olive oil in the 2019/2020 campaign, according to the International Olive Council (IOC) [8]. Data from the last decade (2010–2020) show that the EU alone is responsible, on average, for 69% of the worldwide

production – Fig. 2.1. During that period, Spain was the world's largest olive oil-producing country, with approximately 44% of the global share, followed by Italy (*ca*. 13%) and Greece (*ca*. 10%), while Portugal appears as the 4th biggest producer within the EU (9th at the global scale). Despite the prominence of the Mediterranean countries in the global panorama, other nations such as Argentina, Australia, Chile, China, or the USA, have considerably increased olive tree cultivars over the last few years, and domestic olive oil production is expected to expand further to satisfy the growing market for healthier oils [9].

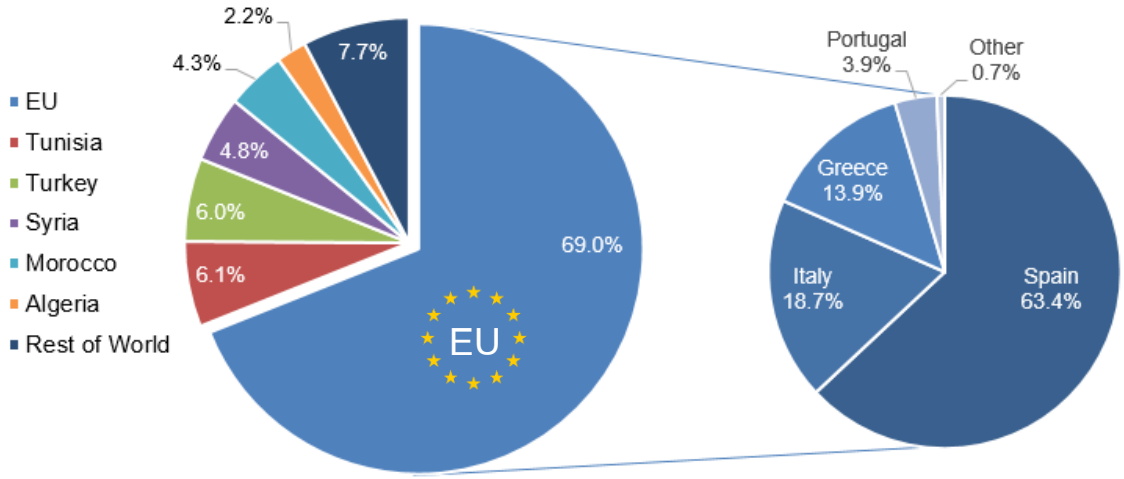


Fig. 2.1 Average worldwide olive oil production (in %) for the last decade campaigns (2010–2020), according to figures published by IOC (data collected from December 2021) [8].

Olive oil extraction is carried out in "olive mills", either by centrifugation processes or by traditional pressing methods. The extraction process initially involves a series of stages that are common to both extraction systems, namely [10,11]:

- Olives washing, to remove any physical impurities resultant from harvestings, such as leaves, twigs, and dirt;
- Grinding/crushing, to tear the flesh cells of olives and help release the oil from the fruit's vacuoles;
- Mixing/malaxation, which consists of slowly stirring the olive paste to increase the percentage of available oil for extraction.

Despite its outdated technology, the more traditional and discontinuous pressing method is still in use today. The extraction of the oil from the olives occurs by application of mechanical or hydraulic pressure to achieve the separation of the liquid phase (i.e., an emulsion of oil and vegetation water/wastewater) from the "solid fraction" (also known as pomace or olive cake, which is the

mixture of olive pulp and pits from the press phase and the added water/vegetation water generated during the process). The olive oil is finally separated from the liquid fraction through decantation or vertical centrifugation [12,13] – Fig. 2.2.

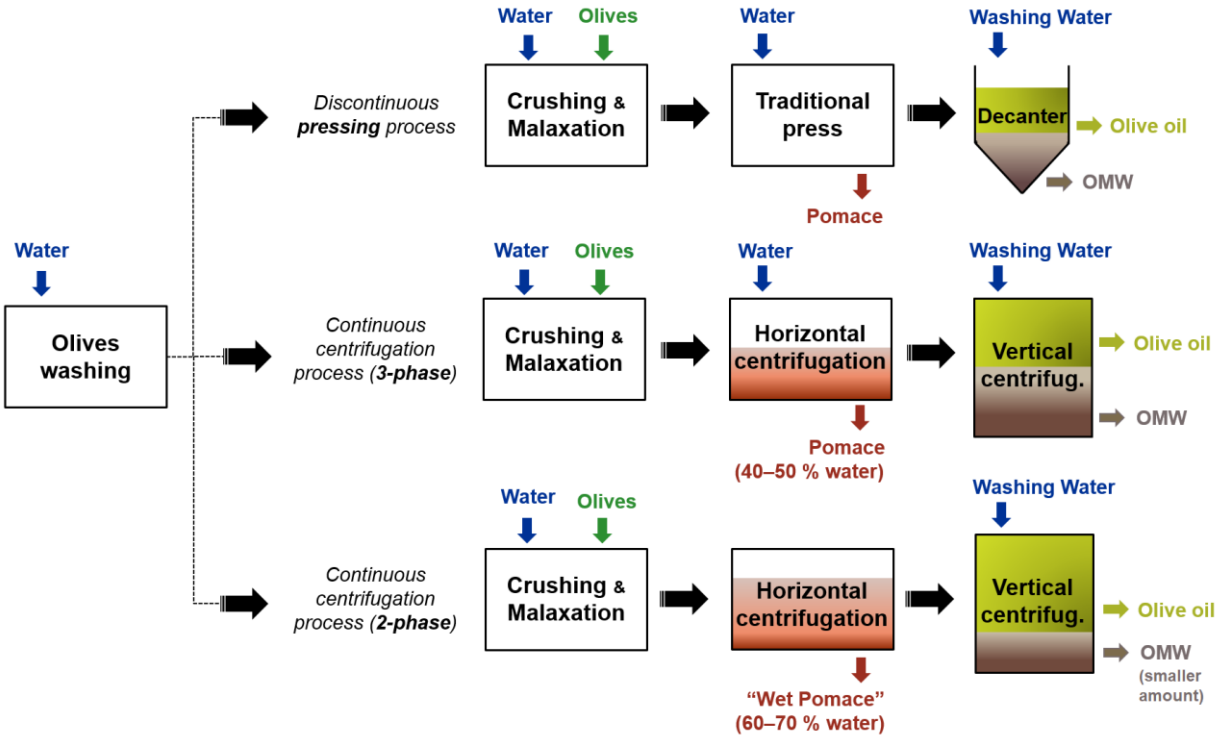


Fig. 2.2 Stages of the different olive oil extraction processes with indication of the main inputs/outputs.

Similar to the traditional process, the 3-phase decanter centrifugation system generates two streams of waste – OMW and pomace – and one stream of olive oil (Fig. 2.2). The 3-phase extraction system is based on the differences in density of the olive paste's constituents (water, olive oil, and insoluble solids). The continuous solid/liquid horizontal decanting system has higher productivity when compared to the traditional process due to its complete automation and smaller area of installation needed, allowing a higher ratio of olives processed over space and time. However, water and energy requirements are also higher, leading to higher operating costs and generation of larger wastewater streams [14].

Due to the ever-growing concern with environmental issues, a more "ecological" extraction unit was developed and commercialized under the denomination of 2-phase decanter centrifuge. The 2-phase system eliminates almost completely water consumption during the centrifugation stage, which consequently reduces the high amount of OMW produced otherwise. In this system, as the name indicates, two major fractions are generated: a "solid fraction" (commonly called wet pomace, due to the higher moisture content than the one generated in 3-phase systems) and

olive oil [13] – Fig. 2.2. Table 2.1 highlights the estimated values of water requirements per ton of olives processed for each system, the expected liquid and "solid" fractions generated, and the resultant olive oil yield.

Over the last three decades, the 2-phase technology has progressively substituted the 3-phase centrifugation system, particularly in Spain, where the large-scale implementation of this "ecological system" occurred just a few years after its arrival into the market. Growing environmental issues arising from poor OMW handling and disposal led to the rapid transition, which was supported by Spanish national policies through public funding, along with other preventive measures such as the construction of hundreds of storage ponds to promote OMW evaporation during summer time [13,15].

Table 2.1 Estimated input/output data for different olive oil extraction systems (adapted from refs. [12–14]).

(→) Inputs / (←) Outputs	**Traditional press**	**3-phase process**	**2-phase process**
(→) Olives	1000 kg	1000 kg	1000 kg
(→) Cold water[1]	0.10 – 0.12 m^3	0.10 – 0.12 m^3	0.10 – 0.12 m^3
(→) Heated water[2]	0.4 – 0.6 m^3	0.6 – 1.3 m^3	0.2 m^3
(←) OMW	0.6 m^3	1.0 – 1.6 m^3	0.2 m^3
(←) Pomace	400 kg (25% water content)	500 – 600 kg (40–50% water content)	800 – 950 kg (60–70% water content
(←) Olive oil	200 kg	200 kg	200 kg

[1] Cold water for olives washing

[2] Heated water for the press/centrifuges

In other olive oil-producing countries such as Italy, Greece, and Portugal, the switch has been much slower for several reasons, being the lack of financial resources to convert the existing 3-phase centrifuges the major one, particularly for small and medium-sized facilities [10,16]. Fig. 2.3 shows the evolution of olive oil extraction technologies adopted by Portuguese producers (particular, cooperative, and industrial facilities) since 1998, emphasizing the slower shift to the 2-phase system and the persistence of some traditional mills in the national panorama. The data also depicts the slow decay of the number of facilities in operation over recent years, highlighting

the drop that occurred in late 1999 due to the producers' financial inability to meet the newly adopted EU environmental standards during that period.

Despite its ecological label, the 2-phase system operation entails a major drawback often taken into consideration by olive oil producers: the management of the "new waste" generated by such centrifuges, with distinct physicochemical properties and higher moisture percentage. Pomace from 3-phase and traditional extraction systems are easily processed with organic solvents for the recovery of residual olive oil. This oil may then be used in soap production or even for human consumption, provided that minimum quality standards for consumption are met (in which case the oil is commercialized as olive pomace oil). The resulting dried solid fraction (mainly olive stones) is typically burned for energy recovery. However, due to the moisture content (*cf*. Table 2.1), wet pomace from 2-phase centrifuges presents major hindrances related to the drying process, as well as the day-to-day handling, transportation, and storage [12,13]. The high moisture and polysaccharides content often leads to waste agglomeration on the dryer walls. This can result in the blockage of gaseous streams, which poses a potential explosion hazard, forcing manufacturers to perform an additional purification step before drying [17]. Often, the excess of liquid from wet pomace is previously drained from the storage tanks in the extraction facilities, resulting in the accumulation of a smaller but concentrated fraction of OMW (in comparison to the 3-phase waste stream), which also requires adequate handling [18].

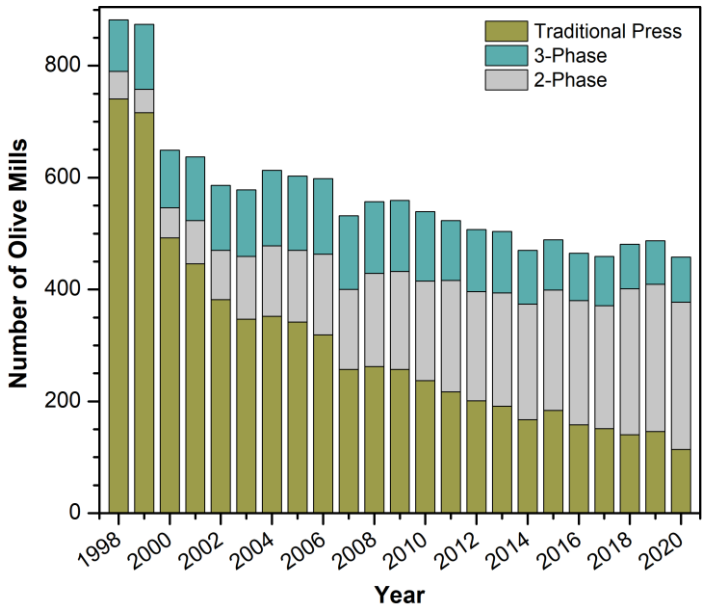


Fig. 2.3 Evolution of the olive oil extraction systems used in Portugal (1998–2020). Data collected from INE (Instituto Nacional de Estatística) [19].

2.1.2. Olive mill wastewater: characteristics and environmental issues

OMW is the common denomination for the olive's vegetable water and the water added during the oil extraction process. It's the main pollutant resulting from 3-phase and traditional press processes. Since auxiliary agents are rarely used for the extraction of olive oil, OMW composition will mostly depend on the intrinsic characteristics of the olives and vegetation water [14]. Still, the physicochemical properties of OMW are extremely variable depending on the olive variety, growing technique, harvest periods, and extraction method, to name a few. Some of the general characteristics include the dark-red to black coloration, slightly acidic pH, foul and very distinct smell, high organic content – as determined by analytical parameters such as chemical oxygen demand (COD), total organic carbon (TOC), or biochemical oxygen demand (BOD_5) – that include several phenolic compounds, lipids, fats, sugars, organic acids, tocopherols, carotenoids, tannins, etc.), and solid matter (e.g., total suspended solids, TSS, and total solids, TS), as well as the presence of residual oil and grease (O&G) [10,12,20]. Table 2.2 shows data collected from the literature on the main properties of OMW, highlighting the resulting wastewater composition heterogeneity even for the same extraction process.

Table 2.2 Summary of the main physicochemical characteristics of OMW according to the extraction method.

	Press		3-phase centrifuge				2-phase centrifuge		
pH	5.2	4.8	4.3	5.5–5.7	5.3	5.0	6.3–7.2	5.6	5.0
COD (g/L)	64.4	92.5	60.5	57.4–70.1	43.3	27.4	1.7–4.1	45.9	16.3
BOD_5 (g/L)	13.7	32.1	10.2	17.3–20.1	11.0	4.5	0.4–1.1	13.7	-
BOD_5/COD	0.21	0.35	0.17	0.25–0.35	0.25	0.16	0.23–0.27	0.30	-
TOC (g/L)	26.0	-	-	-	-	8.3	-	-	-
TPh (g GA_{eq}/L)	6.4	2.1	0.6	8.7–9.0	1.7	0.3	0.4–0.5	4.9	0.2
TS (g/L)	61.9	-	-	-	94.3	-	-	-	-
TSS (g/L)	-	67.5	6.8	-	34.1	-	-	-	3.1–5.8
TDS (g/L)	-	-	-	-	-	-	-	-	-
Salinity (g/L)	18.3	-	-	0.9–1.1	-	-	-	0.6	-
O&G (g/L)	-	-	-	-	-	11.0	-	-	-
Conductivity (mS/cm)	-	-	-	1984-2120	-	-	1.2–2.1	1277	1.8
Ash (% *w/w*)	-	-	-	9.0–9.7	-	-	0.1–0.5	9.3	-
Total P (g/L)	-	1.82	-	-	0.17	0.11	-	0.88	-
TKN (g/L)	-	-	-	-	0.23	0.18	-	1.3	-
Reference	[21]	[22]	[23]	[24]	[25]	[26]	[27] [1]	[24]	[28]

TPh: Total phenolic content; TDS: Total dissolved solids; Total P: Total phosphorus; TKN: Total Kjeldahl nitrogen.

[1] Mixture of OMW from decanters and water from washing tanks/olives.

- Values not reported by the authors.

OMW is mainly comprised of water (83–94% *w/w*) and organic compounds (4–16% *w/w*), which generally include organic acids, polyphenols, sugars, lipids, fats, and tannins. A smaller fraction (0.4–2.5% *w/w*), corresponding to mineral salts such as potassium, calcium, sodium, iron, copper, and traces of other elements, is usually reported [29–31]. Of particular importance is the phenolic fraction of olive stones and pulp (2–5% *w/w*) that tend to be more soluble in water than oil [31,32]. Phenolic compounds include several organic substances with at least one hydroxyl group directly bonded to an aromatic hydrocarbon group. It has been widely reported that phenolic compounds, along with some organic acids such as acetic and formic acids, are responsible for the phytotoxic and antibacterial action of OMW [33,34]. Table 2.3 shows a literature survey on the most

commonly reported phenolic compounds found in OMW samples, although more than 30 compounds were already identified [35,36].

Table 2.3 Phenolic compounds identified in different OMW samples, according to scientific literature data.

Phenolic Compound	Reference							
	[11]	[37]	[18]	[38]	[39]	[40]	[41]	[42]
3,4-dihydroxyphenylacetic acid	×							
4-hydroxyphenylacetic acid	×		×					×
4-hydroxybenzoic acid						×		
Apigenin	×		×					
Caffeic acid	×	×	×	×		×	×	×
Cinnamic acid			×					
Ferulic acid		×	×					
Gallic acid	×		×	×				×
Hydroxytyrosol	×		×	×		×	×	
Luteolin	×							
Luteolin-7-O-glucoside	×		×					
Oleuropein			×	×			×	×
Protocatechuic acid		×				×	×	
Sinapic acid			×					
Syringic acid		×	×		×			
Tyrosol	×		×	×	×	×	×	
Vanillic acid	×	×	×			×		
Veratric acid								×
ρ-coumaric acid		×	×	×			×	×

The effluent's high organic load and bio-recalcitrant nature of some of its compounds make the proper treatment of OMW a complex subject and thus a potential threat to the environment. The uncontrolled disposal of OMW in olive crops may reduce soil fertility and cause phytotoxic effects on olive trees [17,43]. Also, the direct discharge of untreated OMW on water bodies is known to cause, among others, the following major impacts [14,17,44,45]:

- Discoloration, as a result of oxidation and subsequent polymerization of tannins;
- Formation of impenetrable films in the water surface due to the presence of lipids, resulting in the blockage of sunlight and oxygen to microorganisms and plants;

- The proliferation of strong odors related to the fermentation phenomena that occurs whenever OMW is stored in natural lagoons or open reservoirs (tanks, evaporation ponds);
- Overall threat to aquatic life, since the organic load can be more than one hundred times higher than the one from domestic sewage, causing the overall reduction of the oxygen availability and thus an imbalance in the whole ecosystem. Excess nutrients also result in unwanted development of algae and consequent eutrophication.

Considering that an average-sized olive mill generates more than 15 m^3 of OMW per day [9,14], it is estimated that 10–30 million cubic meters are released to the environment in the Mediterranean region every year [31]. The seasonality of the olive oil industry (usually from November to February), the territorial scattering of most small/medium-sized facilities, and the large amounts of highly loaded and hardly degradable OMW generated pose severe technical and economic barriers to the appropriate wastewater management [32,46]. The insufficiency or lack of specific treatment plants/processes combined with occasional bad practices of producers – like direct dumping of OMW in soils or rivers nearby – make OMW a very pollutant and troublesome waste in several regions [13].

2.1.3. Management practices and EU environmental policy

By the end of the last century, stricter legal actions against the disposal of untreated OMW have been put into force, particularly in Europe. However, since there is no common policy among EU members, the adoption of a specific legislative framework concerning olive mill discharges is still left for each country. The lack of common regulation led to the adoption of different standards, physicochemical parameters, and threshold values for olive mill waste safe disposal and use across EU members [12,15].

The discharge of untreated OMW into natural water bodies is strictly forbidden in all EU countries due to the negative environmental impacts already mentioned in the previous section. Direct discharge of OMW into public/municipal sewage collectors is also often prohibited (or limited), as the low pH, high organic load, and high level of refractory organic compounds may originate imbalances in the biological reactors of domestic wastewater treatment plants. Nonetheless, dumping of OMW in nearby rivers, lakes, or municipal collectors is still known to happen nowadays, particularly in remote locations where small-sized facilities deal with financial and

operational struggles in waste management (related to transportation, storage, and treatment) [9,34,47].

As discussed earlier, the main residual products generated during olives processing are leaves and twigs, olive pomace, and OMW. Leaves and twigs are, most frequently, either landfilled or used for animal feeding, while olive pomace's commercial value will depend on its oil and water content, variable upon the extraction method used. As for OMW, the common management practice in many Mediterranean countries for 3-phase and traditional press liquid fraction is the storage in evaporation ponds, where the slow and progressive degradation of the organic matter occurs via the microorganism's action (under aerobic or anaerobic conditions). Nonetheless, this method requires a large installation area, and it is prone to the contamination of groundwater/aquifers, odor nuisance, and proliferation of insects [13,32].

The controlled spreading of OMW on crops offers an alternative and cost-effective solution to the illegal dumping practices often observed. Some reports suggest that irrigation with OMW improves the nutrient content and enhances soil fertility [48,49], while others advocate that it may increase the crop yield or even replace conventional fertilizers [50]. However, this management solution is controversial since the physicochemical characteristics and the amount of OMW are highly variable, and negative effects are commonly reported, namely the ones related to the presence of phytotoxic compounds (e.g., polyphenolic fraction), high salinity, and low pH [13,51].

To prevent such problems, many countries limit volumes, flow rates, and timings for OMW soil/land disposal. In Portugal, each municipality is responsible to define the discharge limit value for industrial wastewaters, according to the physicochemical parameters defined in "Decreto-lei (Decree-law) 236/98" [52]. The point of discharge and receiving water body, as well as the frequency of discharges, are subject to approval and licensing by local regulatory entities. Portuguese legislation ("Despacho conjunto 626/2000" [53]) also defines the terms in which OMW may be used for irrigation purposes: besides the obligation to have a permit emitted by responsible entities, olive mills must own a pond (or lagoon) dedicated to wastewater storage during the harvest season; neutralized OMW may be used for trees and bushes irrigation (under defined geographical limits) to the maximum of 80 m^3/ha per year [6,15].

According to environmental legislation in Italy, all OMW must be preventively treated to reach a minimum of 50% organic load reduction. However, due to the operational and financial difficulties to comply with these standards, new legislation was promulgated (Law no. 574/1996 along with

the Ministry Decree from 6th of July 2005) that outlines the terms for OMW disposal and use. For instance, it is defined that the storage of untreated OMW in any reservoirs should not be extended for more than 30 days, whereas direct land application is limited to 50 m^3/ha per year if traditional press process is used, or to 80 m^3/ha per year for wastewater resulting from continuous centrifuge systems.

In Spain, the discharge of untreated OMW is prohibited since 1981, when most olive oil extraction took place in three-phase process units (and consequently massive amounts of effluents were generated). The pollution of river basins was so problematic that the Spanish government established a legal framework to completely prohibit discharges and subsidized the construction of hundreds of evaporation ponds nation-wide. More recently, similarly to the Italian legislation, the Andalusian Regional Government has passed a law (Decree-law no. 4/2011) that establishes threshold limits for OMW disposal in agricultural soils [10,12,31].

2.1.4. OMW treatment/valorization technologies

Several treatment/valorization processes and integrated treatment schemes have been evaluated and implemented to address the challenges posed by OMW management. Fig. 2.4 presents a brief overlook of the state-of-the-art concerning OMW management, highlighting the scientific research's focus distribution by the treatment scheme studied. The survey comprises close to 350 scientific papers available on the Scopus database over the last 15 years (2006-2021), mostly reporting technologies implemented at lab-scale, though some studies at pilot-scale and industrial-scale are also available.

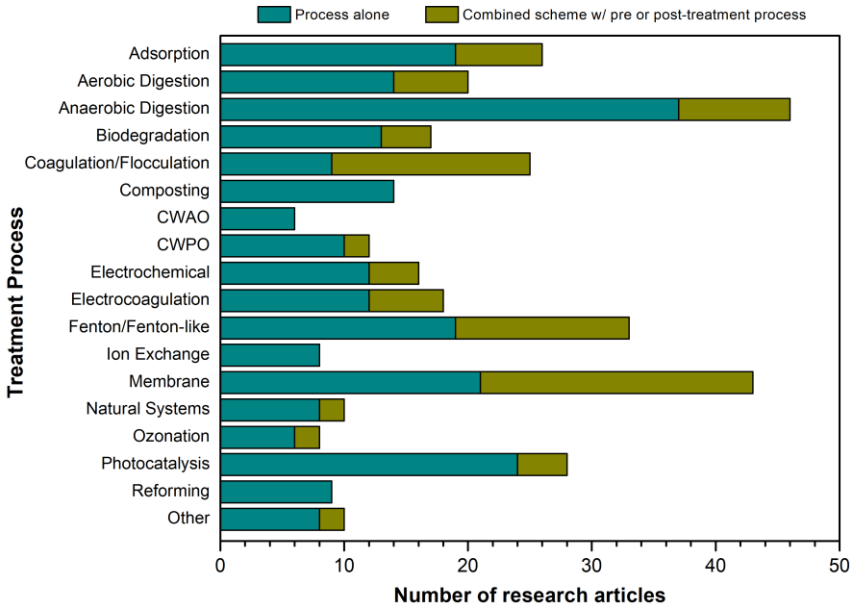


Fig. 2.4 Overlook of the different OMW treatment processes from several research articles published between 2006-2021 (based on Scopus database search with combinations of keywords such as "OMW" or "olive mill wastewater" with "CWPO", "Ion Exchange", etc.).

From the survey, it is clear that early on, most management technologies reported in the literature were primarily focused on bioremediation technologies by aerobic [54–56] and anaerobic digestion [57–59]/co-digestion [60–62] processes, often coupled with conventional pre-treatment units such as coagulation/flocculation [63–65], and/or adsorption [66], to preventively reduce the strong antibacterial activity of polyphenols. Other physicochemical processes such as electro-coagulation [67,68] and sedimentation [69] were also commonly investigated, either as a single-stage process or as a pre-treatment step [70]. Apart from the simple remediation of OMW, the two main olive waste valorization techniques proposed were: (1) the generation of biogas through anaerobic digestion, and (2) the production of organic fertilizers from co-composting of olive cake (pomace/wet pomace) and/or olive mill wastewater [71–73].

More recently, following the reports that some polyphenols from OMW present interesting antioxidant and potential cancer-preventing activities [74], which may be useful in pharmaceutical, cosmetic, and food industries [36,75], the extraction and recovery of polyphenols from OMW gained traction in the scientific community [41,76,77]. Despite the new insights on polyphenols properties, OMW detoxification technologies remained the main focus of scientific papers, with efforts being shifted from biological processes to advanced oxidation processes, primarily by photocatalysis [25,28,78,79], catalytic wet air oxidation (CWAO) [23,80], and ozonation [81,82], followed by Fenton [83–85] and Fenton-based processes, such as Fenton-like [86–88],

photo-Fenton [25,89,90], electro-Fenton [91–93], and CWPO (also known as heterogeneous Fenton process) [94–97].

Over the last decade, the integration of different membrane-related processes for OMW treatment/valorization has also become increasingly predominant in scientific reports. Due to the availability of new membrane materials and designs [31,98], as well as increasing general know-how on membrane fouling mechanisms [9], many researchers turned their attention to the potential of microfiltration, nanofiltration, ultrafiltration, biofiltration, reverse osmosis, and membrane distillation, for both OMW management and polyphenol concentration/recovery [99–107].

Since the success of any given technology not only depends on the intrinsic characteristics of OMW, but also on the socio-economic landscape of the olive oil industry, it is vital to prioritize the adoption of simple and cost-effective strategies adaptable to this agro-industrial sector [16]. The consensus acquired from the literature survey is that stand-alone processes are frequently unable to cost-effectively produce treated-OMW that meets legislated thresholds for safe discharge (either in water bodies or wastewater treatment plants). Within this context, many authors propose the implementation of integrated or hybrid treatment schemes, often including physicochemical units (natural evaporation, thermal concentration, coagulation/flocculation, or adsorption) and/or chemical remediation technologies (namely AOPs). Due to their simplicity, the first are commonly used as pre-treatment strategies to reduce the effluent's initial volume through concentration of organic and inorganic compounds, though only transferring the pollutant from one phase to another; the latter are known for their potential to degrade a wide range of substances, including OMW bio-refractory and recalcitrant compounds, but efficiencies are typically dependent on operating conditions (oxidant and catalyst doses, temperature, pressure, among others) and may require specific equipment and technology.

Among the different AOPs, Fenton-based technologies are known for their oxidative potential towards complex effluents and the equipment's simplicity and operational ease (particularly in the case of the classic Fenton reagent and heterogeneous Fenton-like processes). The next section provides a brief overview of this topic, emphasizing the most recent advances in the development and application of heterogeneous Fenton-like catalysts for wastewater depuration.

2.2. ADVANCED OXIDATION PROCESSES

AOPs are based on the generation of highly reactive and non-selective radicals (including the hydroxyl radical, •OH), capable of attacking most organic and many inorganic solutes with high rate constants (typically in the range of 10^6–10^9 L/mol·s), and are among the most promising techniques for water and wastewater treatment [108,109]. The versatility of AOPs is also enhanced by the fact that there are multiple ways to produce •OH species – chemical, electrochemical and photochemical – which allows selecting the process that better suits any specific treatment requirement [110]. The diagram presented in Fig. 2.5 showcases the most common AOPs used for water/wastewater treatment, classified as to their reactive phase: homogeneous, when the catalyst is dissolved in the solution forming a single phase, and heterogeneous, whenever catalytically active species are anchored or supported onto the matrix of a solid phase such as activated carbon, zeolite, clay, xerogel, nanotube, etc. [111,112].

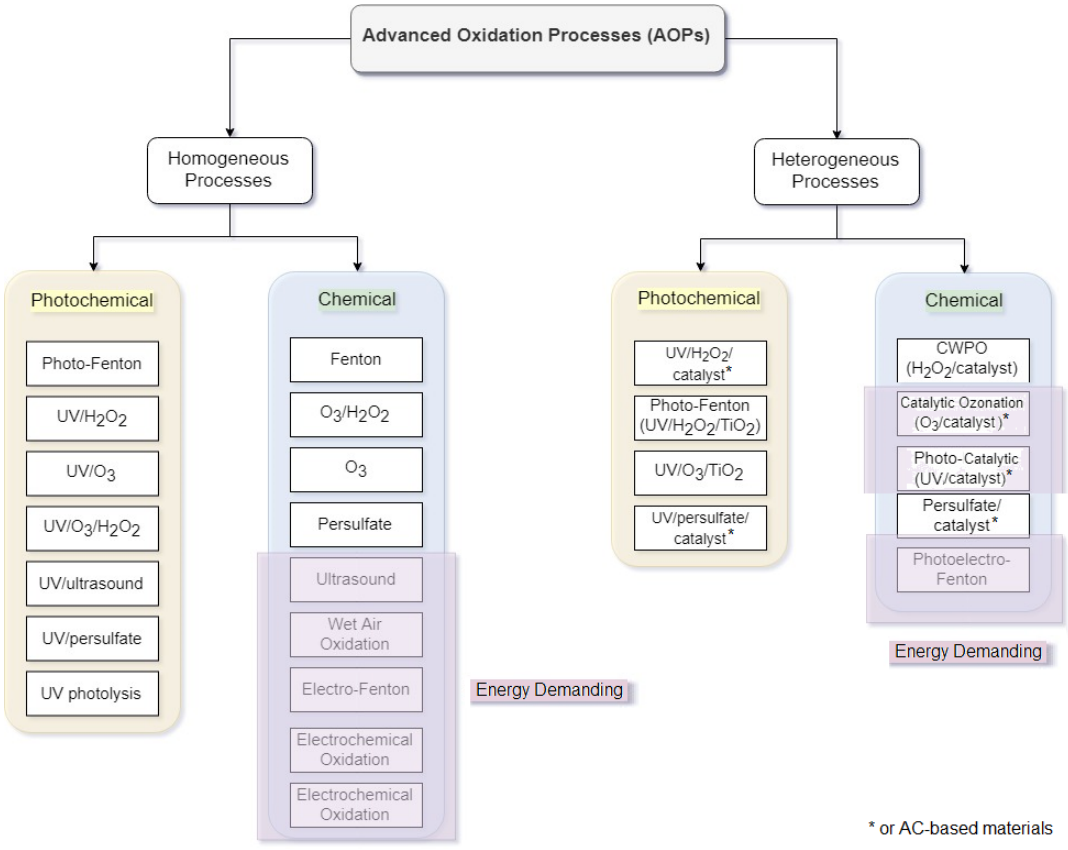


Fig. 2.5 Diagram representation and classification of several AOPs for water/wastewater treatment.

2.2.1. Fenton process

2.2.1.1. Free radical mechanism

The Fenton process is one of the most well-known AOPs and its reaction mechanism has been thoroughly described in the literature over the last decades [113–115]. More than a century ago, H. J. Fenton (1894) reported that the oxidative potential of hydrogen peroxide is strongly improved in the presence of ferrous ions [116]. Later, Haber and Weiss (1934) identified the highly oxidative species in that reaction as hydroxyl radicals, generated by the catalytic decomposition of H_2O_2 in the presence of ferrous ions in an acidic medium, according to Eq. (2.1) [117]. Organic compounds (RH) are non-selectively attacked and oxidized by •OH species – Eq. (2.2) – either by hydrogen abstraction, addition to double bonds, or electron transfer, depending on the structure and ionization potential of the target organic pollutant [118]. Complete mineralization of the organic compounds may be achieved, provided that the lower molecular weight oxidized intermediates are completely decomposed up to H_2O and CO_2 – Eq. (2.3).

$$Fe^{2+} + H_2O_2 \rightarrow Fe^{3+} + {}^{\bullet}OH + OH^- \quad (2.1)$$

$${}^{\bullet}OH + RH \rightarrow H_2O + intermediates \quad (2.2)$$

$${}^{\bullet}OH + intermediates \rightarrow H_2O + CO_2 \quad (2.3)$$

Additionally to the reaction shown in Eq. (2.1), Fenton's complex free radical and chain mechanism can be summarized and described by Eqs. (2.4)–(2.10), whereas common reaction rates for each step may be found in the literature [119]. One of the main steps is the regeneration of Fe^{2+} that guarantees the cyclical continuity of the process, known as the Fenton-like stage – Eqs. (2.4) and (2.5). This stage, which is much slower than the Fenton one – Eq. (2.1) – involves the generation of less oxidative hydroperoxyl radicals ($HO_2^{\bullet}$) that also contribute to the regeneration of ferrous ions – Eq. (2.6). Competing reactions involving hydroxyl radicals may also occur depending on the operating conditions. Excess of oxidant and/or catalyst – Eqs. (2.7) and (2.8) respectively – are usually responsible for the scavenging of •OH radicals and may limit the overall process efficiency. Likewise, the occurrence of radical-radical reactions depicted in Eqs. (2.9) and (2.10) may result in process hindrance [115].

$$Fe^{3+} + H_2O_2 \leftrightarrow \mathrm{Fe-OOH}^{2+} + H^+ \quad (2.4)$$

$$\mathrm{Fe-OOH^{2+}} \rightarrow Fe^{2+} + HO_2^{\bullet} \quad (2.5)$$

$$Fe^{3+} + HO_2^{\bullet} \rightarrow Fe^{2+} + \mathrm{O_2} + H^{+} \quad (2.6)$$

$$^{\bullet}OH + H_2O_2 \rightarrow H_2\mathrm{O} + HO_2^{\bullet} \quad (2.7)$$

$$^{\bullet}OH + Fe^{2+} \rightarrow Fe^{3+} + OH^{-} \quad (2.8)$$

$$^{\bullet}OH + HO_2^{\bullet} \rightarrow O_2 + H_2\mathrm{O} \quad (2.9)$$

$$^{\bullet}OH + {}^{\bullet}OH \rightarrow H_2\mathrm{O_2} \quad (2.10)$$

Among the wide range of advantages related to the Fenton process, operation at near-ambient temperature and atmospheric pressure stand out in comparison to other energy-demanding advanced oxidation techniques (i.e., the so-called hybrid methods that enhance the process, such as photo-Fenton, electro-Fenton, etc.). The equipment's simplicity and ease of operation, along with the use of an environmentally safe oxidant (H_2O_2), which can be broken (or decomposed) down into H_2O and O_2, are also major advantages of Fenton's reagent [16]. The application of Fenton's oxidation for the treatment of different industrial wastewaters containing a wide range of organic compounds has been extensively studied ever since Fenton's reagent has been discovered, particularly by the pharmaceutical, textile, agro-food, pulp and paper, and cosmetic industries. High reduction of organic load (in terms of COD and TOC), mineralization of hazardous compounds, reduction of overall toxicity, and biodegradability improvement are often achieved with Fenton oxidation. Pignatello *et al.* [109] extensive review offers additional insights on the reaction mechanism and pathways, also providing several examples of Fenton reagent's application for water, wastewater, and soil treatment.

2.2.1.2. Key operational parameters

The main operational parameters governing Fenton/Fenton-like reactions are related to the process characteristics, including reaction's pH and temperature, pollutant load (both concentration and characteristics of the compounds in solution), and reagents (i.e., catalyst and oxidant doses).

A strict acidic range of operation (pH of 3.0–3.5) is well-known to maximize Fenton reagent's efficiency, as the maximum concentration of Fe^{2+} active species is achieved at the lowest rate of H_2O_2 parasitic decomposition [120]. Lower pH values are reported to slow down the formation of iron (III)-peroxo complexes (as intermediates, *cf.* Eq. (2.4)), interfering with the Fe^{3+}/Fe^{2+}

regeneration cycle [109]. High pH values may lead to the precipitation of relatively inactive and insoluble ferric oxyhydroxides reducing ferric ions availability, and reaction depicted in Eq. (2.4) becomes the rate-limiting step, while at low pH the decomposition of H_2O_2 is accelerated [108].

The system's temperature also plays an important role since oxidation proceeds at a faster rate for higher temperatures due to the exponential dependence of kinetic constants (*k*) – either for radical production, iron regeneration, or organics attack – with the Arrhenius law (Eq. (2.11)),

$$k = A_0 exp\left(-\frac{E_a}{RT}\right) \quad (2.11)$$

where A_0 is the pre-exponential factor, R is the ideal gas constant, E_a the activation energy, and T the temperature. This dependence is particularly evident between 10 and 40/50 °C, as reported by several researchers [121–123]. Apart from the added energy consumption costs, the excessive increase of reaction temperature can promote H_2O_2 self-decomposition into molecular oxygen (Eq. (2.12)), hindering the formation of oxidizing species (and thus oxidation rates) [27,124].

$$2H_2O_2 \rightarrow O_2 + 2H_2O \quad (2.12)$$

The cost-effective application of most AOPs also depends on the nature and concentration of the pollutant(s)/wastewater matrix. High or close to complete mineralization via Fenton/Fenton-like processes is almost always favored at lower concentrations of the target compound(s) [125,126]. Nonetheless, while the mineralization of aromatic substances (e.g., phenol) by ring cleavage and subsequent oxidation may be easily accomplished by •OH action, the electrophilic attack of conjugate C=C bonds is much less effective (e.g., cyclohexanol, as reported by Ruppert *et al.* [127]).

The vast majority of scientific studies in the literature report the treatment of phenolic compounds/solutions and dye molecules/solutions. Phenolic compounds are among the most abundant pollutants present in industrial wastewaters, owing to their widespread utilization in the synthesis of pesticides, solvents, lubricating oils, dyes, and resins [128], but also as naturally-occurring compounds, such as the case of olive mill wastewater [129] or winery wastewater [130]. Dyes and pigments are also frequently reported due to their widespread use as coloring agents in the textile, food, and pharmaceutical industries [131]. In brief, Fenton-like processes have proved to be effective on the degradation of both classes of refractory compounds, but technical and economic drawbacks arise when dealing with high organic loads

since the amount of oxidant required becomes substantially greater, and inherently so does the concentration of transition metal to catalyze all H_2O_2.

Lastly, catalyst and oxidant doses are intrinsically related. For the vast majority of target compounds/wastewaters and operational conditions, an increase in the relationship between catalyst/oxidant mass ratio leads to higher degradation efficiencies [114]. However, excess of either reagent may cause unwanted parallel reactions, particularly via the scavenging reactions mentioned earlier (Eqs. (2.7)–(2.10)). When $[Fe]_0 << [H_2O_2]_0$, the decomposition of H_2O_2 is slower and •OH generated may react with available H_2O_2 (via Eq. (2.7)) at a greater extent than with RH or reaction intermediates (Eqs. (2.2)–(2.3)). On the contrary, if $[Fe]_0 >> [H_2O_2]_0$ the chain reaction mechanism is quickly terminated as •OH produced in Eq. (2.1) reacts primarily with Fe^{2+} via Eq. (2.8), since this reaction is about ten times faster than the one with H_2O_2 (Eq. (2.7)) [132,133]. The presence of organic compounds under such operational conditions may lead to the competition with ferrous ions for •OH (Eqs. (2.8) and (2.2)-(2.3), respectively), also negatively affecting the process' efficiency.

Consequently, the estimation of the stoichiometric H_2O_2 amount required to theoretically mineralize all the organic carbon (C) present in the solution is often a useful tool. Following the stoichiometry of the reaction presented in Eq. (2.13), an H_2O_2/C molar ratio of 2 (equivalent to a 5.7 mass ratio) is necessary to complete carbon depletion (as TOC content) [134]. Alternatively, assuming complete conversion of H_2O_2 into O_2, the stoichiometric weight ratio between oxidant and effluent's initial COD can also be used: H_2O_2/COD = 2.125 [85]. In practice, because H_2O_2 participates in unwanted parallel reactions, the oxidant dose applied is often higher than the theoretical stoichiometric one.

$$C + 2H_2O_2 \rightarrow CO_2 + 2H_2O \quad (2.13)$$

2.2.1.3. OMW treatment by Fenton processes

Of particular interest for this thesis is Fenton's application for olive mill wastewater depuration. Several articles dealing with OMW treatment by Fenton and Fenton-like reactions (i.e. catalyzed by ferric ions or other transition metals such as Cu, Co, or Mn), often coupled with pre-treatment steps (such as coagulation/flocculation) or post-treatment biological stages (aerobic and anaerobic), are available in the literature. Table 2.4 summarizes the main research findings in this

field, with indication of OMW source, the scale of operation, operational conditions, and achieved standards.

Lucas *et al*. [85] reported on the application of Fenton's reagent for the removal of COD from an OMW resulting from a traditional press process in Portugal. The authors concluded that the application of the process alone is a viable method to partially treat diluted OMW samples, achieving a significant chemical oxygen demand reduction (*ca*. 70%) at pH = 3.5, T = 30 °C, $[H_2O_2]/[Fe^{2+}]$ = 15, and H_2O_2/COD = 1.75 (*w*/*w*).

Iboukhoulef *et al*. [86] examined the removal of phenolic compounds from a diluted OMW sample by the Cu(II)/H_2O_2 system. Total phenolic content (TPh) removal yield increased with reaction temperature, from 43% at 30 °C to 62% at 50 °C, after 65 min of treatment. Alver *et al*. [26] performed a parametric study to optimize the different conditions of the sequential coagulation/flocculation and Fenton system. Different Fe^{2+} and H_2O_2 dosages, pH, and $[Fe^{2+}]/[H_2O_2]$ ratios were evaluated and optimized by statistical analysis. At pH = 3, $[Fe^{2+}]$ = 2.5 g/L, and $[Fe^{2+}]/[H_2O_2]$ = 2.5 (*w*/*w*), over 65% of COD and 87% TPh removals were obtained; as expected, higher treatment efficiency was achieved from the integrated process than with the coagulation step alone.

Amor *et al*. [22] concluded that the combination of Fenton oxidation with the anaerobic biological treatment resulted in a better performance of the biological step since some inhibitory compounds were previously removed from the wastewater by oxidation. A similar assessment was drawn by Maamir *et al.* [135] as the Fenton stage resulted in an increase of 82, 43, and 32% soluble COD, delignification, and hemicellulose degradation, respectively, allowing higher methane yields (10% increase) from pre-treated samples of OMW.

Hodaifa *et al*. [87] conducted a study on the optimization of OMW reclamation by the Fenton-like process in a continuous stirred-tank reactor (CSTR) at a pilot-scale. The authors found that the reaction with Fe^{3+} was strongly pH-dependent (optimum pH = 3), and that operating with $[FeCl_3]/[H_2O_2]$ in the 0.026–0.058 (*w/w*) range, the produced water was suitable for irrigation or discharge into municipal wastewater collectors (final COD = 129 mg/L and TPh = 0.5 mg/L, upon 3 h residence time). Martínez-Nieto *et al*. [136] conducted experiments at an industrial-scale with a similar OMW, i.e., a mixture of olives and olive-oil washing wastewaters 1:1 (*v/v*) from a 2-phase extraction system. The industrial plant layout consisted of an oxidation reactor, followed by a neutralization tank, decanter, and filtration system. The iron-sludge accumulated in the decanter

was recirculated to the system and successfully used in the oxidation process. The exit wastewater stream was free of pesticides, odor, and color, with negligible phenolic content.

As most case studies underline, the efficiency of homogeneous Fenton and Fenton-like processes for OMW depuration typically rely on:

- The acidification of the effluent to pH values in the 2–4 range to maximize global removal efficiencies, though the naturally-occurring acidic pH of OMW combined with catalyst addition may help reduce costs associated with reagents, as pointed by Hodaifa *et al.* [87];
- The use of stoichiometric (or higher) catalyst/oxidant amounts to face the high organic load of most OMW samples, increasing the associated reagents' costs and enhancing the drawbacks related to the downstream generation of iron-rich sludges. Typically, such constraints are also only partially solved, either by the implementation of pre/post-treatment steps or by dilution of the effluent before treatment to decrease reagents' consumption requirements;
- The adoption of H_2O_2 addition strategies to help reduce the competitive H_2O_2-consuming and radical scavenging reactions resulting from the high oxidant doses required, namely the step addition of H_2O_2 or its continuous feed over time [137,138].

Table 2.4 Summary of Fenton and Fenton-like processes applied for OMW treatment, either as single stage units, or combined with other treatment processes.

OMW Source	Process Flow-Scheme	Scale	Oxidation Experimental Conditions	Achieved Standards	Observations	Ref.
Traditional press (Spain) pH_0 = 4.8, COD_0 = 92.5 g/L, TPh_0 = 2.1 g/L, BOD_5 = 32.1 g/L	Fenton + Anaerobic Digestion	Lab-scale	T = 30 ºC, pH = 3.5, $[H_2O_2]$ = 0.55 mol/L, $[Fe^{2+}]$ = 0.0367 mol/L	Fenton removals: COD = 17.6%, TPh = 82.5% Global: COD = 64–88%	Global process leads to increase in CH_4 yield and COD removal (compared to anaerobic step alone)	[22]
3-phase centrifuges (Turkey) pH_0 = 5, TOC_0 = 8.3 g/L, COD_0 = 27.4 g/L, TPh_0 = 0.26 g/L	Coagulation + Fenton	Lab-scale	pH = 3, $[Fe^{2+}]$ = 2.5 g/L $[Fe^{2+}]/[H_2O_2]$ = 2.5, t = 20 min	Global removals: COD = 65.5%, TPh = 87.2%	Coagulation step alone: COD = 51%; TOC = 39%, TPh = 52%	[26]
2-phase storage lagoon (Spain) pH_0 = 10, COD_0 = 12.2 g/L, TPh_0 = 0.55 g/L, TSS = 2.1 g/L	Coagulation/ Flocculation + Fenton	Lab-scale	T = 21 °C, pH = 3, $[H_2O_2]/[Fe^{2+}]$ = 4–6	Global removals: COD = 90%, TPh = 92%, TSS = 95%, BOD_5/COD from 0.05 to 0.52	Pre-treatment step allowed for 82%, 59% and 90% COD, TPh and TSS removal	[84]
Traditional press (Portugal) pH_0 = 4.3, COD_0 = 60.5 g/L, TPh_0 = 0.56 g/L	Fenton	Lab-scale	pH = 3.5, T = 30 °C, $[H_2O_2]/[Fe^{2+}]$= 15, H_2O_2/COD=1.75	Removal: COD = 70%	Effluent diluted 30 times prior to oxidation experiments to reduce COD_0 to *ca*. 2 g/L	[85]
3-phase centrifuges (Algeria) pH_0 = 4.7, COD_0 = 74 g/L, TPh_0 = 20.6 g/L	Fenton-like	Lab-scale	pH = unadjusted, T = 50 °C, $[H_2O_2]$ = 12 M, $[Cu^{2+}]$ = 0.5 g/L, t = 90 min	Removal: TPh = 62%	Experiments were performed with previously decanted and diluted OMW	[86]
2-phase process (Granada, Spain) pH_0 = 6.1, COD_0 = 4.0 g/L, TPh_0 = 0.07 g/L	Fenton-like (continuous)	Pilot-scale	pH = 3, $[FeCl_3]/[H_2O_2]$ = 0.026-0.058 *w/w*; $[Fe^{3+}]$ = 0.35-0.40 g/L; HRT = 3 h	Removals: COD = 97%, TPh = 99%	Effluent is a mixture of olives and olive-oil washing wastewaters 1:1 (*v/v*)	[87]
2-phase process (Granada, Spain) pH_0 = 6.1, COD_0 = 2684 mg/L, TPh_0 = 283 mg/L	Fenton-like +Filtration (continuous)	Industrial-Scale	pH = unadjusted, $[FeCl_3]/[H_2O_2]$ = 0.025 *w/w*; HRT = 2.5 h	Removals (average): COD = 86%, TPh = 99%	Final water was transparent and odorless, suitable for irrigation	[136]

Table 2.4 (cont.) Summary of Fenton and Fenton-like processes applied for OMW treatment, either as single stage units, or combined with other treatment processes.

OMW Source	Process Flow-Scheme	Scale	Oxidation Experimental Conditions	Achieved Standards	Observations	Ref.
Storage pond (Portugal) pH_0 = 5.5, COD_0 = 8.5 g/L, TPh_0 = 0.59 g/L	Fenton + Ion Exchange	Pilot-scale	pH = 3.5, $[Fe^{2+}]$ = 50 mg/L, $[Fe^{2+}]/[H_2O_2]$ = 0.002	Removal: COD = 81% (after 1 h)	Ion Exchange was applied to recover Fe ions resulting from Fenton process	[139]
Industrial pond (Badajoz, Spain) pH_0 = 4.9, COD_0 = 6450 mg/L, $BOD_{5\,0}$ = 2130 mg/L TPh_0 = 21 mg/L	Coagulation + Fenton + Aerobic digestion	Lab- & Industrial-Scale	pH = 3.4 (after coagulation), $[Fe_2SO_4]$ = 1500 mg/L, $[H_2O_2]$ = 4500 mg/L	Lab-scale: 38% COD and 40% TSS (coagulation step), 75% (Fenton) COD Industrial-scale: 43% (coagulation) and 62% (Fenton) COD removals	Ferric ions from coagulation used in oxidation step. Biodegradability increase: $BOD_5/COD_{\,average}$ from 0.03 to 0.42	[140]

2.2.2. Catalytic wet peroxide oxidation

In recent years, many researchers have tried to overcome the main drawback related to Fenton's process: the management/recovery of the iron-rich sludge formed during the process. For most applications, the amount of dissolved catalyst required is above the thresholds defined by EU directives for safe discharge. Consequently, the adoption of Fenton/Fenton-like processes implies the downstream removal of iron to comply with legislated values ([Fe] = 2.0 and 5.0 mg/L for discharge into natural water bodies and irrigation purposes, respectively) [141].

The most common process for Fe recovery is by chemical precipitation in a decanter [142], although in some cases the use of tertiary treatment processes such as ion exchange resins [139,143] or membrane technology [144] is proposed to either comply with legislated values or for posterior recirculation to the oxidation tank to reduce catalyst consumption [139]. However, an additional depuration step increases the global cost and complexity of the process, prompting the study and development of heterogeneous catalysts for CWPO, where the active metal phase is incorporated/supported onto a solid matrix. This approach simplifies the catalyst's recovery and re-utilization step, while preventing secondary contamination of the treated effluent by dissolved metals in the solution.

Another advantage of the use of heterogeneous catalysts is the ability of operation at a wider range of pH values without significant loss of activity. In fact, the activity of some catalyst surface active sites may even be improved by increasing pH values above the optimum reported for the classic Fenton oxidation (*ca*. 3.0–3.5), as reported by several authors [145–147]. Under such conditions, leaching of the active phase can also be significantly reduced, extending the catalyst lifetime [148].

Drawbacks of the process include the slower kinetics in comparison to the homogeneous phase due to the mass transfer limitations (either of H_2O_2 or contaminants) occurring at the solution-catalyst interface (and within catalyst pores), and potential agglomeration of catalyst particles that reduce the free surface available [149,150].

The main principles of the homogeneous Fenton process can be applied to CWPO, although the heterogeneous process is intrinsically more complex due to the co-existence of adsorption and catalysis phenomena. In the heterogeneous Fenton process, $^{\bullet}OH$ radicals are generated on the catalyst surface (represented by letter *X* in Eqs. (2.14) and (2.15)), which results from the developed porosity of the support where the metallic active phase is highly dispersed, forming

small nanoparticles that favor the contact and reaction with H_2O_2 [118]. After oxidation, the reaction products may be desorbed from the surface and catalytically active sites become available again for new reactant molecules [138].

$$X - Fe^{2+} + H_2O_2 \rightarrow X - Fe^{3+} + {}^{\bullet}OH + OH^- \quad (2.14)$$

$$X - Fe^{3+} + H_2O_2 \rightarrow X - Fe^{2+} + HO_2^{\bullet} + H^+ \quad (2.15)$$

2.2.2.1. Heterogeneous catalysts for CWPO

Notwithstanding the nature of the heterogeneous catalysts, some of the key features for their suitability for the CWPO process should include: high activity for radicals' generation, physicochemical stability (either to deactivation by leaching of the metal phase, poisoning of active sites, or mechanical abrasion), easily modified/adjusted surface properties (e.g., tunable selectivity towards specific treatment requirements), and production low-cost [110,151]. Consequently, the selection of materials for catalyst synthesis/preparation, along with the operational conditions, are of utmost importance for the process efficiency.

Heterogeneous catalysts may be obtained from different sources, such as: natural iron-bearing materials, namely pyrite [152,153], magnetite [154], or hematite [155]; synthetized materials with the transition metal supported on activated carbons [111,156,157], zeolites [158,159], mesoporous silica [160,161], pillared clays [162,163], or alumina [164,165], just to name a few; catalysts can also be prepared from industrial by-products, such as sludge and fly ash [166,167].

Numerous parameters regarding heterogeneous catalysts are reported to directly affect the process efficiency and the stability of the catalyst itself, namely the type/source of support, catalyst's incorporation/synthesis method [161], and the particle size [168]. Therefore, many scientific studies are focused on synthesis' morphology control [169], surface modification [170,171], and/or metal-doping techniques for different supports [172,173] and various metallic active phases [123].

Rodríguez *et al*. [172] compared the catalytic activity of Fe-supported catalysts (4.2–4.9 wt.% Fe) prepared over nine different supports for the degradation of the model acid Orange II dye. The resulting catalysts' properties widely ranged in specific surface area (S_{BET} = 69.7–857.4 m^2/g) and average pore size (18.5–169.9 Å). Since adsorption of organic molecules on the surface of the catalyst can enhance the efficiency of the CWPO process, additional experiments were performed

to evaluate whether adsorption or chemical reaction was occurring under identical experimental conditions. The study showed that overall TOC reduction by adsorption phenomena was more preponderant on carbon supports – AC, carbon nanotubes (CNT), carbon nanofibers (CNF) – and hydrotalcite, than in siliceous and clays minerals supports (e.g., sepiolite).

The influence of the iron precursor used in the synthesis of Fe/AC catalysts (7 wt.% Fe) was evaluated by Duarte *et al*. [123]. Three Fe-salts were tested: iron acetate (Ac_2Fe), iron sulfate ($FeSO_4$), and iron nitrate ($Fe(NO_3)_3$). It was observed that different precursors led to different Fe particle sizes and location within the AC-support (represented by letter N): for the N-Ac_2Fe catalyst, a good iron dispersion with Fe-particles located inside the micropores was observed; with the N-$FeSO_4$ one, larger Fe-particles were found in the catalyst surface (thus on larger micropores/mesopores); finally, an intermediate behavior was detected using N-$Fe(NO_3)_3$. Good iron dispersion appears to influence the mineralization efficiency of the azo-dye Orange II since N-Ac_2Fe presented the highest TOC degradation efficiencies while maintaining low levels of iron loss from the support.

Leaching of the active species is also closely related to the method and conditions of the catalyst preparation. Botas *et al*. [174] tested several catalysts that consisted of iron oxide, mostly crystalline hematite particles, over different silica supports. The authors found that samples prepared by post-synthesis incipient wetness impregnation displayed higher leaching levels in the outlet stream (Fe concentrations above 100 mg/L) than the ones prepared by direct incorporation during the synthesis (i.e., co-condensation of iron and silica sources).

In another work of Duarte *et al*. [168], the influence of particle size on adsorption and heterogeneous Fenton oxidative catalysis was also addressed. A commercial AC was impregnated with iron (7 wt.% Fe) and was milled from the original pellet (cylinders of *ca* 3 × 5 mm) and sieved to obtain particle sizes in the intervals of 0.8–1.6, 0.25–0.8, and <0.15 mm (powder). The performance of the catalysts was evaluated regarding TOC removal of a dye-containing solution and Fe leaching from the AC support in batch runs. Results confirmed that the Fe-powder catalyst reached higher levels of mineralization. However, leaching levels were also the highest for the smaller particle sizes tested (Fig. 2.6). Taking into account the TOC mineralization degree and the iron leaching from the supports, the authors concluded that particle sizes in the 0.8–1.6 mm range were the most adequate for the operational conditions tested.

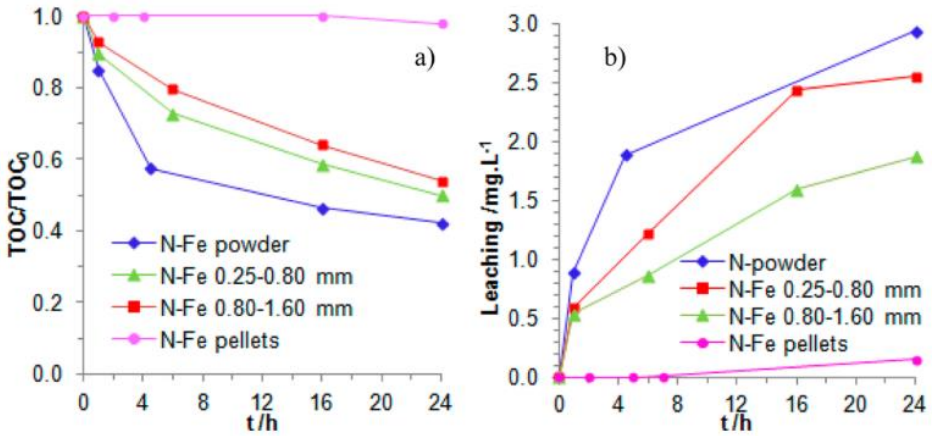


Fig. 2.6 (a) Mineralization degree and (b) leaching values over time using catalysts with different particle sizes (data taken from ref. [168]).

Lu *et al*. [175] also tested different sets of particle sizes of a $Fe_2O_3/\gamma\text{-}Al_2O_3$ catalyst in the intervals of 0.45–0.9, 0.9–1.5, and 1.5–2 mm. The catalytic performance of the continuous Fenton-like oxidation in a fixed-bed reactor was evaluated by COD mineralization levels and phenol degradation ($[Phenol]_{feed}$ = 1 g/L). Phenol oxidation levels were *ca*. 100% for all particle sizes tested and only a minor COD mineralization decrease was observed for 1.5–2 mm. Hence, for this case, the effect of internal diffusion on the catalytic reaction can be disregarded for the smaller particle sizes tested. Although catalysts within that range are preferable to avoid internal diffusion problems, small particles experience a bigger pressure drop across the reactor and may eventually be cleared away by the liquid stream, so an intermediate-range was selected as the optimum size by the authors.

Regarding the active phase selection, continuous research efforts aiming at solving the main bottleneck of iron-based AOPs (i.e., leaching of the active phase at acidic pH) include the synthesis of catalysts different transition metals (e.g., Cu [163,176], Mn [177], Co [178]), as well as the development of mixed metal-oxides supported-catalysts [179,180]. The review of iron-free Fenton-like systems by Bokare and Choi [181] provides further insights on this topic, including the specificity of H_2O_2 activation mechanisms and practical/environmental limitations to their widespread application.

Nevertheless, iron presents definite advantages by comparison to the alternatives, including the fact that it is a cheap and abundant element with low-toxicity and environmentally compatible properties. The high reactivity of Fe^{2+} and Fe^{3+} species for H_2O_2 decomposition makes iron-supporting catalysts the main focus for the majority of AOP applications, including the CWPO

(e.g., [134,182–184]). For such applications, the main functions of the support are to improve the available surface area of the active phase, to limit the sintering phenomena (though in the process addressed herein this may be neglected), and increase the hydrophobicity, thermal and chemical stability of the catalyst [110].

2.2.2.2. Activated carbon as support for catalysts synthesis

Carbon-based materials, particularly activated carbons, are widely known for their versatility in environmental applications, namely in water/wastewater treatment, either as adsorbents of contaminants [185,186], catalysts on their own [187], or more relevant to the present work, suitable catalyst's supports [188,189]. AC precursors are usually selected based on their cost, availability, mechanical and chemical stability. Biomass materials, which include agricultural by-products, are often used as AC precursors due to their abundance, low cost, and availability across the planet, although any organic material may be used for this purpose.

As mentioned earlier, the chemical and physical properties of ACs, namely texture and surface chemistry, are determinant parameters affecting their catalytic performance that can be tailored to satisfy specific needs. For catalysts that consist of metals or metal compounds supported on such materials, their primary role is to maintain the catalytically active phase in a highly dispersed state, which typically leads to higher catalytic activity [188]. The well-developed porous structure of ACs is an important aspect to obtain a large active surface per unit weight of support used. According to the activation extent, it's possible to prepare carbons with different proportions of micro (<2 nm), meso (2–50 nm), and macropores (>50 nm) – Fig. 2.7.

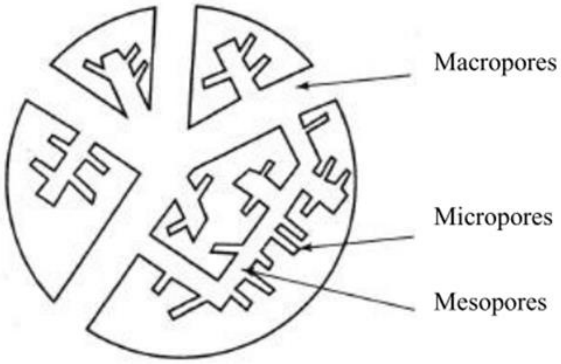


Fig. 2.7 Activated carbon's porous structure schematic representation and classification (adapted from [188]).

The main contributor to the high surface area of activated carbons is typically the microporosity range, where most of the adsorption phenomena occur. However, high microporosity is not always desirable, as a well-developed structure of meso and macropores is fundamental to the

adsorption process since they act as a passage of the adsorbate to the micropores located at the end of larger pores [112,188]. Additionally, unwanted internal mass transfer resistances may play a key role in materials where microporosity prevails [190].

Traditionally, ACs are prepared by either physical or chemical activation. In the case of physical activation, the precursor is initially subjected to a thermal decomposition step at elevated temperatures in an inert atmosphere, in a process known as pyrolysis (or carbonization, because the solid residue is carbon). This step results in the formation of volatile or liquid products and a carbon enriched residue known as char. The porosity of the char is not always accessible because it becomes filled or blocked by disorganized carbon as a consequence of deposition and decomposition of tars [191]. The use of an activating agent (such as air, carbon dioxide, or water steam) at high temperatures (e.g., in the 600–900 °C range) allows a significant development of the material's porosity and pore size distribution [188]. The choice of such activating conditions (i.e., activating agent, precursor, temperature, time, etc.) is crucial to tailor the AC to specific needs. In alternative, for the called chemical activation, the precursor or char are impregnated with a chemical agent (often $ZnCl_2$, KOH or H_3PO_4) and subjected to thermal treatment for the carbonization/activation in a single-step process (typically in the temperature range of 450–650 °C) [192]. Likewise, the activating agent selected, concentration, temperature, and activation time, will also determine the reaction extension and thus the characteristics of the AC produced.

Demiral *et al*. [193] evaluated the effects of steam-activation temperature (750–900 °C) and duration (30–60 min) on the properties of carbonized olive bagasse (500 °C in N_2-atmosphere). The produced activated carbons were mainly microporous materials, with BET surface areas in the 523–1106 m^2/g range and total pore volumes of *ca*. 0.3–0.6 cm^3/g, which were generally improved by temperature and activation time. As the activation temperature increased, the material weight loss also increased due to a combination of volatile matter release and carbon burn-off through carbon-steam oxidation.

The work of Rodríguez-Reinoso and Molina-Sabio [191] showed that the selection of activation mechanism of chars prepared from different lignocellulosic materials (olive stones, peach stones, and almond shells) result in the flexible tune of the ACs pore size distribution. For example, physical activation with CO_2 opens and widens the microporosity of the char (which is even shifted to meso and macro-porosity); nonetheless, at high burn-offs the ablation of the particle's exterior pore walls becomes preponderant. In order to obtain a well-developed porosity in the entire range, the authors tested CO_2-activation catalyzed by iron and also by nitrogen-H_2O steam mixtures.

Both methods produced ACs with well-developed macropores, although the latter has the advantage of preserving the micro- and mesoporosity range. The differences observed between CO_2- and steam- activation methods could be due to the lower partial pressure of H_2O, resulting in a more selective attack of the carbon structure and uniform widening of pores, as opposed to the attack by the much larger concentration of CO_2. Albeit the differences observed, the development of all ranges of porosity is constricted to the reduction of carbon mass and often its mechanical properties (e.g., stability, abrasion resistance), so the synthesis yields are typically low. The authors also showed that direct chemical oxidation with $ZnCl_2$ produces, in a single carbonization/activation step and at lower temperatures, a larger yield of AC with well-developed microporosity (comparable to that of CO_2-activation) and much larger mesopore volume. The amount and distribution of activating agent incorporated in the precursor was found to govern the resulting porosity of the carbon.

Direct chemical activation of olive stones with KOH was evaluated by Ubago-Pérez *et al*. [194]. The synthesized activated carbon presented higher S_{BET} and wider micropores that the same KOH/AC obtained from a previously carbonized sample (840 °C for 1 h under a N_2 flow) – Fig. 2.8a. However, due to the extensive fragmentation and dissolution of lignin and hemicellulose produced by the attack of strongly nucleophilic hydroxyl ions, the AC resultant from direct KOH-activation presented very low density (Fig. 2.8d). The authors proposed the synthesis of monoliths by hot pressing a mixture of the powdered AC and polyvinyl alcohol (acting as binder). Furthermore, the authors also evaluated the properties of ACs prepared with different KOH/carbon weight ratios and distinct particle sizes of the chars prepared from olive stones (Fig. 2.8b, c). The best textural characteristics were obtained for a ratio of 2:1 and with particle size ranging from 0.63–0.80 mm.

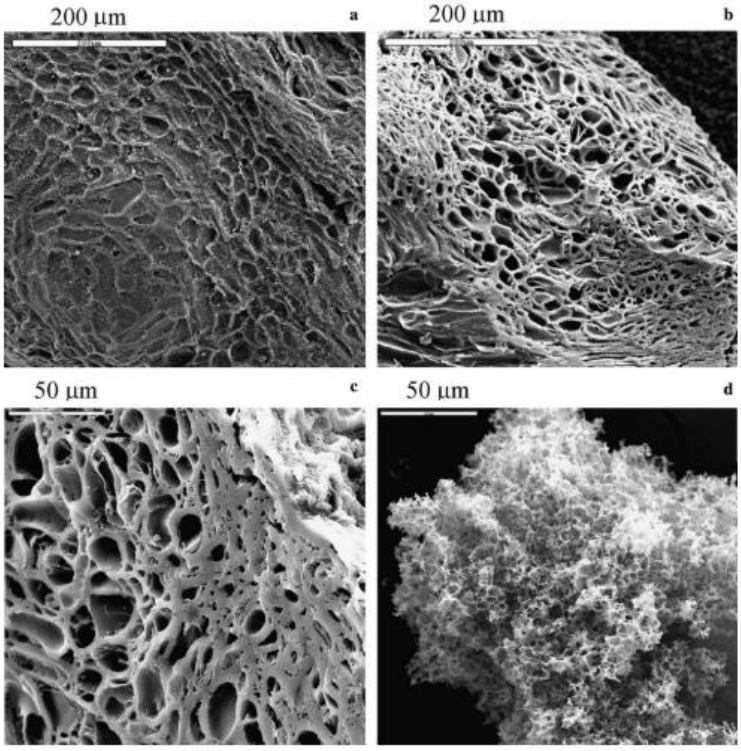


Fig. 2.8 Scanning electron microscopy (SEM) micrographs of (a) carbonized olive stones, (b) KOH/AC (2:1 wt. ratio), (c) KOH/AC (2:1 wt. ratio) with particle size range 0.63–0.80 mm, (d) direct chemical activation (KOH) of raw olive stones (taken from ref. [194]).

Stavropoulos and Zabaniotou [195] also evaluated the use of KOH as an activating agent for olive stone chars. The structure of the produced ACs were mainly composed of micropores at the early stages of activation (i.e., low burn-offs), while at higher burn-offs an increase of the mesoporosity was detected. In that sense, the materials' surface area and pore volume increased with the degree of burn-off (i.e., activation time and temperature).

Recently, the use of hydrothermal carbonization (HTC) for the conversion of biomass waste into valuable carbon materials has received increasing attention in the scientific community [185,196]. The process consists of the conversion of wet or dry biomass into carbonaceous products through fractioning of the raw feedstock by a thermo-chemical technique, using subcritical water at temperatures in the 150–350 °C range. During HTC, the biomass components are hydrolyzed and dehydrated, producing a carbon-rich solid known as hydrochar. Some studies have highlighted the high content of oxygenated functional groups in hydrochars produced by HTC, making them effective precursors for the production of chemically activated carbons with distinct physicochemical characteristics [197]. Other authors have reported on the good self-binding properties of hydrochars, which are particularly important for pelletization and, consequently, industrial application [198]. The milder conditions of hydrothermal carbonization and the needless

use of gases (when compared to pyrolysis/carbonization) can make the process energetically and economically favorable [185].

The adsorptive/catalytic behavior of carbon-based materials is intrinsically dependent on their surface properties, which is correlated with the carbon structure. Due to the graphitic structure of such porous carbons, unsaturated C atoms present at the edges of the graphene layers and basal planes can easily react with O, H_2O, or N, and thus form surface groups (e.g., carboxyl, phenol, carbonyl, pyridine, etc.) [187]. The presence of oxygen surface groups (OSG) at the carbon's surface is particularly relevant for catalyst's synthesis since those complexes also act as anchorage sites that interact with the metallic phase to improve its dispersion [188,199]. Among the OSG, carboxylic acids, phenols or lactones are acidic, while carbonyl and ether groups form basic centers such as quinone and pyrone groups. The controlled removal of such groups can be performed to selectively tune parameters such as the acidic/basic nature and/or hydrophobicity of the carbon surface.

The nature and concentration of different functional groups at the carbon's surface can be modified by chemical or thermal post-treatment, or by changes introduced in the synthesis step. For instance, oxidation in the gas (using oxygen, ozone, or nitrogen oxides) or liquid phase (using H_2O_2 or HNO_3) is commonly performed to increase the surface's oxygen groups, whilst the selective removal of functional groups can be achieved by heating the AC under an inert atmosphere [156,170,200]. This is especially important because some groups can influence H_2O_2 decomposition into unreactive species rather than active $^{\bullet}OH$, which is an unwanted outcome for Fenton-based applications [189]. Nonetheless, there is almost always an intrinsic relationship between these treatments and the textural properties of the resulting material [190]. The duration of the oxidative step and the selected heat temperature (or concentration of reactants) will directly influence the textural morphology of the resulting material, either by widening the existing pores and/or by opening previously inaccessible pores [191]. It is therefore essential to tune these conditions in order to avoid extensive damages to the solid and thus its textural properties.

For instance, the work of Vivo-Vilches *et al*. [170] highlights the possible reorganization of OSG (via different thermal treatments in N_2-atmosphere) of an highly-oxidized AC produced from olive stones. The high activation degree of the olive stones achieved by the use of ammonium peroxydisulfate resulted in the weakening of pore walls and consequent gasification of the resulting AC during the oxidative treatment carried out to functionalize the carbon surface. A thermal treatment (N_2 flow) between 300 and 500 °C allowed the reorganization of OSG within

the chemical structure of the AC, where CO_2-evolving groups (carboxylic acids) were selectively transformed and fixed again as CO-evolving groups (semiquinone).

Lastly, the preparation of carbon-supported iron catalysts can be achieved by several techniques, including impregnation (excess solution or incipient wetness impregnation – IWI), co-precipitation, or ion exchange [162,190,201]. This implies that the AC-support is in contact with the solution containing the metal-active species, reinforcing the importance of suitable surface and textural properties of the AC-support [161,188]. One expected outcome of supporting/anchoring a metal/metal oxide onto an activated carbon is the decrease in porosity and surface area of the material. Still, it is not always easy to predict the influence that metal deposition produces on the catalytic activity of the material, as a number of crossed effects need to be considered.

Rey *et al*. [171] evaluated the catalytic activity of several activated carbons prepared via IWI using two iron precursors – iron nitrate and iron pentacarbonyl. Although no significant differences were observed from the two iron precursors, a more uniform Fe-dispersion was obtained in catalysts using the pentacarbonyl precursor, which makes them more suitable Fenton-type catalysts; still, lower stability was observed when compared to the ones prepared with the nitrate precursor. Catalysts with demarked external Fe-distribution were also related to the poorest oxidative behaviors, ascribed to the faster decomposition of H_2O_2 to non-reactive O_2, according to the auto-scavenging reactions previously mentioned due to excess $^{\bullet}OH$ in the earlier stage of Fenton reaction.

Xu and Teja [202] proposed the deposition of iron oxide (α-Fe_2O_3) onto the pores of two commercial ACs pellets using supercritical water. The immersion time and precursor load $(FeNO_3)_3 \cdot 9H_2O$) produced ACs with higher α-Fe_2O_3 loadings, but the temperature did not affect the process. Nonetheless, at higher concentrations of precursor, the HNO_3 resultant from the synthesis reactions was found to be responsible for detrimental changes in the morphological structure and mechanical stability of the material. Moreover, the deposited Fe-nanoparticles did not produce changes in the micropore size (L_0), but other morphological features were considerably altered, including a decrease in surface area, micropore and total pore volume in line with other similar studies [171,176,201].

2.2.2.3. OMW treatment by CWPO

There are numerous reports in the literature on the application of CWPO for the degradation of model compounds such as phenol [150,155,171,175,201,203], or individual phenolic molecules

commonly found in OMW such as tyrosol [163,204], vanillic acid [205], or 4-hydroxybenzoic acid [205]. Nonetheless, the application of the catalytic wet peroxide oxidation for the depuration of real OMW matrixes is still a very scarce topic of research in the literature. Table 2.5 summarizes the main findings in this field, highlighting the operational conditions and achieved standards after CWPO of synthetic (simulated) and real OMW samples, both relevant for this thesis.

To the best of the author's knowledge, the first study addressing OMW depuration by a CWPO process was reported by De Rosa *et al*. [206] in 2005. The authors evaluated the effluent's biodegradability before and after oxidation, using a Cu-containing metal-organic framework (MOF) as the heterogeneous catalyst. The metal-organic polymer presented a microporous structure similar to the one of zeolite frameworks, with well-developed microporosity, large pore size, and high metal content. The reaction was carried in a semi-batch reactor with 0.97 g/L of catalyst and 113.2 mg/L of H_2O_2. Under such conditions, the polyphenol content was reduced by 96% to 0.10 g/L while the COD_{total} by 18% only (from initial COD of 74.4 to 60.8 g/L) after 27 h. The CWPO pretreatment improved the effluent's biodegradable COD fraction (bCOD) from 52.0 to 84.5%, and the kinetic tests showed that the bCOD removing rate increased after CWPO.

A similar report was published two years later by the same research group [207]. The two new catalysts tested (Cu-silicalite-1 and Cu-pillared clay) presented a high conversion of COD and polyphenolic fraction, on both a 1-year weathered OMW (COD_{total} = 8.2 g/L) and "fresh" sample from a 3-phase centrifugation unit (COD_{total} = 87.6 g/L). Partial recuperation of the used catalyst was achieved by a posterior calcination step, with good catalytic results and only partial copper leaching in re-use tests. By the same time, Caudo *et al*. [208] synthesized copper and iron-based pillared clays (PILC) for the oxidation of a model solution containing several phenolic compounds and a real OMW. The performance of the catalysts was similar for both the model solution and OMW, and the catalysts were used several times without significant metal leaching from the support. After 4 h of reaction, TOC reduction was *ca*. 20% and total phenol removal was *ca*. 45%. The resulting effluent also presented an overall reduction of its toxicity after CWPO.

Azabou *et al*. [209] studied a system based on the combination of CWPO in semi-batch operation mode and anaerobic digestion. The catalyst used was a pillared interlayered clay impregnated with a mixture of aluminum and iron ((Al-Fe)PILC). The initial OMW was extremely resistant to oxidation, so a 5-fold dilution was necessary. Operating at 50 ºC, [Cat.] = 0.5 g/L, and H_2O_2 (30% *w*/*w*) of 0.5 mL/h, considerable COD and TPh reduction (50 and 83%, respectively) were obtained after 8 h. The authors also showed that the oxidized wastewater was much less toxic

than the non-treated effluent and the yield of biogas production in the biological step was improved by the oxidation step.

Martins *et al.* [210] tested the activity of three low-cost materials (sepiolite, volcanic rock, iron shavings) for the treatment of a synthetic solution containing 5 phenolic molecules commonly found in real OMW. Among the materials, iron shavings (ZVI) proved to be the most promising for the mineralization of the solution. At high catalyst dose ([ZVI] = 40 g/L, [H_2O_2] = 35 mM, pH = 3.0), 90% TPh, 60% TOC, and 30% COD removals were obtained after 120 min for a real OMW sample. Stability tests performed in a fixed-bed reactor (FBR) showed: (1) a moderate decrease in the catalyst activity after 168 h of operation for the synthetic solution, and (2) a more rapid decline in oxidation efficiency after only 4 h on stream for the OMW solution.

More recently, Maduna *et al*. [96] reported on the catalytic activity of copper-containing zeolite catalysts for the CWPO of olive mill wastewater. Under optimized operational conditions (T = 80 ºC, [H_2O_2] = 0.5 M, and [Cat] = 10 g/L), total conversion of the phenolic fraction and 52% mineralization (TOC removal) were achieved. Moreover, the authors reported that the rate of phenol oxidation and H_2O_2 decomposition increased with the stirrer speed, catalyst loading, H_2O_2 concentration, temperature, and the decrease of the catalyst particle size.

In more recent years, Domingues *et al.* [97,211] screened the activity of different low-cost iron-rich materials (namely red mud from the aluminum processing industry and volcanic rocks) as catalysts for the CWPO of polyphenolic synthetic solutions. High activity towards the oxidation of phenolic acids was achieved with red mud (TPh removal of 100% after 1 h), but the solution's mineralization remained low (25% TOC removal). The authors also hinted that a single-step H_2O_2 addition is more efficient than its staged addition for both TPh removal and preventing residual oxidant in the solution (Fig. 2.9).

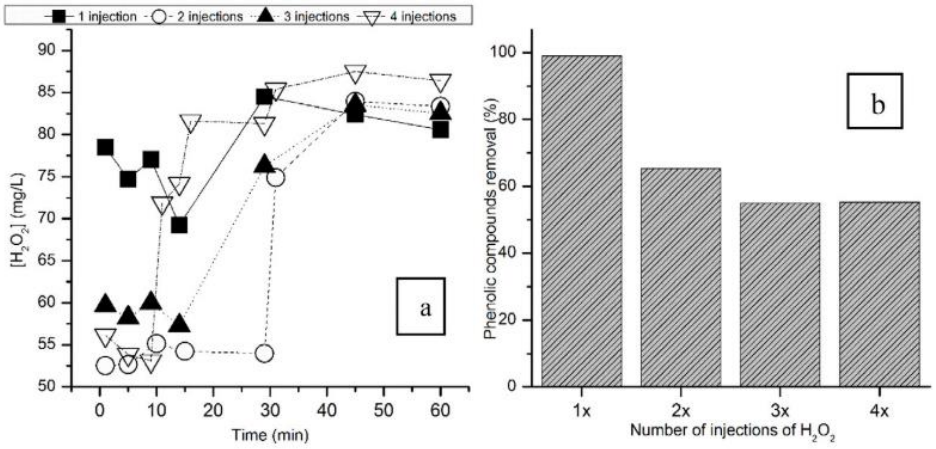


Fig. 2.9 (a) Concentration of residual H_2O_2 in solution over time and (b) total degradation of phenolic content according to the number of H_2O_2 injections (taken from ref. [97]).

In summary, the oxidation of organic compounds from real OMW matrixes seems to rely on the use of higher doses of catalyst by comparison with the homogeneous process. Still, the use of heterogeneous catalysts allows, in many cases, the operation at the naturally-occurring pH of OMW (i.e., 4.0–5.5) without significant loss in degradation efficiencies. The effective mineralization of organic compounds appears to be highly dependent upon the initial physicochemical conditions of the wastewater, as it does for homogenous Fenton-based processes. On the other hand, high removal of the OMW polyphenolic content is commonly reported after CWPO, alongside an overall increase of biodegradability and decrease of the toxic nature of the resulting effluent.

Table 2.5 Main research findings on the treatment of simulated and real OMW by catalytic wet peroxide oxidation.

OMW Source	Process Flow-Scheme/Catalyst	Scale	CWPO Experimental Conditions	Oxidation Achieved Standards	Observations	Ref.
Traditional press (Sfax, Tunisia) pH_0 = 5.2, TOC_0 = 26 g/L, COD_0 = 19 g/L, TPh_0 = 6.4 g/L	Batch CWPO w/ Fe-BEA zeolite	Lab-scale	T = 28 ºC, pH = 5.2, $[H_2O_2] = 2\times10^{-2}$ M, [Cat] = 0.5 g/L	Removals: TOC = 28%, COD = 30%, TPh = 40%, Color = 59% (after 12 h)	OMW diluted to TOC_0 = 1.3 g/L	[21]
Evaporation pond (Portugal) pH_0 = 6.3, TOC_0 = 0.31 g/L, COD_0 = 1.7 g/L, TPh_0 = 0.18 g/L	Batch CWPO w/ Fe-Ce-O 70/30 catalyst	Lab-scale	pH = 4, $[H_2O_2]$ = 115 mM, [Cat] = 1.5 g/L	Removals: COD = 24%, TPh = 100% (after 2 h)	1-year weathered OMW (subject to rain dilution, biological stabilization)	[94]
3-phase centrifuges (Croatia) pH_0 = 4.8, TOC_0 = 10.7 g/L, COD_0 = 36 g/L, TPh_0 = 1.8 g/L	Batch CPWO w/ Cu-13X zeolite catalysts	Lab-scale	T = 80 ºC, d_p = 0.40–0.63 mm, $[H_2O_2]$ = 0.5 M, $m_{Cat.}$ = 2.5 g, V = 250 mL	Removals: TOC = 52%, TPh >99% 3.3 wt.% Cu leached (after 10 h)	Filtered (100 μm Nylon filter) & diluted OMW (*v/v* = 50/50)	[96]
Synthetic polyphenolic solution (5 compounds, 100 mg/L each)	Batch CWPO, Red mud, volcanic rocks	Lab-scale	pH = 3.0, $[H_2O_2]$ = 100 mg/L, [Cat] = 1 g/L	Removals: TPh of 100% for red mud, 72–75% for volcanic rocks (after 60 min)	Catalysts from naturally-occurring iron-rich materials	[97]
Undisclosed process (Calabria, Italy) pH_0 = 3.58, COD_0 = 74.4 g/L, TPh_0 = 2.65 g/L; TSS_0 = 52.4 g/L	Semi-Batch CPWO w/ Cu-BTC catalyst	Lab-scale	T = room, H_2O_2 = 113.2 mg/L (10 mL aliquots every 10 min), [Cat] = 0.97 g/L	Removals: COD = 18%, TPh = 96% (after 27 h)	Biodegradability increased from 52.0 to 84.5%	[206]
3-phase centrifuges (Calabria, Italy) pH_0 = 4.5–5.5, TOC_0 = 20–28 g/L, COD_0 = 8.2–87.6 g/L, TPh_0 = 0.4–3.6 g/L	Batch CWPO w/ Cu-zeolite & Cu-pillared clays	Lab-scale	T = 50–80 ºC, pH = unadjusted, [Cat] = 0.6–5.0 g/L	Removals: COD = 78–87%, TPh = 94.5–97% (after 3-4 h)	H_2O_2 (35% *w/w*) added stepwise for 20 min.	[207]
Undisclosed process (Sicily, Italy) pH_0 = 4.8, TOC_0 = 28.0 g/L, TPh_0 = 0.78 g/L	Semi-Batch slurry reactor CPWO w/ Fe- and Cu-PILC catalysts	Lab-scale	T = 60–90 ºC, pH = unadjusted H_2O_2 = 0.15–0.50 mL/h, $m_{Cat.}$ = 0.5 g	Polyphenolic conversion of ≈45%, ≈20% TOC mineralization for both catalysts (after 4 h)	Filtered (400 mesh filter) & diluted (1:2) OMW	[208]

Table 2.5 (cont.) Main research findings on the treatment of simulated and real OMW by catalytic wet peroxide oxidation.

OMW Source	Process Flow-Scheme	Scale	CWPO Experimental Conditions	Oxidation Achieved Standards	Observations	Ref.
Evaporating pond (Sfax, Tunisia) pH_0 = 5.2, COD_0 = 64.2 g/L, TPh_0 = 6.4 g/L, TS = 62 g/L	Semi-Batch CPWO w/ (Al–Fe) PILC + Anaerobic Digestion	Lab-scale	T = 50 ºC, H_2O_2 = 0.5 mL/h, [Cat] = 0.5 g/L	Removals: COD = 50%, TPh = 83% (after 8 h)	OMW diluted: TPh = 1.25 g/L & COD = 12.5 g/L Treated and untreated OMW remained toxic to anaerobic bacteria	[209]
Synthetic solution/OMW: TOC_0 = 302 / 1150 mg/L TPh_0 = 358 / 332 mg/L COD_0 = 1055 / 2065 mg/L	Batch & continuous FBR operation w/ sepiolite, volcanic rock, iron shavings (ZVI)	Lab-scale	ZVI screened as the most promising material pH = 3.0, [ZVI] = 40 g/L, [H_2O_2] = 35 mM, T = room	Removals (synthetic sol.): TPh = 94%, COD = 54%, TOC = 60% Removals (OMW): TPh = 90%, COD = 30%, TOC = 60%	FBR operation (Q = 1 mL/min, 168 h): TPh = 73%, COD = 44%, TOC = 39%	[210]
Synthetic polyphenolic solution (5 compounds, 100 mg/L each)	Batch CWPO, Red mud	Lab-scale	pH = 3.0, [H_2O_2] = 100 mg/L, [Cat] = 1 g/L	Removals: TPh = 100% TOC = 25% (after 60 min)	Catalysts obtained from waste of the aluminum industry; phenols adsorption onto red mud was negligible	[211]
Undisclosed process (Italy) pH_0 = 4.6–5.1, TOC_0 = 28.0–89.3 g/L, TPh_0 = 0.7–3.4 g/L	Semi-Batch slurry reactor w/ Cu-PILC catalyst	Lab-scale	T = 80 ºC, V = 7000 mL, $m_{Cat.}$ = 15 g, H_2O_2 = 30 mL/h	Removals: COD = 8–21%, TOC = 7–30%, TPh = 18–39% (after 5 h)	Three different OMW samples were tested	[212]

2.3. MEMBRANE TECHNOLOGY

Over the last three decades, similarly to advanced oxidation processes, membrane-based separation techniques have also gained increasing popularity, either for water/groundwater purification [213–215], desalination of seawater [216,217], or wastewater reclamation from different sources/industries, including urban wastewaters [218,219], textile [220,221], pulp and paper [222,223], and agro-industrial industries, such as winery [224,225], dairy [226], and olive oil [100,144,227,228].

Membranes are of great interest because they provide a physical barrier for several constituents of water/wastewater based on their size, allowing for selective separation of undesired molecules, and/or recovery of valuable products [229]. In wastewater treatment, membranes are most commonly used as a tertiary advanced treatment for the removal of colloidal and suspended solids, non-biodegradable organics, heavy metal ions, and human pathogens such as bacteria and viruses [230].

Traditional membrane techniques in wastewater depuration include microfiltration (MF), ultrafiltration (UF), nanofiltration (NF), reverse osmosis (RO), and membrane bioreactors (MBRs – combination of a membrane unit with a biological process) [231]. The selection of the appropriate technique depends on the target particle/molecule size of the solute in the effluent to be treated: MF is commonly used for removal of suspended solids, including microorganisms; UF for the removal of both large, dissolved solute molecules and suspended colloidal particles; NF for the selective removal of multivalent ions and charged or polar molecules; and RO is conventionally applied for inorganic ions removal, although it is capable of removing a wide range of dissolved species [229,232]. Fig. 2.10 highlights the range of application for the above-mentioned membrane technologies, based on the dimension of the solute to separate.

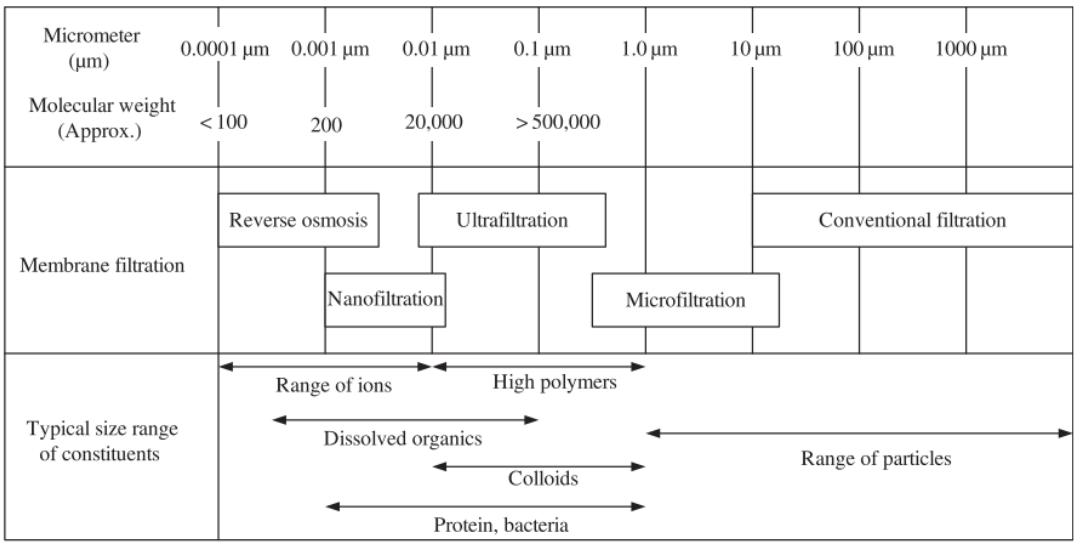


Fig. 2.10 Adequacy of traditional membrane technologies as a function of the size or molecular weight of the target compound (adapted from [233]).

In comparison to conventional wastewater treatment processes, these membrane techniques are considered an attractive alternative since they reduce the number of unit operations, require low space, and are easier to operate and scale up. Moreover, the absence of chemicals required for water/wastewater purification, as well as the continuous and automatic operation, modular configuration possibilities, and non-stopping development of new membrane materials, are key advantages of such technologies [9,31].

On the other hand, one of the major drawbacks associated with membrane processes is the rapid drop of permeate flux (*J*) over time, particularly by the fouling phenomena. These systems may be operated at constant permeate flux (i.e., flow rate per unit area of membrane) with variable transmembrane pressure (TMP), which is the most common procedure, or at variable permeate flux with constant TMP. Fouling typically leads to an increase in the TMP (to maintain the permeate flux), or to a decrease in flux whenever the system is operating at a constant transmembrane pressure [231].

Membrane fouling is a complex phenomenon that may involve pore blocking, clogging, chemical degradation, and/or cake formation on the membrane surface, which result in the loss of its permeability and selectivity, and ultimately its durability. The increase in solutes over the membrane boundary region – concentration polarization – is the first causer of membrane fouling; if the concentration is high enough, it may lead to the formation of gel layers over the membrane's surface that will result in the accumulation of solute. The fouling may be classified as reversible if techniques like backwashing, surface washing, or chemical cleaning, can regenerate the

membrane properties. Whenever the concentration of solutes within the gel layer exceeds solubility concentration values, a solid starts to precipitate and irreversibly clogs the membrane's pores [9].

Membrane contractors, which include membrane distillation (MD) processes, are more recent technologies in which the membrane module is not used as a selective barrier, but rather as a tool for interphase mass transfer. MD technology relies on the vapor/liquid equilibrium to achieve separation, thus heating of the feed solution is required to achieve the necessary latent heat of vaporization [234]. Therefore, it is a thermal-driven membrane process in which the driving force is the partial pressure gradient generated across the membrane module, being widely adopted in desalination, but also in several other environmental applications related to water/wastewater treatment, as comprehensively reviewed by Alkhudhiri *et al*. [235] and by Wang and Chung [236].

2.3.1. Membrane distillation

When compared to other separation technologies, MD processes are operated at a lower temperature than conventional distillation, also involving the generation of lower hydrostatic pressures than NF or RO. Moreover, since solutes are not in direct contact with the membrane, the risk of fouling is significantly reduced and very high rejection of non-volatile solutions is theoretically possible. These compact devices are able to immobilize gas or liquid interface at the membrane micropores by its hydrophobic properties and to create large contact areas for promoting mass transfer efficiency [237–239].

The modular nature of MD makes it easier to scale-up and to integrate into new or pre-existing production lines. Several modules may be added in parallel to increase the capacity of the system or in series to improve the separation degree. Nonetheless, the widespread commercialization of MD technology has been primarily inhibited by the lack of high-performance microporous membranes, and more importantly, the higher energy requirements than RO technology due to the necessary latent heat of water vaporization [237].

Contrary to pressure-driven membrane processes, the permeate flux in membrane distillation processes can't be collected directly at the lower pressure side of the membrane, as condensation of the permeate vapor is necessary. Depending on the method selected to induce the vapor pressure gradient and to collect the transferred vapors from the permeate side, MD processes may be divided into four main configurations (Fig. 2.11) [236,237]:

- Direct contact membrane distillation (DCMD), being the most basic and widespread used MD configuration, since the permeate side (cold) is in direct contact with the retentate side (hot), making the temperature gradient to induce a vapor pressure difference (ΔP) across the membrane. Vapor-molecules formed at the retentate-membrane surface are transported across the hydrophobic membrane and condense in the cold liquid/vapor interface at the permeate side. Since the membrane is the sole barrier separating the hot feed (retentate) and cold (permeate) solutions, this configuration also presents the highest conductive heat loss;
- Vacuum membrane distillation (VMD) requires the use of a pump to create vacuum in the permeate side of the membrane. Condensation may occur inside or outside the membrane module. This configuration is often used to remove volatile organic compounds (VOCs) from aqueous solutions;
- In air gap membrane distillation (AGMD), the feed solution is exclusively in direct contact with the hot side of the membrane surface, as stagnant air is introduced between the membrane and the condensation surface (e.g., metal film, thin dense polymer, etc.). While benefiting from the lower heat loss by conduction, this configuration also offers additional resistance to mass transfer and the flux is typically lower than DCMD or VMD modules;
- In sweep gas membrane distillation (SGMD), a cold inert gas is used to sweep the vapor molecules in the membrane surface at the permeate side. Like AGMD, there is a gas barrier that reduces heat transfer but also enhances mass transfer resistances. An external condenser is typically required to condense vapor molecules on the permeate side, resulting in additional cost with equipment.

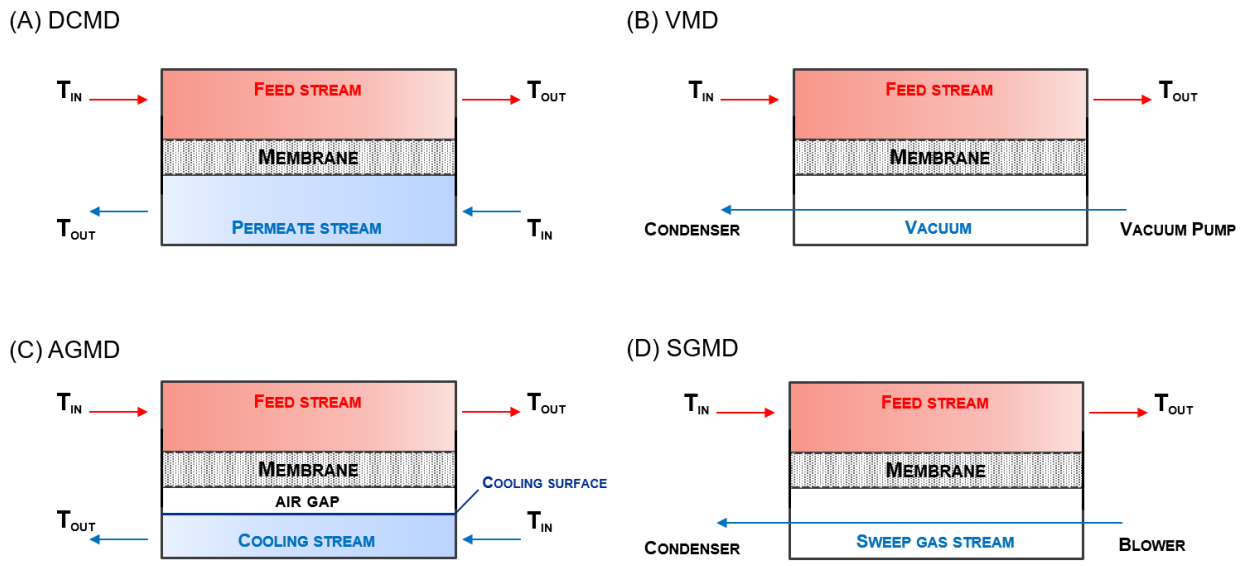


Fig. 2.11 Schematic representation of (A) direct contact membrane distillation (DCMD), (B) vacuum membrane distillation (VMD), (C) air gap membrane distillation (AGMD), and (D) sweeping gas membrane distillation (SGMD) configurations.

The selection of the most appropriate MD configuration may play a key role in determining the separation performance and overall operational costs according to specific needs. As water is typically the main component in the feed stream, a hydrophobic and porous membrane is an essential requirement for most applications, which are typically made from intrinsic or modified hydrophobic polymers with low surface energy (so that a high liquid entry pressure, LEP, can be more easily achieved). Up-to-date the most used polymers in MD are polytetrafluoroethylene (PTFE), polypropylene (PP), and polyvinylidene fluoride (PVDF). Additionally, membranes for MD should present [237,240]:

- Narrow pore size distribution and a high LEP – defined as the minimum TMP required for the feed solution to overcome membrane hydrophobic forces and penetrate the pores, causing membrane wetting. This phenomenon is the main responsible for the decrease in quality and flux rate of permeate production;
- High fouling resistance, although fouling phenomena in MD-based processes is not expected to be as high as in pressure-driven separation technologies;
- Low thermal conductivity, chemical resistance for different feed solutions, and physicochemical stability towards cleaning procedures (e.g., by acid or basic washing);
- Other parameters, such as the tortuosity factor, layer thickness of the membrane, estimated life-cycle, as well as the cost of production, play key roles in the selection of the most appropriate membrane material and design.

Because of their low-surface energy and good wetting resistance, reasonable water flux, and physicochemical stability in various conditions of operation, PTFE membranes are commonly selected in many lab-scale and pilot MD systems [105,239].

2.3.2. Application of MD for OMW treatment/valorization

A survey on the most up-to-date scientific articles revealed a rise in membrane and hybrid membrane driven-processes, particularly over the last decade. However, the application of MD processes for OMW treatment/valorization is a very scarce topic in the literature. Table 2.6 resumes some of the main findings in this field, highlighting achieved standards, either for the depuration of the feed of wastewater, production of purified water at the permeate stream (thus potentially attaining zero level waste discharge in this agro-industrial activity), or concentration/recovery of valuable bio phenolic compounds (as discussed in previous subchapters).

El-Abbassi *et al.* [238] evaluated the operation of a DCMD unit for concentration of polyphenols of OMW from a traditional press process. The authors tested two commercial flat-sheet hydrophobic membranes (PTFE and PVDF) and compared their performance by evaluating the permeate flux achieved and polyphenols (TPh) retention. Both the separation coefficient ($\alpha = 1 - [C_{permeate}(t)/C_{feed,0}] \times 100$, where $C_{permeate}$ is the TPh concentration on the permeate side) and concentration factor ($\beta = C_{feed}(t)/C_{feed,0}$, where C_{feed} is the TPh concentration in the feed), were higher for the PFTE membrane. In addition, the permeate flux (J) attained with the PTFE membrane was 7.68 L/h·m^2, substantially higher than the one of the thicker PVDF membrane (J = 4.95 L/h·m^2). In this preliminary work, the authors also pointed out the load of OMW (COD_0 = 156 g/L) and the role of its complex composition in membrane fouling by deposition of solid particles, oil, sugars, proteins, and other soluble compounds, and the challenges expected ahead to overcome this limitation.

In an ensuing work, the same authors [241] tested three PTFE membranes with distinct average pore sizes. The goal was to assess the possible production of pure water and recovery of polyphenols from OMW (COD_0 = 175 g/L, TPh_0 = 8.7 g/L). DCMD permeate fluxes were evaluated as a function of the feed temperature (30–70 °C) for a fixed permeate temperature (20 °C), which increased with both the temperature difference across the module and the membrane pore size (0.20, 0.45, and 1.0 µm). Since no significant differences were found in α values for the membranes (*ca*. 100% rejection after 8 h of operation), the authors concluded that

it is preferable to work with the membrane with a higher pore size due to the higher fluxes achieved. Nonetheless, the relatively low initial permeate flux attained with OMW and its decrease over time (concentration polarization effect, fouling phenomena), are the process's main limitations. Although water recovery was also a goal of this study, no permeate water quality parameters were evaluated by the authors.

Further on, the authors also evaluated pre-treatment processes (coagulation/flocculation and microfiltration) and their effect on the separation efficiency of the same DCMD unit [38]. For the conditions tested, the authors found that MF was the best pre-treatment route to remove suspended solids from OMW (30% *vs*. 23% with coagulation/flocculation), and enhance the initial permeate flux in DCMD (J_0 = 7.7, 6.9, and 5.6 L/h·m^2 for MF-treated, coagulation/flocculation-treated, and raw OMW, respectively) – Fig. 2.12. Still, even for the MF-treated OMW, the flux also declined considerably in the first 30 h of operation down to a constant value of 1.44 L/ h·m^2, due to the OMW concentration over time and membrane fouling. HPLC analysis denoted that β values close to 3 were observed for some phenolic acids, including tyrosol and gallic acid, and that only monocyclic phenols were observed in the permeate side, due to their smaller size and relative volatility.

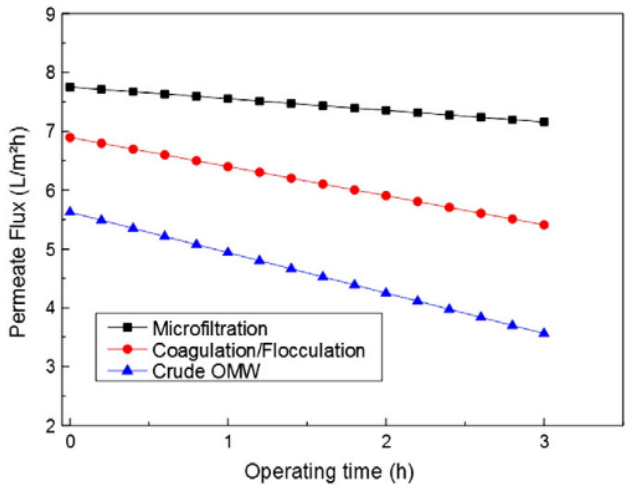


Fig. 2.12 Permeate flux (J) of OMW over time before and after microfiltration or coagulation/flocculation pre-treatments at T_{feed} = 40 °C and $T_{permeate}$ = 20 °C (taken from ref. [38]).

The integrated process proposed by Garcia-Castello *et al*. [41] includes MF followed by NF, and then VMD or OD units, for the recovery and concentration of polyphenols from OWM. Direct application of MF resulted in 91% TSS and 26% TOC reductions, while 78% of polyphenols were recovered in the permeate stream. The TOC of the permeate solution was further reduced by 63% after NF (from 15 to 5.6 g/L), while almost all polyphenols were recovered in the permeate

stream. Finally, VMD and OD were applied for the concentration of the NF permeate solution. Despite the higher transmembrane fluxes achieved with VMD, the OD unit was deemed more energetically advantageous by the authors for the final concentration of a phenol-enriched retentate.

More recently, Carnevale *et al*. [105] studied DCMD and VMD configurations as OMW treatment technologies to obtain a purified stream of water to reuse and a concentrate solution rich in polyphenols. A simple filtration was previously performed to remove suspended particles from the wastewater. The capillary compact module (with a commercial PP membrane) allowed to work with higher membrane area/volume ratios. In the case of DCMD configuration, 99.9% TPh rejection (feed concentration of 2500 ppm) and 89% TOC rejection in the permeate stream were achieved at T_{feed} = 50 °C, with an average J = 6.5 kg/h·m^2. In a prolonged test (20 h, same feed temperature), J value drop was below 25% and the rejection remained >99%. In the case of VMD, similar rejection percentages were achieved (99.6%) while the permeate flux was considerably higher (J = 19 kg/h·m^2). Restoration of the initial flux was achieved by a simple cleaning procedure of the membrane module with distilled water, with only a slight reduction on the average permeate flux (11.4% reduction). Overall, both configurations produced a permeate stream with very low concentration of polyphenols (3.0 and 10.0 ppm for DCMD and VMD, respectively, at TPh_0 of 2500 ppm).

Despite the lack of studies in this field for OMW specifically, the common denominator reported seems to be the rapid decline of the permeate flux, either through the concentration polarization effect, or scaling and membrane fouling on the surface. Both situations appear to be mitigated (up to some extent), by the adoption of pre-treatment strategies or by posterior cleaning procedures to the membrane module to restore its initial properties. The potential application of CWPO as a pre-MD treatment strategy has yet to be investigated for OMW application, though a few works have been recently reported in that sense, including the application of different AOPs (e.g., ozonation, photolytic ozonation, Fenton reaction, photo-Fenton) combined with DCMD for secondary municipal wastewater treatment [239], and the evaluation of Fenton and a modified-Fenton system coupled with DCMD to desalinate produced water (the byproduct of oil and natural gas extraction) [242].

Table 2.6 Summary of membrane distillation technologies applied for the treatment and/or valorization of OMW.

OMW Source	Process scheme	Scale	Membrane Characteristics	MD operational conditions	Achieved Standards	Observations	Ref.
Traditional press (Morocco) COD_0 = 156 g/L, TPh_0 = 8.3 g/L	Coagulation/ flocculation → DCMD & MF → DCMD	Pilot-scale	PFTE flat-sheet membrane (TF200, Gelman), 0.2 µm mean pore size, δ = 178 µm (support included)	T_{feed} = 40 °C T_{perm} = 20 °C (H_2O) t = 40 h Membrane area (*S*): 2.75×10^{-3} m^2 Stirring rate = 500 rpm	J_0 = 7.9 *vs*. 6.9 L/h·m^2 for MF *vs*. coagulation/flocculation pre-treatment; Concentration factor values (*β*) ranged from 1.56 to 2.93, depending on the phenolic compound;	Main phenolic compound in OMW was hydroxytyrosol, which was concentrated *ca*. 2 times after DCMD (from 4.01 to 8.16 g/L)	[38]
3-phase centrifuges (Italy) TOC_0 = 20.2 g/L TSS_0 = 17.6 g/L	MF → NF → VMD/OD	Pilot-scale	Flat-sheet membrane of PVDF, 0.2 µm mean pore size	T_{Feed} = 30 °C S = 55 cm^2 Vacuum = 30 mbar Q = 180 L/h	91% TSS and 26% TOC reductions after the MF step; 63% TOC reduction after NF; *J* of *ca*. 8 L/h·m^2 after 360 min for VMD	Almost all polyphenols were recovered in the permeate solution after NF; both OD and VMD allowed to obtain an enriched polyphenol solution	[41]
Undisclosed process (Italy) Filtered OMW TOC_0 = 37 g/L TPh_0 = 2500 ppm	DCMD	Pilot-scale	Capillary membrane of PP, 0.2 µm mean pore size, d_{int} = 1.8 mm, δ = 0.4 mm	T_{feed} = 30–50 °C T_{perm} = 15 °C (H_2O) S = 30 cm^2 Q_{feed} = 70 L/h Q_{perm} = 60 L/h $[TPh]_{feed}$ = 2500 ppm	$J_{average}$ = 1.1–6.5 kg/h·m^2 $[TPh]_{permeate}$ = 3.0–3.3 ppm $[TOC]_{permeate}$ = 450 –615 mg/L (depending on the feed temperature values)	Membrane cleaning procedure allowed to restore membrane performance with only slight *J* reduction (11.4%)	[105]
Undisclosed process (Italy) Filtered OMW TOC_0 = 37 g/L TPh_0 = 2500 ppm	VMD	Pilot-scale	Capillary membrane of PP, 0.2 µm mean pore size, d_{int} = 1.8 mm, δ = 0.4 mm	T_{feed} = 50 °C S = 30 cm^2 Q_{feed} = 70 L/h Vacuum = 5 mbar $[TPh]_{feed}$ = 150–2500 ppm	$J_{average}$ = 19 kg/h·m^2 (at TPh of 2500 ppm) $[TPh]_{permeate}$ = 4.4–10 ppm (depending on initial concentration)	Both high rejections and higher flux values; Lower $[TPh_0]$ lead to higher *J* values (e.g., *J* >21 kg/h·m^2 at 900 ppm)	[105]

Table 2.6 (cont.) Summary of membrane distillation technologies applied for the treatment and/or valorization of OMW.

OMW Source	Process scheme	Scale	Membrane Characteristics	MD operational conditions	Achieved Standards	Observations	Ref.
3-phase centrifuges (Italy)	MF → DCMD	Pilot-scale	Flat-sheet PVDF, 0.22 µm mean pore size	T_{feed} = 40 °C T_{perm} = 10 °C (H_2O) S = 40 cm^2 Q_{feed} = 150 L/h, Q_{perm} = 80 L/h	35% flux decrease after *ca*. 7 h (4.8 to 3.0 kg/h·m^2)	No thermal degradation of bioactive compounds under the feed temperature tested	[106]
Traditional press (Morocco) COD_0 = 156 g/L, TPh_0 = 4.1 g/L	DCMD	Pilot-scale	Two commercial membranes tested: PTFE (δ = 55 µm, 0.2 µm mean pore size) PVDF (δ = 118 µm, 0.28 µm mean pore size)	T_{feed} = 40 °C T_{perm} = 20 °C (H_2O) t = 9 h Stirring rate = 500 rpm	PTFE membrane with higher separation coefficient (*α*) for polyphenols (99%) than PVDF (89%)	OMW concentration factor (*β*) of 1.72 for the PTFE membrane and 1.40 for PVDF	[238]
3-phase process (Morocco) COD_0 = 175 g/L, TPh_0 = 8.7 g/L	DCMD	Pilot-scale	Three commercial PFTE membranes with distinct mean pore sizes: 0.20, 0.45, and 1.0 µm	T_{feed} = 40 °C T_{perm} = 20 °C (H_2O) t = 8 h S = 2.75 × 10^{-3} m^2 Stirring rate = 500 rpm	*α* values for TPh close to 100% after 8 h independently of the membrane used; higher *J* values for the membrane with higher pore size.	Limitation of DCMD unit related to the relatively low permeate fluxes for OMW and its decline over time	[241]

2.4. SUMMARY

The extraction of olive oil still poses several challenges related to its environmental footprint, mainly caused by the volume and composition of the waste/wastewater generated in the process. The scientific research in the field of OMW treatment shows that different combinations of both traditional and/or advanced technologies may be used to effectively treat olive mill effluents to reach desired standards. Nonetheless, the OMW management problem is still far from being realistically solved in most cases due to economic and practical reasons, owing to the small-scale operation and disperse location of most facilities, as well as the seasonality of olive oil production.

Recent studies show that these effluents can also be regarded as a source of high-added value products, whereas solid, agro-industrial wastes such as olive pomace, olive stones, leaves, and wood cuttings, may be used for the production of carbonaceous materials for different environmental applications, including the synthesis of highly-tunable AC-supported catalysts for wastewater treatment.

In line with the circular economy model trend, the integrated process proposed in this thesis includes the simultaneous recovery/valorization of solid agricultural wastes for the production of AC-based catalysts to be used in the CWPO of olive mill wastewater. Then, water recovery by membrane distillation technology using a hydrophobic membrane is expected to be facilitated by the proposed catalytic pre-treatment of OMW, which can then be used within the same industry for machinery washing activities or irrigation of crops, closing the cycle. Although some reports dealing with CWPO or MD for olive mill wastewater treatment/valorization may be found in the literature, the integrated process is yet to be explored.

REFERENCES

1. European Commission - Water Scarcity & Droughts in the European Union Available online: https://ec.europa.eu/environment/water/quantity/about.htm (accessed on Oct 3, 2021).
2. Casani, S.; Rouhany, M.; Knøchel, S. A discussion paper on challenges and limitations to water reuse and hygiene in the food industry. *Water Res.* **2005**, *39*, 1134–1146.
3. Kirby, R.M.; Bartram, J.; Carr, R. Water in food production and processing: Quantity and quality concerns. *Food Control* **2003**, *14*, 283–299.
4. Mekonnen, M.M.; Hoekstra, A.Y. The green, blue and grey water footprint of crops and derived crop products. *Hydrol. Earth Syst. Sci.* **2011**, *15*, 1577–1600.
5. FAOSTAT - Food and Agriculture Organization Corporate Statistical Database Available online: http://www.fao.org/statistics/en/ (accessed on Jan 2, 2022).
6. Fragoso, R.A.; Duarte, E.A. Reuse of drinking water treatment sludge for olive oil mill wastewater treatment. *Water Sci. Technol.* **2012**, *66*, 887–894.
7. Directive 2008/98/EC of the European Parliament and of the Council of 19 November 2008 on waste and repealing certain Directives. *Off. J. Eur. Union* 2008, *L312*, 3–30.
8. International Olive Council - World olive oil and table oil figures Available online: https://www.internationaloliveoil.org/what-we-do/economic-affairs-promotion-unit/#figures (accessed on Dec 7, 2021).
9. Ochando-Pulido, J.M. A review on the use of membrane technology and fouling control for olive mill wastewater treatment. *Sci. Total Environ.* **2016**, *563–564*, 664–675.
10. Kapellakis, I.E.; Tsagarakis, K.P.; Crowther, J.C. Olive oil history, production and by-product management. *Rev. Environ. Sci. Biotechnol.* **2008**, *7*, 1–26.
11. Aggoun, M.; Arhab, R.; Cornu, A.; Portelli, J.; Barkat, M.; Graulet, B. Olive mill wastewater microconstituents composition according to olive variety and extraction process. *Food Chem.* **2016**, *209*, 72–80.
12. Azbar, N.; Bayram, A.; Filibeli, A.; Muezzinoglu, A.; Sengul, F.; Ozer, A. A review of waste management options in olive oil production. *Crit. Rev. Environ. Sci. Technol.* **2004**, *34*, 209–247.
13. Roig, A.; Cayuela, M.L.; Sánchez-Monedero, M.A. An overview on olive mill wastes and their valorisation methods. *Waste Manag.* **2006**, *26*, 960–969.
14. Awad, A.; Salman, H. Olive Oil Waste Treatment. In *Handbook of Industrial and Hazardous Wastes Treatment*; Wang, L.K., Hung, Y.-T., Lo, H.H., Yapijakis, C., Eds.; CRC Press: Boca Raton, 2004; pp. 737–808 ISBN 9780824741143.
15. Koutsos, T.M.; Chatzistathis, T.; Balampekou, E.I. A new framework proposal, towards a common EU agricultural policy, with the best sustainable practices for the re-use of olive mill wastewater. *Sci. Total Environ.* **2018**, *622–623*, 942–953.
16. Ochando-Pulido, J.M.; Pimentel-Moral, S.; Verardo, V.; Martinez-Ferez, A. A focus on advanced physico-chemical processes for olive mill wastewater treatment. *Sep. Purif. Technol.* **2017**, *179*, 161–174.
17. Rus, W..; Schnappinger, M. *Utilization of by-products and treatment of waste in the food industry*; 2007; ISBN 0387335110.
18. Dermeche, S.; Nadour, M.; Larroche, C.; Moulti-Mati, F.; Michaud, P. Olive mill wastes: Biochemical characterizations and valorization strategies. *Process Biochem.* **2013**, *48*, 1532–1552.
19. Instituto Nacional de Estatística - Statistics Portugal Available online: https://www.ine.pt/xportal/xmain?xpid=INE&xpgid=ine_indicadores&userLoadSave=Load&userTableOrder=9286&tipoSeleccao=1&contexto=pq&selTab=tab1&submitLoad=true&xlang=pt (accessed on Dec 20, 2021).
20. Rodrigues, F.; Pimentel, F.B.; Oliveira, M.B.P.P. Olive by-products: Challenge application in cosmetic industry. *Ind. Crops Prod.* **2015**, *70*, 116–124.
21. Najjar, W.; Azabou, S.; Sayadi, S.; Ghorbel, A. Screening of Fe-BEA catalysts for wet hydrogen peroxide oxidation of crude olive mill wastewater under mild conditions. *Appl. Catal. B Environ.* **2009**, *88*, 299–304.
22. Amor, C.; Lucas, M.S.; García, J.; Dominguez, J.R.; De Heredia, J.B.; Peres, J.A. Combined treatment of olive mill wastewater by Fenton's reagent and anaerobic biological process. *J. Environ. Sci. Heal. - Part A Toxic/Hazardous Subst. Environ. Eng.* **2015**, *50*, 161–168.
23. Gomes, H.T.T.; Figueiredo, J.L.L.; Faria, J.L.L. Catalytic wet air oxidation of olive mill wastewater. *Catal. Today* **2007**, *124*, 254–259.
24. Zorpas, A.A.; Costa, C.N. Combination of Fenton oxidation and composting for the treatment of the olive solid residue and the olive mill wastewater from the olive oil industry in Cyprus. *Bioresour.*

Technol. **2010**, *101*, 7984–7987.
25. Papaphilippou, P.C.; Yiannapas, C.; Politi, M.; Daskalaki, V.M.; Michael, C.; Kalogerakis, N.; Mantzavinos, D.; Fatta-Kassinos, D. Sequential coagulation-flocculation, solvent extraction and photo-Fenton oxidation for the valorization and treatment of olive mill effluent. *Chem. Eng. J.* **2013**, *224*, 82–88.
26. Alver, A.; Baştürk, E.; Kiliç, A.; Karataş, M. Use of advance oxidation process to improve the biodegradability of olive oil mill effluents. *Process Saf. Environ. Prot.* **2015**, *98*, 319–324.
27. Nieto, L.M.; Hodaifa, G.; Rodriguez, S.; Gimenez, J.A.; Ochando, J. Degradation of organic matter in olive-oil mill wastewater through homogeneous Fenton-like reaction. *Chem. Eng. J.* **2011**, *173*, 503–510.
28. Ochando-Pulido, J.M.; Hodaifa, G.; Víctor-Ortega, M.D.; Martínez-Ferez, A. A novel photocatalyst with ferromagnetic core used for the treatment of olive oil mill effluents from two-phase production process. *Sci. World J.* **2013**, *2013*, 1–9.
29. Paraskeva, P.; Diamadopoulos, E. Technologies for olive mill wastewater (OMW) treatment: a review. *J. Chem. Technol. Biotechnol.* **2006**, *81*, 1475–1485.
30. Davies, L.C.; Vilhena, A.M.; Novais, J.M.; Martins-Dias, S. Olive mill wastewater characteristics: modelling and statistical analysis. *Grasas y Aceites* **2008**, *55*, 233–241.
31. Gebreyohannes, A.Y.; Mazzei, R.; Giorno, L. Trends and current practices of olive mill wastewater treatment: Application of integrated membrane process and its future perspective. *Sep. Purif. Technol.* **2016**, *162*, 45–60.
32. McNamara, C.J.; Anastasiou, C.C.; O'Flaherty, V.; Mitchell, R. Biorremediation of olive mill wastewater. *Int. Biodeterior. Biodegrad.* **2008**, *61*, 127–134.
33. Khoufi, S.; Hamza, M.; Sayadi, S. Enzymatic hydrolysis of olive wastewater for hydroxytyrosol enrichment. *Bioresour. Technol.* **2011**, *102*, 9050–9058.
34. Tsagaraki, E.; Lazarides, H.N.; Petrotos, K.B. Olive mill wastewater treatment. In *Utilization of By-Products and Treatment of Waste in the Food Industry*; Oreopoulou, V., Russ, W., Eds.; Springer US: Boston, MA, 2007; pp. 133–157 ISBN 0387335110.
35. Justino, C.I.; Duarte, K.; Loureiro, F.; Pereira, R.; Antunes, S.C.; Marques, S.M.; Gonçalves, F.; Rocha-Santos, T.A.P.; Freitas, A.C. Toxicity and organic content characterization of olive oil mill wastewater undergoing a sequential treatment with fungi and photo-Fenton oxidation. *J. Hazard. Mater.* **2009**, *172*, 1560–1572.
36. Agalias, A.; Magiatis, P.; Skaltsounis, A.L.; Mikros, E.; Tsarbopoulos, A.; Gikas, E.; Spanos, I.; Manios, T. A new process for the management of olive oil mill waste water and recovery of natural antioxidants. *J. Agric. Food Chem.* **2007**, *55*, 2671–2676.
37. Beltran De Heredia, J.; Torregrosa, J.; Dominguez, J.R.; Peres, J.A. Kinetic model for phenolic compound oxidation by Fenton's reagent. *Chemosphere* **2001**, *45*, 85–90.
38. El-Abbassi, A.; Hafidi, A.; Khayet, M.; García-Payo, M.C. Integrated direct contact membrane distillation for olive mill wastewater treatment. *Desalination* **2013**, *323*, 31–38.
39. El-Gohary, F.A.; Badawy, M.I.; El-Khateeb, M.A.; El-Kalliny, A.S. Integrated treatment of olive mill wastewater (OMW) by the combination of Fenton's reaction and anaerobic treatment. *J. Hazard. Mater.* **2009**, *162*, 1536–1541.
40. Kallel, M.; Belaid, C.; Mechichi, T.; Ksibi, M.; Elleuch, B. Removal of organic load and phenolic compounds from olive mill wastewater by Fenton oxidation with zero-valent iron. *Chem. Eng. J.* **2009**, *150*, 391–395.
41. Garcia-Castello, E.; Cassano, A.; Criscuoli, A.; Conidi, C.; Drioli, E. Recovery and concentration of polyphenols from olive mill wastewaters by integrated membrane system. *Water Res.* **2010**, *44*, 3883–3892.
42. El Hajjouji, H.; Pinelli, E.; Guiresse, M.; Merlina, G.; Revel, J.C.; Hafidi, M. Assessment of the genotoxicity of olive mill waste water (OMWW) with the Vicia faba micronucleus test. *Mutat. Res. - Genet. Toxicol. Environ. Mutagen.* **2007**, *634*, 25–31.
43. Rinaldi, M.; Rana, G.; Introna, M. Olive-mill wastewater spreading in southern Italy: Effects on a durum wheat crop. *F. Crop. Res.* **2003**, *84*, 319–326.
44. Danellakis, D.; Ntaikou, I.; Kornaros, M.; Dailianis, S. Olive oil mill wastewater toxicity in the marine environment: Alterations of stress indices in tissues of mussel Mytilus galloprovincialis. *Aquat. Toxicol.* **2011**, *101*, 358–366.
45. Karaouzas, I.; Skoulikidis, N.T.; Giannakou, U.; Albanis, T.A. Spatial and temporal effects of olive mill wastewaters to stream macroinvertebrates and aquatic ecosystems status. *Water Res.* **2011**, *45*, 6334–6346.
46. Mantzavinos, D.; Kalogerakis, N. Treatment of olive mill effluents: Part I. Organic matter degradation by chemical and biological processes - An overview. *Environ. Int.* **2005**, *31*, 289–295.

47. Moraetis, D.; Stamati, F.E.; Nikolaidis, N.P.; Kalogerakis, N. Olive mill wastewater irrigation of maize: Impacts on soil and groundwater. *Agric. Water Manag.* **2011**, *98*, 1125–1132.
48. Mechri, B.; Mariem, F. Ben; Baham, M.; Elhadj, S. Ben; Hammami, M. Change in soil properties and the soil microbial community following land spreading of olive mill wastewater affects olive trees key physiological parameters and the abundance of arbuscular mycorrhizal fungi. *Soil Biol. Biochem.* **2008**, *40*, 152–161.
49. Mekki, A.; Dhouib, A.; Sayadi, S. Changes in microbial and soil properties following amendment with treated and untreated olive mill wastewater. *Microbiol. Res.* **2006**, *161*, 93–101.
50. Paredes, C.; Cegarra, J.; Bernal, M.P.; Roig, A. Influence of olive mill wastewater in composting and impact of the compost on a Swiss chard crop and soil properties. *Environ. Int.* **2005**, *31*, 305–312.
51. Barbera, A.C.; Maucieri, C.; Cavallaro, V.; Ioppolo, A.; Spagna, G. Effects of spreading olive mill wastewater on soil properties and crops, a review. *Agric. Water Manag.* **2013**, *119*, 43–53.
52. *Decreto-lei no. 236/98, In: Diário da República, Série I-A, no. 176 de 1 de agosto de 1998*; Ministério do Ambiente, Lisboa, Portugal, pp. 3676–3722.;
53. *Despacho Conjunto no. 626/2000 - Normas para a utilização de águas russas na rega de solos agrícolas, In: Diário da República. Série II, no. 131 de 6 de Junho de 2000*; Ministérios da Agricultura, do Desenvolvimento rural e das Pescas e do Ambiente e do Ordenamento do Território, Lisboa, Portugal, pp. 9676–9677.;
54. Fadil, K.; Chahlaoui, A.; Ouahbi, A.; Zaid, A.; Borja, R. Aerobic biodegradation and detoxification of wastewaters from the olive oil industry. *Int. Biodeterior. Biodegrad.* **2003**, *51*, 37–41.
55. Tziotzios, G.; Michailakis, S.; Vayenas, D. V. Aerobic biological treatment of olive mill wastewater by olive pulp bacteria. *Int. Biodeterior. Biodegrad.* **2007**, *60*, 209–214.
56. El Hajjouji, H.; Fakharedine, N.; Ait Baddi, G.; Winterton, P.; Bailly, J.R.; Revel, J.C.; Hafidi, M. Treatment of olive mill waste-water by aerobic biodegradation: An analytical study using gel permeation chromatography, ultraviolet-visible and Fourier transform infrared spectroscopy. *Bioresour. Technol.* **2007**, *98*, 3513–3520.
57. Filidei, S.; Masciandaro, G.; Ceccanti, B. Anaerobic digestion of olive oil mill effluents: Evaluation of wastewater organic load and phytotoxicity reduction. *Water. Air. Soil Pollut.* **2003**, *145*, 79–94.
58. Ammary, B.Y. Treatment of olive mill wastewater using an anaerobic sequencing batch reactor. *Desalination* **2005**, *177*, 157–165.
59. Azbar, N.; Tutuk, F.; Keskin, T. Biodegradation performance of an anaerobic hybrid reactor treating olive mill effluent under various organic loading rates. *Int. Biodeterior. Biodegrad.* **2009**, *63*, 690–698.
60. Azbar, N.; Keskin, T.; Yuruyen, A. Enhancement of biogas production from olive mill effluent (OME) by co-digestion. *Biomass and Bioenergy* **2008**, *32*, 1195–1201.
61. Gelegenis, J.; Georgakakis, D.; Angelidaki, I.; Christopoulou, N.; Goumenaki, M. Optimization of biogas production from olive-oil mill wastewater, by codigesting with diluted poultry-manure. *Appl. Energy* **2007**, *84*, 646–663.
62. Boubaker, F.; Cheikh Ridha, B. Anaerobic co-digestion of olive mill wastewater with olive mill solid waste in a tubular digester at mesophilic temperature. *Bioresour. Technol.* **2007**, *98*, 769–774.
63. Jaouani, A.; Vanthournhout, M.; Penninckx, M.J. Olive oil mill wastewater purification by combination of coagulation- flocculation and biological treatments. *Environ. Technol.* **2005**, *26*, 633–41.
64. Azbar, N.; Keskin, T.; Catalkaya, E.C. Improvement in anaerobic degradation of olive mill effluent (OME) by chemical pretreatment using batch systems. *Biochem. Eng. J.* **2008**, *38*, 379–383.
65. Neffa, M.; Hanine, H.; Lekhlif, B.; Ouazzani, N.; Taourirte, M. Improvement of biological process using biocoagulation–flocculation pretreatment aid in olive mill wastewater detoxification. *Desalin. Water Treat.* **2014**, *52*, 2893–2902.
66. Aytar, P.; Gedikli, S.; Sam, M.; Farizoglu, B.; Cabuk, A. Sequential treatment of olive oil mill wastewater with adsorption and biological and photo-Fenton oxidation. *Environ. Sci. Pollut. Res. Int.* **2013**, *20*, 3060–3067.
67. Tezcan Ün, Ü.; Uğur, S.; Koparal, A.S.; Bakir Öğütveren, Ü. Electrocoagulation of olive mill wastewaters. *Sep. Purif. Technol.* **2006**, *52*, 136–141.
68. Hanafi, F.; Assobhei, O.; Mountadar, M. Detoxification and discoloration of Moroccan olive mill wastewater by electrocoagulation. *J. Hazard. Mater.* **2010**, *174*, 807–812.
69. Khoufi, S.; Feki, F.; Sayadi, S. Detoxification of olive mill wastewater by electrocoagulation and sedimentation processes. *J. Hazard. Mater.* **2007**, *142*, 58–67.
70. Coskun, T.; Ilhan, F.; Demir, N.M.; Debik, E.; Kurt, U. Optimization of energy costs in the pretreatment of olive mill wastewaters by electrocoagulation. *Environ. Technol.* **2012**, *33*, 801–807.
71. Plaza, C.; Senesi, N.; Brunetti, G.; Mondelli, D. Cocomposting of sludge from olive oil mill

wastewater mixed with tree cuttings. *Compost Sci. Util.* **2005**, *13*, 217–226.
72. Hachicha, S.; Sellami, F.; Cegarra, J.; Hachicha, R.; Drira, N.; Medhioub, K.; Ammar, E. Biological activity during co-composting of sludge issued from the OMW evaporation ponds with poultry manure-Physico-chemical characterization of the processed organic matter. *J. Hazard. Mater.* **2009**, *162*, 402–409.
73. Aviani, I.; Laor, Y.; Medina, S.; Krassnovsky, A.; Raviv, M. Co-composting of solid and liquid olive mill wastes: management aspects and the horticultural value of the resulting composts. *Bioresour. Technol.* **2010**, *101*, 6699–6706.
74. Obied, H.K.; Allen, M.S.; Bedgood, D.R.; Prenzler, P.D.; Robards, K.; Stockmann, R. Bioactivity and analysis of biophenols recovered from olive mill waste. *J. Agric. Food Chem.* **2005**, *53*, 823–837.
75. Choi, D.Y.; Lee, Y.J.; Hong, J.T.; Lee, H.J. Antioxidant properties of natural polyphenols and their therapeutic potentials for Alzheimer's disease. *Brain Res. Bull.* **2012**, *87*, 144–153.
76. Ochando-Pulido, J.M.; González-Hernández, R.; Martinez-Ferez, A. On the effect of the operating parameters for two-phase olive-oil washing wastewater combined phenolic compounds recovery and reclamation by novel ion exchange resins. *Sep. Purif. Technol.* **2018**, *195*, 50–59.
77. Frascari, D.; Rubertelli, G.; Arous, F.; Ragini, A.; Bresciani, L.; Arzu, A.; Pinelli, D. Valorisation of olive mill wastewater by phenolic compounds adsorption: Development and application of a procedure for adsorbent selection. *Chem. Eng. J.* **2019**, *360*, 124–138.
78. Chatzisymeon, E.; Xekoukoulotakis, N.P.; Mantzavinos, D. Determination of key operating conditions for the photocatalytic treatment of olive mill wastewaters. *Catal. Today* **2009**, *144*, 143–148.
79. Hodaifa, G.; García, C.A.; Borja, R. Study of catalysts' influence on photocatalysis/photodegradation of olive oil mill wastewate. Determination of the optimum working conditions. *Catalysts* **2020**, *10*, 554.
80. Pham Minh, D.; Gallezot, P.; Azabou, S.; Sayadi, S.; Besson, M. Catalytic wet air oxidation of olive oil mill effluents. 4. Treatment and detoxification of real effluents. *Appl. Catal. B Environ.* **2008**, *84*, 749–757.
81. Chedeville, O.; Debacq, M.; Porte, C. Removal of phenolic compounds present in olive mill wastewaters by ozonation. *Desalination* **2009**, *249*, 865–869.
82. Martins, R.C.; Silva, A.M.T.; Castro-Silva, S.; Garção-Nunes, P.; Quinta-Ferreira, R.M. Adopting strategies to improve the efficiency of ozonation in the real-scale treatment of olive oil mill wastewaters. *Environ. Technol.* **2010**, *31*, 1459–1469.
83. Vilardi, G.; Ochando-Pulido, J.M.; Stoller, M.; Verdone, N.; Di Palma, L. Fenton oxidation and chromium recovery from tannery wastewater by means of iron-based coated biomass as heterogeneous catalyst in fixed-bed columns. *Chem. Eng. J.* **2018**, *351*, 1–11.
84. Amaral-Silva, N.; Martins, R.C.; Castro-Silva, S.; Quinta-Ferreira, R.M. Integration of traditional systems and AOP´s technologies on the industrial treatment for Olive Mill Wastewaters. *Environ. Technol.* **2016**, *3330*, 1–41.
85. Lucas, M.S.; Peres, J.A. Removal of COD from olive mill wastewater by Fenton's reagent: Kinetic study. *J. Hazard. Mater.* **2009**, *168*, 1253–1259.
86. Iboukhoulef, H.; Amrane, A.; Kadi, H. Removal of phenolic compounds from olive mill wastewater by a Fenton-like system H_2O_2/Cu(II)—thermodynamic and kinetic modeling. *Desalin. Water Treat.* **2014**, *3994*, 1–6.
87. Hodaifa, G.; Ochando-Pulido, J.M.; Rodriguez-Vives, S.; Martinez-Ferez, A. Optimization of continuous reactor at pilot scale for olive-oil mill wastewater treatment by Fenton-like process. *Chem. Eng. J.* **2013**, *220*, 117–124.
88. Ciggin, A.S.; Sarica, E.S.; Doğruel, S.; Orhon, D. Impact of ultrasonic pretreatment on Fenton-based oxidation of olive mill wastewater - towards a sustainable treatment scheme. *J. Clean. Prod.* **2021**, *313*.
89. Agabo García, C.; Hodaifa, G. Real olive oil mill wastewater treatment by photo-Fenton system using artificial ultraviolet light lamps. *J. Clean. Prod.* **2017**, *162*, 743–753.
90. Agabo-García, C.; Calderón, N.; Hodaifa, G. Heterogeneous Photo-Fenton Reaction for Olive Mill Wastewater Treatment—Case of Reusable Catalyst. *Catalysts* **2021**, *11*, 557.
91. Khoufi, S.; Aloui, F.; Sayadi, S. Treatment of olive oil mill wastewater by combined process electro-Fenton reaction and anaerobic digestion. *Water Res.* **2006**, *40*, 2007–2016.
92. Un, U.T.; Altay, U.; Koparal, A.S.; Ogutveren, U.B. Complete treatment of olive mill wastewaters by electrooxidation. *Chem. Eng. J.* **2008**, *139*, 445–452.
93. Ltaïef, A.H.; Gadri, A.; Ammar, S. Olive mill wastewater treatment by electro-Fenton with heterogeneous iron source. In *Wastes: Solutions, Treatments and Oportunities II*; CRC Press: London, 2020; pp. 333–338 ISBN 9780367257774.

94. Martins, R.C.; Gomes, T.; Quinta-ferreira, R.M. Fenton's depuration of weathered olive mill wastewaters over a Fe-Ce-O solid catalyst. *Ind. Eng. Chem. Res.* **2010**, *49*, 9043–9051.
95. Maduna Valkaj Kaselj, I., Smolkovic, J., Zrncevic, S., Kumar, N., Murzin, D.Yu., K. Catalytic wet peroxide oxidation of olive oil mill wastewater over zeolite based catalyst. *Chem. Eng. Trans.* **2015**, *43*, 853–858.
96. Maduna, K.; Kumar, N.; Aho, A.; Wärnå, J.; Zrnčević, S.; Murzin, D.Y. Kinetics of catalytic wet peroxide oxidation of phenolics in olive oil mill wastewaters over copper catalysts. *ACS Omega* **2018**, *3*, 7247–7260.
97. Domingues, E.; Rodrigues, F.; Gomes, J.; Quina, M.J.; Castro-Silva, S.; Martins, R.C. Screening of low-cost materials as heterogeneous catalysts for olive mill wastewater Fenton's peroxidation. *Energy Reports* **2020**, *6*, 161–167.
98. Fraga, M.; Sanches, S.; Crespo, J.; Pereira, V. Assessment of a New Silicon Carbide Tubular Honeycomb Membrane for Treatment of Olive Mill Wastewaters. *Membranes (Basel).* **2017**, *7*, 12.
99. Ochando-Pulido, J.M.; Hodaifa, G.; Martinez-Ferez, A. Fouling inhibition upon fenton-like oxidation pretreatment for olive mill wastewater reclamation by membrane process. *Chem. Eng. Process. Process Intensif.* **2012**, *62*, 89–98.
100. El-Abbassi, A.; Kiai, H.; Raiti, J.; Hafidi, A. Application of ultrafiltration for olive processing wastewaters treatment. *J. Clean. Prod.* **2014**, *65*, 432–438.
101. Ochando-Pulido, J.M.; Verardo, V.; Segura-Carretero, A.; Martinez-Ferez, A. Technical optimization of an integrated UF/NF pilot plant for conjoint batch treatment of two-phase olives and olive oil washing wastewaters. *Desalination* **2015**, *364*, 82–89.
102. Bazzarelli, F.; Poerio, T.; Mazzei, R.; D'Agostino, N.; Giorno, L. Study of OMWWs suspended solids destabilization to improve membrane processes performance. *Sep. Purif. Technol.* **2015**, *149*, 183–189.
103. Stoller, M.; Azizova, G.; Mammadova, A.; Vilardi, G.; Di Palma, L.; Chianese, A. Treatment of olive oil processing wastewater by ultrafiltration, nanofiltration, reverse osmosis and biofiltration. *Chem. Eng. Trans.* **2016**, *47*, 409–414.
104. Kontos, S.S.; Katrivesis, F.K.; Constantinou, T.C.; Zoga, C.A.; Ioannou, I.S.; Koutsoukos, P.G.; Paraskeva, C.A. Implementation of membrane filtration and melt crystallization for the effective treatment and valorization of olive mill wastewaters. *Sep. Purif. Technol.* **2018**, *193*, 103–111.
105. Carnevale, M.C.; Gnisci, E.; Hilal, J.; Criscuoli, A. Direct Contact and Vacuum Membrane Distillation application for the olive mill wastewater treatment. *Sep. Purif. Technol.* **2016**, *169*, 121–127.
106. Tundis, R.; Conidi, C.; Loizzo, M.R.; Sicari, V.; Romeo, R.; Cassano, A. Concentration of bioactive phenolic compounds in olive mill wastewater by direct contact membrane distillation. *Molecules* **2021**, *26*, 1808.
107. Ochando-Pulido, J.M.; Martinez-Ferez, A. Operation setup of a nanofiltration membrane unit for purification of two-phase olives and olive oil washing wastewaters. *Sci. Total Environ.* **2018**, *612*, 758–766.
108. Comninellis, C.; Kapalka, A.; Malato, S.; Parsons, S.A.; Poulios, I.; Mantzavinos, D. Advanced oxidation processes for water treatment: advances and trends for R&D. *J. Chem. Technol. Biotechnol.* **2008**, *83*, 769–776.
109. Pignatello, J.J.; Oliveros, E.; MacKay, A. Advanced oxidation processes for organic contaminant destruction based on the fenton reaction and related chemistry. *Crit. Rev. Environ. Sci. Technol.* **2006**, *36*, 1–84.
110. Poyatos, J.M.; Muñio, M.M.; Almecija, M.C.; Torres, J.C.; Hontoria, E.; Osorio, F. Advanced oxidation processes for wastewater treatment: State of the art. *Water. Air. Soil Pollut.* **2010**, *205*, 187–204.
111. Duarte, F.; Morais, V.; Maldonado-Hódar, F.J.; Madeira, L.M. Treatment of textile effluents by the heterogeneous Fenton process in a continuous packed-bed reactor using Fe/activated carbon as catalyst. *Chem. Eng. J.* **2013**, *232*, 34–41.
112. Ramirez, J.H.; Costa, C.A.; Madeira, L.M.; Mata, G.; Vicente, M.A.; Rojas-Cervantes, M.L.; López-Peinado, A.J.; Martín-Aranda, R.M. Fenton-like oxidation of Orange II solutions using heterogeneous catalysts based on saponite clay. *Appl. Catal. B Environ.* **2007**, *71*, 44–56.
113. Walling, C. Fenton's reagent revisited. *Acc. Chem. Res.* **1975**, *8*, 125–131.
114. Neyens, E.; Baeyens, J. A review of classic Fenton's peroxidation as an advanced oxidation technique. *J. Hazard. Mater.* **2003**, *98*, 33–50.
115. Bautista, P.; Mohedano, A.F.; Casas, J.A.; Zazo, J.A.; Rodriguez, J.J. An overview of the application of Fenton oxidation to industrial wastewaters treatment. *J. Chem. Technol. Biotechnol.* **2008**, *83*, 1323–1338.
116. Fenton, H.J.H. Oxidation of tartaric acid in presence of iron. *J Chem Soc* **1894**, *65*, 899–910.

117. Haber, F.; Weiss, J. The catalytic decomposition of hydrogen peroxide by iron salts. *Proc. R. Soc. London A* **1934**, *147*, 332–351.
118. Navalon, S.; Dhakshinamoorthy, A.; Alvaro, M.; Garcia, H. Heterogeneous Fenton catalysts based on activated carbon and related materials. *ChemSusChem* **2011**, *4*, 1712–1730.
119. Sychev, A.Y.; Isak, V.G. Iron compounds and the mechanisms of the homogeneous catalysis of the activation of O_2 and H_2O_2 and of the oxidation of organic substrates. *Russ. Chem. Rev.* **1995**, *64*, 1105–1129.
120. Guo, J.; Al-Dahhan, M. Catalytic wet oxidation of phenol by hydrogen peroxide over pillared clay catalyst. *Ind. Eng. Chem. Res.* **2003**, *42*, 2450–2460.
121. Ramirez, J.H.; Maldonado-Hódar, F.J.; Pérez-Cadenas, A.F.; Moreno-Castilla, C.; Costa, C.A.; Madeira, L.M. Azo-dye Orange II degradation by heterogeneous Fenton- like reaction using carbon-Fe catalysts. *Appl. Catal. B Environ.* **2007**, *75*, 312–323.
122. Esteves, B.M.; Rodrigues, C.S.D.; Boaventura, R.A.R.; Maldonado-Hódar, F.J.; Madeira, L.M. Coupling of acrylic dyeing wastewater treatment by heterogeneous Fenton oxidation in a continuous stirred tank reactor with biological degradation in a sequential batch reactor. *J. Environ. Manage.* **2016**, *166*, 193–203.
123. Duarte, F.M.; Maldonado-Hódar, F.J.; Madeira, L.M. Influence of the iron precursor in the preparation of heterogeneous Fe/activated carbon Fenton-like catalysts. *Appl. Catal. A Gen.* **2013**, *458*, 39–47.
124. Herney-Ramirez, J.; Lampinen, M.; Vicente, M.A.; Costa, C.A.; Madeira, L.M. Experimental design to optimize the oxidation of orange II dye solution using a clay-based fenton-like catalyst. *Ind. Eng. Chem. Res.* **2008**, *47*, 284–294.
125. Di Luca, C.; Massa, P.; Fenoglio, R.; Cabello, F.M. Improved Fe_2O_3/Al_2O_3 as heterogeneous Fenton catalysts for the oxidation of phenol solutions in a continuous reactor. *J. Chem. Technol. Biotechnol.* **2014**, *89*, 1121–1128.
126. Babuponnusami, A.; Muthukumar, K. A review on Fenton and improvements to the Fenton process for wastewater treatment. *J. Environ. Chem. Eng.* **2014**, *2*, 557–572.
127. Ruppert, G.; Bauer, R.; Heisler, G.; Novalic, S. Mineralization of cyclic organic water contaminants by the photo-fenton reaction — Influence of structure and substituents. *Chemosphere* **1993**, *27*, 1339–1347.
128. Gil, A.; Korili, S.A.; Trujillano, R.; Vicente, M.A. *Pillared clays and related catalysts*; 2010; ISBN 9781441966698.
129. Rahmanian, N.; Jafari, S.M.; Galanakis, C.M. Recovery and removal of phenolic compounds from olive mill wastewater. *JAOCS, J. Am. Oil Chem. Soc.* **2014**, *91*, 1–18.
130. Ioannou, L.A.; Puma, G.L.; Fatta-Kassinos, D. Treatment of winery wastewater by physicochemical, biological and advanced processes: A review. *J. Hazard. Mater.* **2015**, *286*, 343–368.
131. Ramirez, J.H.; Costa, C.A.; Madeira, L.M. Experimental design to optimize the degradation of the synthetic dye Orange II using Fenton's reagent. *Catal. Today* **2005**, *107–108*, 68–76.
132. Buxton, G. V; Greenstock, C.L.; Helman, P.; Ross, A.B. Critical Review of rate constants for reactions of hydrated electrons, hydrogen atoms and hydroxyl radicals ($^{\bullet}OH/^{\bullet}O^-$) in aqueous solution. *J. Phys. Chem. Ref. Data* **1988**, *17*, 513–886.
133. Yoon, J.; Lee, Y.; Kim, S. Investigation of the reaction pathway of $^{\bullet}OH$ radicals produced by Fenton oxidation in the conditions of wastewater treatment. *Water Sci. Technol.* **2001**, *44*, 15–21.
134. Melero, J.A.; Martínez, F.; Botas, J.A.; Molina, R.; Pariente, M.I. Heterogeneous catalytic wet peroxide oxidation systems for the treatment of an industrial pharmaceutical wastewater. *Water Res.* **2009**, *43*, 4010–4018.
135. Maamir, W.; Ouahabi, Y.; Poncin, S.; Li, H.Z.; Bensadok, K. Effect of fenton pretreatment on anaerobic digestion of olive mill wastewater and olive mill solid waste in mesophilic conditions. *Int. J. Green Energy* **2017**, *14*, 555–560.
136. Nieto, L.M.; Hodaifa, G.; Vives, S.R.; Casares, J.A.G. Industrial Plant for Olive Mill Wastewater from Two-Phase Treatment by Chemical Oxidation. *J. Environ. Eng.* **2010**, *136*, 1309–1313.
137. Zazo, J.A.; Casas, J.A.; Mohedano, A.F.; Rodriguez, J.J. Semicontinuous Fenton oxidation of phenol in aqueous solution. A kinetic study. *Water Res.* **2009**, *43*, 4063–4069.
138. Ribeiro, J.P.; Nunes, M.I. Recent trends and developments in Fenton processes for industrial wastewater treatment – A critical review. *Environ. Res.* **2021**, *197*.
139. Reis, P.M.; Martins, P.J.M.; Martins, R.C.; Gando-Ferreira, L.M.; Quinta-Ferreira, R.M. Integrating Fenton's process and ion exchange for olive mill wastewater treatment and iron recovery. *Environ. Technol. (United Kingdom)* **2018**, *39*, 308–316.
140. Amaral-Silva, N.; Martins, R.C.; Nunes, P.; Castro-Silva, S.; Quinta-Ferreira, R.M. From a lab test to industrial application: scale-up of Fenton process for real olive mill wastewater treatment. *J.*

Chem. Technol. Biotechnol. **2017**, *92*, 1336–1344.
141. Directive 2000/60/EC of the European Parliament and of the Council establishing a framework for community action in the field of water policy, OJ L 327, 22.12.2000, 1–73.
142. Nieto, L.M.; Hodaifa, G.; Rodríguez, S.; Giménez, J.A.; Ochando, J. Flocculation-Sedimentation Combined with Chemical Oxidation Process. *Clean - Soil, Air, Water* **2011**, *39*, 949–955.
143. Víctor-Ortega, M.D.; Ochando-Pulido, J.M.; Martínez-Ferez, A. Iron removal and reuse from Fenton-like pretreated olive mill wastewater with novel strong-acid cation exchange resin fixed-bed column. *J. Ind. Eng. Chem.* **2016**, *36*, 298–305.
144. Ochando-Pulido, J.M.; Rodriguez-Vives, S.; Hodaifa, G.; Martinez-Ferez, A. Impacts of operating conditions on reverse osmosis performance of pretreated olive mill wastewater. *Water Res.* **2012**, *46*, 4621–4632.
145. Feng, Y.; Wu, D.L.; Duan, D.; Lu, M.M. Fenton-Like oxidation of refractory chemical wastewater using pyrite. In Proceedings of the Advances in Environmental Science and Engineering; Trans Tech Publications Ltd, 2012; Vol. 518, pp. 2518–2525.
146. Huang, Y.; Su, C.; Yang, Y.; Lu, M. Degradation of aniline catalyzed by heterogeneous Fenton-like reaction using iron oxide/SiO_2. *AIChE J.* **2013**, *32*, 187–192.
147. Yao, Y.; Mao, Y.; Zheng, B.; Huang, Z.; Lu, W.; Chen, W. Anchored iron ligands as an efficient fenton-like catalyst for removal of dye pollutants at neutral pH. *Ind. Eng. Chem. Res.* **2014**, *53*, 8376–8384.
148. Vorontsov, A. V. Advancing Fenton and photo-Fenton water treatment through the catalyst design. *J. Hazard. Mater.* **2019**, *372*, 103–112.
149. Garcia-segura, S.; Bellotindos, L.M.; Huang, Y.; Brillas, E.; Lu, M. Fluidized-bed Fenton process as alternative wastewater treatment technology — A review. *J. Taiwan Inst. Chem. Eng.* **2016**, *67*, 211–225.
150. Zazo, J.A.; Casas, J.A.; Mohedano, A.F.; Rodríguez, J.J. Catalytic wet peroxide oxidation of phenol with a Fe/active carbon catalyst. *Appl. Catal. B Environ.* **2006**, *65*, 261–268.
151. Wang, N.; Zheng, T.; Zhang, G.; Wang, P. A review on Fenton-like processes for organic wastewater treatment. *J. Environ. Chem. Eng.* **2016**, *4*, 762–787.
152. Ammar, S.; Oturan, M.A.; Labiadh, L.; Guersalli, A.; Abdelhedi, R.; Oturan, N.; Brillas, E. Degradation of tyrosol by a novel electro-Fenton process using pyrite as heterogeneous source of iron catalyst. *Water Res.* **2015**, *74*, 77–87.
153. Aghdasinia, H.; Bagheri, R.; Vahid, B.; Khataee, A. Central composite design optimization of pilot plant fluidized-bed heterogeneous Fenton process for degradation of an azo dye. *Environ. Technol. (United Kingdom)* **2016**, *37*, 2703–2712.
154. Munoz, M.; de Pedro, Z.M.; Casas, J.A.; Rodriguez, J.J. Preparation of magnetite-based catalysts and their application in heterogeneous Fenton oxidation - A review. *Appl. Catal. B Environ.* **2015**, *176–177*, 249–265.
155. Munoz, M.; Domínguez, P.; de Pedro, Z.M.; Casas, J.A.; Rodriguez, J.J. Naturally-occurring iron minerals as inexpensive catalysts for CWPO. *Appl. Catal. B Environ.* **2017**, *203*, 166–173.
156. Figueiredo, J.L.; Pereira, M.F.R.; Freitas, M.M.A.; Órfão, J.J.M. Modification of the surface chemistry of activated carbons. *Carbon N. Y.* **1999**, *37*, 1379–1389.
157. Zazo, J.A.; Bedia, J.; Fierro, C.M.; Pliego, G.; Casas, J.A.; Rodriguez, J.J. Highly stable Fe on activated carbon catalysts for CWPO upon $FeCl_3$ activation of lignin from black liquors. *Catal. Today* **2012**, *187*, 115–121.
158. Granato, T.; Katović, A.; Valkaj, K.M.; Zrnčević, S. Zeolite based ceramics as catalysts for wet hydrogen peroxide catalytic oxidation of phenol and poly-phenols. In *Zeolites and related materials: Trends, targets and challenges*; Gédéon, A., Massiani, P., Babonneau, F., Eds.; Studies in Surface Science and Catalysis; Elsevier, 2008; Vol. 174, pp. 1171–1174.
159. Rache, M.L.; García, A.R.; Zea, H.R.; Silva, A.M.T.; Madeira, L.M.; Ramírez, J.H. Azo-dye orange II degradation by the heterogeneous Fenton-like process using a zeolite Y-Fe catalyst-Kinetics with a model based on the Fermi's equation. *Appl. Catal. B Environ.* **2014**, *146*, 192–200.
160. Zhong, X.; Barbier, J.; Duprez, D.; Zhang, H.; Royer, S. Modulating the copper oxide morphology and accessibility by using micro-/mesoporous SBA-15 structures as host support: Effect on the activity for the CWPO of phenol reaction. *Appl. Catal. B Environ.* **2012**, *121–122*, 123–134.
161. Navalon, S.; Alvaro, M.; Garcia, H. Heterogeneous Fenton catalysts based on clays, silicas and zeolites. *Appl. Catal. B Environ.* **2010**, *99*, 1–26.
162. Hartmann, M.; Kullmann, S.; Keller, H. Wastewater treatment with heterogeneous Fenton-type catalysts based on porous materials. *J. Mater. Chem.* **2010**, *20*, 9002–9017.
163. Ben Achma, R.; Ghorbel, A.; Dafinov, A.; Medina, F. Synthesis of stable Cu-supported pillared clays for wet tyrosol oxidation with H_2O_2. *J. Phys. Chem. Solids* **2012**, *73*, 1524–1529.

164. di Luca, C.; Ivorra, F.; Massa, P.; Fenoglio, R. Iron-alumina synergy in the heterogeneous Fenton-type peroxidation of phenol solutions. *Chem. Eng. J.* **2015**, *268*, 280–289.
165. Chergui, S.; Yeddou, A.R.; Chergui, A.; Halet, F.; Amaouche, H.; Nadjemi, B.; Ould-Dris, A. Removal of cyanide in aqueous solution by oxidation with hydrogen peroxide in presence of activated alumina. *Toxicol. Environ. Chem.* **2015**, *97*, 1289–1295.
166. Zhuang, H.; Han, H.; Hou, B.; Jia, S.; Zhao, Q. Heterogeneous catalytic ozonation of biologically pretreated Lurgi coal gasification wastewater using sewage sludge based activated carbon supported manganese and ferric oxides as catalysts. *Bioresour. Technol.* **2014**, *166*, 178–186.
167. Mohedano, A.F.; Monsalvo, V.M.; Bedia, J.; Lopez, J.; Rodriguez, J.J. Highly stable iron catalysts from sewage sludge for CWPO. *J. Environ. Chem. Eng.* **2014**, *2*, 2359–2364.
168. Duarte, F.; Maldonado-Hódar, F.J.; Madeira, L.M. Influence of the particle size of activated carbons on their performance as fe supports for developing fenton-like catalysts. *Ind. Eng. Chem. Res.* **2012**, *51*, 9218–9226.
169. Duarte, F.; Maldonado-Hódar, F.J.; Madeira, L.M. Influence of the characteristics of carbon materials on their behaviour as heterogeneous Fenton catalysts for the elimination of the azo dye Orange II from aqueous solutions. *Appl. Catal. B Environ.* **2011**, *103*, 109–115.
170. Vivo-Vilches, J.F.; Bailón-García, E.; Pérez-Cadenas, A.F.; Carrasco-Marín, F.; Maldonado-Hódar, F.J. Tailoring the surface chemistry and porosity of activated carbons: Evidence of reorganization and mobility of oxygenated surface groups. *Carbon N. Y.* **2014**, *68*, 520–530.
171. Rey, A.; Faraldos, M.; Casas, J.A.; Zazo, J.A.; Bahamonde, A.; Rodríguez, J.J. Catalytic wet peroxide oxidation of phenol over Fe/AC catalysts: Influence of iron precursor and activated carbon surface. *Appl. Catal. B Environ.* **2009**, *86*, 69–77.
172. Rodríguez, A.; Ovejero, G.; Sotelo, J.L.; Mestanza, M.; García, J. Heterogeneous fenton catalyst supports screening for mono azo dye degradation in contaminated wastewaters. *Ind. Eng. Chem. Res.* **2010**, *49*, 498–505.
173. Wang, W.; Liu, Y.; Li, T.; Zhou, M. Heterogeneous Fenton catalytic degradation of phenol based on controlled release of magnetic nanoparticles. *Chem. Eng. J.* **2014**, *242*, 1–9.
174. Botas, J.A.; Melero, J.A.; Martínez, F.; Pariente, M.I. Assessment of Fe_2O_3/SiO_2 catalysts for the continuous treatment of phenol aqueous solutions in a fixed bed reactor. *Catal. Today* **2010**, *149*, 334–340.
175. Lu, M.; Yao, Y.; Gao, L.; Mo, D.; Lin, F.; Lu, S. Continuous Treatment of Phenol over an $Fe_2O_3/\gamma\text{-}Al_2O_3$ Catalyst in a Fixed-Bed Reactor. *Water. Air. Soil Pollut.* **2015**, *226*, 87.
176. Li, H.; Cheng, R.; Liu, Z.; Du, C. Waste control by waste: Fenton–like oxidation of phenol over Cu modified ZSM–5 from coal gangue. *Sci. Total Environ.* **2019**, *683*, 638–647.
177. Li, H.; Gao, Q.; Wang, G.; Han, B.; Xia, K.; Zhou, C. Unique electron reservoir properties of manganese in Mn(II)-doped CeO_2 for reversible electron transfer and enhanced Fenton-like catalytic performance. *Appl. Surf. Sci.* **2020**, *502*, 144295.
178. Chaliha, S.; Bhattacharyya, K.G. Wet oxidative method for removal of 2,4,6-trichlorophenol in water using Fe (III), Co (II), Ni (II) supported MCM41 catalysts. *J. Hazard. Mater.* **2008**, *150*, 728–736.
179. Moreno-Castilla, C.; López-Ramón, M.V.; Fontecha-Cámara, M. ángeles; Álvarez, M.A.; Mateus, L. Removal of phenolic compounds from water using copper ferrite nanosphere composites as fenton catalysts. *Nanomaterials* **2019**, *9*.
180. Fida, H.; Zhang, G.; Guo, S.; Naeem, A. Heterogeneous Fenton degradation of organic dyes in batch and fixed bed using La-Fe montmorillonite as catalyst. *J. Colloid Interface Sci.* **2017**, *490*, 859–868.
181. Bokare, A.D.; Choi, W. Review of iron-free Fenton-like systems for activating H_2O_2 in advanced oxidation processes. *J. Hazard. Mater.* **2014**, *275*, 121–135.
182. Huaccallo-Aguilar, Y.; Álvarez-Torrellas, S.; Larriba, M.; Águeda, V.I.; Delgado, J.A.; Ovejero, G.; Peres, J.A.; García, J. Naproxen removal by CWPO with Fe_3O_4/multi-walled carbon nanotubes in a fixed-bed reactor. *J. Environ. Chem. Eng.* **2021**, *9*, 105110.
183. Shukla, P.; Wang, S.; Sun, H.; Ang, H.M.; Tadé, M. Adsorption and heterogeneous advanced oxidation of phenolic contaminants using Fe loaded mesoporous SBA-15 and H_2O_2. *Chem. Eng. J.* **2010**, *164*, 255–260.
184. Zhu, Y.; Zhu, R.; Xi, Y.; Zhu, J.; Zhu, G.; He, H. Strategies for Enhancing the Heterogeneous Fenton Catalytic Reactivity: A review. *Appl. Catal. B Environ.* **2019**, *255*, 117739.
185. Román, S.; Valente Nabais, J.M.; Ledesma, B.; González, J.F.; Laginhas, C.; Titirici, M.M. Production of low-cost adsorbents with tunable surface chemistry by conjunction of hydrothermal carbonization and activation processes. *Microporous Mesoporous Mater.* **2013**, *165*, 127–133.
186. Kannan, N.; Sundaram, M.M. Kinetics and mechanism of removal of methylene blue by adsorption on various carbons - A comparative study. *Dye. Pigment.* **2001**, *51*, 25–40.

187. Figueiredo, J.L.; Pereira, M.F.R. The role of surface chemistry in catalysis with carbons. *Catal. Today* **2010**, *150*, 2–7.
188. Rodriguez-Reinoso, F. The role of carbon materials in heterogeneous catalysis. *Carbon N. Y.* **1998**, *36*, 159–175.
189. Rey, A.; Faraldos, M.; Bahamonde, A.; Casas, J.A.; Zazo, J.A.; Rodríguez, J.J. Role of the activated carbon surface on catalytic wet peroxide oxidation. *Ind. Eng. Chem. Res.* **2008**, *47*, 8166–8174.
190. Figueiredo, J.L. Functionalization of porous carbons for catalytic applications. *J. Mater. Chem. A* **2013**, *1*, 9351–9364.
191. Rodríguez-Reinoso, F.; Molina-Sabio, M. Activated carbons from lignocellulosic materials by chemical and/or physical activation: an overview. *Carbon N. Y.* **1992**, *30*, 1111–1118.
192. Jain, A.; Balasubramanian, R.; Srinivasan, M.P. Hydrothermal conversion of biomass waste to activated carbon with high porosity: A review. *Chem. Eng. J.* **2016**, *283*, 789–805.
193. Demiral, H.; Demiral, I.; Karabacakoğlu, B.; Tümsek, F. Production of activated carbon from olive bagasse by physical activation. *Chem. Eng. Res. Des.* **2011**, *89*, 206–213.
194. Ubago-Pérez, R.; Carrasco-Marín, F.; Fairén-Jiménez, D.; Moreno-Castilla, C. Granular and monolithic activated carbons from KOH-activation of olive stones. *Microporous Mesoporous Mater.* **2006**, *92*, 64–70.
195. Stavropoulos, G.G.; Zabaniotou, A.A. Production and characterization of activated carbons from olive-seed waste residue. *Microporous Mesoporous Mater.* **2005**, *82*, 79–85.
196. Zhang, H.; Xue, G.; Chen, H.; Li, X. Magnetic biochar catalyst derived from biological sludge and ferric sludge using hydrothermal carbonization: Preparation, characterization and its circulation in Fenton process for dyeing wastewater treatment. *Chemosphere* **2018**, *191*, 64–71.
197. Sevilla, M.; Fuertes, A.B. The production of carbon materials by hydrothermal carbonization of cellulose. *Carbon N. Y.* **2009**, *47*, 2281–2289.
198. Czégény, Z.; Jakab, E.; Bozi, J.; Blazsó, M. Pyrolysis of wood–PVC mixtures. Formation of chloromethane from lignocellulosic materials in the presence of PVC. *J. Anal. Appl. Pyrolysis* **2015**, *113*, 123–132.
199. Gil, A.; Puente, G. De; Grange, P. Evidence of textural modifications of an activated carbon on liquid-phase oxidation treatments. *Microporous Mater.* **1997**, 51–61.
200. Moreno-Castilla, C.; Ferro-García, M.A.; Joly, J.P.; Bautista-Toledo, I.; Carrasco-Marín, F.; Rivera-Utrilla, J. Activated Carbon Surface Modifications by Nitric Acid, Hydrogen Peroxide, and Ammonium Peroxydisulfate Treatments. *Langmuir* **1995**, *11*, 4386–4392.
201. Xiang, L.; Royer, S.; Zhang, H.; Tatibouët, J.M.; Barrault, J.; Valange, S. Properties of iron-based mesoporous silica for the CWPO of phenol: A comparison between impregnation and co-condensation routes. *J. Hazard. Mater.* **2009**, *172*, 1175–1184.
202. Xu, C.; Teja, A.S. Characteristics of iron oxide/activated carbon nanocomposites prepared using supercritical water. *Appl. Catal. A Gen.* **2008**, *348*, 251–256.
203. Jiang, S.; Zhang, H.; Yan, Y. Catalytic wet peroxide oxidation of phenol wastewater over a novel Cu-ZSM-5 membrane catalyst. *Catal. Commun.* **2015**, *71*, 28–31.
204. Achma, R. Ben; Ghorbel, A.; Dafinov, A.; Medina, F. Copper-supported pillared clay catalysts for the wet hydrogen peroxide catalytic oxidation of model pollutant tyrosol. *Appl. Catal. A Gen.* **2008**, *349*, 20–28.
205. Vega-Aguilar, C.A.; Barreiro, M.F.; Rodrigues, A.E. Catalytic wet peroxide oxidation of vanillic acid as a lignin model compound towards the renewable production of dicarboxylic acids. *Chem. Eng. Res. Des.* **2020**, *159*, 115–124.
206. De Rosa, S.; Giordano, G.; Granato, T.; Katovic, A.; Tripicchio, F.; Siciliano, A. Chemical Pretreatment of Olive Oil Mill Wastewater Using a Metal-Organic Framework Catalyst. *J. Agric. Food Chem.* **2005**, *53*, 8306–8309.
207. Giordano, G.; Perathoner, S.; Centi, G.; De Rosa, S.; Granato, T.; Katovic, A.; Siciliano, A.; Tagarelli, A.; Tripicchio, F. Wet hydrogen peroxide catalytic oxidation of olive oil mill wastewaters using Cu-zeolite and Cu-pillared clay catalysts. *Catal. Today* **2007**, *124*, 240–246.
208. Caudo, S.; Centi, G.; Genovese, C.; Perathoner, S. Copper- and iron-pillared clay catalysts for the WHPCO of model and real wastewater streams from olive oil milling production. *Appl. Catal. B Environ.* **2007**, *70*, 437–446.
209. Azabou, S.; Najjar, W.; Bouaziz, M.; Ghorbel, A.; Sayadi, S. A compact process for the treatment of olive mill wastewater by combining wet hydrogen peroxide catalytic oxidation and biological techniques. *J. Hazard. Mater.* **2010**, *183*, 62–69.
210. Martins, R.C.; Henriques, L.R.; Quinta-Ferreira, R.M. Catalytic activity of low cost materials for pollutants abatement by Fenton's process. *Chem. Eng. Sci.* **2013**, *100*, 225–233.
211. Domingues, E.; Assunção, N.; Gomes, J.; Lopes, D. V.; Frade, J.R.; Quina, M.J.; Quinta-Ferreira,

R.M.; Martins, R.C. Catalytic efficiency of red mud for the degradation of Olive mill wastewater through heterogeneous Fenton's process. *Water (Switzerland)* **2019**, *11*.
212. Caudo, S.; Genovese, C.; Perathoner, S.; Centi, G. Copper-pillared clays (Cu-PILC) for agro-food wastewater purification with H_2O_2. *Microporous Mesoporous Mater.* **2008**, *107*, 46–57.
213. Chu, K.H.; Yoo, S.S.; Ahn, J.Y.; Jo, J.S.; Ko, K.B. Determining flux behavior via a modified flux-step method for surface water treatment: Pilot-scale ultrafiltration membrane operation. *Desalination* **2014**, *341*, 19–26.
214. Guo, X.; Zhang, Z.; Fang, L.; Su, L. Study on ultrafiltration for surface water by a polyvinylchloride hollow fiber membrane. *Desalination* **2009**, *238*, 183–191.
215. Yarlagadda, S.; Gude, V.G.; Camacho, L.M.; Pinappu, S.; Deng, S. Potable water recovery from As, U, and F contaminated ground waters by direct contact membrane distillation process. *J. Hazard. Mater.* **2011**, *192*, 1388–1394.
216. Subramanian, S.; Seeram, R. New directions in nanofiltration applications - Are nanofibers the right materials as membranes in desalination? *Desalination* **2013**, *308*, 198–208.
217. Hegab, H.M.; Zou, L. Graphene oxide-assisted membranes: Fabrication and potential applications in desalination and water purification. *J. Memb. Sci.* **2015**, *484*, 95–106.
218. Yoon, Y.; Westerhoff, P.; Snyder, S.A.; Wert, E.C.; Yoon, J. Removal of endocrine disrupting compounds and pharmaceuticals by nanofiltration and ultrafiltration membranes. *Desalination* **2007**, *202*, 16–23.
219. Kimura, K.; Toshima, S.; Amy, G.; Watanabe, Y. Rejection of neutral endocrine disrupting compounds (EDCs) and pharmaceutical active compounds (PhACs) by RO membranes. *J. Memb. Sci.* **2004**, *245*, 71–78.
220. Lau, W.J.; Ismail, A.F. Polymeric nanofiltration membranes for textile dye wastewater treatment: Preparation, performance evaluation, transport modelling, and fouling control - a review. *Desalination* **2009**, *245*, 321–348.
221. Lin, J.; Ye, W.; Baltaru, M.C.; Tang, Y.P.; Bernstein, N.J.; Gao, P.; Balta, S.; Vlad, M.; Volodin, A.; Sotto, A.; et al. Tight ultrafiltration membranes for enhanced separation of dyes and Na2SO4 during textile wastewater treatment. *J. Memb. Sci.* **2016**, *514*, 217–228.
222. Beril Gönder, Z.; Arayici, S.; Barlas, H. Advanced treatment of pulp and paper mill wastewater by nanofiltration process: Effects of operating conditions on membrane fouling. *Sep. Purif. Technol.* **2011**, *76*, 292–302.
223. Pizzichini, M.; Russo, C.; Di Meo, C.D. Purification of pulp and paper wastewater, with membrane technology, for water reuse in a closed loop. *Desalination* **2005**, *178*, 351–359.
224. Valderrama, C.; Ribera, G.; Bahí, N.; Rovira, M.; Giménez, T.; Nomen, R.; Lluch, S.; Yuste, M.; Martinez-Lladó, X. Winery wastewater treatment for water reuse purpose: Conventional activated sludge versus membrane bioreactor (MBR). A comparative case study. *Desalination* **2012**, *306*, 1–7.
225. Ioannou, L.A.; Michael, C.; Vakondios, N.; Drosou, K.; Xekoukoulotakis, N.P.; Diamadopoulos, E.; Fatta-Kassinos, D. Winery wastewater purification by reverse osmosis and oxidation of the concentrate by solar photo-Fenton. *Sep. Purif. Technol.* **2013**, *118*, 659–669.
226. Luo, J.; Ding, L.; Wan, Y.; Paullier, P.; Jaffrin, M.Y. Application of NF-RDM (nanofiltration rotating disk membrane) module under extreme hydraulic conditions for the treatment of dairy wastewater. *Chem. Eng. J.* **2010**, *163*, 307–316.
227. Cassano, A.; Conidi, C.; Giorno, L.; Drioli, E. Fractionation of olive mill wastewaters by membrane separation techniques. *J. Hazard. Mater.* **2013**, *248–249*, 185–193.
228. Brenes, M.; Garcıia, P.; Romero, C.; Garrido, A. Treatment of green table olive waste waters by an activated-sludge process. *J. Chem. Technol. Biotechnol.* **2000**, *75*, 459–463.
229. Mulder, M. *Basic Principles of Membrane Technology*; 2nd ed.; Kluwer: Dordrecht, 1996;
230. Fu, F.; Wang, Q. Removal of heavy metal ions from wastewaters: a review. *J. Environ. Manage.* **2011**, *92*, 407–18.
231. Guo, W.; Ngo, H.H.; Li, J. A mini-review on membrane fouling. *Bioresour. Technol.* **2012**, *122*, 27–34.
232. Judd, S. Chapter 2 - Membrane technology. In *Membranes for Industrial Wastewater Recovery and Re-use*; Judd, S., Jefferson, B.B.T.-M. for I.W.R. and R., Eds.; Elsevier Science: Amsterdam, 2003; pp. 13–74 ISBN 978-1-85617-389-6.
233. Chiam, C.K.; Sarbatly, R. Purification of aquacultural water: Conventional and new membrane-based techniques. *Sep. Purif. Rev.* **2011**, *40*, 126–160.
234. Aime Mudimu, O.; Peters, M.; Brauner, F.; Braun, G. Overview of membrane processes for the recovery of polyphenols from olive mill wastewater. *Am. J. Environ. Sci.* **2012**, *8*, 195–201.
235. Alkhudhiri, A.; Darwish, N.; Hilal, N. Membrane distillation: A comprehensive review. *Desalination*

2012, *287*, 2–18.
236. Wang, P.; Chung, T.S. Recent advances in membrane distillation processes: Membrane development, configuration design and application exploring. *J. Memb. Sci.* **2015**, *474*, 39–56.
237. Khayet, M. Membranes and theoretical modeling of membrane distillation: A review. *Adv. Colloid Interface Sci.* **2011**, *164*, 56–88.
238. El-Abbassi, A.; Hafidi, A.; García-Payo, M.C.; Khayet, M. Concentration of olive mill wastewater by membrane distillation for polyphenols recovery. *Desalination* **2009**, *245*, 670–674.
239. Vinoth Kumar, R.; Barbosa, M.O.; Ribeiro, A.R.; Morales-Torres, S.; Pereira, M.F.R.; Silva, A.M.T. Advanced oxidation technologies combined with direct contact membrane distillation for treatment of secondary municipal wastewater. *Process Saf. Environ. Prot.* **2020**, *140*, 111–123.
240. El-Bourawi, M.S.; Ding, Z.; Ma, R.; Khayet, M. A framework for better understanding membrane distillation separation process. *J. Memb. Sci.* **2006**, *285*, 4–29.
241. El-Abbassi, A.; Kiai, H.; Hafidi, A.; García-Payo, M.C.; Khayet, M. Treatment of olive mill wastewater by membrane distillation using polytetrafluoroethylene membranes. *Sep. Purif. Technol.* **2012**, *98*, 55–61.
242. Farinelli, G.; Coha, M.; Minella, M.; Fabbri, D.; Pazzi, M.; Vione, D.; Tiraferri, A. Evaluation of Fenton and modified Fenton oxidation coupled with membrane distillation for produced water treatment: Benefits, challenges, and effluent toxicity. *Sci. Total Environ.* **2021**, *796*, 148953.

PART II

ANALYTICAL METHODS

CHAPTER 3

ANALYTICAL METHODS AND CHARACTERIZATION TECHNIQUES

This chapter provides a detailed description of the analytical determinations and techniques used to characterize the wastewater samples and all materials (adsorbents and catalysts) presented in the ensuing chapters of this thesis.

3.1. METHODS FOR WASTEWATER ANALYSIS

The following analytical procedures were performed according to Standard Methods for wastewater examination of the American Public Health Association (APHA) [1]: total organic carbon (TOC) was determined by catalytic oxidation at 680 °C (method 5310 D) with a TC/TOC apparatus (Shimadzu, mod. TOC-L); the closed reflux method (5220 D) was applied for chemical oxygen demand (COD) determinations (using a Nanocolor mod. Vario 4 heating block, and mod. 500D photometer from Macherey Nagel); biochemical oxygen demand after 5 days (BOD_5) was measured following method 5210 B using a WTW OxiTop Thermostat Box; the total iron concentration in solution was assessed by flame absorption spectrometry (AAS) following method 3111 B; the total suspended solids (TSS) and volatile suspended solids (VSS) were evaluated by gravimetric analysis (methods 2540 B and 2540 E, respectively); the total dissolved solids (TDS) were calculated following Method 2540 C; turbidity was measured with a HI88703 turbidimeter (Hanna Instruments) following method 2130 B

The determination of H_2O_2 concentration in solution was performed by spectrophotometry (Thermo Scientific, mod. Genesys 10-S) following the method developed by Sellers [2] in virtue of its speed, simplicity, and accuracy. In brief, titanium (IV) oxalate reacts with the hydrogen peroxide to form a yellow-orange complex, which is measured by spectrophotometry at 400 nm using a Helios ϒ spectrophotometer (Thermo Electron Corporation). Since residual H_2O_2 in solution interferes in COD measurements overestimating the results obtained [3], a correction was applied following Eq. (3.1), where COD (mg O_2/L) is obtained by the standard method and $[H_2O_2]_{res}$ the residual concentration of oxidant (mg/L) in the sample.

$$COD_{corr} = COD - 0.468\,[H_2O_2]_{res} \tag{3.1}$$

The evaluation of the individual concentration of each compound and the total phenolic content (TPh, sum of individual concentrations) of the synthetic solutions used in this work was achieved through high-performance liquid chromatography (HPLC). A Hitachi Elite LaChrom apparatus (equipped with L-2310 pump, L-2220 auto-sampler, and L-2455 diode-array detector) was used, and the chromatographic separation was achieved using a Purospher STAR RP-18 column (240 × 4 mm, 5 µm). The mobile phase consisted of 70% ultra-pure H_2O (acidified with 1% *v*/*v* orthophosphoric acid) and 30% methanol (≥99.8%, Fischer Chemicals). The system was operated at isocratic conditions, with the oven temperature at 50 °C, a flow rate of 1 mL/min, and

the spectra recorded at 280 nm. In the case of real OMW samples, the evaluation of the total phenolic content was achieved through the Folin-Ciocalteau reagent (Panreac), using gallic acid as standard (TPh_{FC} values reported as mg GA_{eq}/L). In summary, 1 mL of the sample supernatant and 5 mL of the Folin-Ciocalteau reagent (1:10 dilution) were mixed together and vortexed for 3 min, adding 4 mL of Na_2CO_3 (7.5% *w*/*v*) afterward. The color intensity, developed for 2 h in the dark, was measured at 765 nm against a blank prepared in the same way with distilled water.

Samples' toxicity was assessed from the light inhibition of *Vibrio fischeri* bacteria when in contact with samples of the effluent according to the standard test DIN/EN/ISO 11348-3 [4], using a Microtox model 500 (5, 15, and 30 min of contact time at 15 °C). The effluent biodegradability was estimated based on the ratio between BOD_5 and COD, as well as by the carbon and average oxidation state indices (COS and AOS) *cf*. Eqs.(3.2) and (3.3), respectively [5].

$$COS = 4 - 1.5\left[\frac{COD}{TOC_0}\right] \tag{3.2}$$

$$AOS = 4 - 1.5\left[\frac{COD}{TOC}\right] \tag{3.3}$$

All analytical determinations were performed at least in duplicate, and the coefficient of variation was ≤ 2% for TOC, TPh, and dissolved Fe, 4% for COD, and 5% for the remaining parameters.

3.2. MATERIALS CHARACTERIZATION TECHNIQUES

The carbon materials used in this thesis have been characterized by several complementary techniques to evaluate their morphology, porous structure, and surface chemistry, as well as the nature and dispersion of the active metal phase of the corresponding catalysts. The characterization methods employed help understand the adsorptive and catalytic behavior of the materials used. A brief description of the methods used and their operating principles (which were summarized from relevant literature in this area [6–12]) are provided below.

3.2.1. TGA

Thermogravimetry analysis (TGA) was performed under an N_2 or air atmosphere (heating rate of 5 or 20 °C/min depending on the experiment, up to 800 °C) with a TGA-50H (Shimadzu) thermobalance. Experiments carried out in an inert atmosphere allow simulate the conditions of carbonization of the bio-residues used as adsorbents/catalyst supports and also the regeneration

of spent adsorbents. The metallic content of the catalysts was also determined by burning (in air) a fraction of the sample until constant weight.

3.2.2. N_2 and CO_2 adsorption

Physical adsorption of gases is one of the most commonly used procedures for the characterization of porous materials. Although several gases may be used (including He, N_2, Ar, and CO_2), the most widely employed one is N_2 at -196 °C, owning to the fact that it covers a relatively high range of relative pressures (10^{-8} to 1) and thus provides adsorption in the entire range of porosity of the materials. Still, diffusional problems of N_2 molecules inside narrow pores (i.e., ultramicropores with <0.7 nm) are known to occur. For such determinations, the use of CO_2 or He is recommended. Because of the higher saturation pressure of CO_2 at 0 °C that results in larger kinetic energy, the molecules are only adsorbed in the microporosity of the sample, and thus it is a good complementary technique to tackle the limitation of N_2 adsorption.

This procedure relies on the evaluation of the volume of gas adsorbed (V_{gas}) per adsorbent mass unit, at a constant temperature (T), which depends on the pressure recorded at each point (P) and the saturation vapor pressure of the gas (P_0) – the relative pressure (P/P_0) – according to Eq. (3.4).

$$V_{gas} = f\left(\frac{P}{P_0}\right)T \tag{3.4}$$

Adsorption/desorption isotherms are obtained by plotting V_{gas} *vs*. (P/P_0); there are several types of isotherms, which are presented in great detail in a recent IUPAC Technical Report [13].

The textural characterization was carried out by physical adsorption of N_2 and CO_2 at -196 °C and 0 °C, respectively, using a Quantachrome Quadrasorb SI equipment; samples were degasified for 12 h (at 120 °C) before analysis. The Brunauer–Emmett–Teller (BET) equation was applied to N_2 adsorption isotherms (at P/P_0 <0.10) to obtain the apparent surface area (S_{BET}) of the materials [14]. Micropore volume (W_0) and mean micropore width (L_0) were determined by the Dubinin-Radushkevich and Stoeckli equations, respectively [15,16]. The total pore volume (V_T) was considered as the volume of N_2 adsorbed at P/P_0 = 0.95, and the mesopore volume (V_{meso}) obtained from the difference between V_T and the volume of N_2 adsorbed at P/P_0 = 0.40, following Gurvich rule [9]. The pore size distribution (PSD) was derived from the quenched solid density functional theory (QSDFT) method applied to N_2 isotherms and assuming slit-shaped pores [17].

3.2.3. SEM

Scanning electron microscopy (SEM) is an imaging technique commonly used to analyze the morphology of a sample. A common preparation technique is to “coat” the sample with a layer (with several nanometres thickness) of a conductive material, such as gold, by the use of Sputter Coater.

After that, the morphology of the carbonaceous materials used in this study was analyzed by high resolution scanning electron microscopy (HRSEM), using a LEO (Carl Zeiss) GEMINI-1530 microscope equipped with an energy dispersive X-ray (EDX) microanalysis system (Oxford Instruments).

3.2.4. XRD

X-ray diffraction (XRD) spectroscopy is a technique capable of identifying the phase of a crystalline material, thus providing valuable information about the nature of the iron particles at the catalysts’ surface.

In this work, XRD analysis was performed using a Bruker D8 Advance diffractometer (Cu Kα radiation at λ = 1.5406 Å), with 2θ angles ranging from 10° to 80° (scan rate of 1°/100 s). ICDD (International Centre for Diffraction Data) cards were used to identify the main iron-oxides formed, including α-Fe_2O_3 (card no. 33-0664) and Fe_3O4 (card no. 19-0629). The average Fe-crystallite diameter (d_{XRD}) was estimated by application of Scherrer equation (Eq. (3.5)) [19], where D is the full-width at half maximum (FWHM) from the main peak in each spectrum.

$$d_{XRD} = \frac{0.94\,\lambda}{D\,cos\theta} \tag{3.5}$$

3.2.5. TEM

Dispersion and Fe-particle sizes were analyzed using a FEI Titan G2 60-300 scanning transmission electron microscopy (STEM) equipped with a high brightness electron gun (X-FEG) operated at 300 kV, and energy-dispersive X-ray spectroscopy (EDX) microanalysis and mapping systems. For that, a small amount of the powdered sample is dispersed in ethanol with the aid of ultrasounds and then mounted onto a 300-mesh carbon-coated Cu-grid.

3.2.6. XPS

The surface chemistry of the samples was analyzed by X-ray photoelectron spectroscopy (XPS). The XPS spectra and elemental analysis were obtained using a Kratos Axis Ultra-DLD X-ray photoelectron spectrometer equipped with a hemispherical electron analyzer connected to a DLD (delay-line detector). Survey and multi-region spectra were recorded at C1s, O1s, and Fe2p photoelectron peaks, and each spectral region was scanned until good signal-to-noise ratios were achieved.

3.2.7. FTIR

The analysis of chemical bonding of functional groups in the supports/catalysts was complemented by Fourier-transform infrared spectroscopy (FTIR) analysis. FTIR spectra were recorded using a Perkin-Elmer Spectrum One apparatus with tablets of KBr, which were prepared by diluting the sample to 0.1% (by weight), and evaluated in the range of 400–4000 cm^{-1} and at a scanning rate of 0.5 $cm^{-1} \cdot s^{-1}$.

3.2.8. pH_{pzc}

The pH at the point of zero charge (pH_{pzc}) is an analytical procedure that gives information about the surface acid/basic character of a material. In this work, the “drift method” was used to determine pH_{pzc} values [18]. Distilled water was first bubbled with N_2 to prevent the dissolution of CO_2 (and consequent acidification of the water). Then, several solutions were prepared by varying the initial pH values in the 2–12 range using HCl (0.1 M) or NaOH (0.1 M), and adding 50 mL of an electrolyte (NaCl 0.01M). A determined amount of the sample (0.15 g) was placed in each solution and the vials were stirred during 24 h in a water bath shaker (T = 21 °C). After that time, the pH was measured and the pHpzc value was determined in the interception of the “final-pH values *vs*. the initial pH values” with the straight line of “final-pH = initial-pH”.

REFERENCES

1. APHA; AWWA; WEF Standard methods for the examination of water and wastewater; 22nd ed.; American Public Health Association: Washington, DC, **2012**; ISBN 9780875530130.
2. Sellers, R.M. Spectrophotometric determination of hydrogen peroxide using potassium titanium(IV) oxalate. *Analyst* **1980**, 105, 950–954.
3. Melero, J.A.; Martínez, F.; Botas, J.A.; Molina, R.; Pariente, M.I. Heterogeneous catalytic wet peroxide oxidation systems for the treatment of an industrial pharmaceutical wastewater. *Water Res*. **2009**, 43, 4010–4018.
4. ISO 11348-3: Water Quality: Determination of the inhibitory effect of water samples on the light emission of *Vibrio fischeri* (luminescent bacteria test). **2007**.
5. Moradi, S.; Sobhgol, S.A.; Hayati, F.; Isari, A.A.; Kakavandi, B.; Bashardoust, P.; Anvaripour, B. Performance and reaction mechanism of MgO/ZnO/Graphene ternary nanocomposite in coupling with LED and ultrasound waves for the degradation of sulfamethoxazole and pharmaceutical wastewater. *Sep. Purif. Technol*. **2020**, 251, 117373.
6. Groen, J.C.; Peffer, L.A.A.; Pérez-Ramírez, J. Pore size determination in modified micro- and mesoporous materials. Pitfalls and limitations in gas adsorption data analysis. *Microporous Mesoporous Mater*. **2003**, 60, 1–17.
7. Kruk, M.; Jaroniec, M. Gas adsorption characterization of ordered organic-inorganic nanocomposite materials. *Chem. Mater*. **2001**, 13, 3169–3183.
8. Ghosh Chaudhuri, R.; Paria, S. Core/shell nanoparticles: Classes, properties, synthesis mechanisms, characterization, and applications. *Chem. Rev*. **2012**, 112, 2373–2433.
9. Rouquerol, J.; Rouquerol, F.; Llewellyn, P.; Maurin, G.; Sing, K.S.W. Adsorption by Powders and Porous Solids: Principles, Methodology and Applications; 2nd ed.; Academic Press: Oxford, **2013**; ISBN 9780080970356.
10. Figueiredo, J.L.; Ribeiro, F.R. Catálise Heterogénea; 2ª ed.; Fundação Calouste Gulbenkian, Lisboa, **2007.**
11. Williams, D.B.; Carter, C.B. Transmission Electron Microscopy: A Textbook for Materials Science; 2nd ed.; Springer: New York, **1996**; ISBN 9780387765006.
12. Figueiredo, J.L.; Pereira, M.F.R. The role of surface chemistry in catalysis with carbons. *Catal. Today* **2010**, 150, 2–7.
13. Thommes, M.; Kaneko, K.; Neimark, A. V.; Olivier, J.P.; Rodriguez-Reinoso, F.; Rouquerol, J.; Sing, K.S.W. Physisorption of gases, with special reference to the evaluation of surface area and pore size distribution (IUPAC Technical Report). *Pure Appl. Chem*. **2015**, 87, 1051–1069.
14. Brunauer, S.; Emmett, P.H.; Teller, E. Adsorption of gases in multimolecular layers. *J. Am. Chem. Soc*. **1938**, 60, 309–319.
15. Bansal, R.C.; Donnet, J.B.; Stoeckli, F. Active Carbon; Dekker: New York, **1998**; ISBN 978-0824778422.
16. Stoeckli, F.; Guillot, A.; Slasli, A.; Hugi-Cleary, D. Microporosity in carbon blacks. *Carbon* **2002**, 40, 211–215.
17. Neimark, A. V.; Lin, Y.; Ravikovitch, P.I.; Thommes, M. Quenched solid density functional theory and pore size analysis of micro-mesoporous carbons. *Carbon*. **2009**, 47, 1617–1628.
18. Newcombe, G.; Hayes, R.; Drikas, M. Granular activated carbon: Importance of surface properties in the adsorption of naturally occurring organics. *Colloids Surfaces A Physicochem. Eng. Asp*. **1993**, 78, 65–71.
19. Scherrer, P. Nachrichten von der Gesellschaft der Wissenschaften zu Göttingen. *Math. Klasse* **1918**, 2, 98–100.

PART III

TREATMENT OF OMW BY HOMOGENEOUS PROCESSES

CHAPTER 4

SYNTHETIC OLIVE MILL WASTEWATER TREATMENT BY FENTON'S PROCESS IN BATCH AND CONTINUOUS REACTORS OPERATION

Highlights

- Fenton process was optimized for the oxidation of a polyphenolic solution;
- H_2O_2 and Fe^{2+} doses, operation temperature, and initial pH were evaluated;
- TPh >99% and TOC >56% under the best operational conditions;
- Analogous efficiencies were observed at steady-state for CSTR operation;
- Removals of COD (>75%) and BOD_5 (>70%) were achieved for both systems.

The contents of this chapter were adapted from:

Esteves, B.M., Rodrigues, C.S.D., Madeira, L.M., Environmental Science and Pollution Research, 2018, 25(35), 34826-34838. https://doi.org/10.1007/s11356-017-0532-y

ABSTRACT

Degradation of total phenolic content (TPh) and organic matter (expressed as total organic carbon, TOC) of simulated olive mill wastewater was evaluated by the Fenton oxidation process under batch and continuous mode conditions. A mixture of six phenolic acids usually found in this agro-industrial wastewater was used for this purpose. The study focused on the optimization of key operational parameters of the Fenton process in a batch reactor, namely: Fe^{2+} dosage, hydrogen peroxide concentration, pH, and reaction temperature. On the assessment of the process efficiency, >99% of TPh and >56% of TOC removals were attained when [Fe^{2+}] = 100 ppm, [H_2O_2] = 2.0 g/L, T = 30 °C and initial pH = 5.0, after 300 min of reaction. Under those operational conditions, experiments on a continuous stirred-tank reactor (CSTR) were performed for different space-time values (τ). TOC and TPh removals of 47.5 and 96.9%, respectively, were reached at steady-state (for τ = 120 min). High removal of chemical oxygen demand – COD (>75%) and biochemical oxygen demand – BOD_5 (>70%) were achieved for both batch and CSTR optimum conditions; analysis of the BOD_5/COD ratio also revealed an increase in the effluent's biodegradability. Despite the high removal of lumped parameters, the treated effluent did not meet the Portuguese legal limits for direct discharge of wastewaters into water bodies, which indicates that coupled chemical-biological process may be the best solution for real olive mill wastewater treatment.

4.1. INTRODUCTION

Lab-scale study/optimization of Fenton's process for the treatment of OMW has already proved its relevance since the industrial application of this technology as a stage unit in a wastewater treatment plant (located in Badajoz, Spain) was successfully implemented [1]. Moreover, the acidic pH of such effluents makes the application of the Fenton process economically attractive, as little to no previous acidification may be required. Up to the author's knowledge, few works reported in the literature deal with the application of the homogeneous Fenton process in a CSTR [2-4], and none addresses the treatment of synthetic olive mill wastewater.

The goal of the work presented in this chapter is to evaluate the effectiveness of Fenton's process on the abatement of the organic load (expressed as total organic carbon and total phenolic content, TOC and TPh, respectively) of a synthetic effluent containing 6 phenolic acids typically present in olive mill wastewater (OMW). First, batch experiments were conducted to determine the operational conditions (pH, temperature, Fe^{2+} and H_2O_2 doses) that maximized the mineralization degree and the efficiency of H_2O_2 consumption. Then, the best experimental conditions found on the batch experiments were used for further investigation on a reactor operating continuously (continuous stirred-tank reactor, CSTR), which entails a large number of advantages for industrial application as compared to the classical batch reactors addressed in the large majority of research studies. Therefore, the effect of space-time (τ) was assessed for the CSTR operation. Finally, the efficiency of the process was also addressed in terms of chemical and biochemical oxygen demand (COD and BOD_5, respectively), biodegradability (BOD_5/COD ratio), and toxicity assessment of the treated effluent, to analyze the possibility of safe disposal/use after Fenton's oxidation, according to Portuguese legislation (e.g., washing and irrigation activities within the olive mills).

4.2. MATERIALS AND METHODS

4.2.1. Synthetic wastewater preparation

The synthetic effluent used in this study consists of a mixture of six different phenolic acids typically present in abundance in real OMW. The phenolic compounds concentrations used for simulating the wastewater was adjusted according to works reported in the literature (*cf*. Table A.1, Appendix A) [5–8] as follows: 50 mg/L of vanillic, caffeic, gallic, and 3,4-dihyroxyphenlyacetic

acids, 100 mg/L of *p*-coumaric acid, and 200 mg/L of tyrosol (all compounds were purchased from Alfa Aesar except the caffeic acid, from Acros Organics). The concentrations used were selected to meet TPh values within the range 300–500 mg GA_{eq}/L, commonly found in OMW samples. The compounds were dissolved in distilled water and then the solution was submitted to ultrasounds (Sonorex, mod. Super RK255H) for 15 min, to ensure full dissolution, and no further purification was applied before use. The main characteristics of the synthetic effluent are summarized in Table 4.1.

Table 4.1 Main characteristics of the synthetic effluent (average values).

pH	TOC (mg C/L)	TPh (mg GA_{eq}/L)	COD (mg O_2/L)	BOD_5 (mg O_2/L)	BOD_5:COD
3.7	321.4	361.9	805.9	207.3	0.26

4.2.2. Experimental procedure

Fenton's oxidation of the synthetic OMW was carried out in two distinct cylindrical jacketed reactors: the first one was a batch reactor, while the second was a CSTR, with 300 and 920 mL capacity, respectively. For both cases, the reaction's medium temperature was kept constant by recycling water from a thermostatic bath (VWR International, mod. 89202-912) through the reactor's jacket. The reactors were also equipped with a VWR VS-CT magnetic stirrer, keeping agitation at *ca*. 200 rpm. The pH of the solution was constantly measured by a pH meter (Inolab, WTW) and adjusted by adding NaOH 2.5 M (Merck) and/or H_2SO_4 1.0 M (Fluka) when needed. Fig. 4.1 shows Fenton's oxidation experimental set-up for the batch (Fig. 4.1a) and the CSTR (Fig. 4.1b) operation. For the batch experiments, the reactor was initially loaded with the synthetic OMW (250 mL) and the desired catalyst concentration, after pH adjustment to the desired value. Three different iron salts were tested as catalysts in this work: $FeCl_3 \cdot 6H_2O$ (LabChem), $FeSO_4 \cdot 7H_2O$ (Panreac), and $Fe(NO_3)_3 \cdot 9H_2O$ (Riedel-de Haën). Fenton's oxidation runs started when hydrogen peroxide (30% *w/v*, Fisher Chemical) was added to the previous mixture (this induced a dilution <2%).

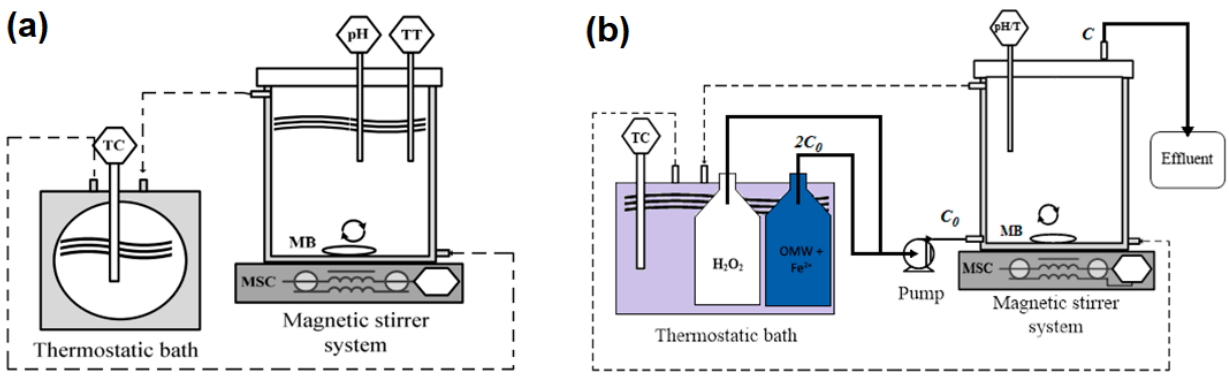


Fig. 4.1 Fenton's oxidation experimental set-up for batch (a) and CSTR (b) operation. TT – thermometer, pH – pH meter, MB – magnetic bar, MSC – magnetic stirrer controller, TC – temperature controller.

For the CSTR operation, the synthetic OMW (containing the selected dissolved iron catalyst concentration) and hydrogen peroxide solutions were pumped (Gibson M312 peristaltic pump) through two distinct streams to the reactor, allowing the use of total flow rates between. 2-26 mL/min. To avoid working with very concentrated H_2O_2 solutions, a single peristaltic pump was used for both solutions fed. Therefore, the effect of the 1:2 dilution that occurs at the reactor's inlet, where the two streams are combined (see Fig. 4.1b), was taken into account; this implied to experimentally prepare more concentrated solutions, to have at the reactor entrance concentrations similar to those used in the batch experiments and that simulate a real OMW. For the %TOC and TPh removal determinations, Eq. (4.1) was used:

$$X_{TOC/TPh}(\%) = \frac{C_0 - C}{C_0} \times 100 \qquad (4.1)$$

where X stands for conversion, C_0 for the inlet concentration, and C for the concentration of either TOC or TPh at reactor outlet, in any given instant. The vials containing the feed solutions were immersed in a Huber Polystat thermostatic bath for better temperature control and set at a maximum of 50 °C to prevent possible thermal decomposition of the hydrogen peroxide. For each experiment in continuous mode, the reactor was initially half-filled with the synthetic wastewater and half-filled with distilled water.

During both sets of experiments, samples of the effluent were taken at regular intervals to assess the evolution of the following parameters: TOC and TPh (after stopping the possible reaction in the sampling flask by adding NaOH until pH >10 and immediate cooling of the sample at 4 °C), and residual H_2O_2 (to determine the oxidant consumption efficiency). For the optimum operating conditions found on the batch and CSTR experiments, a larger sample of the final treated effluent

was collected to the posterior determination of COD, BOD_5, and toxicity (for the CSTR operation, the sample was collected whenever steady-state was reached). For those determinations, the pH of the samples was raised to ≈10 by the addition of NaOH, to stop the possible homogeneous reaction with residual H_2O_2; then, the samples were neutralized to pH ≈ 7.0 with H_2SO_4 0.5 M.

4.3. RESULTS AND DISCUSSION

4.3.1. Batch catalytic tests

A parametric study on the influence of the main operational conditions influencing Fenton's process is presented in the following sections.

4.3.2. Selection of iron salt

The presence of inorganic substances (e.g., Cl^-, PO_4^{3-}, NO_3^-, or SO_4^{2-}) in wastewaters or added as reagents (iron salt counter ion) is reported to influence the overall efficiency of Fenton and Fenton-like processes. Possible consequences include the scavenging of $^\bullet OH$ and formation of less reactive species (e.g., $SO_4^{\bullet-}$, $Cl_2^{\bullet-}$), and/or complexation reactions with ferrous or ferric iron [9–11]. Since different inorganic ions in solution may influence the rate of reaction between H_2O_2 and ferrous/ferric ions (and thus the rate of oxidation of organic species), a preliminary study was performed using three commercially available iron salts: $FeCl_3 \cdot 6H_2O$, $FeSO_4 \cdot 7H_2O$, and $Fe(NO_3)_3 \cdot 9H_2O$.

Fig. 4.2 reports the evolution of TOC and TPh removal along time for the three catalysts tested under identical experimental conditions based on similar reports in the literature [12,13]. For the conditions tested, TPh removal was always greater than 97% after 300 min of reaction without significant performance differences between the three iron salts. In respect to TOC degradation, a slightly higher efficiency was observed for the iron(II) sulfate salt (*ca*. 44%) when compared to the iron(III) chloride and iron(III) nitrate (*ca*. 41 and 39%, respectively).

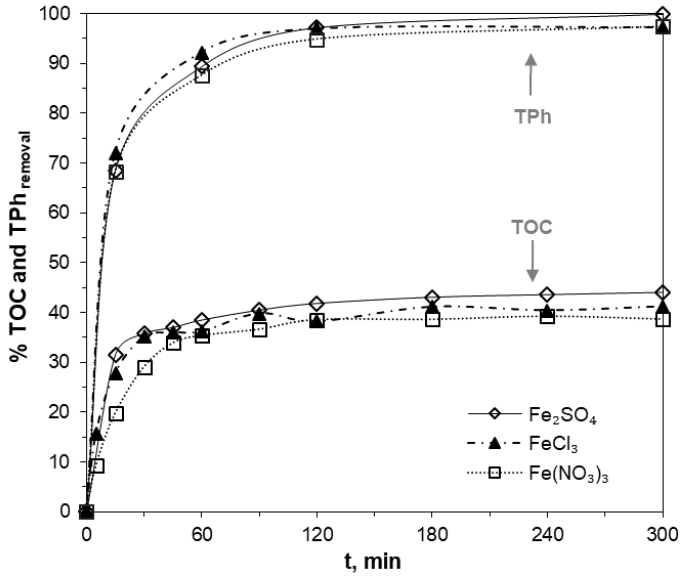


Fig. 4.2 Influence of the iron salt used as catalyst on the TOC and TPh removal efficiency (%) along time. Experimental conditions: $[Fe^{2+}/Fe^{3+}]$ = 50 mg/L, $[H_2O_2]$ = 2.0 g/L, pH_0 = 3.7, T = 30 °C.

In the work of Deng *et al*. [14], the authors reported that the presence of SO_4^{2-} and particularly Cl^- hinders Fenton's oxidation of landfill leachate, while the presence of NO_3^- in solution didn't impact the COD removal rate. Similar results were found by Siedlecka *et al*. [10] regarding the inhibition effect of chloride ions, particularly in the degradation of methyl *t*-butyl by Fenton's oxidation. Nonetheless, under the operational conditions tested, the slightly lower TOC degradation efficiencies observed when using chloride and nitrate salts may be simply related to the fact that the ferric to ferrous reconversion route (Eqs. (2.4) and (2.5)) is a slower step to initiate Fenton's process. Based on these results, and because industrial prices of such salts are similar, subsequent experiments were carried out with the iron(II) sulfate.

4.3.2.1. Influence of H_2O_2 and Fe^{2+} doses

In Fenton's oxidation, H_2O_2 and Fe^{2+} concentrations are closely related and influence the efficiency of the process, both in terms of mineralization degree of the organic load and overall cost of the process [13,15]. The selection of the H_2O_2 dose relies on the response of specific contaminants to oxidation as well as on the ultimate goal or strategy – i.e., the partial oxidation of the pollutants into intermediate compounds, instead of their full mineralization up to CO_2 and H_2O, often leads to significant abatement of the organic load and/or toxicity reduction of the effluent, with lower operating costs (represented here by the costs of chemical reagents). Given the complexity of such agro-industrial effluents, it is common to report the oxidant dose as the

theoretical stoichiometric weight ratio between H_2O_2 and the effluent's initial COD (2.125 g H_2O_2/g COD) [12]. Since hydrogen peroxide is consumed on side reactions (e.g., Eqs. (2.4) and (2.7)) that don't produce the highly reactive hydroxyl radicals, the dose of oxidant required is usually higher than the stoichiometric one [13,16].

For this set of experiments, H_2O_2 doses corresponding to approximately 0.5, 1.0, 2.0, and 3.0 times the stoichiometric amount where tested (corresponding to $[H_2O_2]$ = 1.0, 2.0, 3.0, and 4.0 g/L, respectively), varying the concentration of the iron catalyst ($[Fe^{2+}]$ = 25, 50, and 100 mg/L). Experimental conditions for this set of trials were: unadjusted initial pH (pH_0 = 3.7), T = 30 °C, and reaction time of 300 min. As an example, Fig. 4.3 shows the evolution of TOC removal (%) for runs with $[Fe^{2+}]$ = 50 mg/L. The figure shows that most of the TOC reduction occurs at the beginning of the reaction (within the first 30 min) and from that point on, the TOC removal profile develops more slowly, approaching a plateau when t ≥180 min. A similar trend was obtained for the other ferrous ion concentrations tested (Fig. A.1, Appendix A for $[Fe^{2+}]$ = 25 and 100 mg/L). Similar TOC and/or COD degradation profiles were observed by other authors in their experiments on organic matter reduction of simulated [13] and real olive mill wastewaters [12,17] by homogeneous Fenton/Fenton-like processes.

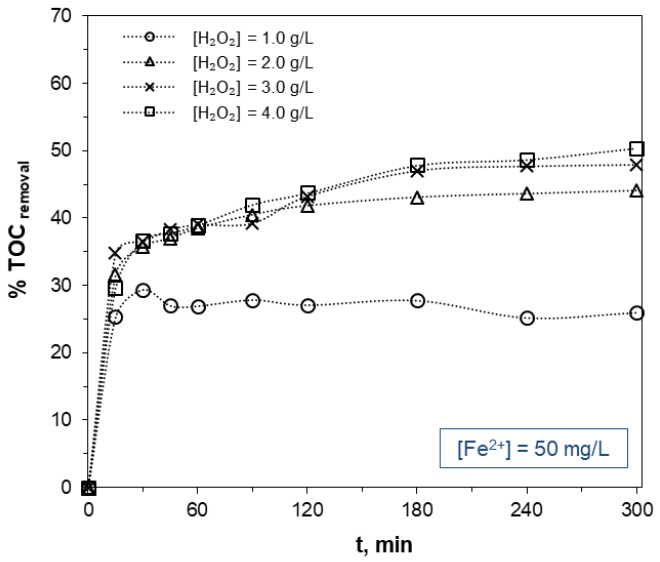


Fig. 4.3 Effect of H_2O_2 dose on the TOC removal efficiency (%) along time on the batch runs. Experimental conditions: $[Fe^{2+}]$ = 50 mg/L, pH_0 = 3.7, T = 30 °C.

Fig. 4.4 reports performances for TPh and TOC removals at the end of Fenton's oxidation runs. For the conditions used, the oxidation process proved to be very efficient in the depletion of the phenolic character of the wastewater, as ≥99% of TPh removal was observed in all experiments,

except for runs with $[H_2O_2]$ = 1.0 g/L. The lower TPh removal achieved whilst using a sub-stoichiometric dose of H_2O_2 could be explained by the results reported by De Heredia *et al*. [18]. The authors established kinetic models for the oxidation of phenolic compounds by Fenton's process, showing that low values of the ratio between the initial concentrations of hydrogen peroxide and phenolic compounds ($R = [H_2O_2]_0/[TPh]_0$) lead to slower degradation rates of those compounds. Also, Kang *et al*. [19] suggested that the availability of Fe^{2+} plays an important role in improving the degradation performance of phenolic compounds, which is in accordance to the higher TPh removed when Fe^{2+} doses go from 25 to 100 mg/L, for $[H_2O_2]$ = 1.0 g/L (81.3 to 88.6%).

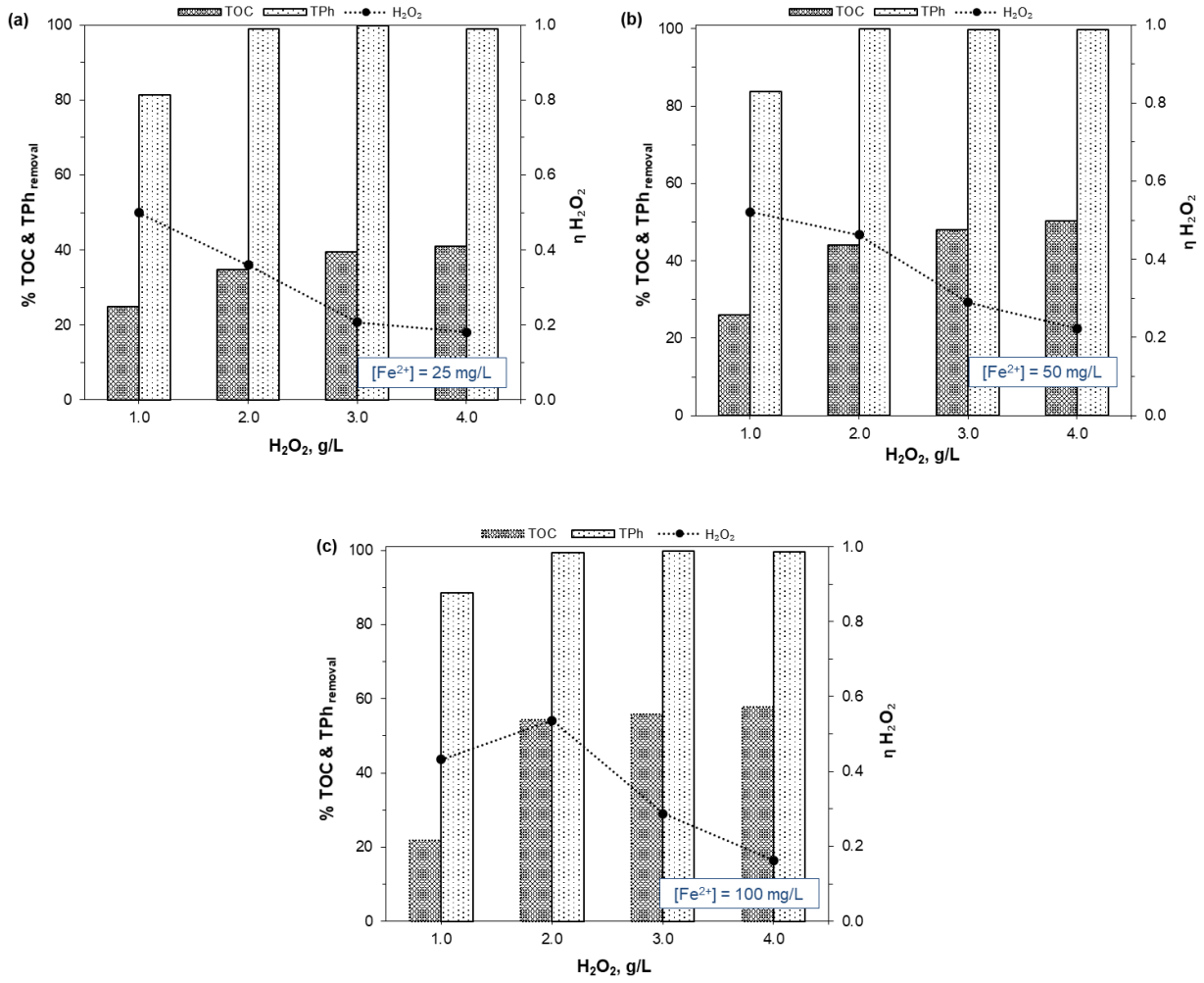


Fig. 4.4 Effect of H_2O_2 concentration on TOC (▒) and TPh (□) removal efficiencies and efficiency of oxidant use (η H_2O_2) (···•···) after the batch runs, for Fe^{2+} concentrations equal to (a) 25, (b) 50, and (c) 100 mg/L. Experimental conditions: pH_0 = 3.7, T = 30 °C, t = 300 min.

Regarding the TOC abatement, an increase in the H_2O_2 amount added to the reaction medium led to the expected enhancement of the mineralization degree [20]. Thus, for each Fe^{2+}

concentration tested, the increase of the hydrogen peroxide dose from 1.0 to 4.0 g/L, improved the organic matter degradation efficiency (e.g., Fig. 4.4b highlights this trend, as TOC removal efficiencies were 26.0, 44.1, 47.9, and 50.4% when $[H_2O_2]$ = 1.0, 2.0, 3.0, and 4.0 g/L, respectively). Despite this improvement, mineralization levels maintained below the TPh removal ones (maximum TOC removal of 57.8% when $[Fe^{2+}]$ = 100 mg/L – Fig. 4.4c), which can be explained by the decomposition of the parent phenolic compounds into refractory low molecular weight compounds (mainly carboxylic acids) that are difficult to be further oxidized by •OH [21,22].

Moreover, for the same fixed amount of H_2O_2, mineralizations are also positively affected by the increase of the Fe^{2+} dose, as it accelerates H_2O_2 conversion into hydroxyl radicals. However, this is only true up to some extent, as an additional experiment was performed with $[Fe^{2+}]$ = 200 mg/L using $[H_2O_2]$ = 4.0 g/L (Fig. A.2, Appendix A), and TOC removal efficiency was lower (53.3%) than the one achieved when $[Fe^{2+}]$ = 100 mg/L for the same H_2O_2 dose (57.8%). A similar behavior was found by Zazo *et al*. [16] in the study of phenol degradation by semi-continuous Fenton oxidation. This can be related to: (i) the scavenging reactions that are promoted in the presence of either excess oxidant or catalyst (*cf*. Eqs. (2.7) and (2.8)); (ii) the higher concentration of sulfate ions in solution (added as iron salt counter ion) that may act as a scavenger of •OH and/or compete with H_2O_2 to form Fe^{3+} complexes, thus inhibiting the Fe^{3+} regeneration cycle (mechanism described by Eqs. (I)–(XI) of Table 4.2) [14,23].

Table 4.2 Key reactions occurring in Fenton's system in the presence of sulfate ions (adapted from [9]).

Eq.	Reaction	Rate constant *k* (M^{-1} s^{-1})
(I)	$FeSO_4 + H_2O_2 \rightarrow Fe^{3+} + {}^{\bullet}OH + OH^- + SO_4^{2-}$	7.8×10^1
(II)	$Fe^{2+} + SO_4^{2-} \leftrightharpoons FeSO_4$	2.29×10^1 $(I = 0.1M)$
(III)	$Fe^{3+} + SO_4^{2-} \leftrightharpoons FeSO_4^+$	3.89×10^2 $(I = 0.1M)$
(IV)	$Fe^{3+} + 2SO_4^{2-} \leftrightharpoons Fe(SO_4)_2^-$	4.47×10^3 $(I = 0.1M)$
(V)	$H^+ + SO_4^{2-} \leftrightharpoons HSO_4^-$	3.47×10^3 $(I = 0.1M)$
(VI)	$HSO_4^- + {}^{\bullet}OH \rightarrow SO^{\bullet}{}_4^- + H_2O$	3.5×10^5
(VII)	$SO^{\bullet}{}_4^- + H_2O \rightarrow H^+ + SO_4^{2-} + {}^{\bullet}OH$	6.6×10^2
(VIII)	$SO^{\bullet}{}_4^- + OH^- \rightarrow SO_4^{2-} + {}^{\bullet}OH$	1.4×10^7
(IX)	$SO^{\bullet}{}_4^- + H_2O_2 \rightarrow SO_4^{2-} + H^+ + HO_2^{\bullet}$	1.2×10^7
(X)	$SO^{\bullet}{}_4^- + HO_2^{\bullet} \rightarrow SO_4^{2-} + H^+ + O_2$	3.5×10^9
(XI)	$SO^{\bullet}{}_4^- + Fe^{2+} \rightarrow Fe^{3+} + SO_4^{2-}$	3.0×10^8

I = Ionic strength

The potential application of the Fenton process for treating highly organic-loaded effluents also depends on the efficient use of the oxidant, since it plays a key role on the operating costs. To assess the H_2O_2 consumption efficiency, a normalized H_2O_2 consumption yield (η H_2O_2) was defined as shown in Eq. (4.2):

$$\eta\, H_2O_2 = \frac{TOC\ removed\ (mg\ C/L) \Big/ H_2O_2\ consumed\ (g\ H_2O_2/L)}{theoretical\ TOC\ removed\ (mg\ C/L) \Big/ H_2O_2\ (g\ H_2O_2/L)} \cdot \frac{1}{R} \qquad (4.2)$$

where the theoretical TOC removed (expressed in mg C/L) per H_2O_2 (expressed in g H_2O_2/L) is the maximum theoretical TOC conversion assuming complete oxidation until CO_2, with the O_2 resulting from the H_2O_2 decomposition (*ca*. 163 mg TOC/g H_2O_2) [24], and R corresponds to the ratio between the H_2O_2 (in g/L) feed and the theoretical stoichiometric dose (*ca*. 1.97 g/L for this effluent). Values for η H_2O_2 range from 0 to 1 (being 1 the maximum H_2O_2 consumption efficiency). Results shown in Fig. 4.4 indicate that H_2O_2 consumption efficiency decreases whilst increasing the oxidant dose unless TOC removal overcomes the increase in the oxidant dose, which only occurs when [Fe^{2+}] = 100 mg/L and [H_2O_2] = 2.0 g/L (Fig. 4.4c). The drop of the H_2O_2 consumption

efficiency when using higher oxidant doses might be attributed to the radical scavenging effect (Eq. (2.7)), which reduces the amount of •OH available to oxidize the organic matter [13,16]. To confirm this, an additional experiment was performed with $[H_2O_2]$ = 6.0 g/L and $[Fe^{2+}]$ = 100 mg/L. As anticipated, a drop in the TOC removal efficiency to 52.8% and η H_2O_2 to 0.06 was observed (results not shown). Taking into account all aspects mentioned so far, the best-operating conditions found were $[H_2O_2]$ = 2.0 g/L and $[Fe^{2+}]$ = 100 mg/L, and further experiments were performed under those conditions.

Additionally, a blank experiment with $[H_2O_2]$ = 2.0 g/L in the absence of Fe^{2+} was performed for the same operating conditions of the previous runs. TOC removal of approximately 8% and TPh of 6% was observed at the end of the 300 min of reaction (data not shown). The low oxidation percentages observed are related to the lower oxidative potential of H_2O_2 when compared to •OH [25]. Moreover, a blank experiment using $[Fe^{2+}]$ = 100 mg/L (without the addition of H_2O_2) was also performed (initial pH of 3.7 and T = 30 °C). No significant TOC or TPh degradation was observed (<2% for both cases – data not shown, which is also in accordance with the experimental error for TOC and TPh determinations).

4.3.2.2. Influence of pH

To evaluate the pH influence on the oxidation process, experiments were carried out at different initial pH values (3.0, natural = 3.7, 5.0, and 7.0). It is worth mentioning that the pH of the reaction medium usually dropped by 1–2 pH unit (depending on the initial pH of the solution) after only 5-15 minutes, and maintained practically constant from that point on (Fig. A.3, Appendix A). This acidification of the solution can be explained by the partial oxidation of the phenolic compounds into low molecular weight carboxylic acids [20], which predominantly occurs within the first stage of Fenton's process, as above mentioned.

Fig. 4.5 shows the effect of the medium's pH on TOC and TPh degradation after 300 min of reaction. A slight improvement on TOC mineralization was observed when initial pH increased from 3.0 to natural (≈3.7) and then to 5.0 (52.8, 54.3, and 56.6%, respectively), while TPh removal was always >99% for this range of pH values. It is well documented in the literature that the performance of Fenton's process is highly affected by the reaction medium pH, and values in the range 2.5–4.0 favor the overall oxidation efficiency of the process [3,20]. As expected, TOC and TPh conversion percentages dropped significantly when initial pH = 7.0. In fact, under neutral-to-alkaline conditions, inhibition of the process may be attributed to: (i) the formation of

ferric hydroxide complexes (*cf*. Eq. (4.3)), resulting in the decline of Fe^{2+} available to react with the hydrogen peroxide [26]; (ii) the lower H_2O_2 stability, catalyzed by $Fe(OH)_3$, which self-decomposes into molecular oxygen and water (*cf*. Eq. (2.12)), hindering the generation of hydroxyl radicals; and (iii) the overall reduction of •OH oxidation potential under basic conditions (e.g., E_0 = 2.65–2.80 V at pH = 3.0, and 1.90 V at pH = 7.0) [27]. The first hypothesis was reinforced by the high concentration of unreacted hydrogen peroxide observed at the end of that run ($[H_2O_2]_{unreacted}$ = 1.47 g/L – corresponding to 73.5% of the initial dose).

$$Fe^{3+} + OH^- \rightarrow Fe(OH)_3 \quad (4.3)$$

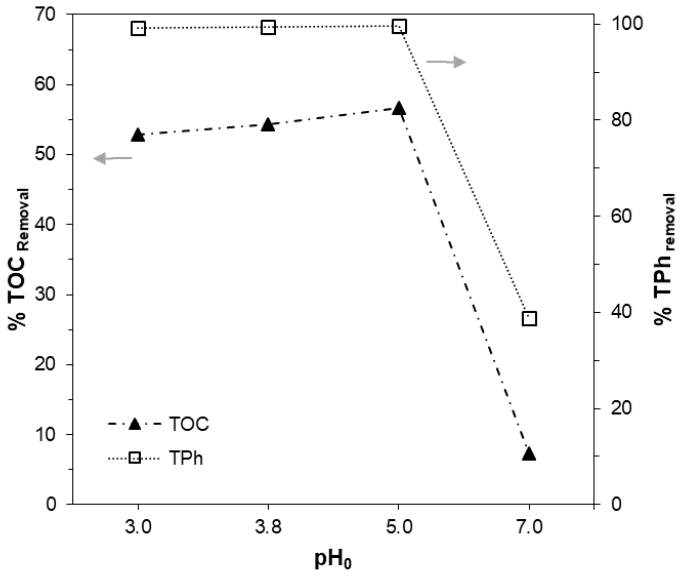


Fig. 4.5 Influence of initial pH value on TOC (▲) and TPh (□) removal after Fenton's oxidation batch runs. Experimental conditions: $[H_2O_2]$ = 2.0 g/L, $[Fe^{2+}]$ = 100 mg/L, T = 30 °C, t = 300 min.

For this set of experiments, maximum TOC removal was achieved at pH = 5.0 (56.6%), bearing in mind that the reaction medium pH dropped to ≈3.2 after only a few minutes (known to be in the range of optimum values for Fenton's oxidation, as previously mentioned). Oxidant use efficiency was also higher for pH = 5.0 then for pH = 3.0 or natural pH (η H_2O_2 = 0.49 *vs*. 0.47 and 0.46, respectively). Moreover, pH values of real OMW usually range from 3.5–5.5 [28], which is an important economical aspect for the possible scale-up of the process, as little to no pH adjustment may be required before the oxidation process. Therefore, the pH of 5.0 was selected as a reference for the following sections.

4.3.2.3. Effect of the reaction temperature

Reaction temperature influence on Fenton's oxidation efficiency was studied in the 20–50 °C range. Following the best results of the parametric study so far, experimental conditions for this set of experiments were [H_2O_2] = 2.0 g/L, [Fe^{2+}] = 100 mg/L, initial pH = 5.0, and reaction time of 300 min. As stated previously, the temperature was controlled and kept constant throughout the entire reaction for each run. Fig. 4.6 shows that near-complete abatement of the phenolic character of the effluent was achieved (>98% TPh removal) for the entire temperature range studied. As to organic matter degradation (expressed as TOC removal), maximum efficiency was achieved in the 30–40 °C range (56.6–57.5%), with η H_2O_2 values around 0.50. Similar results were obtained by Lucas and Peres [12] and Nieto *et al*. [17] on their reports on organic matter degradation of OMW through homogeneous Fenton oxidation.

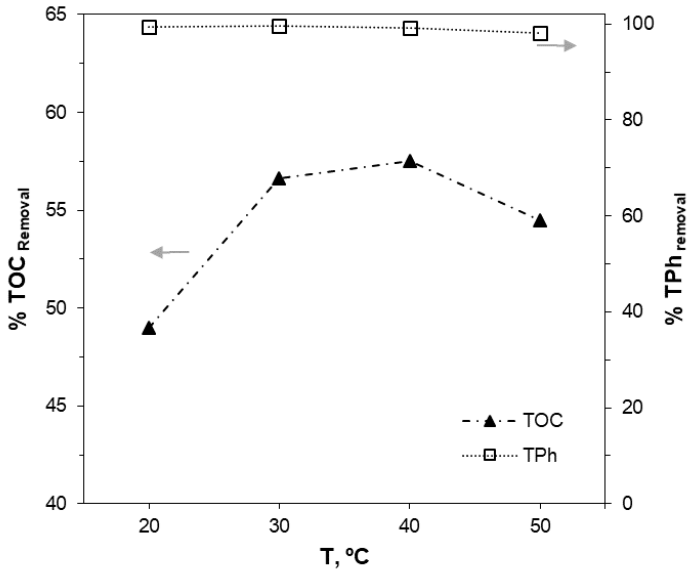


Fig. 4.6 Influence of reaction medium temperature on the TOC (▲) and TPh (□) removal after Fenton's oxidation batch runs. Experimental conditions: [H_2O_2] = 2.0 g/L, [Fe^{2+}] = 100 mg/L, pH_0 = 5.0, t = 300 min.

When operating at lower temperatures (T = 20 °C), the TOC removal performance observed (49.0%) may suggest that the extent of the reaction was not complete within 300 min. Analysis of the residual H_2O_2 detected the highest levels of unreacted oxidant in solution for T = 20 °C (*ca*. 11% of unreacted H_2O_2 after 300 min – Table 4.3). Increasing the temperature to T = 50 °C slightly hindered the TOC depletion efficiency (54.5% – Fig. 4.6), indicating that under those conditions the temperature influences more the thermal decomposition of H_2O_2 into molecular oxygen and water (Eq. (2.12)) than in the degradation of organic matter [17,20]. The hypothesis

is confirmed by the lower levels of residual H_2O_2 in solution, especially after 15 and 30 min of reaction, when compared to the other temperatures tested (see Table 4.3).

Table 4.3 Comparison between residual [H_2O_2] in solution at the early stage of the Fenton process (15 and 30 min) and at the end of the experiment (300 min), for the 20–50 °C range of temperatures tested in the batch runs. Experimental conditions: [H_2O_2] = 2.0 g/L, [Fe^{2+}] = 100 mg/L, pH_0 = 5.0, t = 300 min.

T (°C)	$[H_2O_2]_{unreacted}$ (g/L)		
	After 15 min	After 30 min	After 300 min
20	0.58	0.47	0.22
30	0.59	0.34	0.04
40	0.40	0.17	0.03
50	0.15	0.08	0.03

It is also worth mentioning that an additional experiment was performed at room temperature (T ≈ 22 °C) without control of the reaction medium's temperature throughout the run (Fig. 4.7a). Due to the exothermal nature of the process, the temperature inside the reactor increased approximately 8 °C after 300 min (Fig. 4.7b). However, due to the time gap to achieve the optimum temperature of 30 °C, the TOC degradation rate under such conditions is considerably slower when compared to the experiment performed with temperature control throughout the reaction, although similar overall mineralization levels were achieved. Though this could imply that temperature control would not be required at an industrial level, one should also be aware of the climatic conditions of an actual olive mill installation during the harvest season, since it usually occurs in wintertime (from November to February).

Due to the minor difference on the TOC degradation efficiency for T = 30 *vs*. 40 °C (56.6 and 57.5%, respectively – Fig. 4.6), T = 30 °C was considered the most viable temperature for this process, as the small TOC degradation increase would not make up for the energy used to heat the system the additional 10 °C.

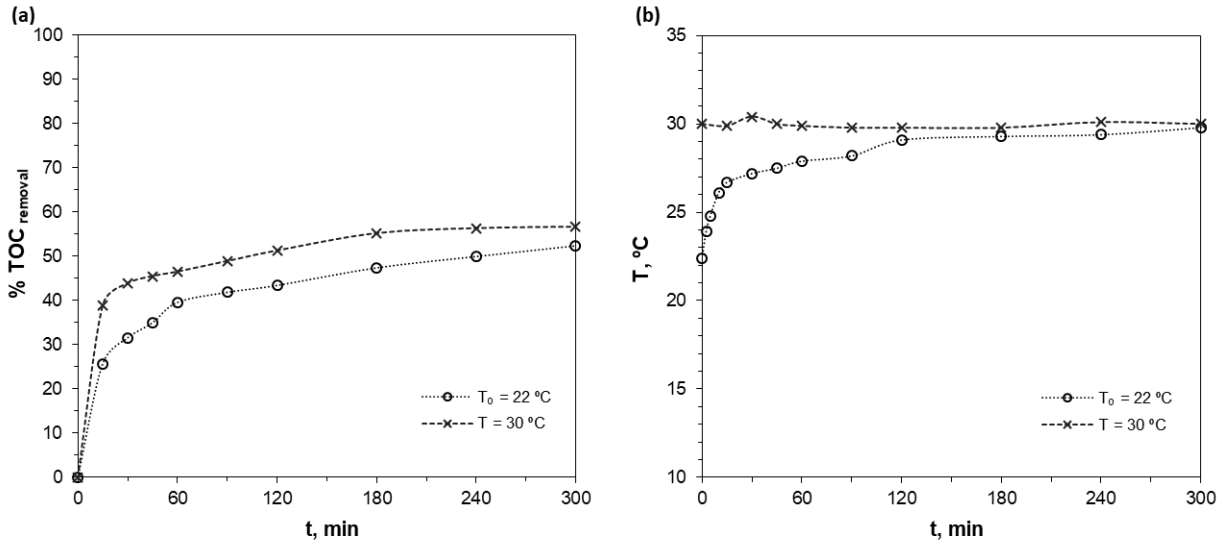


Fig. 4.7 (a) % TOC degradation for constant temperature (T = 30 °C) throughout the entire reaction (×) *vs*. unadjusted temperature (T_0 = 22 °C) (○); (b) reaction's temperature variation throughout the experiments. Experimental conditions: [H_2O_2] = 2.0 g/L, [Fe^{2+}] = 100 mg/L, pH_0 = 5.0, t = 300 min.

4.3.3. CSTR catalytic tests

With the industrial application of Fenton's process in perspective, which entails a large number of advantages when compared to biological or even other oxidative processes such as ozonation or photo-Fenton (e.g., possibility of dealing with refractory or toxic effluents, operation at room pressure and low temperature, equipment and operation simplicity, low operating cost [4,29]), additional experiments were performed in a CSTR to evaluate the process's effectiveness under continuous mode.

As seen in Section 4.3.2.1, Fenton's oxidation for the degradation of synthetic OMW consists in two phases: first, TOC and TPh removal happens quickly within the first minutes of reaction; then, in the second phase (also known as Fenton-like stage), oxidation proceeds at a much slower rate until reaching a plateau [3].This occurs because in the first stage of the process, Fe^{2+} reacts very quickly with H_2O_2 (rate constant of *ca*. 78 $M^{-1}{\cdot}s^{-1}$) to produce large amounts of $^{\bullet}OH$ (Eq. (2.1)) which rapidly mineralize the organic matter in solution; after this stage, ferric ions produced earlier can react with H_2O_2 to produce $HO_2^{\bullet}$ and restore Fe^{2+} (Eqs. (2.4) and (2.5)), although the reaction rate for iron regeneration is much slower (*ca*. 0.02 $M^{-1}{\cdot}s^{-1}$), making the rate of oxidation of this second stage much slower than the first one [30]. This indicates that the space-time (τ) within the CSTR is an important parameter to consider. In an ideal continuous stirred-tank reactor (where

the contents within the vessel are well-stirred and uniform throughout), the space-time is equal to the mean residence time and is calculated according to Eq. (4.4).

$$\tau = \frac{V\ (mL)}{Q\ (mL/min)} \tag{4.4}$$

Before changing the space-time, three runs with an arbitrary space-time value (τ = 90 min, equivalent to Q_{feed} = 10.2 mL/min) were performed varying the H_2O_2 feed dosages ($[H_2O_2]_{feed}$ = 2.0, 3.0, and 4.0 g/L). This set of experiments was performed not only to find the time required to reach steady-state condition but also to determine the best H_2O_2 feed dosage. Both are crucial factors for the efficiency and overall costs of Fenton's process (often holding back its upscale application [4]). An oxidant dose below the stoichiometric one (i.e., $[H_2O_2]_{feed}$ = 1.0 g/L) was not selected due to the poor results achieved in the batch mode operation. The remaining best operational conditions found on the foregoing experiments were applied for the CSTR runs, i.e., $[Fe^{2+}]_{feed}$ = 100 mg/L, initial pH = 5.0, and T = 30 °C. It is worth mentioning that dimensionless reaction time values are presented as $\theta = t/\tau$ – each θ unit is equivalent to one space-time (τ) of that run's experimental conditions. TOC and TPh values were then monitored for 450 min, equivalent to five space-time values.

Results in Fig. 4.8 indicate that steady-state was achieved after *ca*. 2.5–3 space-time values (225–270 min for this set of runs), both for TOC and TPh degradation. Regarding the effluent's TOC abatement, an increase in the hydrogen peroxide dosage led to slightly higher removal efficiencies (steady-state values equal to 45.0, 48.4, and 48.9% for $[H_2O_2]_{feed}$ = 2.0, 3.0, and 4.0 g/L, respectively). Regarding TPh removal, values ≥98% were observed for all experiments in steady-state conditions. The concentration of H_2O_2 at the reactor outlet was also checked, and steady-state values are presented in Table A.2 in Appendix A. Residual H_2O_2 at the reactor outlet shows that, for $[H_2O_2]_{feed}$ = 3.0 g/L, ≈15% of the overall oxidant dose fed was not used. This could imply that, for the operational conditions applied in these runs, no further TOC degradation would be attained. This hypothesis was reinforced when the oxidant dose fed to the reactor was increased to 4.0 g/L, as TOC removal in steady-state maintained practically unchanged (48.9% *vs*. 48.4% for $[H_2O_2]_{feed}$ = 3.0 g/L) and the residual (unreacted) oxidant concentration inside the reactor increased to ≈25% (values for θ = 5). Therefore, increasing the dose of peroxide fed above 2.0 g/L by a factor of 1.5 or 2.0 does not justify the improvement verified in the TOC degradation, which is also evidenced by the decrease in the efficiency of the oxidant use (η H_2O_2 = 0.41, 0.21,

and 0.14 for $[H_2O_2]_{feed}$ = 2.0, 3.0, and 4.0 g/L, respectively), as previously stated in the batch tests. Thus, according to these experimental results, further experiments were performed with $[H_2O_2]_{feed}$ = 2.0 g/L and θ = 4 (which has proved to be enough to reach steady-state conditions).

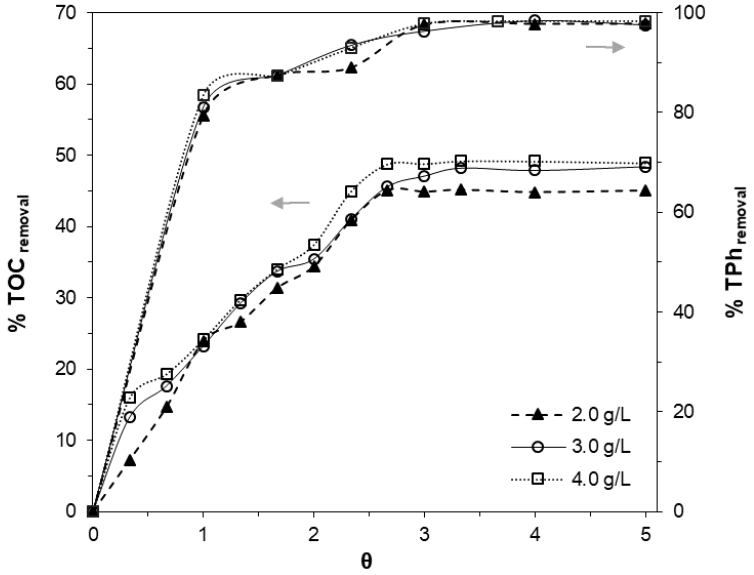


Fig. 4.8 Effect of H_2O_2 dose fed on TOC and TPh removal efficiency, in transient regimen, for the CSTR runs. Experimental conditions: $[Fe^{2+}]_{feed}$ = 100 mg/L, pH_0 = 5.0, T = 30 °C, τ = 90 min.

Runs with five space-time values (τ = 40, 60, 90, 120, and 180 min) were performed. Fig. 4.9 shows TOC and TPh removal values at steady-state (for transient regimen values report to Fig. A.4, Appendix A). Mineralization of the synthetic OMW increases whilst increasing the space-time, with TOC and TPh removals reaching a maximum of 50.4 and 98.2% respectively, in steady-state, when τ = 180 min. Zhang *et al*. [31] have shown the same trend for TOC and COD removal profiles on the treatment of landfill leachate by Fenton's oxidation while operating a CSTR. The higher the space-time, the more time the fluid elements/organic matter will have to react with the radicals because residence time within the reactor is increased. However, it is worth pointing out that operating at τ = 180 min requires the use of very low feed flow rates (*ca*. 5 mL/min), or higher reactor volume if *Q* is kept constant (Eq. (4.4)). Operating at τ = 120 min provided high TOC and TPh degradation levels (48.2 and 96.9%, respectively), with the clear advantage from the up-scale application point-of-view to have reduced by half the residence time of the effluent inside the reactor. It is also worth mentioning that unreacted oxidant concentration at steady-state conditions was less than 10% of the initial feed dose applied on this set of runs, which clearly suggests its efficient use (η H_2O_2 = 0.29, 0.36, 0.41, 0.43, and 0.44 for τ = 40, 60, 90, 120, and 180 min, respectively).

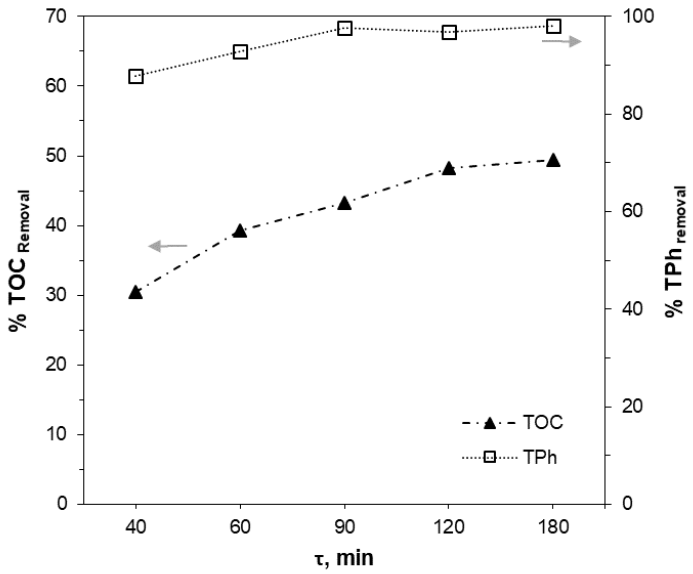


Fig. 4.9 Effect of space-time (τ) on TOC (▲) and TPh (□) removal efficiencies, at steady-state, for the CSTR runs. Experimental conditions: $[H_2O_2]_{feed}$ = 2.0 g/L, $[Fe^{2+}]_{feed}$ = 100 mg/L, pH_0 = 5.0, T = 30 °C.

4.3.4. Overall performance of the batch and CSTR reactors: biodegradability and toxicity evaluation

Table 4.4 shows the main characteristics of the treated solutions for the best operational conditions found on both reactors. For the sake of comparison between the two configurations, Table 4.4 also presents a summary of the TPh and TOC removal efficiency under identical operational times, i.e., 180 min for batch (the plateau for the discontinuous operation, according to considerations in Section 4.3.2.1) and τ = 180 min for the continuous reactor; performances are slightly better in the batch mode, although differences are not too significant.

Table 4.4 Characterization of the synthetic effluent after the batch (after 180 and 300 min) and CSTR (for τ = 120 and 180 min) Fenton's oxidation runs, with respective removal efficiency percentages (within brackets).

Parameter	Final batch	Exit CSTR (steady-state)	Batch	Exit CSTR (steady-state)
	300 min	τ = 120 min	180 min	τ = 180 min
pH	3.18	3.05	3.20	2.98
TOC (mg/L)	142.9 (56.6%)	165.6 (48.2%)	147.7 (55.1%)	159.4 (50.4%)
TPh (mg CA_{eq}/L)	1.2 (99.7%)	10.4 (96.9%)	2.9 (99.2%)	6.3 (98.2%)
COD (mg O_2/L)	164.0 (79.7%)	194.1 (75.9%)	n.d.	n.d.
BOD_5 (mg O_2/)	61.2 (70.5%)	59.9 (71.1%)	n.d.	n.d.
BOD_5:COD ratio	0.37	0.31	n.d.	n.d.
V. fischeri inhibition 5 min (%)	0.0	0.0	n.d.	n.d.
V. fischeri inhibition 15 min (%)	0.0	0.0	n.d.	n.d.
V. fischeri inhibition 30 min (%)	0.0	0.0	n.d.	n.d.

n.d. – not determined

High organic matter degradation was observed for both batch and CSTR operation, with COD falling from 805.9 to 164.0 and 194.1 mg O_2/L, respectively, when operated in the best conditions found. Nonetheless, the synthetic effluent's final COD fell short of accomplishing the Portuguese legal threshold of 150 mg O_2/L for direct discharge of wastewaters on natural water bodies. Also, BOD_5 values slightly above the legal limit of 40 mg O_2/L were obtained after Fenton's oxidation runs in both rector configurations. This could indicate that the application of Fenton's oxidation alone for the treatment of real OMW, which is more complex in its organic constituents [32] when compared to the synthetic effluent used, may be insufficient if the goal is the direct disposal onto aquatic ecosystems or municipal wastewater treatment plants [12,33,34]. Nevertheless, a high reduction of lumped parameters was achieved, with >70% of COD and BOD_5 reductions on both operating modes, as well as >96% removal of the phenolic character of the effluent.

To evaluate the potential application of a coupled chemical-biological treatment, effluent's biodegradability and toxicity were also addressed. Biodegradability of the treated synthetic effluent was assessed by the BOD_5:COD ratio; 0.4 is usually considered the cut-off point value between a biodegradable and difficult to biodegrade effluent [35]. Improvement of this ratio (initially equal to 0.26) was achieved for the batch (0.37) and CSTR (0.31) best runs, although the

cut-off point was not met for the conditions tested. Determination of the toxicity of the effluent was also performed by the acute bioluminescence inhibition assay, using the marine bacterium *V. fischeri*. Although similar works dealing with synthetic OMW report high toxicity of the initial (untreated) samples [13,36], the mixture used in this study was non-toxic for the referred bacterium. Nonetheless, evaluation of this parameter was performed since the effluent's toxicity character may change after the oxidation runs, as Martins *et al*. [13] reported on their study of synthetic phenolic wastewater remediation by Fenton's oxidation. The authors stated that after 15 min, the treated wastewater toxicity was even higher than the one obtained for the initial solution, which shows that this parameter depends on the compounds eliminated and generated by oxidation. For the wastewater used in this study, the toxicity of the treated effluent (after 300 min for the batch run and at steady-state for the CSTR with τ = 120 min) was found to be null.

4.4. CONCLUSIONS

This work focused on a parametric study of homogeneous Fenton oxidation of a synthetic effluent comprising six phenolic acids under batch operation; then, the process was tested in a continuous reactor. First, the effect of hydrogen peroxide dosage, iron load, reaction temperature, and initial pH was addressed for the batch operation mode. It was found that oxidant and catalyst dose are closely related and have a strong influence on treatment efficiency. Up to some extent, increasing the Fe^{2+} and H_2O_2 doses has a positive influence on TOC and TPh removal. Increasing the H_2O_2 concentration from 1.0 to 4.0 g/L improved TOC degradation up to ≈36% and the use of oxidant doses higher than the stoichiometric one lead to ≥99% of TPh depletion. The best initial pH value was found to be 5.0 since it decreases to *ca*. 3.2 a few minutes after the beginning of the reaction, falling in the range of 3.0–3.5 (well-known as the range that maximizes Fenton's efficiency). Also, rising the reaction temperature up to 40 °C had a positive effect on organic matter mineralization. The best conditions for the parameters tested were defined not only based on lumped parameters degradation (TOC, TPh, COD, and BOD_5) but also on oxidant efficient use and actual olive mill conditions.

Based on the best operational parameters found for the batch runs, further experiments were performed on a continuous flow reactor. For the CSTR operation, steady-state conditions were attained after approximately 3 times the space-time (τ) value; enhancement of TOC and TPh

removal values was achieved by increasing τ from 40 to 180 min (30.5 and 87.7% *vs*. 50.4 and 98.2%, respectively). High reduction of COD and BOD_5 values was also verified – over 70% of the initial values both for batch and CSTR experiments; whilst biodegradability was slightly improved (maximum BOD_5:COD ratio equal to 0.37). This study shows that Fenton's oxidation could be effectively applied for the treatment of phenolic wastewaters, such as OMW, under discontinuous or continuous flow operation. A high reduction of lumped parameters leads to a final effluent that almost complies with the legal threshold of Portuguese legislation for direct discharge into water bodies.

REFERENCES

1. Amaral-Silva, N.; Martins, R.C.; Nunes, P.; Castro-Silva, S.; Quinta-Ferreira, R.M. From a lab test to industrial application: scale-up of Fenton process for real olive mill wastewater treatment. *J. Chem. Technol. Biotechnol.* **2017**, 92, 1336–1344.
2. Zhang, H.; Choi, H.; Huang, C. Treatment of landfill leachate by Fenton's reagent in a continuous stirred tank reactor. *J. Hazard. Mater.* **2006**, 136, 618–623.
3. Ramirez, J.H.; Duarte, F.M.; Martins, F.G.; Costa, C.A.; Madeira, L.M. Modelling of the synthetic dye Orange II degradation using Fenton's reagent: From batch to continuous reactor operation. *Chem. Eng. J.* **2009**, 148, 394–404.
4. Hodaifa, G.; Ochando-Pulido, J.M.; Rodriguez-Vives, S.; Martinez-Ferez, A. Optimization of continuous reactor at pilot scale for olive-oil mill wastewater treatment by Fenton-like process. *Chem. Eng. J.* **2013**, 220, 117–124.
5. Allouche, N.; Fki, I.; Sayadi, S. Toward a high yield recovery of antioxidants and purified hydroxytyrosol from olive mill wastewaters. *J. Agric. Food Chem.* **2004**, 52, 267–273.
6. Aggoun, M.; Arhab, R.; Cornu, A.; Portelli, J.; Barkat, M.; Graulet, B. Olive mill wastewater microconstituents composition according to olive variety and extraction process. *Food Chem.* **2016**, 209, 72–80.
7. El-Abbassi, A.; Kiai, H.; Hafidi, A. Phenolic profile and antioxidant activities of olive mill wastewater. *Food Chem.* **2012**, 132, 406–412.
8. Daâssi, D.; Lozano-Sánchez, J.; Borrás-Linares, I.; Belbahri, L.; Woodward, S.; Zouari-Mechichi, H.; Mechichi, T.; Nasri, M.; Segura-Carretero, A. Olive oil mill wastewaters: Phenolic content characterization during degradation by *Coriolopsis gallica*. *Chemosphere* **2014**, 113, 62–70.
9. De Laat, J.; Truong Le, G.; Legube, B. A comparative study of the effects of chloride, sulfate and nitrate ions on the rates of decomposition of H_2O_2 and organic compounds by Fe(II)/H_2O_2 and Fe(III)/H_2O_2. *Chemosphere* **2004**, 55, 715–723.
10. Siedlecka, E.M.; Wieckowska, A.; Stepnowski, P. Influence of inorganic ions on MTBE degradation by Fenton's reagent. *J. Hazard. Mater.* **2007**, 147, 497–502.
11. Ratanatamskul, C.; Chintitanun, S.; Masomboon, N.; Lu, M.C. Effect of chloride ions on nitrobenzene oxidation by the Fluidized-bed Fenton process. *Fresenius Environ. Bull.* **2010**, 19, 2665–2671.
12. Lucas, M.S.; Peres, J.A. Removal of COD from olive mill wastewater by Fenton's reagent: Kinetic study. *J. Hazard. Mater.* **2009**, 168, 1253–1259.
13. Martins, R.C.; Rossi, A.F.; Quinta-Ferreira, R.M. Fenton's oxidation process for phenolic wastewater remediation and biodegradability enhancement. *J. Hazard. Mater.* **2010**, 180, 716–721.
14. Deng, Y.; Rosario-Muniz, E.; Ma, X. Effects of inorganic anions on Fenton oxidation of organic species in landfill leachate. *Waste Manag. Res.* **2012**, 30, 12–19.
15. Bautista, P.; Mohedano, A.F.; Casas, J.A.; Zazo, J.A.; Rodriguez, J.J. An overview of the application of Fenton oxidation to industrial wastewaters treatment. *J. Chem. Technol. Biotechnol.* **2008**, 83, 1323–1338.
16. Zazo, J.A.; Casas, J.A.; Mohedano, A.F.; Rodriguez, J.J. Semicontinuous Fenton oxidation of phenol in aqueous solution. A kinetic study. *Water Res.* **2009**, 43, 4063–4069.
17. Nieto, L.M..; Hodaifa, G.; Rodriguez, S.; Giménez, J.A.; Ochando, J. Degradation of organic matter in olive-oil mill wastewater through homogeneous Fenton-like reaction. *Chem. Eng. J.* **2011**, 173, 503–510.
18. De Heredia, J.B. ; Torregrosa, J.; Dominguez, J.R.; Peres, J.A. Kinetic model for phenolic compound oxidation by Fenton's reagent. *Chemosphere* **2001**, 45, 85–90.
19. Kang, N.; Lee, D.; Yoon, J. Kinetic modeling of Fenton oxidation of phenol and monochlorophenols. *Chemosphere* **2002**, 47, 915–924.
20. Rivas, F.J.; Beltrán, F.J.; Gimeno, O.; Frades, J. Treatment of olive oil mill wastewater by Fenton's reagent. *J. Agric. Food Chem.* **2001**, 1873–1880.
21. Martins, R.C.; Quinta-Ferreira, R.M. Remediation of phenolic wastewaters by advanced oxidation processes (AOPs) at ambient conditions: Comparative studies. *Chem. Eng. Sci.* **2011**, 66, 3243–3250.
22. Kallel, M.; Belaid, C.; Mechichi, T.; Ksibi, M.; Elleuch, B. Removal of organic load and phenolic compounds from olive mill wastewater by Fenton oxidation with zero-valent iron. *Chem. Eng. J*. **2009**, 150, 391–395.
23. Truong, G. Le; De Laat, J.; Legube, B. Effects of chloride and sulfate on the rate of oxidation of ferrous ion by H_2O_2. *Water Res.* **2004**, 38, 2384–2394.

24. Zazo, J.A.; Pliego, G.; García-Muñoz, P.; Casas, J.A.; Rodriguez, J.J. UV-LED assisted catalytic wet peroxide oxidation with a Fe(II)-Fe(III)/activated carbon catalyst. *Appl. Catal. B Environ.* **2016**, 192, 350–356.
25. Bigda, R.J. Consider Fenton´s chemistry for wastewater treatment. *Chem. Eng. Prog.* **1995**, 12, 62–66.
26. Xu, L.J.; Wang, J.L. A heterogeneous Fenton-like system with nanoparticulate zero-valent iron for removal of 4-chloro-3-methyl phenol. J. Hazard. Mater. **2011**, 186, 256–264.
27. Chen, A.; Ma, X.; Sun, H. Decolorization of KN-R catalyzed by Fe-containing Y and ZSM-5 zeolites. *J. Hazard. Mater.* **2008**, 156, 568–575.
28. Ochando-Pulido, J.M. A review on the use of membrane technology and fouling control for olive mill wastewater treatment. *Sci. Total Environ.* **2016**, 563–564, 664–675.
29. Cañizares, P.; Paz, R.; Sáez, C.; Rodrigo, M.A. Costs of the electrochemical oxidation of wastewaters: A comparison with ozonation and Fenton oxidation processes. *J. Environ. Manage.* **2009**, 90, 410–420.
30. Ramirez, J.H.; Costa, C.A.; Madeira, L.M. Experimental design to optimize the degradation of the synthetic dye Orange II using Fenton's reagent. Catal. Today **2005**, 107–108, 68–76.
31. Zhang, H.; Choi, H.J.; Huang, C.P. Treatment of landfill leachate by Fenton's reagent in a continuous stirred tank reactor. *J. Hazard. Mater.* **2006**, 136, 618–623.
32. Dermeche, S.; Nadour, M.; Larroche, C.; Moulti-Mati, F.; Michaud, P. Olive mill wastes: Biochemical characterizations and valorization strategies. *Process Biochem.* **2013**, 48, 1532–1552.
33. Lucas, M.S.; Beltrán-Heredia, J.; Sanchez-Martin, J.; Garcia, J.; Peres, J.A. Treatment of high strength olive mill wastewater by Fenton's reagent and aerobic biological process. *J. Environ. Sci. Heal. - Part A Toxic/Hazardous Subst. Environ. Eng.* **2013**, 48, 954–962.
34. El-Gohary, F.A.; Badawy, M.I.; El-Khateeb, M.A.; El-Kalliny, A.S. Integrated treatment of olive mill wastewater (OMW) by the combination of Fenton's reaction and anaerobic treatment. *J. Hazard. Mater.* **2009**, 162, 1536–1541.
35. Scott, J.P.; Ollis, D.F. Integration of chemical and biological oxidation processes for water treatment: Review and recommendations. *Environ. Prog.* **1995**, 14, 88–103.
36. Silva, A.M.T.; Nouli, E.; Xekoukoulotakis, N.P.; Mantzavinos, D. Effect of key operating parameters on phenols degradation during H_2O_2-assisted TiO_2 photocatalytic treatment of simulated and actual olive mill wastewaters. *Appl. Catal. B Environ.* **2007**, 73, 11–22.

CHAPTER 5

TREATMENT OF HIGH-STRENGTH OMW BY COMBINED FENTON-LIKE OXIDATION AND COAGULATION/FLOCCULATION

Highlights

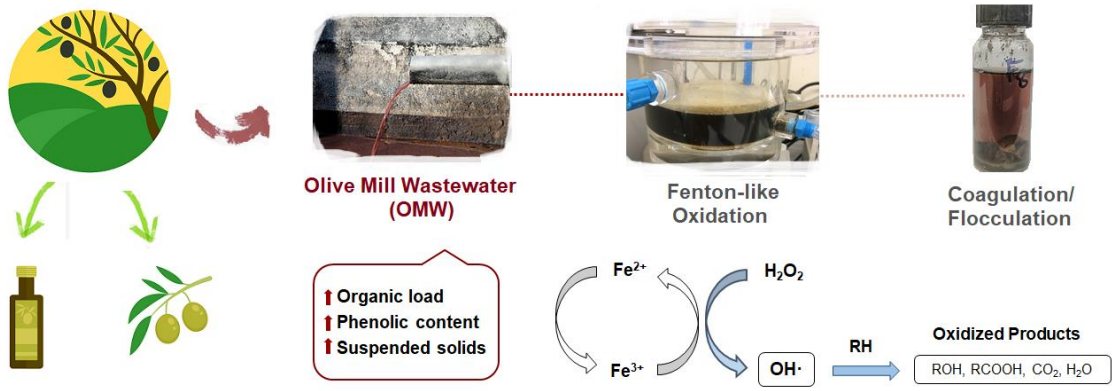
- High organic load and phenolic content difficult OMW treatment and management;
- Fenton-like process efficiency is dependent on pH readjustments along the reaction;
- Fe^{3+}/H_2O_2 mass ratio is a key parameter affecting the process efficiency;
- The catalyst also acts as a coagulant/flocculant agent after the oxidation step;
- COD and TPh global reductions of 77% and 96% were achieved, with toxicity reduction.

The contents of this chapter were adapted from:

Esteves, B.M., Rodrigues, C.S.D., Maldonado-Hódar, F.J., Madeira, L.M., Journal of Environmental Chemical Engineering, 2019, 7(4), 103252. https://doi.org/10.1016/j.jece.2019.103252

ABSTRACT

The efficiency of Fenton/Fenton-like processes on the oxidation of organic matter from real olive mill wastewater (OMW) is described. Tests were performed in lab-scale batch reactors and the influence of different operational parameters was evaluated, namely: type of iron salt, the effect of pH readjustments during the reaction, reactants addition method, and Fe/H_2O_2 mass ratio. For the Fenton-like system (Fe^{3+}/ H_2O_2) it was found that H_2O_2 consumption and consequently total organic carbon (TOC) degradation rate are significantly affected by the reagents addition method, especially in earlier stages of the reaction, although the overall extent of TOC removal is not. Results showed that the gradual addition of H_2O_2 along with pH readjustments during the process led to better chemical oxygen demand (COD) and total phenolic content (TPh) reduction. Operating at pH_0 = 3.0, T_0 = 25 °C, [Fe^{3+}] = 1.0 g/L and Fe/H_2O_2 = 0.04, 34.9% of TOC, 55.7% of COD and 81.4% of TPh were removed after 180 min. The same conditions were applied with the assistance of artificial radiation (photo-Fenton-like process) with slight organic matter degradation improvement (41.8% of TOC, 63.2% of COD, and 83.8% of TPh removals). The catalyst's (ferric chloride salt) ability to act as a coagulant/flocculant after the oxidative process was also checked, being reached a global reduction of 76.7% for COD and 96.4% for TPh after 1 h of sedimentation and no further pH adjustments. Moreover, the effluent's biodegradability (BOD_5:COD ratio) after the combined process improved from the initial value of 0.11 to 0.33, and toxicity against the bioluminescent Vibrio fischeri bacteria decreased from 53% to 4%, putting into evidence the possibility of coupling downstream a biological unit so that the final effluent meets legal discharge limits.



5.1. INTRODUCTION

The decomposition of H_2O_2 may be catalyzed by numerous transition metal ions and their complexes other than Fe^{2+} and undergo redox cycling reactions and produce reactive oxygen species, such as hydroxyl radicals. In such cases, Fenton's reagent is commonly referred to as Fenton-like oxidation. Some reports in this field suggest that the use of Fe^{3+} salts (namely ferric chloride – $FeCl_3$) should also be effective in organics degradation, despite the initial slower rate of H_2O_2 decomposition when compared to Fe^{2+} ones [1]. Additionally, ferric chloride is also reported to act as a coagulant/flocculant agent in wastewater treatment [2,3]. For example, Nieto *et al*. [4] tested the use of Fe^{3+}/H_2O_2 for the degradation of organic matter of olives/olive oil washing wastewaters from a 2-phase mill (COD_0 = 4.1 g/L and TPh_0 = 50.6 mg/L). Operating at ambient temperature, pH = 3, H_2O_2 = 100 g/L and $[FeCl_3]/[H_2O_2]$ ratio = 0.02, >99% of TPh and >92% of COD removal were achieved after 180 min.

The work described in this chapter aims to evaluate the efficiency of Fenton and Fenton-like processes for the treatment of a refractory and highly-loaded OMW from a Portuguese three-phase olive mill facility. This technology was selected because it has the potential to become a technical and economical solution for OMW management, in comparison to other AOPs that require more complex installations and/or higher energy consumption (e.g., ozonation, catalytic wet air oxidation, electro-oxidation), or that may present limitations related to the turbidity and dark color of undiluted OMW (e.g., photo-Fenton).

Few reports deal with the treatment of real OMW by the homogenous Fenton-like process catalyzed by Fe^{3+} ions [4,5] and, to the best of the author's knowledge, none address the treatment of highly-loaded and undiluted OMW from a 3-phase centrifuge. The influence of non-conventional operational parameters, such as the influence of pH readjustments during the process and reactants feeding mode, represent also a novelty in terms of process implementation. The effect of the type of iron salt (Fe^{2+}/Fe^{3+}) and Fe/H_2O_2 mass ratio on the reaction rate and extent of organic matter degradation was also evaluated. Moreover, under the best operational conditions found, experiments with assisted artificial radiation were performed (photo-Fenton-like process) and OMW mineralization efficiency was compared to the dark process.

Additionally to the chemical oxidation process, the organic matter removal occurring afterward through coagulation/flocculation prompted by the remaining iron salts selected as Fenton-like catalysts was also assessed. The efficiency of the combined and sequential process was

evaluated in terms of TOC, COD, and TPh reduction; biodegradability (as inferred from the BOD_5:COD ratio), and toxicity (inhibition of *Vibrio fischeri* photo-bacteria) of treated samples. This strategy aims to investigate the application of simple treatment units for the reduction of OMW's organic load and toxic character, in the context of sustainable water use/reuse.

5.2. MATERIALS AND METHODS

5.2.1. Olive mill wastewater

The OMW used in this study was obtained from a small 3-phase olive mill located in Barcelos, Portugal, in late 2017. The maximum installed olive processing capacity of this unit is ≈9 tons/day (*ca*. 1000 L of olive oil produced daily). The effluent, collected directly from the decanter's exit, had a strong olive smell, dark red-brown color, and a considerable amount of particulate matter. Gridding was carried out to remove coarser particles, then the effluent was homogenized, divided into 0.5 L plastic containers, and stored at -15 °C until needed. Before the experiments, samples were defrosted and allowed to sediment for a period of 12 h before collecting the supernatant. Table 5.1 highlights the main characteristics of the OMW as it was collected and after the sedimentation period. Notably, the sedimentation step alone allowed high organic matter, suspended solids, and turbidity reductions (*ca*. 30% *v/v* sludge separation). In this study, the simple gravity method is suggested as a pre-treatment step since it has no costs associated and could be performed at existing infrastructures in olive mills (such as wastewater tanks/reservoirs). Nonetheless, other methods are reported to efficiently pre-treat OMW, namely by filtration (e.g., 60% COD and 20% TPh removals [6]), coagulation/flocculation (depending on conditions applied, 41–97% TSS, 30–72% COD, and 19–40% TPh removals [7]), or acid cracking (e.g., 58% COD, 43% TOC, and 80% color removals [8]). In our case, performances reached were in such ranges, or even higher (e.g., in terms of TPh reduction).

Table 5.1 Physicochemical characterization of the OMW sample as collected and after the 12 h sedimentation.

Parameter	OMW (as collected)	OMW (after 12h sedimentation)	Removal (%)
pH	4.9 ±0.1	5.1 ±0.1	-
TOC (g/L)	15.5 ±1.2	8.5 ±0.3	45.1
COD (g O_2/L)	49.2 ±2.2	24.4 ±0.8	50.4
BOD_5 (g O_2/L)	7.2 ±0.5	2.6 ±0.2	63.9
TPh (g GA_{eq}/L)	3.36 ±0.10	1.31 ±0.08	61.0
TSS (g/L)	7.8 ±0.1	4.0 ±0.5	48.7
Biodegradability (BOD_5:COD)	0.15	0.11	-
Turbidity (NTU)	22 000 ±500	2 400 ±100	89.1
Conductivity (mS/cm)	4.2 ±0.3	3.1 ±0.1	26.1

5.2.2. Experimental procedure

Fenton/Fenton-like experiments were performed at a lab-scale in a jacketed stirred batch reactor with *ca*. 0.5 L of maximum capacity. Temperature control was performed by recycling water from a model 89202-912 VWR International thermostatic bath through the reactor's jacket. A VWR VS-CT magnetic stirrer was used to keep agitation at *ca*. 150 rpm. The effluent's pH and temperature were constantly monitored using a WTW Inolab pH-meter and a WTW SenTix 81 combined electrode. Photo-Fenton-like trials were also performed at a lab-scale using a 500 mL jacketed cylindrical reactor, equipped with a UV/visible lamp (light from high-pressure mercury vapor Heraeus TQ150 with 150 W, corresponding to a light intensity of 500 W/m^2). For a detailed description of the installation please refer to Rodrigues *et al*. [9].

In a typical Fenton/Fenton-like experiment, the reactor was loaded with 150 mL of OMW and the desired weighted amount of iron salt ($FeSO_4 \cdot 7H_2O$ from Panreac or $FeCl_3 \cdot 6H_2O$ from LabChem), allowing the total dissolution of the catalyst under continuous stirring for a few minutes. Adjustments of the effluent's pH (before and during the reaction) were performed using NaOH 5 M (Merck) and/or H_2SO_4 1 M (Fluka). After achieving the preset temperature of the reaction's medium (25 ±1 °C) and the desired initial pH (3.0 ±0.1), the oxidation process was initiated by adding the desired volume of hydrogen peroxide (30% *w/v*, Fischer Chemical), and the reaction extended for 3 or 4 h, depending on the runs. To highlight the good reproducibility of the

experiments, despite the intrinsically complex composition of the initial effluent used, all experiments were performed at least in duplicate and the mean values are presented along with standard deviations.

In selected experiments, the addition of reagents was performed gradually (i.e., drop by drop, at a flow rate that allowed reaching the total required catalyst and/or oxidant amount in 90 min). For those runs, the reaction started whenever the first drop of H_2O_2/Fe salt solution entered the reactor.

Samples of the treated effluent were periodically withdrawn during the experiments to assess the residual H_2O_2 concentration in solution (immediate analysis) and also the TOC (in this case, after stopping the possible oxidation reaction in the sampling flasks by adding an excess amount of Na_2SO_3, which instantly consumes residual H_2O_2). The evolution of organic matter degradation along the reaction was assessed by the %TOC removal, primarily due to the quickness and accuracy of TOC analysis, when compared to classical methods such as COD and BOD_5.

In experiments where the volume of the reactor is in constant change, due to the gradual addition of H_2O_2 and/or Fe^{3+} solution and the simultaneous collection of samples for analysis, the TOC removed along time was calculated according to Eq. (5.1),

$$TOC_{removed}(\%) = \frac{[TOC_0 \cdot V_0] - [TOC_t \cdot V_t]}{[TOC_0 \cdot V_0]} \cdot 100 \quad (5.1)$$

where *V* is the volume of the reaction mixture and the subscripts “0” and “t” stand for initial conditions and instant of sample collection, respectively.

After the oxidation process, samples of the treated effluent were collected for immediate TPh and COD analysis. In runs where residual H_2O_2 was present, samples were diluted 100× in a strongly basic pH medium (≈12) to decompose residual H_2O_2 and precipitate Fe [10], since Na_2SO_3 has been shown to cause major interference in TPh and COD determinations. Then, a 100 mL sample was collected, neutralized with NaOH 5 M and allowed to sediment for 1 h at 4 °C, to determine the influence of the coagulation/flocculation process (temperatures in the 4–30 °C range and pH in the 3–7 range showed no significant influence in the coagulation/flocculation process – data not shown). The cooling process and the sample neutralization are important steps to prevent the chemical reaction to proceed whenever residual H_2O_2 was found in the solution. After coagulation, samples of the supernatant were collected for COD, TPh, BOD_5, and inhibition towards *V. fischeri*

bacteria analysis with the same procedure as previously described, but neutralized to pH = 7 ±0.1 with H_2SO4 1 M or HCl 1 M prior to BOD_5 and toxicity analysis, respectively.

5.3. RESULTS AND DISCUSSION

5.3.1. Iron salt selection and pH control

For these preliminary tests, experimental conditions were fixed according to data widely reported in literature as suitable for Fenton/Fenton-like processes [11,12], namely pH_0 = 3.0 ±0.1 and T_0 = 25 ±1 °C (near-room temperature). Although some reports show that the process is positively affected when the reaction's temperature is increased [13,14], the efficient use of hydrogen peroxide may be hindered due to its thermal decomposition into H_2O and O_2 when temperatures above 40 °C are employed [4,15]; additionally, energy costs associated with heating the reaction's medium would be prohibitory to most olive oil manufacturing industries [16,17].

Due to the intrinsic complexity of most industrial wastewaters, the effluent's initial COD is frequently used to estimate the theoretical stoichiometric amount of H_2O_2 required to completely mineralize the organic load (R = H_2O_2/COD = 2.125) [18]. Bearing in mind the costs associated with the reactants, R ≈ 0.5 was defined as the starting point (i.e., half the theoretical stoichiometric dosage, [H_2O_2] = 25 g/L) as well as a Fe/H_2O_2 mass ratio of 0.04, which stands in the range of other reports in the field [4,5].

The rate and extent of OMW organic matter degradation over time (expressed as %TOC removal) were evaluated using iron(II) sulfate as Fe^{2+} source (Fenton process) and iron(III) chloride as Fe^{3+} source (Fenton-like process) – Fig. 5.1a. For both systems, the mineralization of phenolic compounds into low molecular weight carboxylic acids caused a significant drop in the medium's pH during the reaction, also reported by other authors [4,10]. Since Fenton/Fenton-like processes typically show greater efficiency at pH ≈ 3, the effect of performing small adjustments during the reaction whenever pH dropped below ≈2.5 was also checked – data for pH evolution over time is shown in Fig. 5.1b.

Results indicate that the rate of TOC oxidation (and consequently H_2O_2 consumption – Fig. 5.1c) is much faster using Fe^{2+}/H_2O_2 instead of Fe^{3+}/H_2O_2, which has been reported as the result of the faster formation of •OH that occurs via Fenton reagent, *cf*. Eq. (2.1) [1,15]. In fact, the kinetic constant for the "Fenton stage" described in Eq. (2.1) ranges from 51–100 $M^{-1}{\cdot}s^{-1}$, while the

regeneration of Fe^{3+} to Fe^{2+} (also known as the "Fenton-like stage") proceeds at a much slower rate (*ca*. 0.02–0.05 $M^{-1}{\cdot}s^{-1}$) [13].

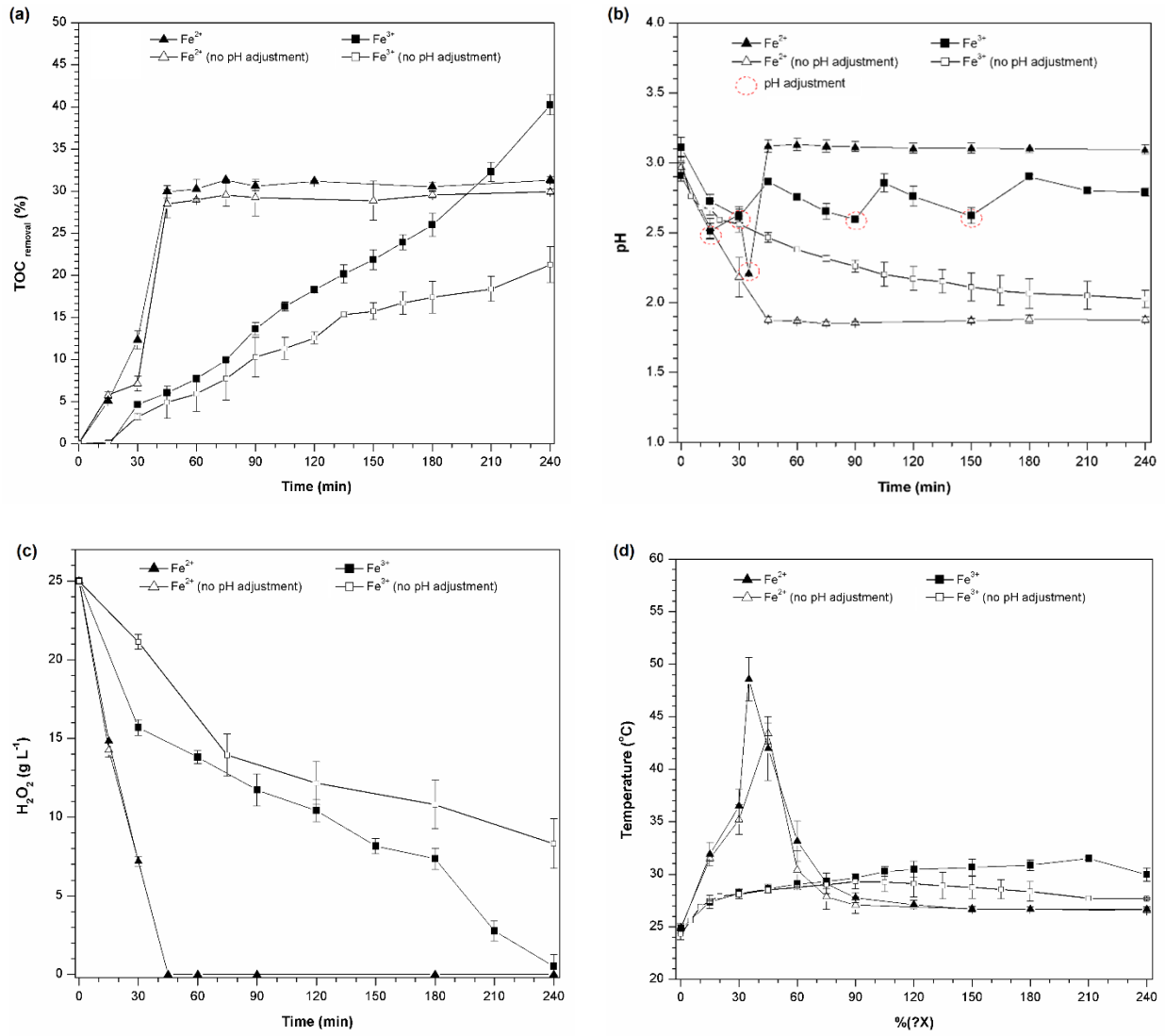


Fig. 5.1 Comparison of Fenton (Fe^{2+}/H_2O_2) and Fenton-like (Fe^{3+}/H_2O_2) reactions, with and without pH adjustments, on the (a) TOC removal, (b) pH evolution, (c) H_2O_2 concentration profile, and (d) temperature profile along time. Experimental conditions: $[Fe^{2+}/Fe^{3+}]$ = 1.0 g/L, $[H_2O_2]$ = 25 g/L, pH_0 = 3.0, T_0 = 25 °C.

When comparing both systems it is observed that with the Fe^{2+}/H_2O_2 one pH quickly drops to ≈1.9 (Fig. 5.1b) after consuming the oxidant available in 45 min (Fig. 5.1c). Such an acidic pH is never reached by the Fe^{3+}/H_2O_2 system. This is probably related to the degradation mechanism in each case: the faster generation of •OH achieved with Fe^{2+}/H_2O_2 promotes the rapid oxidation of more organic molecules into intermediate carboxylic acids (thus the more acidic pH). The absence of any TOC removal observed for the Fe^{2+}/H_2O_2 system after 45 min could be also linked with the inefficient use of H_2O_2. In fact, the high heat generated by the oxidation of the organics in a short

period of time produces a $\Delta T \approx 24$ °C after 45 min (Fig. 5.1d), which could have promoted the unwanted thermal decomposition of hydrogen peroxide.

Experimental data also suggest that the Fenton-like process is strongly pH-dependent, in agreement with previous studies in this subject [5,19]. In fact, with Fe^{3+}/H_2O_2, a severe decrease in the TOC removal (Fig. 5.1a) and overall H_2O_2 consumption (Fig. 5.1c) were observed in the run without pH readjustments regarding the process carried out with pH control, reinforcing the importance of this step to improve the overall efficiency. This could be related to the scavenging effect of $^{\bullet}OH$ by H^+, as reported by Hsueh *et al*. [20] in their study of azo dyes degradation by Fenton and Fenton-like systems.

The influence of the pH control is harder to point out using the Fe^{2+}/H_2O_2 system due to the very fast reaction rate obtained. Nevertheless, it seems that pH adjustment also promoted a slight enhancement on the reaction rate until t = 30 min (i.e., while oxidant was still available), although not improving considerably the final mineralization performance when compared to the run without pH control. For example, Amaral-Silva *et al*. [21] reported a 10% increase in COD degradation and phenolic compounds mineralization by continuous pH control to 3.0 ±0.1 throughout Fenton oxidation of OMW (after 180 min).

Despite the differences in oxidation rate, the overall TOC removal after 240 min was higher for the Fe^{3+}/H_2O_2 system when combined with pH readjustments. Higher removal efficiencies of COD and TPh of a pre-treated OMW were also observed by Mert *et al*. [22] using the Fenton-like process over the Fenton one, across a wide range of H_2O_2 and Fe dosages. Moreover, using the Fenton system the high temperatures reached in the first instants of the oxidation process (with values close to 50 °C) accelerate not only organics degradation but also hydrogen peroxide consumption, which concentration is null after 45 min of reaction (Fig. 5.1c). Failure to rapidly dissipate the heat generated by the quick and violent chemical reaction, which also entails the unwanted formation of excessive foam, may result in hazardous situations at full-scale application. So, subsequent runs were focused on the Fenton-like system.

It is also worth mentioning that the use of $FeCl_3$ makes the effluent's pH quickly drop from its initial value of ≈5 to pH ≈ 3 due to the dissociation of Fe(III) ions that tend to hydrolyze with water. This is an important techno-economical aspect since the acidification of the initial solution often limits the applicability of Fenton-related processes in environmental technology. Another noteworthy consideration is the fact that Fe^{3+} salts are typically cheaper than Fe^{2+} ones [4].

5.3.2. Reagents addition strategy

Fenton/Fenton-like mechanism and kinetics are quite complex, particularly if working with real effluent matrixes. The oxidation reactions are dependent on numerous factors, including the ratio of organic matter to catalyst and/or oxidant [23]. If a high concentration of Fe is present in the solution, iron ions and organics (RH) may compete for $^{\bullet}OH$, according to Eqs. (2.2) and (2.8). Likewise, scavenging of $^{\bullet}OH$ occurs when excess H_2O_2 is fed to the system, reducing hydroxyl radicals' availability to degrade organic matter, generating the less reactive hydroperoxyl radical, *cf*. Eq. (2.7).

In most lab-scale studies, the addition of Fe and H_2O_2 is frequently performed in a single step at the beginning of the process, which usually promotes a high generation of $^{\bullet}OH$ in a short period of time [10,24]. In such conditions, especially when treating high strength wastewaters that require higher doses of chemicals, the competitive scavenging reactions involving reactants, organic matter and hydroxyl radicals may prevail [15].

To better understand the behavior of the Fenton-like system, three distinct methods of reagents addition were tested:

(i) single addition of Fe and H_2O_2 at the beginning of the reaction (t = 0);

(ii) gradual addition of H_2O_2 (same volume of 30% *w/v* H_2O_2 as in method (i) – 12.5 mL – but fed dropwise at a rate of 2–3 drops/min) during the first 90 min of reaction, with a single step addition of Fe at t = 0;

(iii) gradual and simultaneous addition of both Fe and H_2O_2, also for 90 min (the iron salt was dissolved in the minimum amount of distilled water – 2 mL – and also fed dropwise at an approximate rate of 1 drop every 2.5 min).

The results in Fig. 5.2a show that TOC removal proceeds at different rates for the three feeding methods tested, despite the similar final degree of mineralization. In Fenton-like processes, Eq. (2.4) is the chain-initiation step for the production of the reactive hydroxyl radicals (i.e., the kinetic rate-limiting step). Hence, the formation of Fe-peroxo complexes and their unimolecular decomposition into Fe^{2+} (Eq. (2.5)) that sustains the formation of $^{\bullet}OH$ (Eq. (2.1)) is strongly dependent on the availability of H_2O_2 [25].

The great amount of hydrogen peroxide available in case (i) causes a short lag phase in the earlier stage of the reaction (i.e., up to t = 15 min). In this initial step, H_2O_2 consumption is faster indicating the oxidation of organics but the TOC removal does not increase since only

intermediate oxidation products are formed. This consumption is also influenced by the scavenging reactions, particularly the one depicted in Eq. (2.7). This path, along with the chain-initiation step, also generates the less reactive $HO_2^{\bullet}$ resulting in a more steady pace removal of TOC throughout the reaction.

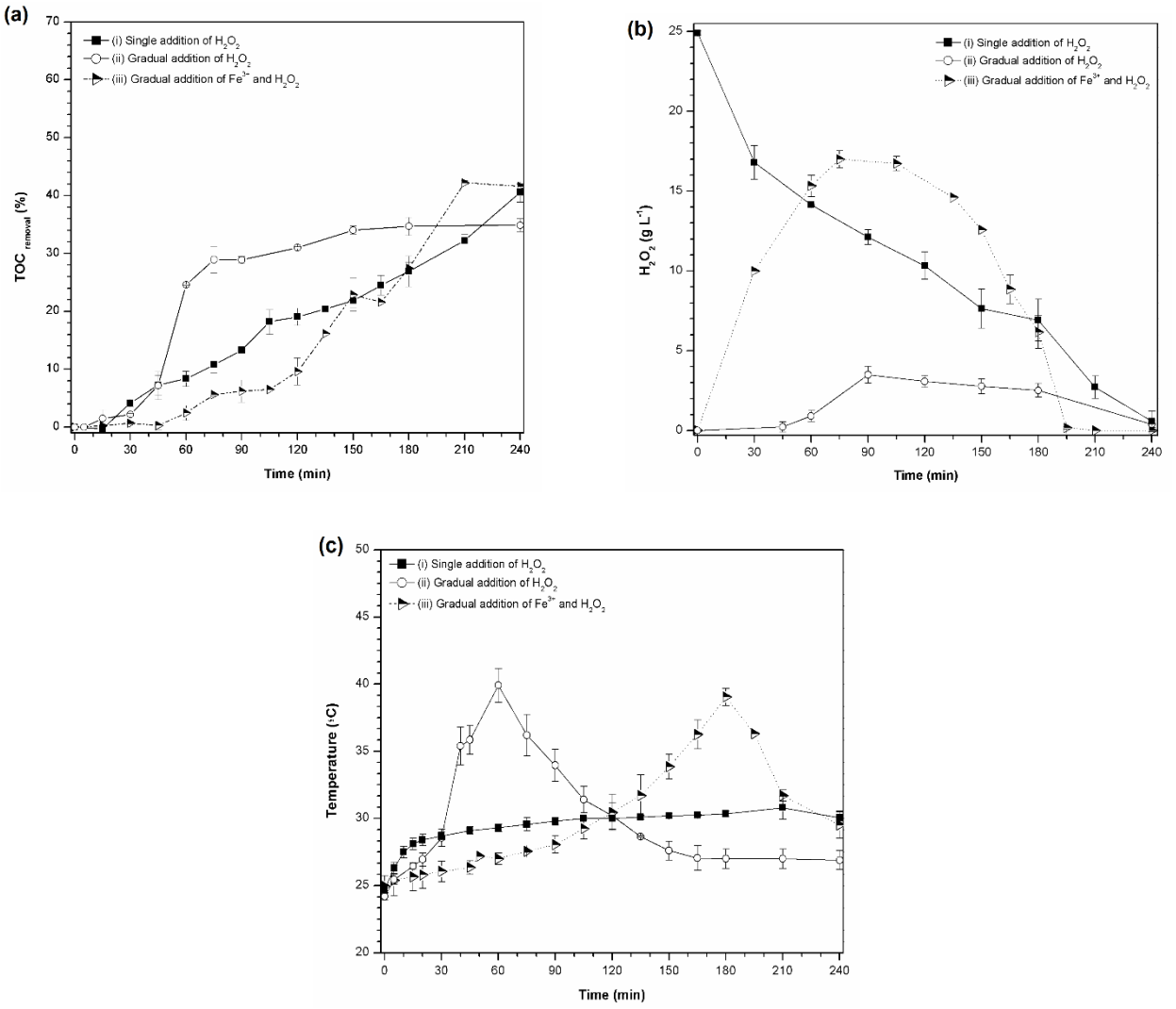


Fig. 5.2 Effect of the different reagent addition methods on (a) TOC removal, (b) H_2O_2 concentration profile, and (c) temperature profile over time for. Experimental conditions: $[Fe^{3+}]$ = 1.0 g/L, $[H_2O_2]$ = 25 g/L, pH_0 = 3.0, T_0 = 25 °C.

In case (ii), when H_2O_2 is gradually supplied to the reactor, despite that initially all H_2O_2 is consumed by the excess amount of ferrous ions in solution (Fig. 5.2b), a bigger time-lag is observed (up to t = 30 min) for the TOC removal. From that moment up to t = 60 min a fast degradation of organic matter and a strongly exothermic process is observed – $\Delta T \approx 15$ °C (Fig. 5.2c); but thereupon (after 90 min), the mineralization rate and the reactor temperature decrease, together with a small build-up of H_2O_2. Evidently, the oxidation of the starting organic compounds is easier (and more exothermic) than the intermediate oxidation products remaining after 90 min

of reaction. Also, the formation of iron complexes with organics or intermediates may occur, affecting the availability of Fe to react (at the same rate) with H_2O_2, thus the slight accumulation of oxidant in the reactor and, consequently, the decrease of hydroxyl radicals formation and slower TOC removal profile. The higher Fe/H_2O_2 ratio in the reaction medium from that point on (as compared to case (i)) may also result in competitive reactions for •OH, particularly the one depicted in Eq. (2.8), which inevitably would also lead to a slower TOC removal profile.

In contrast, case's (iii) simultaneous and gradual addition of both reactants results in the build-up of H_2O_2 inside the reactor up to t = 90 min. The shortage of catalyst and oxidant in that time frame results in a lengthy initial lag-phase (up to t = 45 min) and even a slower TOC removal rate is observed between 45 and 120 min. However, from t = 120 min onwards, a stronger increase of the degradation rate compared with methods (i) or (ii) is observed. This process is also accompanied by an increase of the temperature inside the reactor until t = 195 min, which corresponds to the maximum %TOC removal slope and also H_2O_2 exhaust (Fig. 5.2b). Thus, in contrast with method (ii), the exothermic mineralization of organics only occurs after a significant advance of the reaction, so the intermediate degradation products should be quite different. The Fe-concentration is clearly a limiting factor, and only after a certain Fe-concentration the oxidant is totally consumed.

In respect to COD removal after Fenton oxidation reported in Fig. 5.3, Zhang *et al*. [23] showed that the efficiency of the Fenton process for the treatment of landfill leachate also improved by the stepwise addition of H_2O_2 in comparison to the single-dose method. For COD_0 = 2000 mg/L, degradation increased from 42% to 50%, which is in the same order of magnitude as the results presented in this study. However, contrary to our findings, the same authors reported increasingly better COD removals with the simultaneous and step-wise addition of both oxidant and catalyst in multiple steps (e.g., for five feedings, COD removal was ≈58%). As to TPh removal, Martins *et al*. [26] also reported on the stepwise injection of H_2O_2 for the Fenton oxidation of a mixture of different phenolic compounds typically present in OMW. Higher mineralization of phenolic compounds was achieved when H_2O_2 was divided into 12 injections during the reaction when compared to a single-stage addition at t = 0. The author's results are in accordance with TPh removals attained in this study.

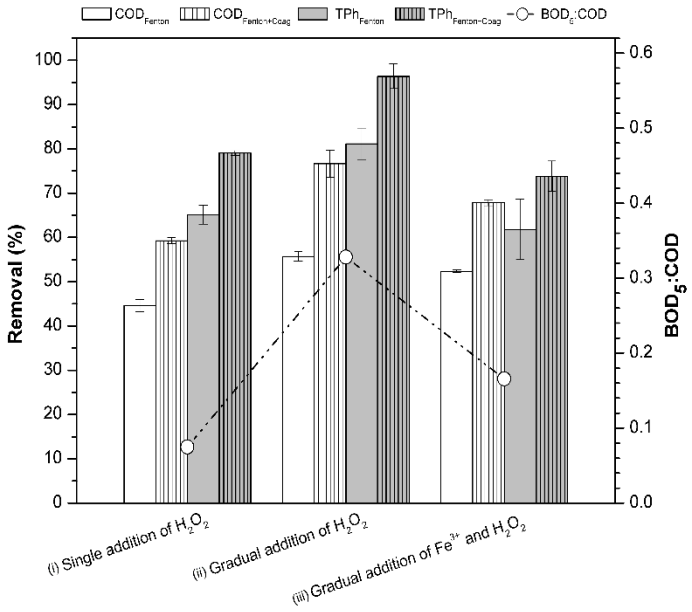


Fig. 5.3 Overall COD and TPh removal (after Fenton oxidation and Fenton + coagulation/flocculation processes) and BOD_5:COD ratio of the final effluent for the different reagent addition methods tested. Experimental conditions: $[Fe^{3+}]$ = 1.0 g/L, $[H_2O_2]$ = 25 g/L, pH_0 = 3.0, T_0 = 25 °C, t = 240 min.

As previously mentioned, Fe(III) may also act as a coagulant/flocculant agent, either as a pre-treatment stage or polishing step after Fenton reaction. Ginos *et al*. [27] reported that a Fe(III) dose of 1000 mg/L reduced the initial COD, TSS, and TPh load of an OMW by 50%, 14%, and 10%, respectively (initial average values for such parameters were 61.1, 52.7, and 3.5 g/L, respectively). Iakovides *et al*. [28] also presented similar results but used 10 times the amount of Fe(III). As shown in Table 5.1, the initial sedimentation step alone reduces the organic load and suspended solids on the original OMW in the same order of magnitude as the ones reported in the literature with coagulation/flocculation pre-treatments. Moreover, for the OMW in this study, preliminary pre-treatment coagulation/flocculation tests were performed with Fe(III) concentrations in the range of 0.25–1.50 g/L. The adopted procedure – rapid stirring at 200 rpm for 3 min, followed by 20 min at 30 rpm and 2 h sedimentation period – resulted in lower COD, TSS, and TPh reductions (results not shown) when compared to the ones obtained by sedimentation alone. Considering all of the above, the effect of the coagulation/flocculation step was only evaluated for the oxidation products, since Fe(III) was already available from the Fenton stage. Moreover, oxidation products of OMW usually comprise carboxylic acids (negatively charged) that are destabilized under the presence of soluble inorganic metal salts, resulting in charge neutralization, consequent agglomeration of colloidal particles in large flocs, and finally precipitation [21].

Overall TPh and COD depletion results are also presented in Fig. 5.3, along with effluent's final biodegradability (BOD_5:COD ratio). Results obtained suggest that the removal of dissolved organic matter that occurs via coagulation/flocculation after the Fenton-like oxidation is quite similar, regardless of the method of reagents addition applied, probably because the same overall dosage of ferric chloride was applied in all runs. On average, additional removal between 15-20% for COD and 12–15% for TPh were achieved through coagulation/flocculation of dissolved organics in solution. Nonetheless, higher COD (≈56%) and particularly TPh removals (≈81%) were reached by Fenton-like oxidation when method (ii) was employed – i.e., the gradual addition of H_2O_2. Achieving high mineralization of the phenolic fraction is a very important aspect if a downstream biological process or discharge in agricultural lands is envisaged since phenolic compounds are known for their recalcitrant behavior and toxicity towards microorganisms and plants. The BOD_5:COD ratio is commonly used as a rough indicator of the biodegradability of the effluent. For instance, Kallel *et al*. [10] reported OMW biodegradability improvement from 0.14 to 0.22 after 5 h zero-valent iron Fenton-like oxidation ($[H_2O_2]$ = 0.95 M, $[Fe^0]$ = 20 g/L, COD_0 = 19 g/L), reaching the value of 0.53 but only after 24 h of reaction. In this study, the highest BOD_5:COD of 0.33 was achieved with method (ii), corresponding to an important biodegradability improvement regarding the initial value of 0.11.

Due to the overall promising results, additional experiments were performed with method (ii), i.e., single-step addition of Fe^{3+} at t = 0 and gradual addition of H_2O_2.

5.3.3. Fe^{3+}/H_2O_2 ratio

As already stated, the relationship between Fe^{3+} and H_2O_2 seems to play a central role in the overall kinetics and extent of organics oxidation. To try to improve the process's efficiency, Fe^{3+} dosages varying from 0.75–1.25 g/L and H_2O_2 from 15–30 g/L were applied (corresponding to Fe^{3+}/H_2O_2 mass ratios in the range of 0.033–0.083). Again, operating costs were considered when selecting the range of reagents doses, aiming not only to maximize the treatment efficiency but also to promote the lowest residual levels of unreacted/residual hydrogen peroxide in the treated effluent.

Fig. 5.4a shows the evolution of %TOC removed with time for the different Fe^{3+}/H_2O_2 mass ratios selected. For comparative purposes, the oxidative potential of H_2O_2 in the absence of the catalyst was also evaluated. For the array of dosages selected, higher TOC degradation efficiencies are achieved for smaller Fe^{3+}/H_2O_2 ratios. This trend is clear for experiments with the same initial Fe^{3+}

dosage of 1.0 g/L and progressively higher H_2O_2 concentrations (20, 25, and 30 g/L, achieving *ca*. 27%, 35%, and 40% TOC removal after 180 min, respectively). However, the amount of unreacted oxidant left in the medium also increases in the same sense (*ca*. 3.2, 8.8, and 10.6% – 0.4, 2.1, and 3.5 g/L – relatively to the total amount of H_2O_2 fed, respectively) – see Fig. 5.4b for H_2O_2 evolution with time inside the reactor.

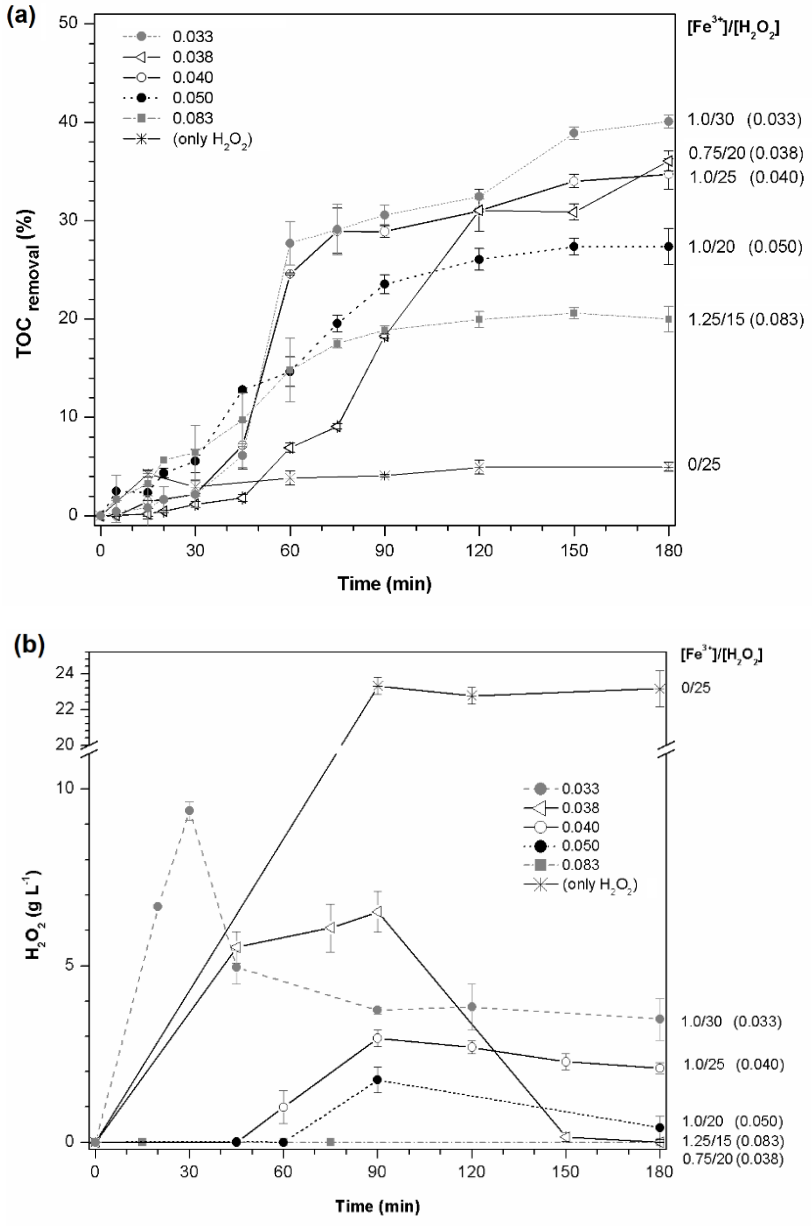


Fig. 5.4 (a) TOC removal and (b) H_2O_2 concentration over time for different Fe^{3+}/H_2O_2 ratios. Experimental conditions: $[Fe^{3+}]$ = 0.75–1.25 g/L, $[H_2O_2]$ = 15–30 g/L, pH0 = 3.0, T_0 = 25 °C, and H_2O_2 gradually added until t = 90 min.

On the other hand, the %TOC removed and the H_2O_2 consumption is influenced by the concentration of catalyst in solution. Comparing Fe^{3+}/H_2O_2 = 0.038 and 0.050 (i.e., $[H_2O_2]$ = 20 g/L and $[Fe^{3+}]$ = 0.75 and 1.0 g/L, respectively), it is possible to say that: (1)

degradation kinetics are way slower in the earlier stages of reaction (i.e., up to t = 45 min) for lower catalysts doses (in this sense, even Fe^{3+}/H_2O_2 = 0.083 can be looked at to support this tendency, despite the lower H_2O_2 dose applied); and (2) the effect of scavenging reactions involving excess iron ions and hydroxyl radicals – Eq. (2.8) – considerably reduces the overall process efficiency.

COD and TPh removal percentages for both Fenton-like process alone and combined oxidation and coagulation/flocculation processes are shown in Fig. 5.5. The best %COD reduction for the Fenton-like oxidation alone was reached for Fe^{3+}/H_2O_2 = 0.040, whose ratio is in the range reported by Nieto *et al*. [4] for the Fenton-like oxidation of OMW from olives and olive oil washing activities (COD_0 of only 4137 mg/L). Working with Fe^{3+}/H_2O_2 ratios in the 0.02–0.04 range ($[H_2O_2]$ = 100–200 g/L and $[Fe^{3+}]$ = 2–4 g/L) the authors reported over 90% COD removal.

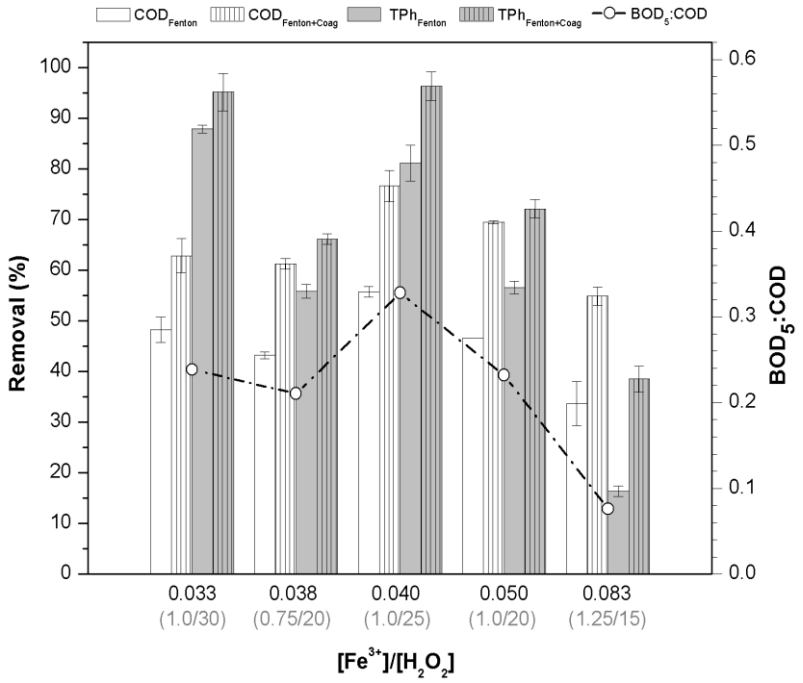


Fig. 5.5 Overall COD and TPh removal (after Fenton oxidation and Fenton + coagulation/flocculation processes), and BOD_5:COD ratio of the final effluent for the different $[Fe^{3+}]/[H_2O_2]$ ratios tested. Experimental conditions: $[Fe^{3+}]$ = 0.75–1.25 g/L, $[H_2O_2]$ = 15–30 g/L, pH_0 = 3.0, T_0 = 25 °C, t = 180 min, and H_2O_2 gradually added until t = 90 min.

Since COD removal by the coagulation/flocculation phenomena alone is very similar across the spectrum of ratios selected, operating with such ratio (i.e., $[H_2O_2]$ = 25 g/L and $[Fe^{3+}]$ = 1.0 g/L) also resulted in the highest global COD removal (76.7%) for the combined process. Lucas *et al*. [29] performed oxidation tests under different H_2O_2/COD mass ratios (R) for a ten-fold diluted OMW (COD = 5.34 g/L) and Fe^{2+}/H_2O_2 = 0.067. For the same R value as the one in this study

(R ≈ 0.5), COD removal reached 57.7% after Fenton oxidation and lime-coagulation, which is in close agreement with this work's findings.

In respect to the phenolic content removed by the oxidation process alone, the general trend is that lower catalyst/oxidant ratios promote higher %TPh degradation, which was also observed by Alver *et al*. [24] in OMW treatment by Fenton's process when the Fe^{2+}/H_2O_2 ratio decreased from 10 to 0.25 (TPh removals from 75.4 to 98.5%, respectively, for OMW with TPh_0 = 260 mg/L). More importantly, the dosage of oxidant seems to be closely linked to this trend, as progressively higher doses result in higher removal percentages. For $[H_2O_2]$ = 15 g/L (run with Fe^{3+}/H_2O_2 ratio of 0.083) TPh removal was ≈16%; in runs where $[H_2O_2]$ = 20 g/L (ratios 0.038 and 0.050) it was ≈56 and 57%, respectively; finally, for oxidant dosages of 25 and 30 g/L (ratios 0.040 and 0.030, respectively) ≈81 and 86% removals were reached, respectively. As to the combined process, the effect of the coagulation/flocculation process is more accentuated for experiments with higher ferric chloride concentration in solution (e.g., compare runs with $[Fe^{3+}]$ = 0.75 and 1.25 g/L, i.e., Fe^{3+}/H_2O_2 = 0.038 and 0.083, respectively).

Except for the run whit the highest catalyst/oxidant ratio, the biodegradability of the treated effluent has improved on all runs, confirming the trend that TPh removal efficiency is closely related to the BOD_5:COD ratio achieved at the end of the experiments, in line with the findings of Amaral-Silva *et al*. [21].

5.3.4. Photo-Fenton-like oxidation

The photo-Fenton process is based on the same principles and reagents as the dark Fenton one, but with the simultaneous application of UV/visible radiation, that should enhance the formation of hydroxyl radicals via, for example, the photolysis of H_2O_2 (Eq. (5.2)) or upon Fe^{2+} regeneration (Eq. (5.3)), ultimately resulting in the acceleration and increase of the mineralization degree [9].

$$H_2O_2 + \lambda v \rightarrow 2\ {}^{\bullet}OH \tag{5.2}$$

$$Fe^{3+}\ H_2O_2 + \lambda v \rightarrow Fe^{2+}\ {}^{\bullet}OH + H^+ \tag{5.3}$$

To assess the ability of the photo-Fenton-like process to improve the mineralization degree of OMW in comparison to the dark Fenton-like one, we have performed tests under the same operational conditions as previously reported as optimum (i.e., $[Fe^{3+}]/[H_2O_2]$ = 0.040, gradual

addition of H_2O_2 and pH control during the reaction). Additionally, we have also checked the performance of H_2O_2 photolysis alone.

Experimental results for TOC mineralization reported in Fig. 5.6 evidence that the photo-assisted Fenton-like treatment performs slightly better than the dark process. Nonetheless, the effect of inner filtering inside the photo-reactor, promoted by the strong dark color and turbidity of the OWM used, clearly inhibit the performance of the photo-assisted process. The enhancement of organics degradation for the conditions tested – 34.9 *vs*. 41.8% on TOC, 55.7 *vs*. 63.2% on COD, 81.4 *vs*. 83.8% on TPh, and no residual H_2O_2 after 240 min – is possibly not sufficient to make the process an economically-viable solution for undiluted OMW, especially if artificial light assistance is required; however, an economic analysis is required.

As to the UV/Vis + H_2O_2 process, TOC mineralization degree was slightly higher than the value reported for the application of H_2O_2 alone (Fig. 5.4a), as expected.

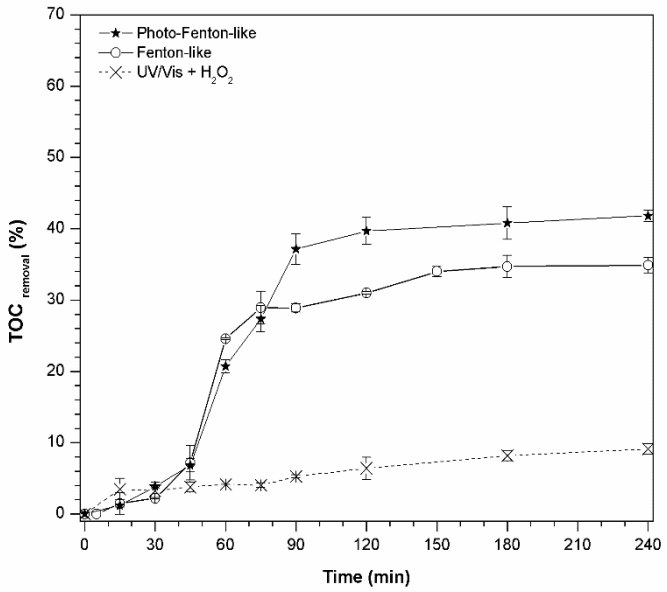


Fig. 5.6 Comparison of TOC removal over time for the photo-Fenton-like and Fenton-like processes. Experimental conditions: $[Fe^{3+}]$ = 1.0 g/L, $[H_2O_2]$ = 25 g/L, pH_0 = 3.0, T_0 = 25 °C, I = 500 W/m^2, and H_2O_2 added gradually until t = 90 min

5.3.5. Toxicity and quality of the treated effluent

The toxicity of the effluent was determined by the %Inhibition caused to the bioluminescent *V. fischeri* bacteria over different contact times – 5, 15, and 30 min. Fig. 5.7 highlights the bacteria's %Inhibition over the untreated OMW and treated effluent samples after the combined process (Fenton-like + coagulation/flocculation) for the range of Fe^{3+}/H_2O_2 ratios studied in the previous section. As expected, higher inhibition rates were recorded as contact time between the

bacteria and the effluent increased. Due to the high concentration of phenolic compounds (TPh_0 = 1.31 g/L – *cf*. Table 5.1), toxicity values for the untreated OMW sample reached 53% inhibition after 30 min contact time with the bacteria. Similarly to results and reports in the literature [10,34], the level of toxicity attenuation of the treated OMW is related to the removal of phenolic compounds (Fig. 5.8 highlights this trend). For the runs where almost total TPh removal was achieved, namely Fe^{3+}/H_2O_2 ratios 0.033 and 0.040 (95.2 and 96.4% removal, respectively – Fig. 5.3), the inhibition values were as low as 4% for both cases after 30 min. For the remaining ratios tested, toxicity reduction was found to be lower (following the same tendency as TPh removal), but the overall process still improved the final toxicity in relation to the initial values. This is an important factor that could make the effluent amenable for further biological depuration, as other authors have already pointed out. For instance, Amor *et al*. [35] reported an increase in organic matter conversion, bio-kinetics, and methane yield by the combined treatment of OMW by Fenton oxidation followed by anaerobic digestion, when compared to the biological step alone. Azabou *et al*. [18] performed catalytic tests with (Al–Fe)PILC/H_2O_2 as pre-treatment step of anaerobic digestion of OMW. The inhibition decrease of the *V. fischeri* bacteria after the catalytic step was 70% and biomethane production increased compared to raw OMW.

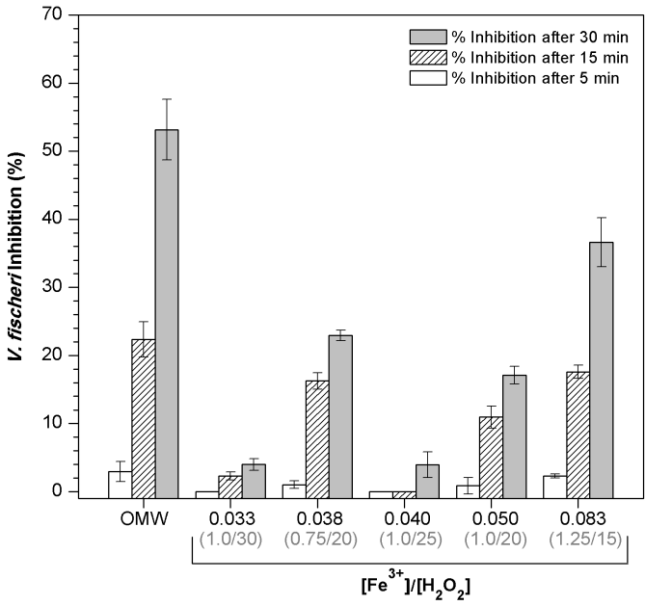


Fig. 5.7 Inhibition of the *V. fischeri* bacteria of the OMW before and after the combined treatment process for different contact time (5, 15, and 30 min)

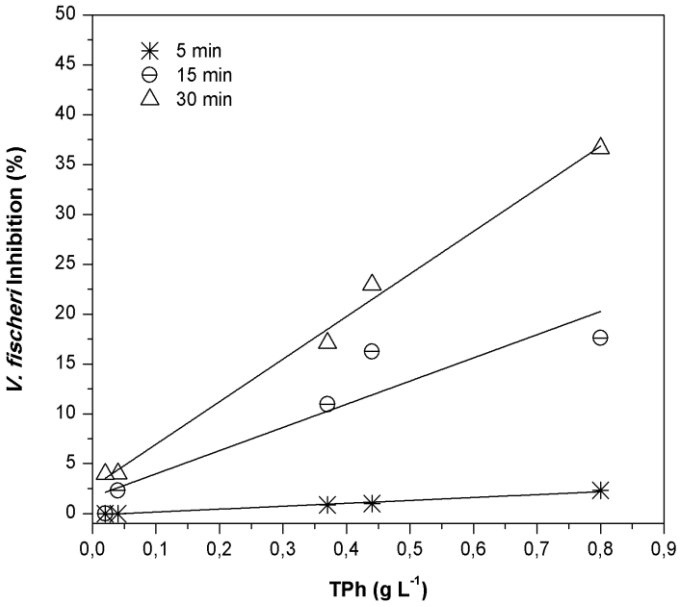


Fig. 5.8 Relationship between *V. fischeri* inhibition (%) and residual TPh (g/L) after the combined treatment process, for different contact times (5, 15, and 30 min).

Table 5.2 shows the effluent's physicochemical characteristics after the combined treatment process. Fe^{3+}/H_2O_2 ratios 0.033 and 0.040 were highlighted due to the most promising results in terms of the overall organic matter degradation (TOC, COD), TPh reduction, and biodegradability/toxicity improvement. Maximum allowable limits for wastewater discharge into water bodies in Portugal are specified in the Decree-Law no. 236/98 of August 1st. However, as mentioned, wastewater discharges into municipal collectors are regulated locally by municipalities or water management entities, each being adapted to the reality of the respective region and subject to acceptance by regulatory authorities.

Despite the satisfactory results, the effluent is not suitable for direct discharge in sewage collectors, according to legal limits imposed by the local water management entity of the Municipality of Braga (northern region of Portugal). To meet discharge limits presented in Table 5.2, a 5–10 fold dilution or a subsequent treatment unit would be required. Nonetheless, this approach constitutes a simple and effective pre-treatment stage for the degradation of refractory pollutants in OMW – not only phenolic compounds but also traces of pesticides residues (used in olive trees to ensure crop protection, since auxiliary agents are hardly used in the processing of olives) – that may hinder a biological step [5]. The fact that the effluent has considerably higher biodegradability and lower toxicity as compared to the raw OMW opens the door for a downstream biological treatment unit. The literature suggests that anaerobic digestion may constitute a suitable option, mainly due to the reduced energy consumption requirements, potential energy

recovery from the methane generated (that can be used for energy production), and low sludge generation [31,32]. The co-digestion of OMW with another wastewater stream (e.g., piggery effluent, poultry manure) [32,33] may not only improve the degradation efficiency and methane yield, but also provide the required pH and alkalinity levels required for successfully implementing the biological stage.

Table 5.2 Physicochemical characteristics of the OMW before and after the combined process for two Fe^{3+}:H_2O_2 ratios (supernatant's mean values). Legal discharge limits for industrial effluents into (a) water bodies in force in Portugal and (b) into municipal collectors of Braga Municipality (northern region of Portugal) are also presented.

Parameter	**OMW**	**Fe^{3+}:H_2O_2**		**Discharge Limit**
		0.033	**0.040**	
pH	5.1	2.4*	2.7*	6–9
TOC (g/L)	8.5	3.7	4.2	n.e.
COD (mg O_2/L)	24 400	9360	5560	150[(a)]/1000[(b)]
BOD_5 (mg O_2/L)	2600	1970	1820	40[(a)]/500[(b)]
TPh (g GA_{eq}/L)	1.31	0.04	0.02	n.e.
TSS (mg&/L)	4000	n.d.	n.d.	60[(a)]/1000[(b)]
Biodegradability (BOD_5:COD)	0.11	0.21	0.33	n.e.
30 min. *V. fischeri* inhibition (%)	53.0	3.9	4.0	n.e.
Visible color after 1:20 dilution	Visible	Not visible	Not visible	Not visible
Conductivity (mS/cm)	3.1	10.3	8.8	n.e.
Fe_{total} (mg/L)	n.d.	109.1	87.2	2.0[(a),(b)]

[(a)] According to Decree Law no. 236/98, August 1st
[(b)] According to the "Regulation for Industrial Discharges no. 169/2015" in force in Braga Municipality (DR 2ª Série – Nº 71 – April 13th 2015)
n.d. – not detected
n.e. – not established
*pH values after the oxidation step, prior to neutralization

One parameter of particular concern is the dissolved iron in solution after the process since relatively high Fe concentrations were applied for the oxidation step and the legal threshold for wastewater discharge is greatly exceeded (2.0 and 5.0 mg/L for discharge in natural water bodies and irrigation, respectively). For the two experiments reported in Table 5.2, *ca*. 10% of the initial iron load of 1.0 g/L stays dissolved in solution after the combined process. The most commonly accepted method for dissolved iron removal after Fenton oxidation is chemical precipitation by

raising the solution's pH, although it may not suffice to achieve the legal threshold value, as the experimental results show (Table 5.2). In such cases, tertiary treatment by ion exchange, adsorption, or membrane technology is usually required [34]. Another solution, which is currently being developed by several research groups for this particular application, is the immobilization of the active phase (Fe catalyst) in a support – the so-called heterogeneous Fenton-like process.

As to the major fraction of iron precipitated after the combined process, the sludge formation was less than 5% *v/v* for all $[Fe^{3+}]/[H_2O_2]$ ratios tested. The installation of lamellar decanters to collect and re-use the iron rich-sludge as an effective catalyst is a simple and economically attractive way to deal with the disposal problem, as reported by Ochando-Pulido *et al*. [35]. This would eliminate the sludge handling, reduce the catalyst consumption costs and, more importantly, reduce secondary pollution of natural water bodies.

5.4. CONCLUSIONS

High-strength olive mill wastewater (TOC_0 = 8.5 g/L and COD_0 = 24.4 g/L, both after sedimentation), coming from the operation of a 3-phase olive mill, was treated through Fenton-like oxidation followed by coagulation/flocculation. The aim of this study was to present a solution for the management of undiluted highly-loaded OMW, using simple treatment units using few and environmentally friendly reagents, and adaptable to the reality of small to medium-size olive oil extraction facilities. The performance of the process was monitored by TOC, COD, and TPh reduction; biodegradability and toxicity were also evaluated. Following the results obtained for the conditions tested, some conclusions may be drawn:

(i) The extent of organic matter oxidation (TOC removal) is higher with Fenton-like oxidation (Fe^{3+}/H_2O_2) when compared with the classic Fenton process (Fe^{2+}/H_2O_2), although the degradation rate is higher for the latter, particularly in the early stages of the reaction;

(ii) Fenton-like oxidation efficiency is strongly pH-dependent. To improve H_2O_2 utilization efficiency and consequently the organic matter degradation, small pH readjustments during the process are required;

(iii) For the Fe^{3+}/H_2O_2 system, the TOC removal rate in the earlier stages of the reaction is enhanced with the gradual addition of the oxidant. Removals of COD and TPh are also improved by this addition method when compared to a single-step addition.

(iv) The main parameter affecting the efficiency of the process is the Fe^{3+}/H_2O_2 mass ratio. Operating at $pH_0 = 3$, $T_0 = 25$ °C, t = 180 min, and $Fe^{3+}/H_2O_2 = 0.040$, the oxidation process alone was responsible for 55.7% COD and 81.1% TPh removal;

(v) The salt selected as catalyst (ferric chloride) also acts as a coagulant/flocculant agent. For the same conditions, 1 h of sedimentation after the oxidation process allowed global reductions of 76.7% for COD and 96.4% for TPh;

(vi) Under the same operational conditions, the photo-assisted Fenton-like process was tested. In comparison to the dark-process, only a slight enhancement of organic matter degradation was achieved, due to the effect of radiation filtration by the dark color and high turbidity of the OMW tested;

(vii) Direct discharge limits were not met after the proposed treatment scheme. However, the improvement in biodegradability and toxicity values, along with the considerable diminution of the organic matter load, evidenced the suitability for further biological depuration by anaerobic digestion, for example.

(viii) A downstream unit is required for iron recovery after the proposed treatment scheme, as the dissolved iron concentration in the solution significantly exceeds the legal threshold for discharge, even after chemical precipitation.

REFERENCES

1. Gallard, H.; De Laat, J. Kinetic modelling of Fe(III)/H_2O_2 oxidation reactions in dilute aqueous solution using atrazine as a model organic compound. *Water Res*. **2000**, 34, 3107–3116.
2. Verma, A.K.; Dash, R.R.; Bhunia, P. A review on chemical coagulation/flocculation technologies for removal of colour from textile wastewaters. *J. Environ. Manage*. **2012**, 93, 154–168.
3. Jaouani, A.; Vanthournhout, M.; Penninckx, M.J. Olive oil mill wastewater purification by combination of coagulation- flocculation and biological treatments. *Environ. Technol*. **2005**, 26, 633–41.
4. Nieto, L.M.; Hodaifa, G.; Rodriguez, S.; Giménez, J.A.; Ochando, J. Degradation of organic matter in olive-oil mill wastewater through homogeneous Fenton-like reaction. *Chem. Eng. J.* **2011**, 173, 503–510.
5. Hodaifa, G.; Ochando-Pulido, J.M.; Rodriguez-Vives, S.; Martinez-Ferez, A. Optimization of continuous reactor at pilot scale for olive-oil mill wastewater treatment by Fenton-like process. *Chem. Eng. J.* **2013**, 220, 117–124.
6. Filidei, S.; Masciandaro, G.; Ceccanti, B. Anaerobic digestion of olive oil mill effluents: Evaluation of wastewater organic load and phytotoxicity reduction. *Water. Air. Soil Pollut.* **2003**, 145, 79–94.
7. Papaphilippou, P.C.; Yiannapas, C.; Politi, M.; Daskalaki, V.M.; Michael, C.; Kalogerakis, N.; Mantzavinos, D.; Fatta-Kassinos, D. Sequential coagulation-flocculation, solvent extraction and photo-Fenton oxidation for the valorization and treatment of olive mill effluent. *Chem. Eng. J.* **2013**, 224, 82–88.
8. Gursoy-Haksevenler, B.H.; Arslan-Alaton, I. Profiling olive oil mill wastewater by resin fractionation: Effect of acid cracking, coagulation, electrocoagulation, and Fenton's reagent. *Clean - Soil, Air, Water* **2014**, 42, 1384–1392.
9. Rodrigues, C.S.D.; Silva, R.M.; Carabineiro, S.A.C.; Maldonado-Hódar, F.J.; Madeira, L.M. Dye-containing wastewater treatment by photo-assisted wet peroxidation using Au nanosized catalysts. *J. Chem. Technol. Biotechnol*. **2018**, 93, 3223–3232.
10. Kallel, M.; Belaid, C.; Mechichi, T.; Ksibi, M.; Elleuch, B. Removal of organic load and phenolic compounds from olive mill wastewater by Fenton oxidation with zero-valent iron. *Chem. Eng. J.* **2009**, 150, 391–395.
11. Wang, N.; Zheng, T.; Zhang, G.; Wang, P. A review on Fenton-like processes for organic wastewater treatment. *J. Environ. Chem. Eng*. **2016**, 4, 762–787.
12. Babuponnusami, A.; Muthukumar, K. A review on Fenton and improvements to the Fenton process for wastewater treatment. *J. Environ. Chem. Eng*. **2014**, 2, 557–572.
13. Ramirez, J.H.; Duarte, F.M.; Martins, F.G.; Costa, C.A.; Madeira, L.M. Modelling of the synthetic dye Orange II degradation using Fenton's reagent: From batch to continuous reactor operation. *Chem. Eng. J.* **2009**, 148, 394–404.
14. Azabou, S.; Najjar, W.; Bouaziz, M.; Ghorbel, A.; Sayadi, S. A compact process for the treatment of olive mill wastewater by combining wet hydrogen peroxide catalytic oxidation and biological techniques. *J. Hazard. Mater.* **2010**, 183, 62–69.
15. Wang, S. A Comparative study of Fenton and Fenton-like reaction kinetics in decolourisation of wastewater. *Dye. Pigment.* **2008**, 76, 714–720.
16. Rivas, F.J.; Beltrán, F.J.; Gimeno, O.; Frades, J. Treatment of olive oil mill wastewater by Fenton's reagent. *J. Agric. Food Chem.* **2001**, 49, 1873–1880.
17. Ochando-Pulido, J.M.; Pimentel-Moral, S.; Verardo, V.; Martinez-Ferez, A. A focus on advanced physico-chemical processes for olive mill wastewater treatment. *Sep. Purif. Technol.* **2017**, 179, 161–174.
18. Lucas, M.S.; Peres, J.A. Removal of COD from olive mill wastewater by Fenton's reagent: Kinetic study. *J. Hazard. Mater.* **2009**, 168, 1253–1259.
19. Hashemian, S. Fenton-like oxidation of malachite green solutions: Kinetic and thermodynamic study. *J. Chem.* **2013**, 2013.
20. Hsueh, C.L.; Huang, Y.H.; Wang, C.C.; Chen, C.Y. Degradation of azo dyes using low iron concentration of Fenton and Fenton-like system. *Chemosphere* **2005**, 58, 1409–1414.
21. Amaral-Silva, N.; Martins, R.C.; Castro-Silva, S.; Quinta-Ferreira, R.M. Integration of traditional systems and AOP´s technologies on the industrial treatment for Olive Mill Wastewaters. *Environ. Technol.* **2016**, 3330, 1–41.
22. Kiril Mert, B.; Yonar, T.; Yalili Kiliç, M.; Kestioğlu, K. Pre-treatment studies on olive oil mill effluent using physicochemical, Fenton and Fenton-like oxidations processes. *J. Hazard. Mater.* **2010**, 174, 122–128.

23. Zhang, H.; Heung, J.C.; Huang, C.P. Optimization of Fenton process for the treatment of landfill leachate. *J. Hazard. Mater.* **2005**, 125, 166–174.
24. Alver, A.; Baştürk, E.; Kiliç, A.; Karataş, M. Use of advance oxidation process to improve the biodegradability of olive oil mill effluents. *Process Saf. Environ. Prot.* **2015**, 98, 319–324.
25. De Laat, J.; Truong Le, G.; Legube, B. A comparative study of the effects of chloride, sulfate and nitrate ions on the rates of decomposition of H_2O_2 and organic compounds by Fe(II)/H_2O_2 and Fe(III)/H_2O_2. *Chemosphere* **2004**, 55, 715–723.
26. Martins, R.C.; Rossi, A.F.; Quinta-Ferreira, R.M. Fenton's oxidation process for phenolic wastewater remediation and biodegradability enhancement. *J. Hazard. Mater*. **2010**, 180, 716–721.
27. Ginos, A.; Manios, T.; Mantzavinos, D. Treatment of olive mill effluents by coagulation-flocculation-hydrogen peroxide oxidation and effect on phytotoxicity. *J. Hazard. Mater.* **2006**, 133, 135–142.
28. Iakovides, I.C.; Pantziaros, A.G.; Zagklis, D.P.; Paraskeva, C.A. Effect of electrolytes/polyelectrolytes on the removal of solids and organics from olive mill wastewater. *J. Chem. Technol. Biotechnol*. **2016**, 91, 204–211.
29. Lucas, M.S.; Peres, J.A. Treatment of olive mill wastewater by a combined process: Fenton's reagent and chemical coagulation. *J. Environ. Sci. Heal. - Part A Toxic/Hazardous Subst. Environ. Eng.* **2009**, 44, 198–205.
30. Khoufi, S.; Feki, F.; Sayadi, S. Detoxification of olive mill wastewater by electrocoagulation and sedimentation processes. *J. Hazard. Mater.* **2007**, 142, 58–67.
31. Amor, C.; Lucas, M.S.; García, J.; Dominguez, J.R.; De Heredia, J.B.; Peres, J.A. Combined treatment of olive mill wastewater by Fenton's reagent and anaerobic biological process. *J. Environ. Sci. Heal. - Part A Toxic/Hazardous Subst. Environ. Eng.* **2015**, 50, 161–168.
32. Paraskeva, P.; Diamadopoulos, E. Technologies for olive mill wastewater (OMW) treatment: a review. *J. Chem. Technol. Biotechnol.* **2006**, 81, 1475–1485.
33. Khoufi, S.; Louhichi, A.; Sayadi, S. Optimization of anaerobic co-digestion of olive mill wastewater and liquid poultry manure in batch condition and semi-continuous jet-loop reactor. *Bioresour. Technol.* **2015**, 182, 67–74.
34. Reis, P.M.; Martins, P.J.M.; Martins, R.C.; Gando-Ferreira, L.M.; Quinta-Ferreira, R.M. Integrating Fenton's process and ion exchange for olive mill wastewater treatment and iron recovery. *Environ. Technol.* **2018**, 39, 308–316.
35. Ochando-Pulido, J.M.; Hodaifa, G.; Victor-Ortega, M.D.; Rodriguez-Vives, S.; Martinez-Ferez, A. Reuse of olive mill effluents from two-phase extraction process by integrated advanced oxidation and reverse osmosis treatment. *J. Hazard. Mater.* **2013**, 263, 158–167.

PART IV

TREATMENT OF OMW BY HETEROGENEOUS PROCESSES

CHAPTER 6

SPECIFIC ADSORBENTS FOR THE TREATMENT OF OMW PHENOLIC COMPOUNDS BY ACTIVATION OF BIO-RESIDUES FROM THE OLIVE OIL INDUSTRY

Highlights

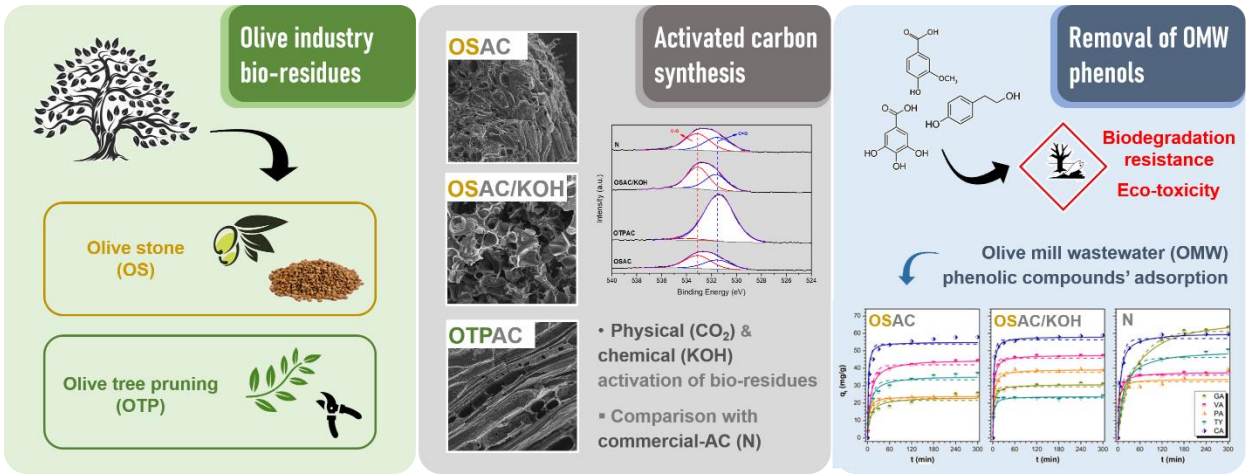
- Olive stone and tree pruning are used to synthesize a series of AC-biosorbents;
- Single & competitive removal of olive mill wastewater phenolic compounds is studied;
- Adsorption capacity and rate controlled by larger micropores and BET surface area;
- Olive stone derived-AC capacity can be restored upon simple thermal regeneration.

The contents of this subchapter were adapted from:

Esteves, B.M., Morales-Torres, S., Maldonado-Hódar, F.J., Madeira, L.M., Journal of Environmental Management, 2022, 306, 114490. https://doi.org/10.1016/j.jenvman.2022.114490

ABSTRACT

A series of adsorbents was developed by physical (CO_2) and chemical (KOH) activation of two bio-residues: olive stones (OS) and wood from olive tree pruning (OTP). The physicochemical properties of such materials were determined and correlated with their adsorptive performance in the removal of phenolic compounds of olive mill wastewater (OMW). Adsorption isotherms and kinetics of single phenolic acids, as well as the kinetics for competitive multi-compound adsorption, were fitted by applying different models, though Langmuir and pseudo-second order models fitted better the experimental results, respectively. The intraparticle diffusion model pointed out that mesoporosity reduces the influence of phenolic compounds' restrictions in the external film diffusion of the adsorbent particle–solution interphase, but adsorption capacity linearly increases with the micropore volume accessible to N_2 at -196 °C (and also with BET surface area), while diffusion into ultramicropores (<0.7 nm, determined by CO_2-adsorption) is slow and presents minor influence on the total adsorption capacity. After saturation, thermal regeneration of spent adsorbents allows the removal of adsorbed products, enabling the reuse of samples whilst maintaining a significant performance.



6.1. INTRODUCTION

Adsorption processes are a potential approach for the removal of phenolic compounds from OMW, mainly due to the processes' simplicity of design, operation, and scale-up [1]. Nevertheless, the much higher COD values of OMW (up to 200 g/L) in comparison to the average range for total phenolic content (up to 7.5 g/L) [2], may hinder phenolic compounds' adsorption by competition with different components in solution (e.g., tannins, sugars, organic acids) due to differences in concentration, molecular size and affinity towards the adsorbent [3]. The development of low-cost porous adsorbents with high specificity for phenols contained in OMW is therefore mandatory for this application. Biomass-derived activated carbon (AC) materials emerged as a clear and cheap alternative to commercial adsorbents (zeolites, inorganic oxides, MOFs, etc. [4]), thanks to the wide availability of such by-products from a wide range of industrial activities [5]. The use of organic residues from the olive oil extraction industry, either as biosorbents or as precursors for their preparation, has already been described in the literature. Many authors reported on the purification of effluents containing heavy metals (e.g., Pb^{2+}, Cu^{2+}, Fe^{3+}, Cr^{6+}) using ACs prepared from exhausted olive-waste cakes [6], from olive peel and seed [7], or even raw olive stones [8]. The adsorption of different organic pollutants by similar biosorbents was also already reported, including ACs prepared from olive stones [9] and olive-waste cakes [10] for dye removal, biosorption of phenolic compounds with solvent-washed olive wood [11], solvent-extracted olive husks [12], and AC-derived olive husks [13], as well as ACs prepared from olive stones and solvent-extracted olive pulp [14].

In this chapter, porous ACs prepared from olive stone (OS) and olive tree pruning (OTP), synthesized by physical and chemical activation processes, were tested for the adsorption of several phenolic compounds typically found in real OMW. The combination of different residues and activation processes to produce bio-carbons with different physicochemical properties, along with the knowledge of the relationship of these parameters with the adsorption performances, will favor the development of cheap and specific adsorbents/catalyst supports suitable for phenolic effluent's treatment. This approach allows the revalorization of residues within this industry, the appropriate treatment of OMW by environmentally friendly processes, the potential recovery of valuable substances and reuse of water, in line with the circular economy trend.

6.2. MATERIALS AND METHODS

6.2.1. Synthesis of materials

Olive stone and olive tree pruning were selected as precursors for the synthesis of physically activated carbons. The raw agricultural waste was first washed thoroughly, then ground and sieved to a particle size fraction of 0.45–0.80 mm. Samples were prepared by a two-step process in a horizontal tube furnace: first, the carbonization of raw materials was carried out at 800 °C (10 °C/min heat ramp, 2 h hold time) in a 150 cm^3/min N_2 flow (volumetric flow rates reported at ambient temperature and atmospheric pressure), followed by physical activation by switching the flow of N_2 to CO_2 (300 cm^3/min, 4 h); after that time, the flow is again switched to N_2, the oven turned off, and the samples allowed to reach room temperature [15]. The derived ACs were denoted as OSAC and OTPAC, corresponding to physically-activated carbons from olive stones and olive tree pruning, respectively.

Additionally, a chemically-activated sample of OS was prepared using concentrated potassium hydroxide as the activating agent. Chemical activation with KOH was carried out in one step procedure with a fraction of OS previously carbonized as described earlier, in a weight proportion of 1:1 (50% KOH: 50% OS). KOH was dissolved in the minimum amount of water and mechanically agitated with the OS-derived sample. After drying in an oven at 110 °C overnight to remove water, the OS/KOH mixture was directly heated at 800 °C for 2 h (N_2 flow, 150 cm^3/min, measured at room temperature and atmospheric pressure). After that, the oven was turned off and the sample cooled to room temperature in the same N_2 flow. The sample (designated OSAC/KOH) was treated in an acidic media (HCl) to remove the remaining KOH, and then washed with distilled H_2O until no chlorine ions were detected in the washing waters (adding drops of concentrated $AgNO_3$ solution until absence of AgCl precipitate) [16]. For comparison purposes, a commercially available high-purity steam-activated activated carbon (Norit® RX 3 Extra, from Sigma-Aldrich) was also used in this study (herein denoted as N). Prior to use, all materials were ground and sieved to powder.

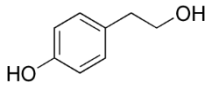
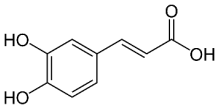
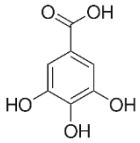
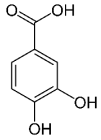
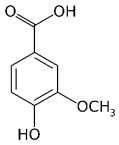
6.2.2. Adsorbates and adsorption runs

Due to the complexity and variability of the OMW characteristics, a polyphenolic synthetic solution was prepared using pure reagents, thus allowing an analysis of the interactions between phenolic compounds typically present in OMW with the prepared ACs. For this, five phenolic compounds

commonly found in real OMW were selected [17–19], and in concentrations similar to those reported by some authors [20,21]: tyrosol and vanillic acid (Sigma-Aldrich), protocatechuic and caffeic acids (ACROS Organics), and gallic acid (Alfa Aesar); their chemical structure and main characteristics are listed in Table 6.1. The solution was prepared by dissolving 30 mg/L of each compound in distilled water (thus yielding a total of 150 mg/L, which was also the concentration employed when using a single compound), ensuring full dissolution with the aid of an ultrasound apparatus (Argo Lab, mod. DU 45). Adsorption experiments were performed in triplicate in a 300 mL-capacity cylindrical jacketed batch reactor, under magnetic agitation at 300 rpm (VWR VS-CT magnetic stirrer) and controlled temperature (T = 25 ºC), recycling water through a model 89202-912 VWR International thermostatic bath. The reactor was initially loaded with 150 mL of the synthetic effluent (total phenolic content, TPh, 150 mg/L and $pH_0 \approx 3.8$) and the adsorbent sample (0.5 g/L) in powder form. This synthetic solution was used to evaluate competitive adsorption processes by following the concentration of each specific compound.

Taking into account the different behavior observed between the different phenols of the mixture (as detailed later in Section 6.3.2), gallic and vanillic acids were also selected for individual sorption studies (particularly because such phenolic compounds are very similar in molecular weight and dimensions, but presented rather distinct adsorptive behavior in the multi-compound solution). The corresponding adsorption isotherms on the different ACs were recorded by varying the initial concentration of pollutants in the aqueous solution (initial concentrations ranging from 25-350 mg/L). Stoppered flasks containing 25 mg of each adsorbent (0.5 g/L) and 50 mL of the phenolic solution were agitated (300 rpm) in a thermostatic water bath shaker (Grant OLS 200) at a constant temperature of 25 °C. A sample of each flask was collected after 24 and 48 h, filtered using 0.45 μm PTFE syringe filters (VWR), and the equilibrium concentrations were determined by HPLC; whenever necessary, samples were diluted with ultrapure water prior to such analysis. It is important to note that the runs were prolonged up to 48 h to confirm that equilibrium was achieved; nevertheless, it was determined that 24 h of contact was sufficient in all cases (data not shown for brevity).

Table 6.1 Chemical characteristics of the phenolic compounds used.

Name	Chemical structure	Molecular formula	Max. linear dim. (Å)	Molecular weight (g/mol)	pKa (25 ºC)	Solubility in water (g/L)
Tyrosol		$C_8H_{10}O_2$	7.8	138.16	10.20	25.3 (25 °C)
Caffeic acid		$C_9H_8O_4$	8.7	180.16	4.62	1.0 (22 °C)
Gallic acid		$C_7H_6O_5$	6.4	170.12	4.40	11.5 (25 °C)
Protocatechuic acid		$C_7H_6O_4$	6.3	154.12	4.48	18.2 (14 °C)
Vanillic acid		$C_8H_8O_4$	6.3	168.14	4.16	1.5 (14 °C)

The equilibrium adsorption capacity of each adsorbent, q_e (mg/g_{ads}), was determined following Eq. (6.1), where C_0 and C_e (mg/L) are the adsorbate's initial and equilibrium concentrations, respectively, W_{ads} (g) the mass of adsorbent, and V (L) the volume of adsorbate solution. Adsorption isotherms were determined at the solution's initial pH, which ranged between 3.5–3.8.

$$q_e = \frac{(C_0 - C_e)}{W_{ads}} \times V \tag{6.1}$$

The adsorption kinetics of these individual compounds were also determined. For that, 150 mL of the phenolic solution (C_0 = 150 mg/L), i.e., with a similar total phenol concentration previously used for the competitive adsorption experiments for comparisons, were mixed with the adsorbents in Erlenmeyer flasks and agitated under the same conditions described previously. Samples (0.5 mL) were periodically withdrawn, filtered, and analyzed by HPLC, as previously described; the total volume withdrawn during each experiment corresponds to only 3% of the initial volume.

6.2.3. Regeneration studies

To check the reusability of the adsorbents, regeneration studies were performed with samples saturated with gallic or vanillic acid. To ensure full saturation of each sample, 100 mg of each adsorbent was placed in a 150 mL solution loaded with 1000 mg/L of the required phenolic acid and the solution was agitated for 48 h; after filtration, samples were dried at 105 ºC and then placed in a desiccator. Thermal regeneration of spent samples was simulated by thermogravimetric analysis (TGA), performed under an N_2 inert atmosphere with a TGA-50H thermobalance. According to these results, the removal of phenolic acids from the ACs was performed by heating the saturated samples at 800 °C for 10 min (heat ramp 20 °C/min) under an inert N_2 flow. After cooling to room temperature, the regenerated samples were used in uptake adsorption studies according to the experimental conditions reported in Section 6.2.2.

6.3. RESULTS AND DISCUSSION

6.3.1. Textural and chemical characterization of the adsorbents

Experimental conditions for chemical and physical activation of OS and OTP bio residues were fitted to produce a similar activation degree in all cases, with solid yields between 14–16 wt.%. Yields within the same range were obtained by Galiatsatou *et al*. [14] using physically-activated samples of olive stone and solvent extracted olive pulp, which were also progressively lower for higher carbonization/activation times. Nonetheless, the morphology of the ACs obtained depends on the precursor used, thus OTPAC is clearly a less dense material than OSAC, also containing a larger concentration of wider channels from the original wood structure, as denoted by HRSEM images (Fig. 6.1). Analogous morphological structures were already reported for ACs prepared from similar bio-residues, both CO_2-activated olive pomace [22] and KOH-activated olive stones [23]. From a practical point of view, due to the different morphology of the materials, the adsorptive behavior may be influenced by parameters such as the volume occupied by the sample or the possibility of floating in solution (if it is less dense than the solution itself – this was mitigated by the high agitation speed employed in the tests).

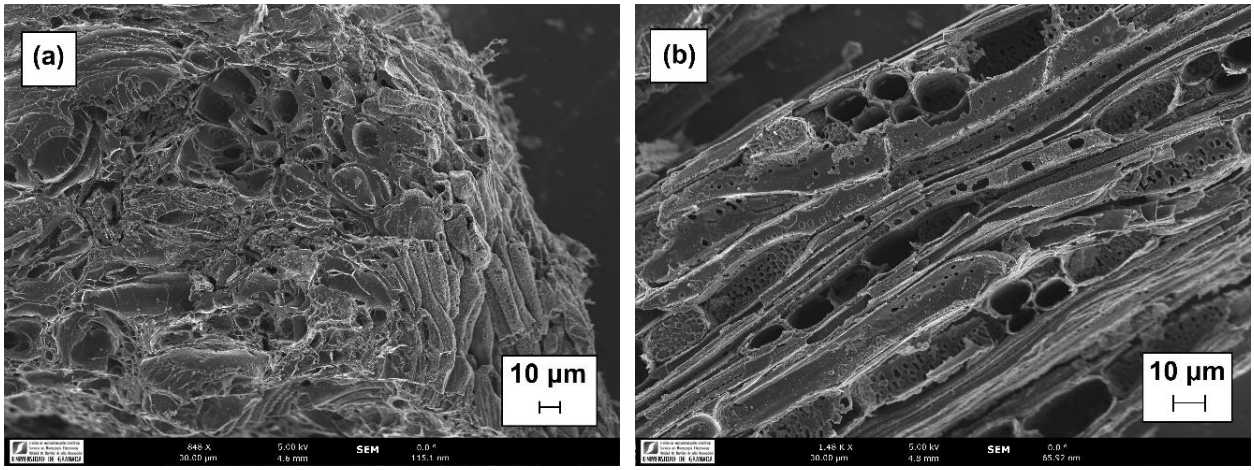


Fig. 6.1 HRSEM micrographs highlighting the morphology of (a) OSAC and (b) OTPAC.

The materials' textural properties were examined by N_2 adsorption-desorption isotherms (Fig. 6.2a) and complemented with CO_2 adsorption isotherms to estimate the narrowest porosity (ultramicropores). In the absence of diffusional restrictions, W_0 (N_2) yields the total micropore volume, while W_0 (CO_2) estimates the narrowest microporosity (diameter <0.7 nm) [24]. A summary of the data is detailed in Table 6.2, which also includes the parameters obtained for the commercial sample N used as reference.

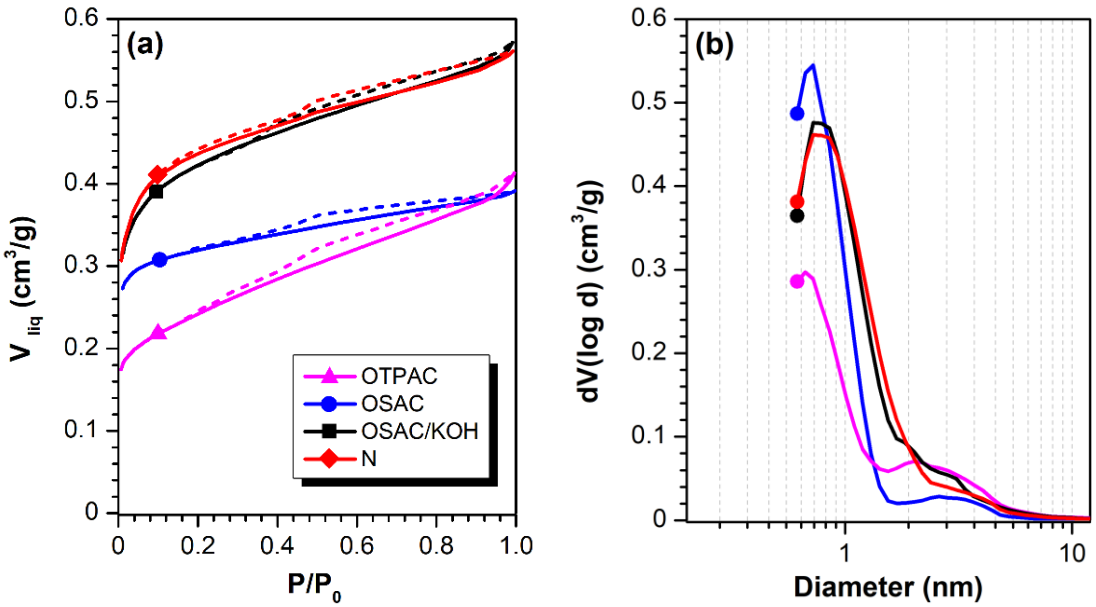


Fig. 6.2 (a) N_2 adsorption-desorption isotherms (P/P_0 is the relative pressure between the equilibrium pressure and the saturation vapor pressure of N_2) and (b) pore size distribution of the adsorbents.

The porosity of the produced samples was influenced by the nature of the raw lignocellulosic residue, as depicted by HRSEM images, but also by the activation process employed. After carbonization and physical activation with CO_2, ACs obtained from both precursors – olive stone

(sample OSAC) and olive tree pruning (sample OTPAC) – present similar total pore volume (V_T = 0.39 cm^3/g) but a very distinct pore size distribution (Fig. 6.2b), as denoted by the different shape of their isotherms in Fig. 6.2a. Thus, the OTPAC isotherm corresponds to the type IV (formation of multilayer overlapping the monolayer adsorption on the mesopore walls, and thus the gradual curvature at increasing values of relative pressure, P/P_0), associated to mesoporous samples, as compared to a practically flat plateau in the isotherm of OSAC (predominantly type I), characteristic of microporous samples, as adsorption occurs primarily at very low P/P_0 due to micropores filling [25]. The higher N_2-adsorption at low P/P_0 pointed out that microporosity is favored in the case of OSAC, as already reported by Ghouma *et al*. [22] during the preparation of ACs from olive pomace through different activation agents, while the marked slope of the N_2-adsorption isotherm of OTPAC denotes a more heterogeneous porosity and the predominant mesoporous character. Moreover, microporosity is narrower and homogeneous in the former but larger and heterogeneous in the latter. The CO_2-adsorption experiments also confirm this heterogeneity, thus, OTPAC present narrower micropores and wider micropores (determined by N_2-adsorption). In both cases, the presence of the hysteresis cycle in the N_2 adsorption-desorption isotherm confirms the presence of a certain volume of mesopores.

After chemical KOH-activation of OS, the AC obtained (OSAC/KOH) presents a more developed porosity regarding OSAC, with a total pore volume (V_T) of 0.55 cm^3/g and surface area (S_{BET}) of 1013 m^2/g (Table 6.2). Similar properties were obtained under analogous conditions of activation (KOH, 800 °C, for 2 h) of olive stone-derived char [26]. The micropore volume also significantly increased, generating mainly large micropores – W_0 (N_2) –, and so did the corresponding mean micropore width (L_0). Nonetheless, the equivalent narrowest microporosity obtained by CO_2 isotherms – W_0 (CO_2) – didn't alter significantly regarding physical activation. The pore opening also resulted in the generation of mesoporosity, as denoted by the slope of the isotherm, being quite similar to the one obtained for the reference commercial material N.

Table 6.2 Textural characteristics and pH_{pzc} of the adsorbents.

Sample	S_{BET} (m^2/g)	W_0 (N_2) (cm^3/g)	L_0 (N_2) (nm)	W_0 (CO_2) (cm^3/g)	L_0 (CO_2) (nm)	V_{meso} (cm^3/g)	V_T (cm^3/g)	pH_{pzc}
OTPAC	565	0.24	1.6	0.11	0.66	0.15	0.39	10.7
OSAC	792	0.33	1.2	0.20	0.74	0.06	0.39	10.6
OSAC/KOH	1013	0.43	1.7	0.18	0.73	0.12	0.55	8.3
N	1058	0.44	1.6	0.21	0.88	0.11	0.55	11.6

It is also recognized that the surface chemistry of ACs influences the adsorption process, particularly concerning the presence of oxygen-containing surface groups that may alter the mechanism and extension of the adsorbate-adsorbent interactions [27]. The oxygenated surface groups (OSG) are the main functionalities present on ACs. The surface oxygen content and nature of OSG were analyzed by XPS. The O1s spectral region can be fitted using two components (Fig. 6.3), assigned to C–O or C=O bonds at ca. 531.8 and 533.4 eV, respectively [28]. The integrated results are summarized in Table 6.3. The highest surface oxygen content was observed for OTPAC, which, moreover, presents a very homogeneous distribution of OSG containing C=O bonds, like carboxylic acids, but also basic ketones. The OS-derived ACs present smaller oxygen content than OTPAC, and although this parameter increased after chemical activation, the distribution of C=O and C–O OSG is quite similar in both cases (around 41% and 59%, respectively), denoting the presence of additional groups such as alcohols, phenols, and carboxylic acids. The commercial sample N also presents a high oxygen content, with a very similar distribution of OSG (45% C=O, 55% C–O). The pH at the point of zero charge indicates that all materials present a basic character (Table 6.2), which was analogous for OSAC and OTPAC samples (pH_{pzc} = 10.6–10.7) in spite of their different OSG distribution, and slightly lower in the case of the KOH activated sample (pH_{pzc} = 8.3).

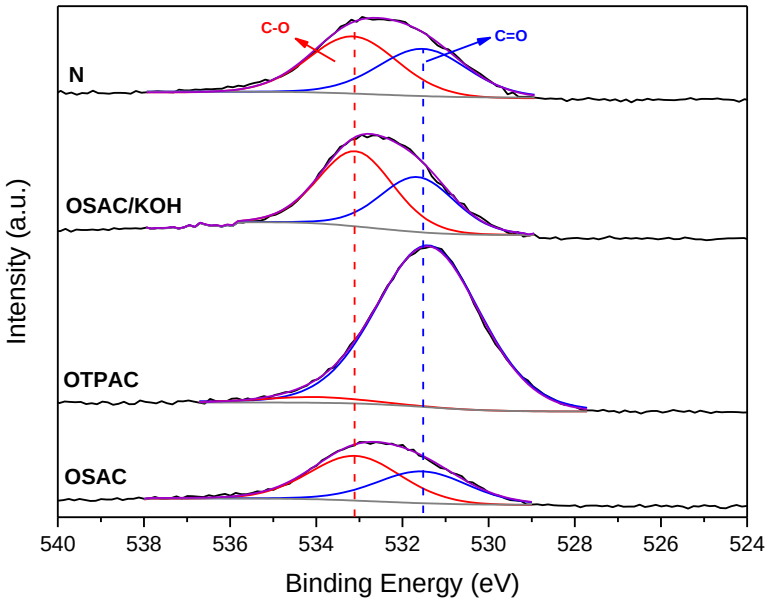


Fig. 6.3 High resolution XPS spectra of the O1s spectral region for the different biosorbents.

Table 6.3 Elemental analysis (atomic content, %), species percentages and corresponding binding energies (in brackets, eV) of the different adsorbents determined by XPS analysis.

Sample	O/C	C	O	O1s (%)	
				C=O	C–O
OTPAC	0.11	90.4	9.6	97 (531.4)	3 (534.0)
OSAC	0.06	94.2	5.8	41 (531.5)	59 (533.1)
OSAC/KOH	0.09	92.1	7.9	42 (531.7)	58 (533.1)
N	0.09	91.6	8.4	45 (531.5)	55 (533.2)

6.3.2. Adsorptive performance of the ACs in the treatment of simulated OMW

To evaluate the potential applicability of biosorbents prepared and examine the influence of the OS-activation procedure, the performance of OSAC and OSAC/KOH samples were compared to the commercial AC (N). A simulated OMW was prepared containing 150 mg/L of a mixture of five phenolic compounds, as described in the experimental section. The total phenol removed (Fig. 6.4) was calculated based on the corresponding concentrations of each product recorded as a function of time along the adsorption experiments (Fig. 6.5).

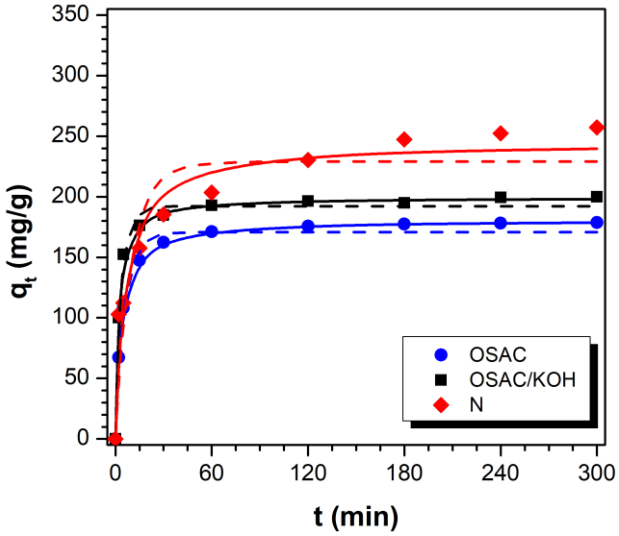


Fig. 6.4 Total phenol removal as a function of adsorption time (dashed lines: PFO model adjustment; solid lines: PSO model adjustment). Experimental conditions: C_0 = 150 mg/L (30 mg/L each phenolic compound) at 25 °C, W_{ads} = 75 mg, pH_0 = 3.5–3.8

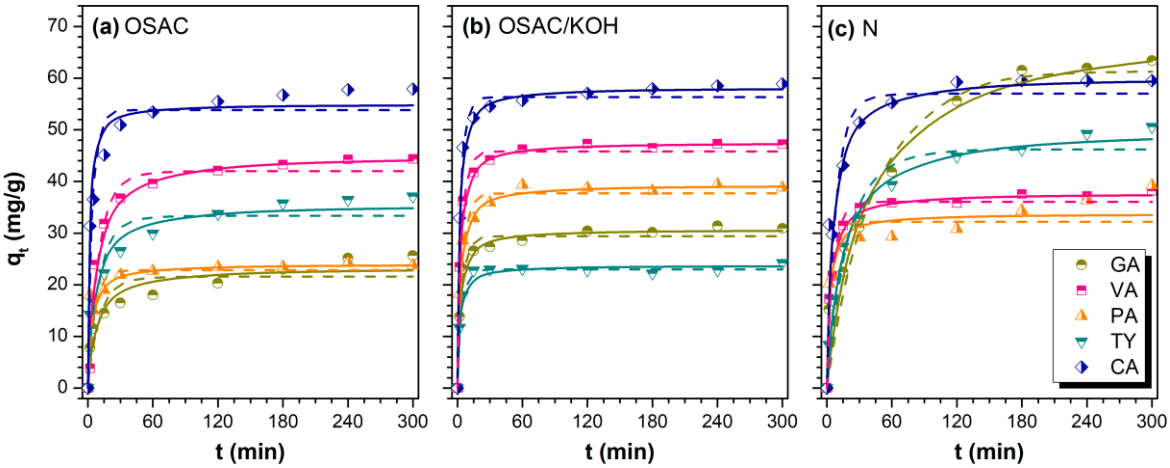


Fig. 6.5 Kinetic curves for competitive adsorption onto (a) OSAC, (b) OSAC/KOH, and (c) N samples (dashed lines: PFO model; solid lines: PSO model). Experimental conditions: C_0 = 150 mg/L (30 mg/L each phenolic compound) at 25 °C, W_{ads} = 75 mg, pH_0 = 3.5–3.8.

The total phenolic content (TPh) uptake decreases in the sense N (257 mg/g) > OSAC/KOH (200 mg/g) > OSAC (189 mg/g). Although sample OSAC/KOH has a very similar porosity as the reference sample N, the TPh removed is approximately 22% lower, which can be related to the lower pH_{pzc} of OSAC/KOH. Chemically activated olive stone presents better performance than the physically activated sample, due to the resulting higher surface area (S_{BET}) and microporosity (W_0) values – Table 6.2. Nevertheless, while the S_{BET} increases from 792 to 1013 m^2/g (i.e., *ca*. 28%), TPh removal only improved by 5.8%, which is also indicative that additional parameters should be considered.

The amount of each compound adsorbed also strongly differs between samples (Fig. 6.5). Only caffeic acid (CA) is quickly and preferentially adsorbed in all samples, with similar qe values (around 60 mg/g), indicating that it is completely removed in all cases. The commercial sample N also totally adsorbs gallic acid (GA), which is poorly adsorbed on both OS-derived ACs (even on OSAC/KOH that has analogous porosity to sample N). Tyrosol (TY), vanillic (VA), and protocatechuic (PA) acids are only partially removed in all cases, being the amount and kinetics of adsorption strongly dependent on the adsorbent used.

Experimental data were fitted using well-established kinetic models commonly suited to describe the adsorption process of liquid-solid systems [29], namely the pseudo-first-order (PFO) [30] and pseudo-second-order (PSO) [31] models. The application of linearized forms of the equations is the most widely used solving method for the determination of both models' parameters, though also entailing the possible introduction of propagation errors by changing the independent/dependent variables [29]. The experimental data was therefore fitted by nonlinear regression, using Microsoft's Excel® solver function with an iterative algorithm that minimizes the residual sum of squares. The results obtained are summarized in Table 6.4.

For the PFO model, the adsorption is determined by diffusion through a boundary, while PSO is based on the sorption capacity of the solid phase, being commonly assumed that chemisorption could be the rate-controlling step in the adsorption process [32–34]. The characteristic adsorption constants of PFO and PSO equations were determined according to the integrated rate laws shown in Eqs. (6.2) and (6.3), respectively, obtained with the initial condition of $q_t = 0$ at t = 0,

$$q_t = q_e \left(1 - e^{-k_1 t}\right) \tag{6.2}$$

$$q_t = \frac{t}{\frac{1}{q_e^2\, k_2} + \frac{t}{q_e}} \tag{6.3}$$

where q_e and q_t are the adsorption capacities (mg/g) at equilibrium and at any given time t (min), respectively, k_1 and k_2 the pseudo-first order (min^{-1}) and pseudo-second order (g/mg·min) rate constants. The initial adsorption rate h (mg/g·min) can be derived from the PSO model and $dq_t/dt = h$ at $t \rightarrow 0$, according to Eq. (6.4) [35].

$$h = q_e^2\, k_2 \tag{6.4}$$

Both model's applicability/selection was assessed by two statistical indicators: root mean square error (RMSE, Eq. (6.5)) and correlation coefficient (R^2, Eq. (6.6)), being $q_{e,exp}$ the measured adsorbate concentration in the solid phase and $q_{e,cal}$ (mg/g) the calculated concentration by any given model [36]. Smaller values of RMSE and R^2 values close to the unit indicate minor variations between experimental and calculated data, thus better fittings.

$$RMSE = \sqrt{\frac{1}{m}\sum_{i=1}^{m}(q_{e,exp,i} - q_{e,cal,i})^2} \quad (6.5)$$

$$R^2 = 1 - \frac{\sum_{i=1}^{n}(q_{e,exp,i} - q_{e,cal,i})^2}{\sum_{i=1}^{n}(q_{e,exp,i} - \bar{q}_{e,exp})^2} \quad (6.6)$$

In all cases, adsorption capacities sharply increase within the first minutes of contact time and the maximum uptake is typically reached after approximately 60 min for the prepared biosorbents, while for commercial sample N it is only reached after 180 min (Fig. 6.4). Data in Table 6.4 shows that both models (PFO and PSO) satisfactorily predict the adsorption process for all adsorbents, although the PSO model describes the data slightly better, as suggested by the lower RMSE values when compared to the PFO model. Moreover, PFO doesn't fit well for the entire range of adsorption time, offering the best fittings at the beginning of the process but deviating afterward, thus failing in the theoretical prediction of the amount adsorbed. A similar behavior denoting the deviation of the PFO model was previously described for several adsorbents prepared from agricultural wastes [37].

Globally, the adsorption process appears to be directly linked to the development of the sample's available surface (and therefore porosity) achieved by each activation process; i.e., despite the better fittings obtained using the PSO that suggest that the limiting step is the chemisorption process, the porosity of the samples should be large enough to avoid several diffusion restrictions. This was in agreement with the larger micropore volumes detected with N_2 at -196 °C regarding those observed with CO_2 at 0 °C, confirming the absence of diffusional problems of N_2 at low temperatures into the micropores.

The simulated OMW presents an acidic character (pH = 3.8) as a result of the dissociation of the four phenolic acids (pKa values ≈4), whereas anionic-neutral species are expected in the case of TY (pKa = 10.2). Under such conditions, all carbon surfaces should be positively charged due to their demarked basic character (pH_{pzc} = 8.3–11.6). Generally speaking, attractive interactions

between adsorbents and adsorbates should favor the adsorption of deprotonated compounds, in agreement with the better fittings observed with the PSO model. Nevertheless, repulsive interactions are observed between TY and the AC surfaces, both positively charged at the solution's pH. In fact, tyrosol is the less adsorbed compound on OSAC/KOH (Fig. 6.5).

Moreover, despite the similar porosity and pore size distribution between OSAC/KOH and N samples, the adsorption capacity of the former is generally smaller in comparison, whereas the initial adsorption rate (*h*, Table 6.4) is always higher. Likewise, despite the complete CA adsorption observed in all cases, it occurs faster than the remaining compounds in solution on either OSAC or OSAC/KOH, whereas h values obtained for CA onto commercial sample N are comparable to those of VA or PA (which were, ultimately, the less adsorbed compounds in this case). The overall worse fittings (higher RMSE values) obtained for sample N also denotes the greater heterogeneity of this sample.

Competitive adsorption processes are complex and determined not only by the combination of porosity and surface area of the adsorbent (determining accessibility and extent of the active surface) and the interaction with the adsorbates (nature and concentration of functional groups) but also by interactions occurring between the different adsorbates in solution. In general, the presence of various adsorbates in solution leads to inhibitory effects and a worse elimination of pollutants [38]. Considering these results, GA and VA were selected to perform individual adsorption experiments to further elucidate the physicochemical properties controlling such adsorbent-adsorbate interactions.

Table 6.4 Fitted kinetic parameters of the competitive adsorption runs using the PFO and PSO models.

Adsorbent	Adsorbate	$q_{e,\,exp}$ (mg/g)	Pseudo-first order				Pseudo-second order				
			$q_{e,\,cal}$ (mg/g)	k_1 (min^{-1})	RMSE	R^2	$q_{e,\,cal}$ (mg/g)	k_2 (g/mg·min)	h (mg/g·min)	RMSE	R^2
OSAC	GA	25.7	21.6	1.06×10^{-1}	3.2	0.859	23.3	6.19×10^{-3}	3.4	2.2	0.929
	VA	44.4	42.0	1.10×10^{-1}	3.2	0.962	45.0	3.32×10^{-3}	6.7	2.7	0.974
	PA	23.7	22.9	2.25×10^{-1}	1.4	0.970	24.0	1.39×10^{-2}	8.0	0.4	0.997
	TY	37.1	33.4	1.08×10^{-1}	4.2	0.896	35.5	4.66×10^{-3}	5.9	2.7	0.955
	CA	57.9	53.8	3.05×10^{-1}	4.7	0.936	56.2	8.23×10^{-3}	26.0	2.5	0.982
	TPh	188.9	170.8	2.12×10^{-1}	17.8	0.915	180.7	1.64×10^{-3}	53.5	10.2	0.972
OSAC/KOH	GA	30.9	29.4	3.07×10^{-1}	1.5	0.979	30.7	1.51×10^{-2}	14.2	0.9	0.991
	VA	47.2	45.8	3.33×10^{-1}	1.7	0.988	47.5	1.12×10^{-2}	25.3	0.8	0.998
	PA	38.8	37.7	2.98×10^{-1}	1.9	0.978	39.3	1.16×10^{-2}	17.9	0.9	0.995
	TY	24.3	23.0	3.31×10^{-1}	0.6	0.995	23.7	2.41×10^{-2}	13.6	0.9	0.987
	CA	58.9	56.3	4.02×10^{-1}	2.1	0.986	58.1	1.18×10^{-2}	39.8	0.9	0.998
	TPh	200.0	192.2	3.40×10^{-1}	7.2	0.988	199.3	2.75×10^{-3}	109.1	3.0	0.998

N	GA	63.4	61.3	2.42×10^{-2}	4.4	0.979	70.1	4.40×10^{-4}	2.2	3.3	0.986
	VA	38.2	36.1	2.20×10^{-1}	2.2	0.970	37.7	9.11×10^{-3}	12.9	1.1	0.993
	PA	39.2	32.2	3.33×10^{-1}	4.1	0.865	33.7	1.43×10^{-2}	16.2	3.1	0.922
	TY	50.6	46.2	5.52×10^{-2}	3.8	0.963	50.2	1.58×10^{-3}	4.0	1.8	0.990
	CA	59.5	57.0	1.39×10^{-1}	4.2	0.963	60.3	3.47×10^{-3}	12.6	1.7	0.993
	TPh	257.1	229.0	1.17×10^{-1}	29.5	0.889	244.1	7.18×10^{-4}	42.8	19.2	0.950

6.3.3. Performance of ACs in the adsorption of single phenolic compounds

Adsorption models allow us to infer the adsorption mechanism occurring in such solid-liquid/gas systems and to determine specific equilibrium parameters, key to the design and development of adsorption processes [5,39]. To better describe and quantify the equilibrium relationship between each solute and the adsorbents tested, several isotherms were fitted to the experimental data, including Langmuir, Freundlich, Sips, Langmuir-Freundlich, and Radke-Prausnitz [40]. To check the models' adhesion, a mathematical/model selection criterion (MSC) was applied in addition to R^2 and RMSE. As detailed elsewhere [36], MSC takes also into account the number of fitting parameters of the model and the number of experimental points. For brevity, the results presented here are those where better models adhesion to experimental data was achieved: with the Langmuir and Freundlich isotherms.

The Langmuir isotherm is based on the hypothesis that adsorbate molecules form a uniform and finite monolayer on the adsorbent's surface [41]. The nonlinear form of the Langmuir model can be represented according to Eq. (6.7),

$$q_e = \frac{q_m \, K_L \, C_e}{1 + K_L C_e} \tag{6.7}$$

where C_e is the equilibrium solute concentration (mg/L), qm is the maximum uptake of adsorbed molecules per unit mass of adsorbent (mg/g) for the formation of a complete monolayer on the adsorbent's surface, q_e the equilibrium concentration in the adsorbent phase (mg/g), and K_L the adsorption constant of the Langmuir isotherm equation (L/mg). The product $K_L \cdot q_m$ is often used to describe the relative affinity of the adsorption process [42].

The Freundlich isotherm is commonly apt to describe non-ideal sorption on highly heterogeneous surfaces that provide adsorption sites of varying affinities [41]. The model's nonlinear form can be represented as described in Eq. (6.8),

$$q_e = K_F \, C_e^n \tag{6.8}$$

where K_F the Freundlich constant related to adsorption capacity ((mg/g)(mg/L)^n), and n an empirical parameter related to the adsorption intensity.

Overall, both models describe the experimental adsorption data reasonably well (fittings shown in Fig. 6.6). Based on the calculated statistical parameters (Table 6.5), the overall uptake process of gallic acid approaches the Freundlich model better (higher R^2 and lower RMSE values) than

the Langmuir one, whereas the latter seems to better describe the adsorption of vanillic acid (except for N). Moreover, the Langmuir isotherm typically predicted more accurately the behavior at lower concentrations of sorbate in equilibrium (formation of a monolayer), while at higher concentrations the Freundlich model was better apt to describe the process of multilayer adsorption in some cases (*cf*. Fig. 6.6). The highest values of the RMSE parameter were always obtained for the commercial activated carbon N, which is the only material that obeys the Freundlich isotherm for both GA and VA, thus suggesting a multilayer adsorptive behavior independently of the adsorbate.

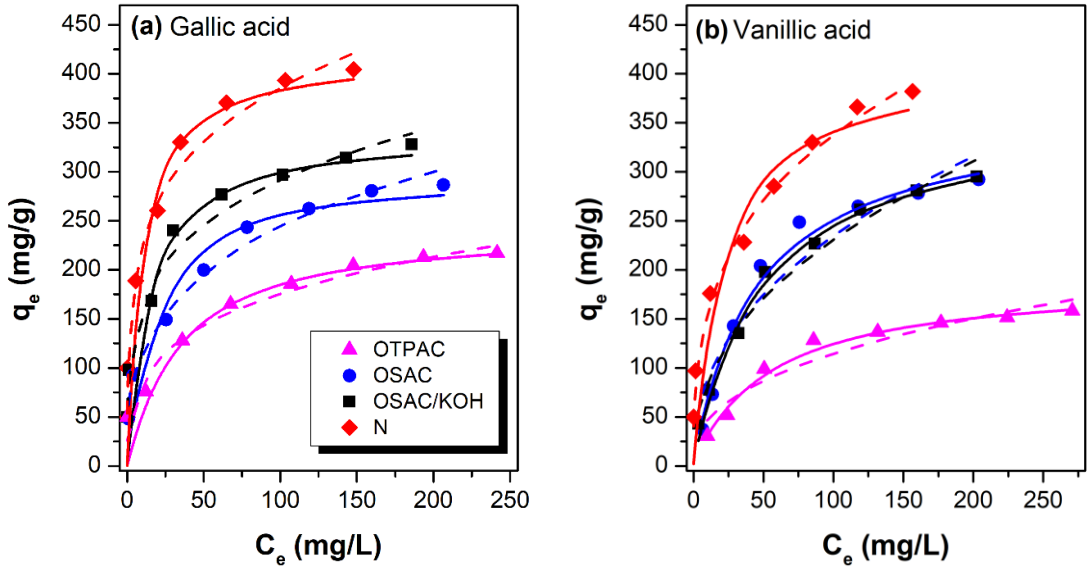


Fig. 6.6 Adsorption isotherms of (a) gallic acid and (b) vanillic acid (solid lines: experimental data fit with Langmuir isotherm; dashed lines: fit with Freundlich isotherm). Experimental conditions: 25 °C, C_0 = 25–350 mg/L, W_{ads} = 25 mg, V = 50 mL, pH_0 = 3.5–3.8.

As in the case of the TPh analysis provided in Section 6.3.2 for the competitive process, the adsorption isotherms of both GA and VA reflect the smaller adsorption capacity of OTPAC for the range of materials studied, and that commercial sample N always offers the best results. Comparing the influence of the raw bio-residue material on physically activated samples, GA is preferentially adsorbed regarding VA in the case of OTPAC, while the contrary performance is observed for OSAC. Nevertheless, the chemically activated OSAC/KOH has a similar GA or VA adsorption capacity, and this performance is also observed for the reference N-sample. The values of both constants (K_L and K_F) were always higher for the uptake of gallic acid than the corresponding ones for vanillic acid. Thus, the product $K_L \cdot q_m$, related with the affinity of the adsorption processes, is almost always higher for GA than for VA, independently of the adsorbent used, and increases upon increasing the microporosity and surface area of the materials. Thus,

adsorbents derived from the olive stone precursor showed higher maximum monolayer adsorption capacities (q_m) than the one prepared from olive tree pruning. Likewise, chemical activation also favors microporosity and consequently the uptake capacity (Table 6.5).

Despite the lower capacity obtained for the OTPAC sample, the morphological and porous characteristics of this sample, including the well-developed network of wider channels, may favor de adsorption (removal/recovery) of larger molecules, or its use for the development of micro/mesoporous metal supports for heterogeneous catalysts.

Table 6.5 Langmuir and Freundlich isotherm models' parameters for gallic and vanillic acids.

Adsorbate	Adsorbent	Langmuir				Freundlich			
		q_m (mg/g)	K_L (L/mg)	RMSE	R^2	n	K_F ((mg/g)(mg/L)^n)	RMSE	R^2
Gallic Acid	OTPAC	244.0	0.032	18.0	0.972	0.27	50.1	16.0	0.943
	OSAC	296.0	0.067	19.6	0.970	0.29	65.7	10.7	0.984
	OSAC/KOH	337.6	0.082	32.1	0.966	0.24	98.5	12.7	0.983
	N	416.6	0.120	40.6	0.971	0.21	144.4	14.8	0.987
Vanillic Acid	OTPAC	188.6	0.020	5.0	0.988	0.39	19.3	12.4	0.927
	OSAC	359.0	0.024	10.3	0.989	0.42	34.2	26.4	0.920
	OSAC/KOH	358.5	0.022	9.2	0.992	0.42	33.0	13.5	0.978
	N	406.9	0.053	34.7	0.960	0.31	82.4	9.3	0.994

Adsorption kinetics were also investigated based on the uptake of gallic and vanillic acids at 25 °C. Fig. 6.7 compares the PFO and PSO models prediction for each adsorbent (dashed and solid lines, respectively) with the experimental values (dots) for the two phenolic compounds.

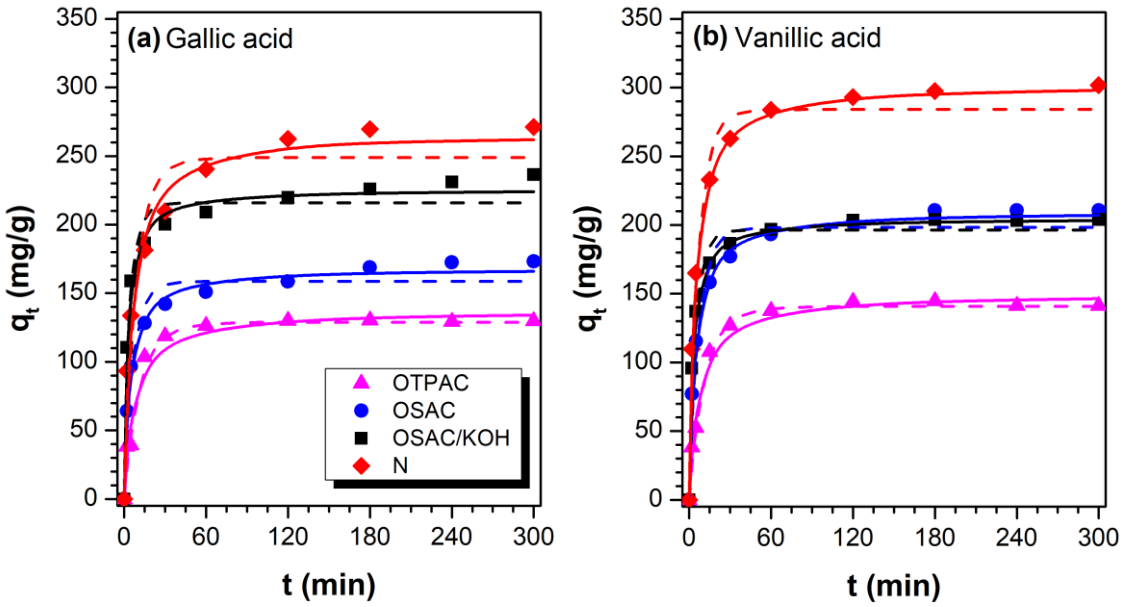


Fig. 6.7 Kinetic curves for (a) gallic acid and (b) vanillic acid adsorption at C_0 = 150 mg/L, 25 °C, V = 50 mL, pH_0 = 3.5-3.8 (dashed lines: fitting of PFO model to experimental data; solid lines: fitting of PSO model).

There is a good agreement between the experimental adsorption capacity values and those predicted by the models. As postulated in the previous section, the experimental adsorption capacities obtained in this series of experiments (q_e values, Table 6.6) are, in general, higher than those obtained for the same experimental conditions (same C_0 as the ones here reported) when various adsorbates compete for adsorption sites (*cf*. TPh values in Table 6.4). All PSO kinetic parameters values progressively increased in the sense OTPAC <OSAC <OSAC/KOH. However, in spite of the higher q_e values obtained for sample N, smaller k_2 and h values are obtained regarding OSAC/KOH, as well as in general, worse fittings.

Table 6.6 Fitted parameters for the pseudo-first order and pseudo-second order kinetic models.

			Pseudo-first order				Pseudo-second order				
Adsorbate	**Adsorbent**	$q_{e,\,exp}$ (mg/g)	$q_{e,\,cal}$ (mg/g)	k_1 (min^{-1})	RMSE	R^2	$q_{e,\,cal}$ (mg/g)	k_2 (g/mg·min)	h (mg/g·min)	RMSE	R^2
	OTPAC	129.8	128.6	1.02×10^{-1}	5.7	0.987	136.6	1.12×10^{-3}	20.8	6.6	0.982
Gallic	OSAC	173.3	158.7	1.87×10^{-1}	12.8	0.956	168.1	1.55×10^{-3}	43.8	5.9	0.989
Acid	OSAC/KOH	236.4	215.8	3.00×10^{-1}	15.0	0.966	225.7	1.96×10^{-3}	100.0	7.5	0.989
	N	271.1	248.9	1.33×10^{-1}	24.7	0.936	267.4	7.04×10^{-4}	50.3	12.3	0.983
	OTPAC	141.3	140.7	9.90×10^{-2}	5.4	0.991	149.7	9.86×10^{-4}	22.1	5.2	0.990
Vanillic	OSAC	210.6	198.2	1.70×10^{-1}	14.5	0.962	209.9	1.16×10^{-3}	51.2	5.2	0.995
Acid	OSAC/KOH	203.9	196.2	2.70×10^{-1}	10.5	0.977	204.9	2.02×10^{-3}	84.6	2.2	0.999
	N	301.8	284.1	1.74×10^{-1}	17.8	0.973	302.1	8.30×10^{-4}	75.8	4.3	0.998

When using physically activated olive stone-derived sample (OSAC), the experimental equilibrium adsorption capacity for TPh removal in the competitive adsorption run is 189 mg/g (Table 6.4), an intermediate value regarding the GA (173 mg/g) and VA (211 mg/g) removals when this biosorbent was applied in the single adsorption process (Table 6.6). Regarding the kinetic constant k_2, the computed value is 1.64 x 10^{-3} in the competitive run, which is also comparable to the k_2 values for single GA (1.55 x 10^{-3}) or VA (1.16 x 10^{-3}) adsorption processes. It is worth noting that, for the same conditions of C_0, the apparent reaction rate constants were always in the same order of magnitude, except for commercial sample N (with k_2 values one order of magnitude lower).

Similarly, for the chemically activated sample (OSAC/KOH), TPh is 200 mg/g (Table 6.4), also comparable to 204 mg/g of VA or the 236 mg/g of GA (Table 6.6). However, using the commercial sample N, $q_{e,exp}$ values for TPh in competitive adsorption experiments is 257 mg/g, thus significantly smaller than the 302 mg/g of VA or 271 mg/g of GA removed from single adsorption experiments. Thus, a greater inhibitory effect is observed for commercial N sample than in our biosorbents, which could favor their application for the treatment of real OMW.

The mass transfer process of gallic and vanillic acids was analyzed using a known intraparticle diffusion model, based on the theory proposed by Weber and Morris [43], according to Eq. (6.9),

$$q_t = K_{id}\, t^{1/2} + C \tag{6.9}$$

where K_{id} is defined as the intraparticle diffusion rate constant (mg/g·$min^{1/2}$), and C (mg/g) is a constant related to the boundary layer thickness, i.e., larger values of C suggest a greater boundary layer effect [44]. The plot of q_t *vs*. $t^{1/2}$ (Fig. 6.8) shows that a linear behavior is not obtained for the entire time range, indicating that different steps influence the adsorption processes [45]. Results of the fittings of each linear section are collected in Table 6.7. From a mechanistic point-of-view, the adsorption process may be controlled by one or more steps, including: i) solute diffusion from the bulk solution to the adsorbent's external surface; ii) mass transfer within the particle (pore diffusion); iii) solute's uptake onto adsorption-sites, which can involve different mechanisms (e.g., adsorption, ion-exchange, complexation, chelation) [34,46,47].

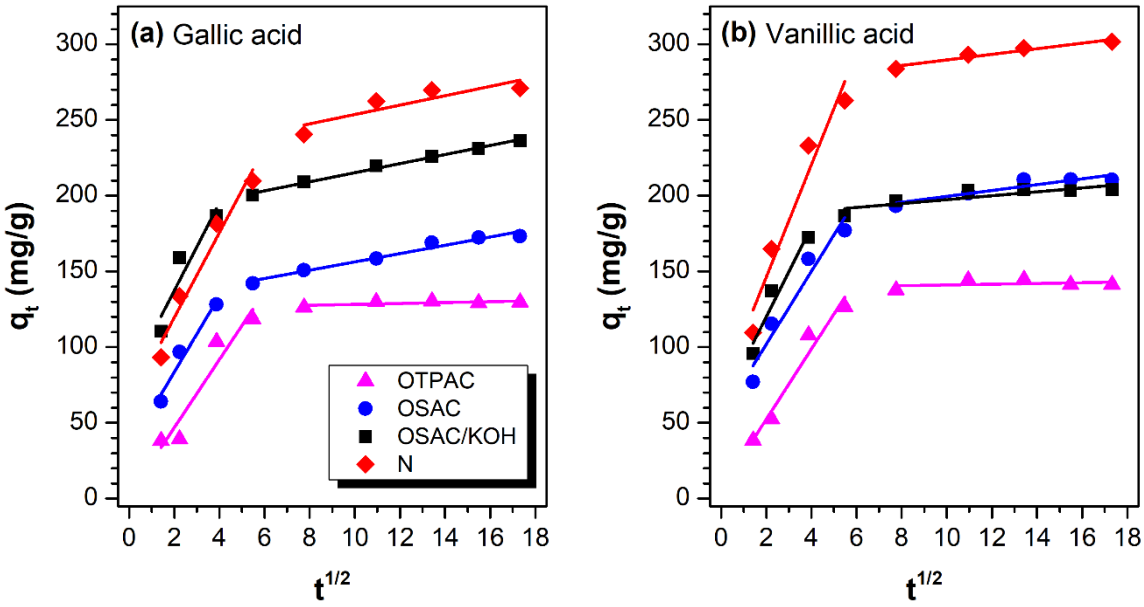


Fig. 6.8 Intraparticle diffusion adsorption kinetics for (a) gallic acid and (b) vanillic acid at C_0 = 150 mg/L, 25 °C, V = 50 mL, and pH_0 = 3.5–3.8.

The two straight lines in Fig. 6.8 indicate that the GA or VA intra-particle transport to the carbon surface occurs in two steps with very different adsorption rates (slope, K_{id}). The first one corresponds to diffusion into the open porosity (macro-meso-large micropores) and the second one, slower, corresponds to diffusion into narrow micropores [47,48]. The smallest *C* values are observed for OTPAC, suggesting a smaller boundary layer effect for both GA and VA adsorption onto this sample, which is a direct consequence of the predominant open porosity (large channels observed by SEM, Fig. 6.1). The boundary layer effect increased in the same order: OTPAC <OSAC <OSAC/KOH. The highest *C* values are always observed for the most porous samples, OSAC/KOH and N, due to the fundamental microporous character of these samples, in spite of the significant mesopore volume observed (Table 6.2). After that, phenolic molecules diffuse into the microporosity [34,49], first occupying large micropores (typically determined by N_2-adsorption), and in a second step to the ultramicropores (narrower than 0.7 nm, determined by CO_2-adsorption). The intraparticle diffusion rate constant K_{id} values increased with increasing the microporous volume (surface) accessible to the adsorbate and are typically greater for VA than GA. It is also noteworthy that $K_{id,1} >> K_{id,2}$ because ultramicropores present a size that approaches the phenolic molecules' size (Table 6.1), which strongly limits their diffusion inside this microporosity range [34,47,49]. A plateau is even approached in the case of OTPAC, indicating a very low adsorption rate/capacity in the second stage, which seems to be related to the least developed and narrower ultra-microporosity observed in this sample (Table 6.2).

Table 6.7 Intraparticle diffusion parameters for the adsorption of gallic and vanillic acids.

Adsorbate	Adsorbent	1st linear part of the curve			2nd linear part of the curve		
		$K_{id,1}$ (mg/g·min$^{1/2}$)	C_1 (mg/g)	R^2	$K_{id,2}$ (mg/g·min$^{1/2}$)	C_2 (mg/g)	R^2
Gallic acid	OTPAC	21.8	4.8	0.944	0.4	123.9	0.912
	OSAC	25.1	33.3	0.961	2.7	128.9	0.969
	OSAC/KOH	29.0	79.4	0.884	3.0	185.2	0.993
	N	28.0	63.5	0.962	5.0	195.9	0.802
Vanillic acid	OTPAC	23.2	6.1	0.961	0.2	142.5	0.936
	OSAC	32.0	36.7	0.975	2.8	168.3	0.868
	OSAC/KOH	29.8	60.4	0.947	1.3	184.5	0.722
	N	37.1	71.9	0.946	1.8	271.3	0.946

Thus, the adsorptive performance of the samples in this series, including adsorption capacity or mass transfer process, is mainly determined by the differences in the pore structure. A relation between adsorption capacities and textural properties (S_{BET} and W_0 (N_2)) can therefore be established, as shown in Fig. 6.9. The highest adsorption capacities were achieved with the AC with better developed large micropores (sample N), whereas the pruning waste-derived adsorbent OTPAC exhibited the lowest adsorption capacity towards both contaminants. However, narrow ultramicropores have a very low influence on the adsorption capacity or adsorption rate (Table 6.7). Similarly, in spite of the predominant mesoporous character of the OTPAC sample that leads to the smaller restriction in the external film diffusion, the initial adsorption rate h for GA and VA calculated from the PSO model (Table 6.6) is also the lowest (20.8 and 22.1 mg/g·min, whereas *h* values ranging from 43.8–100.0 mg/g·min are observed for the remaining ACs). Thus, the extent of S_{BET}, more than the microporous surface, seems to be the main parameter governing the adsorption of phenolic compounds, mesopores, and large micropores W_0 (N_2) are determining the adsorption rate and uptake of the adsorbate molecules (Fig. 6.9). In general, adsorption capacities determined at equilibrium by the PSO model were globally higher in the case of vanillic acid (Table 6.6). However, from the analysis of the GA or VA isotherms (Table 6.5) it is observed that affinity presents the contrary trend, namely pointed out by the higher values of K_L and K_F for GA.

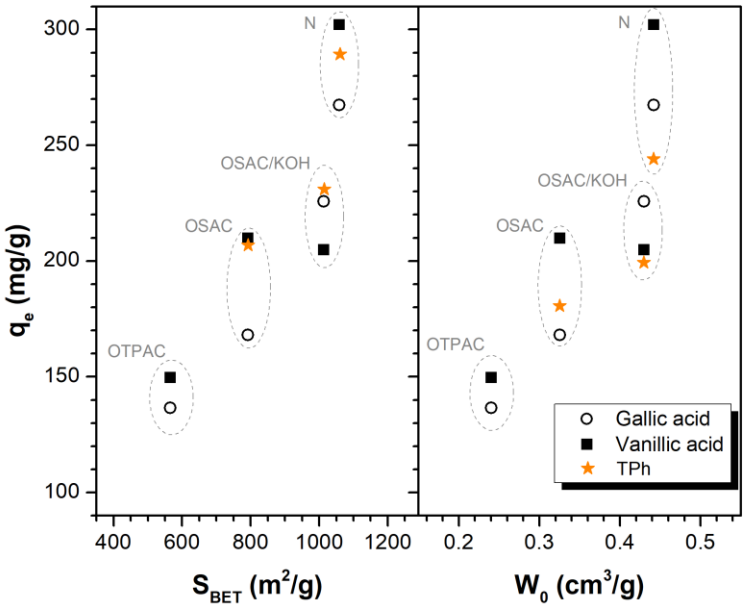


Fig. 6.9 Relationship between equilibrium adsorption capacities (qe) and the textural characteristics (S_{BET} and W_0 (N_2)) of the adsorbents for gallic and vanillic acids (C_0 = 150 mg/L); q_e values for TPh on competitive runs shown for comparison (same experimental conditions).

Nevertheless, additional parameters, associated to the characteristics of the phenolic compounds should also be taken into account. The influence of interactions adsorbent-adsorbate was pointed out by the best fittings reached with the PSO model. In previous works, it was demonstrated that carbon materials' adsorption of phenols is influenced by parameters such as their solubility in water (the higher solubility the smaller absorbability, i.e., greater affinity by water) [13,27,50]. Nonetheless, results in this study show that caffeic and vanillic acids, with similar solubility and pKa (Table 6.1), exhibited very distinct adsorption behaviors. Similarly, the higher solubility of TY regarding the rest of phenolic acids should induce a smaller adsorption, however, an intermediate adsorption behavior is observed in many cases. The affinity of different phenols by the carbon surface also varies according to the nature of the aromatic rings substituents [51]. Adsorption of phenols is favored by the withdrawing effect of substituents, which modify the electron density of the aromatic rings and consequently the strength of the π–π interactions with the carbon surface. In a previous work by Michailof *et al*. [13], the following order of deactivation of the aromatic ring was established: vanillic acid > caffeic acid > gallic acid, though caffeic acid was also the best adsorbed compound in spite of the degree of deactivation of the aromatic ring (in line with the results obtained in our study). The shape and molecular dimensions of phenols can also determine the accessibility and interactions with the adsorbent surface. The molecular shape of CA is almost linear with a length of 8.7 Å, while the maximum linear dimension of VA and GA is

similar and approximately 6.4 Å. Thus, the micropore size determined from the N_2-adsorption isotherms is, in all cases, clearly larger than the molecular dimension of the adsorbates.

Regarding the chemical characteristics of the carbon surface, oxygenated surface groups are the main functionalities, and it was demonstrated that by increasing the oxidation degree, phenols' adsorption is progressively reduced [52]. Fierro *et al*. [44] described the beneficial effect of basic sites and carbonyl groups located in larger micropores leading to donor-acceptor interactions, in competition with the π–π interactions mainly developed inside the narrowest micropores. In our case, the oxygen content increases with the chemical activation, but this process is accompanied by a development of the porosity, similarly, the larger amount of C=O found in OTPAC can be countered by the smaller microporosity of this sample, thus the variation in the oxygen content of these biosorbents do not provide clear information. Table 6.8 shows a summary of the maximum adsorptive capacities of similar adsorbents (i.e., prepared from olive mill's agro-industrial by-products) reported in the scientific literature for various adsorbates. Despite of the different raw materials and activation processes used and activation degrees reached, it is noteworthy that in general, our adsorbents present a better performance than those typically described. For instance, S. Eder *et al*. [53] prepared olive pit derived-AC by physical activation with water vapor and reported on the application of the resulting material for hydroxytyrosol removal. The resulting adsorbent presented considerably high specific surface area (S_{BET} = 1040 m^2/g), total pore volume (0.69 cm^3/g), and average pore size (4.4 nm), and the maximum adsorption capacity achieved was 375 mg/g. These values are of the same order as those obtained in our case by one-step chemical activation of OS with KOH. Hamadneh *et al*. [54] selected olive husk for the synthesis of AC using $MgCl_2$ as activating agent. The biosorbent presented BET surface area, total pore volume, and average pore size of 484 m^2/g, 0.07 cm^3/g, and 1.5 nm, respectively. The maximum adsorbent capacities reported for phenol, *p*-methoxyphenol, and *p*-nitrophenol were 43.9, 98.0, and 122.0 mg/g, respectively, and the process was well described by the Langmuir isotherm model in all cases. Thus, the selection of the raw materials and the adequate activation procedure is the key factor to obtain optimized biosorbents.

The results obtained with our biosorbents also clearly improve those presented in studies using commercial neutral or ionic exchange resins for the recovery of phenols from OMW, which showed a maximum adsorption capacity of 81 mg/g [55]. Nevertheless, macroreticular polymers displayed poor adsorption capacity, but allow a high selectivity for the separation of some compounds from OMW, such as hydroxytyrosol [56]. Other advanced carbon materials, like

graphene oxide foams with hierarchical interconnected porous texture [57] showed a maximum phenol adsorption capacity of 135.6 mg/g, although increased for different chlorobenzenes.

In sum, the development of the porous structure is a key parameter to improve the adsorptive capacity, but the synthesis procedure should also be modeled/tuned to consider the functionalization of the adsorbents to target specific compounds within a complex matrix (such is the case of some phenolic compounds, often suitable for applications related to their antioxidant properties in different industries), which should be subsequently recovered through and optimized desorption process, aiming to isolate and concentrate them (e.g., tyrosol and hydroxytyrosol).

Table 6.8 Comparison of maximum adsorptive capacities (mg/g) of various low-cost adsorbents derived from agro-industrial residues for different organic pollutants (at 25 °C).

Adsorbent	Adsorbate	q_m (mg/g)	Ref.
OS and OTP derived-ACs	Phenolic compounds	188.6–359.0	This work
Partially-combusted OP	Total phenol from OMW	11.4	[12]
OS-derived AC	Dye (Methylene blue)	16.1	[9]
Olive-waste cake derived AC	Dye (Lanaset grey G)	108.7	[10]
Solvent-washed OWs	Phenol, nitrophenols, clorophenols	5.5–12.3	[11]
OH-derived ACs	Phenolic compounds	58.3–284.6	[13]
OS-derived AC	Total phenol / COD from OMW	91.7 / 1667	[14]
Solvent-extracted olive pulp AC		71.4 / 1429	
OS- derived AC	Hydroxytyrosol	375.0	[53]
OH-derived $MgCl_2$-AC	Phenol, PMP, PNP	43.9–122.0	[54]
OS-derived KOH-ACs	Dye (Methylene blue)	190–263	[26]

OP – Olive pomace; OW – Olive wood; OH – Olive husk; PMP – *p*-methoxyphenol ; PNP – *p*-nitrophenol

6.3.4. Regeneration of adsorbents

For practical applications, the stability and reusability of the adsorbents are of utmost importance. After adsorption capacities were evaluated for the uptakes of GA or VA, spent samples were

thermally regenerated in N_2 flow, and the regenerated samples were used again in the same experimental conditions. To determine if thermal regeneration is an appropriate technique (and the required experimental conditions), the thermal behavior of GA and VA acids were tested by TG/DTG experiments (Fig. 6.10). For VA, single-step and complete decomposition take place at around 330 ºC, while the decomposition of GA presents an initial small weight loss (WL) at low temperature and then total decomposition occurs slower in comparison to VA and up to higher temperatures.

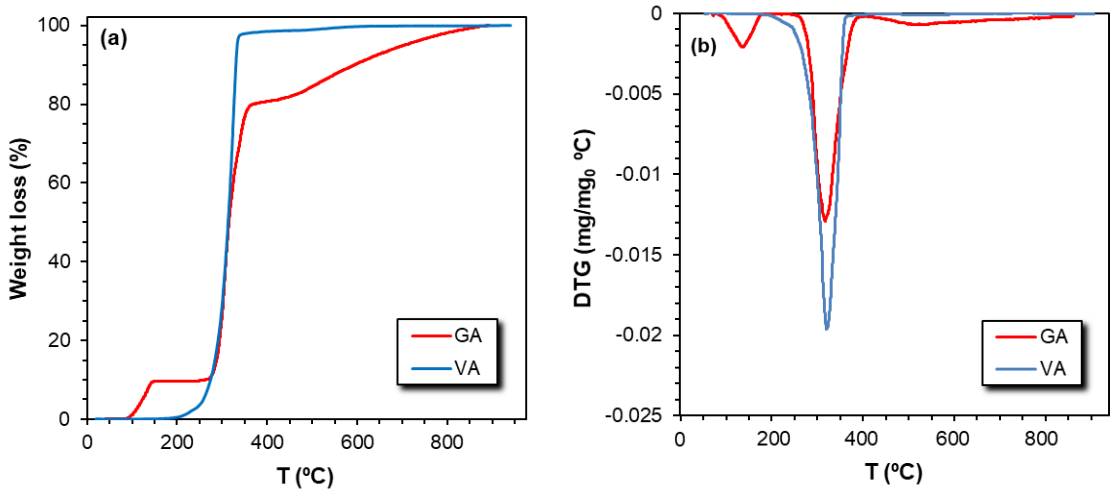


Fig. 6.10 (a) TG and (b) DTG profiles of gallic acid (GA) and vanillic acid (VA) decomposition.

Fig. 6.11 compares TG/DTG curves of fresh and spent OSAC/KOH samples. The WL of the fresh sample is associated with desorption of adsorbed compounds, namely water, and the removal of oxygenated surface groups of different thermal stability that evolve as CO and CO_2. Carboxylic acid groups present in the adsorbent are typically desorbed as CO_2 at low temperature (<400 °C), while CO-desorption in this range corresponds to carbonyl groups in *α*-substituted ketones and aldehydes. Anhydride groups decompose evolving a mixture of CO + CO_2 at around 550 °C, and lactones as CO_2 at 650 °C. Finally, the more stable and basic surface groups evolve as CO at high temperature, phenolic and hydroquinone groups at around 720 °C, and carbonyl or quinones above 900 °C [58].

TG profiles of fresh and spent samples are coincident with increasing temperature up to around 330 °C, i.e., the temperature range where the decomposition of GA and VA occurs. However, the DTG of spent samples does not show a sharp peak at 330 °C corresponding to the decomposition of adsorbed GA or VA observed for pure adsorbates (Fig. 6.10). When fixed on the adsorbent surface, their decomposition takes place progressively with increasing temperature. From 600 °C on, the WL observed is also enhanced by the release of OSG present in the fresh sample.

According to data in Table 6.5, spent samples contain 337 mg/g of GA and 358 mg/g of VA, i.e., between 34–36% of the total weight, corresponding approximately to the difference observed in the TGs profiles of fresh and spent samples at 800 °C.

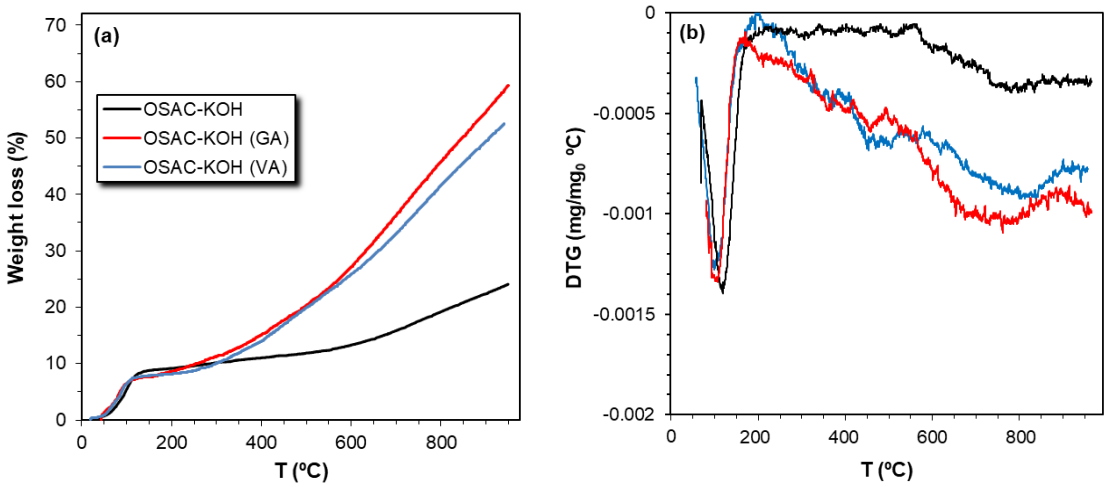


Fig. 6.11 (a) TG and (b) DTG profiles of fresh and spent OSAC/KOH after adsorption of GA or VA.

Thus, regeneration of spent samples was carried out in 40 min, by heating at a rate of 20 °C/min up to 800 °C without soak time. After cooling, regenerated samples were used again in identical adsorption experimental conditions, and results are summarized in Fig. 6.12. Comparing the results obtained with those of Fig. 6.7 and Table 6.6, it is clear that adsorption capacities after 300 min decreased by different degrees depending on the adsorbent. Both textural and chemical transformations associated with the formation of permanent deposits, or on the contrary, gasification processes of the supports, will be responsible for this adsorption capacity decrease. Although significant deactivation was observed for OSAC/KOH and N (i.e., the best microporous adsorbents), OSAC shows a minor adsorption capacity decrease of approximately 8–12%, depending on the adsorbate. This means that the thermal cycle for the regeneration process should be optimized according to the biosorbents characteristics, although heating in an inert atmosphere is an efficient, cheap, and fast regeneration procedure.

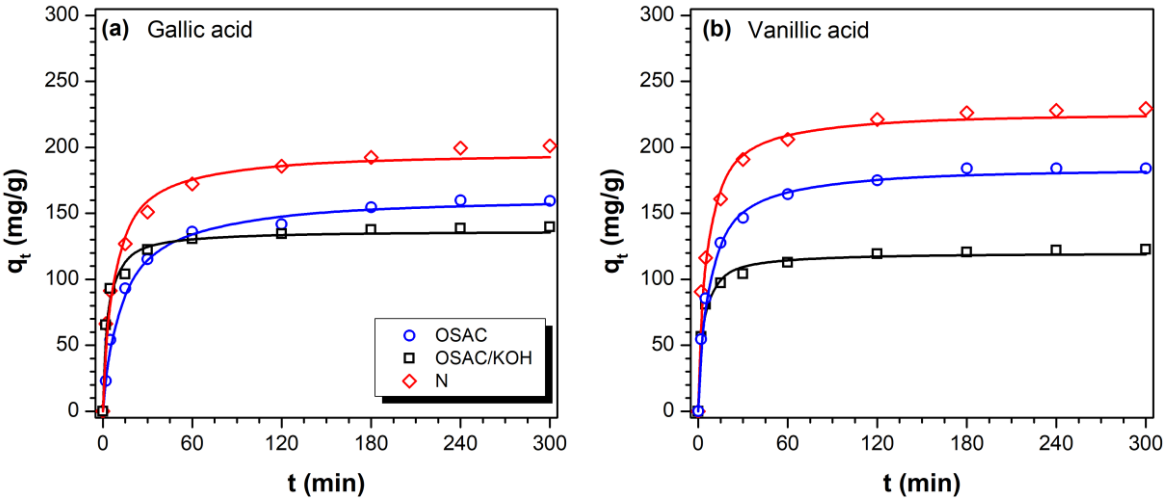


Fig. 6.12 Kinetic curves for (a) gallic and (b) vanillic acids using regenerated samples at C_0 = 150 mg/L and 25 °C (PSO model adjustment).

6.4. CONCLUSIONS

A series of biosorbents (ACs) was prepared by physical or chemical activation of residues from the olive oil production (olive stone, OS, and rest of pruning, OTP). The resulting porosity and chemical nature depend on the raw materials, OTPAC showing a more open structure and homogeneous oxygenated surface groups but smaller microporosity and surface area. Chemical activation of OS with KOH produces, in only one synthesis step, greater development of porosity, namely the microporosity. The total pore volume of the materials tested ranged from 0.39-0.55 cm^3/g and S_{BET} from 565–1013 m^2/g.

The competitive adsorptive performance in simulated OMW was compared with the adsorption of single phenolic compounds (vanillic and gallic acids, VA and GA). Adsorption kinetics were fitted using PFO and PSO models, as well as the intraparticle diffusion model. The adsorption isotherms of VA and GA were fitted by applying the Langmuir and Freundlich equations. The best fittings were obtained using the PSO model, suggesting the influence of chemical interactions in the global process. The transport of the phenolic compounds to the carbon surface occurs in two steps, corresponding to the process inside large pores and narrow micropores, respectively, with the latter showing a scarce influence in the global adsorptive process. Thus, the adsorption capacity and adsorption rate are mainly determined by the porosity, specifically by the larger micropores and the BET surface area, rather than the samples' total micropore volume.

High total phenolic content (TPh) adsorption capacities (q_e) were observed along the competitive adsorption process with simulated OMW, also comparable to those obtained in single VA or GA

adsorption processes, while a commercial AC from Norit, used as a reference, shows a significant inhibition degree in the competitive adsorption runs. Regeneration by thermal treatment demonstrated high efficiency for OSAC, allowing the reuse of this adsorbent, though the process should be further optimized for the entire range of materials studied. These results evidenced the applicability of such biosorbents in the removal of OMW phenolic compounds.

REFERENCES

1. Soto, M.L.; Moure, A.; Domínguez, H.; Parajó, J.C. Recovery, concentration and purification of phenolic compounds by adsorption: A review. *J. Food Eng*. **2011**, 105, 1–27.
2. Ochando-Pulido, J.M.; Pimentel-Moral, S.; Verardo, V.; Martinez-Ferez, A. A focus on advanced physico-chemical processes for olive mill wastewater treatment. *Sep. Purif. Technol.* **2017**, 179, 161–174.
3. Al-Malah, K.; Azzam, M.O.J.; Abu-Lail, N.I. Olive mills effluent (OME) wastewater post-treatment using activated clay. *Sep. Purif. Technol.* **2000**, 20, 225–234.
4. Ahmaruzzaman, M. Adsorption of phenolic compounds on low-cost adsorbents: A review. *Adv. Colloid Interface Sci.* **2008**, 143, 48–67.
5. Jeguirim, M.; Belhachemi, M.; Limousy, L.; Bennici, S. Adsorption/reduction of nitrogen dioxide on activated carbons: Textural properties versus surface chemistry – A review. *Chem. Eng. J.* **2018**, 347, 493–504.
6. Baccar, R.; Bouzid, J.; Feki, M.; Montiel, A. Preparation of activated carbon from Tunisian olive-waste cakes and its application for adsorption of heavy metal ions. *J. Hazard. Mater*. **2009**, 162, 1522–1529.
7. Petrella, A.; Spasiano, D.; Acquafredda, P.; De Vietro, N.; Ranieri, E.; Cosma, P.; Rizzi, V.; Petruzzelli, V.; Petruzzelli, D. Heavy metals retention (Pb(II), Cd(II), Ni(II)) from single and multimetal solutions by natural biosorbents from the olive oil milling operations. *Process Saf. Environ. Prot.* **2018**, 114, 79–90.
8. Hodaifa, G.; Ochando-Pulido, J.M.; Driss Alami, S. Ben; Rodriguez-Vives, S.; Martinez-Ferez, A. Kinetic and thermodynamic parameters of iron adsorption onto olive stones. *Ind. Crops Prod.* **2013**, 49, 526–534.
9. Hazzaa, R.; Hussein, M. Adsorption of cationic dye from aqueous solution onto activated carbon prepared from olive stones. *Environ. Technol. Innov.* **2015**, 4, 36–51.
10. Baccar, R.; Blánquez, P.; Bouzid, J.; Feki, M.; Sarrà, M. Equilibrium, thermodynamic and kinetic studies on adsorption of commercial dye by activated carbon derived from olive-waste cakes. *Chem. Eng. J.* **2010**, 165, 457–464.
11. El-Sheikh, A.H.; Newman, A.P.; Said, A.J.; Alzawahreh, A.M.; Abu-Helal, M.M. Improving the adsorption efficiency of phenolic compounds into olive wood biosorbents by pre-washing with organic solvents: Equilibrium, kinetic and thermodynamic aspects. *J. Environ. Manage.* **2013**, 118, 1–10.
12. Stasinakis, A.S.; Elia, I.; Petalas, A. V.; Halvadakis, C.P. Removal of total phenols from olive-mill wastewater using an agricultural by-product, olive pomace. *J. Hazard. Mater.* **2008**, 160, 408–413.
13. Michailof, C.; Stavropoulos, G.G.; Panayiotou, C. Enhanced adsorption of phenolic compounds, commonly encountered in olive mill wastewaters, on olive husk derived activated carbons. *Bioresour. Technol.* **2008**, 99, 6400–6408.
14. Galiatsatou, P.; Metaxas, M.; Arapoglou, D.; Kasselouri-Rigopoulou, V. Treatment of olive mill waste water with activated carbons from agricultural by-products. *Waste Manag.* **2002**, 22, 803–812.
15. Baçaoui, A.; Dahbi, A.; Yaacoubi, A.; Bennouna, C.; Maldonado-Hódar, F.J.; Rivera-Utrilla, J.; Carrasco-Marín, F.; Moreno-Castilla, C. Experimental design to optimize preparation of activated carbons for use in water treatment. *Environ. Sci. Technol.* **2002**, 36, 3844–3849.
16. Morales-Torres, S.; Silva, A.M.T.; Pérez-Cadenas, A.F.; Faria, J.L.; Maldonado-Hódar, F.J.; Figueiredo, J.L.; Carrasco-Marín, F. Wet air oxidation of trinitrophenol with activated carbon catalysts: Effect of textural properties on the mechanism of degradation. *Appl. Catal. B Environ.* **2010**, 100, 310–317.
17. Aggoun, M.; Arhab, R.; Cornu, A.; Portelli, J.; Barkat, M.; Graulet, B. Olive mill wastewater microconstituents composition according to olive variety and extraction process. *Food Chem.* **2016**, 209, 72–80.
18. El-Abbassi, A.; Kiai, H.; Hafidi, A. Phenolic profile and antioxidant activities of olive mill wastewater. *Food Chem.* **2012**, 132, 406–412.
19. Kapellakis, I.E.; Tsagarakis, K.P.; Crowther, J.C. Olive oil history, production and by-product management. *Rev. Environ. Sci. Biotechnol.* **2008**, 7, 1–26.
20. De Marco, E.; Savarese, M.; Paduano, A.; Sacchi, R. Characterization and fractionation of phenolic compounds extracted from olive oil mill wastewaters. *Food Chem.* **2007**, 104, 858–867.
21. Tundis, R.; Conidi, C.; Loizzo, M.R.; Sicari, V.; Romeo, R.; Cassano, A. Concentration of bioactive phenolic compounds in olive mill wastewater by direct contact membrane distillation. *Molecules* **2021**, 26, 1808.

22. Ghouma, I.; Jeguirim, M.; Sager, U.; Limousy, L.; Bennici, S.; Däuber, E.; Asbach, C.; Ligotski, R.; Schmidt, F.; Ouederni, A. The potential of activated carbon made of agro-industrial residues in NOx emissions abatement. *Energies* **2017**, 10, 1508.
23. Alslaibi, T.M.; Abustan, I.; Ahmad, M.A.; Foul, A.A. Kinetics and equilibrium adsorption of iron (II), lead (II), and copper (II) onto activated carbon prepared from olive stone waste. *Desalin. Water Treat.* **2014**, 52, 7887–7897.
24. Cazorla-Amorós, D.; Alcañ Iz-Monge, J.; De La Casa-Lillo, M.A.; Linares-Solano, A. CO_2 as an adsorptive to characterize carbon molecular sieves and activated carbons. *Langmuir* **1998**, 14, 4589–4596.
25. Thommes, M.; Kaneko, K.; Neimark, A. V.; Olivier, J.P.; Rodriguez-Reinoso, F.; Rouquerol, J.; Sing, K.S.W. Physisorption of gases, with special reference to the evaluation of surface area and pore size distribution (IUPAC Technical Report). *Pure Appl. Chem.* **2015**, 87, 1051–1069.
26. Stavropoulos, G.G.; Zabaniotou, A.A. Production and characterization of activated carbons from olive-seed waste residue. *Microporous Mesoporous Mater.* **2005**, 82, 79–85.
27. García-Araya, J.F.; Beltrán, F.J.; Álvarez, P.; Masa, F.J. Activated carbon adsorption of some phenolic compounds present in agroindustrial wastewater. *Adsorption* **2003**, 9, 107–115.
28. Moreno-Castilla, C.; Pérez-Cadenas, A.F.; Maldonado-Hódar, F.J.; Carrasco-Marín, F.; Fierro, J.L.G. Influence of carbon-oxygen surface complexes on the surface acidity of tungsten oxide catalysts supported on activated carbons. *Carbon* **2003**, 41, 1157–1167.
29. Wang, J.; Guo, X. Adsorption kinetic models: Physical meanings, applications, and solving methods. *J. Hazard. Mater.* **2020**, 390, 122156.
30. Lagergren, S. About the theory of so-called adsorption of soluble substances. *K. Sven. Vetenskapsakademiens Handl.* **1898**, 24, 1–39.
31. Blanchard, G.; Maunaye, M.; Martin, G. Removal of heavy metals from waters by means of natural zeolites. *Water Res.* **1984**, 18, 1501–1507.
32. Ho, Y.S.S.; McKay, G. Pseudo-second order model for sorption processes. *Process Biochem.* **1999**, 34, 451–365.
33. Srivastava, V.C.; Mall, I.D.; Mishra, I.M. Adsorption of toxic metal ions onto activated carbon. Study of sorption behaviour through characterization and kinetics. *Chem. Eng. Process. Process Intensif.* **2008**, 47, 1269–1280.
34. Toor, M.; Jin, B. Adsorption characteristics, isotherm, kinetics, and diffusion of modified natural bentonite for removing diazo dye. *Chem. Eng. J.* **2012**, 187, 79–88.
35. Alhamed, Y.A. Adsorption kinetics and performance of packed bed adsorber for phenol removal using activated carbon from dates' stones. *J. Hazard. Mater.* **2009**, 170, 763–770.
36. Macedo, E.; Santos, M.S.F.; Maldonado-Hódar, F.J.; Alves, A.; Madeira, L.M. Insights on Carbonaceous Materials Tailoring for Effective Removal of the Anticancer Drug 5-Fluorouracil from Contaminated Waters. *Ind. Eng. Chem. Res.* **2018**, 57, 3932–3940.
37. Salleh, M.A.M.; Mahmoud, D.K.; Karim, W.A.W.A.; Idris, A. Cationic and anionic dye adsorption by agricultural solid wastes: A comprehensive review. *Desalination* **2011**, 280, 1–13.
38. Li, Z.; Sellaoui, L.; Luiz Dotto, G.; Bonilla-Petriciolet, A.; Ben Lamine, A. Understanding the adsorption mechanism of phenol and 2-nitrophenol on a biopolymer-based biochar in single and binary systems via advanced modeling analysis. *Chem. Eng. J.* **2019**, 371, 1–6.
39. Ayawei, N.; Ebelegi, A.N.; Wankasi, D. Modelling and Interpretation of Adsorption Isotherms. *J. Chem.* **2017**, 2017.
40. Wanassi, B.; Hariz, I. Ben; Ghimbeu, C.M.; Vaulot, C.; Hassen, M. Ben; Jeguirim, M. Carbonaceous adsorbents derived from textile cotton waste for the removal of Alizarin S dye from aqueous effluent: kinetic and equilibrium studies. *Environ. Sci. Pollut. Res*. **2017**, 24, 10041–10055.
41. Seader, J.D.; Henley, E.J.; Keith Roper, D. Separation Process Principles; 3rd ed.; John Wiley Incorporated: Hoboken, NJ, **2010**; ISBN 9781118139622.
42. Rivera-Utrilla, J.; Moreno-Castilla, C.; Utrera-Hidalgo, E.; Carrasco-Marín, F. Removal of tannic acid from aqueous solutions by activated carbons. Chem. Eng. J. 1993, 52, 37–39.
43. Weber Jr., W.J.; Morris, J.C. Kinetics of Adsorption on Carbon from Solution. *J. Sanit. Eng. Div.* **1963**, 89, 31–59.
44. Fierro, V.; Torné-Fernández, V.; Montané, D.; Celzard, A. Adsorption of phenol onto activated carbons having different textural and surface properties. *Microporous Mesoporous Mater.* **2008**, 111, 276–284.
45. Pholosi, A.; Naidoo, E.B.; Ofomaja, A.E. Intraparticle diffusion of Cr(VI) through biomass and magnetite coated biomass: A comparative kinetic and diffusion study. *South African J. Chem. Eng.* **2020**, 32, 39–55.

46. Viegas, R.M.C.; Campinas, M.; Costa, H.; Rosa, M.J. How do the HSDM and Boyd's model compare for estimating intraparticle diffusion coefficients in adsorption processes. *Adsorption* **2014**, 20, 737–746.
47. Conde, E.; Moure, A.; Domínguez, H. Recovery of phenols from autohydrolysis liquors of barley husks: Kinetic and equilibrium studies. *Ind. Crops Prod.* **2017**, 103, 175–184.
48. Allen, S.J.; McKay, G.; Khader, K.Y. Intraparticle diffusion of a basic dye during adsorption onto sphagnum peat. *Environ. Pollut.* **1989**, 56, 39–50.
49. Mohd Din, A.T.; Hameed, B.H.; Ahmad, A.L. Batch adsorption of phenol onto physiochemical-activated coconut shell. *J. Hazard. Mater.* **2009**, 161, 1522–1529.
50. Kumar, A.; Kumar, S.; Kumar, S. Adsorption of resorcinol and catechol on granular activated carbon: Equilibrium and kinetics. *Carbon* **2003**, 41, 3015–3025.
51. Moreno-Castilla, C.; Rivera-Utrilla, J.; López-Ramón, M. V.; Carrasco-Marín, F. Adsorption of some substituted phenols on activated carbons from a bituminous coal. *Carbon*. **1995**, 33, 845–851.
52. Sun, J.; Liu, X.; Zhang, F.; Zhou, J.; Wu, J.; Alsaedi, A.; Hayat, T.; Li, J. Insight into the mechanism of adsorption of phenol and resorcinol on activated carbons with different oxidation degrees. *Colloids Surfaces A Physicochem. Eng. Asp.* **2019**, 563, 22–30.
53. Eder, S.; Müller, K.; Azzari, P.; Arcifa, A.; Peydayesh, M.; Nyström, L. Mass Transfer Mechanism and Equilibrium Modelling of Hydroxytyrosol Adsorption on Olive Pit–Derived Activated Carbon. *Chem. Eng. J.* **2021**, 404, 126519.
54. Hamadneh, I.; Abu-Zurayk, R.A.; Al-Dujaili, A.H. Removal of phenolic compounds from aqueous solution using MgCl2-impregnated activated carbons derived from olive husk: the effect of chemical structures. *Water Sci. Technol.* **2020**, 81, 2351–2367.
55. Frascari, D.; Rubertelli, G.; Arous, F.; Ragini, A.; Bresciani, L.; Arzu, A.; Pinelli, D. Valorisation of olive mill wastewater by phenolic compounds adsorption: Development and application of a procedure for adsorbent selection. *Chem. Eng. J.* **2019**, 360, 124–138.
56. Yangui, A.; Njimou, J.R.; Cicci, A.; Bravi, M.; Abderrabba, M.; Chianese, A. Competitive adsorption, selectivity and separation of valuable hydroxytyrosol and toxic phenol from olive mill wastewater. *J. Environ. Chem. Eng.* **2017**, 5, 3581–3589.
57. Wang, W.; Gong, Q.; Chen, Z.; Wang, W.D.; Huang, Q.; Song, S.; Chen, J.; Wang, X. Adsorption and competition investigation of phenolic compounds on the solid-liquid interface of three-dimensional foam-like graphene oxide. *Chem. Eng. J.* **2019**, 378, 122085.
58. Morales-Torres, S.; Maldonado-Hódar, F.J.; Pérez-Cadenas, A.F.; Carrasco-Marín, F. Design of low-temperature Pt-carbon combustion catalysts for VOC's treatments. *J. Hazard. Mater.* **2010**, 183, 814–822.

CHAPTER 7

FITTING BIOCHARS AND ACTIVATED CARBONS FROM RESIDUES OF THE OLIVE OIL INDUSTRY AS SUPPORTS OF FE-CATALYSTS FOR THE FENTON-LIKE OXIDATION OF SIMULATED OMW

Highlights

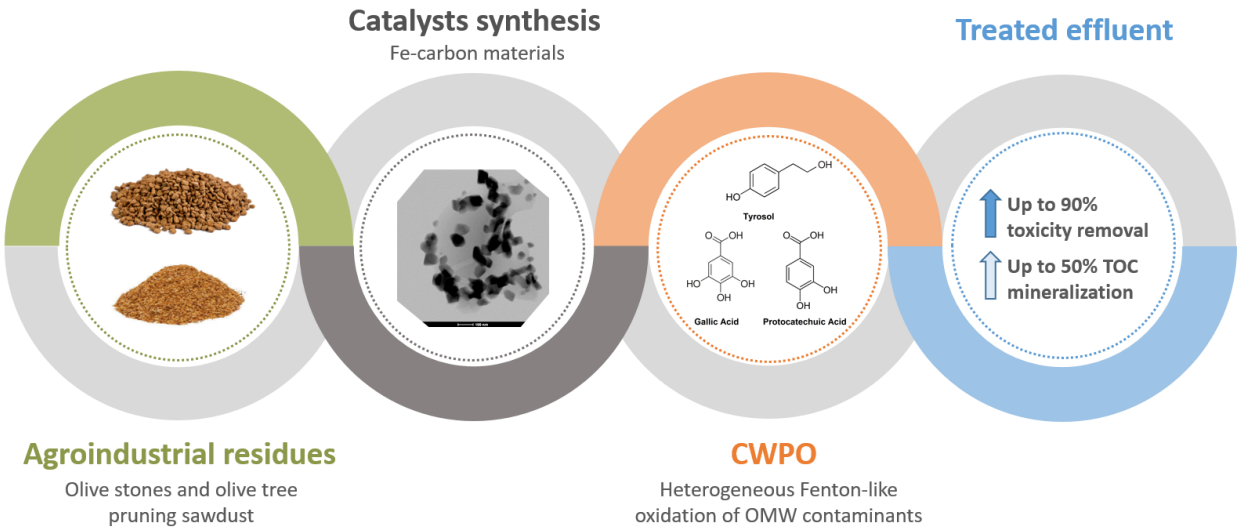
- Fe-supports were prepared by carbonization and activation of bio-residues;
- Synthesized catalysts were compared to ones supported into commercial-ACs;
- Morphological and chemical properties were correlated to the catalytic performances;
- TPh removals were generally higher for commercial-AC Fe-catalysts;
- Improved stability & mineralization achieved with prepared Fe-AC catalysts.

The contents of this subchapter were adapted from:

Esteves, B.M., Morales-Torres, S., Maldonado-Hódar, F.J., Madeira, L.M., Nanomaterials, 2020, 10(5), 876. https://doi.org/10.3390/nano10050876

ABSTRACT

A series of biochars and activated carbons (ACs) were prepared, combining carbonization and physical or chemical activation of cheap and abundant residues of the olive oil industry. These materials were used as Fe-support to develop low-cost catalysts for the heterogeneous Fenton-like oxidation of simulated olive mill wastewater (OMW), the highly polluting effluent generated by this agroindustry. Two commercial ACs were also used for reference. All catalysts were extensively characterized and their properties correlated to the performances in the catalytic wet peroxide oxidation (CWPO). Results showed a linear relationship of the textural properties of the catalysts with the adsorptive and catalytic performance, as well as the preferential adsorption and degradation of some phenolic compounds (caffeic and gallic acids) by specific interactions with the catalysts' surface. Despite the best performance of catalysts developed using commercial supports, those prepared from agro-industrial residues present some advantages, including a smaller catalyst deactivation by iron leaching. CWPO results show that catalysts from physically activated olive stones are the most promising materials, reaching total organic carbon and toxicity reductions of 35% and 60%, respectively, as well an efficient use of H_2O_2, comparable with those obtained using commercial supports. This approach showed that the optimized treatment of this type of residue allows their integration in the circular economic process of olive oil production.



7.1. INTRODUCTION

Solid by-products such as olive stones and olive tree pruning, as well as semi-solid residues usually known as pomaces, also require management alternatives, as they comprise an important fraction of the total residues generated by olive mills. Several authors have already tested such residues as precursors for the preparation of adsorbents (as also shown in Chapter 6), with applications on adsorption of OMW contaminants [1,2] or heavy metals removals from water [3,4]. In this chapter, the catalytic activity of different Fe-based catalysts, prepared from olive stones and olive tree pruning's sawdust biochars, is evaluated for the treatment of a phenolic mixture simulating the polyphenolic composition of real OMW. The activity and stability of the synthesized materials will be compared to commercially available ones. Performance of the CWPO process will be monitored following the solution's mineralization degree (total organic carbon – TOC), degradation of individual parent phenolic compounds, and H_2O_2 consumption efficiency. The bioluminescence inhibition of *V. fischeri* bacteria will be used as a toxicity indicator, and the Fe leaching assessed to infer the stability of the catalysts. The goal of this work is to check the suitability of two olive oil extraction by-products as Fe-support catalysts on the oxidation of OMW's characteristic phenolic compounds and reduction of the solution's overall toxicity, in the perspective of a circular and sustainable economy, which to the best of author's knowledge has never been reported yet.

7.2. MATERIALS AND METHODS

7.2.1. Catalysts synthesis

Catalysts were prepared using two agricultural by-products from the olive oil extraction operation: olive stones (OS) and sawdust (SD) from olive tree pruning. The raw starting materials were provided by local manufacturers from the region of Granada, Spain. Before use, olive stones and sawdust were thoroughly washed, ground, and sieved to a particle size fraction of 0.45–1.0 mm.

Biochars were prepared through the carbonization of the raw materials using a horizontal tube furnace at 800 °C (heat ramp of 10 °C/min, 2 h of hold time) under N_2 flow (flow rate of 150 cm^3/min). All volumetric flow rates were measured at room temperature and atmospheric pressure. Physically activated biochars were obtained using CO_2 as the activating agent. For that, the flow of N_2 was exchanged for that of CO_2 (flow rate of 300 cm^3/min and 4 h of hold time) after

the carbonization period, and finally, the oven turned off and the sample was allowed to cool to room temperature, again under an inert (N_2) atmosphere. These samples were denominated indicating the thermal treatments of the corresponding raw materials, thus OSC and SDC correspond to biochar from OS and SD, while OSC-AC and SDC-AC to the physically activated biochars, respectively. Additionally, another fraction of OS was chemically activated, using KOH as activating agent (sample OS-AC/KOH). For that, a mixture of OS/KOH was prepared in a weight ratio of 1 and thermally treated at 800 °C for 2 h and allowed to cool to room temperature. Samples were finally washed with diluted HCl and then with distilled water until the absence of chloride ions in the washing waters was observed.

Fe-supported catalysts were then prepared by incipient wetness impregnation (IWI) using the appropriate amount of $FeCl_2 \cdot 4H_2O$ (Acros Organics) aqueous solution as the metal precursor, to obtain an iron load of 5 wt.%. Impregnated samples were dried overnight at 100 °C, then treated for 1 h under N_2 flow of 150 cm^3/min at 350 °C (heat ramp of 10 °C/min), and finally stored in air-tight sealed containers until needed. For comparative purposes, two commercial activated carbons were also used as Fe-supports: one from Norit (Norit RX-3 Extra) and the other from Merck (ref. 102514 AC pure), commercialized in granular form, which was also grounded and sieved to the particle size fraction of 0.45–1.0 mm. The designation and synthesis conditions of each catalyst used in this study are reported in Table 7.1.

Table 7.1 Summary of synthesis conditions, nomenclature of catalysts and yield values of the carbonization/activation processes.

Catalyst	Starting material	Carbonization	Activation agent	Carb/Act yield (%)
OSC-Fe	Olive Stone	800 °C/N_2/2 h	-	24
OSC-AC-Fe	Olive Stone	800 °C/N_2/2 h	CO_2	16
OS-AC/KOH-Fe	Olive Stone	-	KOH	14
SDC-Fe	Sawdust	800 °C/N_2/2 h	-	23
SDC-AC-Fe	Sawdust	800 °C/N_2/2 h	CO_2	16
N-Fe	AC (Norit RX-3 Extra)	Commercial, used as received		-
M-Fe	AC (Merck)	Commercial, used as received		-

7.2.2. Synthetic wastewater and experimental procedure

Experiments were performed with a synthetic effluent comprising five phenolic compounds typically present in real olive mill wastewaters. The concentration/occurrence of each compound was adjusted according to data reported in the literature for real OMW as follows: 100 mg/L of tyrosol (2-(4-hydroxyphenyl)ethanol, Sigma-Aldrich), 75 mg/L of gallic (3,4,5-trihydroxybenzoic acid, Alfa Aesar) and caffeic (3,4-dihydroxycinnamic acid, Acros Organics) acids, 50 mg/L of vanillic (4-hydroxy-3-methoxybenzoic acid, Sigma-Aldrich) and protocatechuic (3,4-dihydroxybenzoic acid, Acros Organics) acids. The compounds were dissolved in distilled water under sonication for 15 min to ensure full dissolution. The chemical characteristics of each compound used in this study are presented in Table B.1 (Appendix B). Table 7.2 highlights the main physicochemical characteristics of the synthetic effluent used in this study as well as the range of values reported for real wastewater: weathered OMW from storage ponds, olives washing waters, and OMW from olive oil production (centrifuges).

Table 7.2 Physicochemical characterization of the synthetic effluent; overview of OMW characteristics from different sources: storage pond (weathered), olives washing and centrifuges.

Effluent	pH	COD (g/L)	BOD_5 (g/L)	TOC (g/L)	TPh (g/L)	TSS (g/L)	Ref.
Synthetic	3.8	0.77	0.19	0.21	0.35	-	This work
OMW (weathered)	6.3	1.7	0.47	0.31	0.18	0.25	[5]
OMW (olives washing)	6.3–7.2	0.8–4.1	0.3–1.5	-	0.04–0.10	8–18	[6,7]
OMW (centrifuges)	3.5–6.0	4–200	0.8–100	8.3–26.0	0.1–7.4	2–35	[7–10]

CWPO runs were performed in triplicate in a 300 mL-capacity cylindrical jacketed batch reactor, under magnetic agitation at *ca*. 300 rpm (VWR VS-CT magnetic stirrer) and controlled temperature (T = 25 °C), recycling water through a model 89202-912 VWR International thermostatic bath. The reactor was initially loaded with 150 mL of the synthetic effluent ($pH_0 \approx 3.8$), followed by the catalyst (0.5 g/L) in powder form and the reaction started after the single-step addition of 0.5 mL of H_2O_2 (30% *w/v*, VWR Chemicals), yielding an initial concentration of 1.0 g/L. The concentration of hydrogen peroxide selected corresponds to approximately the theoretical stoichiometric amount (H_2O_2 = 1.25 g/L) for complete mineralization of the total organic carbon of the mixture to CO_2 and H_2O. The effluent's pH and temperature were monitored

using a WTW Inolab pH-meter and a WTW SenTix 81 combined electrode, respectively. Samples of the effluent were collected at regular intervals and filtered (0.45 μm pore diameter filters) prior to analysis in order to remove the catalyst from solution. Samples were neutralized with NaOH 1 M and immediately analysed by high performance liquid chromatography (HPLC), whilst Na_2SO_3 was used as quencher of H_2O_2 before TOC determinations in order to prevent the homogenous reaction catalyzed by dissolved Fe. The same procedure was adopted for total phenolic content and TOC determinations of the influent and the procedure repeated on all runs. Pure adsorption of the phenolic compounds was also evaluated for all catalysts in the same operational conditions but in the absence of H_2O_2. TOC/TPh removals and H_2O_2 consumptions (%) were calculated according to Eq. (4.1), where X stands for removal/consumption efficiency, C_0 for the initial TOC/TPh/H_2O_2 concentration (mg/L) and C for the concentration at any given time (mg/L).

The theoretical TOC removal values reported were calculated assuming that all H_2O_2 was consumed to completely mineralize organic carbon of each compound up to CO_2 and H_2O. For each phenolic compound in the selected mixture, the reaction's stoichiometry was calculated and the theoretical (mass) rate between TOC and H_2O_2 (R) is approximately 0.17. The efficiency of H_2O_2 consumption (η) can then be calculated following Eq. (7.1).

$$\eta\, H_2O_2(\%) = \frac{TOC_{removed}\,(\frac{mg\ C}{L})}{H_2O_{2_{consumed}}(\frac{mg}{L}) \times R} \times 100 \qquad (7.1)$$

7.3. RESULTS AND DISCUSSION

7.3.1. Textural and chemical characterization

As mentioned in the previous section, two solid residues from different steps of the olive oil production were selected to develop Fenton catalysts' supports: sawdust (SD) from the olive tree pruning and olive stones (OS) obtained after the oil's extraction process. The objective is, evidently, the valorization and integration of such waste/cheap materials in a more efficient and clean olive oil production, by facilitating the treatment and reuse of water and reducing the pollution load of the produced effluents in the same agro-industrial activity sector.

Both lignocellulosic residues were carbonized to increase their chemical stability and the development of porous textures. Initially, the carbonization process was simulated by TGA to fit

experimental conditions of samples' preparation. TG-DTG (differential thermogravimetric analysis) curves obtained in each case are compared in Fig. 7.1. It is noteworthy the good coincidence of pyrolysis curves, denoting a similar chemical structure and stability of both raw materials. The carbonization process of lignocellulosic materials is complex [11–13] and it starts with the decomposition of hemicellulose, typically occurring between 200–290 °C with the formation of volatile compounds. In this case, however, it is observed that the first weight loss (WL) process occurs at around 100 °C, then weight remains constant up to 250 °C. Thus, probably only dehydration process occurs in this temperature range. The main carbonization step takes place between 250–380 °C, associated with the cellulose decomposition that is the main component in both residues. Afterward, carbonization continues with increasing temperature, although at a slower and nearly constant rate, due to the greater thermal stability of lignin regarding cellulose. Those processes are more clearly observed in the DTG profiles, corresponding respectively to the small minimum at 100 °C, the shoulder around 300 °C, and the maximum carbonization rate at *ca*. 350 °C. Finally, the DTG curves remain practically constant at high temperatures because, as commented, the observed lignin decomposition rate is nearly constant. In both cases, the WL up to 800 °C was around 85 wt.%. The ash content determined after burning a sample fraction in air was also similar in both cases (*ca*. 2.5 wt.%). The experimental conditions of OSC and SDC physical activation, as well as the chemical activation of OS, were fitted to have a similar activation degree, with an activated carbon yield between 14-16 wt.%.

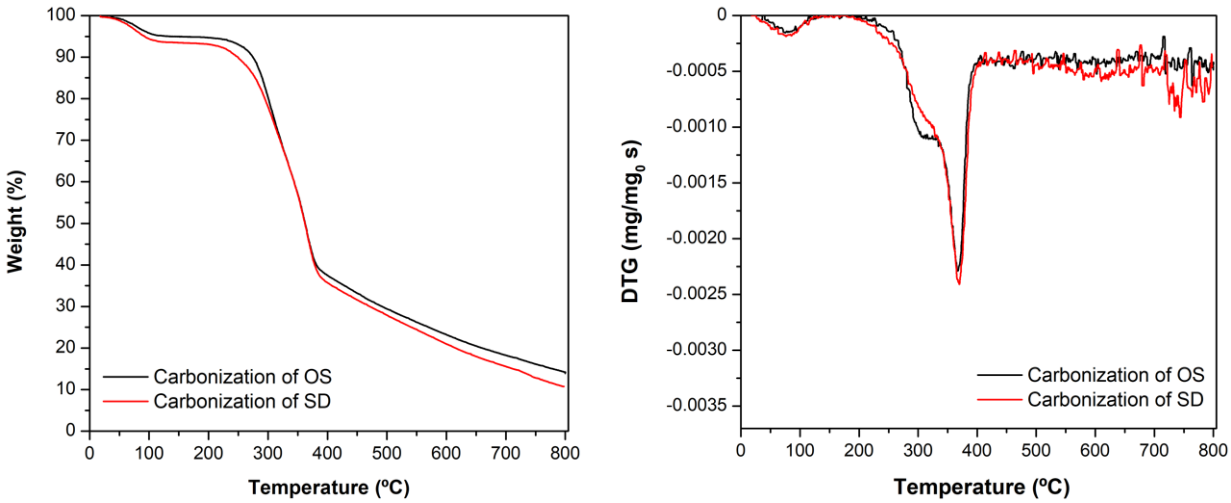


Fig. 7.1 TG-DTG profiles for the carbonization of OS and SD residues.

The morphology of the samples was studied by HRSEM (Fig. 7.2). The cellular structure of wood is visible in the physically-activated carbon obtained from SDC (Fig. 7.2A) with long, wide, and

parallel channels aligned in the direction of the tree's growth. Although the particles of AC obtained from OSC also exhibit a highly porous structure (Fig. 7.2B), closed vesicles are observed and the channels are clearly narrower than the ones in SDC-AC and not so clearly aligned; thus, most compact particles are observed. After chemical activation, the cellular structure of OS is strongly damaged and the tangled combination of crisscrossed channels leads to the foam-like aspect (Fig. 7.2C) instead of regular channels.

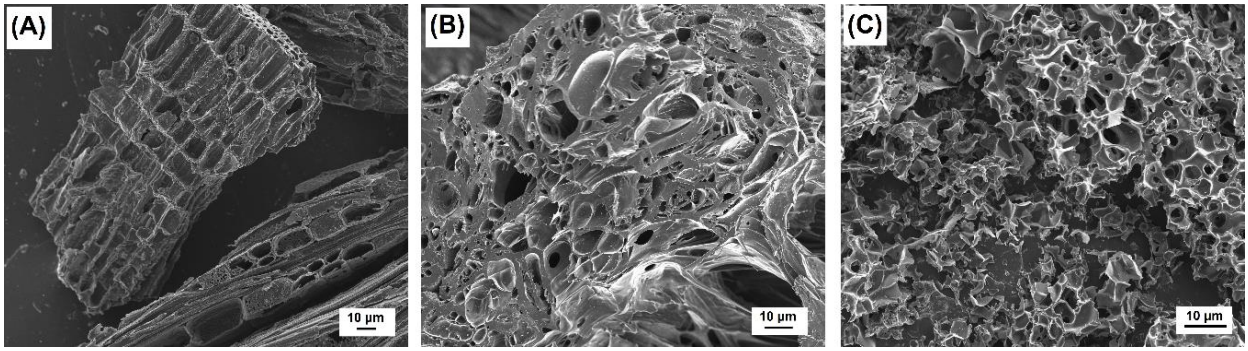


Fig. 7.2 HRSEM images of (A) SDC-AC, (B) OSC-AC and (C) OS-AC/KOH supports (without Fe).

Samples' porosity was determined by N_2 and CO_2–adsorption isotherms and the textural characterization results are compiled in Table 7.3. Both prepared activated samples and commercial materials present predominantly N_2-adsorption isotherms of type I–IV, characteristic of microporous/mesoporous materials. The N_2–adsorption isotherms of all supports and their corresponding catalysts presented a hysteresis loop, indicating some contribution of mesopores in their porous structure (Fig. B.1, Appendix B). N_2–adsorption allows determining the total porosity of samples in the absence of diffusional restriction, while CO_2 is used to characterize the narrowest micropores (ultramicropores with diameter <0.7 nm), where the accessibility of N_2 at -196 °C can be limited. However, CO_2 is only adsorbed into the microporosity because of the higher saturation pressure (P_0) at 0 °C. In this case, only OSC and SDC biochars present a close microporosity inaccessible to N_2, thus the micropore volume $W_0(N_2) < W_0(CO_2)$ and the surface area (S_{BET}) is low in both cases (around 100 m^2/g). On the contrary, for both synthesized and commercial activated carbon samples, $W_0(N_2) > W_0(CO_2)$, denoting that physical activation develops the porosity, avoiding diffusional restriction of N_2 and also favoring the adsorption in larger micropores. Nonetheless, the narrowest microporosity – $W_0(CO_2)$ – varies only slightly. Activation leads to a significant increase of the surface area, reaching a value close to 800 m^2/g for OSC-AC. When comparing OSC-AC and SDC-AC supports it is noticeable the similarities in total porosity (V_T = 0.39 cm^3/g). Nonetheless, the formation of more opened porosity, wider

micropores, and greater mesoporosity is favored in the latter, and thus, despite the similar total pore volume, the surface area value is significantly smaller (565 m^2/g). The highest porosity is obtained after the chemical activation of OS, which strongly favors the formation of a large micropore volume. This well-developed microporosity leads to higher surface area values (*ca*. 1000 m^2/g). Both commercial activated carbons are also eminently microporous samples: N sample shows similar porous characteristics as compared to OS-AC/KOH support, and sample M is comparable with OSC-AC.

Table 7.3 pH_{pzc} and textural characteristics of supports and corresponding catalysts.

Sample	pH_{pzc}	S_{BET} (m^2/g)	W_0 (N_2) (cm^3/g)	L_0 (N_2) (nm)	W_0 (CO_2) (cm^3/g)	V_{meso} (cm^3/g)	V_T (cm^3/g)
OSC	10.3	136	0.06	n.a.	0.17	0.08	0.17
OSC-Fe	2.2	10	0.01	n.a.	0.16	0.03	0.04
OSC-AC	10.6	792	0.33	1.2	0.20	0.04	0.39
OSC-AC-Fe	2.4	546	0.23	1.4	0.13	0.05	0.30
OS-AC/KOH	8.3	1013	0.43	1.7	0.18	0.09	0.55
OS-AC/KOH-Fe	2.0	526	0.23	2.0	0.17	0.08	0.33
SDC	11.5	82	0.04	n.a.	0.11	0.08	0.14
SDC-Fe	4.2	9	0.00	n.a.	0.10	0.02	0.03
SDC-AC	10.7	565	0.24	1.6	0.15	0.10	0.39
SDC-AC-Fe	3.2	176	0.08	n.a.	0.12	0.10	0.21
N	11.6	1058	0.44	1.6	0.21	0.08	0.55
N-Fe	2.4	777	0.33	1.7	0.23	0.07	0.42
M	7.0	831	0.35	1.5	0.25	0.07	0.44
M-Fe	1.9	663	0.28	1.6	0.22	0.06	0.36

After Fe-impregnation, all catalysts present a smaller porosity than the corresponding supports because Fe-nanoparticles are partially blocking or occupying this porosity (Fig. 7.3). Such blockage affects mainly the microporosity range (which is blocked and not accessible to N_2), thus increasing the mean pore size L_0 on all catalysts regarding their corresponding supports. Fe-nanoparticles seem to be located mainly on the larger micropores, but the porosity larger than 1.5–2.0 nm is preserved (Fig. 7.3). This fact is corroborated by the strong decrease of W_0 values

after impregnation of supports with large micropores, particularly for OS-AC/KOH and SDC-AC. Due to the low micropore volume and large micropore size of SDC-AC, microporosity is practically blocked in the obtained SDC-AC-Fe, thus showing the lowest S_{BET} of catalysts derived from activated supports. Consequently, the support's porous attributes also define the characteristics of the Fe-active phase in the catalysts derivatives. The acid/basic character of the samples is discussed based on their pH_{pzc} values (Table 7.3). The pH_{pzc} of the supports range from 7.0-11.6, being consequently basic materials. However, after impregnation with the Fe-active phase, catalysts become acidic materials.

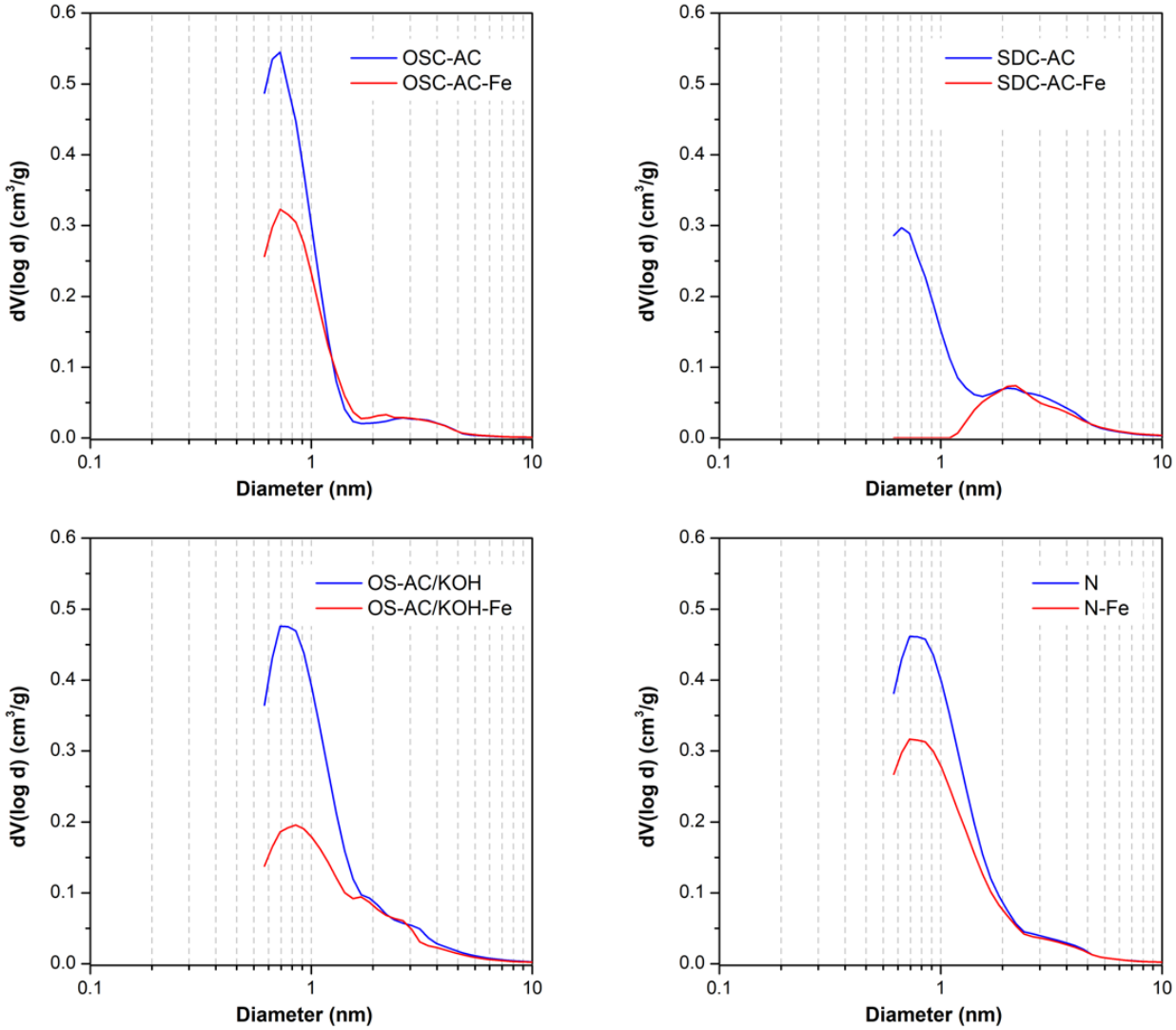


Fig. 7.3 Pore size distribution obtained by QSDFT applied to N_2-adsorption isotherms for selected activated carbon supports and Fe-derivative catalysts: effect of Fe-impregnation.

Nature and dispersion of the Fe-active phase were analyzed by the combination of HRSEM and HRTEM-EDX analysis, XRD, and XPS techniques. After impregnation, as expected, catalysts

maintain the same morphology as previously described, but it is clearly observed the formation of a high concentration of new nanoparticles coating the carbon surface (Fig. 7.4).

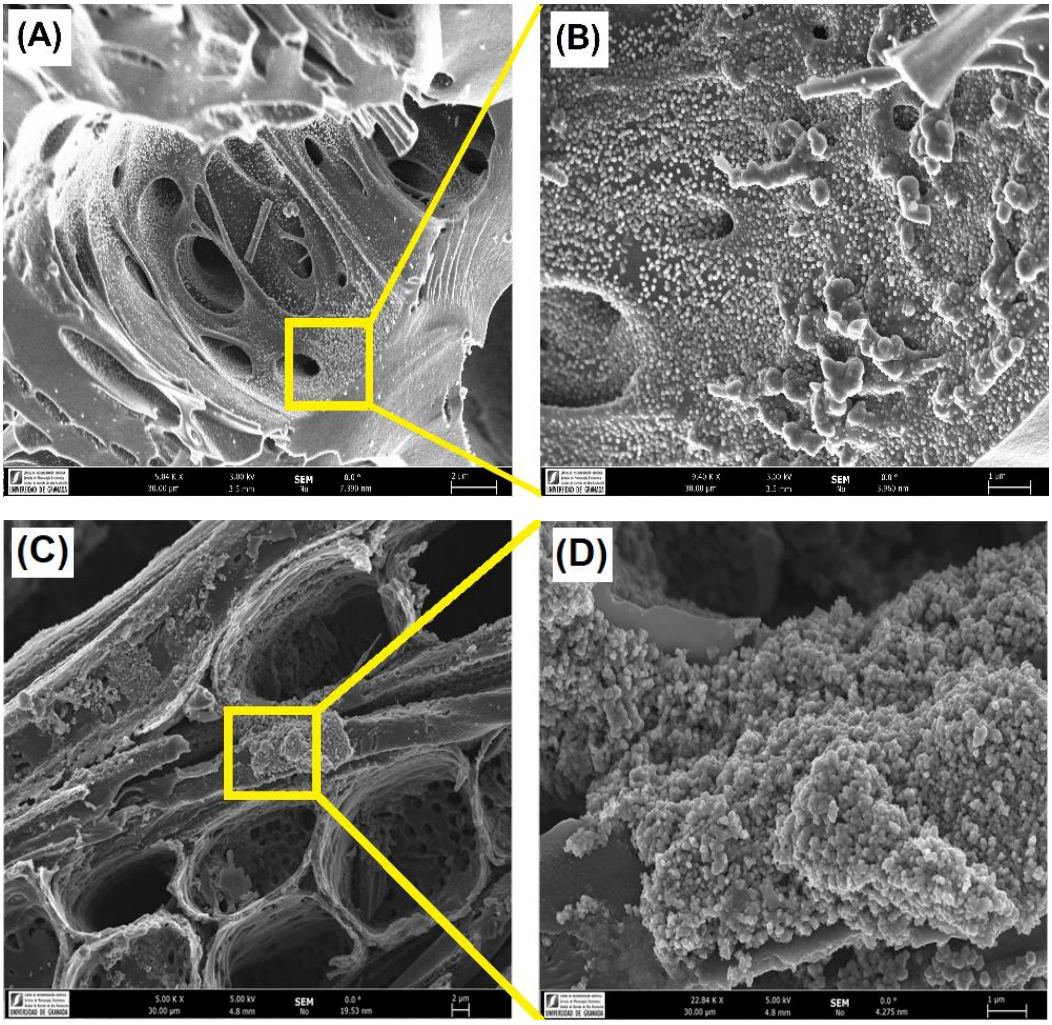


Fig. 7.4 Morphology of (A) OSC-AC-Fe, and (C) SDC-AC-Fe; (B, D) detail of Fe-nanoparticles coating the carbon surface.

The XRD patterns presented in Fig. 7.5 point out that iron nanoparticles are transformed into oxides after pretreatment of the impregnated samples. Basically, hematite, α-Fe_2O_3 (JCPDS card no. 79-0149) is detected, although magnetite, Fe_3O_4 (JCPDS card no. 79-0149) was also identified in a minor proportion. X-ray diffraction patterns also show two broad peaks for all catalysts at 2θ values around 26° and 44° (JCPDS card no. 89–8487), corresponding to the (002) and (101) diffraction peaks of graphite, respectively. No significant differences were noticed between the nanocrystal sizes of such Fe-phases among the catalysts, being in all cases between 19–23 nm (as obtained from the Scherrer equation – Eq. (3.5)). Although Fe-particles were detected by HRSEM on the samples' surface, it is also expected the formation of smaller

nanoparticles which can be located into the porosity, as previously denoted by textural characterization.

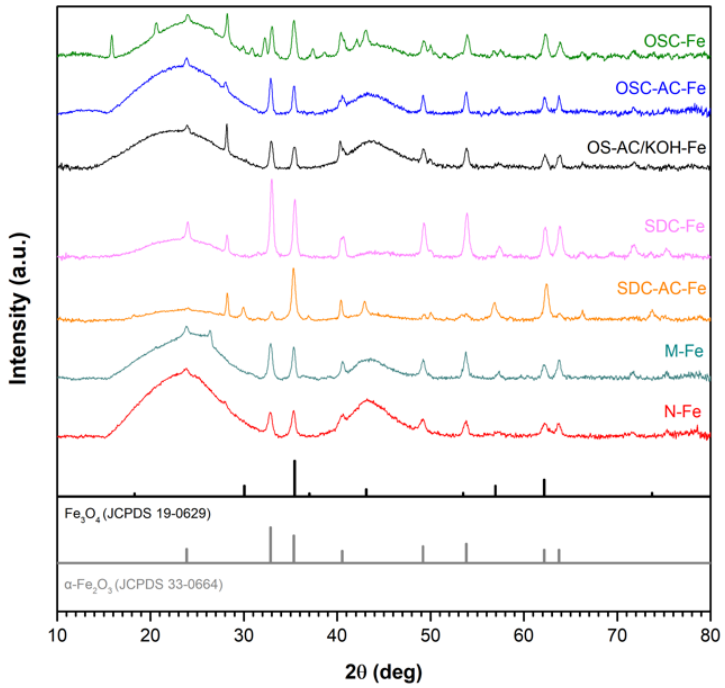


Fig. 7.5 XRD patterns of the catalysts tested; standard patterns of Fe_3O_4 and α-Fe_2O_3 (JCPDS cards no. 19-0629 and 33-0664, respectively) are also presented.

HRTEM images (Fig. 7.6) show heterogeneity in both size and distribution of iron particles. Differences are based on the distinct interactions of the aqueous precursor's solutions with the supports. The distribution of Fe-nanoparticles on physically activated biochars and commercial N-support is very heterogeneous, with particle sizes ranging from very small particles of a few nanometers to large ones exceeding 100 nm, responsible for the XRD peaks. Additionally, in some cases, the morphology of the Fe-particles changed from dense units with a high contract to "cloud" shape structures. In the case of chemically activated OS, however, the distribution, shape, and good contrast of Fe-particle size (at around 50 nm) are quite homogeneous.

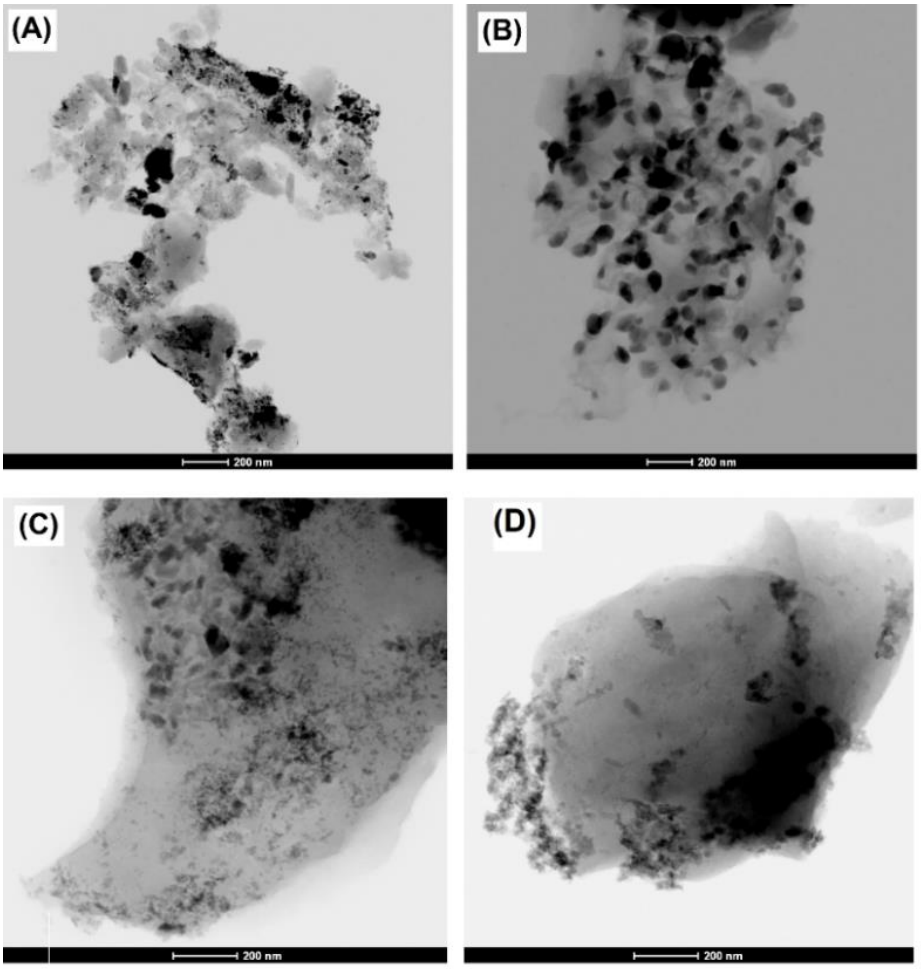


Fig. 7.6 HRTEM images of (A) OSC-AC-Fe, (B) OS-AC/KOH-Fe, (C) SDC-AC-Fe, and (D) N-Fe catalysts.

The catalysts' surface composition obtained by XPS is summarized in Table 7.4. The surface Fe-content is higher in the SD series than in the OS one and increased from carbonized to activated samples in both situations, thus also confirming that the opened porosity enhances the Fe-dispersion and/or the localization of the Fe-nanoparticles in a more external surface accessible to the XPS analysis. The surface oxygen content increased with the Fe-content (Fig. 7.7), though the slope of this line is around 2.5, greater than the O/Fe for any possible oxides (1.5 for Fe_2O_3 and 1.33 for Fe_3O_4) because the determined oxygen content evidently included the oxygenated surface groups of the carbon supports. The analysis of a catalyst after an oxidative reaction (denoted as "OSC-AC-Fe used") shows a similar Fe-content to the analogous "fresh" one, denoting that the Fe-leaching is not significant in this sample. Nevertheless, the oxygen content strongly increased, indicating the oxidation of the carbon surface by H_2O_2 during the reaction or the adsorption of pollutants (or their oxidation intermediates) on the catalyst surface. In fact, this increased oxygen content in activated carbons was also determined when used in catalytic wet air oxidation (CWAO) of aniline [14].

Table 7.4 Atomic surface composition determined by XPS analysis of the prepared catalysts.

Catalyst	Atomic content (%)				
	C	O	N	Fe	Others
OSC-Fe	91.5	7.2	0.3	0.8	0.2
OSC-AC-Fe	88.5	9.6	0.2	1.6	0.1
OSC-AC-Fe (used)	75.8	20.8	1.5	1.9	-
OS-AC/KOH-Fe	86.9	10.7	0.4	1.7	0.3
SDC-Fe	80.8	13.7	-	2.4	3.1
SDC-AC-Fe	77.5	15.7	0.7	4.6	1.5
N-Fe	76.2	17.4	0.3	4.2	1.9
M-Fe	89.8	8.0	0.3	1.8	0.1

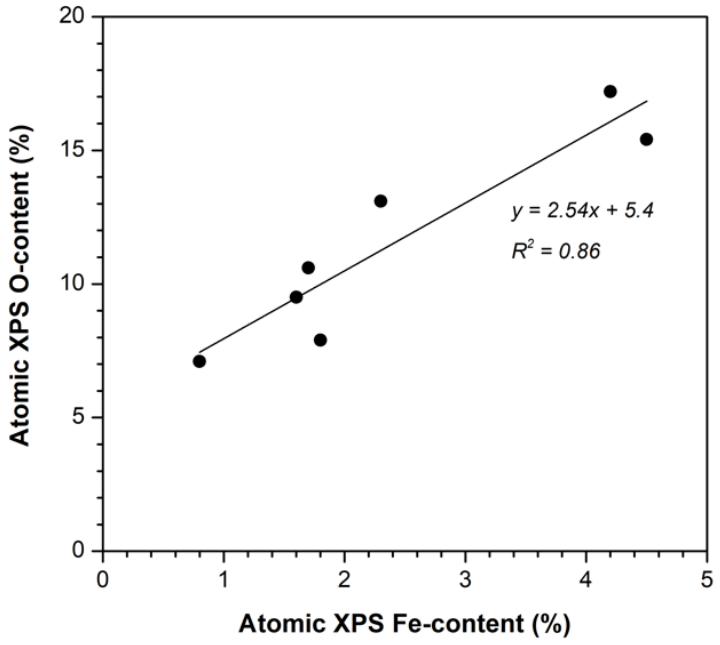


Fig. 7.7 Relationship between the surface Fe and O atomic contents (%) for all the prepared catalysts.

The different high resolution XPS spectral regions (C1s, O1s, and Fe2p) were treated to obtain the surface chemistry composition and results are summarized in Table 7.4 and Table 7.5.

Table 7.5 Distribution of oxygen and iron species on the catalysts surface.

Peak (eV)	**OSC-Fe**	**OSC-AC-Fe**	**OSC-AC-Fe (used)**	**OS-AC/KOH-Fe**	**SDC-Fe**	**SDC-AC-Fe**	**M-Fe**	**N-Fe**
O1s				*Area %*				
Fe–O (530.1)	12	20	8	20	37	35	34	30
C=O (531.6)	58	48	33	43	43	44	30	27
C–O (533.2)	30	32	59	37	20	21	36	43
$Fe2p_{3/2}$				*Area %*				
Fe^{2+} (709.9)	13	22	29	25	29	23	27	20
Fe^{3+} (710.9)	30	45	32	40	28	37	36	41
Fe^{3+} (712.0)	34	19	18	18	28	17	19	21
Fe^{3+} (713.0)	13	10	16	15	9	12	13	11
Fe^{3+} (714.1)	10	4	5	2	6	11	5	7

The Cs1 spectra were fitted using four components [15,16]. The first component at 284.6 eV is used as a reference, and is due to aliphatic and aromatic C–C bonds, while the rest of the components were assigned to carbon forming oxygen functionalities: single C–O bonds (285.7 eV), double C=O bonds (286.8 eV) and O=C–OH carboxylic structures (288.4 eV). The proportion of carbon linked to oxygen increased from chars to their derivative activated carbons due to the surface oxidation by CO_2–treatment (e.g., C–C contribution at 284.6 eV decreased from 71 to 66% in OSC-Fe and OSC-AC-Fe, respectively – Fig. B.2). The oxygen content (Table 7.4) also increased but, as previously commented, due to the greater Fe-surface content. The distribution of oxygenated surface groups (OSG) is more clearly pointed out by analyzing the O1s spectral region (Fig. 7.8, Table 7.5). In this case, three components were used, being the first one located at 530.1 eV and assigned to the Fe–O bonds [17,18], clearly differentiated in the O1s profile by important shoulder at this binding energy that in some cases increased to an independent maximum. The other two components located at 531.6 and 533.2 eV are assigned to the OSG on the carbon surface, double C=O and C–O bonds, respectively [15,16]. Broadening of the peak at around 531 eV is suggested to be due to the interactions of the Fe-nanoparticles with the OSG of the carbon supports, forming Fe–O–C bonds [18,19].

As previously mentioned, the surface composition determined by XPS indicated that Fe-leaching was not significant for the OSC-AC-Fe catalyst during the reaction. Nevertheless, the oxygen

content strongly increases, and the analyses of oxygen nature (Fig. 7.8, Table 7.5) pointed out that this was due to the oxygen linked to carbon (either to the carbon supports or the adsorbed species). The Fe–O ratio decreased from 20 to 8%, highly increasing the proportion of the C–O bonds, likely indicating the adsorption of phenols (C–OH) and their derivatives. It is noteworthy the higher contribution of oxygen linked to iron (Fe-O) in catalysts supported on commercial and SD-derived supports regarding those supported on OS-derived supports, clearly related also with the higher surface Fe-content of these samples (Table 7.4), induced by a more opened porosity (as previously stated).

To determine the chemical state of the surface iron, the Fe2p spectral region was fitted with five components (Fig. 7.9), according to the procedure of McIntyre [20]. This region presents a similar profile for all catalysts. The peak maximum in this region is fixed at 710.9 eV with a full width half maximum (FWHM) value of 1.4 eV, that together with the Gupta and Sen (GS) multiplets at 711.9, 713.0, and 714.1 eV, with FWHM = 1.2 eV, were assigned to Fe^{3+} species [17,18,21], whilst the component located at 709.9 eV corresponds to the Fe^{2+} ones. Except for the OSC-Fe catalyst, which exhibits a lower Fe^{2+} content, the remaining samples present a quite similar Fe^{2+}/Fe^{3+} ratio, which is in agreement with the XRD results, showing the preferential formation of Fe_2O_3-particles. Nevertheless, it is noteworthy that the Fe^{2+} content is in general significantly high, suggesting the possibility of the formation of non-crystalline phases of partially reduced oxides, including magnetite (Fe_3O_4), detected as a minority phase by XRD.

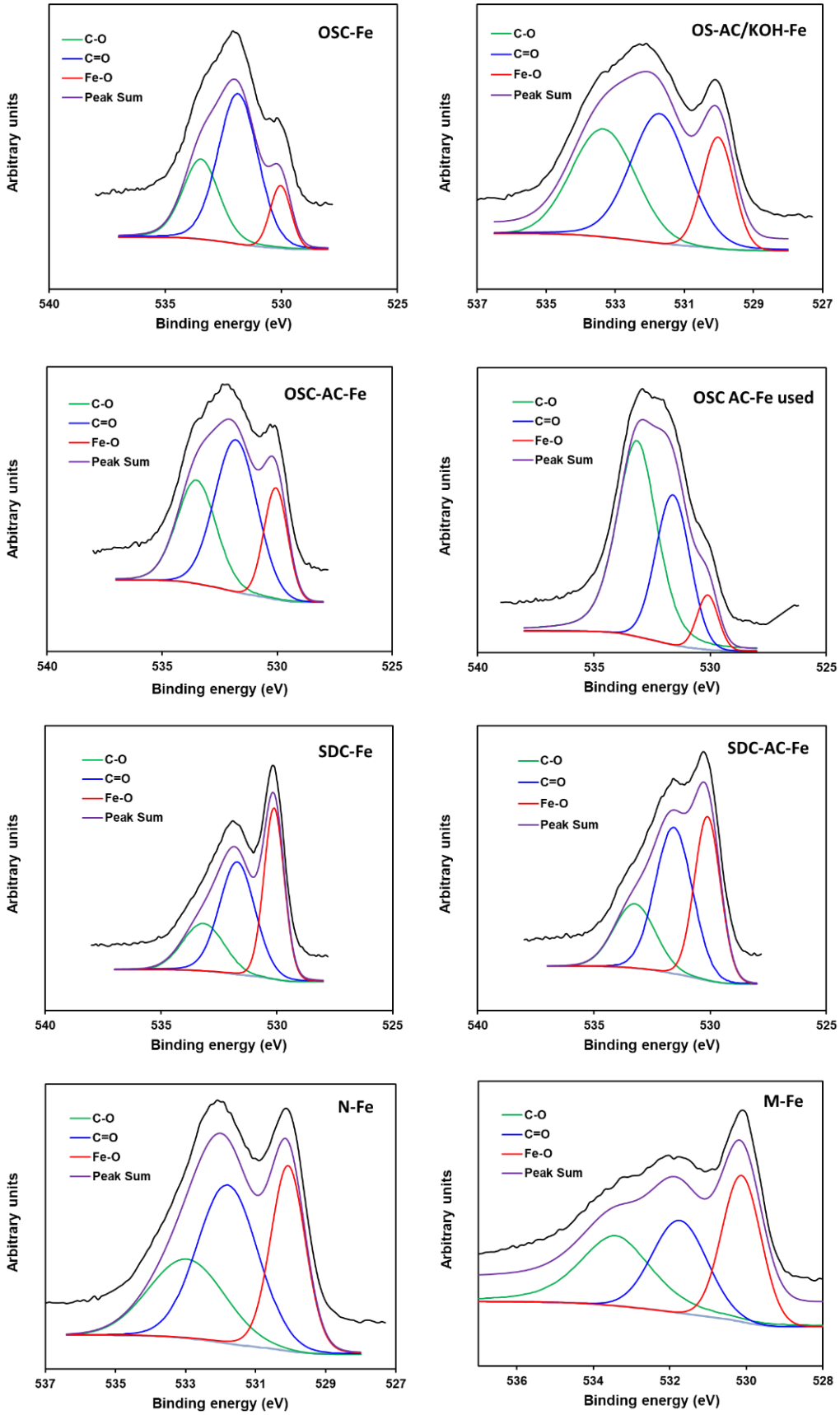


Fig. 7.8 O1s XPS spectral region of the different catalysts.

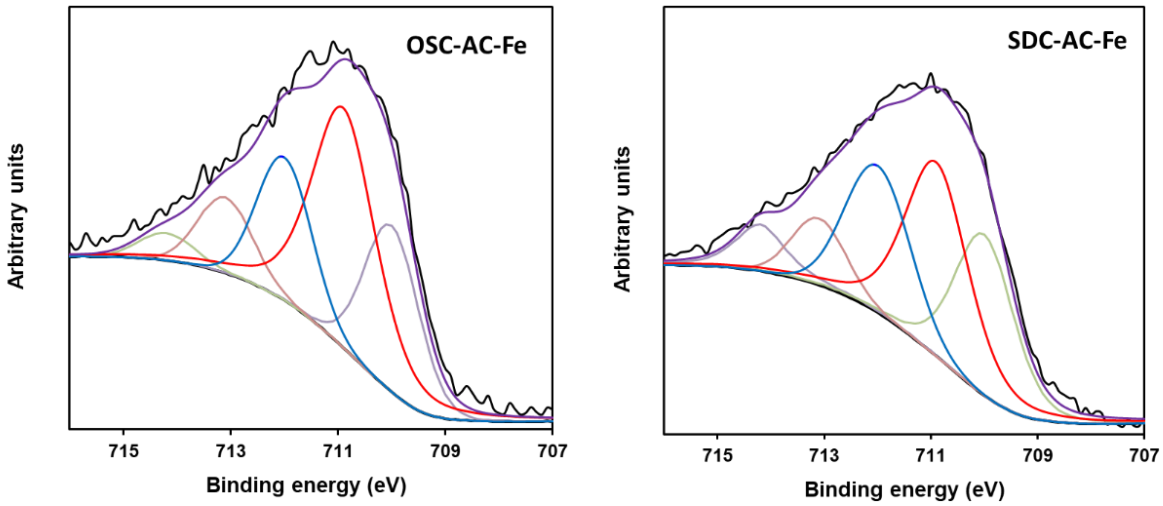


Fig. 7.9 Fitting the Fe2p$_{3/2}$ spectral region of OSC-AC-Fe and SDC-AC-Fe.

7.3.2. Treatment of simulated OMW

The CWPO of OMW was studied. In order to estimate the influence of the adsorptive character of the catalysts in the CWPO process, experiments in the absence of H_2O_2 were carried out in such a way that the pollutant removal obtained in each case is evidently only due to the adsorption phenomena. The performance of the catalysts in the removal of TPh by adsorption and catalytic processes is summarized in Fig. 7.10a.

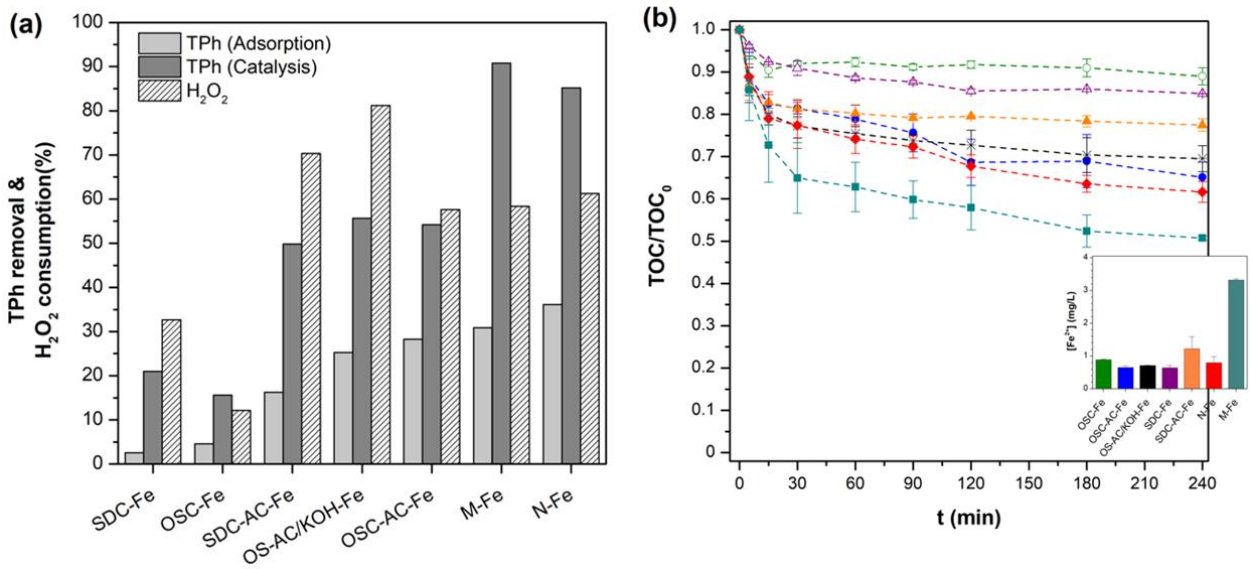


Fig. 7.10 (a) TPh removal efficiencies by adsorption and catalytic processes, and H_2O_2 consumption for each catalyst after 4 h of reaction; (b) evolution of TOC conversion as a function of reaction time for CWPO experiments (inset: mean Fe-leaching values after the reaction).

Using catalysts prepared on the biochar supports OSC and SDC results in low adsorption of pollutants from the initial mixture (below 5% of total phenolic content). When using catalysts

prepared from activated supports, adsorption is still low for the SD-AC-Fe catalyst because, as previously shown, microporosity is practically blocked after Fe incorporation, resulting in a TPh removal of 16% after 240 min. Using OS-AC/KOH-Fe and OSC-AC-Fe, higher removals were achieved by adsorption (25% and 28%, respectively) because both catalysts present a similar surface area (*ca*. 550 m^2/g – Table 7.3). In the case of the commercial supports based catalysts, both M-Fe and N-Fe achieved the highest adsorptive performance of pollutants after 4 h, with *ca*. 31 and 36%, respectively. Individual contaminants' removal by adsorption (C/C_0) over time for each catalyst is reported in Fig. B.3.

Regarding CWPO experiments, it was demonstrated that in the absence of any catalyst and under the same experimental conditions reported hereafter, the degradation of contaminants by H_2O_2 alone is negligible (Fig. B.4, Appendix B), due to the low oxidation potential of hydrogen peroxide. Fe-catalysts prepared from biochar OSC and SDC supports exhibited the lowest removal of TPh (Fig. 7.10a). Nonetheless, while OSC-Fe is slightly more effective as an adsorbent, SDC-Fe is more active in CWPO, associated with the more developed porosity of the first (Table 7.3) and the higher surface iron-content of the second (Table 7.4). This points out the importance of a developed porosity and accessible Fe-nanoparticles. In this sense, the catalytic performance also improved using activated supports because physical or chemical activation of residues improves both factors. Therefore, the better performance of catalysts supported on commercial activated carbons is due to their higher surface area and surface Fe-content.

While TPh removal values show good coincidence with TOC ones in adsorption experiments, both parameters present differences in the oxidation runs due to the formation/adsorption of intermediate/final reaction products. In Fig. 7.10b, catalysts' performance over time in the CWPO process are compared in terms of mineralization. Although the same order of activity is generally observed, being M-Fe catalyst the most active with *ca*. 50% total reduction in TOC, it is observed a very similar performance of OSC-AC-Fe and OS-AC/KOH-Fe catalysts in respect to the N-Fe one. As observed in Fig. 7.10a, the adsorptive capacity of such materials is quite similar, while TPh removals achieved with N-Fe are considerably higher, suggesting the formation of a significant amount of intermediates that remain in solution during the synthetic OMW treatment with such catalyst.

The concentration of Fe dissolved in solution (in mg/L) after the CWPO runs was also analyzed and the mean values for each catalyst are reported in the inset graph of Fig. 7.10b. The Fe-leaching of M-Fe is around four times greater than the values obtained when Fe is supported

on biochars or activated carbons from the olive oil industry's residues. Thus, despite M-Fe seems to be at a glance the most active material of this series, it can be related to the higher activity of Fe in solution, where it can work as a homogeneous rather than a heterogeneous catalyst. The lack of stability is evidently a significant hindrance regarding the catalyst's life and possible reuse. Moreover, the leaching of metal ions to the solution has to be avoided to prevent additional contamination and respect environmental legislation (maximum of 2 mg/L in EU directives [22]). With the exception of the aforementioned material, the leaching of iron was typically below 1 mg/L for the remaining materials, which corresponds to <1.5% of the initial theoretical Fe load in the catalysts, indicating a strong supporting of the metal to the carbon surface. To check the influence of the homogeneous Fenton process in the mineralization efficiency, two experiments in the homogeneous phase were performed using Fe concentrations corresponding to the average minimum and the maximum observed for this series of catalysts. It was found that 1 mg/L of Fe is only able to remove *ca*. 6% of TOC, whilst 3.5 mg/L results in *ca*. 20% mineralization after 240 min (results not shown).

The removal of each phenolic compound along adsorption and CWPO processes was followed by HPLC – full details are provided in Fig. B.3 and Fig. B.5 of Appendix B, respectively. Fig. 7.11 shows, as an example, the comparison of performances for synthesized OSC-AC-Fe and N-Fe catalysts in adsorptive and catalytic experiments. It is observed the occurrence of preferential adsorption of caffeic and gallic acids regarding the tyrosol, vanillic or protocatechuic acids. This behavior is common for all the catalysts prepared and tested in this study. After 240 min of CWPO reaction, both catalysts showed a similar TOC/TOC_0 ratio of 0.65 and 0.62, respectively, although the oxidation of each compound is evidently distinct. Results also showed that the oxidation of each compound is related with the previous adsorption process, highlighting the dependence on the pollutant/catalyst surface interaction, as they follow the same degradation order.

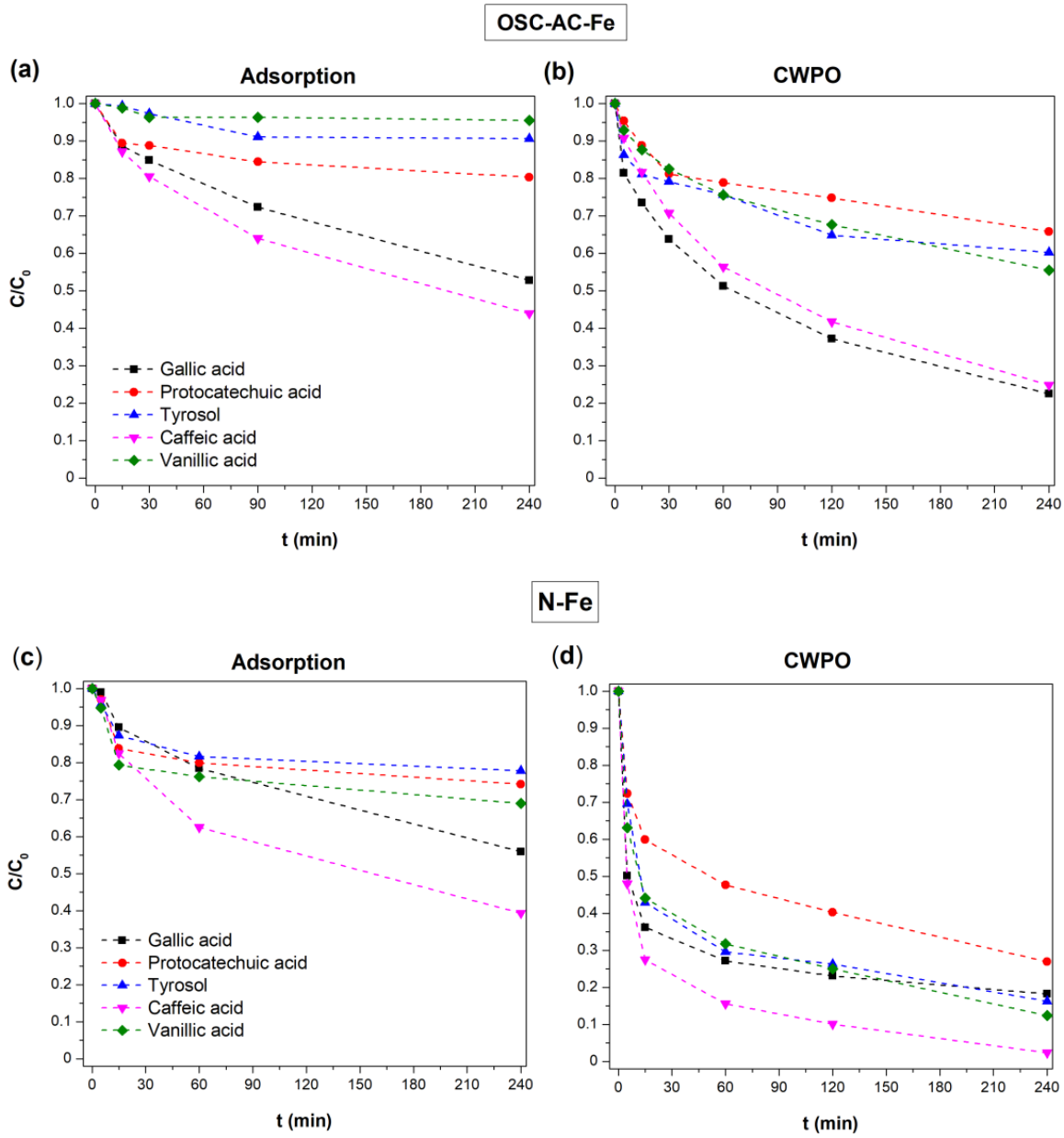


Fig. 7.11 Comparison of phenolic compounds' removal by adsorption or CWPO using OSC-AC-Fe and N-Fe catalysts.

The interactions of phenolic compounds with the catalysts surface are dependent on the catalysts porous structure (determining diffusion, adsorption rate and adsorption capacity) but also on the chemical interactions between pollutants and the adsorbent's surface, thus, on the nature and distribution of the surface chemical groups on the catalysts and the chemical structure of phenols. The main role of the porous texture of the catalysts on their adsorptive and catalytic performance is highlighted in Fig. 7.12.

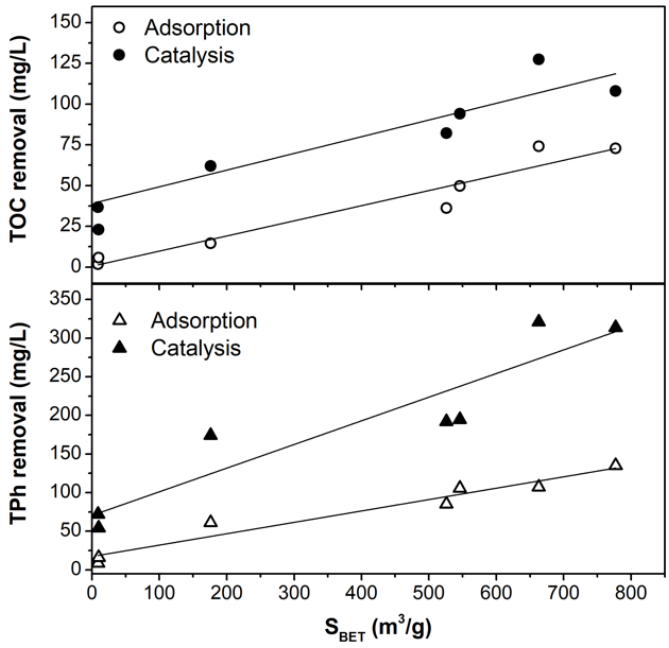


Fig. 7.12 Influence of the specific surface area (S_{BET}) on the TPh and TOC removals by adsorption and catalysis (in mg/L).

In previous works, it was demonstrated that carbon materials' adsorption of phenols is related to parameters such as their solubility in water [23]. Nonetheless, results in this study show that caffeic and vanillic acids, which present similar solubility (Table B.1), exhibited opposite adsorption behavior (Fig. 7.11). Also, the affinity of different phenols by the carbon's surface varies according to the nature of the aromatic rings' substituents [24]. Adsorption of phenols is favored by the basic character of the adsorbent and by the withdrawing effect of substituents. Electron withdrawing groups from the aromatic rings such as halogens (–X) or nitrites ($–NO_2$) enhance adsorption regarding electron donor groups such as hydroxyl (–OH) or amino ($–NH_2$) substituents [24]. Different positions were therefore activated on the aromatic rings depending on the substituents' nature and position, also determining the reactivity and degradation mechanism in Fenton reactions [25]. Iron species can also induce various chelation degrees with the different phenolic acids [26]. Results showed that hydroxycinnamic acids (in our case the caffeic acid) are typically better ligands for iron than the hydroxybenzoic ones (gallic, vanillic, or protocatechuic acids). The ethylene group between the aromatic ring and the carboxylic group in hydroxycinnamic acids influence not only the chelating activity but can also work as a scavenger, preventing free radical reactions. Regarding the hydroxybenzoic acids, the number and position of hydroxyl groups also influence the chelating effect and the galloyl moiety improving chelation regarding catechol groups, thus gallic acid is a better chelating agent than the protocatechuic one. The stability of the Fe-phenolic acid complexes was compared by determining their binding

constants [26], with the following order: protocatechuic acid < gallic acid < caffeic acid. Our experimental data showed a preferential removal of caffeic and gallic acids, which can be related to this effect. Nevertheless, specific experiments of characterization of used samples still need to be performed in order to clarify this aspect.

Once the phenolic compounds were adsorbed, the oxidation also depends on the reactivity of each molecule. The electrophilic attack of hydroxyl radicals to phenols' aromatic rings is facilitated by the presence of electron donating groups (EDG), explaining the fact that oxidation of gallic acid (with three EDG) is always higher than the remaining benzoic acid derivatives (vanillic and protocatechuic acids). Previous studies [27] also showed that degradation of cinnamic acid derivatives is generally faster than benzoic acid derivatives, which justifies the high reactivity of the caffeic acid (containing two reactive groups in its structure) observed in this study. S. Azabou *et al*. [28] reported on the catalytic photo-oxidation of a phenolic mixture containing, among others, tyrosol, vanillic and caffeic acids. Under the experimental conditions employed in that work, the degradation yield of caffeic acid (86%) was higher than vanillic acid (50%) and tyrosol (31%), also proceeding at a faster oxidation rate than the last two, which is also observed as a trend in our study.

The degradation profiles of contaminants by Fe-AC based catalysts (Fig. 7.10b, Fig. 7.11b, d), also point to a two-stage process, characteristic of Fenton-related processes, with a very fast initial oxidation of organics up to t = 15–30 min followed by a slower degradation rate, likely associated to the Fe regeneration cycle [29]. The catalytic oxidation of the phenolic solution is accompanied by the formation of reaction intermediates, namely carboxylic acids and also their complexes with iron ions [8], to greater or lesser extent depending on the physicochemical properties of the catalysts used. Such reaction intermediates are commonly responsible for the drop of the solution pH [6], which was also observed on all runs (from $pH_0 \approx 3.8$ to 3.0–3.4, depending on the catalyst – data not shown). Oxalic acid was identified as the main reaction intermediate in solution after the treatment, while oxamic and maleic acids were also identified in some cases but in a smaller proportion (data not shown).

High TOC removal and efficient H_2O_2 conversions are indispensable for assessing any catalyst's performance in the CWPO process. Conversions of H_2O_2 (%) are displayed in Fig. 7.10a, while the oxidant consumption (mg/L) for each catalyst *vs*. the correspondent TOC removal is plotted in Fig. 7.13.

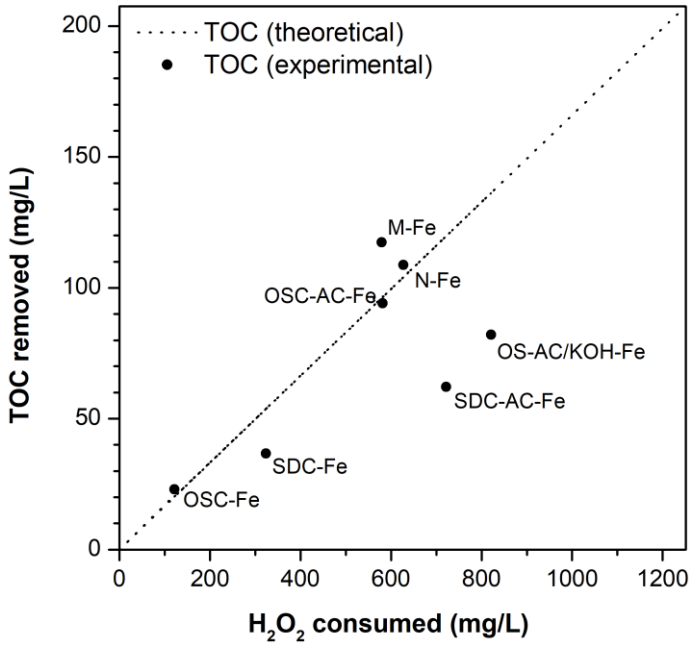


Fig. 7.13 H_2O_2 consumed *vs*. experimental and theoretical TOC removals for each catalyst.

The plot of H_2O_2 conversion *vs*. TOC removal shows that OSC-AC-Fe presents one of the highest oxidant use efficiencies among the catalysts obtained using supports prepared from activated residues (the highest was obtained using OSC-Fe, but mineralization is very low). The performance of this catalyst is similar to those obtained using the commercial support N-Fe and M-Fe. In comparison, this catalyst presents a surface area and surface iron content similar to OS-AC/KOH-Fe, but a narrowest microporosity and more heterogeneous Fe-particles distribution. Compared with SDC-AC-Fe, OSC-AC-Fe exhibits a larger surface area but smaller surface iron content (Table 7.3 and Table 7.4). Owning to the complexity and diversity of processes occurring simultaneously, but also on the physicochemical heterogeneity among the materials tested, it is virtually impossible to correlate them with all the results obtained. In that sense, the lower H_2O_2 consumption efficiencies of some materials may be related to the fast scavenging of •OH radicals and/or non-selective decomposition of the oxidant by bulk Fe-oxides and hydroxides, as already reported by other authors [30]. Moreover, it is also well-known the ability of carbon materials to catalytically decompose H_2O_2 molecules via different routes, even in the absence of any transition metal [31], for which the real yield of •OH radicals generated may vary according to the intrinsic properties of each material.

The level of toxicity and biodegradability of OMW is commonly related to the amount of TPh present in solution [9]. Toxicity values were evaluated following the inhibition (%) caused to the bioluminescent *V. fischeri* bacteria when in contact with the phenolic solutions (contact times of

5, 15, and 30 min). The initial untreated effluent presented 99% bioluminescence inhibition after only 5 min of contact time, clearly denoting its toxic character towards these bacteria. A relation between the amount of TPh removed from each solution (by each catalyst) after the CWPO process and V. fischeri inhibition (after 30 min) was established (Fig. 7.14). As anticipated, the highest toxicity reduction was achieved by N-Fe and M-Fe catalysts (only 19 and 11% bioluminescence inhibition, respectively), related to the higher TPh oxidation achieved by those catalysts. Nonetheless, more than 60% of the initial toxic character of the phenolic solution was eliminated using Fe-catalysts prepared from physically activated olive stones (OSC-AC-Fe), whilst 56 and 44% reductions were achieved by OS-AC/KOH-Fe and SDC-AC-Fe catalysts, respectively.

As previously mentioned, the formation of reaction intermediates, potentially more refractory than the original ones, is a major drawback related to AOP applications. However, the correlation obtained between the toxicity values of the treated effluent samples and the removal of initial pollutants clearly suggest that, despite the formation of intermediates, they exhibit a nontoxic behavior or, at least, less toxic than the original pollutants.

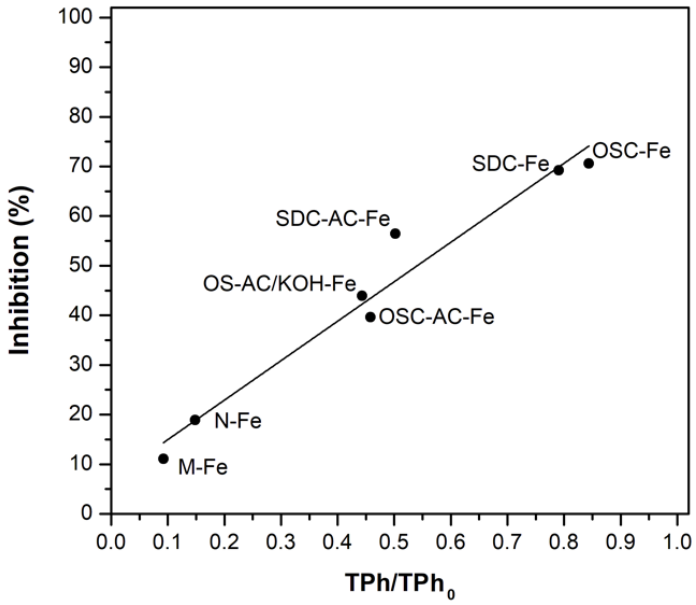


Fig. 7.14 TPh/TPh_0 *vs*. inhibition (%) of the *V. fischeri* bacteria after 30 min in contact with the different solutions after CWPO.

7.3.3. Further considerations

This study presents an approach with double interest for the olive oil sector, combining the valorization and integration of solid residues in the management of wastewaters generated by

this industry, resulting in a more environmentally friendly process. However, it is primarily focused on a particular category of refractory pollutants that comprise the overly-complex physicochemical character of olive mill wastewaters. The reduction of the phenolic content of OMW (and thus its overall toxic character), whilst unveiling the specific interaction of those contaminants with the synthesized materials, is the first step to understanding and improving catalysts' synthesis for such applications.

As reported, the proposed process is clearly able to degrade a broad range of phenolic contaminants and thus reduce the toxicity of the treated effluent. Evidently, the application of the proposed process to more complex wastewater matrixes would require the optimization of the operational conditions – e.g., range of pH operation, temperature, and particularly H_2O_2 and catalyst concentrations – depending on the specific treatment requirements. In fact, the efficiency of most AOPs is often improved by the integration of pre- and post-treatment units in a multi-step treatment scheme. Simple but finely tuned physicochemical steps, such as coagulation/flocculation or filtration processes, will considerably reduce costs associated with subsequent treatment stages and improve the overall efficiency of the process. Likewise, the oxidation of recalcitrant compounds and overall mineralization of organics would favor the action of microorganisms in a subsequent (downstream) biological treatment unit, or even allow its discharge on crops or wastewater collectors (provided the compliance with local discharge environmental regulations).

In that sense, and despite the limitations of CWPO processes related to catalysts' deactivation through Fe-leaching and costs associated with H_2O_2 consumption (that will depend on the degree of oxidation required), the equipment simplicity, easy-to-handle reagents, and operational conditions required (atmospheric pressure and room temperature) clearly favors the application of CWPO when compared to more energy-demanding processes (e.g., ozonation, catalytic wet air oxidation) or ones limited by the dark color of OMW (e.g., photocatalysis).

In order to enhance the stability of the proposed materials and improve the process's efficiency, ongoing studies are focused on the catalysts' synthesis, to improve the Fe-dispersion and anchorage to the prepared supports, as well as their application to more complex wastewater matrixes, such as pre-treated or diluted real OMW. Then, optimized materials will be tested under a wider range of experimental conditions, including different reactor configurations, particularly operating under conditions closer to continuous operation (e.g., packed-bed column reactor,

continuous stirred tank reactors). If efficient materials are developed, a detailed techno-economic analysis should be done, and effluents characteristics compared with legislated standards.

7.4. CONCLUSIONS

Fe-catalysts were prepared by direct impregnation of biochars and activated carbons obtained from sawdust (tree pruning) and olive stones by combining carbonization with chemical or physical activation processes to yield a similar activation degree. The physicochemical properties of these materials depend on the raw residue and experimental conditions of synthesis. Thus, the synthetized Fe-AC catalysts are essentially microporous materials with BET surface areas ranging from 176–777 m^2/g and with a high concentration of more or less spherical Fe-nanoparticles (mainly as α-Fe_2O_3), covering the carbonaceous surface of the materials, partially blocking or occupying the microporous structure, in particular for supports obtained from sawdust pruning.

Adsorptive and catalytic screening tests of a polyphenolic solution simulating the OMW showed the importance of the porous structure of the materials, which controls the accessibility of phenolic compounds to Fe-active sites and therefore not only the adsorption capacity of the pollutants, but also the catalytic performance. Both TPh removal and the mineralization degree (TOC) increased linearly with increasing the surface area of the catalysts. Thus, ACs showed an enhanced adsorptive and catalytic behaviors regarding the corresponding biochars.

On the other hand, caffeic and gallic acids were preferentially adsorbed and oxidized from solution regardless the catalyst used, either by the higher chelating activity of Fe towards such compounds, and/or by the preferential electrophilic attack of hydroxyl radicals to the phenol's aromatic rings. Under the experimental conditions tested, the greater TPh removal efficiencies were achieved using M-Fe and N-Fe catalysts prepared from commercially available AC supports, reaching 92% for M-Fe. Nonetheless, Fe leaching values in this case was *ca*. 3.5 mg/L (corresponding to >5 wt.%), which leads to the inevitable contribution of the homogeneous process and catalyst's deactivation. In the case of N-Fe, the TOC mineralization degree was significantly lower than the TPh removal which indicates the formation of refractory intermediates. Using Fe-AC catalysts derived from agricultural wastes, the total phenolic content oxidation ranged from 50–56%, but catalysts showed an improved stability and favored the total mineralization of pollutants.

The toxicity of the solutions decreased linearly with TPh reduction. Among the range of materials prepared from organic residues, the physically-activated olive stone catalyst (OSC-AC-Fe) seems to be the most promising, showing a mineralization degree (TOC) and efficiency in the H_2O_2 consumption comparable to N-Fe and M-Fe catalyst, also reducing the toxicity of the initial solution towards the *V. fischeri* bacteria by >60%. Supports and Fe-active phases are being modified by different activation treatments and/or functionalization to improve specific interactions with OMW pollutants, which demonstrated to control adsorption rate and further oxidation degree.

REFERENCES

1. Galiatsatou, P.; Metaxas, M.; Arapoglou, D.; Kasselouri-Rigopoulou, V. Treatment of olive mill waste water with activated carbons from agricultural by-products. *Waste Manag*. **2002**, 22, 803–812.
2. Stasinakis, A.S.; Elia, I.; Petalas, A. V.; Halvadakis, C.P. Removal of total phenols from olive-mill wastewater using an agricultural by-product, olive pomace. *J. Hazard. Mater.* **2008**, 160, 408–413.
3. Alslaibi, T.M.; Abustan, I.; Ahmad, M.A.; Foul, A.A. Kinetics and equilibrium adsorption of iron (II), lead (II), and copper (II) onto activated carbon prepared from olive stone waste. *Desalin. Water Treat*. **2014**, 52, 7887–7897.
4. Petrella, A.; Spasiano, D.; Acquafredda, P.; De Vietro, N.; Ranieri, E.; Cosma, P.; Rizzi, V.; Petruzzelli, V.; Petruzzelli, D. Heavy metals retention (Pb(II), Cd(II), Ni(II)) from single and multimetal solutions by natural biosorbents from the olive oil milling operations. *Process Saf. Environ. Prot*. **2018**, 114, 79–90.
5. Martins, R.C.; Gomes, T.; Quinta-Ferreira, R.M. Fenton's depuration of weathered olive mill wastewaters over a Fe-Ce-O solid catalyst. *Ind. Eng. Chem. Res.* **2010**, 49, 9043–9051.
6. Nieto, L.M.; Hodaifa, G.; Rodríguez, S.; Giménez, J.A.; Ochando, J. Degradation of organic matter in olive-oil mill wastewater through homogeneous Fenton-like reaction. *Chem. Eng. J.* **2011**, 173, 503–510.
7. Ochando-Pulido, J.M.; Pimentel-Moral, S.; Verardo, V.; Martinez-Ferez, A. A focus on advanced physico-chemical processes for olive mill wastewater treatment. *Sep. Purif. Technol.* **2017**, 179, 161–174.
8. Najjar, W.; Azabou, S.; Sayadi, S.; Ghorbel, A. Screening of Fe-BEA catalysts for wet hydrogen peroxide oxidation of crude olive mill wastewater under mild conditions. *Appl. Catal. B Environ.* **2009**, 88, 299–304.
9. Esteves, B.M.; Rodrigues, C.S.D.; Maldonado-Hódar, F.J.; Madeira, L.M. Treatment of high-strength olive mill wastewater by combined Fenton-like oxidation and coagulation/flocculation. *J. Environ. Chem. Eng.* **2019**, 7, 103252.
10. Alver, A.; Baştürk, E.; Kiliç, A.; Karataş, M. Use of advance oxidation process to improve the biodegradability of olive oil mill effluents. *Process Saf. Environ. Prot.* **2015**, 98, 319–324.
11. Cagnon, B.; Py, X.; Guillot, A.; Stoeckli, F.; Chambat, G. Contributions of hemicellulose, cellulose and lignin to the mass and the porous properties of chars and steam activated carbons from various lignocellulosic precursors. *Bioresour. Technol.* **2009**, 100, 292—298.
12. Miranda, M.; Bica, C.; Nachtigallm, S.; Rehman, N.; Rosa, S. Kinetical thermal degradation study of maize straw and soybean hull celluloses by simultaneous DSC-TGA and MDSC techniques. *Thermochim. Acta* **2013**, 565, 65–71.
13. Alejandro, A.-C.; Lobato-Peralta, D.R.; Arreola-Ramos, C.E.; Martínez-Casillas, D.C.; Pacheco-Catalán, D.E.; Cuentas-Gallegos, A.K.; Arancibia-Bulnes, C.A.; Villafán-Vidales, H.I. Exploring the influence of solar pyrolysis operation parameters on characteristics of carbon materials. *J. Anal. Appl. Pyrolysis* **2019**, 140, 290–298.
14. Morales-Torres, S.; Silva, A.M.T.; Maldonado-Hódar, F.J.; Machado, B.F.; Pérez-Cadenas, A.F.; Faria, J.L.; Figueiredo, J.L.; Carrasco-Marín, F. Pt-catalysts supported on activated carbons for catalytic wet air oxidation of aniline: Activity and stability. *Appl. Catal. B Environ.* **2011**, 105, 86–94.
15. Pérez-Cadenas, A.F.; Maldonado-Hódar, F.J.; Moreno-Castilla, C. On the nature of surface acid sites of chlorinated activated carbons. *Carbon* **2003**, 41, 473–478.
16. Vivo-Vilches, J.F.; Bailón-García, E.; Pérez-Cadenas, A.F.; Carrasco-Marín, F.; Maldonado-Hódar, F.J. Tailoring the surface chemistry and porosity of activated carbons: Evidence of reorganization and mobility of oxygenated surface groups. *Carbon* **2014**, 68, 520–530.
17. Zhang, S.; Li, X. Yan; Chen, J.P. An XPS study for mechanisms of arsenate adsorption onto a magnetite-doped activated carbon fiber. *J. Colloid Interface Sci.* **2010**, 343, 232–238.
18. Saiphaneendra, B.; Saxena, T.; Singh, S.A.; Madras, G.; Srivastava, C. Synergistic effect of co-existence of hematite (α-Fe_2O_3) and magnetite (Fe_3O_4) nanoparticles on graphene sheet for dye adsorption. *J. Environ. Chem. Eng.* **2017**, 5, 26–37.
19. Zubir, N.A.; Yacou, C.; Motuzas, J.; Zhang, X.; Diniz da Costa, J.C. Structural and functional investigation of graphene oxide–Fe_3O_4 nanocomposites for the heterogeneous Fenton-like reaction. *Sci. Rep.* **2014**, 4, 4594.
20. McIntyre, N.S.; Zetaruk, D.G. X-ray photoelectron spectroscopic studies of iron oxides. *Anal. Chem.* **1977**, 49, 1521–1529.
21. Li, X.; Wang, H.; Shao, G.; Wang, G.; Lu, L. Low temperature reduction of NO by activated carbons impregnated with Fe based catalysts. *Int. J. Hydrogen Energy* **2019**, 44, 25265–25275.

22. EEC Council Directive 75/440. European Economic Community; Brussels, **1975**.
23. Liu, J.C.; Huang, C.P. Adsorption of some substituted phenols onto hydrous ZnS(s). *J. Colloid Interface Sci.* **1992**, 153, 167–176.
24. Moreno-Castilla, C.; Rivera-Utrilla, J.; López-Ramón, M. V.; Carrasco-Marín, F. Adsorption of some substituted phenols on activated carbons from a bituminous coal. *Carbon* **1995**, 33, 845–851.
25. Moreno-Castilla, C.; López-Ramón, M.V.; Fontecha-Cámara, M. Ángeles; Álvarez, M.A.; Mateus, L. Removal of phenolic compounds from water using copper ferrite nanosphere composites as Fenton catalysts. *Nanomaterials* **2019**, 9.
26. Andjelković, M.; Van Camp, J.; De Meulenaer, B.; Depaemelaere, G.; Socaciu, C.; Verloo, M.; Verhe, R. Iron-chelation properties of phenolic acids bearing catechol and galloyl groups. *Food Chem.* **2006**, 98, 23–31.
27. Silva, A.M.T.; Nouli, E.; Xekoukoulotakis, N.P.; Mantzavinos, D. Effect of key operating parameters on phenols degradation during H_2O_2-assisted TiO_2 photocatalytic treatment of simulated and actual olive mill wastewaters. *Appl. Catal. B Environ.* **2007**, 73, 11–22.
28. Azabou, S.; Najjar, W.; Gargoubi, A.; Ghorbel, A.; Sayadi, S. Catalytic wet peroxide photo-oxidation of phenolic olive oil mill wastewater contaminants. Part II. Degradation and detoxification of low-molecular mass phenolic compounds in model and real effluent. *Appl. Catal. B Environ.* **2007**, 77, 166–174.
29. Ramirez, J.H.; Duarte, F.M.; Martins, F.G.; Costa, C.A.; Madeira, L.M. Modelling of the synthetic dye Orange II degradation using Fenton's reagent: From batch to continuous reactor operation. *Chem. Eng. J.* **2009**, 148, 394–404.
30. Satishkumar, G.; Landau, M. V.; Buzaglo, T.; Frimet, L.; Ferentz, M.; Vidruk, R.; Wagner, F.; Gal, Y.; Herskowitz, M. Fe/SiO_2 heterogeneous Fenton catalyst for continuous catalytic wet peroxide oxidation prepared in situ by grafting of iron released from $LaFeO_3$. *Appl. Catal. B Environ.* **2013**, 138–139, 276–284.
31. Ribeiro, R.S.; Silva, A.M.T.; Figueiredo, J.L.; Faria, J.L.; Gomes, H.T. The influence of structure and surface chemistry of carbon materials on the decomposition of hydrogen peroxide. *Carbon* **2013**, 62, 97–108.

CHAPTER 8

INTEGRATION OF OLIVE STONES IN THE PRODUCTION OF FE/AC-CATALYSTS FOR THE CWPO TREATMENT OF SYNTHETIC AND REAL OLIVE MILL WASTEWATER

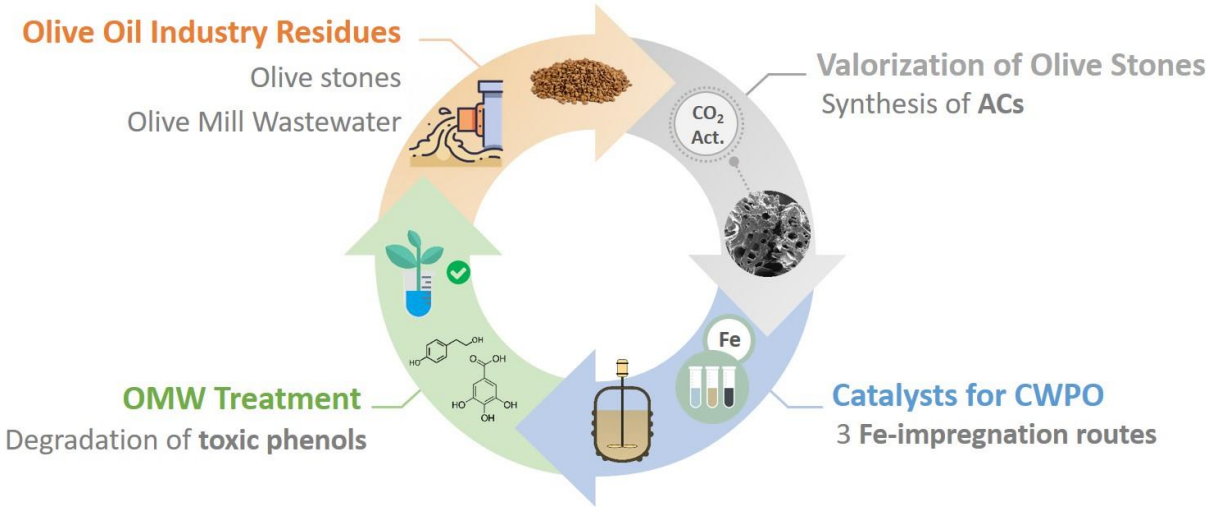
Highlights

- Cheap & efficient CWPO Fe-catalysts developed by integrating agricultural residues;
- Efficiency of three Fe-impregnated catalysts is compared for simulated and real OMW;
- 55% TPh, 37% COD, and 71% H_2O_2 conversions under smooth operational conditions;
- 64% toxicity reduction and biodegradability enhancement after only 240 min;
- High catalyst stability and reusability with Fe leaching <2.8 wt.% after 4 runs.

The contents of this chapter were adapted from:
Esteves, B.M., Morales-Torres, S., Maldonado-Hódar, F.J., Madeira, L.M., Chemical Engineering Journal, 2021, 411, 128451. https://doi.org/10.1016/j.cej.2021.128451

ABSTRACT

A by-product of olive mill operation (olive stone, OS) was transformed into activated carbon (AC) and used as support to prepare Fe-based catalysts, which were employed on the catalytic wet peroxide oxidation (CWPO) of olive mill wastewater (OMW). Three Fe-impregnation routes were tested: incipient wetness impregnation (IWI), adsorption (Ads), and hydrothermal (HT) resulting in catalysts with distinct iron loadings, particle sizes, and surface dispersion. OSAC-Fe catalysts were characterized by N_2 and CO_2 physisorption, XRD, XPS, FTIR, HRTEM, EDX, and HRSEM techniques. Catalysts' activity and stability were first compared in the degradation of synthetic polyphenolic solutions. After one cycle (240 min), catalysts' sorption capacity was considerably exhausted and •OH radicals were found to be the main oxidative species responsible for total phenolic content (TPh) removal. OSAC-Fe-IWI and OSAC-Fe-Ads performed better than OSAC-Fe-HT after four consecutive cycles (53 and 48 *vs*. 38% TPh removals, respectively), also showing considerably lower cumulative Fe leaching values (2.2 and 2.8 *vs*. 10 wt.%). The most promising materials were used for the depuration of real OMW samples. Under smooth operational conditions ([OSAC-Fe-IWI] = 2.0 g/L, $[H_2O_2]$ = 0.5 g/L, $pH_0 \approx 4.9$, T_0 = 25 °C), 55 % TPh removal was attained after 240 min, resulting in a significant reduction of the effluent's toxicity (from 100% *Vibrio fischeri* bioluminescence inhibition to 36%), 37% chemical oxygen demand degradation, and 21% total organic carbon mineralization. Promising catalytic performances were also achieved by OSAC-Fe-Ads, despite its considerably lower iron loading, highlighting the importance of Fe surface dispersion.



8.1. INTRODUCTION

Activated carbons are traditionally used for water treatments because they are cheap, non-toxic, with easily adjustable physicochemical properties, and are highly stable in extreme acid/basic media, avoiding leaching/degradation shown by other inorganic supports. In this chapter, an abundant organic by-product of the olive oil industry – olive stones (OS) – was selected for the preparation of activated carbon, which was thereafter used as support in the synthesis of Fe-catalysts. The work described in Chapter 7 highlighted some promising features of OS-AC derived catalysts regarding other ACs and biochars (e.g., synthesized from olive tree pruning), and showed comparable activity to the ones prepared from commercially available AC supports [1]. Other reports also highlight the properties of similar olive mill's by-products as sorbents for water/wastewater purification or heavy metal removal (e.g., [2,3]).

For the first time, the depuration of real OMW samples was evaluated by CWPO using in-house synthetized Fe-catalysts derived from a by-product of the same agro-industrial activity, in a perspective of a circular economy. The deposition of the Fe-active phase was performed following three distinct routes: incipient wetness impregnation (IWI), adsorption (Ads), and hydrothermal precipitation (HT). The physicochemical properties of the synthesized catalysts were determined by a wide set of experimental techniques and their catalytic activity and stability were screened using a synthetic solution comprising five different phenolic compounds commonly present in real OMW. Catalytic performances were evaluated following TPh and COD degradation, TOC mineralization, and H_2O_2 consumption, while catalysts' deactivation degree was inferred by Fe dissolved in solution.

After the catalysts' screening, further experiments and optimization of operational conditions were assessed with the most promising materials but using real OMW samples. Additionally, BOD_5 and biodegradability indices were evaluated, while *Vibrio fischeri* bacteria bioluminescence decay was selected as a toxicity indicator, all used to compare raw OMW and the final effluent produced.

8.2. MATERIALS AND METHODS

8.2.1. Catalysts synthesis

Olive stones (OS) were used as precursors for the synthesis of OS-derived activated carbons (OSAC). Prior to use, OS were thoroughly washed with distilled water and then ground and sieved

to a particle size fraction of 0.45–1.0 mm. The first step for the OSAC synthesis involved the carbonization of raw OS in a horizontal tube furnace under a 150 cm^3/min flow rate of N_2 (2 h of hold time at 800 °C, 10 °C/min heat ramp). Then, the flow of N_2 was switched to CO_2 (300 cm^3/min) for the physical activation of the produced biochars (4 h of hold time at 800 °C, 10 ºC/min heat ramp); finally, the flow was switched again to the original N_2 flowrate as to allow the furnace to cool to room temperature for approximately 20 h. The synthesis yield of OSAC was ≈16 wt.%, whereas the ash content, determined by burning a fraction of OS in air up to 800 °C, was ≈2.5 wt.% [1].

Different fractions of OSAC (6.0 g) were impregnated to a theoretical 4 wt.% Fe-loading using 0.85 g of $FeCl_2 \cdot 4H_2O$ (Acros Organics) as the precursor salt. Three procedures were adopted: (i) incipient wetness impregnation (IWI), where the iron precursor was dissolved in the minimum volume of water (according to its solubility) and this solution was then slowly and evenly dropped on the support filling the porosity, with the aid of manual shaking, until complete addition of the solution; (ii) adsorption (Ads), by adding OSAC in an 80 mL aqueous Fe-solution, keeping the suspension sealed and in constant magnetic agitation (300 rpm) for 48 h, and then recovering the impregnated OSAC particles by filtration (removing the excess solution); and (iii) hydrothermal deposition (HT), where the fitted amount of Fe-precursor was dissolved in 80 mL of distilled water with pH adjusted to ≈10, and the solution magnetically stirred (300 rpm) for 1 h. This solution was then mixed with OSAC in a 125-mL PTFE vessel, filling to 2/3 of its capacity. The vessel was then transferred into a stainless-steel autoclave (Parr Instruments, USA Mod. 4748), sealed, and placed in an oven at 200 °C for 20 h; after cooling to room temperature the solution was filtered to recover the catalyst. Lastly, all impregnated samples were washed with distilled water several times, rinsed, dried for 12 h at 100 °C, and thermally treated in a horizontal tube furnace (1 h hold time at 350 °C, 10 °C/min heat ramp) under a N_2 flow rate of 150 cm^3/min. All volumetric flow rates were measured at 25 ºC and 1 atm. The derived catalysts were named (i) OSAC-Fe-IWI, (ii) OSAC-Fe-Ads, and (iii) OSAC-Fe-HT.

8.2.2. Wastewater and experimental procedure

The CWPO experiments were performed with a synthetic solution comprising a mixture of five phenolic compounds (70 mg/L each) commonly present in real olive mill wastewaters: tyrosol (2-(4-hydroxyphenyl)ethanol, Sigma-Aldrich), gallic acid (3,4,5-trihydroxybenzoic acid, Alfa Aesar), caffeic acid (3,4-dihydroxycinnamic acid, Acros Organics), vanillic acid

(4-hydroxy-3-methoxybenzoic acid, Sigma-Aldrich), and protocatechuic acid (3,4-dihydroxybenzoic acid, Acros Organics). The selection of the pollutants was adjusted to simulate the occurrence in real OMW, according to data reported in the literature [4–6]. The compounds were dissolved in distilled water and sonicated for 15 min until full dissolution. The prepared solution presented a TOC of 203 mg/L and a TPh of 350 mg/L.

The real OMW used in this study was collected from the decanter's exit of a 3-phase olive mill located in Barcelos (Portugal), in late 2019. Before storage, the effluent was left to settle for 24 h to remove most of suspended particulate matter. The supernatant was then collected, homogenized, and stored at -15 °C until needed. Since OMW is commonly mixed with olives washing wastewaters and then stored in open air ponds (i.e. subject to climatic conditions, namely dilution by rain and biological stabilization) [7], CWPO experiments were performed with ten-fold diluted samples to simulate the wastewater in such conditions.

All CWPO experiments were performed in a 300-mL capacity cylindrical jacketed batch reactor under magnetic agitation (300 rpm) and controlled temperature (25 °C), using a magnetic stirrer (VWR, model VS-CT) and a thermostatic bath (VWR, model 89202-912), respectively. Solution's pH was continuously recorded using a WTW Inolab pH-meter, and adjustments to the medium's pH during the reaction were not performed.

In a typical run, the reactor was loaded with 150 mL of the polyphenolic synthetic solution ($pH_0 \approx 3.8$) or the ten-fold diluted OMW ($pH_0 \approx 4.9$), followed by the desired amount of catalyst (particle size fraction of 0.45–1.0 mm); preliminary experiments showed intraparticle mass transfer limitations to be negligible. The reaction started (t = 0) after the single-step addition of 0.5 mL of H_2O_2 (30 % *w/v*, VWR Chemicals), equivalent to $[H_2O_2]_0$ = 1.0 g/L (29 mM). The amount of oxidant used corresponds to approximately the theoretical stoichiometric value required for complete mineralization of the synthetic solution up to CO_2 and H_2O[1].

Samples were periodically collected from the reactor, filtered through 0.45 μm pore diameter filters to separate the catalyst, and diluted in a 1:5 ratio with distilled water. For the synthetic solution, the determination of the phenolic content was performed instantly by HPLC to prevent further oxidation to occur by unreacted H_2O_2 present in the vial containing the sample (or via the homogeneous reaction catalyzed by leached Fe dissolved in solution). Likewise, the determination of residual H_2O_2 in solution was immediately performed after each sample's collection. For the TOC measurements, an excess of Na_2SO_3 (3 times the initial stoichiometric

amount) was used as H_2O_2 quencher. An additional sample was also collected at the end of each experiment (t = 240 min), filtered, neutralized with NaOH 1 M, and kept refrigerated until needed for the assessment of toxicity and dissolved Fe. All catalysts present magnetic characteristics in greater (–HT) or lesser extent (–IWI and –Ads), according to the Fe-loading and Fe-phase formed. The magnetic character was not quantified, but this property can facilitate the catalysts recovery after reaction.

8.3. RESULTS AND DISCUSSION

8.3.1. Catalysts characterization

Table 8.1 summarizes the physicochemical transformation from the OSAC support to the resulting Fe-containing catalysts. Changes in the porosity of the materials were analyzed by gas adsorption (N_2 and CO_2). In all cases, the programmed Fe-loading was 4 wt.%, though results obtained by atomic absorption measurements denoted that the iron loading for Ads and HT impregnation methods were considerably smaller. The impregnation with Fe-nanoparticles produces simultaneously two effects: the blockage of the support's porosity (as inferred from the BET surface area decrease) and a change in the pH_{pzc} of the materials.

Table 8.1 Textural characteristics and pH_{pzc} values for the OSAC support and derived Fe-catalysts.

Sample	S_{BET} (m^2/g)	W_0 (N_2) (cm^3/g)	L_0 (N_2) (nm)	W_0 (CO_2) (cm^3/g)	V_{meso} (cm^3/g)	V_T (cm^3/g)	Fe (wt.%)	pH_{pzc}
OSAC	792	0.33	1.2	0.20	0.04	0.39	-	10.6
OSAC-Fe-IWI	546	0.23	1.4	0.13	0.05	0.30	4.0	2.4
OSAC-Fe-Ads	740	0.30	0.9	0.28	0.05	0.37	1.8	4.3
OSAC-Fe-HT	736	0.30	1.0	0.28	0.05	0.37	1.2	7.8

The catalysts' morphology is defined by the support, which in all cases was obtained by the consecutive carbonization and CO_2–activation of olive stones. The morphology evaluation was carried out by HRSEM (Fig. 8.1). The catalysts' micrographs in Fig. 8.1A, C clearly shows a heterogeneous network of channels and wide-open cavities derived from the original cellulosic biomaterial. After impregnation, the sample's micrographs also reveal the occurrence of spherical-like shaped Fe-nanoparticles, frequently overlapping and thus forming agglomerates,

as highlighted in Fig. 8.1B, D. Analogous findings were already reported for different OS-impregnation procedures [8].

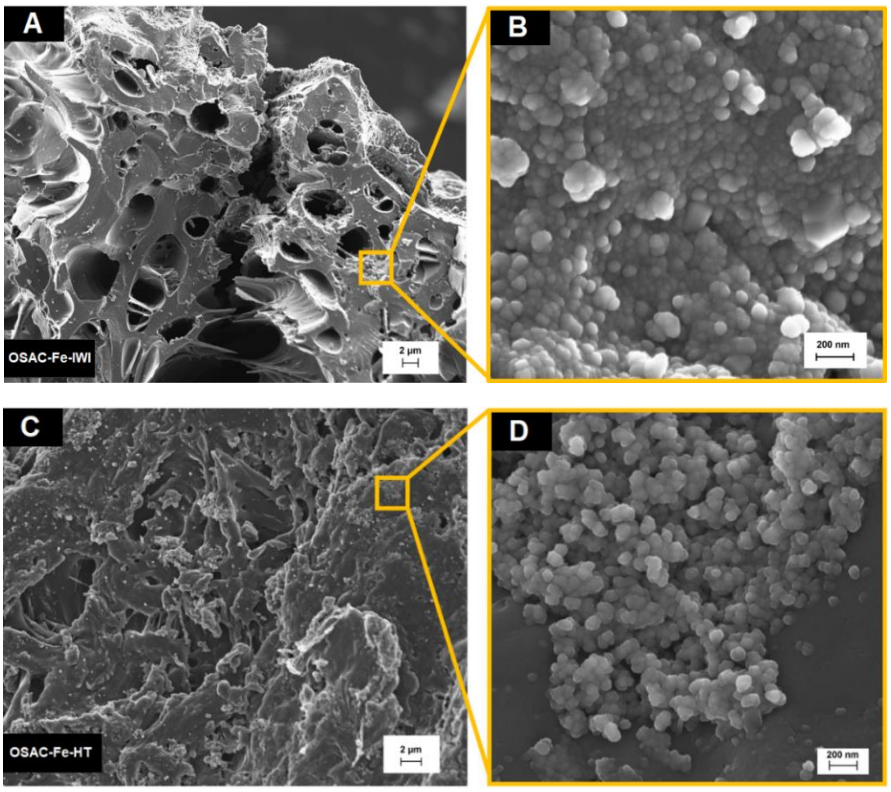


Fig. 8.1 HRSEM micrographs of samples: (A) OSAC-Fe-IWI and (C) OSAC-Fe-HT; (B) and (D) show details of Fe-particles coating OSAC-Fe-IWI and OSAC-Fe-HT surfaces, respectively

As observed, metal nanoparticles are blocking the porosity of the activated carbon used as support. The magnitude of the blockage is influenced by the amount, distribution, shape, and dimension of these nanoparticles, which in turn depend on the impregnation method used. N_2 adsorption-desorption isotherms are depicted in Fig. 8.2a, and pore size distribution profiles, calculated by applying the QSDFT method to N_2 isotherm data, are shown in Fig. 8.2b. Both the support and derived catalysts show a mixture of type I and type IV isotherms (according to the IUPAC classification), typical of predominantly microporous materials with a slight mesoporosity contribution on the isotherm profile, which is denoted by a certain slope of the isotherm (instead of the plateau observed in microporous materials – type I isotherms), and the formation of a small hysteresis loop [9]. All materials display parallel isotherms, with changes mainly occurring at low P/P_0 values. Thus, a similar pore size distribution profile, with a maximum centered at approximately 0.7 nm pore width, was obtained in all cases. The porosity in this range is blocked regarding the support, particularly on the OSAC-Fe-IWI sample, whereas the porosity larger than 2.0 nm is preserved in all cases after Fe-doping. This indicates that microporosity plays an

important role in the formation and localization of iron nanoparticles. For this catalyst specifically, the L_0 value significantly increased while the micropore volume (W_0) decreased (Table 8.1). However, for the other two materials, W_0 remained practically unchanged while L_0 decreased. Therefore, at low Fe-loading, the nanoparticles can be formed inside the microporosity thus decreasing the dimension of the micropores, but with increasing the Fe-content, micropores are blocked and N_2 adsorption mainly occurs in larger pores.

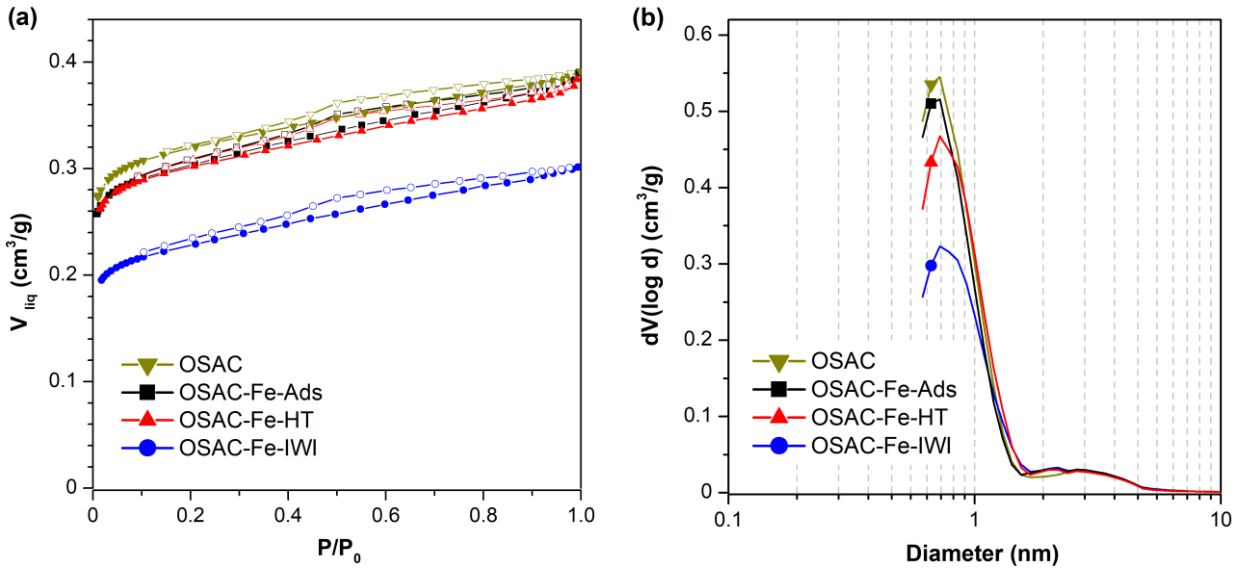


Fig. 8.2 (a) N_2 adsorption-desorption isotherms at -196 °C; (b) pore size distribution of the materials obtained by QSDFT applied to N_2 adsorption isotherms.

In this sense, the microporosity characterization was complemented by CO_2 adsorption. In the absence of diffusional restrictions, the micropore volume obtained from the N_2 adsorption corresponds to the total micropore volume of the sample: W_0 (N_2) = W_0 (CO_2). However, when microporosity is narrow, N_2-diffusional restriction occurs and W_0 (N_2) < W_0 (CO_2), whereas when the sample contains large pores where N_2-condensation occurs, W_0 (N_2) > W_0 (CO_2). Thus, CO_2 at 0 °C is used to characterize the narrowest microporosity (i.e., micropores with diameter <0.7 nm). For the prepared catalysts, W_0 (N_2) > W_0 (CO_2), denoting the absence of diffusional restriction and the contribution of mesoporosity (that is always preserved, as commented) to the adsorption capacity of the samples.

The surface acid/basic character of the materials also changed depending on the impregnation method. The activated carbon support is clearly a basic material (pH_{pzc} = 10.6 – Table 8.1), but this parameter progressively decreased with increasing Fe-loadings, with catalysts becoming acid materials and reaching a pH_{pzc} = 2.4 in the case of the catalyst obtained by IWI. A similar trend

was reported by G. Vilardi *et al*. [8] for the synthesis of mixed-iron coating materials on raw olive stones.

Nonetheless, this change is not only influenced by the Fe content but also by the nature of the iron oxide formed after the pre-treatment. The iron phase and crystallite size were studied by XRD. X-ray diffraction peaks presented in Fig. 8.3 show that the broad band centered at (002) diffraction peak ($2\theta \approx 24\text{-}26°$) corresponds to an eminently amorphous carbon structure, while (101) diffraction peak at $2\theta \approx 44°$ is due to the axis of a graphitic framework (ICDD card no. 89-8487) [10], denoting a certain ordering of the structure. A mixture of iron oxides was formed after the thermal decomposition of the iron salt precursor upon thermal treatment, as also observed by other authors [11]. Diffraction peaks characteristic of hematite (α-Fe_2O_3, ICDD/JCPDS card no. 33-0664) are primarily detected for OSAC-Fe-IWI and OSAC-Fe-Ads samples, whilst magnetite (Fe_3O_4, ICDD card no. 19-0629) is the predominant active phase found on the OSAC-Fe-HT catalyst. It is noteworthy that, despite the unequivocal identification of these phases, the intensity of the peaks is generally even weaker than the broad bands associated with the amorphous structure of the support. This fact, together with the broadening of α-Fe_2O_3 and Fe_3O_4 characteristic XRD peaks, is suggestive of poor crystallinity and/or small nanoparticles' crystallite size [12]. The crystallite sizes were calculated from the full width at half maximum (FWHM) of the stronger intensity peaks using Scherrer equation (Eq. (3.5)). Average crystallite sizes are estimated to be 24.0, 14.5, and 18.2 nm for OSAC-Fe-IWI, OSAC Fe Ads, and OSAC-Fe-HT, respectively.

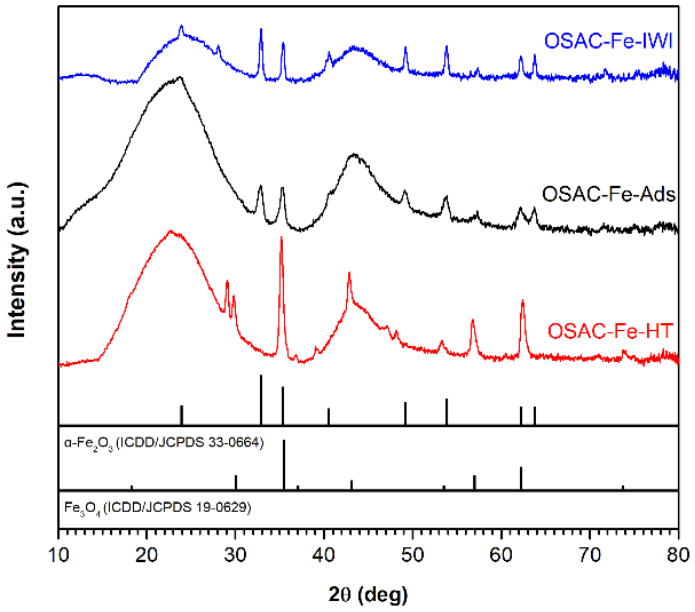


Fig. 8.3 XRD patterns of the synthetized catalysts. Standard patters of *α*-Fe_2O_3 (ICDD card no. 33-0664) and Fe_3O_4 (ICDD card no. 19-0629) are shown for reference.

Further characterization, conducted by HRTEM analysis (Fig. 8.4) to determine the Fe-dispersion on the catalysts' surface, confirmed the heterogeneous distribution of iron particles, also denoting a distinct shape profile and distribution of these nanoparticles. In the case of the OSAC-Fe-IWI catalyst (Fig. 8.4A-C), the higher Fe-content clearly favors a wider distribution of nanoparticle sizes. The formation of a significant concentration of big particles exceeding 100 nm is observed, together with a large fraction of smaller nanoparticles more homogeneously distributed. Evidently, large Fe-particles are formed on the external surface of the support and are significantly bigger than results predicted for crystallites by XRD, also confirming the low crystallinity of such metal nanoparticles. The appearance of Fe-particles in this catalyst is similar to that of the one prepared by HT (Fig. 8.4G–I). Nonetheless, in this case, the lower Fe-content favors the formation of smaller nanoparticles, which also appear better distributed in the carbon matrix (Fig. 8.4H–I). At a glance, the aspect of the catalyst prepared by adsorption is clearly different from the other two. The long adsorption periods employed during the synthesis allowed a more uniform and deeper diffusion of the metal precursor solution into the porosity of the support, favoring the formation of "needle-like" metal particles (Fig. 8.4D–E), together with smaller and round-shaped nanoparticles (Fig. 8.4F). The Fe-distribution on the different supports was also always confirmed along the experiments using the EDX-microanalysis (*cf*. Fig. C.1, Appendix C).

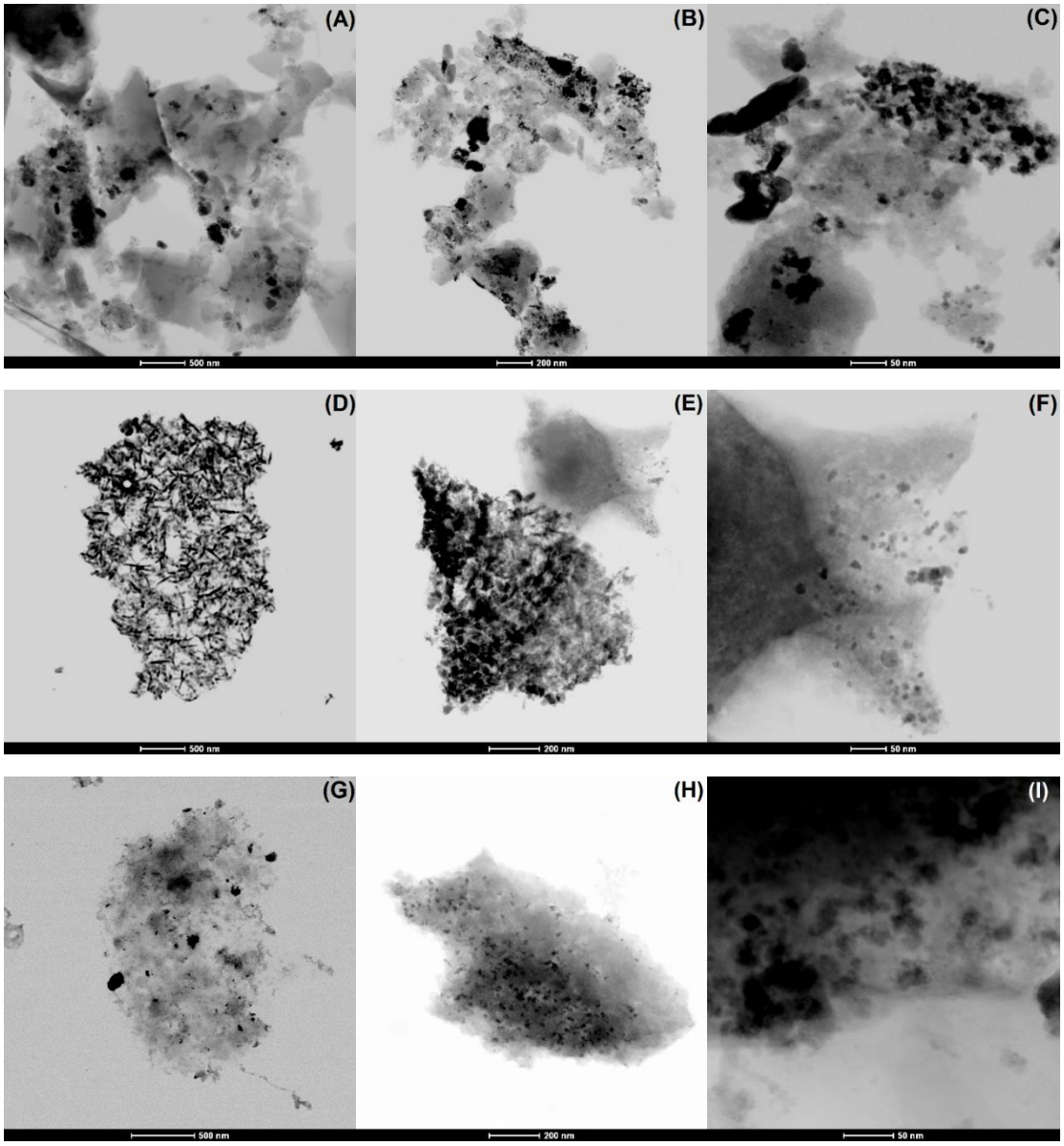


Fig. 8.4 HRTEM images of Fe-catalysts: (A-C) OSAC-Fe-IWI, (D-F) OSAC-Fe-Ads, and (G-I) OSAC-Fe-HT.

The surface chemistry composition of the synthesized catalysts was analyzed by XPS and the results are summarized in Table 8.2; high-resolution XPS spectra of O1s and Fe2p regions are shown in Fig. 8.5 and Fig. 8.6, respectively. The oxygen and iron contents were comparable for all catalysts with exception of OSAC-Fe-HT, which presented the lowest oxygen and iron contents (Table 8.2), as a consequence of the hydrothermal treatment. The O1s spectral region was deconvoluted in three components, being the first peak placed at 530.1 eV due to Fe–O bonds [11], and the other two contributions located at 531.6 and 533.2 eV assigned to oxygen-containing groups (C=O and C–O bonds, respectively) on the carbon surface (Fig. 8.5) [13]. The distribution of the different oxygen species was comparable for all catalysts synthesized (Table C.1). However, the contribution of Fe–O bonds was different and increased with the iron surface

content (Table 8.2 and Table C.1). Complementary FTIR analyses were recorded (Fig. C.2) confirming the presence of different oxygen surface groups (C=O, C–O, –OH) on the carbon support/catalysts, as denoted by the assignation of the corresponding vibration bands [14].

Table 8.2 Elemental analysis of the prepared catalysts determined by XPS (atomic content %).

Sample	C	O	Fe
OSAC-Fe-IWI	89.1	9.2	1.7
OSAC-Fe-Ads	88.1	9.7	2.2
OSAC-Fe-HT	92.2	7.0	0.8

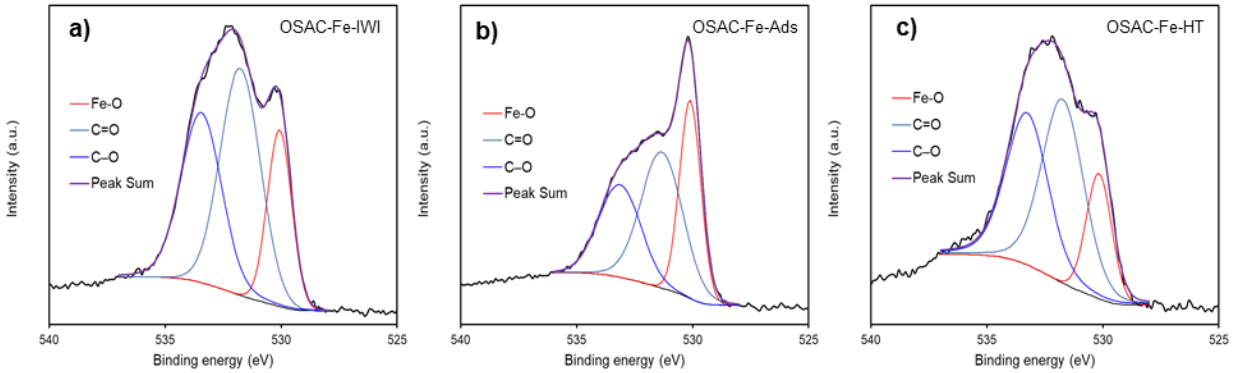


Fig. 8.5 O1s XPS spectral region of the different catalysts.

The Fe2p spectral region was fitted with five components (Fig. 8.6), according to the procedure of McIntyre and Zetaruk [15]. The peak maximum was fixed at 710.9 eV with an FWHM value of 1.4 eV, that together with the Gupta and Sen (GS) multiplets at 712.0, 713.1, and 714.2 eV, with an FWHM of 1.2 eV, were assigned to Fe^{3+} species [11,15], whilst the component located at 710.0 eV corresponds to Fe^{2+} ones. In general, all catalysts presented a comparable Fe^{2+}/Fe^{3+} ratio, indicating a preferential formation of Fe_2O_3-particles. However, the Fe^{2+} content detected can be present in other non-crystalline phases of partially reduced oxides, including magnetite (Fe_3O_4), also detected by XRD.

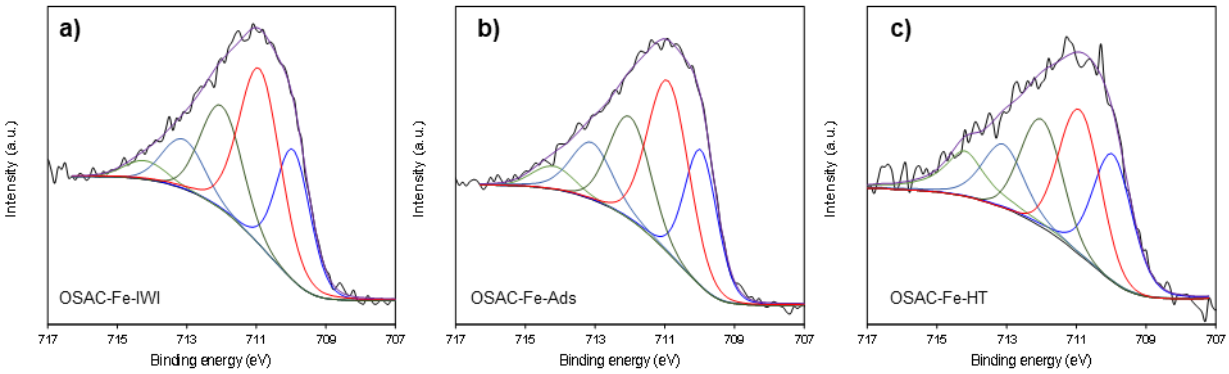


Fig. 8.6 Fitting of the Fe2p$_{3/2}$ spectral region of the different catalysts.

8.3.2. CWPO of synthetic OMW

8.3.2.1. Adsorption experiments

Experiments in the absence of H_2O_2 were performed to evaluate the adsorptive capacity of each material – Fig. 8.7. For the experimental conditions tested, the highest overall adsorption of the phenolic content was achieved by OSAC-Fe-HT and OSAC-Fe-Ads (20.9 and 19.7% TPh removals, respectively, after 240 min). The adsorption of phenols by the catalyst prepared by IWI was slightly lower, reaching an overall phenolic content removal of 16.6% after 4 h, similar to that reached by the OSAC support. Expectably, the percentage of TOC removal verified after each experiment was similar to that of TPh (not shown).

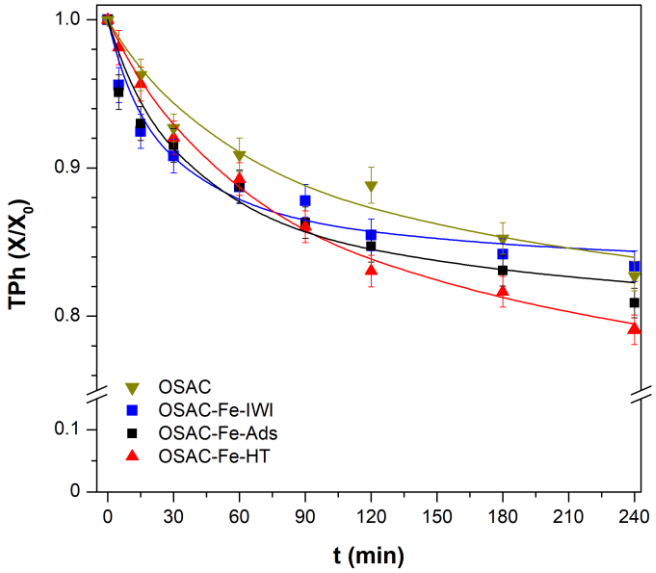


Fig. 8.7 Comparison of total phenolic content (TPh) adsorption over time by the OSAC support and derived Fe-catalysts (solid lines: pseudo-second order kinetic model fitting). [Cat] = 0.5 g/L, T_0 = 25 ºC, and pH_0 = 3.5.

It is noteworthy the influence of the parameters summarized in Table 8.1 on the adsorptive behavior of the catalysts. At a glance, the smaller adsorption capacity of the OSAC-Fe-IWI

catalyst is due to the stronger blockage of the porosity by the highest Fe-content of this sample, as previously commented. The other two catalysts exhibited similar porosity and surface area values, and thus also similar TPh removal capacity. The adsorption of the phenolic compounds is analogous to the total pore volume decrease (i.e., around 20 %), denoting that all the porosity of the samples is accessible to the pollutants and that there are no major diffusion problems of the compounds in the porous network.

Experimental adsorption capacities were calculated according to Eq. (6.1). The pseudo-second order (PSO) kinetic model, widely applied to describe adsorption processes [16], was found to fit the experimental data reasonably well. The characteristic kinetic constants were determined using the PSO model (Eq. (6.3)). The kinetic parameters were obtained by non-linear regression of the experimental data using Microsoft's Excel® solver function, following an iterative algorithm that minimizes the root mean square error. A graphic representation of the predicted adsorptive behavior is provided in Fig. 8.7 (solid lines), while the computed kinetic parameters and respective correlation factors (R^2) are presented in Table 8.3. Good adherence of the model to experimental data was in general observed, with a higher sorption capacity (q_e) for sample OSAC-Fe-HT (in line with data shown above), and a higher kinetic constant for sample OSAC-Fe-IWI, the one with larger mean micropores width (Table 8.1).

Table 8.3 Calculated adsorption parameters for PSO kinetic model fitting.

Sample	$q_{e,\,cal}$ **(mg/g)**	k_2 **(g/mg·min)**	R^2
OSAC	151.5	7.99×10^{-5}	0.979
OSAC-Fe-IWI	118.9	3.46×10^{-4}	0.972
OSAC-Fe-Ads	150.6	1.74×10^{-4}	0.966
OSAC-Fe-HT	165.0	5.93×10^{-5}	0.995

The concentration of each phenolic compound present in the synthetic solution was also followed over time and normalized concentrations are depicted in Fig. C.3. Adsorption data highlights the preferential removal of gallic and caffeic acids, independently of the catalyst used; still, this trend is not observed in the case of the OSAC support. The chelating activity of iron towards different phenolic acids was already reported [17], being found that due to the ethylene group of hydroxycinammic acids, caffeic acid is a better ligand for Fe than hydroxybenzoic acids (e.g., protocatechuic, vanillic, or gallic acids). Thus, as shown in Fig. C.3, faster and higher adsorption

of caffeic acid is always observed using the catalysts, despite the greater surface area and total pore volume of the support. Those authors also suggest that the number and position of hydroxyl groups on hydroxybenzoic acids could determine the chelating properties [17]. Comparing the binding constants of different Fe-phenolic acid complexes, it was concluded that gallic acid is a better chelating agent than protocatechuic acid, which could also help explain the lower removal of this compound by the support (and thus the lower overall TPh adsorption of the OSAC support regarding the derived OSAC-Fe-Ads and OSAC-Fe-HT catalysts – Fig. 8.7).

8.3.2.2. Catalytic experiments

Prior to the CWPO runs, a homogenous process was conducted to evaluate the action of H_2O_2 alone towards the polyphenolic solution ([H_2O_2] = 1.0 g/L, T_0 = 25 °C, and pH_0 = 3.5). Results confirm that in the absence of a catalyst, the oxidizing capacity of H_2O_2 is practically negligible, resulting in approximately 4% TPh removal and 3% TOC mineralization after 240 min of reaction (results not shown).

Screening of the catalysts was performed under the same experimental conditions mentioned in the Section 8.3.2.1 but with the addition of H_2O_2. Fig. 8.8 compares the pollutants' removal performance by adsorption (dashed bars) and adsorption + oxidation (blank bars) after 240 min. Since adsorption is an intrinsically bound process to the heterogeneous oxidation, columns denoted as CWPO depict the simultaneous effect of both phenomena. The higher removal of TPh on CWPO runs confirms that Fe-sites on the materials' surface are able to catalytically decompose H_2O_2 [18]. Under the experimental conditions mentioned, the catalyst with the highest oxidative capacity was OSAC-Fe-IWI, reaching TPh removals of 48.9%, with this parameter decreasing to 36.4% and 28.6% for OSAC-Fe-Ads and OSAC-Fe-HT, respectively. The same trend is observed for H_2O_2 consumptions after each run: 31.7, 16.4, and 8.4% of the initial amount of 1.0 g/L, respectively (right y-axis, Fig. 8.8).

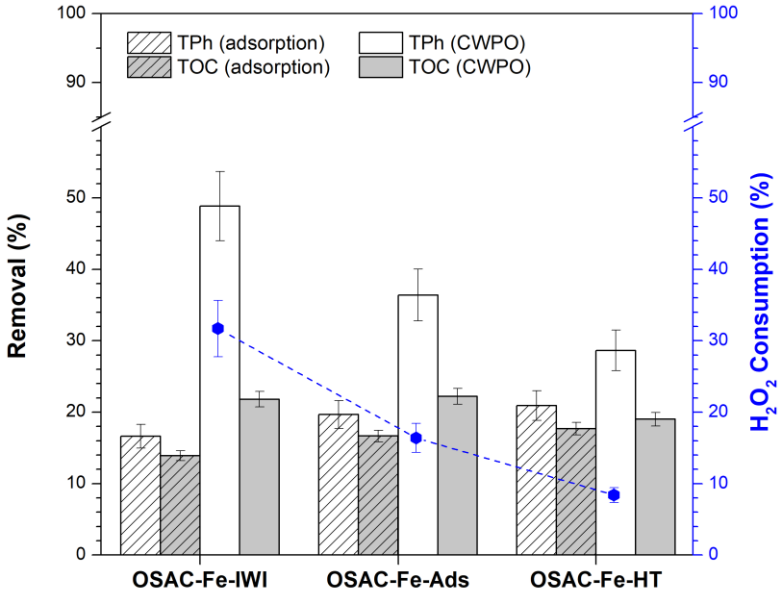


Fig. 8.8 Comparison of TOC and TPh removals by adsorption (dashed bars), and adsorption + oxidation = CWPO (blank bars) after 240 min of reaction. H_2O_2 consumptions for CWPO runs are shown in the right y-axis. [Cat] = 0.5 g/L, [H_2O_2] = 1.0 g/L, T_0 = 25 ºC, and pH_0 = 3.5.

Despite the different removal degrees of the parent phenolic compounds, TOC depletion is rather similar between the different catalysts. This puts in evidence that the greater activity of OSAC-Fe-IWI is not traduced in deeper oxidation of pollutants, but the formation of intermediate compounds that accumulate in the solution. Several authors have already reported on the formation of low molecular weight carboxylic acids from the oxidation of phenolic effluents [19,20], which are often more refractory to oxidation than the initial compounds and also responsible for the drop of the solution's pH. This trend was also observed in this study (*cf*. Fig. C.4) in the case of OSAC-Fe-IWI and OSAC-Fe-Ads catalysts, whereas for the OSAC-Fe-HT one, the rise in pH during the reaction highlights the contribution of the higher pH_{pzc} of this material (*cf*. Table 8.1) and the possibly different route of TPh removal (and thus the formation of distinct reaction intermediates).

Fig. 8.9 depicts the degradation of each phenolic compound of the synthetic solution over time. It is observed the higher activity of OSAC-Fe-IWI and also how gallic and caffeic acids are preferentially removed. This trend is similar to that observed in adsorption tests, and denotes the importance of such interactions since the pollutants can be adsorbed before being oxidized.

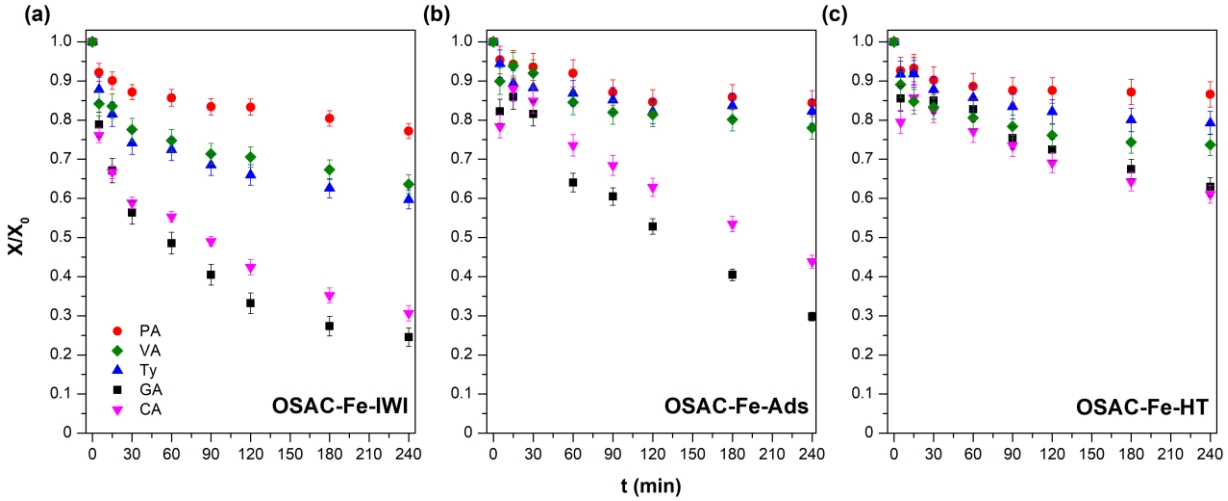


Fig. 8.9 Removal of phenolic compounds over time by CWPO (normalized concentrations) using: (a) OSAC Fe IWI, (b) OSAC-Fe-Ads, and (c) OSAC-Fe-HT (PA – Protocatechuic acid; VA – Vanillic acid; Ty – Tyrosol; GA – Gallic acid; CA – Caffeic acid). [Cat] = 0.5 g/L, [H_2O_2] = 1.0 g/L, T_0 = 25 ºC, and pH_0 = 3.5.

Since low H_2O_2 conversions were observed on this set of runs, the catalytic efficiency of the process could be limited by the catalyst dosage, as the presence of a larger number of Fe-active sites is expected to prompt •OH generation and improve oxidation/mineralization efficiencies. For abbreviation, results in Fig. 8.10 only show the total phenolic content removal over time, as removal trends for individual compounds are very similar to the ones presented in Fig. 8.9 (independently of the catalyst's concentration used, shown in Fig. C.5 and Fig. C.6). It is worth mentioning that caffeic and gallic acids were completely removed after 240 min of reaction on all cases with the higher catalyst dosage.

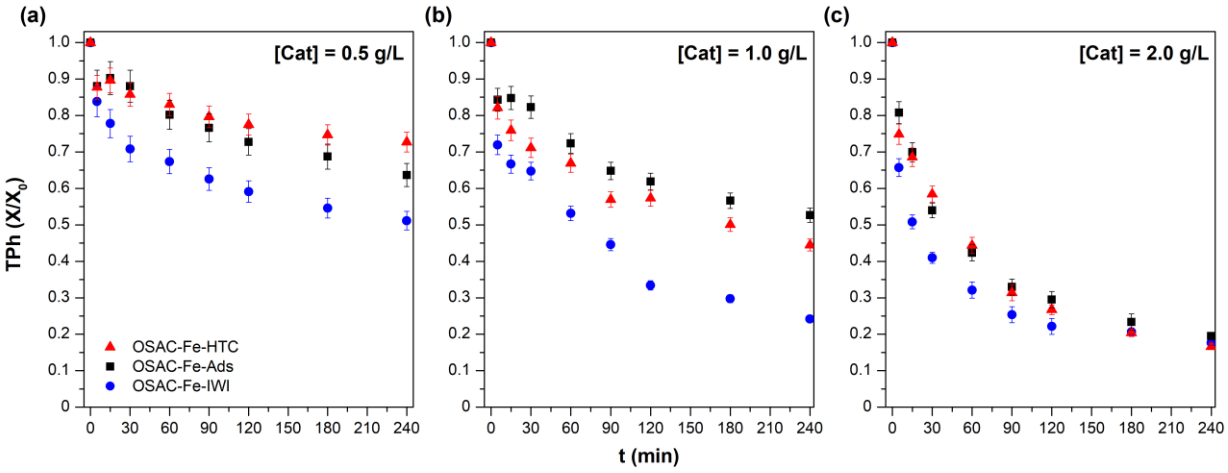


Fig. 8.10 Effect of catalyst dosage on the removal of TPh: (a) 0.5 g/L (75 mg), (b) 1.0 g/L (150 mg), and (c) 2.0 g/L (300 mg). [H_2O_2] = 1.0 g/L, T_0 = 25 ºC, and pH_0 = 3.5.

Results for this set of experiments are also summarized in Table 8.4. As the catalysts' concentration increased, both TPh and TOC removals improved. Maximum total phenol content

removal was around 80% for all catalysts after 240 min, though the process was initially faster for the OSAC-Fe-IWI sample (Fig. 8.10); still, the total organic carbon mineralization (*ca*. 50%) was lower in respect to TPh removal values. Results also show that H_2O_2 consumptions increased as higher catalysts' concentrations were used, though the complete decomposition of the oxidant was never reached under such conditions. Nonetheless, H_2O_2 consumption using OSAC-Fe-HT is considerably lower than the other two catalysts, even when higher dosages are used, suggesting that the major driving agent of the pollutants' depletion is the adsorptive process. Regarding the iron leaching, this catalyst also presented the highest percentages of Fe losses after the catalytic runs, implying a weaker metal-support interaction. This can be related to the structural changes to the carbon matrix promoted by the hydrothermal synthesis route, as evidenced in Fig. 8.1. Even so, the dissolved iron concentrations recorded at the end of each run were always lower than 2 mg/L, the legislated limit imposed by the EU for surface water intended for the abstraction of drinking water [21].

Table 8.4 Summary of TPh and TOC removals, H_2O_2 conversions, and Fe leaching after each run.

Catalyst	**[Cat] (g/L)**	**TPh $_{removal}$ (%)**	**TOC $_{removal}$ (%)**	**H_2O_2 $_{conversion}$ (%)**	**Fe $_{leached}$ (mg/L)**	**Fe $_{leached}$ (wt.%)**
OSAC-Fe-IWI	0.5	48.9	21.8	31.7	0.25	1.2
	1.0	75.8	34.0	42.6	0.36	0.8
	2.0	82.3	46.7	71.0	0.77	0.9
OSAC-Fe-Ads	0.5	36.3	22.2	16.4	0.07	0.8
	1.0	47.3	26.2	31.5	0.14	0.8
	2.0	80.5	52.8	73.0	0.36	1.0
OSAC-Fe-HT	0.5	27.3	19.0	8.4	0.14	2.9
	1.0	55.5	24.6	10.6	0.36	3.6
	2.0	83.4	53.0	13.0	1.12	5.6

8.3.2.3. Catalysts stability and reuse

The loss of activity of the materials is an important issue for the practical implementation of catalytic heterogeneous systems. Long-term stability and/or reusability of the catalysts may be hindered by different factors, such as iron leaching or pore blockage. Recyclability of the catalysts was assessed through four consecutive cycles under the experimental conditions that resulted in

the best catalytic results so far, i.e., [Cat] = 2.0 g/L, [H_2O_2] = 1.0 g/L, T_0 = 25 °C, and pH_0 = 3.5. After each cycle, the catalyst was filtered, washed with distilled water, and finally dried overnight at 100 °C before being used again with a new/fresh synthetic solution.

As shown in Fig. 8.11 there is a sharp decrease in TPh removals from the first to the second runs, as the adsorbed products (phenolic compounds or even reaction by-products) occupied most of the porosity of the catalysts after the first cycle. Thereafter the adsorption capacity of the materials is progressively exhausted and thus TPh depletion is primarily achieved by catalytic oxidation. Nonetheless, from the second run on, a small drop in the catalytic performance of the materials was observed and TPh removals decreased from *ca*. 63 to 53% for OSAC-Fe-IWI, from 56 to 48% for OSAC-Fe-Ads, and 43 to 38% for OSAC-Fe-HT; TOC mineralizations followed the same trend (*cf*. Table C.2).

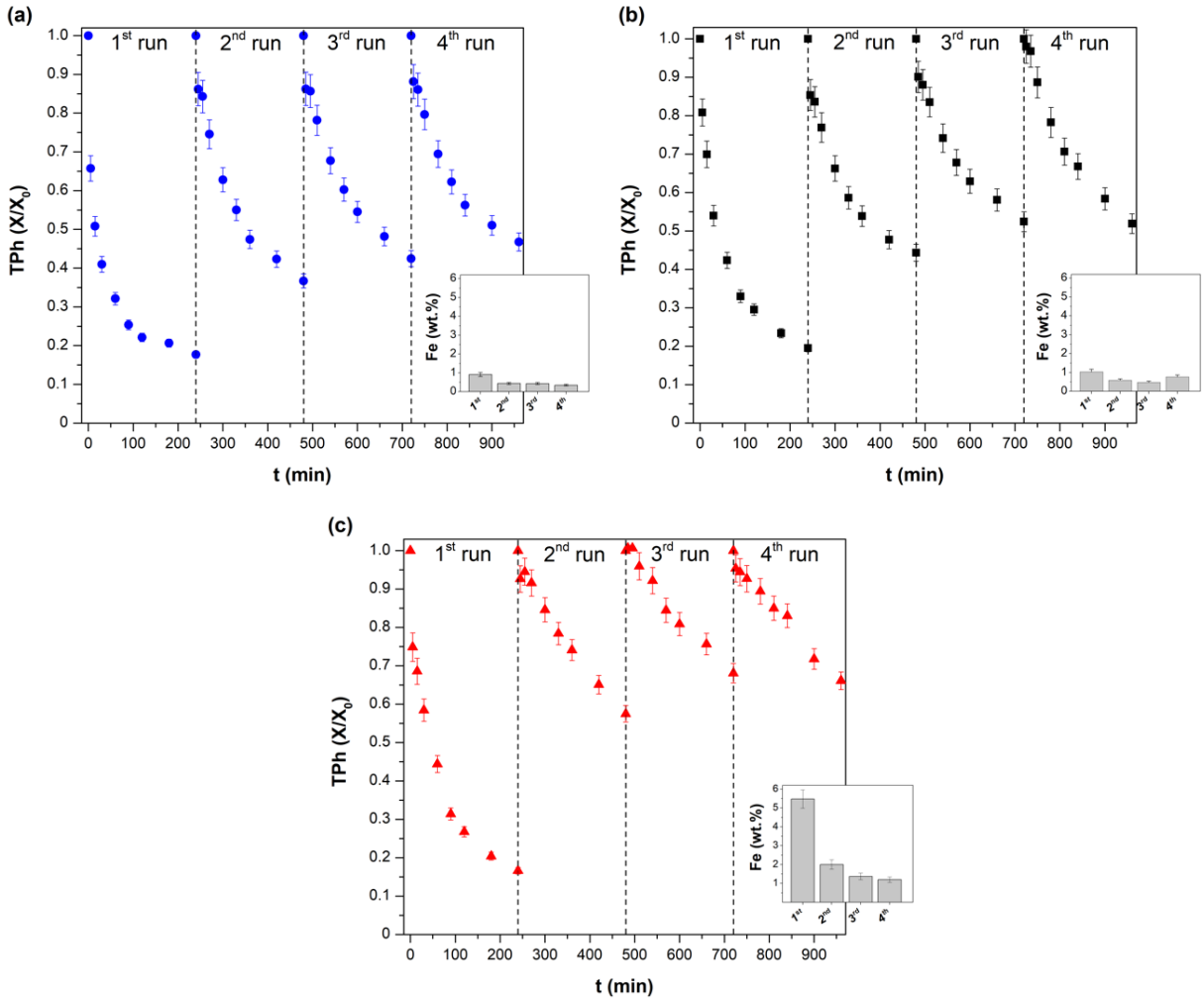


Fig. 8.11 Total phenolic content removal in consecutive cycles using: (a) OSAC-Fe-IWI, (b) OSAC-Fe-Ads, and (c) OSAC-Fe-HT. Inset graphs show Fe leached (wt.%) after each run.

This decay was also accompanied by a progressive decrease in H_2O_2 conversion (*cf*. Fig. C.7), which should be linked to the surface blockage of pores by the adsorbed compounds (and thus the accessibility to active sites), and/or related to the progressively smaller leaching of iron from the materials' surface, as depicted in the inset graphs of Fig. 8.11 (and therefore contribution of the homogeneous Fenton oxidation to the overall performance is smaller from cycle to cycle). As previously commented, this phenomenon is particularly relevant for the OSAC-Fe-HT catalyst, as the initial relative loss of Fe was the highest among the three materials, and the cumulative lixiviation after 4 runs amounted to approximately 10 wt.% (whereas this value was 2.2 and 2.8 wt.% for the other two catalysts).

The catalytic activity and stability of such materials can strongly depend on the calcination procedure adopted after Fe-impregnation, as reported by Achma *et al*. [22]. In this study, calcination procedures were not individually tuned for each catalyst, which could've played a role in the catalytic and stability of the OSAC-Fe-HT catalyst due to its clearly distinct physicochemical properties.

8.3.2.4. Scavenging tests and catalytic mechanism

To better understand the mechanism responsible for the degradation of phenolic compounds, radical scavenging tests were performed using dimethyl sulfoxide (DMSO) as a selective $^{\bullet}OH$ trapper [23]. The catalytic activity of saturated catalyst samples (avoiding the influence of adsorptive contributions) was compared to those obtained under the same conditions reported in the previous section, but with DMSO in solution – Fig. 8.12.

The presence of DMSO in the OSAC-Fe/H_2O_2 systems studied was able to considerably reduce TPh removal efficiencies. As an example, the TPh removal decreased from 57.6% to 18.2% for the OSAC-Fe-IWI sample when DMSO was used, thus confirming the generation of $^{\bullet}OH$ as the predominant oxidative species (via the Fe(III)/Fe(II)-initiated chain shown in Eqs. (2.1), (2.4), and (2.5)). Nevertheless, other less oxidative radicals as the hydroperoxyl ($^{\bullet}HO_2$) and, to a lesser extent, the oxidative action of H_2O_2 alone (as already stated on Section 8.3.2.2), contribute to the degradation of TPh even in the presence of DMSO.

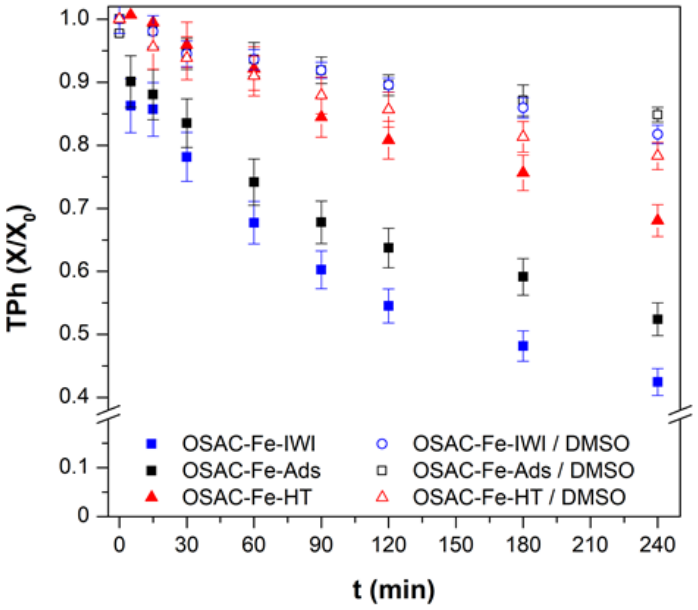


Fig. 8.12 Comparison of TPh removal efficiencies in the absence *vs*. presence of DMSO quencher for all catalysts (DMSO:H_2O_2 molar ratio of 10).

The •OH attack to organic molecules can occur through different pathways, including hydroxylation, abstraction of hydrogen atoms from C–H bonds, and redox reactions [24]. As oxidative radicals are generated through interaction between H_2O_2 and surface Fe-active sites, the first step of phenolic compounds degradation is the formation of aromatic intermediates (which caused the solution to acquire a pale-brown hue). Therefore, •OH attack on aromatic intermediates leads to the cleavage of the benzene ring, yielding the formation of short-linear aliphatic carboxylic and dicarboxylic acids. From that point on, radical attack is responsible for shortening the open-chain of such compounds and the appearance of oxalic, formic, and maleic acids, for example, known to accumulate in the solution as refractory reaction by-products [6,25]. The complete degradation of such compounds leads to the formation of CO_2 and H_2O. In fact, we have detected by HPLC (Fig. C.8) the formation of these acids (oxamic and oxalic) as intermediate oxidation products, in agreement with the bibliography.

Due to the multiple possibilities for chain-initiation/propagation/termination reactions (briefly presented in Eqs.(2.1)–(2.10)) [24,26], and possible oxidative pathways for phenolic compounds' degradation, drawing a tentative oxidation mechanism of such intricate system involving five contaminants – and therein their reaction intermediates – is not feasible; such complexity would considerably increase for the real effluent, addressed herein below, but remains as an interesting open topic for future work.

8.3.2.5. Kinetic studies

Since the catalysts have markedly distinct Fe loadings (as a result of the impregnation procedures adopted – *cf*. Table 8.1) and also show different lixiviation degrees, it is best to compare their performances in terms of the activity of the metal phase rather than in terms of catalyst (metal + support). Developing a kinetic model that accurately describes every reaction pathway occurring during this complex process is not only a hard task but also out of the scope of this work. In such complex systems, lumped parameters that represent a group of compounds – such as TPh or TOC – should be adopted to calculate reaction rates and/or to develop simplified kinetic models [27,28]. Assuming a pseudo-steady state of •OH generation along with the reaction for the saturated catalysts, a simple mass balance for TPh removal in a constant-volume batch reactor ($V = V_0$), where an n-order reaction occurs, yields [29]:

$$-\frac{dC}{dt}V = (-r)\,W_{cat} = k_{app}\,C^n\,W_{cat} \tag{8.1}$$

where C is the TPh concentration (mg/L), V the reaction volume (L), $(-r)$ the reaction rate for TPh degradation, W_{cat} the mass of catalyst (g), and k_{app} the apparent overall kinetic constant. To determine the reaction rates and apparent kinetic constants per active metal phase, W_{cat} was multiplied by γ_{Fe} (iron content) of each catalyst (*cf*. Table 8.1) at the beginning of each cycle, thus also taking into account the cumulative Fe leaching that occurs in the consecutive previous cycles.

The differential method [30] of data analysis was applied for $-dC/dt\,|_{t=0}$ to determine the observed initial rate rates $(-r)_0$ of TPh depletion. The integral method was applied to compute the apparent reaction order (n), being that a pseudo-second-order kinetic behavior was found to be the best fit for the experimental data ($R^2 \geq 0.960$). From the linear plot of $1/C$ *vs*. t of Eq. (8.2) (obtained upon integration of Eq. (8.1) with $n = 2$), it is possible to determine the apparent kinetic constants in each run. Table 8.5 lists the kinetic results obtained, normalized for the Fe content of each material. The proposed kinetic modeling only considers the catalytic removal of contaminants, thus it's just applicable from 2nd and onward runs (i.e., after catalysts' sorption capacities were considerably minimized due to the exhaustion of adsorption sites that occurred after the 1st cycle).

$$\frac{1}{C} = k_{app}\,\frac{W_{cat}\cdot\gamma_{Fe}}{V}\,t + \frac{1}{C_0} \tag{8.2}$$

The computed kinetic results reveal that the initial rate of TPh depletion and apparent kinetic constants for OSAC-Fe-Ads are always higher than the ones for OSAC-Fe-IWI, despite the higher removal values achieved by the latter. This indicates that the metal content and dispersion on OSAC-Fe-Ads surface (*cf*. Fig. 8.4 and Table 8.2) are determining factors for the efficiency of the catalyst. A similar conclusion was drawn by W. Najjar *et al*. [19] regarding the catalytic activity of several Fe-zeolites with different Fe-contents. The authors reported higher specific initial rates of phenolic compounds' oxidation with increasing iron loadings but only to a certain extent, as the formation of bulky iron oxides in catalysts with high Fe-content ultimately hindered reaction rates and catalytic efficiencies. On the other hand, the lowest values of $(-r)_0$ were verified with the OSAC-Fe-HT catalyst, highlighting the poor capacity of this material to rapidly decompose H_2O_2 into hydroxyl radicals, and thus oxidize the target compounds (also traduced in the lowest TOC mineralization efficiencies – Table C.2).

Table 8.5 Kinetic parameters of TPh depletion for the stability cycles after saturation of the catalysts ($(-r)_0$: mg/min·g_{Fe}; k_{app}: L^2/mg·min·g_{Fe}).

Catalyst	$(-r)_0$	k_{app} ($\times10^{-4}$)	R^2	$(-r)_0$	k_{app} ($\times10^{-4}$)	R^2	$(-r)_0$	k_{app} ($\times10^{-4}$)	R^2
	2nd run			*3rd run*			*4th run*		
OSAC-Fe-IWI	43.8	2.2	0.982	33.5	1.6	0.984	33.6	1.4	0.968
OSAC-Fe-Ads	95.6	3.8	0.962	69.2	2.6	0.973	37.2	3.1	0.995
OSAC-Fe-HT	26.0	3.5	0.992	17.4	2.3	0.993	20.5	2.5	0.960

Despite the complexity of CWPO reactions, it's fairly common to assume that the rate-limiting step of Fenton-like systems is the generation of hydroxyl radicals, which in this case occurs through the adsorption of H_2O_2 molecules onto Fe-active sites on the catalysts' surface [31]. Experimental results indicate that the decomposition of H_2O_2 follows pseudo-first order reaction kinetics, and the apparent kinetic constants are summarized in Table 8.6. A sharp decrease in the k_{app} values was observed in all cases after the first run since the consumption rate of H_2O_2 is proportional to the catalytic surface area (progressively smaller as the catalysts' porosity is occupied by the initial phenolic compounds and reaction products). As anticipated, the rate constant of H_2O_2 catalytic decomposition for the OSAC-Fe-HT material was the lowest on all runs among the catalysts tested, limiting the extent of organics mineralization as shown in Table C.2.

Table 8.6 Apparent rate constants of H_2O_2 consumption (k_{app}: L/min·g_{Fe}).

Catalyst	k_{app} (×10^{-2})	R^2	k_{app} (×10^{-2})	R^2	k_{app} (×10^{-2})	R^2	k_{app} (×10^{-2})	R^2
	1st run		*2nd run*		*3rd run*		*4th run*	
OSAC-Fe-IWI	6.2	0.999	3.4	0.990	2.9	0.996	2.4	0.994
OSAC-Fe-Ads	1.4 (×10^{-1})	0.995	5.2	0.991	3.7	0.984	2.7	0.957
OSAC-Fe-HT	2.3	0.946	1.8	0.951	1.1	0.944	0.7	0.929

8.3.3. CWPO application to real OMW

8.3.3.1. Catalyst selection

The two most promising materials (based on the catalytic and stability results with the synthetic solution) were selected for the depuration of more complex and highly-loaded real OMW samples. Operational conditions employed were the same as reported so far, using the highest concentration of catalyst tested (2 g/L). Results in Fig. 8.13a display the performance of previously saturated samples of OSAC-Fe-IWI and OSAC-Fe-Ads.

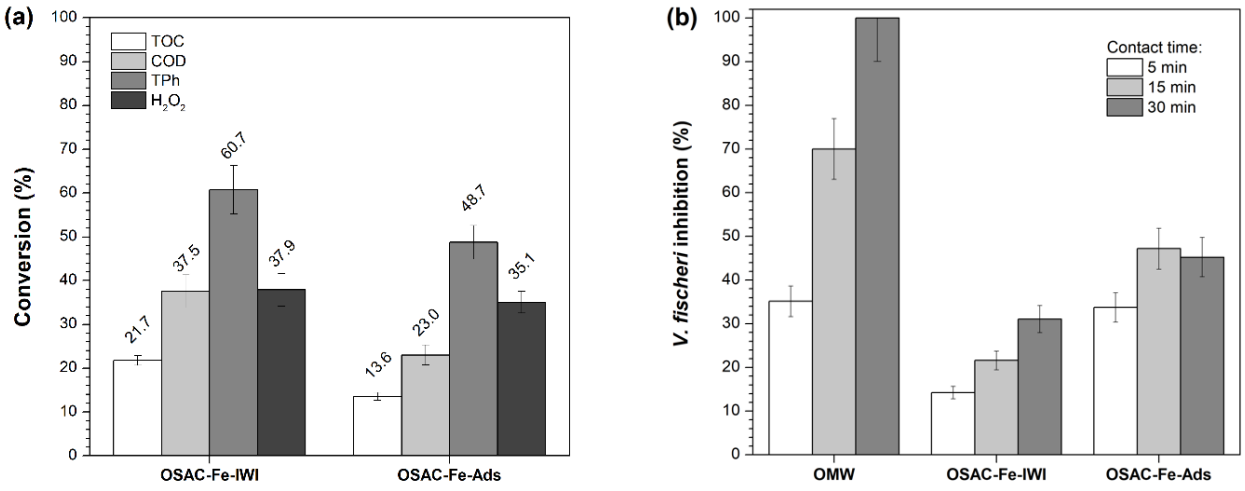


Fig. 8.13 (a) TOC, COD, and TPh removals of real OMW samples, and H_2O_2 conversions by OSAC-Fe-IWI and OSAC-Fe-Ads (after 240 min); (b) Inhibition (%) of the Vibrio fischeri at different contact times in the presence of ten-fold diluted OMW sample and after CWPO.

Similar to the results observed in the experiments with the synthetic solution, only a fraction of the initial organic load is completely oxidized, as TOC removals were lower than COD ones in both cases. M. Lucas and J. Peres [32] also reported on the treatment of real ten-fold diluted

OMW but by the homogeneous Fenton process. Using an H_2O_2/COD mass ratio of 0.5 (close to the one reported in this study – 0.6), the authors recorded 36% COD abatement (COD_0 = 5.34 g/L). Employing a mass ratio of 1, the removal of COD increased to 42% while TOC mineralization was fixed at 26%, following the same trend and range of values here reported.

As shown in Fig. 8.13a, the polyphenolic fraction of the effluent was also considerably reduced in both cases, which led to the decrease of the effluent's toxicity, as inferred by the *V. fischeri* luminescence inhibition values recorded at different contact times – Fig. 8.13b. The untreated ten-fold diluted OMW used showed high toxicity towards the marine bacteria (70% inhibition after 15 min in contact, reaching 100% inhibition after 30 min), which was considerably lowered after CWPO (e.g., using the OSAC-Fe-IWI catalyst, only 30 % inhibition was recorded after 30 min of contact time).

S. Azabou *et al*. [33] also reported on the CWPO of 5-fold diluted OMW but using an Al/Fe-pillared clay catalyst. Operating at 25 °C in a semi-batch mode (8 h of continuous H_2O_2 feed up to a final concentration of 2×10^{-2} M, catalyst concentration of 0.5 g/L), approximately 37% COD reduction and 54% phenol removal were registered. Furthermore, a significant reduction of the effluent's toxicity towards the marine bacteria *V. fischeri* was achieved (from 80 to 30% inhibition after CWPO), which was linked to the reduction of the polyphenolic fraction of the OMW, in line with the results obtained in this work.

In spite of the promising results obtained by OSAC-Fe-Ads, the ultimate goal is the selection of a catalyst that maximizes removal efficiencies (although also producing a less toxic effluent after the process), so OSAC-Fe-IWI was used in further studies.

8.3.3.2. Influence of key operational parameters: pH and H_2O_2 dose

Unlike the classic Fenton process, the reported optimum pH range of values for heterogeneous catalytic processes is not always limited to pH close to 3 [26], which is advantageous as it expands the scale of CWPO application to a wider range of wastewaters [34]. Additionally to the results obtained with the effluent's unaltered initial value (i.e., pH ≈ 4.9), two more initial pH values were evaluated, corresponding to the optimum widely reported in the literature (pH ≈ 3) and a circumneutral value of ≈6.8.

Fig. 8.14a shows that, after 240 min, removals slightly improved upon acidification of OMW to pH_0 ≈ 3 regarding the unaltered initial pH value of this effluent (even for TOC, improvement was

small – 26.1 *vs*. 21.7%), whereas operating at near-neutral pH the oxidative process was noticeably hindered. Higher pH values may contribute to the formation of surface ferric-hydroxide complexes [35] that preferentially decompose H_2O_2 to molecular oxygen and water instead of •OH, as already reported by other authors [6,36]. Despite the higher initial rate of organics degradation at $pH_0 \approx 3$ (e.g., as shown in Fig. C.9 for COD removals up to t = 60 min), the overall efficiency after 240 min is practically the same when operating at $pH_0 \approx 4.9$, which is very advantageous from an operational point-of-view as no initial pH adjustments are required.

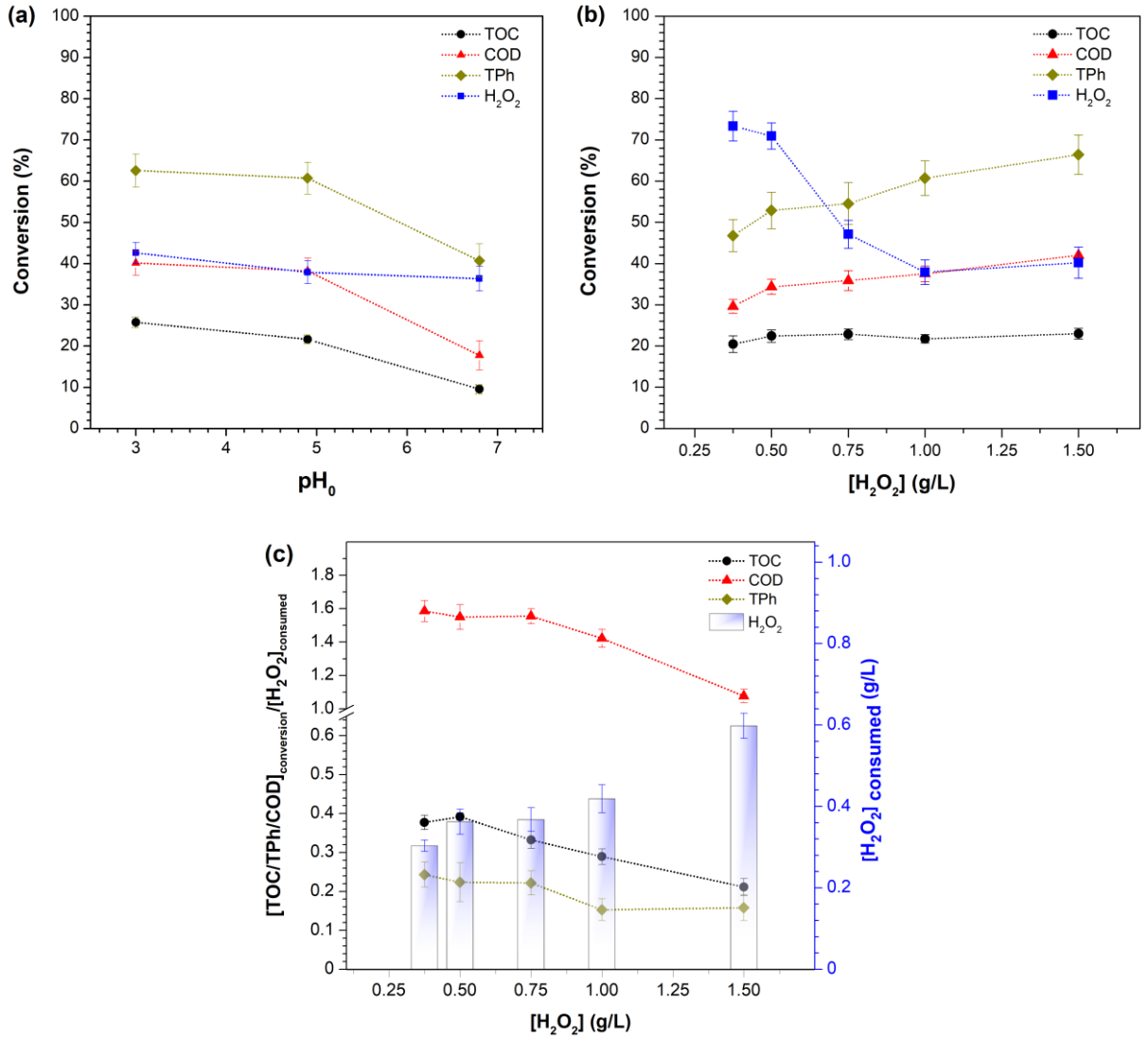


Fig. 8.14 Conversion efficiencies after 240 min with OSAC-Fe-IWI catalyst with different (a) initial pH ([Cat] = 2.0 g/L, $[H_2O_2]$ = 1.0 g/L, T_0 = 25 °C), and (b) H_2O_2 dosages ([Cat] = 2.0 g/L, pH_0 = 4.9, T_0 = 25 °C); (c) Efficiency of degradation *vs*. H_2O_2 conversions (right y-axis: H_2O_2 consumed (g/L)).

Low H_2O_2 decomposition efficiencies (<50%) were also observed in this set of runs using an initial H_2O_2 concentration of 1.0 g/L. The use of excessive H_2O_2 can lead to the scavenging of •OH via the diffusion-controlled reactions shown in Eqs. (2.7) and (2.9) [26], whereas a deficiency of

oxidant may limit the extent of oxidation. Thus, the optimization of this parameter is essential in CWPO and Fig. 8.14b highlights the influence of the initial H_2O_2 dose on the catalytic process (for oxidant concentrations in the 0.375–1.50 g/L range). According to the catalytic results, TPh and COD removals increased as higher H_2O_2 concentrations were used, while TOC mineralization remained practically unchanged, in line with results obtained in other studies [6,37]. For the range studied, complete conversion of H_2O_2 was never achieved after 240 min of reaction, as the diffusion rate of H_2O_2 molecules to Fe-active sites is slower for smaller oxidant doses.

The selection of an optimum oxidant dose (and catalyst too) will entirely depend on the required characteristics of the wastewater after the treatment. Nonetheless, in order to keep the process economically attractive, a compromise should be made to minimize the amount of unconverted H_2O_2 in the effluent whilst trying to maintain degradation levels as high as possible. Fig. 8.14c presents a graphical representation of H_2O_2 consumption efficiency, where the ratio between the amount of TOC or TPh or COD removed (in g/L) per H_2O_2 consumed (g/L) is plotted for each concentration of oxidant used. As the catalyst concentration is the same in all cases (and so the expected number of Fe-active sites), that ratio is progressively smaller as oxidant concentrations increase, since the higher H_2O_2 consumed (right-y axis) is not traduced in deeper oxidation of contaminants but undesired oxidant scavenging reactions. Following the results obtained, the H_2O_2 dosage of 0.50 g/L was selected for further studies.

8.3.3.3. Evaluation of the treated wastewater quality

Despite the importance of TOC, TPh, and H_2O_2 analysis for a performance evaluation point-of-view, these parameters are not considered in many environmental laws, hence analysis of COD, BOD_5, and discoloration is also imperative. Table 8.7 compiles the effluent's physicochemical parameters before and after CWPO treatment ([Cat] = 2.0 g/L, $[H_2O_2]$ = 0.50 g/L, $pH_0 \approx 4.9$, T_0 = 25 °C). Under the operational conditions selected for an operation time of 240 min, the wastewater is not suitable for direct discharge in natural water bodies according to legislated values. Still, COD values close to the thresholds defined for controlled industrial discharges in local sewage collectors were reached, although TPh ones were not. It is however worth noting the discoloration achieved after oxidation. In contrast to the initial brown hue characteristic of OMW, treated samples displayed a pale-yellow coloration after the process (*cf*. Fig. C.10 – sample (2) also highlights the easiness to recover the catalyst by sedimentation), indicative of the

combined depolymerization of high molecular-mass molecules (such as tannins) and oxidation of some smaller aromatic compounds [6].

Table 8.7 Physicochemical properties of OMW before and after CWPO, and legal discharge limits for industrial effluents: (a) direct discharge to natural water resources, (b) industrial discharge in municipal collectors; values and standard deviations reported result from 3 independent analyses.

Parameter	OMW	After CWPO	Discharge limit
pH	4.9 ± 0.1	3.7 ± 0.1	6 – 9[(a),(b)]
TOC (mg/L)	545 ± 16.3	430 ± 9.1	n.e.
COD (mg O_2/L)	1648.2 ± 45.2	1079 ± 34.9	150[(a)]/1000[(b)]
BOD_5 (mg O_2/L)	360.8 ± 38.3	220.0 ± 20.0	40[(a)]/500[(b)]
TPh (mg GA_{eq}/L)	153.0 ± 9.8	69.3 ± 7.8	-[(a)]/0.5[(b)]
Fe_{total} (mg/L)	n.d.	0.42 ± 0.09	2.0[(a),(b)]
V. fischeri inhibition % (30 min)	100	36.4 ± 3.7	n.e.
Biodegradability (COS/AOS indices)	-0.48/-0.48	1.25/0.24	n.e.
Visible color after 1:20 dilution	Visible	Not visible	Not visible

[(a)] According to Portuguese Decree Law no. 236/98, August 1st
[(b)] According to "Regulation for Industrial Discharges no. 169/2015" (DR 2nd series – no. 71 – April 13th 2015)
n.d. – not detected
n.e. – not established

As mentioned in the introductory section, a cost-effective solution commonly proposed to meet discharge limits is the coupling of biological degradation processes [38,39]. Therefore, the evaluation of the effluent's biodegradability indices and toxicity values are important factors to determine if the wastewater is amenable for further biological depuration. Carbon oxidation state (COS) and average oxidation state (AOS) – Eqs. (3.3) and (3.4), respectively – can provide an indication as to the biodegradability of the resulting effluent. Findings show that COS and AOS indices increased from -0.48 to 1.25 and 0.24, respectively (Fig. C.11 shows COS and AOS variation along time), highlighting the enhancement of biodegradability after the treatment but also the formation of non-oxidized reaction intermediates. In spite of the lower oxidant dosage selected in this case ([H_2O_2] = 0.5 g/L), toxicity values reported are in the same order of magnitude as those reported in Fig. 8.13b, with the final effluent only producing *ca*. 36% inhibition to *V. fischeri* bacteria (after a contact time of 30 min).

8.4. CONCLUSIONS

Olive stones were used as Fe-supports for the catalytic heterogeneous Fenton-like oxidation of olive mill wastewater, in the perspective of simultaneous valorization and treatment of both by-products of this agro-industrial activity. Fe-supports have been prepared by carbonization and CO_2-activation, by three different Fe-impregnation strategies. Despite the same initial theoretical Fe load, the impregnation routes led to markedly distinct materials, both in resulting metal loading, particles' size and dispersion, and morphological features of the catalysts.

Screening of the synthesized materials with a synthetic polyphenolic solution showed that all catalysts were able to achieve *ca*. 80 % removal of phenolic compounds, correspondent to *ca*. 50 % TOC mineralization, under smooth conditions (25 °C, pH = 3.5, [Cat] = 2.0 g/L, $[H_2O_2]$ = 1.0 g/L, t = 240 min). Nonetheless, the catalyst prepared via the hydrothermal route (OSAC-Fe-HT) displayed worse catalytic results in consecutive cycles, not only as a result of the smaller Fe content but also as a consequence of the higher extent of Fe leaching observed. From the stability tests, and apparent kinetic constants and initial reaction rates computed, wherein the effect of different iron contents is discarded, the most promising catalysts – OSAC-Fe-IWI and OSAC-Fe-Ads – were selected for the depuration of a real OMW solution.

After optimization of key operational parameters, experiments with OSAC-Fe-IWI performed at room temperature, without adjustment of the effluent's initial pH, and at a moderate concentration of reagents ($[H_2O_2]$ = 0.5 g/L, [Cat] = 2.0 g/L), resulted in *ca*. 55% TPh and 37% COD removals, with 71% H_2O_2 conversion, after only 240 min. Despite not achieving the threshold values legally imposed for direct discharge under such soft conditions, the produced effluent could reduce the stress of subsequent treatment processes, including biological steps commonly found in wastewater treatment plants. In fact, COS and AOS indices confirmed the biodegradability improvement of the resulting effluent (despite the presence of some refractory compounds), whereas tests with *V. fischeri* bacteria highlighted a significant reduction in the effluent's toxicity (from initial 100% bioluminescence inhibition to *ca*. 36% after CWPO).

Although the synthesis of heterogeneous catalysts from organic by-products is an energy-intense process, the heterogeneous catalytic process presents advantages regarding the homogeneous one (and also other AOPs) that should be weighted on: soft operational conditions, the possibility for catalyst reuse in consecutive cycles without major activity loss (or operation in a continuous mode in a flow-through reactor), easiness of recuperation of the catalyst after use, and more

importantly, no secondary waste generated by dissolved Fe in solution (that ultimately would require a downstream management solution with added costs associated with reagents and equipment).

REFERENCES

1. Esteves, B.M.; Morales-Torres, S.; Maldonado-Hódar, F.J.; Madeira, L.M. Fitting biochars and activated carbons from residues of the olive oil industry as supports of Fe-catalysts for the heterogeneous Fenton-like treatment of simulated olive mill wastewater. *Nanomaterials* **2020**, 10, 876.
2. Stasinakis, A.S.; Elia, I.; Petalas, A. V.; Halvadakis, C.P. Removal of total phenols from olive-mill wastewater using an agricultural by-product, olive pomace. *J. Hazard. Mater.* **2008**, 160, 408–413.
3. Vilardi, G.; Rodriguez-Rodriguez, J.; Miguel Ochando-Pulido, J.; Di Palma, L.; Verdone, N. Fixed-bed reactor scale-up and modelling for Cr(VI) removal using nano iron-based coated biomass as packing material. *Chem. Eng. J*. **2019**, 361, 990–998.
4. Aggoun, M.; Arhab, R.; Cornu, A.; Portelli, J.; Barkat, M.; Graulet, B. Olive mill wastewater microconstituents composition according to olive variety and extraction process. *Food Chem.* **2016**, 209, 72–80.
5. Dermeche, S.; Nadour, M.; Larroche, C.; Moulti-Mati, F.; Michaud, P. Olive mill wastes: Biochemical characterizations and valorization strategies. *Process Biochem.* **2013**, 48, 1532–1552.
6. Kallel, M.; Belaid, C.; Mechichi, T.; Ksibi, M.; Elleuch, B. Removal of organic load and phenolic compounds from olive mill wastewater by Fenton oxidation with zero-valent iron. *Chem. Eng. J.* **2009**, 150, 391–395.
7. Martins, R.C.; Gomes, T.; Quinta-Ferreira, R.M. Fenton's depuration of weathered olive mill wastewaters over a Fe-Ce-O solid catalyst. *Ind. Eng. Chem. Res.* **2010**, 49, 9043–9051.
8. Vilardi, G.; Ochando-Pulido, J.M.; Verdone, N.; Stoller, M.; Di Palma, L. On the removal of hexavalent chromium by olive stones coated by iron-based nanoparticles: Equilibrium study and chromium recovery. *J. Clean. Prod.* **2018**, 190, 200–210.
9. Bansal, R.C.; Donnet, J.B.; Stoeckli, F. *Active Carbon*; Dekker: New York, **1998**; ISBN 978-0824778422.
10. Demir, M.; Kahveci, Z.; Aksoy, B.; Palapati, N.K.R.; Subramanian, A.; Cullinan, H.T.; El-Kaderi, H.M.; Harris, C.T.; Gupta, R.B. Graphitic biocarbon from metal-catalyzed hydrothermal carbonization of lignin. *Ind. Eng. Chem. Res.* **2015**, 54, 10731–10739.
11. Saiphaneendra, B.; Saxena, T.; Singh, S.A.; Madras, G.; Srivastava, C. Synergistic effect of co-existence of hematite (α-Fe_2O_3) and magnetite (Fe_3O_4) nanoparticles on graphene sheet for dye adsorption. *J. Environ. Chem. Eng.* **2017**, 5, 26–37.
12. Hu, X.; Liu, B.; Deng, Y.; Chen, H.; Luo, S.; Sun, C.; Yang, P.; Yang, S. Adsorption and heterogeneous Fenton degradation of 17α-methyltestosterone on nano Fe_3O_4/MWCNTs in aqueous solution. *Appl. Catal. B Environ.* **2011**, 107, 274–283.
13. Pérez-Cadenas, A.F.; Maldonado-Hódar, F.J.; Moreno-Castilla, C. On the nature of surface acid sites of chlorinated activated carbons. *Carbon* **2003**, 41, 473–478.
14. Morales-Torres, S.; Maldonado-Hódar, F.J.; Pérez-Cadenas, A.F.; Carrasco-Marín, F. Design of low-temperature Pt-carbon combustion catalysts for VOC's treatments. *J. Hazard. Mater.* **2010**, 183, 814–822.
15. McIntyre, N.S.; Zetaruk, D.G. X-ray photoelectron spectroscopic studies of iron oxides. *Anal. Chem.* **1977**, 49, 1521–1529.
16. Wang, J.; Guo, X. Adsorption kinetic models: Physical meanings, applications, and solving methods. *J. Hazard. Mater.* **2020**, 390, 122156.
17. Andjelković, M.; Van Camp, J.; De Meulenaer, B.; Depaemelaere, G.; Socaciu, C.; Verloo, M.; Verhe, R. Iron-chelation properties of phenolic acids bearing catechol and galloyl groups. *Food Chem.* **2006**, 98, 23–31.
18. Zazo, J.A.; Casas, J.A.; Mohedano, A.F.; Rodríguez, J.J. Catalytic wet peroxide oxidation of phenol with a Fe/active carbon catalyst. *Appl. Catal. B Environ.* **2006**, 65, 261–268.
19. Najjar, W.; Azabou, S.; Sayadi, S.; Ghorbel, A. Screening of Fe-BEA catalysts for wet hydrogen peroxide oxidation of crude olive mill wastewater under mild conditions. *Appl. Catal. B Environ.* **2009**, 88, 299–304.
20. Gomes, H.T.T.; Figueiredo, J.L.L.; Faria, J.L.L. Catalytic wet air oxidation of olive mill wastewater. *Catal. Today* **2007**, 124, 254–259.
21. EEC Council Directive 75/440. European Economic Community; Brussels, 1975;
22. Achma, R. Ben; Ghorbel, A.; Dafinov, A.; Medina, F. Copper-supported pillared clay catalysts for the wet hydrogen peroxide catalytic oxidation of model pollutant tyrosol. *Appl. Catal. A Gen.* **2008**, 349, 20–28.

23. Isari, A.A.; Hayati, F.; Kakavandi, B.; Rostami, M.; Motevassel, M.; Dehghanifard, E. N, Cu co-doped TiO_2@functionalized SWCNT photocatalyst coupled with ultrasound and visible-light: An effective sono-photocatalysis process for pharmaceutical wastewaters treatment. *Chem. Eng. J.* **2020**, 392, 123685.
24. Hartmann, M.; Kullmann, S.; Keller, H. Wastewater treatment with heterogeneous Fenton-type catalysts based on porous materials. *J. Mater. Chem.* **2010**, 20, 9002–9017.
25. Yan, Y.; Jiang, S.; Zhang, H. Efficient catalytic wet peroxide oxidation of phenol over Fe-ZSM-5 catalyst in a fixed bed reactor. *Sep. Purif. Technol.* **2014**, 133, 365–374.
26. Navalon, S.; Dhakshinamoorthy, A.; Alvaro, M.; Garcia, H. Heterogeneous Fenton catalysts based on activated carbon and related materials. *ChemSusChem* **2011**, 4, 1712–1730.
27. Gil, A.; Korili, S.A.; Trujillano, R.; Vicente, M.A. Pillared clays and related catalysts; **2010**; ISBN 9781441966698.
28. Lopes, R.J.G.; Silva, A.M.T.; Quinta-Ferreira, R.M. Screening of catalysts and effect of temperature for kinetic degradation studies of aromatic compounds during wet oxidation. Appl. Catal. B Environ. 2007, 73, 193–202.
29. Guedes, A.M.F.M.; Madeira, L.M.P.; Boaventura, R.A.R.; Costa, C.A.V. Fenton oxidation of cork cooking wastewater - Overall kinetic analysis. *Water Res.* **2003**, 37, 3061–3069.
30. Fogler, H.S. Elements of Chemical Reaction Engineering; 4th ed.; Prentice Hall PTR: Massachusetts, **2005**; ISBN 0130473944.
31. Huang, C.P.; Huang, Y.H. Comparison of catalytic decomposition of hydrogen peroxide and catalytic degradation of phenol by immobilized iron oxides. *Appl. Catal. A Gen.* **2008**, 346, 140–148.
32. Lucas, M.S.; Peres, J.A. Treatment of olive mill wastewater by a combined process: Fenton's reagent and chemical coagulation. *J. Environ. Sci. Heal. - Part A Toxic/Hazardous Subst. Environ. Eng.* **2009**, 44, 198–205.
33. Azabou, S.; Najjar, W.; Bouaziz, M.; Ghorbel, A.; Sayadi, S. A compact process for the treatment of olive mill wastewater by combining wet hydrogen peroxide catalytic oxidation and biological techniques. *J. Hazard. Mater.* **2010**, 183, 62–69.
34. Wang, N.; Zheng, T.; Zhang, G.; Wang, P. A review on Fenton-like processes for organic wastewater treatment. *J. Environ. Chem. Eng.* **2016**, 4, 762–787.
35. Kiril Mert, B.; Yonar, T.; Yalili Kiliç, M.; Kestioğlu, K. Pre-treatment studies on olive oil mill effluent using physicochemical, Fenton and Fenton-like oxidations processes. *J. Hazard. Mater.* **2010**, 174, 122–128.
36. Kakavandi, B.; Ahmadi, M. Efficient treatment of saline recalcitrant petrochemical wastewater using heterogeneous UV-assisted sono-Fenton process. *Ultrason. Sonochem.* **2019**, 56, 25–36.
37. Pariente, M.I.; Siles, J.A.; Molina, R.; Botas, J.A.; Melero, J.A.; Martinez, F. Treatment of an agrochemical wastewater by integration of heterogeneous catalytic wet hydrogen peroxide oxidation and rotating biological contactors. *Chem. Eng. J.* **2013**, 226, 409–415.
38. Vuppala, S.; Bavasso, I.; Stoller, M.; Di Palma, L.; Vilardi, G. Olive mill wastewater integrated purification through pre-treatments using coagulants and biological methods: Experimental, modelling and scale-up. *J. Clean. Prod.* **2019**, 236, 117622.
39. Vlyssides, A.G.; Lamprou, G.K.; Vlysidis, A. Industrial case studies on the detoxification of OMWW using Fenton oxidation process followed by biological processes for energy and compost production. *Olive Mill Waste Recent Adv. Sustain. Manag.* **2017**, 119–138.

CHAPTER 9

SUSTAINABLE IRON-OLIVE STONE BASED-CATALYSTS FOR FENTON-LIKE OMW TREATMENT: DEVELOPMENT AND PERFORMANCE ASSESSMENT IN CONTINUOUS FIXED-BED REACTOR OPERATION

Highlights

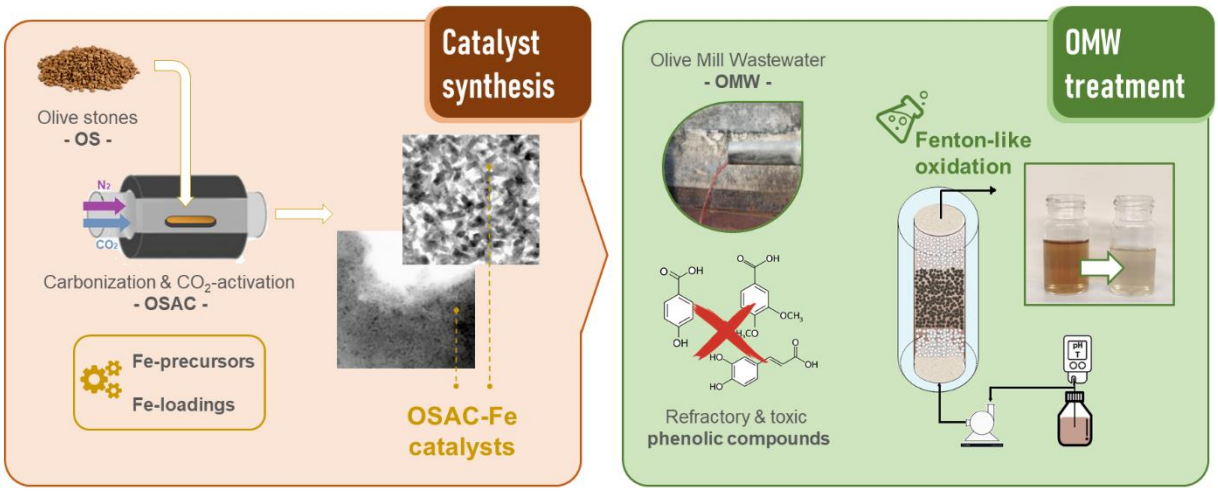
- An organic by-product is integrated in olive mill wastewater Fenton-like treatment;
- Good Fe dispersion is key to improve olive stone-derived catalysts' efficiency;
- The oxidation of toxic phenolic compounds is correlated with their chemical properties;
- OMW organic load and toxicity reduced upon continuous fixed-bed reactor operation.

The contents of this chapter were adapted from:

Esteves, B.M., Morales-Torres, S., Maldonado-Hódar, F.J., Madeira, L.M., Chemical Engineering Journal, 2022, 435, 134809. https://doi.org/10.1016/j.cej.2022.134809

ABSTRACT

Iron oxide catalysts supported on activated carbon prepared from olive stones (OSAC-Fe) were used for the catalytic wet peroxide oxidation of refractory polyphenolic solutions and real olive mill wastewater (OMW) in a fixed-bed reactor (FBR). Catalysts were prepared with different precursors and Fe-loadings. The resulting catalysts were essentially microporous materials with well-developed surface areas (S_{BET} = 588–689 m^2/g), whereas the nature and distribution of metallic nanoparticles were found to be strongly dependent on the precursor used. The stability and catalytic performance were screened in a batch reactor using a synthetic solution and the most promising catalyst – prepared at 5 wt.% Fe using $Fe(NO_3)_3$ as the precursor – was selected for the operation of a continuous FBR. Different operational conditions were evaluated through a parametric study. At 60 °C, $[H_2O_2]_{feed}$ = 1.5 g/L and Q = 0.75 mL/min, 87% total phenolic content removal (TPh), 28% mineralization and 88% H_2O_2 conversion were achieved at steady-state. Real OMW samples were then treated at a fixed $[H_2O_2]$/[COD] in the feed, and TPh removals of 57–71% and COD (chemical oxygen demand) reductions of 26–34% were attained. The resulting effluents showed an overall reduction of eco-toxicity and improvement of biodegradability indices.



9.1. INTRODUCTION

In the previous chapter, olive stone-derived Fe-catalysts were prepared following different impregnation methods and used for the CWPO of both polyphenolic solutions and real OMW [1]. The goal was the recovery of an olive oil industry by-product (olive stone) and its repurpose as an integral part of the treatment of wastewaters generated within the same agro-industrial activity. Nonetheless, the work focused on the application of such materials in a discontinuous operation context (batch reactor), with disadvantages related to the necessity to separate the catalyst from the treated effluent, implying an interruption of the operation (unless working with parallel reactors) [2].

In this chapter, olive stone-derived activated carbons (OSAC) were again selected as support for the synthesis of a series of catalysts with distinct properties regarding the iron salt used as the precursor and the Fe-loading. The catalytic performance of the resulting materials was correlated with their morphological and chemical properties in the oxidation of a synthetic polyphenolic solution. The most promising catalyst was then selected for the treatment of synthetic and real OMW solutions, in a continuous operation mode using a fixed-bed reactor (FBR), with the inherent evaluation of operational parameters (reaction temperature, H_2O_2 feed dose, and volumetric flow rate/contact time). The catalytic performance and stability were monitored through the assessment of several parameters, including the degradation of individual phenolic compounds (followed by high-performance liquid chromatography – HPLC), chemical oxygen demand (COD), total phenolic content (TPh), and total organic carbon (TOC) removals, as well as H_2O_2 consumption and Fe leaching. Moreover, distinct synthetic polyphenolic formulations were prepared, and the properties of the different phenolic compounds used were correlated to the degradation efficiencies obtained. Having established the best operating conditions for the process in the FBR, the treatment of actual OMW samples (with increasing initial organic loads) was finally tested, and the resulting effluent toxicity (inferred from the Vibrio fischeri luminescence inhibition) and biodegradability (BOD_5/COD ratio, and average oxidation state – AOS) were also estimated.

9.2. MATERIALS AND METHODS

9.2.1. Catalysts synthesis

The catalyst supports were prepared by sequential carbonization and CO_2–physical activation at 800 °C of raw olive stones (OS) to produce OS-derived activated carbons (OSAC); the procedure is thoroughly described in Chapter 8. Separate fractions of OSAC with a particle size range of 0.45–0.80 mm were loaded with iron via incipient wetness impregnation (IWI), using either $FeCl_2 \cdot 4H_2O$ (Acros Organics) or $Fe(NO_3)_3 \cdot 9H_2O$ (Merck) as iron precursors. For each case, the amount of salt required to obtain catalysts with theoretical Fe-loads of 1, 2, or 5 wt.% was dissolved in the minimum amount of distilled water (according to the salt solubility) with the aid of ultrasound agitation (Argo Lab, mod. DU-45). Thereafter, each solution was added dropwise and uniformly to agitated fractions of OSAC until the entire volume was homogeneously incorporated in the OSAC particles. After oven-dried overnight at 100 °C, the impregnated OSAC fractions were thermally treated (at 350 °C, under an N_2 flow for 1 h) to decompose the iron salt and to produce OSAC-Fe catalysts.

9.2.2. Synthetic polyphenolic solutions and real OMW

The catalysts screening was performed in a batch reactor using a synthetic solution comprised of different phenolic compounds to simulate the refractory polyphenolic fraction commonly found in real OMW [3–5]. By using synthetic solutions instead of real OMW samples (which entail inherent variability of physicochemical properties from batch to batch), a more equitable comparison between catalytic performances is possible. The polyphenolic solution used in the screening runs (“Synthetic 1”, Table 9.1) comprised five phenolic compounds, each with equal initial concentration (70 mg/L) to produce a solution with a total phenolic content (TPh) of 350 mg/L.

Further experiments, performed in a continuous-flow fixed-bed reactor (FBR), were performed using both polyphenolic and real OMW solutions. For that, two additional synthetic formulations were prepared by varying the phenolic compounds selected according to Table 9.1, though maintaining an analogous initial total phenolic concentration as solution “Synthetic-1”. Gallic, syringic, and 4-hydroxybenzoic acids (Alfa Aesar), protocatechuic, caffeic, and veratric acids (Acros Organics), tyrosol and vanillic acid (Sigma-Aldrich), were the model compounds used in this study – the corresponding chemical structures are presented in Fig. D.1, Appendix D. The

three synthetic solutions were obtained by dissolving the appropriate (and equal) amount of each compound in distilled water with the aid of ultrasound agitation.

Table 9.1 Phenolic compounds selected for each formulation used.

	Synthetic-1	Synthetic-2	Synthetic-3
Gallic acid (GA)	✓	✓	
Syringic acid (SA)		✓	✓
4-Hydroxybenzoic acid (4-HbA)			✓
Protocatechuic acid (PA)	✓		✓
Caffeic acid (CA)	✓	✓	
Veratric acid (VrA)		✓	✓
Tyrosol (Ty)	✓		✓
Vanillic acid (VA)	✓	✓	

Samples of real OMW were collected directly from the decanter's exit of a 3-phase olive mill (northern region of Portugal) in late 2019. Due to the high concentration of suspended solids and overall particulate matter, samples were left to settle for 24 h. Thereafter, the effluent supernatant was collected, filtered, separated into individual 1 L containers, and then frozen until needed. Before the experiments, the initial organic load of OMW samples was adjusted to produce solutions with different initial COD values by dilution with distilled water. The main physicochemical properties of the real effluent filtered supernatant and "Synthetic-1" solution are summarized in Table 9.2.

Table 9.2 Physicochemical properties of the polyphenolic solution and filtered sample of OMW used (supernatant, non-diluted).

Parameter	"Synthetic-1"	OMW
pH	3.5 ±0.1	4.5 ±0.4
COD (mg O_2/L)	546 ±9	17724 ±624
BOD_5 (mg O_2/L)	160 ±10	4300 ±282
TPh (mg GA_{eq}/L)	340 ±7	1247 ±72
TOC (mg C/L)	203 ±4	6340 ±177
BOD_5/COD	0.29	0.24
AOS	-0.06	-0.43
V. fischeri inhibition (%)	>99	71.4
Color (1:20 dilution)	non-visible	visible

9.2.3. Catalytic runs

Preliminary screening experiments were executed in a 300 mL jacketed glass batch reactor connected to a recirculating thermostatic bath (VWR, mod. 89202-912) set at 20 °C. All runs were performed with 150 mL of "Synthetic-1" solution, which was kept in agitation at 300 rpm using a Falc Instruments magnetic stirrer, while the medium pH and temperature were continuously monitored using a WTW Inolab pH-meter. Catalytic runs started with the simultaneous addition of 0.5 mL of H_2O_2 (30% *w/v*, VWR) and 300 mg of catalyst. The same experimental conditions were maintained for all screening tests: [Cat] = 2.0 g/L, $[H_2O_2]_0$ = 1.0 g/L, $pH_0 \approx 3.5$ (i.e., solution initial pH without adjustments). Samples were periodically collected and filtered through Whatman qualitative filter papers (0.45 μm) before HPLC, TOC, and H_2O_2 analyses, as detailed in the next section. After each cycle (t = 300 min), the catalyst was recovered by filtration and dried overnight at 100 °C. Adsorption runs were performed in the same way but without the addition of the oxidant.

Continuous-flow experiments were conducted in a jacketed up-flow fixed-bed reactor (borosilicate glass column, 1.5 cm internal diameter, and 12 cm bed length) also connected to a recirculating thermostatic bath set at the desired system temperature. The column was capped in both ends with glass wool (to prevent the clogging of inlet/outlet tubbing by detached powder catalyst

particles), the required amount of catalyst was placed in the center of the column (1000 mg, corresponding to approximately 1/3 of the column height), bounded by 1 mm diameter inert glass beads (to pack the column and promote more uniform dispersion of the solution) as illustrated in Fig. 9.1.

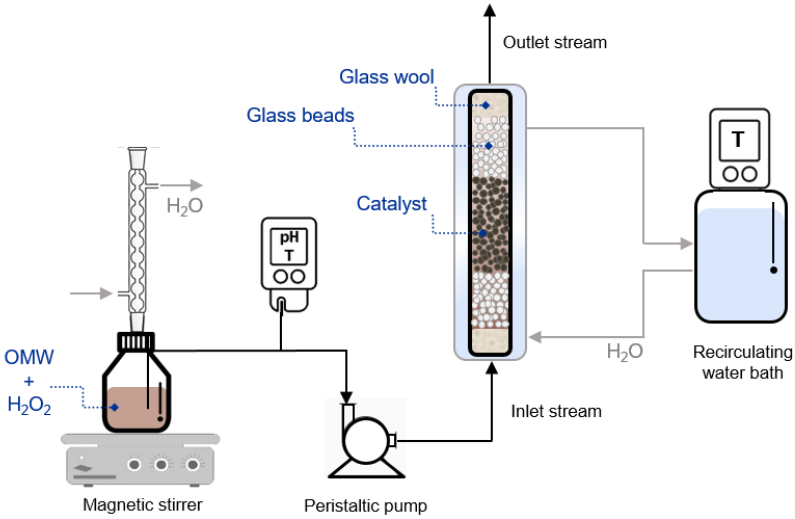


Fig. 9.1 Scheme of the up-flow fixed-bed reactor (FBR) experimental set-up.

Before each run, the column was filled with distilled water. The inlet stream was continuously fed to the reactor by a peristaltic pump (NEW-ERA, mod. NE 900), and the flowrate was adjusted as needed. The temperature of the feed solution was controlled using a magnetic stirrer equipped with a temperature control system. To prevent evaporation of the feed solution when working at high temperatures, a reflux condenser connected to a recirculating water bath, set at T = 15 °C, was installed. After reaching the desired temperature of the feed OMW, the required amount of H_2O_2 was added, the vial sealed, and the solution kept agitated and 300 rpm throughout the experiment. It is worth noticing that the concentration of H_2O_2 in the feed vial was also evaluated over time, being that the initial concentration of oxidant varied less than 5% throughout the entire range of experiments, even when higher temperatures were employed, which suggests that thermal decomposition of H_2O_2 was also negligible. Under such conditions, the action of hydrogen peroxide only resulted in minor oxidation of the contaminants in the vial, as further detailed in Section 9.3.2.1.

9.3. RESULTS AND DISCUSSION

9.3.1. Textural and chemical characterization of the materials

The total metal content (wt.%) of the catalysts was determined by AAS (Fe_{AAS}) and compared to the theoretical programmed values (Fe_{theor}). As shown in Table 9.3, the resulting Fe-loadings only varied slightly from the calculated ones, suggesting that the incipient wetness impregnation procedure is convenient and reliable for the doping of such activated carbons with either chloride or nitrate solutions.

Table 9.3 Textural characteristics of the OSAC support and derived OSAC-Fe catalysts, Fe loadings (wt.%) obtained from AAS analysis.

Sample	Fe_{theor} (wt.%)	Fe_{AAS} (wt.%)	S_{BET} (m^2/g)	W_0 (cm^3/g)	L_0 (nm)	V_{meso} (cm^3/g)	V_T (cm^3/g)
OSAC (support)	-	-	792	0.32	1.0	0.04	0.39
OSAC-$FeCl_2$	2.0	1.96	689	0.28	1.0	0.11	0.43
OSAC-$Fe(NO_3)_3$	1.0	0.83	677	0.27	0.9	0.08	0.39
	2.0	2.07	662	0.26	0.8	0.06	0.36
	5.0	4.83	588	0.24	1.0	0.05	0.31

The textural properties of the OSAC support and the morphological changes produced after Fe-impregnation were determined by analyzing the N_2 adsorption-desorption isotherms (Fig. 9.2a). The parameters obtained are also summarized in Table 9.3. The AC support is essentially a microporous material with a certain volume of mesopores, as depicted by the hybrid type-I and type-IV shape of the isotherms (according to the International Union of Pure and Applied Chemistry – IUPAC – classification). After filling the microporosity at low P/P_0, the amount adsorbed does not approach a plateau typical of type I isotherms, but instead exhibits a slight increase with increasing relative pressures, that together with the hysteresis loop formed by the desorption branch, confirms the presence of mesopores. The pore size distribution (PSD, Fig. 9.2b) showed the preponderance of micropores around 1.0 nm and mesopores of *ca*. 3.0 nm in diameter.

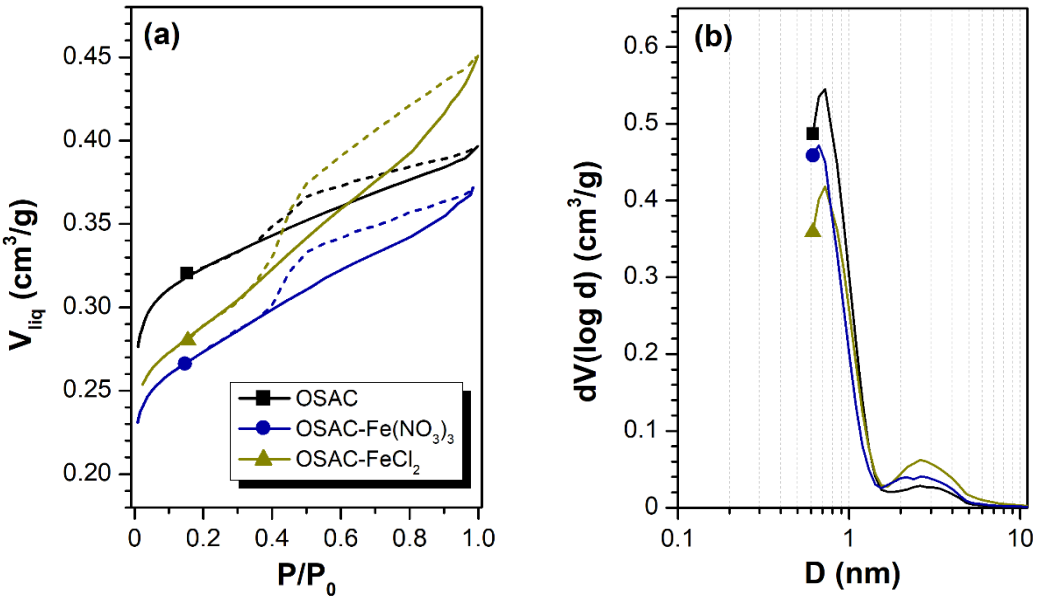


Fig. 9.2 (a) N_2-adsorption/desorption isotherms and (b) pore size distribution (PSD) of OSAC support and derived Fe-catalysts (2 wt.% Fe).

The micropore volume (W_0) of the catalysts decreased in all cases regarding OSAC, being progressively lower with increasing Fe-loadings, which also induces the progressive drop of the surface area values observed (Table 9.3). Nevertheless, although mesoporosity also decreased in the same sense, it increased in all cases regarding the support, especially when using $FeCl_2$ as the precursor. The formation of more open porosity – mesoporosity – is clearly favored for OSAC-$FeCl_2$ when compared to the analogous catalyst prepared with $Fe(NO_3)_3$ (as emphasized by the steeper isotherm shape profile in Fig. 9.2a).

The mean size of microporosity of the OSAC support (L_0 = 1.0 nm) and the average crystallite size of the metallic particles formed (d_{XRD} from <4 up to 12 nm for α-Fe_2O_3, as detailed next), suggests that after impregnation/pre-treatment the metallic nanoparticles should be mainly located at the external surface of the AC (meso/macropores) blocking the micropores. This results in the decrease of W_0 without significant changes in L_0 values, and the increase of mesoporosity by the blockage of narrowest meso/macropores, as denoted by the PSD (Fig. 9.2b). Textural differences should be therefore related to variations in Fe dispersion and distribution depending on the precursor salt.

XRD patterns of the two iron-supported OSAC samples prepared with 2 wt.% Fe loadings are compared in Fig. 9.3. The amorphous character of the carbon support is denoted by the two broad bands observed: one at $2\theta \approx 24–26°$ and a weaker one at ≈ 44°, ascribed to the formation of incipient ordered graphite structure [6]. Identification of the iron oxides formed at the surface of

the catalysts was confirmed by comparison to those of standards in ICDD files for α hematite (card no. 33-0664) and magnetite (card no. 19-0629). XRD patterns show the predominance of the *α*-Fe_2O_3 oxide formation in both cases, though characteristic peaks of Fe_3O_4 are also identified in the OSAC-$FeCl_2$ sample, where a mixture of the two iron oxides was likely formed. Narrower and more intense diffraction peaks were also obtained in this case, indicating the formation of larger iron particles in comparison to OSAC-$Fe(NO_3)_3$. Nonetheless, the weak intensity and broadening of characteristic diffraction peaks of iron oxides suggest an overall poor crystallinity and/or small crystallite size in both cases [7]. By applying Scherrer equation to XRD data (Eq. (3.5)), an average *α*-Fe_2O_3 crystallite size of 4 nm was estimated for OSAC-$Fe(NO_3)_3$ (thus just within the detection limit, in agreement with previous findings [8]) and *ca*. 12 nm for OSAC-$FeCl_2$. A used sample of OSAC-$Fe(NO_3)_3$ after 4 consecutive adsorptive/catalytic cycles (300 min each) was also analyzed. Results indicate a similar nature of the metallic phase with a further broadening of the Fe-oxides characteristic peaks, whose intensity has also decreased (probably as a consequence of some iron leaching).

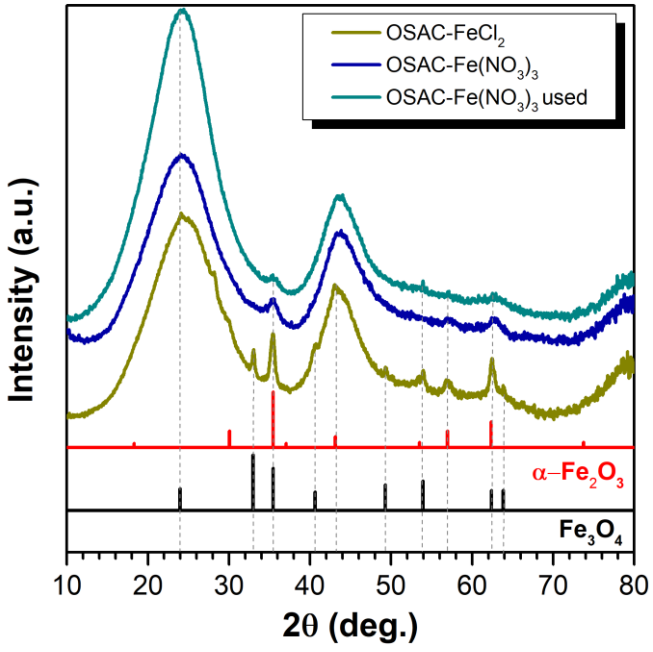


Fig. 9.3 XRD patterns of the two fresh catalysts prepared to theoretical Fe-loads of 2 wt.%, and OSAC $Fe(NO_3)_3$ after 48 h of continuous use. ICDD cards of *α*-Fe_2O_3 and Fe_3O_4 shown for reference.

STEM images of the derived Fe catalysts (2 wt.% Fe, Fig. 9.4) confirmed a better distribution and smaller size of metallic nanoparticles using $Fe(NO_3)_3$ as the precursor in comparison with the same metal loading but using $FeCl_2$. In the latter case, the formation of metallic nanoparticles exceeding 20 nm was clearly observed (Fig. 9.4a). Moreover, the dispersion is more

heterogeneous and the formation of acicular Fe-particles was also detected. The Cu species detected by the EDX microanalysis/mapping (Fig. 9.4c, f, i) are ascribed to the support frame used in the analysis procedure. A very high and homogeneous coating of very small Fe-nanoparticles (1–2 nm) is comparatively observed using $Fe(NO_3)_3$ as the precursor (Fig. 9.4d). This very high dispersion is responsible for the weak XRD peaks previously observed. The micrographs obtained for the used catalyst sample (Fig. 9.4g, h) show an overall decrease of the concentration of smaller surface Fe-nanoparticles, leading to a worse dispersion in comparison to the analogous fresh sample (expectably due to Fe leaching).

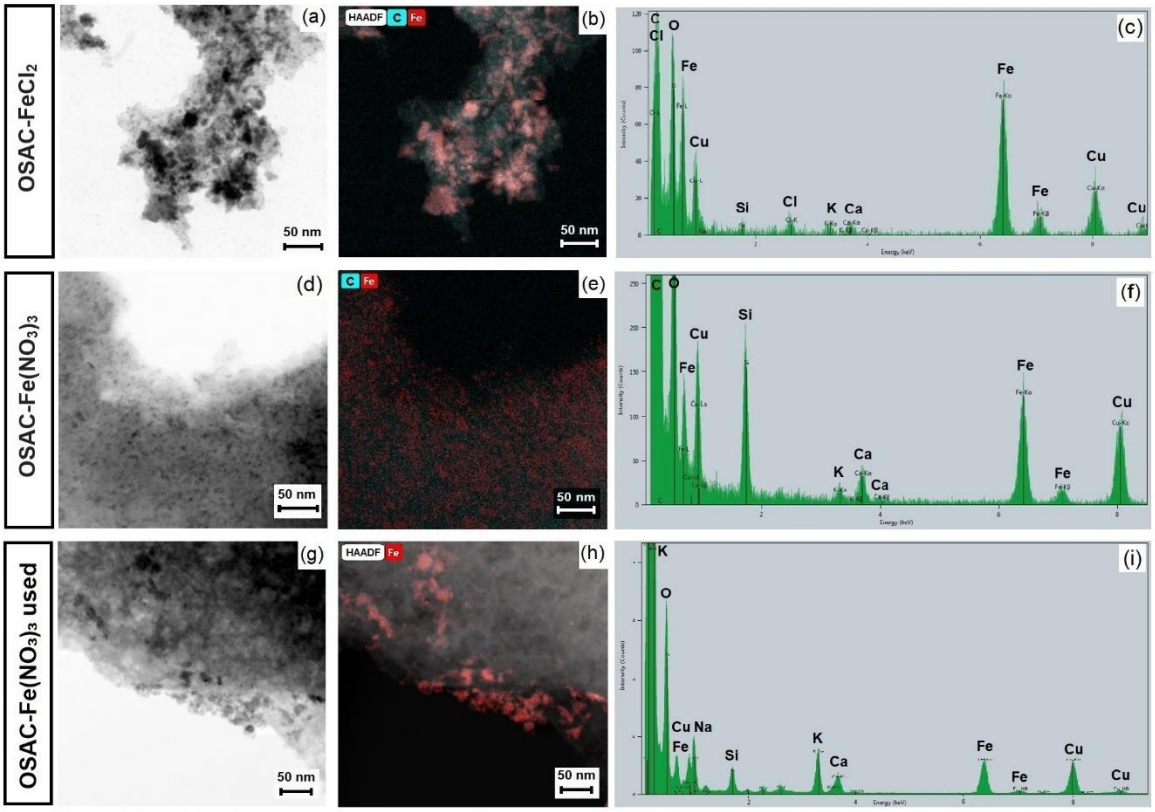


Fig. 9.4 STEM images (1st column), mapping (2nd column), and EDX-spectrum (3rd column) of OSAC-$FeCl_2$ (a, b, c) and OSAC-$Fe(NO_3)_3$ (d, e, f), as well as OSAC-$Fe(NO_3)_3$ after 48 h of operation in the fixed-bed reactor (g, h, i).

The chemical surface composition was also determined by XPS (Table 9.4). High resolution XPS spectra of O1s and Fe2p are shown in Fig. 9.5. The higher Fe and O contents on the OSAC-$Fe(NO_3)_3$ catalyst regarding OSAC-$FeCl_2$ is due to the strong differences in the dispersion and distribution of metallic nanoparticles on the carbon surface, as also previously shown by STEM. The O1s spectrum was deconvoluted in three components: the first peak at 530.1 eV was assigned to Fe–O bonds [1], and the other peaks were due to oxygen-containing groups on the

carbon surface [9]. The increased percentage of Fe–O bonds for OSAC-Fe$(NO_3)_3$ is potentially explained by the higher Fe surface content.

The Fe2p spectrum was deconvoluted in five contributions, according to the procedure proposed by McIntyre and Zetaruk [10]. Briefly, the main contribution of Fe^{3+} species is assigned to the peak placed at 711.2 eV and the corresponding multiplets at 712.1, 713.4 and 714.5 eV, whilst the contribution at 710.1 eV is attributed to Fe^{2+} species. Therefore, it is noteworthy that even if Fe^{2+} and Fe^{3+} were respectively used with the chloride and nitrate salt precursors, after pre-treatment, the proportion of Fe^{2+} species only varies between 35% for OSAC-Fe$(NO_3)_3$ and 41 % for OSAC-$FeCl_2$ (Table 9.4).

After the catalytic reaction, the catalyst surface composition is significantly altered (Table 9.4). The carbon content increased, which led to an overall decrease in the Fe and O contents. This fact can be associated with a certain leaching degree (as show below in Section 9.3.2.1, the cumulative leaching measured after the cycles is around 5 wt.%), but mainly to the deposition of organic compounds of OMW (phenolic compounds and/or oxidation by-products). This conclusion is also supported by the enrichment of the C–O bonds characteristic of phenolic compounds observed by analyzing the oxygen nature (O1s spectral region), while no significant changes occurred in the nature of the Fe-species (Fe2$p_{3/2}$ spectral region) in agreement with the XRD results previously commented.

Table 9.4 Elemental analysis (atomic content %), species percentages and corresponding binding energies (in brackets, eV) of the derived Fe-catalysts (2 wt.% Fe), and of a used sample of OSAC-Fe$(NO_3)_3$, determined by XPS.

Sample	**C**	**O**	**Fe**	**O1s (%)**			**Fe2$p_{3/2}$ (%)**				
				Fe–O	C=O	C–O	Fe^{2+}	Fe^{3+}	Fe^{3+}	Fe^{3+}	Fe^{3+}
OSAC-$FeCl_2$	84.3	13.1	2.6	39 (530.1)	43 (531.3)	18 (533.2)	41 (710.1)	27 (711.2)	19 (712.1)	10 (713.4)	3 (714.5)
OSAC-Fe$(NO_3)_3$	64.8	26.5	8.7	51 (530.1)	41 (531.4)	8 (533.2)	35 (710.1)	30 (711.1)	20 (712.0)	11 (713.2)	4 (714.3)
OSAC-Fe$(NO_3)_3$ used	81.4	17.4	1.2	12 (530.1)	46 (531.6)	42 (533.2)	36 (710.1)	29 (711.1)	19 (712.1)	11 (713.2)	5 (714.5)

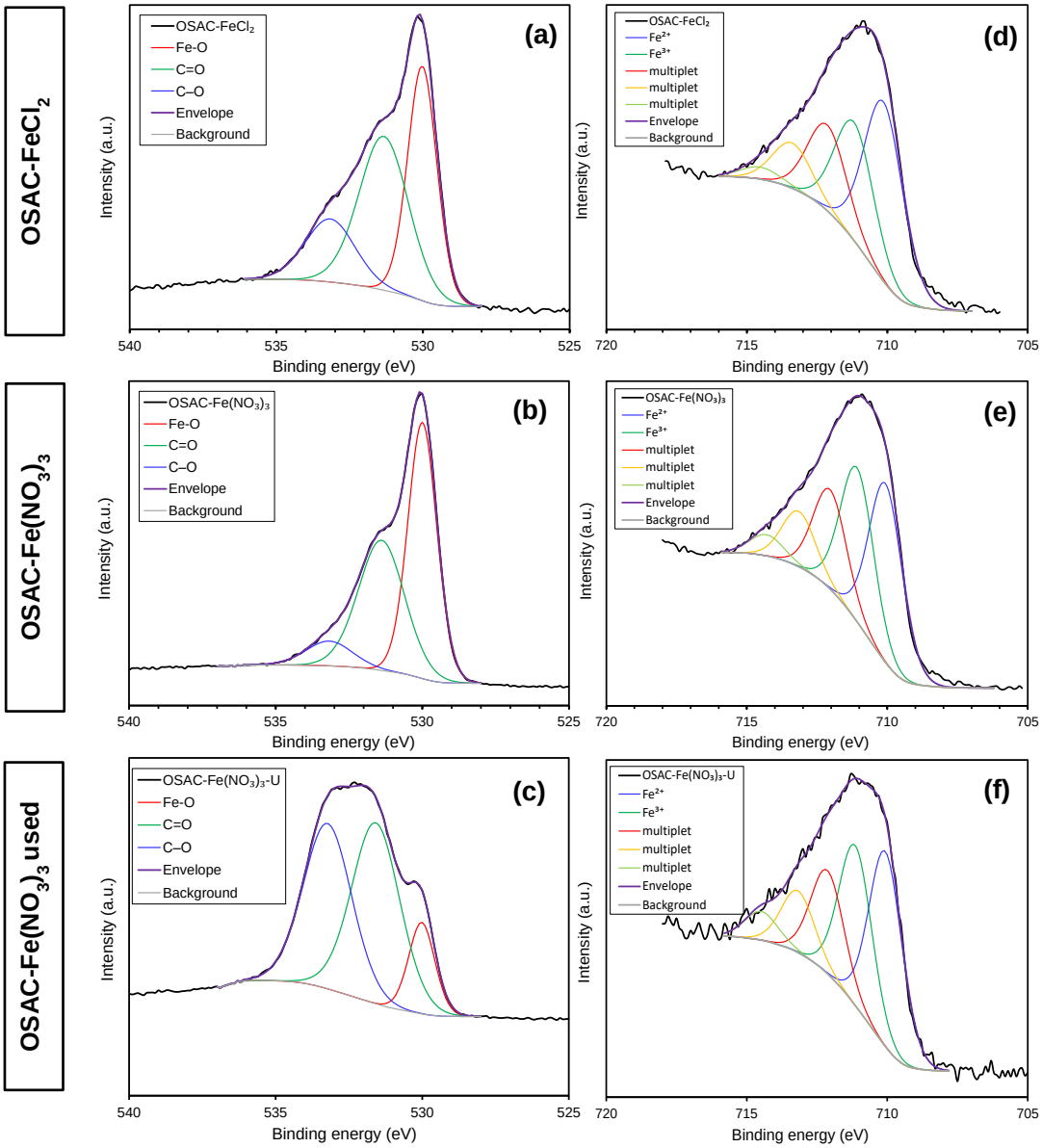


Fig. 9.5 XPS spectra and fitting of the derived Fe-catalysts (2 wt.% Fe) and of a used sample of OSAC-Fe(NO_3)$_3$: (a, b, c) O1s and (d, e, f) Fe2$p_{3/2}$ regions.

9.3.2. Catalysts screening: batch reactor

9.3.2.1. Selection of Fe-precursor

Solution "Synthetic-1" was used for the screening runs. The performance of the two catalysts prepared with different iron precursors (but same Fe load of 2 wt.%) was evaluated following TPh, TOC, and H_2O_2 conversions over time, as well as the Fe leached from the supports after each run. Fig. 9.6a shows the total phenolic content removal over time for four consecutive 300 min runs under the following conditions: [Cat] = 2.0 g/L, [H_2O_2] = 1.0 g/L (when used), pH_0 = 3.5 (unaltered solution pH), 20 °C. The first cycle shows TPh removal by adsorption alone (no H_2O_2

added) and includes the adsorptive capacity of the OSAC support for comparison. Thereafter, three catalytic experiments were performed with the same sample used in the previous run(s). A blank run was also performed to check the oxidative action of H_2O_2 alone; for the same experimental conditions mentioned, only minor TPh and TOC removals were observed after 300 min – 5.7 and 3.2 %, respectively (results not graphically represented).

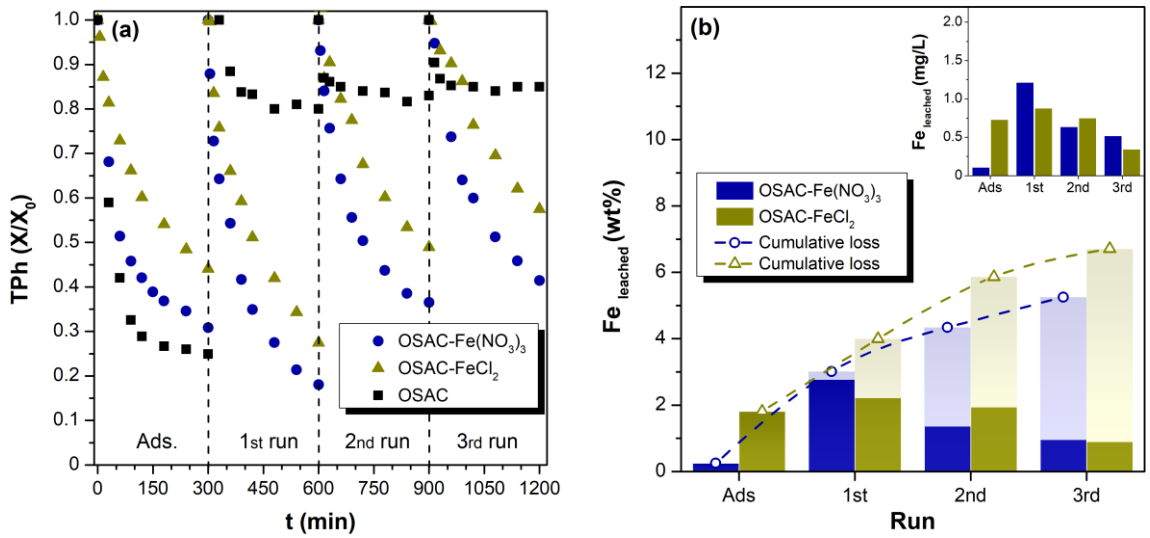


Fig. 9.6 (a) TPh/TPh$_0$ in consecutive adsorption/catalytic runs with OSAC and derived Fe-catalysts (2 wt.% Fe); (b) Fe leaching (wt.%) with indication of the cumulative % after each run (open symbols); Inset graph: Fe concentration in solution (mg/L). [Cat] = 2.0 g/L, [H_2O_2] = 1.0 g/L, pH$_0$ = 3.5, 20 °C.

OSAC became saturated after 300 min in contact with the phenolic solution (Fig. 9.6a), with TPh removal presenting the characteristic plateau. However, in the presence of Fe nanoparticles the adsorption rate decreased, more dramatically for OSAC-$FeCl_2$, as a consequence of the porous blockage and surface chemistry changes discussed earlier, in such a way that the curve decay is less progressive and the same plateau is not observed within 300 min.

The adsorptive behavior varies according to the characteristics of the materials but also with the composition of the synthetic solution, i.e., with the adsorbent-adsorbate interactions. Fig. D.2 (Appendix D) shows the adsorptive performances of all samples for each phenol present in the mixture. As commented, in the case of OSAC support the concentration of all the components in solution reaches a nearly constant value after 300 min of contact (Fig. D.2c). This behavior also occurs for caffeic and protocatechuic acids and tyrosol when adsorbed onto OSAC-$Fe(NO_3)_3$, but adsorption continues for vanillic and gallic acids (Fig. D.2a). However, the adsorption of none of them is complete with OSAC-$FeCl_2$ (Fig. D.2b). Except for tyrosol (pKa = 10.2), the remaining

compounds present p*K*a values around 4.5, thus, all of them are expected to remain in their molecular form in the experimental conditions used (i.e., pH = 3.5).

In the next cycles, oxidation of contaminants by CWPO may occur via different pathways, including heterogeneous and homogeneous catalytic reactions (as Fe leached from the support can promote Fenton-like reactions in the aqueous phase), or even by the oxidative potential of H_2O_2 alone (though this contribution is almost negligible, as discussed above). Moreover, the catalytic contribution of the OSAC support (together with the oxidative potential of H_2O_2, as pointed earlier) was found to be very small in comparison to the derived catalysts (Fig. 9.6a). Similar to the adsorption runs, OSAC-Fe$(NO_3)_3$ presents a better performance regarding OSAC-$FeCl_2$ even after 3 cycles, likely related to the better dispersion of Fe oxides achieved with the iron nitrate precursor (Fig. 9.4d, e). Moreover, residual chloride anions found on the surface of OSAC-$FeCl_2$ (confirmed by EDX analysis, Fig. 9.4c) could potentially harm the process due to their scavenging nature towards hydroxyl radicals [11]. Nevertheless, results in Fig. 9.6a show a progressive decrease in removal efficiencies from cycle to cycle for both catalysts, which could be due to different factors, including: exhaustion of adsorption sites, “poisoning” of the catalyst by intermediate/final reaction products (as shown in Section 9.3.1 through XPS and XRD analyses of a spent sample of OSAC Fe$(NO_3)_3$), and/or Fe leaching (confirmed by the shift in size and distribution of nanoparticles observed by XRD and complemented by STEM micrographs) [12].

Nonetheless, OSAC-Fe$(NO_3)_3$ presented slightly lower cumulative values of iron leaching after four runs, as shown in Fig. 9.6b. It is also worth noting that neither catalysts leaching has resulted in Fe concentrations in solution higher than 1.3 mg/L after each run (Fig. 9.6b, inset graph), hence below the strictest legislated value of 2.0 mg/L imposed by EU guidelines for treated wastewater [13]. In summary, OSAC-Fe$(NO_3)_3$ presents a better dispersion of smaller oxide nanoparticles, showing a better adsorption capacity and catalytic performance, and also greater stability versus leaching than the catalyst prepared with $FeCl_2$.

Mineralization levels were always considerably lower than the removal of the total phenolic content from solution (TOC curves presented in Fig. D.3a, Appendix D), thus confirming the occurrence of partial oxidation of the initial compounds to intermediate ones that were not fully oxidized up to CO_2 under the conditions tested. OSAC-Fe$(NO_3)_3$ also presented slightly better mineralization levels on all runs. H_2O_2 conversions after each cycle were always below 50% (Fig. D.3b) in spite of the amount of oxidant selected being smaller than the estimated theoretical stoichiometric value of 1.25 g/L (according to the solution initial TOC) [4]. A progressive decay on

the oxidant consumption was also recorded after each run, in line with the findings discussed so far.

9.3.2.2. Selection of Fe-loading

Considering the results in the previous section, $Fe(NO_3)_3 \cdot 9H_2O$ was selected as the iron precursor for the synthesis of three OSAC fractions with different iron loadings (Table 3). The resulting catalysts were tested under the same experimental conditions reported before, and the experimental data is summarized in Fig. 9.7.

The progressive blockage of the porous structure of catalysts with increasing metal loading makes catalysts with Fe loadings of 1 and 2 wt.% better adsorbents than the one with 5 wt.%, so TPh (Fig. 9.7a) and TOC removals (Fig. 9.7c) were noticeably lower for the latter after the 300 min long adsorption run. The poorer adsorptive behavior is closely related to the pore blockage promoted by the larger amount of Fe-nanoparticles and Fe clusters that are expectably formed on the catalyst surface.

As to the ensuing catalytic runs, the progressively decreasing trend in TPh removals (and respective mineralizations), more accentuated for catalysts with 1 and 2 wt.% Fe, is in part due to the porosity blockage by adsorbed substances (intermediates and reaction products), but also due to the loss of iron from the support (Fig. 9.7b). In spite of the relatively small concentrations of iron in solution after each catalytic cycle (as shown in the inset graph of Fig. 9.7b), the cumulative leaching from the supports leads to a decay of H_2O_2 conversions after each cycle (Fig. 9.7d) and, ultimately, the generation of less radical species. This is particularly clear for the catalyst with the lowest Fe-loading, where the cumulative amount leached after 4 runs amounts to ca. 14 wt.% of its initial loading, thus significantly hindering TPh and TOC removals in that case (apart from the fact that such sample has the smallest initial load of iron).

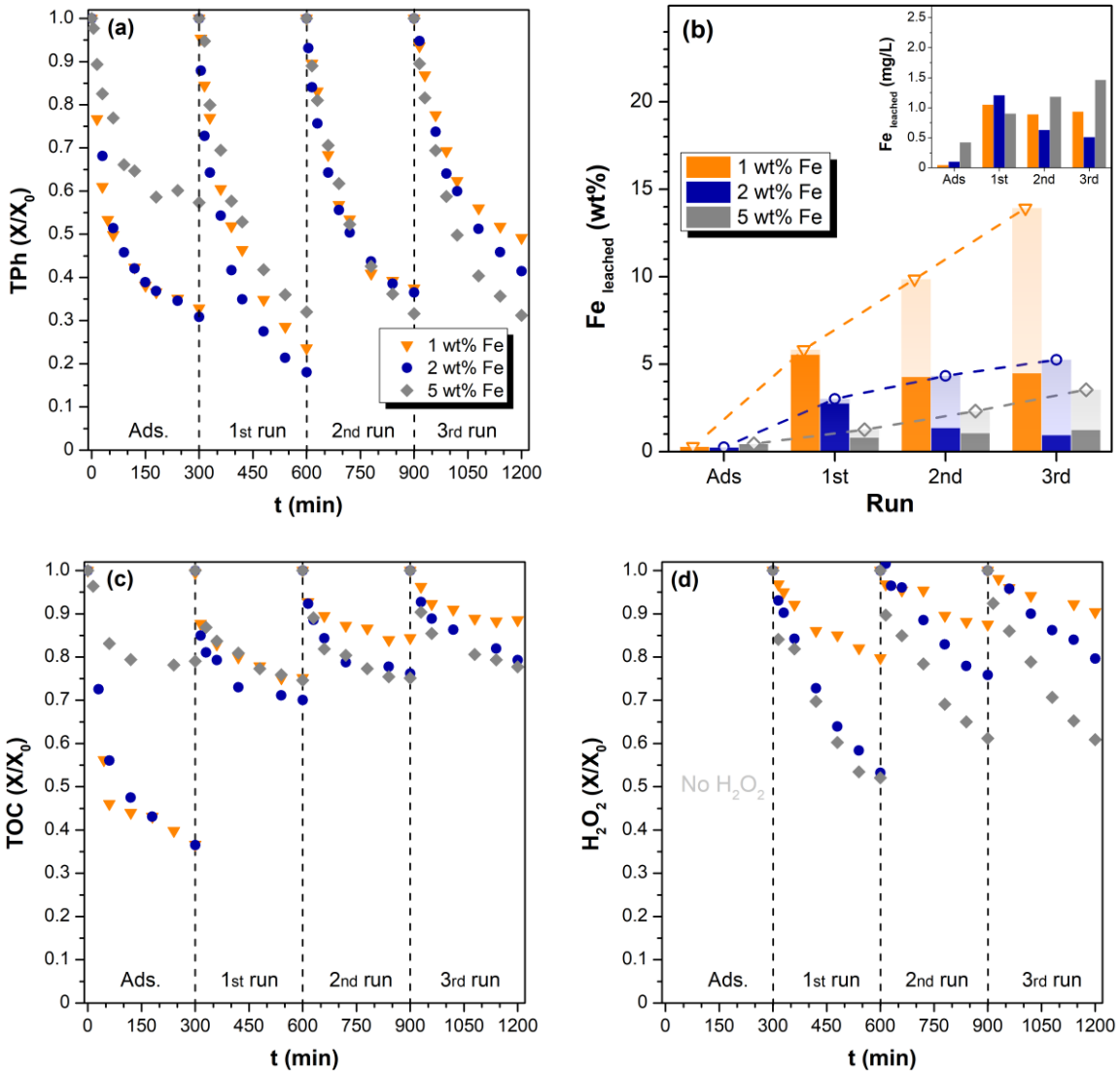


Fig. 9.7 (a) TPh/TPh$_0$ over time in consecutive runs; (b) Fe leaching (wt.%) with indication of the cumulative % after each run (open symbols); Inset graph: concentration of Fe in solution (mg/L), (c) TOC/TOC$_0$, (d) H_2O_2 conversion with different OSAC-Fe$(NO_3)_3$ catalysts. [Cat] = 2.0 g/L, [H_2O_2] = 1.0 g/L, pH$_0$ = 3.5, 20 °C.

After the last run, performances in terms of TPh removal improved with increasing Fe loadings (Fig. 9.7a) although TOC mineralizations were somewhat similar with Fe loadings of 5 and 2 wt.% (22 and 21%, respectively). So, at this point, further improvements in mineralization should be dependent on adjustments to the operational conditions. Finally, comparing the catalysts' stability it was observed that the cumulative wt.% of Fe-leached also decreased in the same sense, which was expected since the concentration in solution remained within the same range in all cases (Fig. 9.7b). Despite the promising performances with samples with lower Fe-loadings, results suggest that superior reusability and stability in continuous treatment is expected for OSAC-Fe$(NO_3)_3$-5%, thus further experiments in the fixed-bed reactor were conducted with this catalyst.

9.3.3. Fixed-bed reactor operation

9.3.3.1. Catalytic bed stability

The dynamic stability of the catalytic bed was first assessed up to 48 h of continuous operation under fixed operational conditions: Q = 0.75 mL/min, $[H_2O_2]_{feed}$ = 0.75 g/L, pH_0 = 3.5, 20 °C. TPh and H_2O_2 removal/conversion profiles, depicted in Fig. 9.8, provide useful insights on the stability and activity of the catalyst in such conditions: 1) steady-state is reached after approximately 4-6 h of continuous operation; 2) TPh removal is practically maintained (49.3–52.4%) after *ca*. 36 h, even if H_2O_2 conversion decrease from 74.6% to 63.9% during that time frame; 3) a slightly higher catalytic activity loss occurs after that point, as the oxidant conversion decrease to 47.7% and TPh removal to 37.6% in the last 6 h of operation.

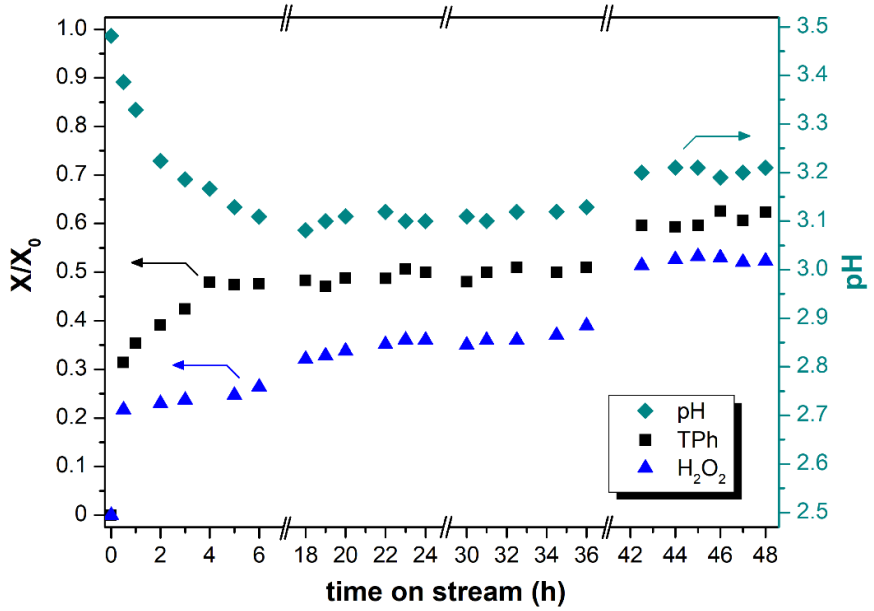


Fig. 9.8 Stability tests for OSAC-Fe$(NO_3)_3$ catalyst (5 wt.% Fe): normalized TPh and H_2O_2 over time. Right y-axis: pH values at the reactor outlet. Q = 0.75 mL/min, $[H_2O_2]_{feed}$ = 0.75 g/L, pH_0 = 3.5, 20 °C.

As suggested by other authors working on similar experimental set-ups [14,15], the progressive decay of oxidant conversion is most likely connected to the partial deactivation of the catalytic bed due to iron leaching from the AC-support, and/or to the blockage of catalytically active sites by adsorption of intermediate/final products of the reaction. The latter case is further supported by the drop of the solution pH to values close to 3.1 (*cf*. right y axis on Fig. 9.8), a behavior typically correlated to the formation of carboxylic acid refractory intermediates that are not further mineralized [14,16], which increases to 3.2 after the 36 h period. As to the leaching of iron from the support, a fraction of the used catalyst was analyzed after the experiments, and a variation

on the Fe content of 9.3% was estimated based on the initial load of the catalyst (i.e., from 4.83 to 4.38 wt.%), suggesting that partial deactivation has indeed occurred. Considering the results, it was assumed that the catalytic bed could only maintain its full catalytic capacity for a period corresponding to six consecutive 6 h-cycles under such conditions, after which point the catalytic bed was substituted.

A non-catalytic run was performed under the same operational conditions to evaluate the system's sorptive behavior – Fig. D.4, Appendix D. Saturation of the catalytic bed was also achieved after 5–6 h of continuous operation, as TPh and TOC concentrations at the reactor outlet are approximately equal to the inlet ones (X/X_0 >0.98) and were maintained up to 12 h of continuous operation. The catalytic contribution of the iron leached into the solution was also evaluated based on the data from the used catalyst. To better estimate the contribution of the homogenous reaction to the global process, a test with dissolved iron in solution was performed. A detailed description of the adopted procedure and the results obtained are presented in Appendix D (Fig. D.5); it was found that the homogenous phase reaction was able to reach ca. 10% of TPh removal.

9.3.3.2. Effect of temperature, H_2O_2 feed dose, and flow rate

A parametric study of different experimental conditions was performed for the fixed-bed reactor operation. First, the effect of the system temperature was evaluated, fixing the remaining operational conditions at Q = 0.75 mL/min, $[H_2O_2]_{feed}$ = 0.75 g/L and pH_0 = 3.5.

The first section of Fig. 9.9 shows conversions at steady-state (i.e., average values between 4 and 6 h of operation at the feed flow rate mentioned) for each set temperature. The kinetic constants of •OH generation (and therefore the rate of organic molecules attack) are exponentially dependent on temperature, according to Arrhenius equation. The experimental data obtained is in agreement with this hypothesis, as higher H_2O_2 conversions and a consequent improvement of TPh/TOC removals were observed when operating the system at higher temperatures. In such cases, it is also worth noting the occurrence of thermal degradation of phenolic compounds in the feed container [17], though the thermal decomposition of H_2O_2 into molecular oxygen and water was negligible (<5% after 6 h, in relation to the initial oxidant dosage), as also reported by other authors (e.g., [18,19]), and so did the solution mineralization levels (TOC <2%). As inferred by HPLC peak analysis, caffeic acid is the most susceptible compound to thermal decomposition in this mixture (over 50%, at 60 °C and after 6 h), whereas this phenomenon was comparatively smaller for the remaining compounds (*cf*. Fig. D.6). Since the decomposition of phenols is not

accompanied by a significant TOC decrease within the feed container, it is therefore expected that smaller decomposition products (with potential anti-oxidative behavior) were formed from the decarboxylation of caffeic acid, as already described by other authors [20]. Fig. 9.9 highlights the overall TPh removals observed at the reactor outlet (open symbols) in each case, but also the extent of TPh abatement when considering the changes produced within the feed vial after 6 h owing to the thermal decomposition at 40 or 60 °C (closed symbols); at 20 ºC such effect was negligible.

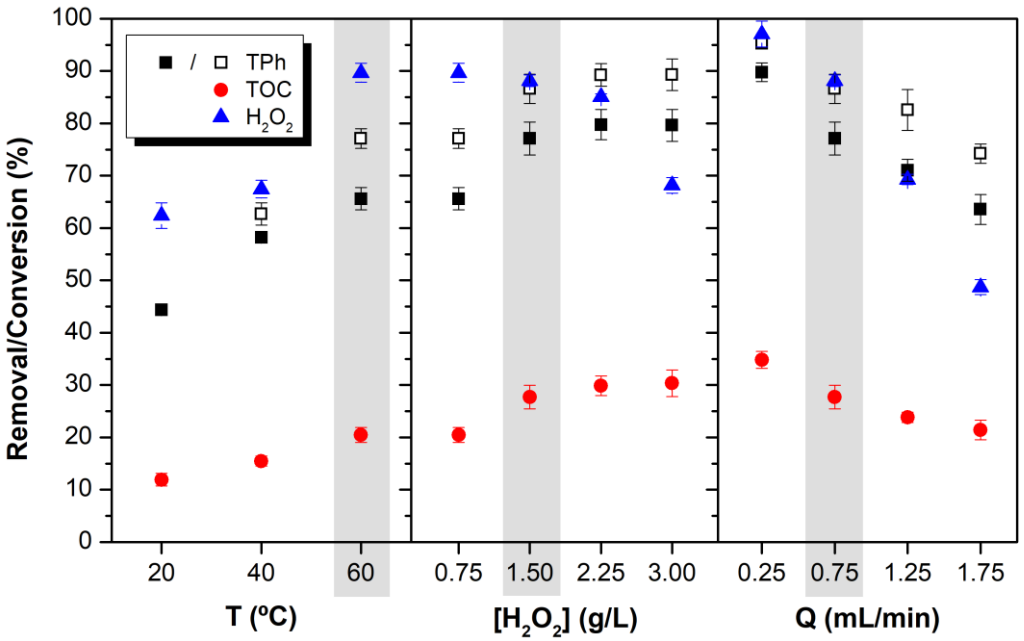


Fig. 9.9 Parametric assessment of the FBR operation: steady-state TPh removals (open symbols: TPh removal considering the thermal degradation effect), TOC removal efficiencies and H_2O_2 conversions for different operational conditions.

Given the superior performance of the system at 60 °C, even eliminating the contribution of thermal degradation, with TPh and TOC removals of 65.6% and 20.4% respectively (and high H_2O_2 conversions of 89.7% at steady-state), further experiments were conducted fixing this parameter and varying the H_2O_2 feed dose in the 0.75–3.0 g/L range. As depicted in the second section of Fig. 9.9, the oxidation of phenolic compounds was also favored with the increase of the oxidant dose up to a feed concentration of 2.25 g/L, after which point conversions remained unchanged and an excess of unreacted H_2O_2 was obtained in the outlet stream at $[H_2O_2]_{feed}$ = 3.0 g/L (with H_2O_2 consumption dropping from the previous 85–90% range to ca. 68% in this case).

The participation of hydrogen peroxide in parallel reactions that lead to the scavenging of reactive radicals (e.g., Eq. (2.7)), and thus the decline of the oxidative potential of the entire process, is often referred in the scientific literature [14,21,22]. Hindrance of the catalytic process at higher oxidant feed doses was also observed in this study, as similar H_2O_2 conversions were obtained for $[H_2O_2]_{feed}$ = 1.50 and 2.25 g/L (88.1% and 85.1%, respectively), but mineralization efficiencies remained almost unchanged despite the 50% increase of the oxidant feed concentration. On the other hand, it is also plausible to assume that the low mineralization observed in those cases (and even at the highest feed dosage) could be attributed to the limited capacity of the catalytic bed (i.e., the availability of active sites for the solution residence time within the reactor) and the refractory nature of some of the products formed. From an economic point of view, not only the waste of reagents in the outlet stream should be avoided, but the increase of H_2O_2 fed to the system should also be justified with a more substantial improvement of the overall mineralization efficiencies. Therefore, a good compromise was achieved with $[H_2O_2]_{feed}$ = 1.5 g/L, where steady-state TPh and TOC removals were close to the highest values obtained for the entire range studied, whilst also maintaining high H_2O_2 conversion yields at steady-state.

Finally, and following the discussion in the previous paragraph, the solution residence time in the FBR was also adjusted by varying the feed flow rate in the 0.25–1.75 mL/min range (fixing the remaining conditions at $[H_2O_2]_{feed}$ = 1.5 g/L, 60 °C – grey bars in Fig. 9.9, at pH_0 = 3.5). Results presented in the last section of Fig. 9 also consider the proportional variation in flow time required to achieve steady-state operation for each volumetric flow rate tested.

Increasing the residence time by 3-fold (by adjusting the feed flow rate to 0.25 mL/min) has resulted in a clear improvement in the mineralization efficiencies, as steady-state TOC removal went from 27.7% (at Q = 0.75 mL/min) to 34.8%. Under such conditions, not only the frequency of interactions between H_2O_2 molecules with more “exposed” surface Fe-sites are improved, but also those with Fe-nanoparticles located inside the microporous structure of the catalyst. Consequently, more radicals are generated, promoting the oxidation of phenolic compounds and their reaction intermediate products, as already pointed out by other authors [8,22]. In contrast, the catalytic bed ability to convert H_2O_2 is markedly reduced when the feed flow rate is increased, which is thereafter reflected in the progressively smaller TPh and TOC removal efficiencies at Q = 1.25 and 1.75 mL/min. Further experiments were performed solely with Q = 0.75 mL/min, which didn’t significantly compromise the catalytic performance of the system and significantly reduces the residence time, thus increasing the amount of effluent treated per unit of time.

9.3.3.3. Effect of synthetic solution composition

Despite the high removal of parent phenolic compounds observed under most conditions tested, the synthetic solution still exhibits an overwhelmingly refractory nature, since the maximum TOC mineralization at steady-state was always below 35%. As detailed in Table 9.1, different phenolic compounds were used to prepare two additional synthetic formulations with similar initial organic loads to the one used so far ("Synthetic 1"). By examining the removal profiles of individual phenolic compounds of each formulation under the same operating conditions, a better understanding of the interaction between contaminants and the catalytic system could be drawn.

Fig. 9.10 shows normalized profiles of each compound under smooth operational conditions for the three solutions at Q = 0.75 mL/min, $[H_2O_2]_{feed}$ = 0.75 g/L, pH_0 = 3.5, and 20 °C. Under these conditions, the decomposition promoted by higher temperatures is practically null and the degradation kinetics are slowed, so individual degradation profiles are better differentiated by HPLC analysis; potential correlations between functional groups of the phenolic compounds and the extent of degradation achieved can be therefore established. Functional groups classified as electron-donors (activating the aromatic rings by increasing the electronic density) include hydroxyl (–OH, strong) and alkyl (–R, weak, stronger the longer the alkyl chain) groups. However, groups such as –COR or –COOH are electron-acceptors (moderate), deactivating the reactivity of the aromatic ring. Results suggest that a higher number of –OH functional groups increase the likelihood of electrophilic attack on the aromatic ring [23]. Removal of GA (gallic acid), with three –OH electron-donating groups (EDG), is always favored in respect to other benzoic acid derivatives with two –OH groups (such as protocatechuic acid, PA – Fig. 9.10a), or only one (e.g., 4-hydroxybenzoic acid, 4-HbA – Fig. 9.10c); please refer also to the structures of the phenolic acids in Fig. D.1. Syringic acid (SA) showed a very distinct behavior from GA (Fig. 9.10b), which could be due to the two methoxy groups (O–CH_3) in its structure that potentially decrease the reactivity, as already pointed by D. Mantzavinos [24] in his study on the removal of cinnamic acid derivatives by Fenton and Fenton-like processes.

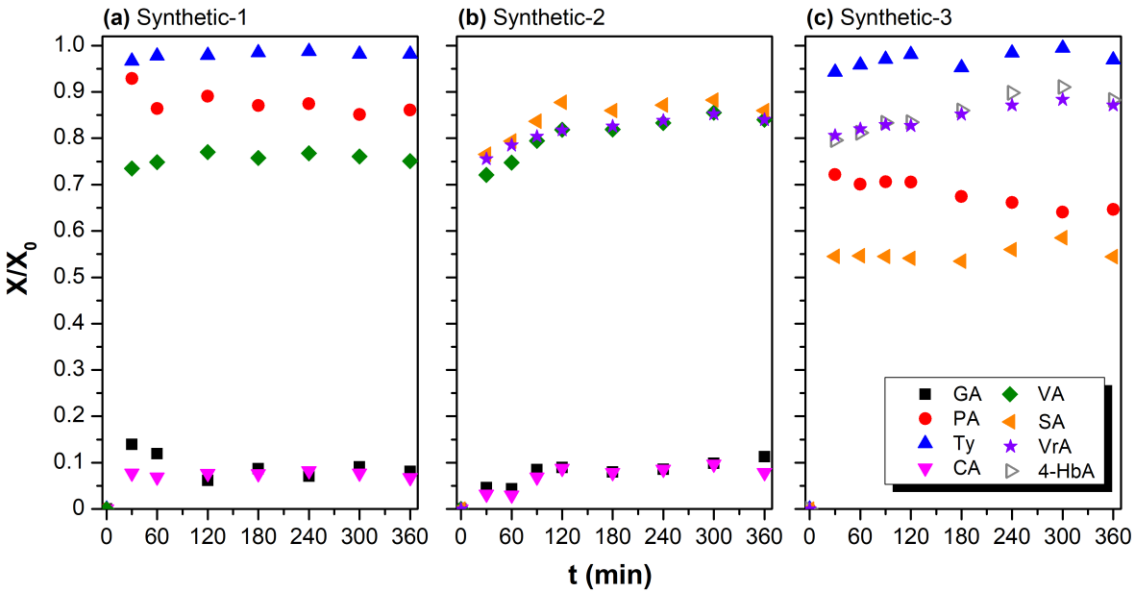


Fig. 9.10 Normalized profiles for the removal of parent phenolic compounds from the different synthetic solutions tested in the fixed-bed reactor. Q = 0.75 mL/min, $[H_2O_2]_{feed}$ = 0.75 g/L, pH_0 = 3.5, 20 °C.

A. Silva *et al*. [23] also showed that the oxidation reaction is generally faster for cinnamic acid derivatives than benzoic acid ones, thus while only having two hydroxy groups in its structure, caffeic acid (CA – Fig. 10a, b) presents a similar removal profile to that of GA (with three –OH). The effect of the different reactivity of the phenol mixture components is clearly observed using solution "Synthetic-3" (Fig. 9.10c), where the reactivity decreases with the specificity of the different EDGs in the sense of SA > PA > VrA ≈ 4-HbA. Among the range of molecules studied, tyrosol (Ty, a phenethyl alcohol derivative) appears as the phenolic compound less susceptible to oxidation by the CWPO process.

The catalytic performance was similar in terms of H_2O_2 conversion for all solutions, though considerably lower TPh and TOC removals were recorded for "Synthetic-3", as represented in Fig. 9.11 (colored bars). For comparison, blank bars show the process efficiency under the best operational conditions previously established (Section 9.3.3.2).

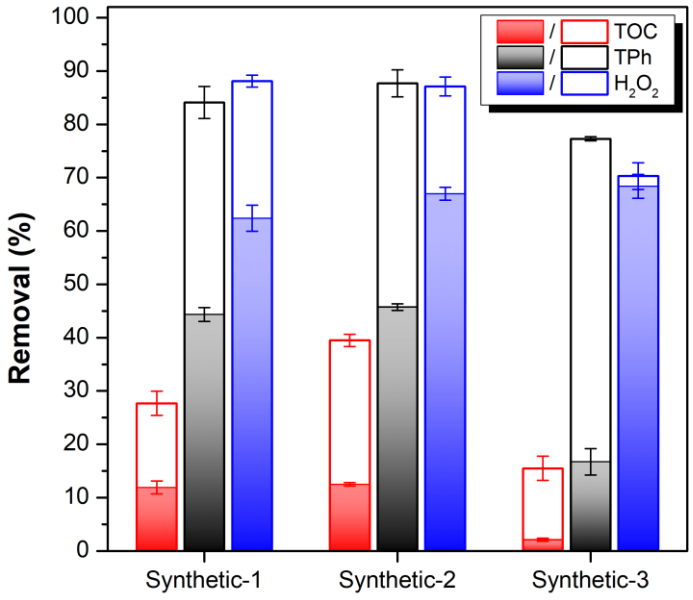


Fig. 9.11 Steady-state TPh and TOC removals and H_2O_2 conversions for each solution under distinct operational conditions. Coloured bars: Q = 0.75 mL/min, $[H_2O_2]_{feed}$ = 0.75 g/L, pH_0 = 3.5, 20 °C (as reported on Fig. 9.10); Blank bars: Q = 0.75 mL/min, $[H_2O_2]_{feed}$ = 1.50 g/L, pH_0 = 3.5, 60 °C.

Degradation efficiencies were visibly dependent on the solution initial composition, even at the best operational conditions (blank bars). "Synthetic-2" showed similar H_2O_2 conversion and TPh removal as "Synthetic 1" but higher TOC mineralization (39.5 and 27.7%, respectively), confirming tyrosol as the most refractory compound. Despite the high degradation of TPh in "Synthetic-3" (>77%), the corresponding TOC removal (15.5%) was the lowest in this series, thus underlining the more refractory behavior of the reaction intermediates generated by the initial compounds of this solution.

A qualitative analysis of the chromatograms of samples collected during CWPO showed a relatively fast disappearance of peaks correspondent to the initial phenolic compounds, and the appearance of new ones that typically elute before the parent compounds (*cf*. shown in Fig. D.7, Appendix D). Ma *et al*. [25] reported on the suppression of •OH production in Fenton and photo-Fenton systems by the presence of such compounds. Specifically, the authors concluded that malonic acid formed organic complexes with Fe^{3+} that impeded the regeneration of Fe^{2+}. A similar behavior could be responsible for the lower mineralizations obtained with "Synthetic-3". In this case, the number of new overlapping peaks recorded at low retention times clearly suggests the presence of low-molecular organic reaction intermediates (not identified in the scope of this work), which are also in higher concentration than those observed for "Synthetic-1" and "Synthetic 2" solutions.

9.3.3.4. Application to real OMW samples

In a final series of experiments, samples of real OMW were fed to the FBR under the same conditions reported earlier to check the process efficiency for the treatment of more complex solutions. Samples of real OMW were diluted 30, 15, 7.5, and 5-fold (Table 9.5) to produce effluents with different initial organic loads. The inlet concentration of H_2O_2 was also adjusted according to the initial COD values of each effluent. M. Lucas *et al*. [26] estimated a stoichiometric weight ratio between H_2O_2 and COD of 2.125 for the complete oxidation of COD in real effluents; preliminary studies (not reported here for brevity) had shown that for the current operational conditions (m_{cat} = 1000 mg, Q = 0.75 mL/min, 60 °C) a ratio of 2.2–2.4 g H_2O_2/g O_2 was required, not only to improve the global process efficiency but also to minimize the amount of unreacted oxidant in the reactor outlet. At steady-state, H_2O_2 conversions were maintained above 94% except for solution "OMW-5×", in which case approximately 28% of unreacted oxidant was obtained at the reactor outlet stream.

A somewhat similar behavior was observed for the entire range of real effluents tested (i.e., with different organic loads), with analogous removals of COD (ranging from 26–34%) and TOC (13-16%) at steady-state, which confirms the good adjustment of the oxidant dose fed to the reactor in each case. It is also noteworthy that efficiencies were maintained, even at the highest influent organic load tested; on the other hand, a high fraction of the oxidizable organic matter present in the OMW samples is not removed by CWPO, independently of the initial organic load.

Table 9.5 Physicochemical properties of the different OMW samples (diluted 30, 15, 7.5 and 5-fold) after CWPO (values at steady-state); removal percentage values shown in parentheses. $[H_2O_2]/[COD]$ = 2.3 ±0.1 g H_2O_2/g O_2, Q = 0.75 mL/min, pH_0 = 3.5, 60 °C.

Parameter	**OMW-30×** *(COD_0 ≈0.6 g/L)*	**OMW-15×** *(COD_0 ≈1.2 g/L)*	**OMW-7.5×** *(COD_0 ≈2.4 g/L)*	**OMW-5×** *(COD_0 ≈3.6 g/L)*
COD (mg O_2/L)	443 ±3 (26%)	793 ±16 (34%)	1717 ±11 (29%)	2411 ±16 (33%)
BOD_5 (mg O_2/L)	130 (16%)	255 (16%)	540 (18%)	745 (17%)
TPh_{FC} (mg GA_{eq}/L)	18 ±1 (57%)	24 ±1 (67%)	52 ±1 (60%)	69 ±5 (71%)
TOC (mg C/L)	166 ±1 (13%)	326 ±4 (16%)	663 ±9 (15%)	1129 ±5 (14%)
BOD_5/COD	0.29	0.32	0.31	0.31
AOS	0	0.35	0.12	0.80
V. fischeri inhibition (%)	4.8	13.3	24.4	36.5
pH	3.0	3.4	3.3	3.7

Additional considerations can be drawn from the results obtained by comparison to those of synthetic solutions. In the case of OMW-30×, which was tuned to have the same overall initial organic load (COD) as the synthetic solutions tested earlier, the mineralization achieved was 13%, which is much lower than those observed in solutions “Synthetic-1” and “Synthetic-2” (*cf*. Fig. 9.11), but in line with that obtained for the most refractory polyphenolic solution tested (“Synthetic-3”). Also, despite presenting an initial phenolic content much smaller (TPh_{FC} = 40 mg GA_{eq}/L, Table D.1 in Appendix D) than those of synthetic solutions (TPh_{FC} ≈ 340 mg GA_{eq}/L), conversions were also much smaller in comparison (57% *vs*. 77–88%, depending on the synthetic solution). Since OMW samples present a much more complex matrix than synthetic solutions, smaller TPh removals are also expected since phenolic compounds must compete with other organic contaminants for radicals.

Many wastewater treatment schemes often include biological degradation step(s) due to their overall higher cost-effectiveness when operated under adequate conditions. Bioremediation is potentially more cost-effective if applied to amenable effluents, particularly to those with less refractory or toxic compounds in their composition. Evaluation of the effluent ecotoxicity towards the *V. fischeri* bacteria showed that the initial effluent inhibited by 71.4% the bioluminescence of the bacteria when in contact with the initial undiluted sample for 30 min (Table 9.2). Decreasing

toxicity values of the effluents were therefore obtained as samples' dilution increased (ranging from 19.2–52.4%, *cf*. *Table S1 of SI*). In virtue of the CWPO process employed, the ecological impact that the effluent could potentially produce on aquatic ecosystems was also reduced in all samples, with the toxic character towards *V. fischeri* decreasing to values ranging from 4.8–36.5% (Table 9.5).

The average oxidation state (AOS) is an index that provides an indication of effluent biodegradability. After oxidation, AOS went from negative values (-0.74 to -0.05, Table D.1), expressive of the poor oxidation degree of the initial samples, to values between 0 and 0.80, which suggests an overall increase in the oxidation state of carbon [27]. Moreover, the effluent BOD_5/COD ratio slightly improved in all cases, indicating some biodegradability enhancement after the treatment, though the threshold commonly accepted as easily amenable for the bioremediation of wastewaters (BOD_5/COD = 0.4) was not met under the operational conditions tested.

9.4. CONCLUSIONS

Activated carbons were prepared from a by-product of the olive oil industry (olive stones) and the conditions of iron impregnation for the synthesis of Fenton-like catalysts were varied as to the Fe-salt used and the Fe-loading. In a perspective of integration and valorization of residues within the same industrial activity, the resulting materials were tested in the catalytic wet peroxide oxidation of refractory polyphenolic solutions and real olive mill wastewater. Although the metallic nanoparticles deposited on the ACs surface are blocking porosity, all catalysts present surface areas greater than 580 m^2/g, thus maintaining a high adsorption capacity. Deeper differences were found to be related to the dispersion of the active phases, which strongly improves using $Fe(NO_3)_3$ regarding $FeCl_2$ precursors, thus favoring a high surface Fe-loading in the corresponding catalysts. The active phase contains a mixture of Fe^{3+}/Fe^{2+} in all cases, with the formation of α-Fe_2O_3 and Fe_3O_4 crystalline nanoparticles.

Screening of the resulting materials was performed with a synthetic solution containing refractory phenols commonly detected in OMW. It was found that the better Fe nanoparticles dispersion in the catalyst prepared with iron nitrate provided higher catalytic activity in relation to the one prepared with iron(II) chloride. Under smooth operational conditions – [Cat] = 2.0 g/L, $[H_2O_2]$ = 1.0 g/L, pH_0 = 3.5 (unaltered solution pH), 20 °C and 300 min – the catalyst prepared

with an Fe-load of 5 wt.% lead to TPh removals of 68% after 4 consecutive runs without significantly compromising its stability (cumulative Fe leaching of only 3.5 wt.%).

OSAC-Fe(NO_3)$_3$-5% was therefore established as to be the most suitable material for CWPO in a continuous operation unit. Three operational parameters of the fixed-bed reactor were studied: temperature, oxidant feed dosage, and volumetric flow rate. The best conditions of operation were determined (60 °C, $[H_2O_2]_{feed}$ = 1.5 g/L, Q = 0.75 mL/min), and the process was tested with different synthetic solutions. Compounds with more –OH electron-donating groups were found to be more susceptible to degradation, while the reactivity seems to decrease in the presence of methoxy groups. Finally, real OMW samples with increasing initial organic loads were tested under the same conditions, fixing the feed $[H_2O_2]$/[COD] ratio at 2.3 ±0.1 g H_2O_2/g O_2. Despite the high H_2O_2 conversions achieved, the efficiency of the catalytic bed was not significantly affected, with steady-state TPh removals of 57–71%, 26–33% for COD, and 13–16% for TOC mineralization. The resulting effluent eco-toxicity was always lower than the inlet stream ones, while outlet biodegradability indices also improved upon catalytic oxidation. Moreover, the proposed methodology could also be suitable for adjacent agro-industries, such as the common case of wineries, which are also responsible for the generation of effluents with a high concentration of phenolic compounds.

REFERENCES

1. Esteves, B.M.; Morales-Torres, S.; Maldonado-Hódar, F.J.; Madeira, L.M. Integration of olive stones in the production of Fe/AC-catalysts for the CWPO treatment of synthetic and real olive mill wastewater. *Chem. Eng. J*. **2021**, 411, 128451.
2. Esteves, B.M.; Rodrigues, C.S.D.; Madeira, L.M. Wastewater Treatment by Heterogeneous Fenton-Like Processes in Continuous Reactors. In Applications of Advanced Oxidation Processes (AOPs) in Drinking Water Treatment; Gil, A., Galeano, L.A., Vicente, M.Á., Eds.; Springer International Publishing: Cham, 2019; pp. 211–255. ISBN 978-3-319-76882-3.
3. Daâssi, D.; Lozano-Sánchez, J.; Borrás-Linares, I.; Belbahri, L.; Woodward, S.; Zouari-Mechichi, H.; Mechichi, T.; Nasri, M.; Segura-Carretero, A. Olive oil mill wastewaters: Phenolic content characterization during degradation by Coriolopsis gallica. *Chemosphere* **2014**, 113, 62–70.
4. Aggoun, M.; Arhab, R.; Cornu, A.; Portelli, J.; Barkat, M.; Graulet, B. Olive mill wastewater microconstituents composition according to olive variety and extraction process. *Food Chem*. **2016**, 209, 72–80.
5. Dermeche, S.; Nadour, M.; Larroche, C.; Moulti-Mati, F.; Michaud, P. Olive mill wastes: Biochemical characterizations and valorization strategies. *Process Biochem.* **2013**, 48, 1532–1552.
6. Domínguez, C.M.; Ocón, P.; Quintanilla, A.; Casas, J.A.; Rodriguez, J.J. Highly efficient application of activated carbon as catalyst for wet peroxide oxidation. *Appl. Catal. B Environ.* **2013**, 140–141, 663–670.
7. Martínez, F.; Molina, R.; Pariente, M.I.; Siles, J.A.; Melero, J.A. Low-cost Fe/SiO_2 catalysts for continuous Fenton processes. *Catal. Today* **2017**, 280, 176–183.
8. Duarte, F.M.; Maldonado-Hódar, F.J.; Madeira, L.M. Influence of the iron precursor in the preparation of heterogeneous Fe/activated carbon Fenton-like catalysts. *Appl. Catal. A Gen.* **2013**, 458, 39–47.
9. Pastrana-Martínez, L.M.; Morales-Torres, S.; Likodimos, V.; Falaras, P.; Figueiredo, J.L.; Faria, J.L.; Silva, A.M.T. Role of oxygen functionalities on the synthesis of photocatalytically active graphene-TiO_2 composites. *Appl. Catal. B Environ.* **2014**, 158–159, 329–340.
10. McIntyre, N.S.; Zetaruk, D.G. X-ray photoelectron spectroscopic studies of iron oxides. *Anal. Chem.* **1977**, 49, 1521–1529.
11. Pastrana-Martínez, L.M.; Morales-Torres, S.; Figueiredo, J.L.; Faria, J.L.; Silva, A.M.T. Graphene oxide based ultrafiltration membranes for photocatalytic degradation of organic pollutants in salty water. *Water Res.* **2015**, 77, 179–190.
12. Soon, A.N.; Hameed, B.H. Heterogeneous catalytic treatment of synthetic dyes in aqueous media using Fenton and photo-assisted Fenton process. *Desalination* **2011**, 269, 1–16.
13. EEC Council Directive 75/440. European Economic Community; Brussels, **1975**.
14. Lu, M.; Yao, Y.; Gao, L.; Mo, D.; Lin, F.; Lu, S. Continuous treatment of phenol over an Fe_2O_3/γ-Al_2O_3 catalyst in a fixed-bed reactor. *Water, Air, Soil Pollut.* **2015**, 226.
15. Martínez, F.; Melero, J.A.; Botas, J.Á.; Isabel Pariente, M.; Molina, R. Treatment of phenolic effluents by catalytic wet hydrogen peroxide oxidation over Fe_2O_3/SBA-15 extruded catalyst in a fixed-bed reactor. *Ind. Eng. Chem. Res.* **2007**, 46, 4396–4405.
16. Botas, J.A.; Melero, J.A.; Martínez, F.; Pariente, M.I. Assessment of Fe_2O_3/SiO_2 catalysts for the continuous treatment of phenol aqueous solutions in a fixed bed reactor. *Catal. Today* **2010**, 149, 334–340.
17. Pariente, M.I.; Siles, J.A.; Molina, R.; Botas, J.A.; Melero, J.A.; Martinez, F. Treatment of an agrochemical wastewater by integration of heterogeneous catalytic wet hydrogen peroxide oxidation and rotating biological contactors. *Chem. Eng. J.* **2013**, 226, 409–415.
18. Nieto, L.M.; Hodaifa, G.; Rodriguez, S.; Giménez, J.A.; Ochando, J. Degradation of organic matter in olive-oil mill wastewater through homogeneous Fenton-like reaction. *Chem. Eng. J.* **2011**, 173, 503–510.
19. Duarte, F.; Morais, V.; Maldonado-Hódar, F.J.; Madeira, L.M. Treatment of textile effluents by the heterogeneous Fenton process in a continuous packed-bed reactor using Fe/activated carbon as catalyst. *Chem. Eng. J.* **2013**, 232, 34–41.
20. Andueza, S.; Manzocco, L.; Paz De Peña, M.; Cid, C.; Nicoli, C. Caffeic acid decomposition products: Antioxidants or pro-oxidants? *Food Res. Int.* **2009**, 51–55.
21. Navalon, S.; Dhakshinamoorthy, A.; Alvaro, M.; Garcia, H. Heterogeneous Fenton catalysts based on activated carbon and related materials. *ChemSusChem* **2011**, 4, 1712–1730.
22. Yan, Y.; Wu, X.; Zhang, H. Catalytic wet peroxide oxidation of phenol over Fe_2O_3/MCM-41 in a fixed bed reactor. *Sep. Purif. Technol. J.* **2016**, 171, 52–61.

23. Silva, A.M.T.; Nouli, E.; Xekoukoulotakis, N.P.; Mantzavinos, D. Effect of key operating parameters on phenols degradation during H_2O_2-assisted TiO_2 photocatalytic treatment of simulated and actual olive mill wastewaters. *Appl. Catal. B Environ.* **2007**, 73, 11–22.
24. Mantzavinos, D. Removal of cinnamic acid derivatives from aqueous effluents by Fenton and Fenton-like processes as an alternative to direct biological treatment. *Water, Air, Soil Pollut. Focus* **2003**, 211–221.
25. Ma, J.; Ma, W.; Song, W.; Chen, C.; Tang, Y.; Zhao, J. Fenton degradation of organic pollutants in the presence of low-molecular-weight organic acids: Cooperative effect of quinone and visible light. Environ. *Sci. Technol.* **2006**, 618–624.
26. Lucas, M.S.; Peres, J.A. Removal of COD from olive mill wastewater by Fenton's reagent: Kinetic study. *J. Hazard. Mater.* **2009**, 168, 1253–1259.
27. Moradi, S.; Sobhgol, S.A.; Hayati, F.; Isari, A.A.; Kakavandi, B.; Bashardoust, P.; Anvaripour, B. Performance and reaction mechanism of MgO/ZnO/Graphene ternary nanocomposite in coupling with LED and ultrasound waves for the degradation of sulfamethoxazole and pharmaceutical wastewater. *Sep. Purif. Technol.* **2020**, 251, 117373.

CHAPTER 10

INTEGRATION OF CATALYTIC WET PEROXIDE OXIDATION AND MEMBRANE DISTILLATION PROCESSES FOR OMW TREATMENT AND WATER RECOVERY

Highlights

- The integration of CWPO/DCMD for OMW management is reported for the first time;
- Higher permeate fluxes were obtained with CWPO pre-treated samples;
- The resulting permeate water presented several parameters suited for irrigation purposes;
- The produced DCMD-retentate was also successfully recirculated and treated by CWPO.

ABSTRACT

The degradation of organic matter present in olive mill wastewater (OMW) and the recovery of water were studied by the integration of catalytic wet peroxidation (CWPO) and direct contact membrane distillation (DCMD). The oxidation step was performed in a fixed bed reactor (FBR) working in continuous mode (pH0 = 4.0±0.2, 60 °C, Q = 0.75 mL/min, [H2O2]/[COD]feed = 2.3±0.1 g H2O2/g O2). Samples of OMW diluted by 5- and 7.5 fold (OMW 5× and OMW-7.5×, respectively) were used, corresponding to inlet chemical oxygen demand (COD) values of 3562 ±68 and 2335±54 mg/L, total phenolic content (TPh) of 177±17 and 143±7 mg GAeq/L, and total organic carbon (TOC) of 1258±63 and 842±45 mg/L, respectively. The FBR was loaded with 2.0 g of a Fe activated carbon derived catalyst, prepared by using olive stones as the precursor. The catalyst was selected based on the activity and stability towards OMW depuration shown in a previous work of the team. CWPO-treated samples of OMW allowed the operation of the DCMD unit at higher fluxes than with the analogous untreated ones, also showing higher rejections of organic matter from the feed solution upon DCMD. Using a pre-treated sample of OMW 7.5× as feed solution (Q = 100 mL/min, Tpermeate ≈ 18 °C, Tfeed ≈ 66 °C), the produced permeate water stream presented several parameters well below the legislated thresholds required for direct discharge, including total suspended solids (TSS <10 mg/L), TPh (<0.01 mg GAeq/L), biochemical oxygen demand (BOD5 <40 mg/L), and dissolved Fe (<0.06 mg/L). Moreover, the resulting concentrated OMW retentate streams could be recirculated to the FBR and maintain the same removal efficiencies obtained previously, despite the increased initial organic loadings of the retentate after DCMD.

10.1. INTRODUCTION

In this last chapter, the integration of an advanced oxidation technology for OMW treatment – the catalytic wet peroxide oxidation (CWPO) – with a downstream membrane separation process for water recovery – the direct contact membrane distillation (DCMD) technology – is studied.

In the first step, the oxidation potential of the highly reactive and non-selective hydroxyl radicals ($^{\bullet}OH$) – generated from the catalytic decomposition of H_2O_2 in the presence of ferrous ions in an acidic medium [1] – is explored for the depuration of OMW. In this stage, the process implementation can benefit from the naturally low pH of OMW to help reduce costs associated with chemicals for wastewater acidification, required for optimum CWPO operation. Additionally, the use of Fe-supported catalysts is known to tackle the generation of the iron-rich sludge characteristic of the homogeneous process, and thus also eliminate its downstream handling costs [2]. For this purpose, the work developed in the previous Chapters 7–9 [3–5] has been focused on the development and detailed characterization of tailored Fenton-like catalysts synthesized from solid by products of the olive oil industry (namely olive stones), and thus, ultimately, to the adoption of an environmental circular economy model within this industry.

Membrane distillation is a thermally-driven separation technology widely adopted in desalination, but also for different environmental applications related to water/wastewater treatment [6]. A module operated at non-isothermal conditions between both sides of a microporous hydrophobic membrane, generates a transmembrane vapor pressure difference (ΔP) between the permeate (cold) and retentate (hot) sides of the module, that allows water vapor (or volatile compounds) to selectively pass the membrane pores, preventing the mass transfer of the liquid [7]. When compared to other separation technologies, membrane distillation processes are operated at a lower temperature than conventional distillation, also involving the generation of lower hydrostatic pressures when compared to nanofiltration or reverse osmosis, for example [6,8].

It has been proved that direct DCMD is an efficient process for wastewater treatment, either as a method to produce a less environmentally-hazardous stream of permeate abd/or to concentrate and recover valuable compounds [9,10]. Thus, aiming at the recovery and reuse of water (e.g., for crops irrigation or machinery washing activities), the second step of the proposed process herein envisaged comprises the use of a DCMD unit. Among the possible configurations, DCMD was selected for its simplicity of operation, as the condensation step occurs inside de membrane module. The downstream application of this technology can also benefit from the capacity of the

advanced oxidation process to cause the dissolution of organic matter and thus reduce the likelihood of membrane fouling [11].

Therefore, the work in this chapter aims to explore the aforementioned advantages of both processes to: (1) reduce OMW organic load, as inferred by its TPh, COD, and TOC; (2) ensure the continuous production of a stream of treated OMW by using an in-house synthesized catalyst in a fixed-bed reactor to operate continuously and feed the DCMD unit; (3) recover and characterize treated water (permeate) to check compliance with legislated standards for irrigation purposes; and (4) evaluate the possibility of recirculating the produced concentrated stream of OMW back to the FBR unit.

Up to the author's knowledge, the application of an integrated process comprising heterogeneous Fenton-like oxidation followed by a DCMD separation for OMW treatment and water recovery has never been addressed in the literature as an integrated solution for the management of residues within this agro-industry.

10.2. MATERIALS AND METHODS

10.2.1. Chemicals, materials, and olive mill wastewater

Methanol (HPLC grade ≥99.8%, Fischer Chemicals), H_2O_2 (30% *w*/*v*, VWR), and Folin Ciocalteau reagent (Panreac) were used. A polytetrafluoroethylene (PTFE) membrane (0.22 μm pore size, 150 μm thickness) from Merck Millipore (FGLP Fluoropore®) was selected for the DCMD unit, based on several reviews [6,12,13] that highlight its efficiency for membrane distillation and good properties related to pore size distribution, hydrophobicity, chemical resistance and thermal stability.

The catalyst used in the FBR runs was prepared via incipient wetness impregnation using $Fe(NO_3)_3 \cdot 9H_2O$ (Merck) as the iron precursor, to a theoretical load of 5 wt.% of Fe. The active iron-phase was anchored to an olive stone derived-activated carbon support, previously synthesized by sequential carbonization (N_2 atmosphere) and activation (CO_2 atmosphere) in a horizontal tube furnace at 800 °C; a detailed report on the synthesis procedure and characterization of the catalyst can be found in Chapters 8 and 9 [3,5].

The OMW used in this study was obtained from the 3-phase decanter's exit of a small-size olive mill from the northern region of Portugal during the 2019 campaign. Imhoff cones were used to

separate particulate and settable suspended matter (24 h of settling time), and the supernatant was collected for physicochemical characterization (Table 10.1). Samples were then divided into several 1 L containers and frozen (-15 °C) until required for the experimental runs. The initial organic load of the effluent was adjusted by dilution with distilled water; the effluent supernatant was diluted by 5-fold and 7.5-fold to recreate the potential biological stabilization and/or rain dilution occurring in a scenario where the effluent would be stored in an open-air pond [14].

Table 10.1 Main physicochemical characteristics of OMW supernatant before and after dilution. Legislated discharge limits for irrigation water and industrial wastewater are shown for reference.

Parameter	OMW (supernatant)	OMW (D = 5-fold)	OMW (D = 7.5-fold)	Discharge limits*
pH	3.5 ±0.3	4.0 ±0.2	4.9 ±0.1	6.0 – 9.0[(b)]
COD (mg/L)	17 878 ±554	3 562 ±68	2 335 ±54	150[(b)]
BOD_5 (mg/L)	3 817 ±483	970 ±10	730 ±10	25[(a)]/40[(b)]
TOC (mg/L)	6 685 ±145	1258 ±63	842 ±45	n.e.
TPh (mg GA_{eq}/L)	1 098 ±48	177 ±17	143 ±7	0.5[(b)]
TSS (mg/L)	370 ±40	130 ±16	28 ±6	35[(a)]/60[(ab)]
TDS (mg/L)	2 120 ±170	455 ±17	338 ±11	n.e.
Fe (mg/L)	1.05	0.23	0.16	2.0[(a,b)]
Conductivity (μS/cm)	3 290 ±120	703 ±4	520 ±7	n.e.
Color (1:20 dilution)	Visible	visible	visible	non-visible

* According to the Portuguese Decree-law 119/2019, 21st August – production of water for reuse in irrigation activities[(a)], and Decree-law 236/98, 1st August in Annex XVIII – standards for industrial discharges[(b)].
n.e. – not established.

10.2.2. Fixed-bed reactor set-up: CWPO experiments

Catalytic runs were performed in an up-flow jacketed fixed-bed reactor (borosilicate glass column) with inner dimensions of H = 12 cm and D = 1.5 cm. The catalyst (W_{cat} = 2.0 g, corresponding to approximately 2/3 of the reactor's height) was placed at the center of the column, 1 mm diameter inert glass spheres were used to fill the remaining void spaces, and both ends were capped with glass wool to prevent clogging of the inlet and outlet tubing – *cf*. Fig. 10.1. The FBR was connected to a recirculating thermostatic bath (VWR, mod. 89202-912), and the temperature was

set to 60 °C. The feed solution (OMW) was placed into a 3-neck round bottom flask (500 mL), agitated at 300 rpm, and heated to 60 °C using a magnetic stirrer with a hot plate (Falc Instruments). To guarantee an equitable comparison between runs, pH values were maintained at 4.0 ±0.2 (i.e., the initial pH of sample OMW-5×) – adjustments to slightly acidify the OMW-7.5× sample were performed using H_2SO_4 1.0 M. As illustrated in Fig. 10.1, the flask was connected to a reflux condenser at 15 °C (to avoid evaporation of the feed OMW), the solution's pH and temperature were continuously measured by a WTW Inolab pH-meter (mod. Level 2P), and fed to the reactor by a peristaltic pump (NEW ERA, mod. NE 900).

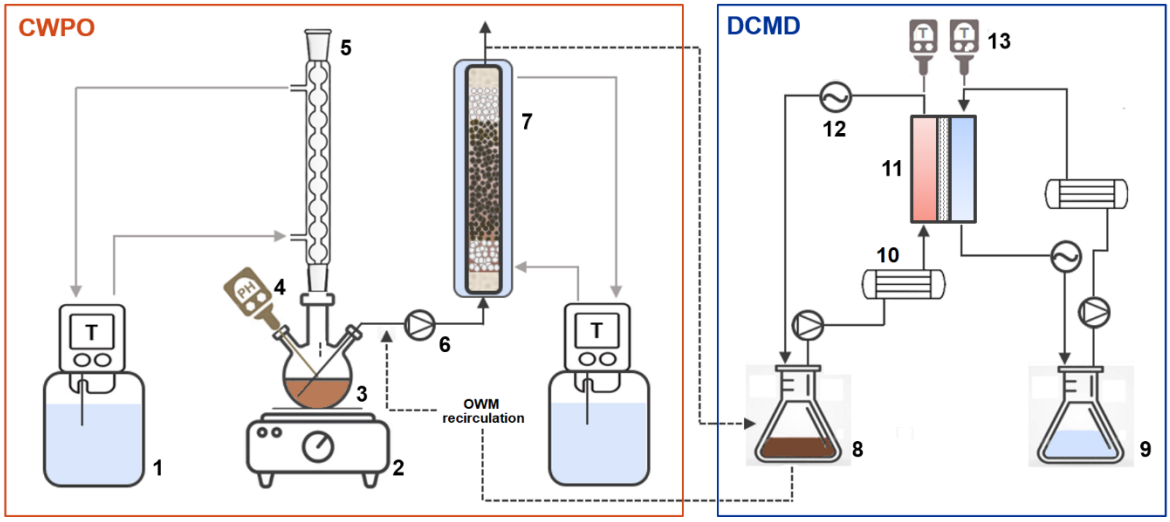


Fig. 10.1 Schematic representation of the combined experimental set-up: (1) recirculating water bath; (2) magnetic stirrer hot plate; (3) 3-neck flask with OMW+H_2O_2; (4) combined pH and temperature electrode; (5) reflux condenser; (6) peristaltic pump; (7) jacketed FBR; (8) retentate; (9) permeate; (10) heat/cool exchangers (both connected to separate recirculating water baths – not graphically represented); (11) DCMD module; (12) conductivity meter; (13) thermocouples.

In a typical run, the column was initially filled with distilled water, the system was allowed to reach the desired temperature, and then the H_2O_2 was added to the feed flask and fed to the FBR (initial instant of the oxidation experiments, t = 0). The oxidative behavior of the H_2O_2 in the feed vial was checked over time, and the maximum removals observed were <4% for TOC, <6% for COD, and <10% for TPh (results not shown for brevity). As detailed in the Chapter 9 [5], the required amount of H_2O_2 is dependent on the solution's initial COD, which was kept at a feed [H_2O_2]/[COD] ratio of 2.3 ±0.1 g H_2O_2/g O_2. In each run, the system was operated continuously for 20 h at a volumetric flow rate (*Q*) of 0.75 mL/min, requiring the addition of untreated OMW to the feed flask approximately every 10 h (i.e., once every run). The operational conditions of the FBR unit were established following the results of the previous chapter [5], and as suggested therein, the contact

time (W_{cat}/Q) was increased by 2 fold to W_{cat}/Q = 2.66 g·min/mL; under such conditions, the activity of the catalyst bed was maintained stable for ≈40 h of operation, and thus it was not substituted for this set of experiments.

10.2.3. DCMD experimental set-up

DCMD experiments were performed in a laboratory set-up similar to that described in a previous study [15]. The commercial PTFE membrane (effective area of 7.0×10^{-3} m^2) was placed into an "LH shaped" polyoxymethylene module working in cross-flow mode in counter current [7]. In a typical run, the CWPO treated OMW (feed) and distilled water (permeate) were recirculated through heat and cool exchangers, respectively, by two peristaltic pumps working at a flow rate of 100 mL/min – Fig. 10.1. These conditions were selected based on the findings of a previous study [7]. Thermocouples placed at both sides of the DCMD module allowed to continuously monitor the cell temperature, which was maintained at ≈57 °C (feed side) and ≈18 °C (permeate side) throughout the experiments, resulting in a pressure differential of ≈16.5 kPa between both sides [16]. Similar runs were also performed with feed temperatures of ≈66 °C and ≈75 °C, resulting in ΔP ≈ 26.2 kPa and ≈41.0 kPa, respectively. The approximate values reported are due to small variations within the set temperature and cell temperature measured during the runs. The permeate fluxes across the membrane were determined by the change in weight of the permeate vial. The initial volumes of permeate (distilled water – DW) and retentate were 300 and 450 mL, respectively. In selected experiments, the retentate was also recirculated to the FBR unit after the DCMD operation (typically 4 h runs) to treat the concentrated OMW produced in this step.

The total dissolved solids (TDS) were also measured over time in the permeate side with a conductivity meter (VWR mod. CO310), by multiplying the measured conductivity (mS) by a set TDS factor of 0.65. Experiments were conducted for 4 h and the permeate flux (J) was calculated for several time intervals following Eq. (10.1), where W is the mass of distillate – permeate (kg), A the effective membrane area (m^2), and t the sampling time (h).

The rejection % (R) was estimated following Eq. (10.2), where Cpermeate is the concentration of any given lumped parameter (TOC, TPh, COD, or TDS) of the permeate solution at a given time t, and $C_{feed,0}$ is the initial concentration of such parameter in the feed solution, respectively. The OMW concentration factor in the retentate side (β) was determined from Eq. (10.3).

$$J = \frac{\Delta W}{A \times \Delta t} \quad (10.1)$$

$$R(\%) = \left(1 - \frac{C_{permeate}\ (t)}{C_{feed_0}}\right) \times 100 \quad (10.2)$$

$$\beta = \frac{C_{retentate}\ (t)}{C_{feed_0}} \quad (10.3)$$

10.3. RESULTS AND DISCUSSION

10.3.1. FBR experiments

One of the main limitations of membrane distillation is the rapid decrease of permeate flux due to the high concentration of solutes in the feed solution [17]. The variety and load of different organic compounds in the OMW feed matrix may also lead to membrane fouling (by deposition of dissolved or colloidal organic matter on the membrane surface) or scaling (by precipitation of sparingly soluble salts), which can cause wetting of the membrane and result in the free passage of contaminants through the pores [18,19]. A pre-treatment capable of reducing the effluent's initial load could prevent membrane fouling and also scaling, as already suggested by V. Kumar *et al*. [11] for the management of secondary municipal wastewater.

In this chapter, the catalytic wet peroxide oxidation was considered as a pre-treatment step for continuous OMW depuration, and the effluent's COD, TPh, TOC, and residual H_2O_2 were monitored at the reactor outlet. Two set of experiments were performed with distinct OMW feed loadings, corresponding to a 5-fold dilution (COD_0 = 3562 ±68 mg/L, TPh_0 = 177 ±17 mg/L) and a 7.5-fold dilution (COD_0 = 2335 ±54 mg/L, TPh_0 = 143 ±7 mg/L) of the raw effluent supernatant (*cf*. Table 10.1). The fixed-bed reactor was fed continuously for 20 h, and the COD and TPh values registered at the outlet stream are shown in Fig. 10.2.

As mentioned before, different operational parameters – including oxidant dose (in the 0.75-3.0 g/L range), reaction temperature (varying from 20 to 60 °C), and volumetric flow rate (between 0.25–1.75 mL/min) – were previously optimized for a similar effluent and experimental set-up; the main difference with the present study was the amount of catalyst loaded into the column (i.e., the contact time of the fluid with the catalyst was doubled). Subsequently, the unreacted H_2O_2 in

the outlet stream was reduced from 28% (as disclosed in the previous work) to an average of 7%, in the run with OMW-5× (results not graphically presented for brevity). Similarly, high oxidant conversions were observed throughout the entire run with OMW-7.5×, with steady state FBR exit conversions >95%. Consequently, the increase in catalyst amount also led to an overall improvement in the reduction of COD and TPh in both cases when compared to the efficiencies previously reported (for instance, steady-state removals of 29% for COD and 60% for TPh were previously obtained with OMW-7.5×)..

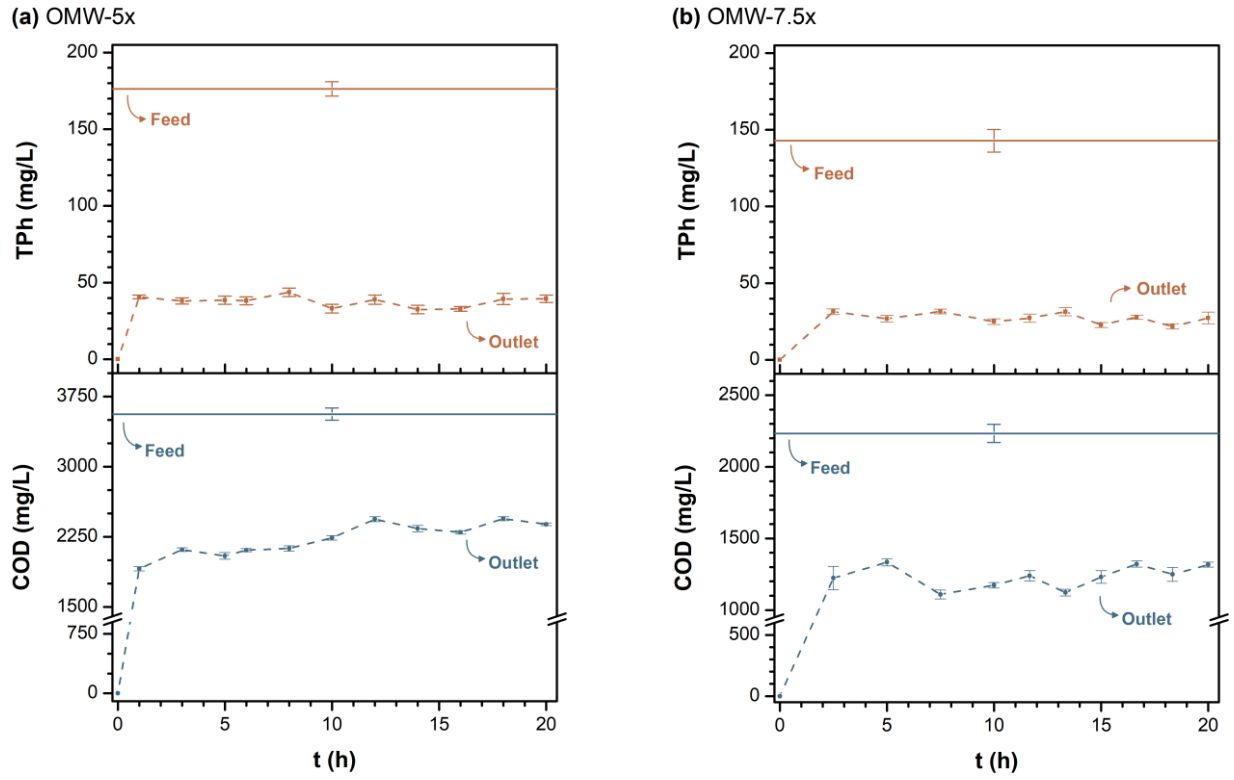


Fig. 10.2 COD and TPh concentrations (mg/L) over time at the FBR feed and outlet streams for (a) OMW-5× and (b) OMW-7.5×. Experimental conditions: $[H_2O_2]_{feed}/[COD]_{feed}$ = 2.3 ±0.1 g H_2O_2/g O_2, W_{cat}/Q = 2.66 g min/mL, T = 60 °C, Q = 0.75 mL/min, pH_0 = 4.0 ±0.2.

On average, removal efficiencies were slightly lower for the OMW with higher initial load (i.e., less diluted effluent – OMW-5x), with COD and TPh removals of 37% and 79%, respectively, whereas 45% and 81% reductions were obtained with OMW-7.5× at steady state. As observed in Fig. 10.2, the TPh values reported at the reactor outlet were practically constant during the 20 h of operation, ranging from 32.4–41.7 mg/L and 21.8 31.6 mg/L, for OMW-5× and OMW-7.5×, respectively. The values of COD of the produced effluent were also maintained in the case of OMW-7.5× (*ca*. 1230 mg/L on average), whilst slightly increasing after ≈10 h for OMW 5× (from an average of 2120 to 2360 mg/L).

A smaller extent of TOC removal (mineralization) after CWPO was observed (removals of 14.2% and 16.8% for OMW-5× and OMW-7.5×, respectively), possibly related to the breakdown of suspended solids during the catalytic process, resulting in the dissolution of this fraction of organic matter to the solution (not previously accounted due to the sample's filtration before TOC analysis – i.e., dissolved organic carbon). This hypothesis was reinforced by the TDS values registered before (455 ±17 mg/L) and after oxidation (649 ±36 mg/L) in the case of the run performed with OMW-5×, along with a decrease in TSS (from 130 ±16 to 42 ±7 mg/L after CWPO). Furthermore, the values of BOD_5 also decrease by 86.6% to 130 ±10 mg/L, while the cumulative values of Fe dissolved in solution were found to be considerably higher (Fe = 5.7 mg/L) than those observed in the original effluent, indicating the leaching of the metallic active phase from the catalyst. Similar trends were also observed for the CWPO-treated sample of OMW-7.5× (results not shown for brevity).

Despite the removals achieved by oxidation, the produced effluents are still non-compliant with legislated emission values (Portuguese Decreto-Lei n. 236/98) for wastewater discharge into natural bodies of water. Nonetheless, the main goal of this step was to produce a continuous stream of pre-treated OMW with steady physicochemical properties over time (e.g., COD and TPh), and then check its suitability for further depuration through membrane distillation with water recovery.

10.3.2. DCMD experiments

The performance of DCMD for the management of the different OMW streams was evaluated by the transmembrane fluxes achieved, the rejection values, and the overall quality of the permeate streams produced. A run with DW was also performed to assess the maximum permeate flux (J) of the distillation module in the absence of membrane fouling, under a defined set of operational conditions ($Q_{feed} = Q_{permeate} = 100$ mL/min, $T_{feed} \approx 57$ °C, $T_{permeate} \approx 18$ °C, t = 4 h). Permeate fluxes and water recovery calculated along time for the two untreated OMW samples (OMW-5× and OMW-7.5×), as well as for the corresponding CWPO-treated samples of OMW, are shown in Fig. 10.3.

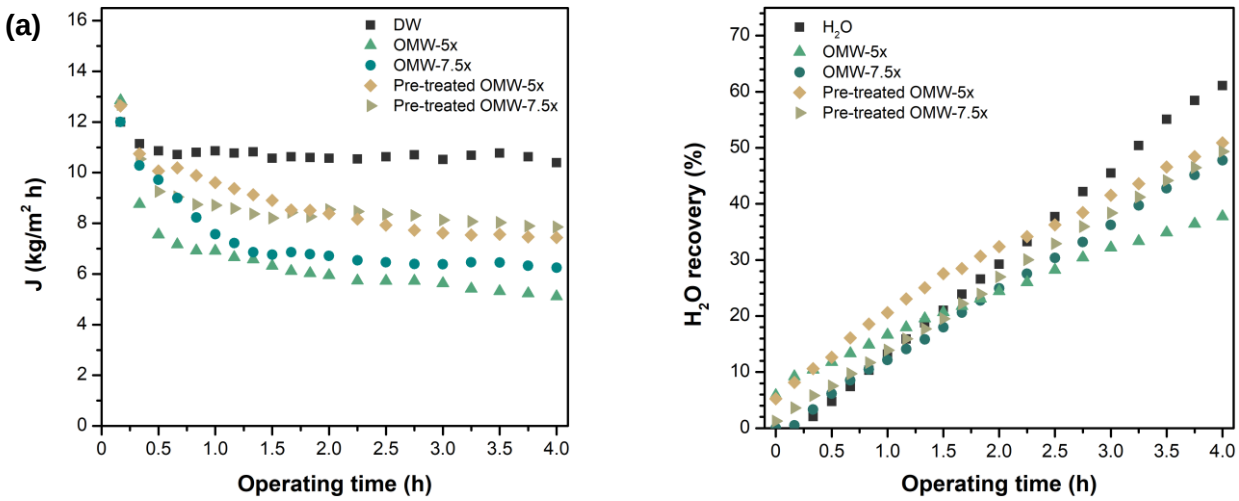


Fig. 10.3 (a) DCMD permeate flux and (b) H_2O recovery over time for DW and for OMW samples (before and after CWPO pre-treatment). Experimental conditions: T_{feed} ≈ 57 °C and $T_{permeate}$ ≈ 18 °C (ΔP ≈ 16.5 kPa), Q = 100 mL/min.

After stabilization of the temperature gradient inside the membrane module (i.e., after *ca*. 20 min) the flux of DW was maintained practically unaltered at ≈10.5 kg/m^2·h for the experimental conditions tested (Fig. 10.3a). Contrarily, different degrees of flux decline were observed for both untreated and pre-treated samples of OMW. Due to the initial composition of OMW comprising several organic (and inorganic) solutes, a lower water vapor pressure is expected and thus also smaller permeation fluxes values in comparison to that of DW [20]. Expectably, OMW-5× (the less diluted effluent) registered the highest permeation flux decline after 4 h of operation (*ca*. 60%), whereas this value was close to 48% for the more diluted untreated sample (OMW-7.5×). A similar trend was reported by Vinoth Kumar *et al*. [11] under analogous experimental conditions but for the treatment of secondary municipal wastewater.

After 4 h of operation, the system achieved similar H_2O recoveries for samples with lower initial loadings (which included the CWPO-treated OMW-5× with similar COD and TOC values as the untreated OMW-7.5×) – Fig. 10.3b. Still, the recoveries were always lower than the one achieved with DW (final recovery of *ca*. 58%). A very distinct profile was obtained in the OMW-5×, which also presented the lowest productivity (*ca*. 38%).

The higher flux decline (and lower H_2O recovery) observed for the sample with higher organic load (OMW-5×) could be partially attributed to the phenomena of concentration polarization occurring due to the rapid increase in solute concentration over time in the retentate side that leads to a decrease in the driving force (i.e., partial vapor pressure) [6]. Additionally, the deposition of particulate matter on the membrane surface (membrane scaling and/or organic fouling) –

visually confirmed after the experiments, *cf*. Fig. 10.4 – suggests the occurrence of a more extensive pore blocking in this sample.

Increased resistance of water vapor transport across the membrane over time is therefore expected, and under such conditions membrane wetting is also possible, further negatively affecting the process efficiency. Wetting phenomena occurs when the transmembrane pressure (ΔP) exceeds the liquid entry pressure (LEP), allowing for the feed to pass through the membrane pores. Among others, LEP is directly influenced by the membrane contact angle and water surface tension, and thus a decrease in both parameters can facilitate membrane wetting. Since the degradation of organic contaminants causes an increase in surface tension that may impede their interaction with the hydrophobic membrane surface [18], the oxidative pre-treatment could be potentially responsible for this phenomenon, thus allowing for higher fluxes.

The measurement of membrane contact angles provided evidence of this phenomenon. For example, in the case of OMW-7.5x, the used membrane presented an average contact angle of 106.0° (measured at the center of the membrane) while this value was clearly improved by the oxidative pre-treatment step to 142.4° (also measured at the center of the membrane). Comparatively, a pristine PTFE membrane exhibits a contact angle of 145.8°, confirming its highly hydrophobic character. The observed behavior is in line with similar reports in the literature for this type of effluents [17,21].

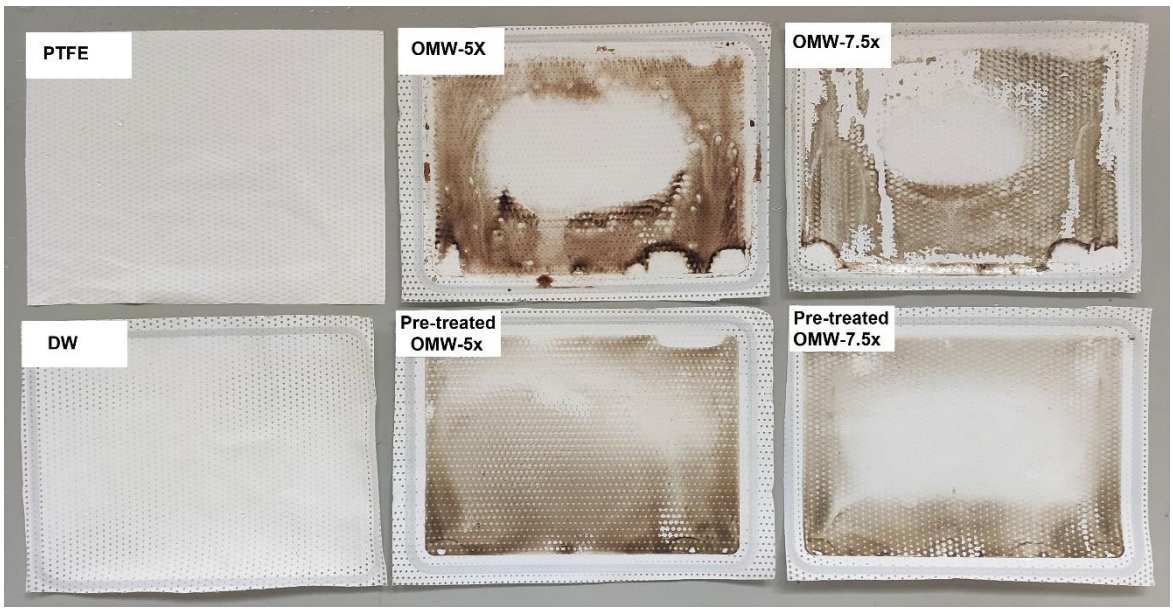


Fig. 10.4 Visual comparison of a neat-PTFE membrane with the used ones in DCMD after 4 h of operation for the different feed solutions tested. Experimental conditions: $T_{feed} \approx 57$ °C and $T_{permeate} \approx 18$ °C ($\Delta P \approx 16.5$ kPa), Q = 100 mL/min.

The extent of membrane scaling and/or fouling is also visibly dependent on the initial load of the effluent, but more importantly, on the oxidative pre-treatment step, as highlighted in Fig. 10.4. The resulting brownish coloration that appears on the membrane surface – noticeably darker in the case of untreated OMW samples – is probably related to the presence of lignin polymerized with phenolic compounds, and constitutes the most resistant fraction of OMW [22,23]. The contact angles observed in such spots are considerably lower than those previously reported for the center of the membrane, with measured average contact angles as low as 45.4° in areas where fouling/scaling is more severe (predominantly in the membrane edges, due to the module's intrinsic design and operation). In general, a less concentrated fouling layer was obtained in the membrane surface of pre-treated samples, expectably as a result of the phenolic content reductions achieved by the CWPO step.

Despite the resemblances in the permeate fluxes obtained for both pre-treated samples, with $J \approx 7.4$ kg/m^2·h after 4 h, the catalytic pre-treatment step resulted in a clear improvement of the fluxes obtained in comparison to those of the respective untreated samples. El Abbassi *et al*. [20] reported a similar behavior for pre-treated samples of OMW via microfiltration and coagulation/flocculation, whereas the work of Farinelli *et al*. [18] showed no specific advantage in the obtained water fluxes by using the homogenous Fenton oxidation as a preliminary stage for the DCMD of hypersaline "produced water" from oil and gas extraction activities.

Both permeate (Table 10.2) and retentate (Table 10.3) streams were analyzed to evaluate the efficiency of the DCMD process in the production of water and concentration of contaminants, respectively. In addition to the improvement in productivity of the DCMD unit by the pre oxidation step of the raw OMW (higher H_2O recovery *cf*. Fig. 10.3b), the resulting water quality after the combined process was also enhanced when compared to that of the membrane distillation stage alone. Table 10.2 shows the characterization of the produced streams of permeate obtained by untreated samples of OMW-5× and OMW-7.5×, as well as the respective CWPO-treated ones. Rejection percentages achieved by the membrane distillation step alone and the combined process (oxidation and membrane distillation) are highlighted between brackets. It is worth noting that the dilution effect occurring in the permeate vial due to the initial volume of DW (300 mL) was taken into consideration and eliminated for the calculation of the concentrations and rejection percentages presented.

Table 10.2 Permeate characterization after 4 h of DCMD; rejection % shown between brackets. Experimental conditions: T_{feed} ≈ 57 °C and $T_{permeate}$ ≈ 18 °C (ΔP ≈ 16.5 kPa), Q = 100 mL/min.

Parameter	OMW-5×	OMW-7.5×	Pre-treated OMW-5×		Pre-treated OMW-7.5×	
	DCMD step		*DCMD step*	*CWPO+DCMD*	*DCMD step*	*CWPO+DCMD*
COD (mg/L)	466 (*87.1%*)	290 (88.4%)	329 (*86.2%*)	(*90.8%*)	265 (85.0%)	(89.2%)
TPh (mg GA_{eq}/L)	1.7 (*99.1%*)	0 (100%)	0.5 (*98.9%*)	(*99.7%*)	0 (100%)	(100%)
TOC (mg/L)	249 (*78.7%*)	199 (76.4%)	220 (*78.6%*)	(*81.6%*)	188 (73.1%)	(77.8%)
TDS (mg/L)	41.0 (*91.0%*)	38.8 (90.0%)	68.4 (*88.8%*)	(*85.0%*)	52.6 (91.4%)	(84.4%)

The characterization results of both OMW samples show that the DCMD unit per se was able to effectively reduce COD, TPh, and TOC in the permeate stream to a similar degree, independently of whether the effluent was pre-treated or not. However, the absolute values of all parameters evaluated were significantly improved by the combined process (and thus also the respective removal efficiencies by comparison to the DCMD step alone, *cf*. highlighted in the columns labelled as "CWPO+DCMD" of Table 10.2). Comparing the global rejection efficiencies (i.e., after CWPO+DCMD) achieved with OMW-5× and OMW-7.5×, the rejection percentages obtained were similar independently of the effluent's organic load after oxidation. The TDS concentrations registered were also small in comparison to the feed solutions, albeit a higher percentage of TDS rejection was attained for the non-treated samples. This behavior was probably due to the breakdown of suspended solids that occurred after CWPO, as mentioned in Section 10.3.1. In both cases, to a greater or lesser extent, the characterization of the permeate side suggests the presence of volatile compounds in the wastewater matrixes (accounted for as COD and TOC) that could also have resulted from the free passage through the membrane pores, or the occurrence of membrane wetting previously discussed. Though not referred to in Table 10.2, the concentration of Fe dissolved in the permeate was also very low in all cases (<0.08 mg/L), thus also providing a key advantage to the integrated process, as the Fe resulting from the catalyst leaching in the catalytic step is almost exclusively maintained in the retentate side

Table 10.3 Retentate characterization after 4 h of DCMD; concentration factors of the retentate ($\beta_{4\ h}$) shown in brackets. Experimental conditions: T_{feed} ≈ 57 °C and $T_{permeate}$ ≈ 18 °C (ΔP ≈ 16.5 kPa), Q = 100 mL/min.

Parameter	OMW-5×	OMW-7.5×	Pre-treated OMW-5×	Pre-treated OMW-7.5×
COD (mg/L)	7111 (*2.0*)	4501 (*1.8*)	4337 (*1.8*)	2689 (*1.5*)
TPh (mg Ga_{eq}/L)	517.9 (*2.9*)	375.1 (*2.6*)	154.5 *(3.3)*	80.3 (*3.2*)
TOC (mg/L)	2729 (*2.3*)	1776 (*2.1*)	2092 (*2.0*)	1198 (*1.7*)
TDS (mg/L)	1085 (*2.4*)	785 (*1.7*)	839 (*1.4*)	988 (*1.6*)

Values of the concentration factors after the 4 h of operation ($\beta_{4\ h}$, Table 10.3) point out the more denoted effect of the concentration polarization effect referred earlier, as slightly higher concentration factors of COD, TOC and TDS were obtained for the untreated samples of OMW. The retentate concentration factors obtained were in line with the water recovery in the permeate side previously shown (Fig. 10.3b). Oppositely, a significantly higher TPh concentration factor in DCMD was observed after processing both untreated and pre-treated samples, potentially explained by the "aggregation" of the phenolic fraction of the wastewater to the TSS one, and that ended up dissolved in solution by the process temperature (in line with the TDS values observed). A similar range of concentration factors was reported by other authors [20,24] for specific OMW phenolic compounds (namely, gallic acid and tyrosol), while others (such as oleuropein) presented considerably smaller β values.

To take advantage of the effluent's temperature after the CWPO step, the membrane unit was initially operated at T_{feed} ≈ 57 °C. Still, DCMD is a thermally driven process and an increase in ΔT is expected to favor the process efficiency, as per previous reports [17,19,20]. In an attempt to further improve the permeate flux and quality of the permeate stream to meet legislated emission values for irrigation purposes (Table 10.1), further experiments were conducted with pre-treated samples of OMW-7.5×. Fixing $T_{permeate}$ at ≈18 °C, two additional feed temperatures were tested (T_{feed} ≈ 66 and 75 °C) resulting in pressure differentials of ≈26.2 and ≈41.0 kPa, respectively. Permeate fluxes and TDS rejection values over time are shown in Fig. 10.5.

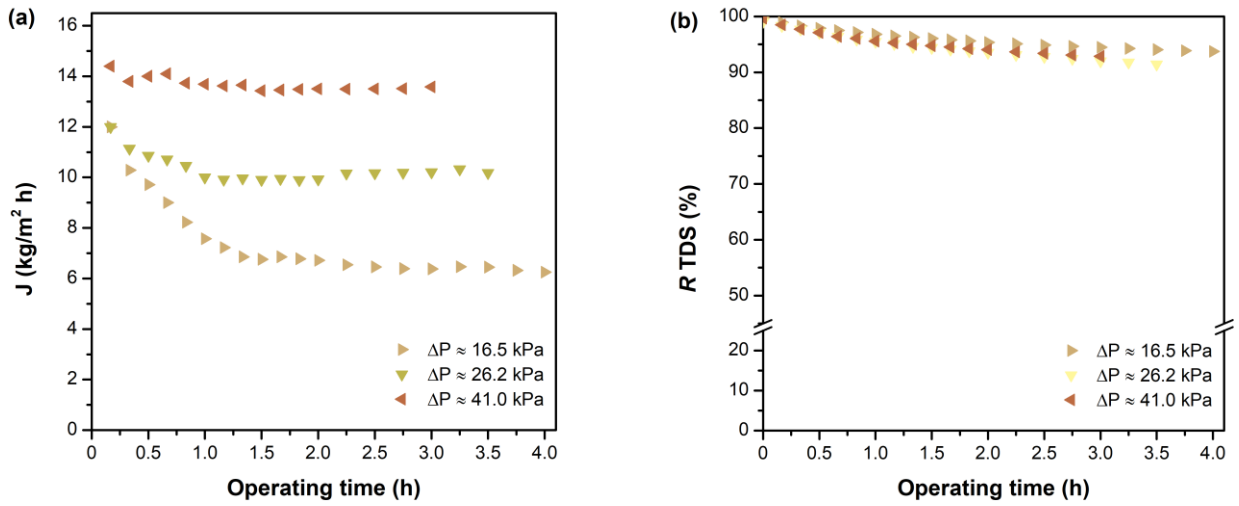


Fig. 10.5 (a) DCMD permeate flux and (b) TDS rejection over time for CWPO pre-treated samples of OMW-7.5× Experimental conditions: $T_{permeate}$ ≈ 18 °C, Q = 100 mL/min.

Increasing the feed temperature by *ca*. 10 °C resulted in 60% improvement of the permeate flux, which was more than doubled when the mean bulk temperature was increased by *ca*. 20 °C – Fig. 10.5a. The TDS rejections (*R*) – Fig. 10.5b – were always below the theoretical maximum and slowly decreased over time in every case to a similar extent, which can be partially attributed to the wetting of the membrane pores [8,25]. It is also worth noting that due to the higher permeate fluxes achieved at higher feed temperatures, the system operation was limited to the fixed initial volume of solution fed to the DCMD unit (450 mL), and thus the values reported in Fig. 10.6 were equitably compared for an operating time of 3 h.

As to the quality of permeate streams obtained after the integrated process reported in Fig. 10.6, all parameters evaluated varied in a close range of values independently of the feed temperature used (and thus transmembrane pressure). This behavior, in addition to the higher permeate fluxes achieved as ΔP increases (Fig. 10.5a), can be advantageously adopted to produce higher volume of permeate over time with steady physicochemical properties, although the higher energy costs associated with heating the feed solution may need to be taken into consideration.

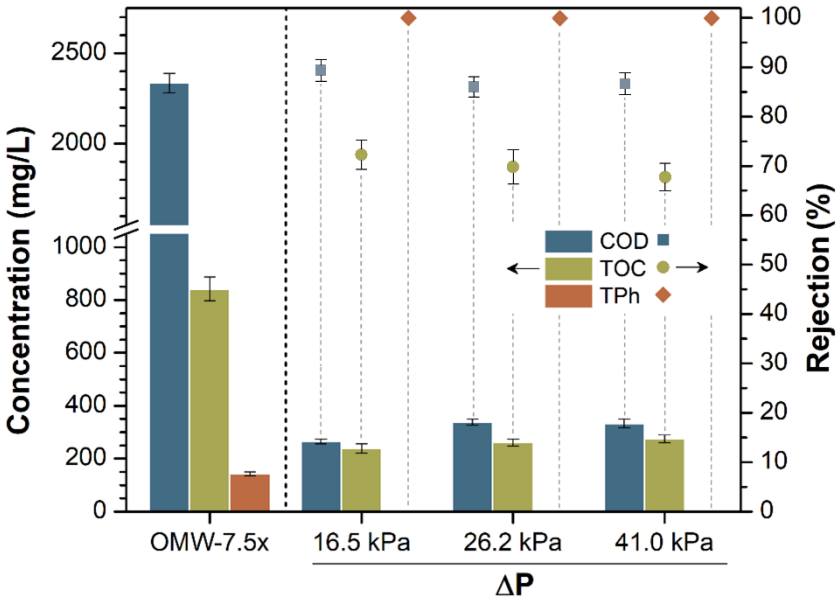


Fig. 10.6 Concentration of COD, TOC, and TPh (permeate) after the integrated process (CWPO+DCMD), initial values of OMW-7.5× presented for reference. Right y-axis shows the global rejection for each parameter. Experimental conditions: $T_{permeate}$ ≈ 18 °C, Q = 100 mL/min, t = 3 h.

The permeate water obtained under the conditions tested was able to meet several criteria thresholds required for irrigation purposes according to Portuguese legislation (*cf*. Table 10.1), including TPh (<0.11 mg GA_{eq}/L), TSS (<10 mg/L), and Fe (<0.08 mg/L) concentrations in all cases. The BOD_5 values reported in the permeate streams also met the criteria when operating at ΔP ≈ 26.2 kPa (<40 mg/L), or were found to be slightly above the emission values in the remaining cases (74–87 mg/L). Likewise, the values of COD obtained were still above the limit emission value of 150 mg/L (e.g., 265 ±9 mg/L in the best scenario, i.e. ΔP ≈ 16.5 kPa – Fig. 10.6). As to the legal scheme for the "production of water for its reuse, obtained from the treatment of wastewater, in the irrigation of crops" from the Portuguese Decree-law 119/2019, values of turbidity (<4.1 NTU), TSS and Fe were also always below the imposed discharge limits, but the more restrictive value for BOD_5 (i.e., below 25 mg/L) was not achieved under the conditions tested.

10.3.3. DCMD-retentate recirculation to the FBR

Notwithstanding the achieved quality parameters of the permeate water produced, the DCMD operation also generates a secondary stream of concentrated waste that requires downstream handling (i.e., the retentate). On another hand, it was previously shown that for a similar experimental set-up (only differing in the amount of catalyst loaded into the FBR), the CWPO

process was able to maintain similar treatment efficiencies independently of OMW initial load (for COD_0 ranging from 594–3595 mg/L – Chapter 9 [5]).

Therefore, three distinct DCMD-retentate solutions were re circulated (in discontinuous mode) from the membrane unit back to the catalytic reactor (i.e., the DCMD run was stopped after 4 h, and the resulting retentate was collected and used to feed the FBR). Fig. 10.7 highlights the main properties (COD, TOC, and TPh) of the retentate samples after the catalytic step (i.e., FBR outlet at steady-state).The results obtained are in good agreement with the previous findings. The overall similar range of COD (37.4–42.7%), TOC (32.2–33.2%), and TPh (77.4–83.9%) removals after the recirculation to the FBR, independently of the initial OMW DCMD retentate load (COD_0 range of 2689–7111 mg/L), confirms the good adjustment between the $[H_2O_2]$/[COD] feed ratio and contact time selected for the FBR operation. Moreover, identical COD and TPh removal percentages were obtained with either samples that were treated by FBR-DCMD-FBR. Finally, an improvement in TOC removal efficiencies by *ca*. 2-fold after the membrane distillation process was also achieved (previously in the 14.2-16.8% range *cf*. results in Section 10.3.1 for FBR alone, to 32.2–33.2% as depicted in Fig. 10.7b for FBR-DCMD-FBR). This enhancement can be justified by the fact that the most hardly degradable compounds were adhered to the membrane (*cf*. Fig. 10.4), or by the transference of some organic solutes to the permeate side (Table 10.2).

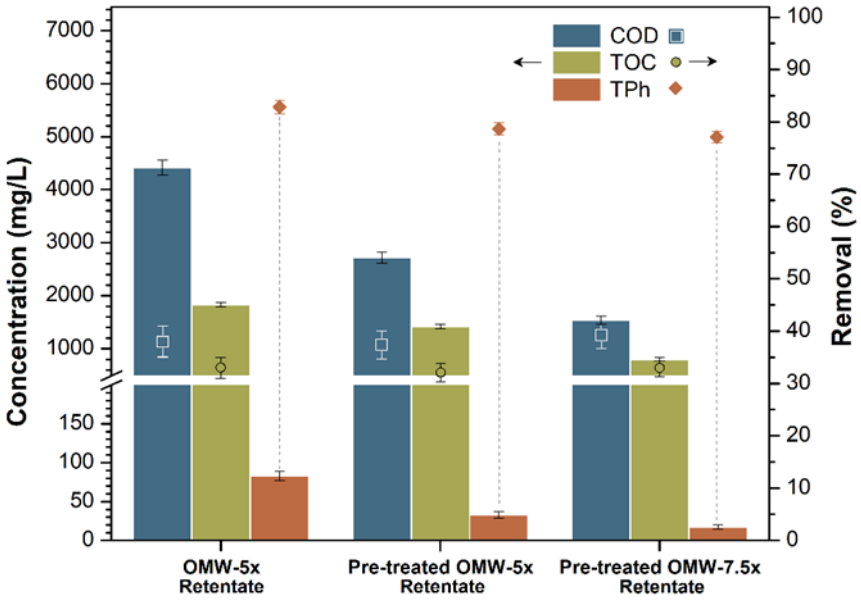


Fig. 10.7 (a) COD, TOC, and TPh of different retentates after recirculation to the FBR with indication of oxidation efficiencies in steady-state (yy-axis). DCMD experimental conditions: T_{feed} ≈ 57 °C, $T_{permeate}$ ≈ 18 °C, ΔP ≈ 16.5 kPa, Q = 100 mL/min; FBR: $[H_2O_2]_{feed}$/$[COD]_{feed}$ =2.3 ±0.1 g H_2O_2/g O_2, W_{cat}/Q = 2.66 g min/mL, T = 60 °C, pH_0 = 4.0 ±0.2; data for the FBR refer to its steady-state operation).

10.4. CONCLUSIONS

This work highlighted the potential of a combined treatment process for OMW management comprising a preliminary oxidative step by CWPO in a fixed-bed reactor and the subsequent recovery of water by DCMD. The pre-treated samples of OMW allowed the operation of the membrane distillation unit at higher fluxes than those registered for analogous untreated samples, due to the oxidation of organic matter and breakdown of suspended matter. The integrated process also showed globally higher rejections of organic matter from the feed solutions. A more accentuated flux decline in the initial stages of the process (i.e., after 1 h) was observed when using non-treated samples of OMW, as a consequence of the higher initial organic load. Further improvement to the permeate flux of pre-treated samples was possible by increasing the feed temperature (at a fixed permeate temperature), but no clear correlation could be established for the resulting permeate quality. In any case, the produced permeate water stream showed several parameters that comply with legislated values for discharge into water bodies, including TSS, TPh, BOD_5, and dissolved Fe, while COD values were always slightly higher than the threshold defined by legislation despite the high removal efficiencies obtained (>89%). The produced DCMD-retentates were also successfully treated by the same CWPO process employed earlier (i.e., FBR-DCMD-FBR), with maximum removal percentages of 42.7% for COD, 83.9% for TPh, and 33.2% for TOC..

REFERENCES

1. Neyens, E.; Baeyens, J. A review of classic Fenton's peroxidation as an advanced oxidation technique. *J. Hazard. Mater*. **2003**, 98, 33–50.
2. Navalon, S.; Alvaro, M.; Garcia, H. Heterogeneous Fenton catalysts based on clays, silicas and zeolites. *Appl. Catal. B Environ*. **2010**, 99, 1–26.
3. Esteves, B.M.; Morales-Torres, S.; Maldonado-Hódar, F.J.; Madeira, L.M. Integration of olive stones in the production of Fe/AC-catalysts for the CWPO treatment of synthetic and real olive mill wastewater. *Chem. Eng. J*. **2021**, 411, 128451.
4. Esteves, B.M.; Morales-Torres, S.; Maldonado-Hódar, F.J.; Madeira, L.M. Fitting biochars and activated carbons from residues of the olive oil industry as supports of Fe-catalysts for the heterogeneous Fenton-like treatment of simulated olive mill wastewater. *Nanomaterials* **2020**, 10, 876.
5. Esteves, B.M.; Morales-Torres, S.; Maldonado-Hódar, F.J.; Madeira, L.M. Sustainable iron-olive stone-based catalysts for Fenton-like olive mill wastewater treatment: development and performance assessment in continuous fixed-bed reactor operation. *Chem. Eng. J*. **2022**, 134809.
6. Khayet, M. Membranes and theoretical modeling of membrane distillation: A review. *Adv. Colloid Interface Sci.* **2011**, 164, 56–88.
7. Silva, T.L.S.; Morales-Torres, S.; Esteves, C.M.P.; Ribeiro, A.R.; Nunes, O.C.; Figueiredo, J.L.; Silva, A.M.T. Desalination and removal of organic micropollutants and microorganisms by membrane distillation. *Desalination* **2018**, 437, 121–132.
8. El-Bourawi, M.S.; Ding, Z.; Ma, R.; Khayet, M. A framework for better understanding membrane distillation separation process. *J. Memb. Sci.* **2006**, 285, 4–29.
9. Pangarkar, B.L.; Sane, M.G.; Guddad, M. Reverse Osmosis and Membrane Distillation for Desalination of Groundwater: A Review. *Mater. Sci.* **2011**, 2011, 1–9.
10. Aime Mudimu, O.; Peters, M.; Brauner, F.; Braun, G. Overview of membrane processes for the recovery of polyphenols from olive mill wastewater. *Am. J. Environ. Sci.* **2012**, 8, 195–201.
11. Vinoth Kumar, R.; Barbosa, M.O.; Ribeiro, A.R.; Morales-Torres, S.; Pereira, M.F.R.; Silva, A.M.T. Advanced oxidation technologies combined with direct contact membrane distillation for treatment of secondary municipal wastewater. *Process Saf. Environ. Prot.* **2020**, 140, 111–123.
12. Zare, S.; Kargari, A. Membrane properties in membrane distillation; Elsevier Inc., **2018**; ISBN 9780128167120.
13. Eykens, L.; De Sitter, K.; Dotremont, C.; Pinoy, L.; Van Der Bruggen, B. How to Optimize the Membrane Properties for Membrane Distillation: A Review. *Ind. Eng. Chem. Res.* **2016**, 55, 9333–9343.
14. Martins, R.C.; Gomes, T.; Quinta-Ferreira, R.M. Fenton's depuration of weathered olive mill wastewaters over a Fe-Ce-O solid catalyst. *Ind. Eng. Chem. Res*. **2010**, 49, 9043–9051.
15. Morales-Torres, S.; Silva, T.L.S.; Pastrana-Martínez, L.M.; Brandão, A.T.S.C.; Figueiredo, J.L.; Silva, A.M.T. Modification of the surface chemistry of single- and multi-walled carbon nanotubes by HNO_3 and H_2SO_4 hydrothermal oxidation for application in direct contact membrane distillation. *Phys. Chem. Chem. Phys.* **2014**, 16, 12237–12250.
16. Zhang, J.; Dow, N.; Duke, M.; Ostarcevic, E.; Li, J. De; Gray, S. Identification of material and physical features of membrane distillation membranes for high performance desalination. *J. Memb. Sci.* **2010**, 349, 295–303.
17. Kiai, H.; García-Payo, M.C.; Hafidi, A.; Khayet, M. Application of membrane distillation technology in the treatment of table olive wastewaters for phenolic compounds concentration and high quality water production*. Chem. Eng. Process. Process Intensif.* **2014**, 86, 153–161.
18. Farinelli, G.; Coha, M.; Minella, M.; Fabbri, D.; Pazzi, M.; Vione, D.; Tiraferri, A. Evaluation of Fenton and modified Fenton oxidation coupled with membrane distillation for produced water treatment: Benefits, challenges, and effluent toxicity. *Sci. Total Environ.* **2021**, 796, 148953.
19. Nghiem, L.D.; Cath, T. A scaling mitigation approach during direct contact membrane distillation. *Sep. Purif. Technol.* **2011**, 80, 315-322.
20. El-Abbassi, A.; Hafidi, A.; Khayet, M.; García-Payo, M.C. Integrated direct contact membrane distillation for olive mill wastewater treatment. *Desalination* **2013**, 323, 31–38.
21. El-Abbassi, A.; Kiai, H.; Hafidi, A.; García-Payo, M.C.; Khayet, M. Treatment of olive mill wastewater by membrane distillation using polytetrafluoroethylene membranes. *Sep. Purif. Technol.* **2012**, 98, 55–61.
22. Dermeche, S.; Nadour, M.; Larroche, C.; Moulti-Mati, F.; Michaud, P. Olive mill wastes: Biochemical characterizations and valorization strategies. *Process Biochem.* **2013**, 48, 1532–1552.

23. Zbakh, H.; El Abbassi, A. Potential use of olive mill wastewater in the preparation of functional beverages: A review. *J. Funct. Foods* **2012**, 4, 53-65.
24. Garcia-Castello, E.; Cassano, A.; Criscuoli, A.; Conidi, C.; Drioli, E. Recovery and concentration of polyphenols from olive mill wastewaters by integrated membrane system. *Water Res.* **2010**, 44, 3883-3892.
25. Silva, T.L.S.; Morales-Torres, S.; Figueiredo, J.L.; Silva, A.M.T. Multi-walled carbon nanotube/PVDF blended membranes with sponge-and finger-like pores for direct contact membrane distillation. *Desalination* **2014**, 357, 233-245.

PART V

CONCLUSIONS

CHAPTER 11

CONCLUSIONS AND FUTURE WORK

This chapter presents a summary of the main conclusions from the work developed during this PhD thesis, the limitations encountered, and recommendations for future work.

11.1. CONCLUSIONS

The present work demonstrates the possibility to develop carbonaceous materials from organic by products of the olive oil industry, suited to be used as adsorbents or supports for the synthesis of Fe-catalysts for OMW treatment by adsorption or heterogeneous Fenton-like oxidation processes. This approach could constitute an environmentally-friendly strategy for the management of two types of residues (solid and liquid) within this sector. Furthermore, in line with the circular economy model, a membrane distillation unit was integrated downstream to recover water that could be potentially used within the same agro-industry for activities related to crops irrigation or machinery washing, among others.

Aiming at better understanding the possibilities and limitations of this advanced oxidation technology for OMW depuration, the homogeneous Fenton process was first evaluated. The reduction of organic matter content (assessed in terms of lumped parameters as COD, TOC, BOD_5, etc.) and oxidation of the phenolic content (TPh) of OMW were studied in discontinuous (batch) and continuous (CSTR) reactors. A thorough parametric study, performed in batch mode with a synthetic solution replicating the phenolic fraction of an actual OMW, revealed that the oxidant (H_2O_2) and catalyst (Fe^{2+}) doses are closely related and have the biggest influence on the process efficiency. The increase of reaction medium's temperature also plays a key role in the mineralization achieved. Based on the parametric study, the process performance in a CSTR was also evaluated, showing high performance towards TPh removal (>98%) in steady-state conditions.

Despite the promising results obtained with a synthetic solution, the more complex matrix of real effluents could hinder the oxidative process efficiency, so further experiments were performed with an actual highly-loaded OMW from a Portuguese manufacturer (COD_0 = 24.4 g/L, TOC_0 = 8.5 g/L, and TPh_0 = 1.31 g GA_{eq}/L). Both Fenton (Fe^{2+}/H_2O_2) and Fenton-like (Fe^{3+}/H_2O_2) processes were studied, and the experimental results showed that slightly higher TOC removals are obtained with the Fe^{3+}/H_2O_2 system, but the mineralization rate is higher for the Fe^{2+}/H_2O_2 one in the earlier stages of the reaction. For the Fenton-like system, it was found that H_2O_2 consumption and consequently mineralization rates are significantly affected by the reagents addition method (gradual addition of oxidant *vs*. single addition or gradual and simultaneous addition of oxidant and Fe^{3+}), especially in earlier stages of the reaction, although the overall extent of TOC removal is not. Operating at pH_0 = 3.0, T_0 = 25 °C, $[Fe^{3+}]$ = 1.0 g/L and an Fe/H_2O_2

mass ratio of 0.04, *ca*. 35% of TOC, 56% of COD, and 81% of TPh were removed after 3 h operation in a batch reactor. Moreover, the selected catalyst (ferric chloride) also acts as a coagulant/flocculant agent; after the oxidation process, 1 h of sedimentation allowed global reductions of *ca*. 77% for COD and 96% for TPh, and thus similar efficiencies than the ones obtained with the synthetic solution were reached, albeit the considerably higher initial load of the real OMW. A correlation between TPh removals and reduction of OMW's toxicity (assessed by the *V. fischeri* inhibition) was also established. Nonetheless, discharge limits for industrial wastewaters were not met and a downstream unit is required for iron recovery, as the dissolved Fe concentration in solution significantly exceeds the legal threshold for discharge (2 mg/L), even after chemical precipitation.

To tackle this constraint of homogeneous processes, the catalytically-active metal phase was "immobilized" in a solid matrix prepared from solid by-products of the industry – olive stones (OS) and olive tree pruning (OTP). Several carbon-based materials – biochars and activated carbons (AC) – were prepared by varying the synthesis conditions of the precursors (physical activation with CO_2, or chemical activation with KOH). The materials were then used as adsorbents or Fe-containing catalysts, for which the Fe impregnation procedure and the active metallic phase (Fe salt and load) were also optimized. Moreover, tests with commercially-available AC materials were performed for comparison purposes.

The physicochemical properties of the resulting materials were dependent upon the organic by-product precursor and the conditions of synthesis. Experimental studies performed with specific phenolic compounds highlighted the increase in the materials' adsorption capacities with the volume of micropores (particularly the larger ones) and specific surface area, while mesoporosity reduces the influence of the phenolic compounds' restrictions in the external film diffusion of the AC particle–solution interphase. AC-derived materials prepared from OTP presented a more open structure and oxygenated surface groups, but less developed micropores and surface area than OSAC materials, while biochars prepared from both precursors presented closed or inaccessible micropores.

The impregnation of Fe-nanoparticles inevitably resulted in the blockage/occupation of porosity (particularly in the microporosity range), also leading to a shift in the materials' surface basic character. The resulting catalytically-active phase generally contained a mixture of Fe^{3+}/Fe^{2+} (in different proportions depending upon the synthesis conditions), with the preferential formation of

α-Fe_2O_3 and Fe_3O4 crystalline nanoparticles with various sizes and shapes according to the sample morphology and Fe-impregnation procedure adopted.

Screening experiments showed that the more developed porosity and morphology of the Fe/AC catalysts (prepared from organic residues) by comparison to the analogous Fe/biochars resulted in greater oxidation of phenolic compounds. Still, catalysts prepared from commercial ACs led to better removal efficiencies of TOC and TPh, but a superior loss of stability (Fe-leaching) was observed. Based on several parameters (including the ratio of H_2O_2 consumed/TOC removal, Fe-leaching, and TPh removal), the catalyst prepared onto physically-activated samples of olive stones (OSAC-Fe) was selected as the most promising material and used in further tests.

Upon selecting the best support, changes to the Fe impregnation procedure adopted resulted in OSAC-Fe catalysts with heterogeneity in surface properties such as the resulting Fe-loading and metallic nanoparticles' size and surface distribution. Based on the adsorptive/catalytic activity and stability towards the removal of phenolic compounds in consecutive cycles, the observed kinetic constants and removal rates (calculated to discard the effect of the distinct Fe-loading between samples), the catalyst prepared by the incipient wetness impregnation (IWI) route was found to be the most promising material. Under smooth operational conditions ([Cat] = 2.0 g/L, $[H_2O_2]$ = 0.5 g/L, $pH_0 \approx 4.9$, T_0 = 25 °C, t = 4 h), the OSAC-Fe-IWI catalyst had the best performances towards both synthetic and real OMW depuration (removals of 55% for TPh and 37% for COD, with a great reduction of the OMW toxicity, from initial 100% *V. fischeri* inhibition to 37%).

Further screening of the synthesis conditions was performed using the IWI method and OSAC support, by varying now the iron salt precursor ($FeCl_2$ or $Fe(NO_3)_3$) and Fe loading (1–5 wt.%). The catalyst prepared with $Fe(NO_3)_3$ and 5 wt.% Fe was established as the most suitable for the CWPO of several synthetic and real OMW samples under continuous operation conditions in a fixed-bed reactor (FBR). In general, phenolic compounds with more –OH electron-donating groups were found to be more susceptible to degradation, while the reactivity seems to decrease in the presence of methoxy groups. OMW samples with increasing initial organic loads were then tested under previously optimized operational conditions (W_{cat}/Q = 1.33 g min/mL, no pH adjustments, $[H_2O_2]/[COD]$ = 2.3 ±0.1 g H_2O_2/g O_2, and T = 60 °C), resulting in TPh removals ranging from 57 to 71% and 26 to 34% for COD, at steady-state, depending on the initial OMW load. Moreover, by fixing the same operating conditions and increasing the amount of catalyst by 2-fold (i.e., contact time), TPh and COD removals improved to 79–81% and 37–45%, respectively.

Finally, a membrane distillation set-up was installed after the FBR unit. The resulting pre-treated samples of OMW allowed the operation of the membrane unit at higher permeation fluxes than those obtained for the equivalent untreated samples, and the integrated process also showed higher rejections of organic matter from the feed solution. At Q = 100 mL/min, $T_{permeate}$ ≈ 18 °C and T_{feed} ≈ 57 °C (i.e., ΔP ≈ 16.5 kPa), the produced permeate stream presented several parameters below the legislated thresholds required for water for irrigation purposes, although COD values (265 ±9 mg/L) were still slightly higher than those defined by legislation (i.e., <150 mg/L). Finally, the concentrated OMW retentate stream was also recirculated to the FBR unit keeping removal efficiencies in the same range as those previously attained.

11.2. LIMITATIONS AND FUTURE WORK

The results obtained during this work pointed out the potential of the biochar/activated carbons and Fe-catalysts developed in the adsorptive or catalytic treatments of OMW from an environmental point of view. Nevertheless, the limitations of the processes for OMW management were also simultaneously identified, providing important perspectives to consider in the future that could complement and/or improve the information reported in this thesis.

On such a basis, the economics side of samples' preparation should be considered in further studies. Although important efforts were carried out to select the raw materials, salts, impregnation procedure, etc., alternative procedures including treatments at low temperature (e.g., hydrothermal synthesis of hydrochars) should also be analyzed to save energy during the carbonization step. In the same line, the experimental findings in Chapter 5 show that the ferric chloride used as a Fenton-like catalyst could also act as a coagulant after the oxidation step, originating an iron-rich sludge. This by-product of the homogenous process could constitute a suitable precursor for the preparation of heterogeneous Fe-catalysts. Thus, the pretreatment of OMW by coagulation (without H_2O_2), also providing valuable precursors of heterogeneous Fe-catalysts, can be an interesting and innovative catalysts' preparation route.

As highlighted throughout Part IV, but particularly in Chapters 6 and 7, carbon-based adsorbents/catalyst-precursors can be successfully prepared from organic by-products by different synthesis conditions. The main focus of this work has been to correlate the textural/morphological and chemical properties of the materials with the adsorption/oxidation of specific phenolic compounds or lumped parameters of OMW. Nonetheless, different factors were

not fully explored in the catalysts' synthesis step, including those related to the thermal/chemical pretreatment conditions (e.g., temperature, time, reduction/oxidation conditions) for a more controlled tuning of the catalysts' surface chemistry functionalities (e.g., oxygenated surface groups).

The experimental results show that adsorption (and therefore also oxidation), were dependent upon different types of interactions between the phenolic compounds and the adsorbent/catalyst, namely by the affinity of specific electron-withdrawing groups or by the chelating activity of surface iron oxides towards specific phenolic compounds in a mixture. The mentioned tuning/modeling of surface functionalities should be aimed at improving the affinity towards the least degraded compounds in the synthetic mixtures teste (e.g., protocatechuic acid or tyrosol). Additionally, a more detailed study should be performed to elucidate the extent and nature of those interactions, but also others, for which it is suggested to increase the complexity of the synthetic solution with other classes of organic compounds of OMW (e.g., sugars, tannins, organic acids), that may compete with phenolic acids for adsorptive/catalytic sites. Thus, the optimization of the surface chemistry and the knowledge of the nature and strength of the interactions between the solid and OMW would allow: i) the selective adsorption of phenols from OMW – it is noteworthy that many phenols are valuable compounds, and adsorption, but mainly desorption processes, should be studied to reutilize the spent adsorbents; ii) the role of OSG (and others) in anchoring the Fe-species should also lead to more stable catalysts (less leaching), thus also improving the reusability of the catalysts prepared.

Apart from the high organic load and complex matrix of OMW, the amount of suspended, dissolved, and volatile solids in the effluent (even after sedimentation) poses a major obstacle for the operation of heterogeneous Fenton-based processes in a column reactor configuration. The adequate removal of the fraction of solids upstream of the column reactor is a key factor to avoid clogging issues (*cf*. highlighted in Chapter 9). In that sense, other reactor configurations should be evaluated, namely continuous slurry reactors such as the CSTR configuration reported in Chapter 4 (used for the treatment of a synthetic phenolic solution); still, the pros and cons must be thoroughly evaluated, since a larger reactor volume may be required to obtain the same desired conversion.

In Chapter 10, several parameters of DCMD operation should be further tested to try to obtain a permeate flux that complies with all parameters required for safe discharge, namely in the case of the final COD concentration. For that, future work should be focused on the optimization of

other operational variables such as the recirculation flow rate and membrane nature/characteristics, in addition to aspects related to the recovery of the membrane productivity by regeneration procedures. Moreover, the proposed treatment scheme was operated in a semi-continuous configuration, with the DCMD unit being operated discontinuously; for future work, it is suggested the connection of the FBR-exit stream to the feed-DCMD vial, as well as the retentate of the latter with the inlet current of the FBR reactor (using a peristaltic pump), thus allowing a fully integrated and continuous process operation scheme.

Finally, the proposed strategy should be also evaluated for the treatment of wastewaters and solid residues from other related agro-industries such as this case of the wine production sector, which also has a considerable socio-economic impact in our country and is responsible for the generation of effluents with similar environmental impacts as OMW (e.g., due to the seasonal production, high organic load, and polyphenolic content).

APPENDIX A

SUPPORTING INFORMATION FOR CHAPTER 4

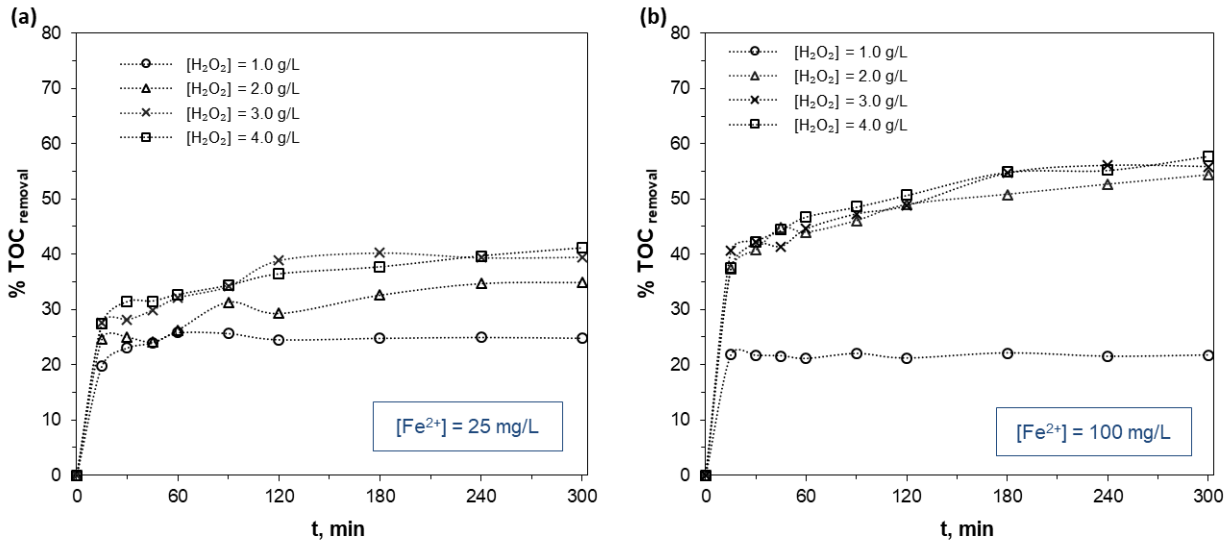


Fig. A.1 Effect of H_2O_2 dose on the TOC removal efficiency (%) along time on the batch runs of the synthetic OMW Fenton's oxidation for $[Fe^{2+}]$ = 25 (a) and (b) 100 mg/L. Experimental conditions: pH_0 = 3.7, T = 30 °C, t = 300 min.

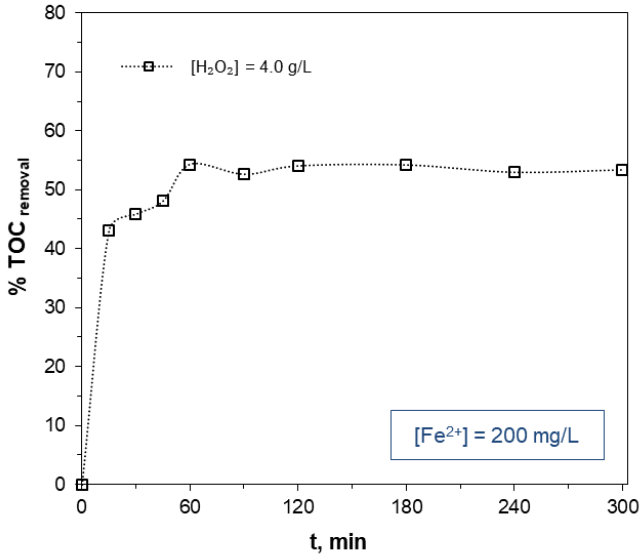


Fig. A.2 Effect of H_2O_2 dose on the TOC removal efficiency (%) along time on the batch runs of the synthetic OMW Fenton's oxidation. Experimental conditions: $[Fe^{2+}]$ = 200 mg/L, pH_0 = 3.7, T = 30 °C, t = 300 min.

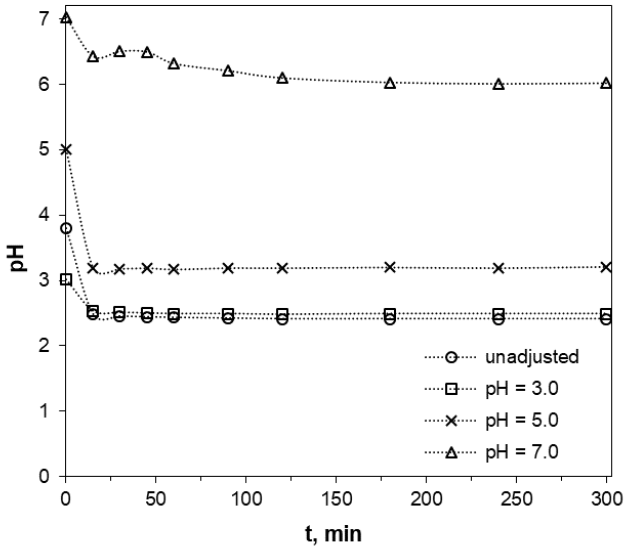


Fig. A.3 Evolution of pH values for the batch runs of the synthetic OMW Fenton's oxidation. Experimental conditions: $[Fe^{2+}]$ = 200 mg/L, $[H_2O_2]$ = 2.0 g/L, pH_0 = 3.7, T = 30 °C, t = 300 min.

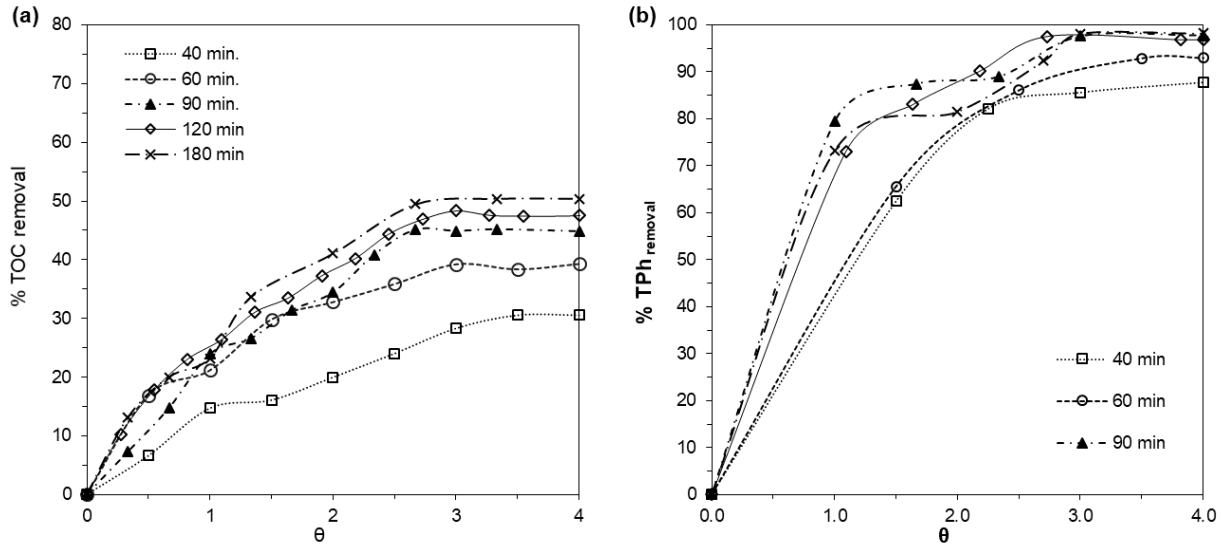


Fig. A.4 Effect of space-time (τ, min) on (a) TOC and (b) TPh removal efficiencies, in transient regimen, for the CSTR runs. Experimental conditions: $[H_2O_2]_{feed}$ = 2.0 g/L, $[Fe^{2+}]_{feed}$ = 100 mg/L, pH_0 = 5.0, T = 30 °C.

Table A.1 Relative percentage of phenolic compounds in relation to the total phenolic content (wt.%) of different untreated OMW, according to literature survey.

Vanillic Acid	Caffeic Acid	Tyrosol	*p*–Coumaric Acid	Gallic Acid	3,4-Dihydroxyphenylacetic acid	Ref.
-	9.6%	25.3%	8.9%	-	2.6%	[15]
7.3%	7.2%	44.1%	-	0.7%	5.9%	[16]
9.0%	7.4%	29.1%	-	9.0%	3.9%	[16]
-	1.6%	5.5%	15.2%	9.7%	-	[17]
9.3%	-	-	22.5%	-	-	[18]

- compound not detected

Table A.2 Outlet H_2O_2 concentration (g/L) at steady-state for different H_2O_2 feed doses to the CSTR. Experimental conditions: $[Fe^{2+}]_{feed}$ = 100 mg/L, pH_0 = 5.0, T = 30 °C, τ = 90 min.

$[H_2O_2]_{feed}$, (g/L)	$[H_2O_2]_{outlet}$ (g/L)	% H_2O_2 unreacted
2.0	0.12	6.2
3.0	0.45	14.9
4.0	1.01	25.2

APPENDIX B

SUPPORTING INFORMATION FOR CHAPTER 7

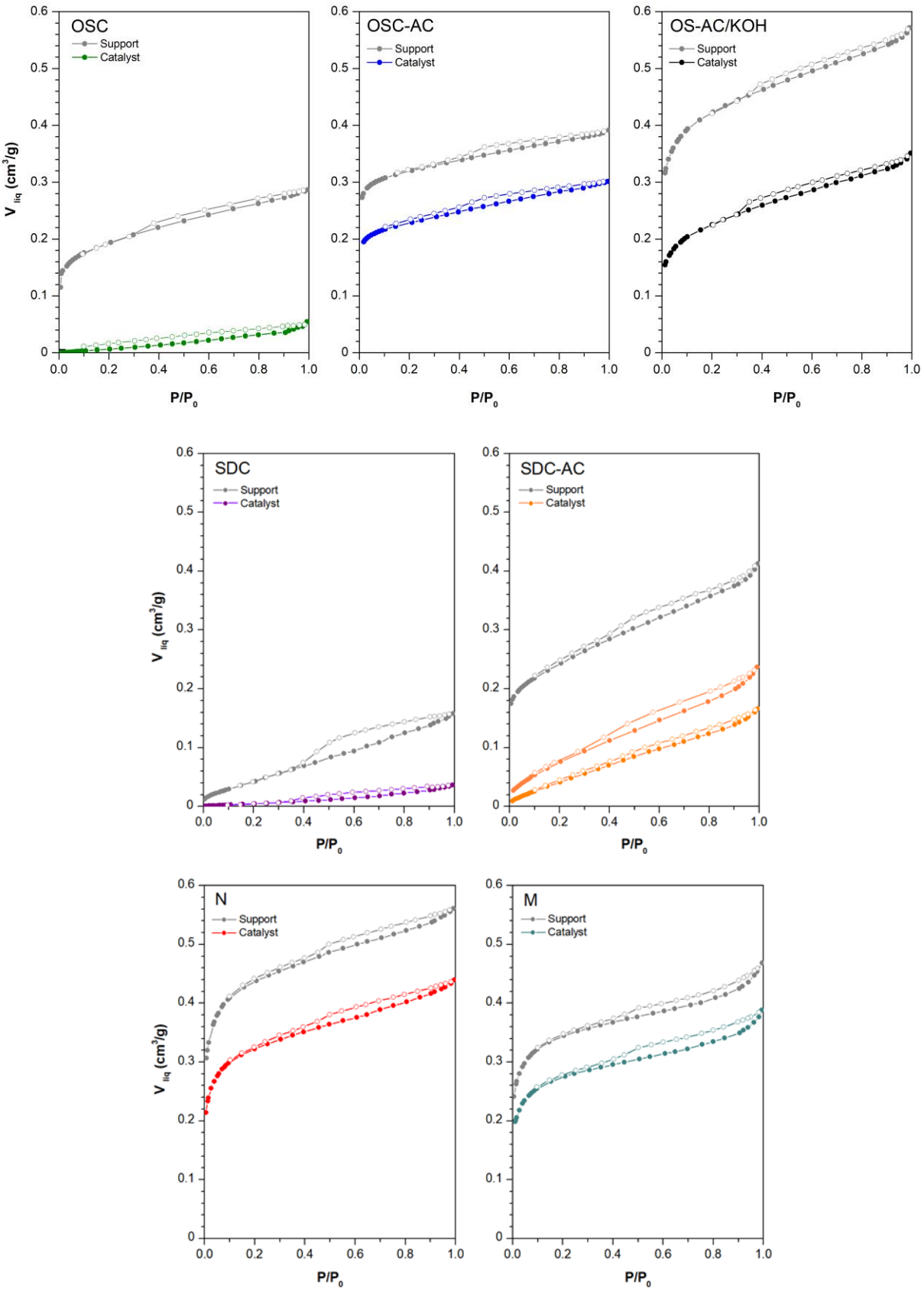


Fig. B.1 N_2 adsorption/desorption isotherms for the supports and corresponding Fe-catalysts tested.

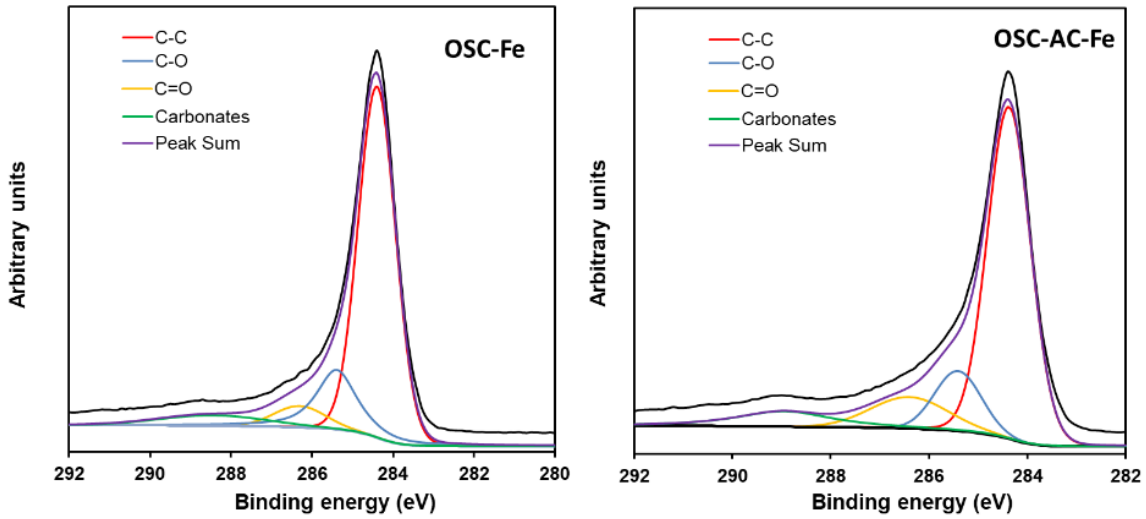


Fig. B.2 C1s spectral region of OSC-Fe and OSC-AC-Fe catalysts.

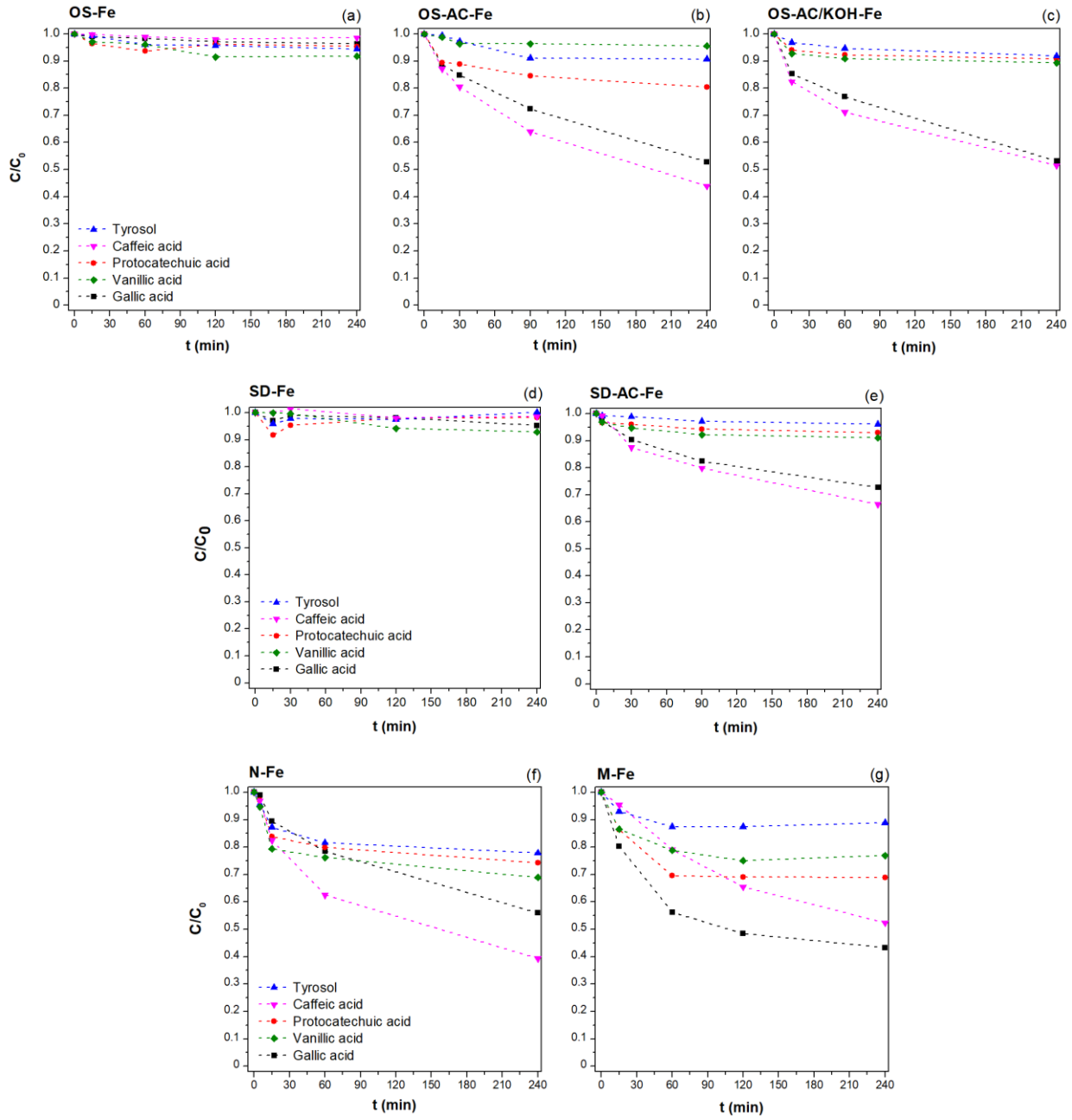


Fig. B.3 Adsorption runs using the catalysts prepared: removal of each phenolic compound (C/C_0) over time. Experimental conditions: [Cat] = 0.5 g/L, T = 25 °C, pH = unadjusted.

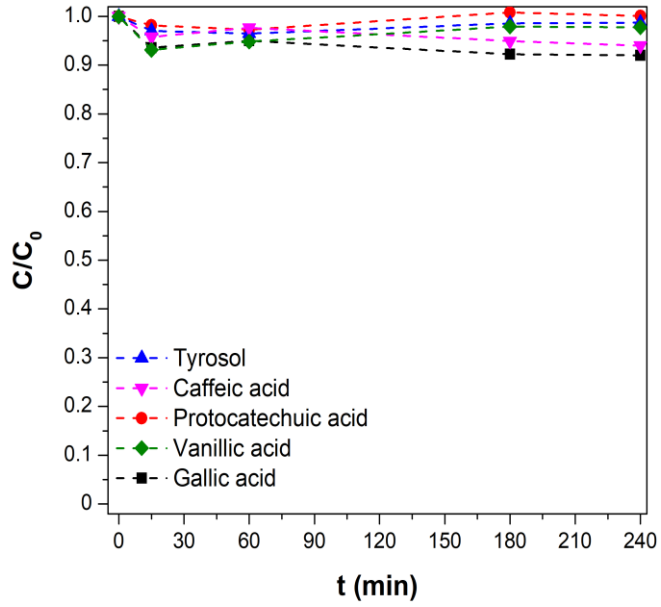


Fig. B.4 Catalytic effect of H_2O_2 on the removal of phenolic compounds (C/C_0) over time. Experimental conditions: [H_2O_2] = 1 g/L, T = 25 °C, pH = unadjusted.

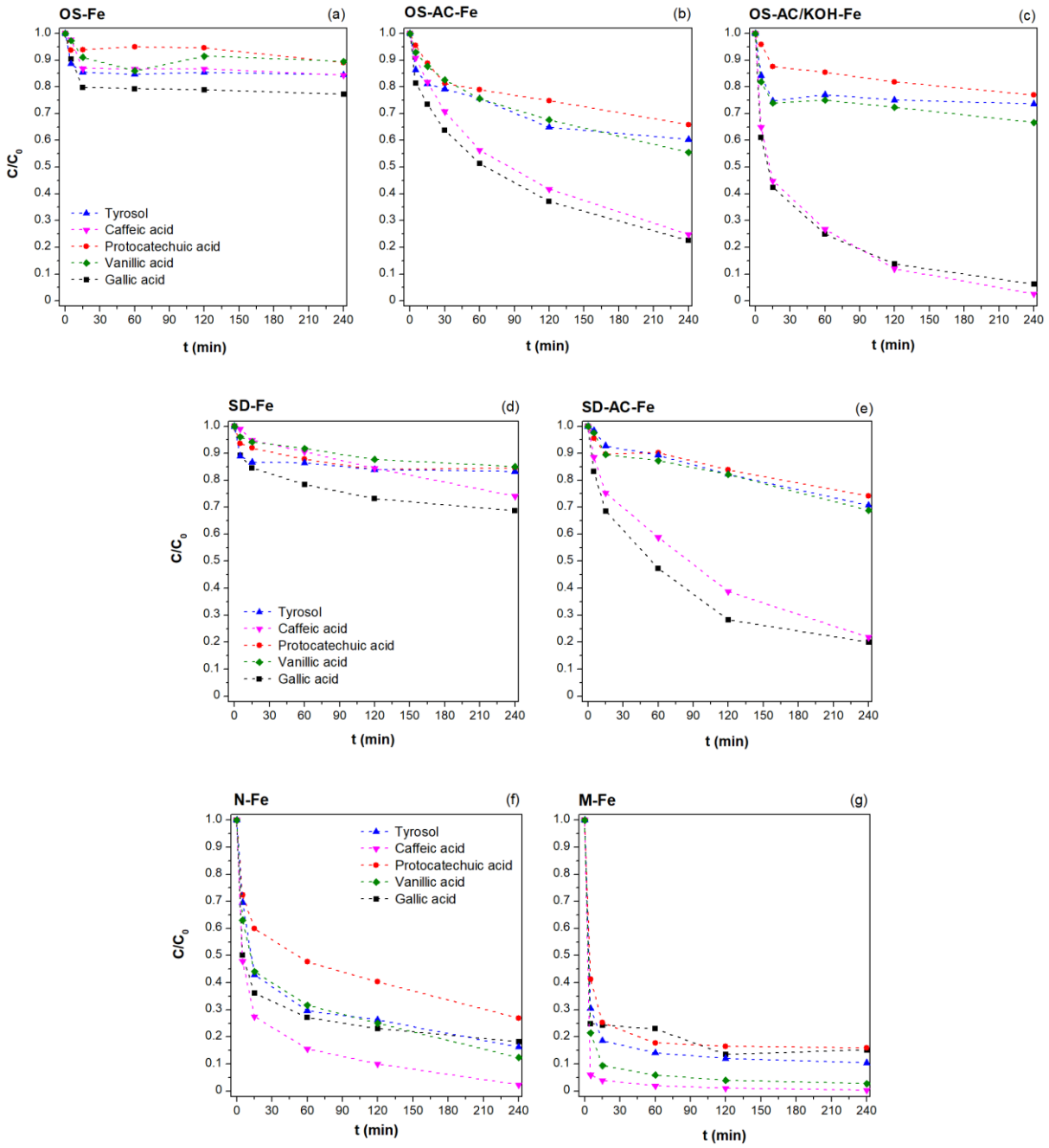
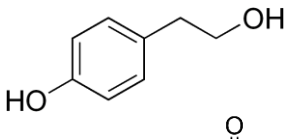
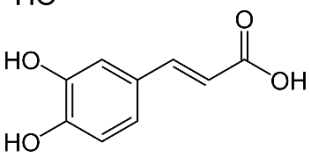
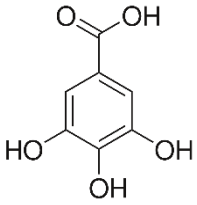
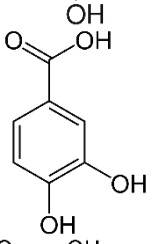
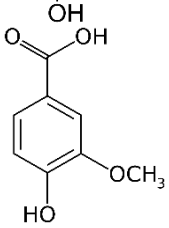


Fig. B.5 Catalytic runs using the Fe/AC catalysts prepared: removal of phenolic compounds (C/C_0) over time. Experimental conditions: [H_2O_2] = 1 g/L, [Cat] = 0.5 g/L, T = 25 °C, pH = unadjusted.

Table B.1 Chemical characteristics of the selected phenolic compounds.

Name	Chemical structure	Molecular formula	Molecular weight (g/mol)	pKa (at 25 °C)	Solubility in water (g/L)
Tyrosol		$C_8H_{10}O_2$	138.16	10.20	25.3
Caffeic acid		$C_9H_8O_4$	180.16	4.62	1.0
Gallic acid		$C_7H_6O_5$	170.12	4.40	11.5
Protocatechuic acid		$C_7H_6O_4$	154.12	4.48	18.2
Vanillic acid		$C_8H_8O_4$	168.14	4.16	1.5

APPENDIX C

SUPPORTING INFORMATION FOR CHAPTER 8

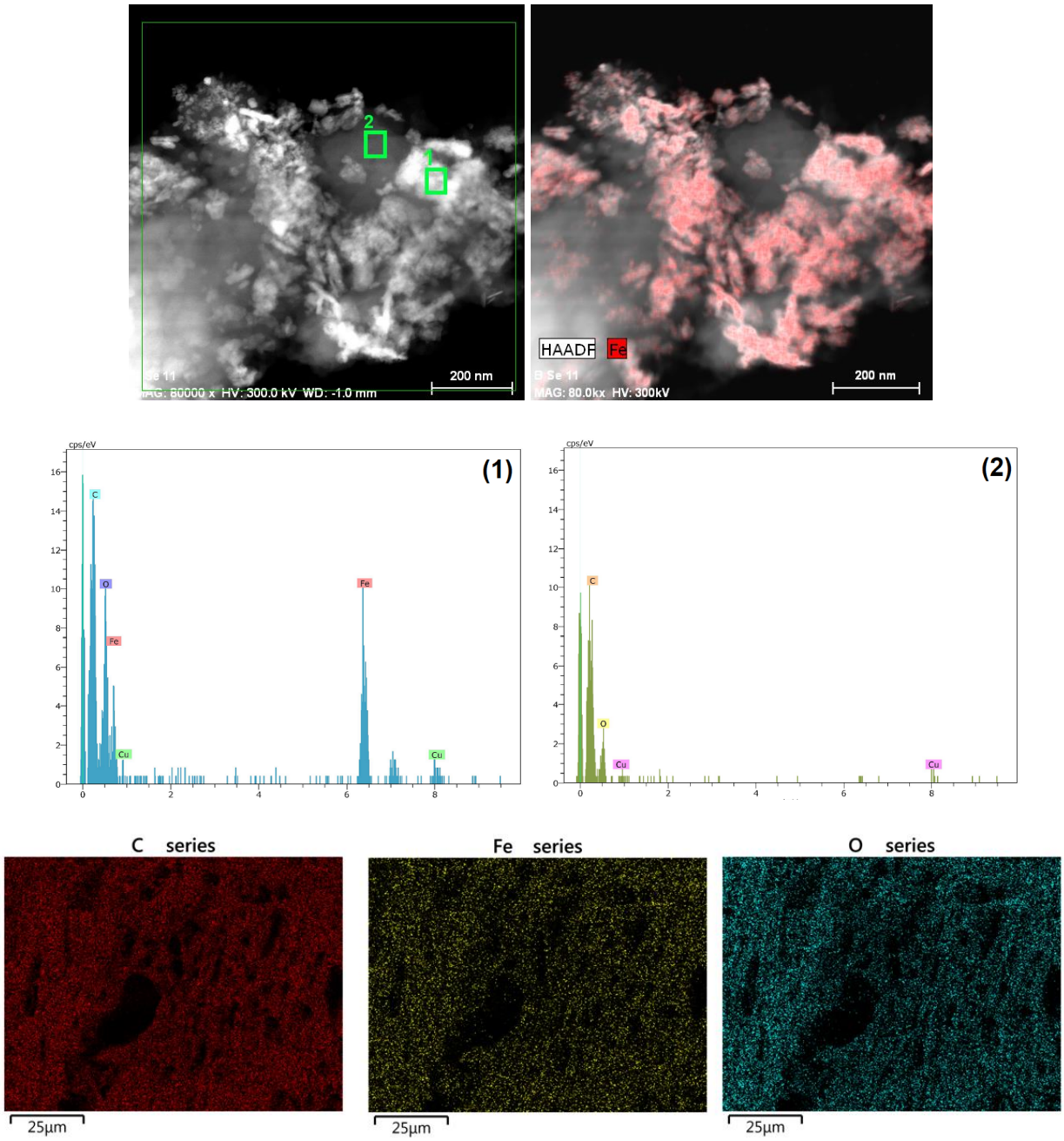


Fig. C.1 EDX microanalysis of the OSAC-Fe-IWI catalyst surface with the mapping of elements C, Fe, and O in the sample. (1) Fe-particles and (2) carbon support.

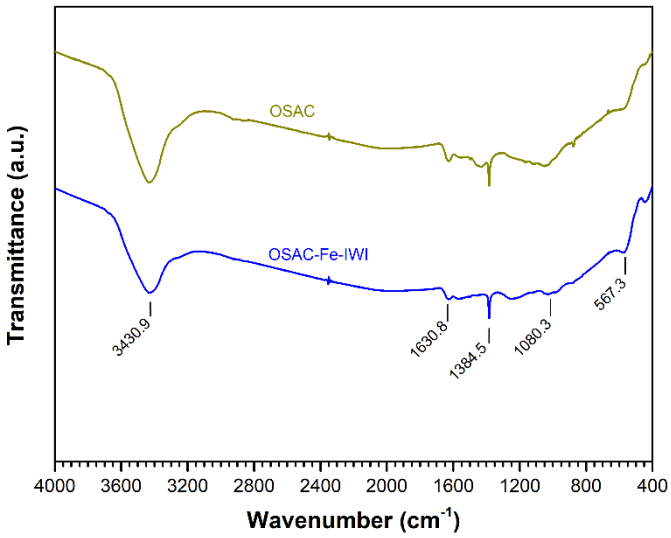


Fig. C.2 FTIR spectra of OSAC support and derived OSAC-Fe-IWI catalyst.

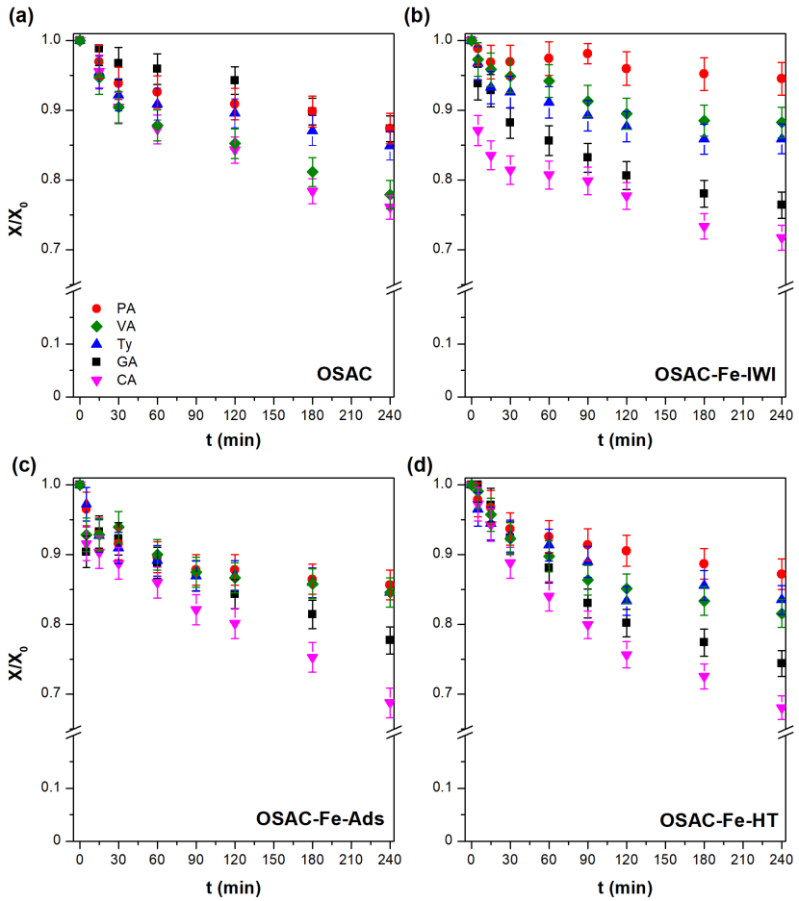


Fig. C.3 Adsorption of phenolic compounds over time (normalized concentrations) by: (a) OSAC, (b) OSAC-Fe-IWI, (c) OSAC-Fe-Ads, and (d) OSAC-Fe-HT (PA – Protocatechuic acid; VA – Vanillic acid; Ty – Tyrosol; GA – Gallic acid; CA – Caffeic acid). [Cat] = 0.5 g/L, T_0 = 25 ºC, and pH_0 = 3.5.

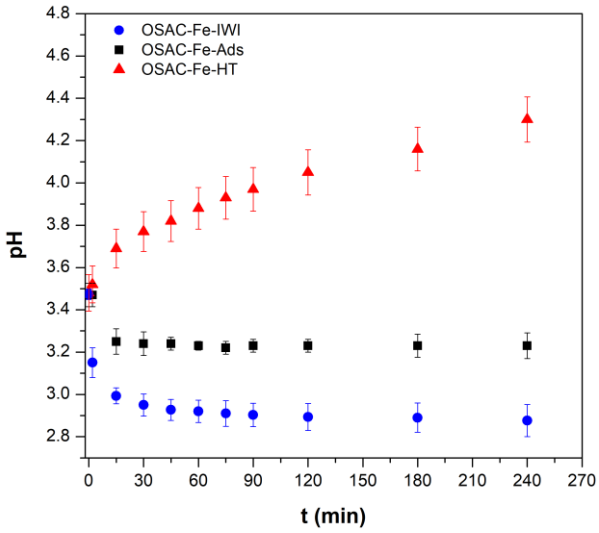


Fig. C.4 pH variation over time for the CWPO runs. [Cat] = 0.5 g/L, [H_2O_2] = 1.0 g/L, T0 = 25 ºC, and pH_0 = 3.5.

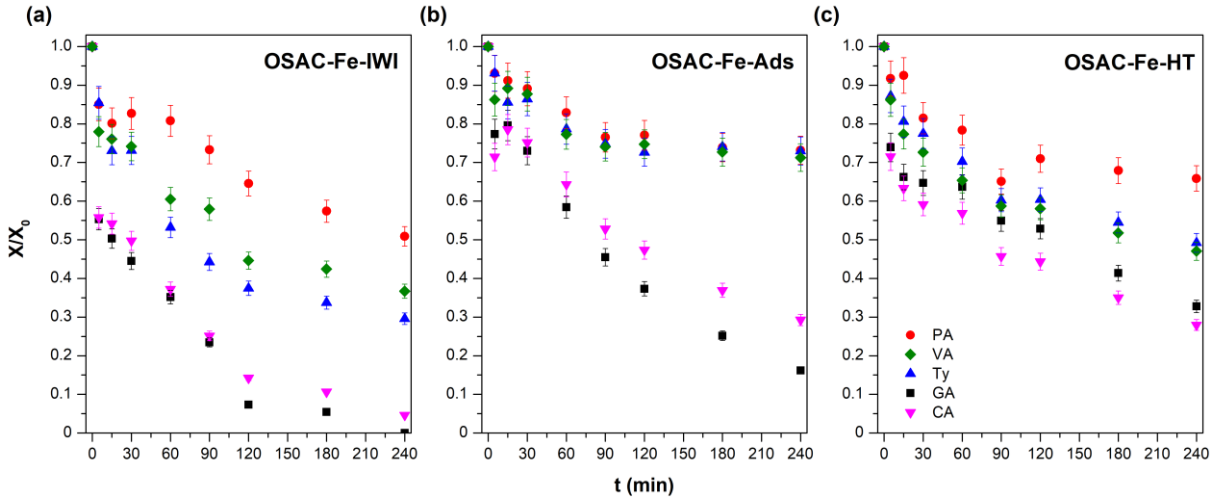


Fig. C.5 Removal of phenolic compounds over time by CWPO (normalized concentrations) using: (a) OSAC-Fe-IWI, (b) OSAC-Fe-Ads, and (c) OSAC-Fe-HT. [Cat] = 1.0 g/L, [H_2O_2] = 1.0 g/L, T_0 = 25 ºC, and pH_0 = 3.5.

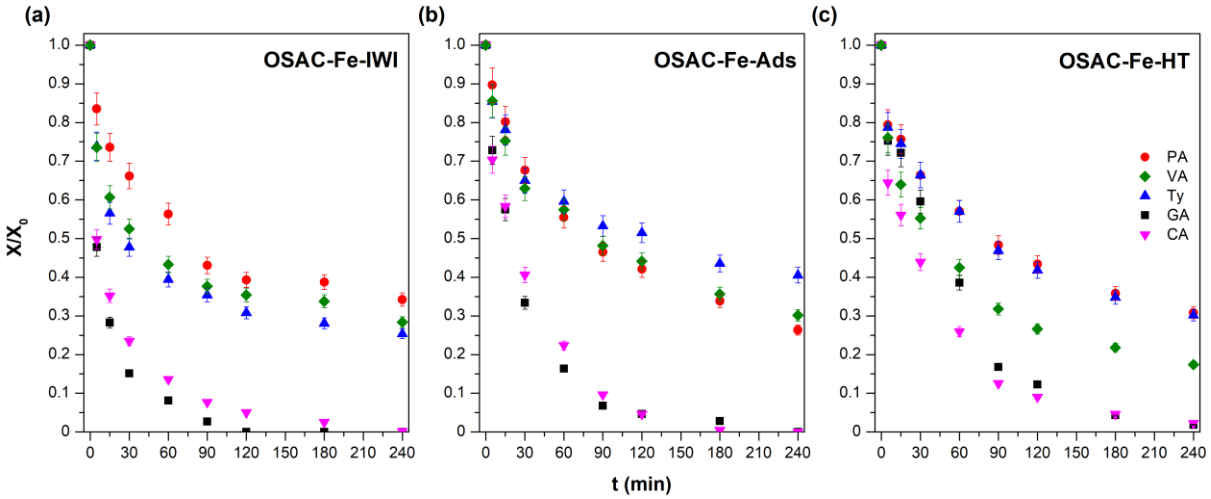


Fig. C.6 Removal of phenolic compounds over time by CWPO (normalized concentrations) using: (a) OSAC-Fe-IWI, (b) OSAC-Fe-Ads, and (c) OSAC-Fe-HT. [Cat] = 2.0 g/L, [H_2O_2] = 1.0 g/L, T_0 = 25 ºC, and pH_0 = 3.5.

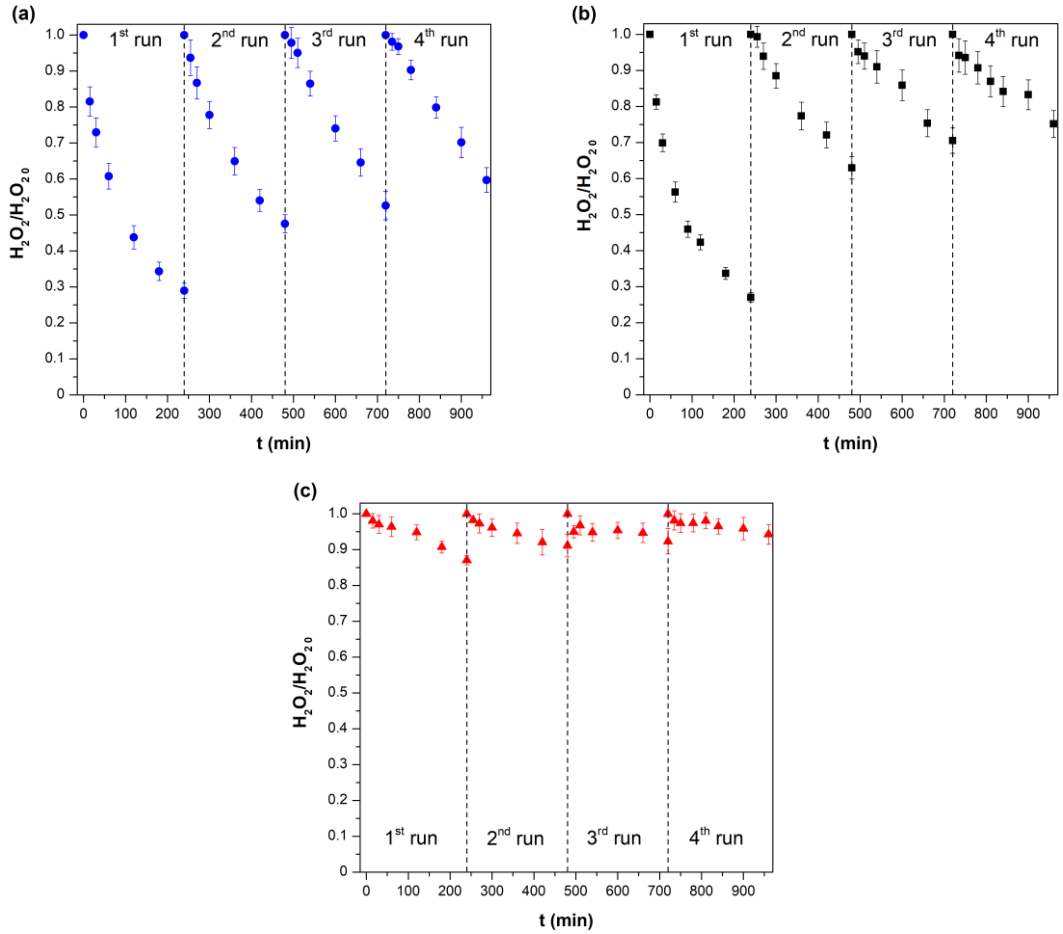


Fig. C.7 Variation in H_2O_2 consumption in consecutive cycles using: (a) OSAC-Fe-IWI, (b) OSAC-Fe-Ads, and (c) OSAC-Fe-HT.

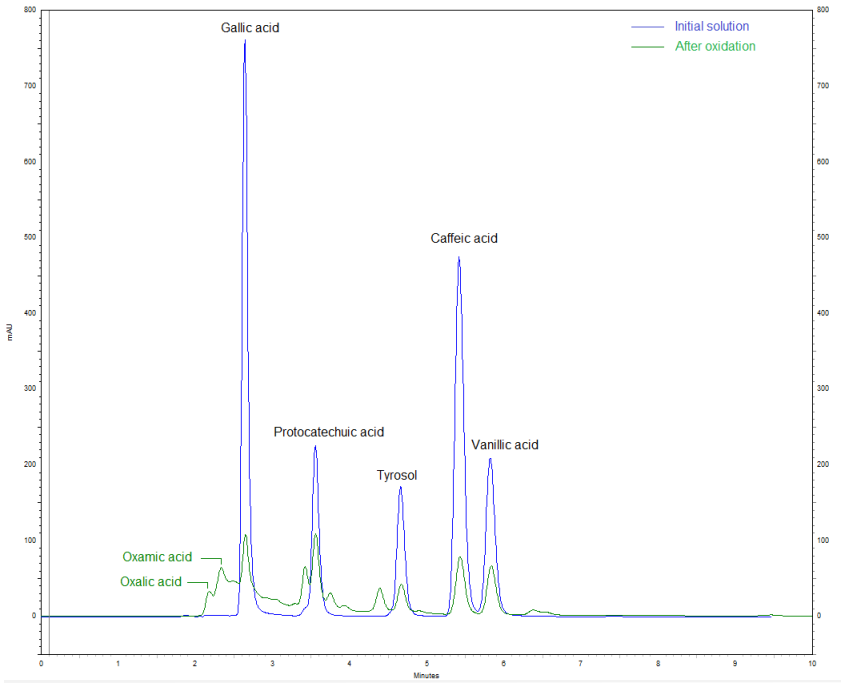


Fig. C.8 HPLC chromatograms of the initial synthetic solution and after 60 min of reaction with OSAC-Fe-IWI ([Cat] = 2.0 g/L, [H_2O_2] = 1.0 g/L, T_0 = 25 ºC, and pH_0 = 3.5).

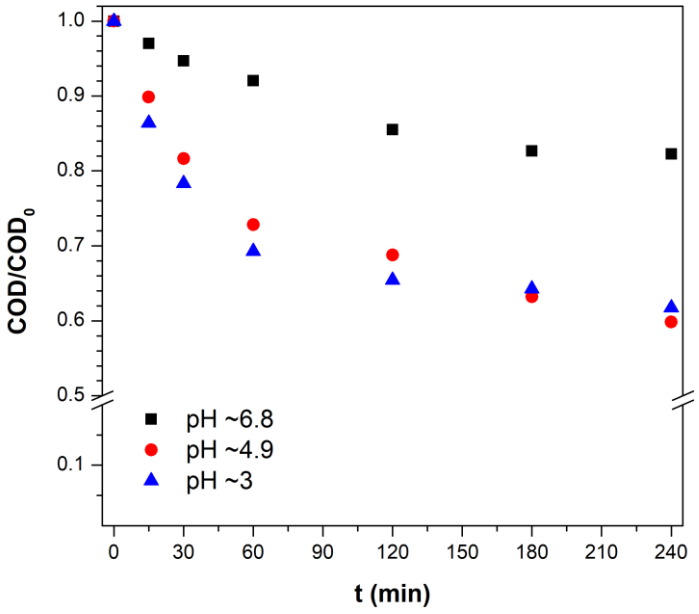


Fig. C.9 COD degradation along time under different initial pH values ([OSAC-Fe-IWI] = 2.0 g/L, [H_2O_2] = 1.0 g/L, and T_0 = 25 ºC).

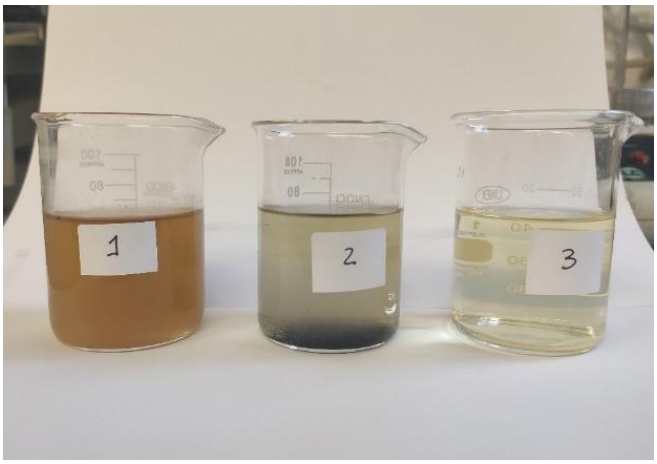


Fig. C.10 (1) Ten-fold diluted OMW, (2) OMW after CWPO (240 min) with OSAC-Fe-IWI deposited, and (3) OMW after CWPO without catalyst.

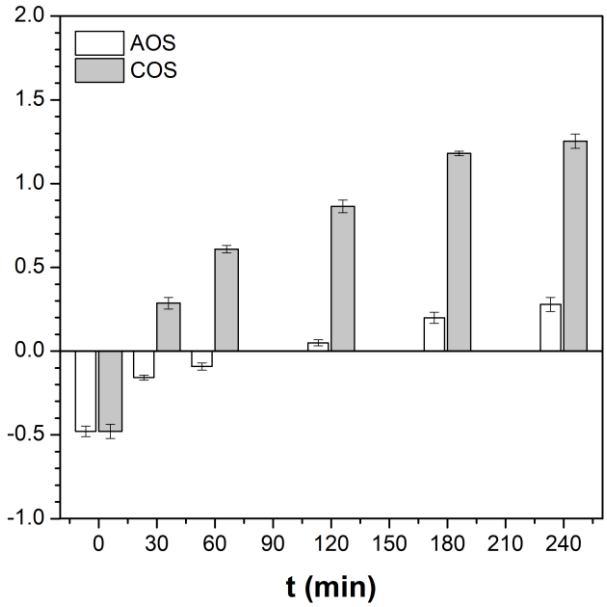


Fig. C.11 AOS and COS indices variation over time during the real OMW treatment by CWPO ((Cat] = 2.0 g/L, $[H_2O_2]$ = 0.50 g/L, $pH_0 \approx 4.9$, T = 25 °C).

Table C.1 Distribution of oxygen and iron species on the catalysts' surface.

Peak (eV)	OSAC-Fe-IWI	OSAC-Fe-Ads	OSAC-Fe-HT
O1s			
Fe–O (530.1)	21	30	17
C=O (531.6)	44	42	45
C–O (533.2)	35	28	38
$Fe2p_{3/2}$			
Fe^{2+} (710.0)	24	24	25
Fe^{3+} (710.9)	40	37	28
Fe^{3+} (712.0)	22	21	20
Fe^{3+} (713.1)	10	13	14
Fe^{3+} (714.2)	4	5	13

Table C.2 TOC removal efficiencies (%) for the consecutive catalytic cycles (after 240 min).

Run	OSAC-Fe-IWI	OSAC-Fe-Ads	OSAC-Fe-HT
1^{st}	46.7	52.8	53.0
2^{nd}	36.4	39.9	20.2
3^{rd}	28.0	31.7	14.7
4^{th}	24.6	26.3	13.5

APPENDIX D

SUPPORTING INFORMATION FOR CHAPTER 9

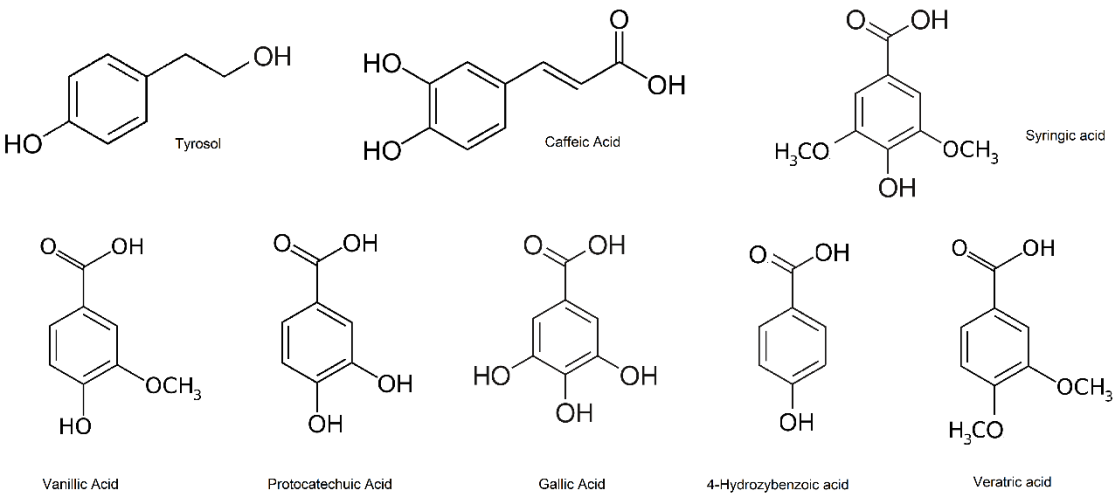


Fig. D.1 Chemical structures of the phenolic acids selected as model compounds.

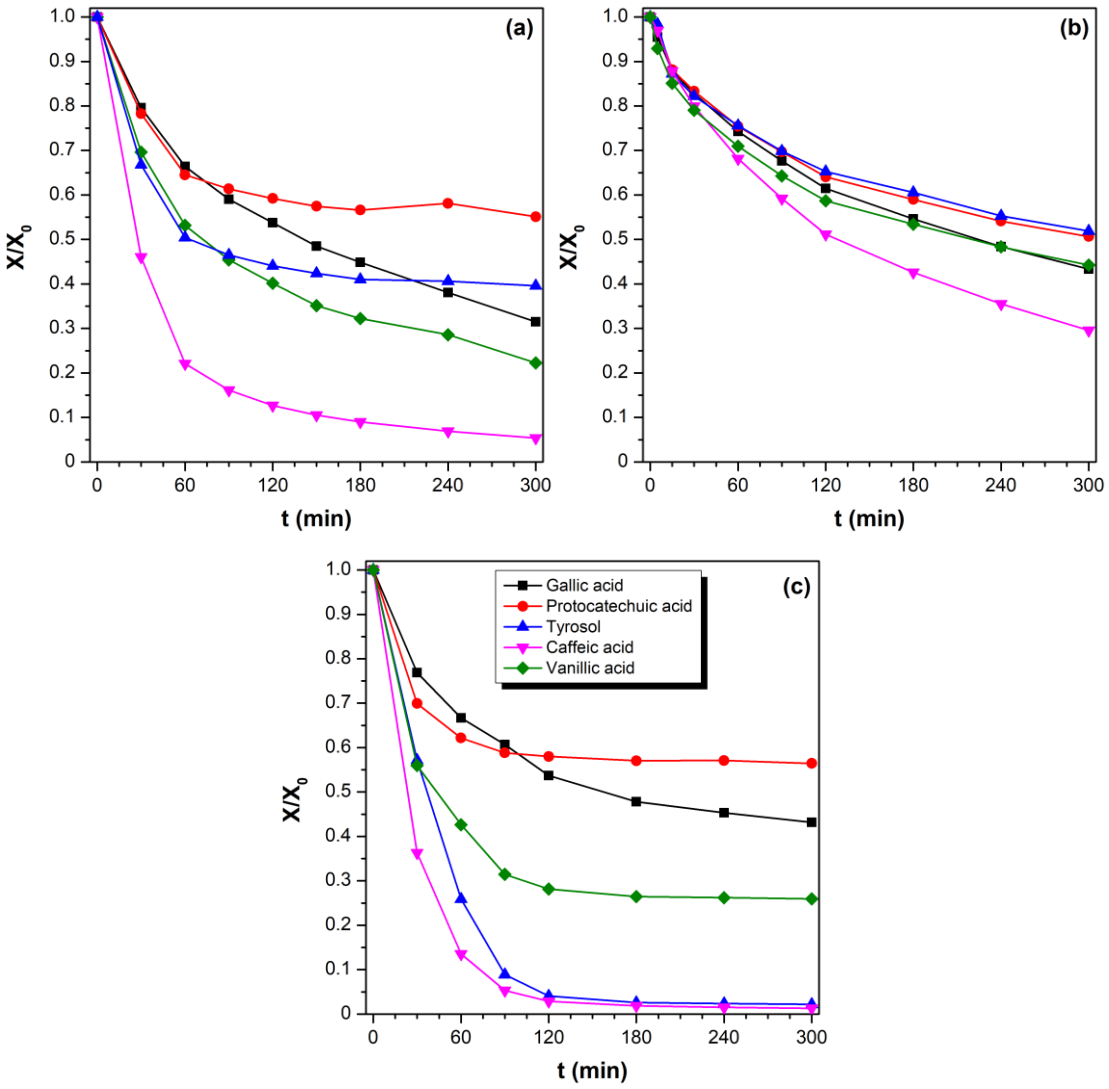


Fig. D.2 Adsorption profiles of each phenolic compound over time obtained by HPLC using (a) OSAC-Fe$(NO_3)_3$, (b) OSAC-$FeCl_2$, and (c) OSAC support. [Cat] = 2.0 g/L, pH_0 = 3.5, 20 °C.

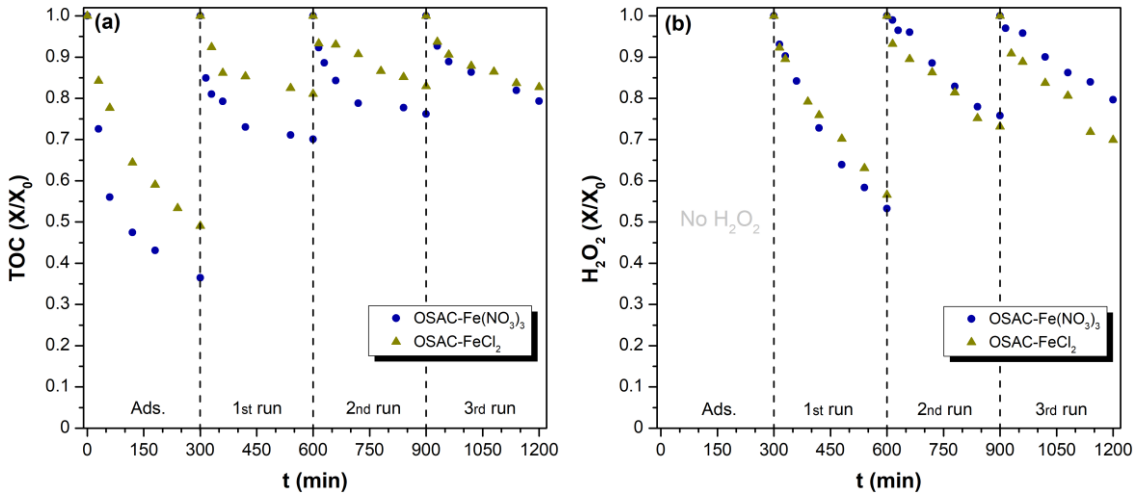


Fig. D.3 (a) Total organic carbon (TOC) removal and (b) H_2O_2 conversion along time in consecutive 300-min cycles using OSAC-Fe$(NO_3)_3$ and OSAC-$FeCl_2$ catalysts (2 wt% Fe). [Cat] = 2.0 g/L, [H_2O_2] = 1.0 g/L, pH_0 = 3.5, 20 °C.

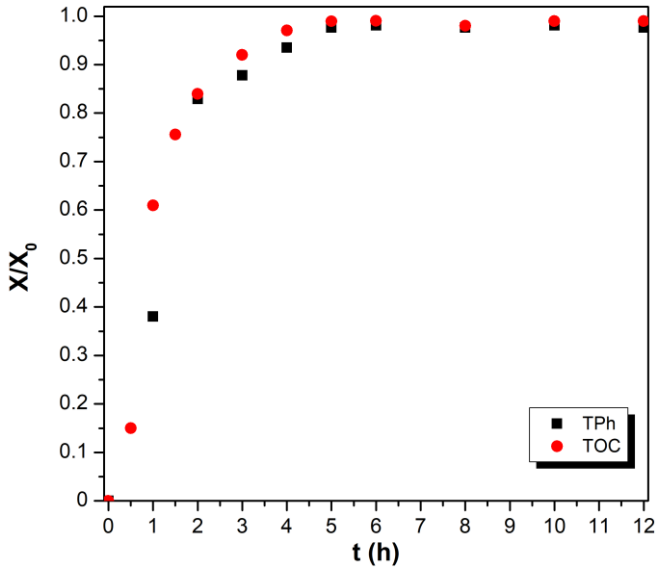


Fig. D.4 TPh and TOC profile at the fixed-bed reactor's outlet in a non-catalytic run. Q = 0.75 mL/min, pH_0 = 3.5, 20 °C.

Evaluation of the Fe-dissolved contribution to the CWPO – Fig. D.5

To estimate the effect of iron leached from the support (9.3 wt.% after 48 h of reaction) in the overall TPh removals achieved by the CWPO process, an additional run was performed according to the following:

- The leaching of iron from the catalytic bed was estimated based on the assumption of constant and linear deactivation rate during the entire operating time;
- Assuming a constant flow rate under the conditions depicted in Fig. 9.8, the residence time was experimentally estimated to be 7.6 min;
- The catalytic bed was replaced by inert glass spheres;
- To avoid the generation of the radicals inside the feed vial, two streams were fed to the reactor: (a) a mixture of the synthetic OMW solution and Fe (using $Fe(NO_3)_3$ $9H_2O$ as iron salt), and (b) a stream of distilled water with H_2O_2;
- To account for the dilution effect occurring at the stream's junction, both reagents and OMW solution concentrations were increased by 2-fold (once the flow rates of the two streams were equal).

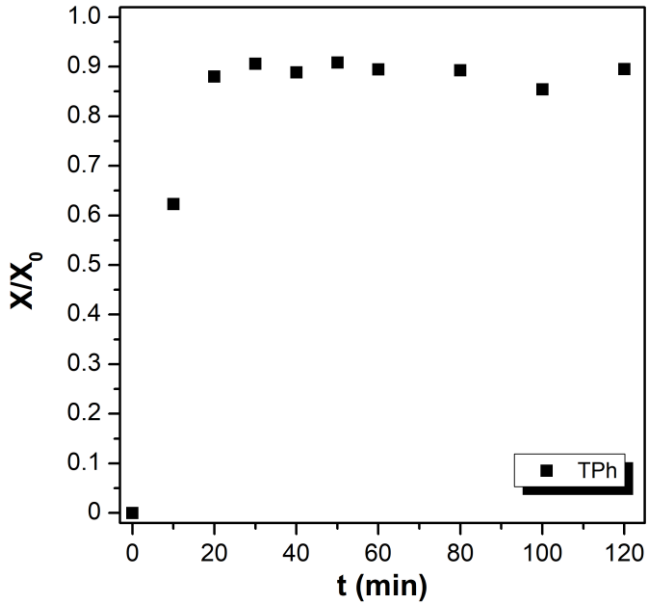


Fig. D.5 TPh concentration profile at the fixed-bed reactor outlet in a catalytic run performed with dissolved iron. $[H_2O_2]_{feed}$ = 0.75 g/L, $[Fe]_{feed}$ = 2.1 mg/L; Q = 0.75 mL/min, pH_0 = 3.5, T = 20 °C.

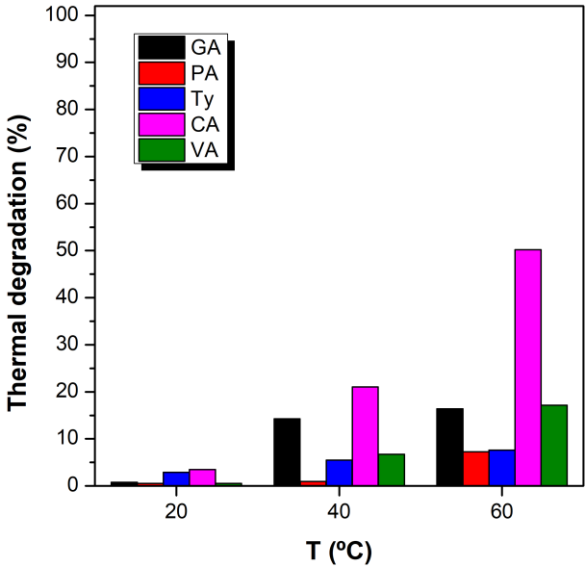


Fig. D.6 Thermal degradation (in %) promoted by different operating temperatures for each parent phenolic compound in solution after 6 h. Q = 0.75 mL/min, $[H_2O_2]_{feed}$ = 0.75 g/L, pH_0 = 3.5.

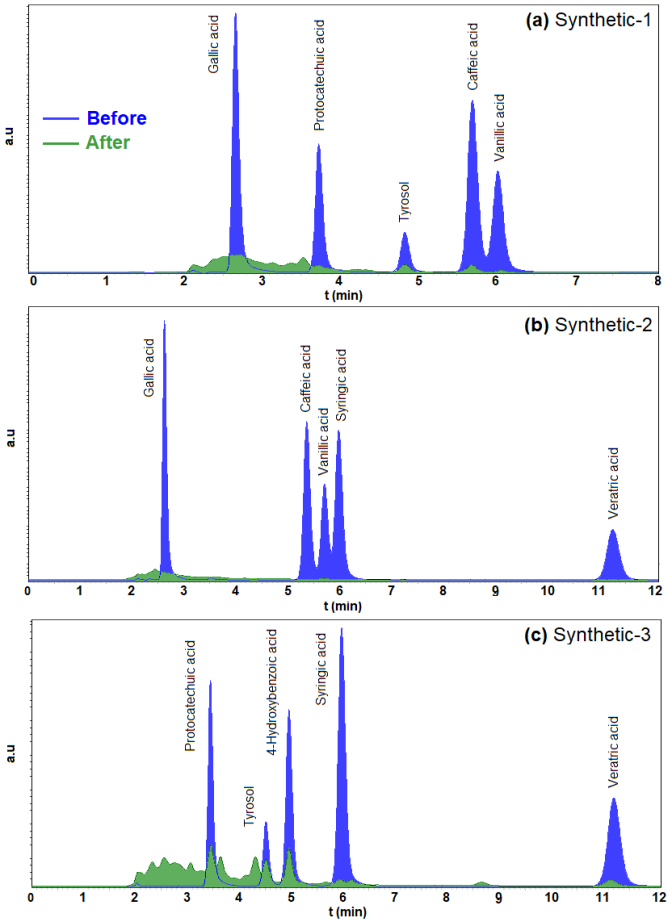


Fig. D.7 HPLC chromatograms of synthetic solutions before and after CWPO in the fixed-bed reactor. Q = 0.75 mL/min, $[H_2O_2]_{feed}$ = 1.50 g/L, pH_0 = 3.5, 60 °C.

Table D.1 Physicochemical characterization of the initial OMW samples used.

Parameter	**OMW-30×** *(COD_0 ≈ 0.6 g/L)*	**OMW-15×** *(COD_0 ≈ 1.2 g/L)*	**OMW-7.5×** *(COD_0 ≈ 2.4 g/L)*	**OMW-5×** *(COD_0 ≈ 3.6 g/L)*
COD (mg O_2/L)	594	1204	2382	3565
BOD_5 (mg O_2/L)	155	305	655	900
TPh_{FC} (mg GA_{eq}/L)	40	71	130	243
TOC (mg C/L)	191	384	783	1320
BOD_5/COD	0.26	0.25	0.27	0.25
AOS	-0.68	-0.74	-0.56	-0.05
V. fischeri inhibition (%)	19.2	33.3	44.4	52.4
pH	4.9	4.7	4.6	4.4

APPENDIX E

PUBLICATIONS AND SCIENTIFIC COMUNICATIONS

SCIENTIFIC PUBLICATIONS IN PEER-REVIEWED INTERNATIONAL SCIENTIFIC JOURNALS

1. **Esteves, B.M.**, Morales-Torres, S., Maldonado-Hódar, F.J., Madeira, L.M., *Sustainable iron-olive stone based-catalysts for Fenton-like olive mill wastewater treatment: development and performance assessment in continuous fixed-bed reactor operation*. Chemical Engineering Journal, 2022, 435, 134809. https://doi.org/10.1016/j.cej.2022.134809
2. **Esteves, B.M.**, Morales-Torres, S., Maldonado-Hódar, F.J., Madeira, L.M., *Specific adsorbents for the treatment of OMW phenolic compounds by activation of bio-residues from the olive oil industry*. Journal of Environmental Management, 2022, 306, 114490. https://doi.org/10.1016/j.jenvman.2022.114490
3. **Esteves, B.M.**, Morales-Torres, S., Maldonado-Hódar, F.J., Madeira, L.M., *Integration of olive stones in the production of Fe/AC-catalysts for the CWPO treatment of synthetic and real olive mill wastewater*. Chemical Engineering Journal, 2021, 411, 128451. https://doi.org/10.1016/j.cej.2021.128451
4. **Esteves, B.M.**, Morales-Torres, S., Maldonado-Hódar, F.J., Madeira, L.M., *Fitting biochars and activated carbons from the from residues of the olive oil industry as supports of Fe-catalysts for the heterogeneous Fenton-like treatment of simulated olive mill wastewater*. Nanomaterials, 2020, 10(5), 876. https://doi.org/10.3390/nano10050876
5. **Esteves, B.M.**, Rodrigues, C.S.D., Maldonado-Hódar, F.J., Madeira, L.M. *Treatment of high-strength olive mill wastewater by combined Fenton-like oxidation and coagulation/flocculation*. Journal of Environmental Chemical Engineering, 2019, 7(4), 103252. https://doi.org/10.1016/j.jece.2019.103252
6. **Esteves, B.M**., Rodrigues, C.S.D., Madeira, L.M. *Synthetic olive mill wastewater treatment by Fenton's process in batch and continuous reactors operation*. Environmental Science and Pollution Research, 2018, 25(35), 34826-34838. https://doi.org/10.1007/s11356-017-0532-y

Other peer-reviews scientific publications not included in this thesis

7. **Esteves, B.M.**, Rodrigues, C.S.D., Madeira, L.M. *Wastewater treatment by heterogeneous Fenton-like processes in continuous reactors*. In: Gil A., Galeano L., Vicente M. (eds) Applications of Advanced Oxidation Processes (AOPs) in Drinking Water

Treatment. The Handbook of Environmental Chemistry, 2019, vol. 67, 211-255, Springer. Cham.
https://doi.org/10.1007/698_2017_81

8. **Esteves, B.M.**, Rodrigues, C.S.D., Boaventura, R.A.R., Maldonado-Hódar, F.J., Madeira, L.M. *Coupling of acrylic dyeing wastewater treatment by heterogeneous Fenton oxidation in a continuous stirred tank reactor with biological degradation in a sequential batch reactor*. Journal of Environmental Management, 2016, 166, 193-203. https://doi.org/10.1016/j.jenvman.2015.10.008

ORAL COMMUNICATIONS IN SCIENTIFIC MEETINGS

1. **Esteves, B.M.**, Morales-Torres, S., Maldonado-Hódar, F.J., Madeira, L.M., *Enhanced Fenton-like degradation of phenolic contaminants by carbon-supported Fe-Mn catalysts prepared from olive stones*. 9th International Symposium on Carbon for Catalysis (CarboCat-IX), Spain, Zaragoza, 28-30 June 2022 (accepted for the 2020 edition; postponed due to the COVID-19 pandemic)
2. **Esteves, B.M.**, Morales-Torres, S., Maldonado-Hódar, F.J., Madeira, L.M., *Valorization of olive stone by-product as Fenton-like catalysts for olive mill wastewater treatment*, 17th International Conference on Environmental Science & Technology (CEST-21), Greece, Athens, 1-4 September 2021.
3. **Esteves, B.M.**, Morales-Torres, S., Maldonado-Hódar, F.J., Madeira, L.M., *Treatment of olive mill wastewater by integration of agroindustrial residues: a circular economy approach*, Proc. of the 4th Doctoral Congress in Engineering (DCE-21) - Symposium on Environmental Engineering, OC24, p. 90, Portugal, Porto, 28-29 June 2021.
4. **Esteves, B.M.**, Morales-Torres, S., Maldonado-Hódar, F.J., Madeira, L.M., *Treatment and valorization of olive mill's residues: integration of Fenton-like oxidation and membrane processes*. International School of Chemistry (web edition) "Chemistry for everyday life", Italy, University of Camerino, 1st September 2020.
5. Madeira, L.M., Rodrigues, C.S.D., **Esteves, B.M.**, *Use of Fenton-like processes for wastewater treatment: technological perspectives and integration with other technologies*. 4th International Conference on Photocatalytic and Advanced Oxidation Technologies for the Treatment of Water, Air, Soil and Surfaces (PAOT-4), Portugal, Porto, 10-13 July 2018.

Oral communications out of the scope of this thesis

6. Madeira, L.M., Lima, V.N., **Esteves, B.M.**, Rodrigues, C.S.D., *Fenton-based processes for effluents treatment: from conventional to innovative approaches.* Dia do Centro de Química de Vila Real – Universidade de Trás-os-Montes e Alto Douro (UTAD), 29th November 2019 (invited speaker).
7. **Esteves, B.M.**, Rodrigues, C.S.D., Boaventura, R.A.R., Maldonado-Hódar, F.J., Madeira, L.M., *Acrylic Textile Dyeing Wastewater Treatment by Combination of Heterogeneous Fenton's Oxidation in a CSTR and Biological Degradation in a SBR*, Proc. of the 4th European Conference on Environmental Applications of Advanced Oxidation Processes (EAAOP-4), B2-4, p. 138-140, Greece, Athens, 21-24 October 2015.

POSTER COMMUNICATIONS IN SCIENTIFIC MEETINGS

1. **Esteves, B.M.**, Morales-Torres, S., Maldonado-Hódar, F.J., Madeira, L.M., *Valorization of olive stones as Fe/AC-catalysts for the catalytic wet peroxide oxidation of phenolic effluents*. 9th International Symposium on Carbon for Catalysis (CarboCat-IX), Spain, Zaragoza, 28-30 June 2022 (accepted for the 2020 edition; postponed due to the COVID-19 pandemic)
2. **Esteves, B.M.**, Morales-Torres, S., Maldonado-Hódar, F.J., Madeira, L.M*., Development of Fe-olive stone-based catalysts for olive mill wastewater treatment in continuous fixed-bed reactor operation*. IV Simposio de La Unidad de Excelencia de Química Aplicada a Biomedicina y Medioambiente, Spain, Granada, 21th January 2022.
3. **Esteves, B.M.**, Morales-Torres, S., Maldonado-Hódar, F.J., Madeira, L.M*., Cheap Fenton catalysts for olive mill wastewater treatment*. III Simposio de La Unidad de Excelencia de Química Aplicada a Biomedicina y Medioambiente, Spain, Granada, 17th January 2020.
4. **Esteves, B.M.**, Rodrigues, C.S.D., Madeira, L.M., *Optimization of Fenton's process for olive mill wastewater treatment: from batch to continuous flow operation*, Proc. of the 5th European Conference on Environmental Applications of Advanced Oxidation Processes (EAAOP-5), P3-10, p. 298, Czech Republic, Prague, 25-29 June 2017.